Influence of Flow Characteristics on the Kinetics of Spherical Agglomeration: An Experimental and Computational Analysis

Victoria Rose Kitching

A thesis submitted in partial fulfilment of the requirements for the degree of
Doctor of Philosophy

The University of Sheffield
Faculty of Engineering
Department of Chemical and Biological Engineering

September 2023

Declaration of Authenticity

This thesis discusses the work conducted to obtain the degree of Doctor of Philosophy in the Department of Chemical and Biological Engineering at the University of Sheffield. The work within this thesis is my own original work, any exceptions to this are explicitly stated with the correct citation. No part of this work has been submitted for any other qualification or degree. I am aware of the University's Guidance on the Use of Unfair Means (www.sheffield.ac.uk/ssid/unfair-means).

Publications in Preparation

Kitching, V.R., Girard, K., Smith, R.M. Investigation into Particle Motion and Settling in Cascading MSMPRs

Kitching, V.R., Pitt, K., Ahmed, B., Litster, J.D., Smith, R.M. A CFD and Experimental Investigation of the Influence of Flow Characteristics on Spherical Agglomeration

Kitching, V.R., Ahmed, B., Pitt, K., Lian, G.J., Litster, J.D., Smith, R.M. Incorporating Impeller Characteristics into a Population Balance Model for Spherical Agglomeration: Methodology and Experimental Validation

Conference Proceedings

Kitching V.R., Ahmed, B., Pitt, K., Litster, J.D., Smith, R.M. Effectiveness of Predicting Spherical Agglomerate Properties Using a Population Balance Model. In 10th International Granulation Workshop 2023 (Poster Presentation)

Kitching V.R., Pitt, K., Ahmed, B., Litster, J.D., Smith, R.M. Influence of Impeller Geometry on the Formation of Spherical Agglomerates. In Particle Agglomeration and Granulation Processes. In 2022 AIChE Annual Meeting (Oral Presentation)

Further details of publication and conference proceedings can be found in Appendix E.

Acknowledgements

My deepest gratitude goes to Professor Rachel Smith and Professor Jim Litster, not only for the opportunity to join the Particle Technology Group, but for their support and advice during my studies. Your help and suggestions were instrumental in shaping my research and I would not be in this position without your guidance. Whilst the journey of my PhD has been challenging on occasion, it has also been extremely rewarding and I have thoroughly enjoyed my time at Sheffield.

I am also extremely grateful to Dr Kevin Girard and the rest of the FAST Group at Pfizer for being so welcoming and encouraging during my industrial placement. It was an incredible opportunity that I feel very lucky to have had.

The support of Dr Kate Pitt has been extremely helpful throughout my studies. I am very thankful to her for the advice and guidance that she has given me. Her incredible proof reading skills have helped me to improve the quality of my writing and her kindness has helped me through my PhD more than she will know.

I would like to thank the Particle Technology Group, past and present, for the incredible research environment that I have enjoyed being a part of. A special thanks to Guo J. Lian for allowing me to use some of the results from his MEng Research Project in my thesis. I would also like to express my gratitude to Dr Neeru Bala and Suruthi Gnanenthiran for their help with proofreading my thesis and their constructive feedback that has improved the quality of my work.

The expertise of Dr Stefan Bellinghausen, Dr Bilal Ahmed and Dr Omid Arjmandi-Tash has been invaluable in developing the population balance model. Their advice and assistance has helped me greatly, and I am very thankful for their assistance over the years.

I would also like to thank the CMAC team at the University of Strathclyde for the incredible opportunities that being a part of CMAC have facilitated. Throughout my PhD, being a CMAC funded student has allowed me an insight into the pharmaceutical industry, and I am so grateful to them for facilitating my industrial placement.

Thank you so much to my wonderful friends and family. To Georgia and Hannah, thank you for being there from the very beginning. I am so lucky to have been on this journey with two people as caring and understanding as the two of you! A special thanks to my friends Lucy, Beth, Bhumika, Marya, Laurel, and Kirsty for being there for me through the highs and lows. Thank you to my Uncle Mick and Auntie Lesley for always being wonderful, supportive godparents. To my family, James, Lauren, and Jess, thank you for putting me up with me every step of the way, with a special thanks to Poppy for being the most wonderful niece! Last, but definitely not least, thank you so much to my parents, for all of your help throughout not only the last four years, but for everything you have done for me.

Abstract

The spherical agglomeration process is gaining increasing interest in the pharmaceutical industry as it has the ability to transform needle-like crystals into dense agglomerates that are spherical in shape. The formed agglomerates have improved micromeritic properties, improving the ease of handling and reducing the number of downstream processing steps. Spherical agglomerates are formed by suspending particles in a solvent and adding an antisolvent to induce crystallisation. An immiscible bridging liquid is then added to the crystal suspension to form spherical agglomerates.

As the success of spherical agglomeration is determined by the composition of the solvent system, this has been the subject of the majority of spherical agglomeration research. However, there is limited consistency in the apparatus used for the various investigations. Spherical agglomeration is a process that occurs in suspension; therefore, the mixing profile will affect the contact between the bridging liquid and particles. In a stirred tank, the impeller conditions are the main factor that influences flow and mixing. This work studied the influence of flow characteristics and mixing on the formation of spherical agglomerates. For this investigation, experiments were performed with different impeller geometries, speeds and clearances. A computational fluid dynamics (CFD) study with corresponding impeller characteristics was also produced.

This work demonstrates that the impeller geometry, clearance, and speed have an enormous influence on the particle size distribution and sphericity of agglomerates formed. The CFD study demonstrates that the impeller clearance influences the flow profile and the mixing between the particles and the bridging liquid. For increased impeller clearances, the circulation loop induced by the impeller covers a greater portion of the liquid height for the pitched blade and propeller impellers. As the flow in the tank greatly influences agglomerate characteristics, it is crucial that the impeller geometry and clearance are accurately included in a population balance model (PBM) for spherical agglomeration.

A PBM has previously been developed by Ahmed et al., 2023 which incorporated the various nucleation mechanisms to predict agglomerate size. Whilst this model did consider impeller diameter and speed, it did not include impeller geometry and clearance. In this work, the PBM by Ahmed et al., 2023 was modified to include different impeller geometries and clearances due to the CFD and experimental study showing that these parameters influence spherical agglomeration. To incorporate impeller geometry, the impeller power number was used as the experimental study observed a clear correlation between power number and agglomerate characteristics. It was found that increased power number produced agglomerates that were more consistent in size and sphericity. The velocity magnitude from the CFD simulations was used in the PBM to include the influence of impeller clearance.

The PBM that was developed as part of this work was experimentally validated using an agglomeration in suspension process in which poly(methylmethacrylate) beads were suspended in water, and a bridging liquid was added. As part of the experimental validation, various process parameters, including impeller geometry, impeller clearance, bridging liquid to solid ratio (BSR) and agglomeration time, were altered. In a comparison of the PBM developed in this work, the PBM by Ahmed et al., 2023 and the experimental data, it was found that the PBM developed in this thesis, predicted a d_{43} value closer to the experimental results than the model by Ahmed et al., 2023 for 56.4 % of the simulations. This is a minimal improvement to the previous model. The predictions for axial impellers were inaccurate, but this PBM was effective at predicting the d_{43} for agglomerates produced with a Rushton turbine impeller, which was the best performing impeller experimentally.

Table of Contents

Table of Figures

Table of Tables

xxi

Nomenclature

Symbol	Description	Units
$\mathbf{A}$	Dip tube surface area	m^2
$\dot{\mathbf{A}}$	Area flux of powder	m^2/s
$\mathbf{b}$	Impeller blade height	M
$\dot{\mathbf{b}}_{\mathbf{a,nuc}}(\mathbf{x},\mathbf{t})$	Birth of nuclei of size x at time t	
$\dot{\mathbf{b}}(\mathbf{x})$	Frequency distribution of birth of particles of size x	m^{-4}/s
$\mathbf{C}$	Impeller clearance	M
$\mathbf{C_{coll}}$	Kinetic parameter found through agglomeration	-
$\mathbf{C_{growth}}$	Growth coefficient	-
$\mathbf{c_i}$	Bridging liquid composition in particle size i	-
$\mathbf{c_j}$	Bridging liquid composition in particle size j	-
$\mathbf{C_L}$	Power number calculation parameter	-
$\mathbf{C_{opt}}$	Optimal bridging liquid composition	-
$\mathbf{c_p}$	Solids concentration	mol/m^3
$\mathbf{C_t}$	Power number calculation parameter	-
$\mathbf{C_{tr}}$	Power number calculation parameter	-
$\mathbf{d}$	Impeller diameter	M
$\mathbf{D}$	Vessel diameter	M
$\dot{\mathbf{d}}(\mathbf{x})$	Frequency distribution of death of particles of size x	m^{-4}/s
$\mathbf{d_{10}}$	Particle size that 10 % of particles are below	m
$\mathbf{d_{43}}$	Mean particle size of distribution	m
$\mathbf{d_{50}}$	Particle size that 50 % of particles are below	m
$\mathbf{d_{90}}$	Particle size that 90 % of particles are below	m
$\mathbf{d_d}$	Diameter of droplets	m
$\mathbf{def^{max}}$	Radius of the contact surface	m
$\mathbf{d_p}$	Particle diameter	m
$\mathbf{D_p}$	Primary particle diameter	m
$\mathbf{eff(i,j,t)}$	Efficiency of agglomeration	-
$\mathbf{f}$	Friction factor	-
$\mathbf{f{\sim}}$	Approximate friction factor	-
$\mathbf{f(i,j,t)}$	Meeting probability of agglomerates	-
$\mathbf{f_{adh}}$	Adhesive force between agglomerates	N
$\mathbf{F_{bridge}}$	Binging force at point of contact between two agglomerates	N
$\mathbf{f_{mi}}$	Mass frequency of particles of size i	m^{-1}
$\mathbf{f_{sep}}$	Disruptive force between agglomerates	N
$\mathbf{g}$	Constant of acceleration due to gravity	m/s
$\mathbf{G}$	Growth of particles	-
$\mathbf{H}$	Liquid height	m
$\mathbf{H}$	Vessel height	m
$\mathbf{h_B}$	Length of the baffles	m

I_{js}	Just suspended impeller tip speed	m/s
k	Turbulent kinetic energy	-
$k(i, j, t)$	Agglomeration kernel	-
L	Agglomerate particle size	m
L	Liquid height	m
L_i	Agglomerates of size i	m
$L_{in,p}$	Bridging liquid volumetric flowrate	m^3/s
L_j	Agglomerates of size j	m
m	Power number calculation parameter	-
m_{BL}	Bridging liquid mass	kg
m_i	Mass of powder in size interval i	kg
m_p	Mass of particles	kg
m_{si}	Mass of empty sieve of size i	kg
m_{spi}	Mass of sieve and powder for sieve size i	kg
m_t	Total system mass	m
N	Impeller rotation speed	rps
$n(x, t)$	Number of particles of size x at time t	-
n_B	Number of Baffles	-
$n_d(x, t)$	Bridging liquid number density	no/m^4
n_{ex}	Number of particles of size x exiting the system	m-4
N_i	Agglomerate particle concentration	nb/m^3
n_{in}	Number of particles of size x into the system	m^{-4}
N_{js}	Critical impeller speed for particle suspension	rps
N_p	Impeller power number	-
n_p	Number of impeller blades	-
N_{P0}	Unbaffled power number	-
N_{Pmax}	Fully baffled power number	-
P	Impeller power requirements	W
$P(t)$	Agglometate porosity	-
Q	Flowrate	m^3/s
$\dot{Q}_{ex}$	Volumetric flowrate out of the system	m^3/s
$\dot{Q}_{in}$	Volumetric flowrate into system	m^3/s
R_A	Rate distribution for agglomeration	$m^{-4} s^{-1}$
r_{agg}	Agglomeration rate	$nb \ m^{-3} \ m^{-1}$
Re_d	Impeller reynolds number	-
Re_G	Modified reynolds number	-
R_{pore}	Pore radius	m
S	Zwietering constant	-
S_i	Agglomerate size i	m
S_j	Agglomerate size j	m
T	Tank diameter	m
u	Velocity of particle collision	m/s

$\mathbf{u(D_d)}$	Relative velocity of the bridging liquid droplets and the mother solution	m/s
$\mathbf{u(D_p)}$	Relative velocity of the particles and mother solution	m/s
$\overline{\mathbf{(u')}}$	Fluctuating turbulent velocity in u direction	m/s
$\mathbf{v}$	Kinematic viscosity	m²/s
$\mathbf{V}$	Suspension volume	m³
$\mathbf{v}$	Velocity	m/s
$\overrightarrow{\mathbf{v_q}}$	Velocity vector for phase q	-
$\mathbf{V_0}$	Volume of liquid droplet	m³
$\mathbf{V_{BL}}$	Bridging liquid volume	m³
$\mathbf{\dot{V}}$	Volumetric spray rate	m³/s
$\mathbf{\dot{V}}$	Volume of formed nuclei	m³
$\mathbf{W}$	Impeller blade width	m
$\mathbf{X}$	Solid loading in the system	-
$\mathbf{x}$	Particle diameter	m
$\mathbf{x}$	Agglomerate diameter	m
$\mathbf{X}$	Power number calculation parameter	-
$\mathbf{x}$	Power number calculation parameter	-
$\overline{\mathbf{x_{43}}}$	Mean particle size of distribution	m
$\overline{\mathbf{x_i}}$	Average of size interval i and $i+1$	m
$\mathbf{y_{mi}}$	Mass fraction of particles of size i	-

Greek Letter	Description	Units
α	Volume fraction	-
α	Liquid droplet weight coefficient	-
$\alpha(i, j, t)$	Target agglomeration efficiency	-
β	Agglomeration rate	-
β	Power number calculation parameter	-
β_0	Agglomeration rate constant	-
γ	Surface tension	N.m
γ	Interfacial tension of bridging liquid and mother solution	N.m
γ	Power number calculation parameter	-
δ	Solid particle weight coefficient	-
Δx_i	Difference between size interval i and $i + 1$	m
ε	Turbulent dissipation	-
ε	Porosity of powder bed	-
η	Power number calculation parameter	-
θ	Impeller blade pitch	°
θ	Contact angle	°
θ_d	Dynamic liquid contact angle	radians
μ	Viscosity	Pa.s
π	Pi	-
ρ	Density	kg/ m^3
τ_p	Drop penetration time	s
φ	Number density function	nb/ ms^3
φ_{cp}	Critical-packing liquid volume fraction	-
φ_{Pb}	Volume fraction of crystals in the mother solution	-
Ψ	Particle sphericity	-
Ψ_a	Dimensionless spray flux	-

Chapter 1 Introduction

Spherical agglomeration is a particle size enlargement process, in which a bridging liquid is added to suspended particles to generate agglomerates (Pitt et al., 2018). This process is generating increasing interest in the pharmaceutical industry, due to the potential to improve micromeritic and powder handling properties of drug particles for tableting (Orlewski et al., 2018). Limited understanding of the mechanisms of agglomerate production and process optimisation are hindering industrial uptake. Most spherical agglomeration studies are in small bench-top scale vessels, ranging from 100 mL to 1 L, and limited scale-up data is available.

There are two primary methods of spherical agglomerate production relevant to pharmaceutical manufacturing, differentiated by the starting solvent system. The first method, antisolvent spherical agglomeration, starts with a typical antisolvent crystallisation process, in which the drug is dissolved in a good solvent, and an antisolvent (or poor solvent) is added to precipitate crystals. Once the crystals have formed, a bridging liquid is added causing the crystals to agglomerate (Zhang et al., 2010). The second method, termed agglomeration in suspension, starts with crystals suspended in a solvent. Bridging liquid is added to induce agglomeration. For both methods, the resultant agglomerates are generally spherical in shape and can often undergo direct tableting due to improved compression characteristics (Saini et al., 2013).

Many parameters are known to influence spherical agglomeration such as the agitation speed, temperature, and bridging liquid to solid ratio. A small number of parametric studies are available in the literature, however these are typically restricted to specific solvent/powder systems and provide little understanding of the mechanisms and kinetics of formation, growth and breakage. Understanding these mechanisms is key to engineering process and product design,

A critical literature review has been conducted to understand the mechanisms and kinetics of spherical agglomeration processes, and to identify gaps in the knowledge. The rate process controlling the spherical agglomeration processes are in fact very similar to the regimes and mechanisms involved in high shear wet granulation and, therefore, there are opportunities to apply our relatively advanced understanding of wet granulation to spherical agglomeration.

There have been limited attempts to model the process of spherical agglomeration. Blandin et al, 2005 proposed a population balance model (PBM) incorporating an agglomeration kernel to describe the growth of agglomerates. Arjmandi-Tash et al, 2019 proposed a mechanistic nucleation/layering model, later incorporated into PBM in the work of Ahmed et al., 2023.

As in all agglomeration kernels, the particle meeting probability is an important factor for spherical agglomeration. Hydrodynamics are stated as the major factor influencing the probability of particles meeting (Blandin et al., 2005). In the case of spherical agglomerate, hydrodynamics are influenced by the mixing action between the components in the fluid system and the particles. The Zwietering correlation proposed in 1958 proposed that the impeller speed needed for particles in a system to be fully suspended was dependent on material properties, the impeller diameter and the Zwietering constant which is to be determined experimentally. Further studies have investigated the Zwietering constant and a study by Devarajulu and Loganathan in 2016 determined that the Zwietering constant varies with impeller geometry, impeller clearance, liquid height and vessel diameter. Despite the crucial role flow and mixing play in agglomerate production, this research avenue has been largely neglected. This represents a conspicuous gap in spherical agglomeration research and will be addressed in this work.

1.1 Aim

The aim of this research is to enable improved design of spherical agglomeration processes, by developing a novel, predictive, population balance model. Critically, this population balance model will incorporate the flow and mixing characteristics in spherical agglomeration vessels, to predict resulting particle attributes.

1.2 Objectives

To achieve the aim, various objectives will be met:

1. An experimental study to identify the effect of stirred tank geometries and operating conditions on particle attributes
2. A corresponding computational fluid dynamics (CFD) study of the influence of impeller and internal geometry of stirred tank reactors (STRs) on flow characteristics
3. Construct a robust population balance model (PBM) for spherical agglomeration that incorporates the influence of flow characteristics. This will be informed by CFD and experiment observation
4. Experimentally verify, validate and evaluate the PBM

1.3 Overall Thesis Outline

A comprehensive analysis of the spherical agglomeration literature will be presented in Chapter 2. This chapter utilises the parametric studies for spherical agglomeration to determine the influence of operating conditions on agglomerate characteristics. An assessment of the current understanding of spherical agglomeration mechanisms, and how they have been modelled is also included in this chapter. As mixing behaviour is a focus for this research, there has been an evaluation of CFD software to determine their applicability for spherical agglomeration CFD simulations. Discussions of CFD simulations for suspensions, slurries, and high shear wet granulation processes are also presented in Chapter 2. Slurries and suspensions were considered due to spherical agglomeration occurring in a dilute solvent system. Research into high shear wet granulation (HSWG) was conducted due to spherical agglomeration being mechanistically similar to HSWG. Research avenues were identified based on gaps in the literature, these are also presented in Chapter 2.

Chapter 3 presents the experimental and CFD methodology used for this research. This thesis contains two experimental stages; the first is to identify the influence of stirred tank geometry on spherical agglomerates, and the second is to experimentally validate the produced PBM. Chapter 3 details the material system and changes to the stirred tank geometry that were made during this investigation. The material systems and reactor geometries tested for the PBM validation are discussed in Chapter 3. The methods used to analyse the produced spherical agglomerates for both experimental studies are also presented in this chapter. A parametric CFD study was conducted in ANSYS Fluent to investigate the influence on stirred tank geometry on flow patterns and mixing characteristics. Construction of the CFD study is discussed in this chapter alongside development of a PBM for spherical agglomeration. Flow characteristics that were determined using the CFD studies were incorporated into the PBM.

The results of the parametric experimental investigation into the influence of impeller geometry, speed and clearance are shown in Chapter 4. This chapter presents the particle size distribution (PSD) of the spherical agglomerates, as well as agglomerate images to determine the effectiveness of different impeller geometries.

Chapter 5 presents the results of the CFD simulations that correspond to the experimental study presented in Chapter 4. The velocity profiles in the tank with different impeller configurations is shown

and the influence of impeller geometry, speed and clearance on the flow profiles is analysed. Chapter 5 also discusses the link between the flow pattern and spherical agglomeration.

In Chapter 6, the methodology used to incorporate the impeller geometry and clearance into the PBM is discussed. This chapter details the adaptations to key equations of the existing spherical agglomeration PBM by Ahmed et al., 2023, based on the findings of the parametric experimental and CFD study presented in Chapter 4 and Chapter 5.

Validation of the PBM is key to ensuring that it is applicable to spherical agglomeration. Chapter 7 contains a comparison of validation experiments with results produced by the PBM. The experimental results will also be compared to the PBM by Ahmed et al., 2023 to determine whether the produced model is an improvement on previous iterations of a spherical agglomeration PBM.

A four month industrial placement at Pfizer was undertaken over the course of this PhD project, and is discussed in Chapter 8. Whilst this research does not pertain to spherical agglomeration, it draws upon understanding gained in Chapter 5. CFD simulations of a crystallisation process were developed to investigate how changing reactor geometry influences particle motion and settling in a series of mixed suspension-mixed product removal (MSMPR) crystallisers.

Figure 1-1 shows the thesis results chapters and how they link together. A major component of this research is the CFD simulations and experimental investigation into how impeller geometry influences agglomerate formation. These results are used to influence the generation of the PBM as previous iterations by Ahmed et al., 2023 did not incorporate the impeller geometry or the flow pattern in the tank. The developed model has been experimentally validated, ensuring that incorporation of flow pattern improves model prediction. This will be performed by comparing the experimental results with the base model and the results generated from the model that incorporates flow. The outcomes from the CFD results in Chapter 5 were useful in determining investigation parameters for the CFD in Chapter 8.
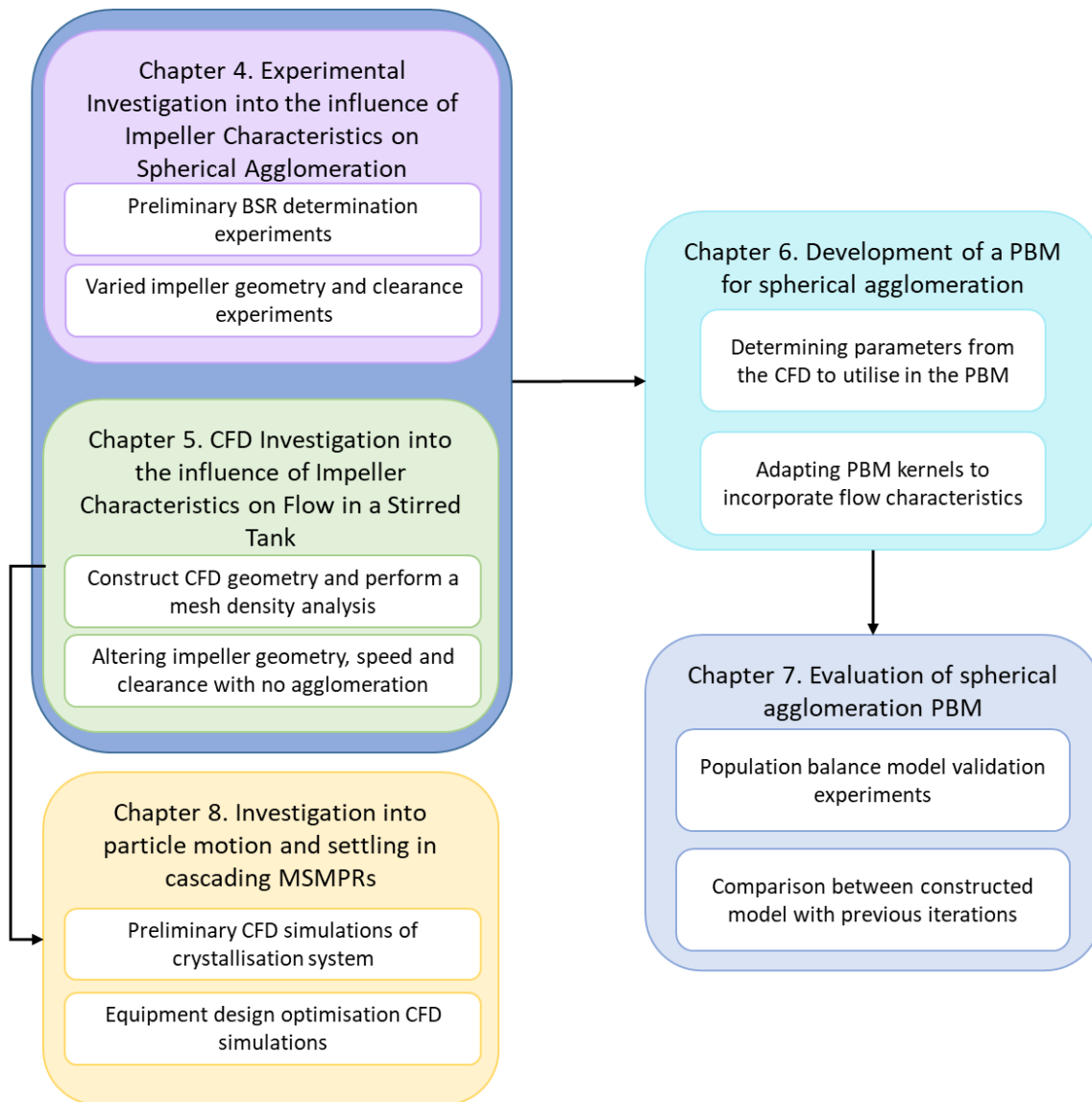
Figure 1-1 Diagram explaining the content of the thesis results chapters and how they link together

1.4 Key Contributions of this Work

The aim of this work was to generate a predictive population balance model for spherical agglomeration that considers the influence of reactor geometry on the flow characteristics in a stirred tank. To do this both experimental and computational analysis of mixing in stirred tank with different impeller geometries, speeds and clearances was conducted. The key contributions from this thesis are:

- Determining that increased impeller power number increases the consistency in the shape and size of spherical agglomerates
- Further confirmation of the importance of clearance when using a Rushton turbine impeller due to the transition between axial and radial flow at clearance to vessel diameter ratios > 0.3
- Incorporating the impeller power number for different impeller geometries into a population balance model for spherical agglomeration
- Using experimental validation to suggest further development areas to increase the accuracy of population balance models for spherical agglomeration

Chapter 2 Literature Review

2.1 Overview of the Spherical Agglomeration Process

The pharmaceutical industry has shown increasing interest in spherical agglomeration in recent years, although it is not currently used for industrial pharmaceutical manufacture. Spherical agglomeration is a promising particle size enlargement technique for pharmaceutical manufacture, due to the products of this technique being spherical particles with improved micrometric properties (Orlewski et al., 2018). It is desirable to improve micrometric properties, such as sphericity, as this can improve the ease of handling of the particles, as they will have improved flowability. Spherical agglomeration also influences porosity, meaning direct tabletting of the spherical agglomerates is possible; reducing the need for further processing which in turn minimises production costs (Saini et al., 2013). The ability to be directly tabletted makes this process extremely attractive to the pharmaceutical industry as oral solid dosage forms are the most common form of administration to patients (Krishna et al., 2012) with 70% of all pharmaceutical products being in solid form (Peña and Nagy, 2015).

Spherical agglomeration is a technique which is one of three types of spherical crystallisation. Section 2.2 discusses spherical crystallisation in more detail. The process of spherical agglomeration begins with an antisolvent crystallisation, then a bridging liquid is added to induce agglomeration. As this process occurs in a ternary mixture, the selection of the liquids is extremely important for the process to work effectively and can be a difficult and time-consuming process (Javadzedah et al., 2016). The three components of the ternary mixture have different purposes in the facilitation of spherical agglomeration. Primary particles of a pharmaceutical compound dissolve in the solvent. The antisolvent induces the precipitation of the pharmaceutical compound, and the bridging liquid acts as a binder and causes bridges to form between the particles of the pharmaceutical compound (H. Zhang et al., 2010b).

Spherical agglomerates can also be manufactured through a process called agglomeration in suspension. In this process, already formed crystals are suspended in a solvent, and then the bridging liquid is added to induce agglomeration. Agglomeration in suspension technique may be used due to it being less complex than conventional spherical agglomeration which has a ternary liquid system.
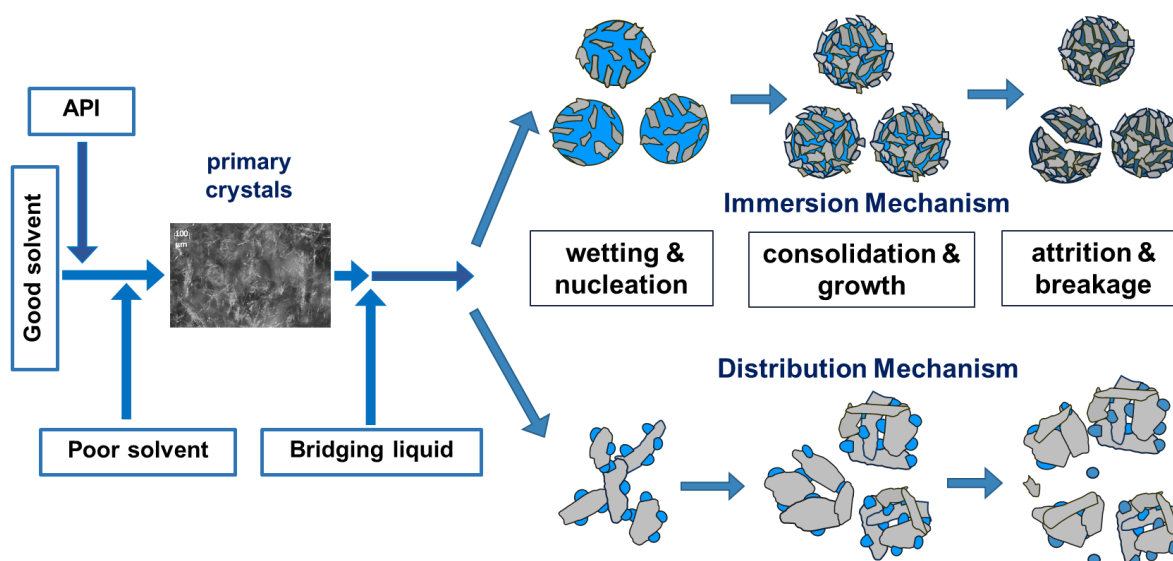
Figure 2-1 Schematic of the spherical agglomeration process, including the different nucleation mechanisms, image from (Arjmandi-Tash et al., 2019)

Figure 2-1 shows a schematic of the spherical agglomeration process, including the different mechanisms of nucleation. In the nucleation regime, the bridging liquid initially wets the powder particles. When the bridging liquid contacts the powder, nuclei form (Maghsoodi et al., 2012; Pitt et al., 2018; Arjmandi-Tash et al., 2019). The formation of spherical agglomerate nuclei can happen in two different ways. The mechanism of nucleation depends on the size of the liquid droplets in relation to the suspended primary particle size. If the particles are larger than the liquid droplets, nucleation occurs through the distribution mechanism (Pitt et al., 2018; Arjmandi-Tash et al., 2019). In the distribution mechanism, the bridging liquid coats the powder particles. The coated particles aggregate together to form the nuclei (Arjmandi-Tash et al., 2019). Alternatively, the droplets of the bridging liquid being larger than the powder particles will result in immersion nucleation occurring (Pitt et al., 2018; Arjmandi-Tash et al., 2019). In immersion nucleation, the powder particles penetrate the liquid droplet to form a nucleus within the droplet (Arjmandi-Tash et al., 2019).

Once the nuclei form, the agglomerates undergo consolidation and growth; consolidation causes the bridging liquid to be squeezed out of the nuclei on to the surface and the particles with wet surfaces undergo collisions; allowing coalescence to occur (Bharti et al., 2013; Pitt et al., 2018). The agitation rate determines the rate of squeezing out the liquid as it influences the collision rate.

Some agglomerates may decrease in size due to breakage or attrition. Although attrition and breakage can occur, it will not reduce the average particle size, as the system will have reached an equilibrium between the increase and decrease of particle size (Bemer, 1979; Bharti et al., 2013; Javadzedah et al., 2016; Pitt et al., 2018).

In a spherical agglomeration study of glass beads suspended in carbon tetrachloride, with a water-glycerol mix as the bridging liquid, Bemer proposed that there were four regimes in spherical agglomeration. The four regimes are the flocculation regime, the zero growth regime, the fast growth regime, and the equilibrium regime (Bemer, 1979; Pitt et al., 2018). The equilibrium regime is sometimes referred to as the constant size regime (Bharti et al., 2013).

The flocculation regime occurs when particles contact the bridging liquid and form loose flocs. The zero growth regime follows the flocculation regime. In the zero growth regime, there is limited bridging available due to flocculation formation, resulting in a constant mean particle size. As spherical agglomeration is very system dependent, the zero growth regime will also vary for each system. Due to the lack of bridging liquid, the zero growth regime is considered the rate limiting step (Bharti et al., 2013; Javadzedah et al., 2016). The fast growth regime comes after the zero growth regime. Fast growth occurs due to consolidation and coalescence of the loose flocs, forming tightly packed agglomerates. This process reaches an equilibrium and the mean size either will remain constant or decrease slightly as there may still be consolidation occurring in the system (Bemer, 1979; Pitt et al., 2018).

2.2 Spherical Crystallisation

Spherical agglomeration is a method in which spherical crystallisation can be achieved and as such, the terms are sometimes used interchangeably. Spherical crystallisation can occur through both typical and non-typical crystallisation techniques. Typical spherical crystallisation techniques involve three solvents which induce crystallisation and agglomeration. Typical spherical crystallisation processes are discussed in Section 2.2.1. The non-typical crystallisation techniques, discussed in Section 2.2.2 generate spherical crystals by controlling physical and chemical properties of the system. Section 2.2.3 analyses the different spherical crystallisation techniques and justifies spherical agglomeration being the spherical crystallisation technique used for this work.

2.2.1 Typical Crystallisation

Typical crystallisation methods for spherical crystallisation are considered a solvent change method of crystallisation, and in these methods either a binary or ternary solvent system is used to induce agglomeration (Krishna et al., 2012). The process of spherical agglomeration has been discussed in Section 2.1 Sections 2.1.1.1 to 2.1.1.4 discuss the other typical spherical crystallisation processes.

2.1.1.1 Quasi-emulsion Solvent Diffusion (QESD)

This technique occurs in a system that contains a good solvent and antisolvent. The good solvent will have a higher affinity for the primary particles than the poor solvent. When the solution of the good solvent and particles are dispersed in the bridging liquid, quasi emulsion droplets are formed. The interfacial tension between the good solvent and poor solvent results in the good solvent diffusing from the emulsion droplets into the poor solvent. Counter diffusion of the poor solvent and good solvent results in crystal formation. A polymer additive as added to the system to stabilise the emulsion (Chadwick et al., 2009; Krishna et al., 2012; Keshwani et al., 2015; Javadzedah et al., 2016; Pitt et al., 2018).

It is difficult to design a QESD process as finding an additive that will keep the system emulsified and improve diffusion of the poor solvent into the solution of the good solvent and the particles is very difficult (Keshwani et al., 2015).

2.1.1.2 Ammonia Diffusion

The ammonia diffusion method is only suitable for amphoteric particles, which are only soluble in alkaline or acidic solutions and not conventional organic, neutral solvents. In the ammonia diffusion method, ammonia will act as the bridging liquid and the good solvent. Poor solvent selection considers the solubility of the drug in the poor solvent and how miscible the poor solvent is with both water and ammonia (Puechagut et al., 1998; Krishna et al., 2012; Keshwani et al., 2015; Javadzedah et al., 2016).

There are three mechanistic steps of ammonia diffusion. In the first stage, the poor solvent enters the ammonia-water solution leading to precipitation of the particles. Whilst this is occurring, the ammonia will diffuse into the organic phase. Diffusion of the ammonia into the organic phase reduces the ability of ammonia to act as a bridging liquid, and this prevents further agglomeration occurring, limiting the agglomerate size.

2.1.1.3 Crystallo-co-agglomeration (CCA)

CCA was developed to allow for the crystallisation and agglomeration of API particles with excipients or another API. In this method, a good solvent is used to dissolve the API and the antisolvent is added to induce crystallisation. An immiscible bridging liquid is then added to form liquid bridges and agglomerate the material. The selection of the solvent system for CCA is very difficult as the solvents selected need to be appropriate for the API and the excipients (Keshwani et al., 2015; Javadzedah et al., 2016).

2.1.1.4 Neutralisation Technique

The neutralisation technique is similar to spherical agglomeration in that bridging liquid is added to formed crystals to induce agglomeration. However, the crystals are formed by dissolving the API in an alkaline solution and adding this to an acidic solution that contains the bridging liquids and any polymers that may also be added (Chuahan et al., 2012; Krishna et al., 2012; Keshwani et al., 2015; Pitt et al., 2018).

2.2.2 Non-Typical Crystallisation

Non-typical crystallisations occur by changing the physical or chemical properties of the mixture to induce crystallisation, and a bridging liquid is then added (Keshwani et al., 2015). Some examples of these crystallisations are given in the following sections:

2.1.1.5 Salting Out Spherical Crystallisation

In 1983, Kawashimi et al. produced spherical agglomerates of sodium theophylline monohydrate using the salting out method. In this work, ethylenediamine solutions of theophylline and sodium chloride were added to a mixture of ethanol and chloroform. At increased concentrations of chloroform, the diameter of the agglomerates increased (Kawashima et al., 1983).

2.1.1.6 Cooling Crystallisation Spherical Agglomeration

In a study by Guo et al., 2022, a cooling crystallisation spherical agglomeration process was used to generate spherical agglomerates of benzoic acid. The benzoic acid particles was dissolved in water at 353.15 K which was then cooled to 293.15 K to form benzoic acid crystals. Oleic acid was added as the bridging liquid to the suspension of benzoic acid crystals with a small amount of sodium dodecyl sulphate being added as a surfactant. These agglomerates had a narrower particle size distribution than conventionally formed spherical agglomerates (Guo et al., 2022).

2.1.1.7 Melt Spherical Crystallisation

Teipel et al., 2000 produced spherical crystals of ammonium dinitramide (AND) using melt crystallisation. The ADN was melted into a liquid which was then added to heated paraffin oil, forming spherical droplets. The mixture was then cooled to allow the spherical droplets to solidify into spherical crystals of ADN. These crystals ranged from 10-600 μm in size (Teipel et al., 2000; Liao et al., 2023).

2.2.3 Analysis of Spherical Crystallisation Techniques

Spherical crystallisation techniques can be used to produce agglomerates for API with poor solubility and has the added benefit of improving micromeritic properties such as flowability and compaction. The different methods of spherical crystallisation all have their advantages and disadvantages, however, this work focusses on spherical agglomeration due to this method having a wider range of applicable solvents (Krishna et al., 2012). As spherical agglomeration can be used with a larger variety of solvent systems, it gives interesting research avenues. The wide range of appropriate solvents also increases the likelihood of it being used industrially as more environmentally friendly solvents may be applicable. Section 2.7 discusses the sustainability of the spherical agglomeration process.

2.3 Ternary System Selection

As previously mentioned, the most common method for spherical agglomeration involves precipitation and agglomeration from a ternary system. The ternary system consists of the solvent, antisolvent and bridging liquid. Choosing the correct solvent and antisolvent is important as they dissolve and precipitate the solid crystals, which are then wetted by the bridging liquid to form nuclei. Solubility studies ensure that the optimal solvent and antisolvent are used. The choice of bridging liquid is also important as it influences the strength of the formed agglomerates (Chuahan et al., 2012). As the bridging liquid needs to wet the particles to induce agglomeration, it is important to accurately measure and understand the system wettability. Section 2.3.2 discusses various methods to study the bridging liquid to powder wettability.

There are general guidelines for the selection of the components of the ternary system, which depend on the pharmaceutical compound that undergoes spherical agglomeration. The guidelines, proposed by (Saini et al., 2013), depend on which group (1-4) the compound falls into:

- Group 1 - If the compound is soluble in water, then a water immiscible organic solvent is the antisolvent with high concentration salt solution being the bridging liquid.
- Group 2 - If the active pharmaceutical ingredient (API) is soluble in organic solvents, then water is the antisolvent. The bridging liquid is an organic solvent that is immiscible in water.
- Group 3 - Some compounds are only soluble in organic solvents that are miscible in water. For these compounds, a saturated aqueous solution of the compound is used as the antisolvent with a mixture of organic solvents being used as the bridging liquid.
- Group 4 - If the compound is insoluble in water and organic solvents, then an organic solvent that is immiscible in water is chosen as the antisolvent with a 20% calcium chloride solution being used as the bridging liquid. The mixture will also need to contain a binding agent such as polyethylene glycol (PEG) to allow agglomeration to occur.

The guidelines proposed by Saini et al., 2013 aid in choosing the correct components for the tertiary system. However, these guidelines may suggest that multiple systems would be suitable for the API. When this occurs, experimentation ensures selection of the optimal system as even a system that meets the proposed guidelines may not result in agglomerate formation. In a study by Thati and Rasmuson, 2012, the spherical agglomeration of benzoic acid with seven different bridging liquids were tested, of which two resulted in no agglomerate formation (Thati and Rasmuson, 2012).

2.3.1 Solubility Studies

When performing spherical agglomeration, it is important that the primary particles sufficiently dissolve in the solvent and this, in turn, will allow for the determination of the ideal antisolvent. Table 2-1 shows a summary of the methods used for measuring solubility.

Table 2-1 Comparison of methods used for solubility Studies, information from (Glomme et al., 2005; Gregory, 2014; Avdeef et al., 2016; Veseli et al., 2019)

Method	Advantages	Disadvantages
Shake Flask	Simple and inexpensive experiment to perform (Veseli et al., 2019) High level of accuracy (Veseli et al., 2019)	Time consuming (Veseli et al., 2019) Large amounts of sample required (Veseli et al., 2019)
Potentiometric Methods	Uses small quantities of the pharmaceutical compound (Veseli et al., 2019) Fast and efficient (Avdeef et al., 2016)	Can only be used on compounds that are ionisable (Glomme et al., 2005)
Column Elution	Simple and inexpensive to set up (Veseli et al., 2019) Relatively short time to find solubility when compared to shake flask methods (Veseli et al., 2019)	Large amount of solid needed (Veseli et al., 2019) Not suitable for inorganic compounds as coating the support material is difficult (Gregory, 2014)

2.3.2　Wettability Studies

To ensure that the bridging liquid is suitable for the agglomeration of the solid particles, the contact angle between the bridging liquid and particle is measured. The contact angle is the angle of the tangent of the liquid-interface and the solid surface (Huhtamäki et al., 2018). If the contact angle is lower than 90° then there is a high level of wettability between the surface and the liquid. A contact angle of 0° indicates that complete wetting has occurred (Yuan and Lee, 2013). In Figure 2-2, a schematic of contact angles can be seen.

Figure 2-2 Schematic diagram of contact angles, one under 90° (wetting) and one over 90° (non-wetting)

Contact angle measurements are extremely useful to be able to analyse the surface energetics of a system. Young's Equation (2.1) is critical for the measurement of contact angle as it relates the angle of a liquid droplet on a solid surface to interfacial tensions (Yuan and Lee, 2013).

$$\gamma_{f1.2} \cos \theta_Y = \gamma_{sf2} - \gamma_{sf1} \tag{2.1}$$

Where:

$\gamma_{f1,2}$ is fluid 1 to fluid 2 surface tension (N.m)

θ_Y is Young's contact angle (°)

γ_{sf1} is solid-fluid 1 surface tension (N.m)

γ_{sf2} is solid-fluid 2 surface tension (N.m)

In Equation 2.1, only the fluid-fluid surface tension and Young's contact angle are measurable. Therefore, another equation is required to calculate the other surface tensions between the solid and the fluids present in the system (Kwok et al., 1997). Often in contact angle measurements, it is only a solid-liquid-vapour system. However, it is possible to get accurate contact angle measurements with a solid-liquid-liquid system using Equation (2.1) (Jiang et al., 2017). There are limitations of using the contact angle to determine the surface energetics as the observed contact angle may not be equal to Young's contact angle as the contact angle can undergo hysteresis if the surface is rough or not ideal (Kwok et al., 1997) . Furthermore, surface roughness, chemical heterogeneity, and hydrophobicity of a solid surface influence contact angle measurements, resulting in less accurate values obtained for surface wettability (Tavana et al., 2004). Table 2-2 shows a summary of various contact angle measurement methods.

Table 2-2 Comparison of various contact angle measurement methods, information from (Río and Neumann, 1997; Bezuglyi et al., 2001; Bachmann et al., 2003; Hoorfar and Neumann, 2004; Galet et al., 2010; Yuan and Lee, 2013; Huhtamäki et al., 2018)

Measurement Method	Advantages	Disadvantages
Sessile-Drop Goniometry	Small volumes of liquid and small surfaces of substrates are needed (Yuan and Lee, 2013) Extremely simple method (Yuan and Lee, 2013; Huhtamäki et al., 2018)	High risk of impurities due to the small volume of liquid required (Yuan and Lee, 2013; Huhtamäki et al., 2018) Can be time consuming if larger areas are used as multiple measurements need to be taken at different points on the sample area (Huhtamäki et al., 2018)
Tilting Plate	Simple and has less dependence on the judgement of the operator (Yuan and Lee, 2013) Can get measurements quickly (Huhtamäki et al., 2018)	The estimation of the liquid surface curvature is often done visually and therefore can be subjective leading to changes in the results if different operators are used (Bezuglyi et al., 2001) Use of tilting plate method to measure advanced and receding contact angle may not be the best use of this method (Pierce et al., 2008) Drop size influences the reported angle (Huhtamäki et al., 2018)
Wilhelmy Plate	No operator error and it can easily be automated (Huhtamäki et al., 2018)	The sample needs to have the same morphology and composition on all surfaces; if the surface is rough, it is difficult to determine the length of the contact line and therefore the contact angle (Huhtamäki et al., 2018)
Axisymmetric Drop Shape Analysis	High levels of accuracy (Río and Neumann, 1997) Can be automated through using computerised image analysis (Río and Neumann, 1997)	Inaccurate results were obtained if the drops were close to spherical (Hoorfar and Neumann, 2004)
Capillary Rise	Washburn equation can be applied with 3.7% precision for a capillary rise height that is 10% of the final height that the liquid rises in the tube (Galet et al., 2010)	If the contact angle is greater than 90° then the testing fluid will not rise into the sample (Bachmann et al., 2003)

2.3.3 Constructing the Ternary Phase Diagram

Once the appropriate solvent, antisolvent and bridging liquid have been selected, a ternary phase diagram is constructed to determine the composition of the solvent system (Jitkar et al., 2016; Kulkarni et al., 2011; Pitt et al., 2018; H. Zhang et al., 2010b). Ternary phase diagrams consist of an equilateral triangle with each corner of the triangle representing 100 % concentration of compounds A, B and C. Ternary phase diagrams are presented as if they are isothermal (Holaň et al., 2014). Figure 2-3 shows an example ternary phase diagram.

In Figure 2-3, the ternary phase diagram is for a mixture of acetone, water, and dichloromethane (DCM). In this system, acetone is the good solvent, water is the antisolvent and DCM is the bridging

liquid. The mixture was prepared by mixing water and acetone in different ratios ranging from 1:9 to 9:1. With DCM added drop by drop, the system underwent intermittent mixing. At each ratio, the volume of DCM that was required for the solution to become clear was noted and this data was plotted to identify the miscible (A) and immiscible (B) regions. For spherical agglomerates to form, the composition of the system must be within the miscible region (Jitkar et al., 2016).
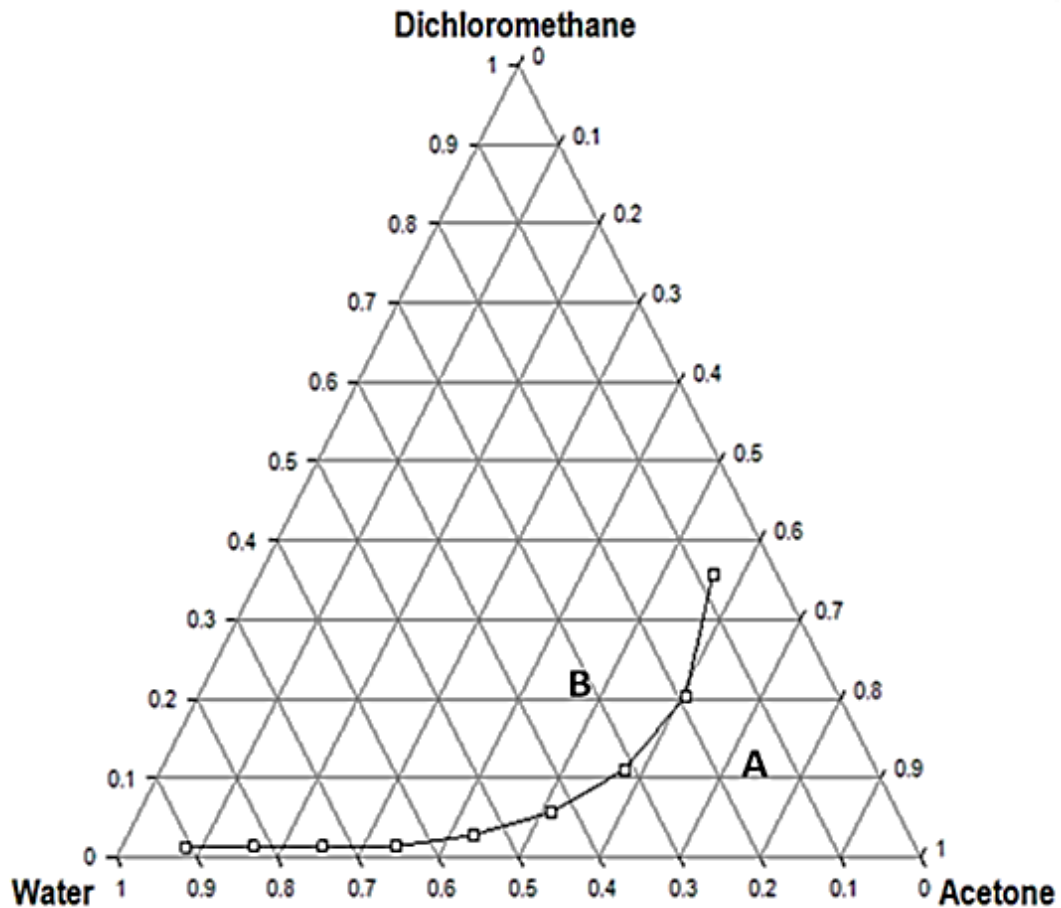
Figure 2-3 Ternary phase diagram of acetone-water-dichloromethane (DCM). Image from (Jitkar et al., 2016)

2.4   Parameters Impacting Spherical Agglomerate Formation

Many parameters control the effectiveness of the spherical agglomeration process; a summary of these parameters and their effects can be found in Table 2-3, with more information about the parameters in the following sub-sections.

Table 2-3 Impact of process parameters on the formed agglomerates, information from (Kawashima et al., 1982; Paradkar et al., 2002; Katta and Rasmuson, 2008; Thati and Rasmuson, 2011; Thati and Rasmuson, 2012; Maghsoodi and Yari, 2013; Peña and Nagy, 2015; Orlewski et al., 2018; Arjmandi-Tash et al., 2019)

Process Parameter	Impact on Agglomerates
Agitation Speed	Higher agitation speed reduces the size of the formed agglomerates (Paradkar et al., 2002; Katta and Rasmuson, 2008)
Temperature	An increased solvent temperature reduces the size of the agglomerated products as well as the sphericity and density (Maghsoodi and Yari, 2013) Increased solvent temperature reduces the fracture stress of the agglomerates (Thati and Rasmuson, 2012)
Bridging Liquid to Solid Ratio (BSR)	There is a range of BSR values that allow agglomeration to work effectively. Too low and no agglomeration occurs; too high and a paste forms (Peña and Nagy, 2015)
Aqueous Solution Feed Rate	Size decreases with higher feed rate of aqueous solution (Pitt et al., 2018). Fracture force increases at higher feed rates of aqueous solution (Thati and Rasmuson, 2011)
Bridging Liquid Feed	Increased feed rate increases the size of the produced agglomerates (Kawashima et al., 1982) The horizontally injected bridging liquid produces smaller agglomerates than vertically injected bridging liquid (Orlewski et al., 2018)
Solvent To Antisolvent Ratio	High values will result in a low yield (Peña and Nagy, 2015)
Residence Time	Increased residence time increases the fracture stress of agglomerates (Thati and Rasmuson, 2012)
Solids Concentration	Increased solid concentration results in faster agglomeration and increased agglomerate size until a certain level of solid concentration is reached; increasing it further will have no effect (Peña, Oliva, et al., 2017)
Size of Solid Particles	If the solid particles are smaller in size than bridging liquid droplets then immersion nucleation takes place, resulting in denser particles that can have easily controlled size distribution (Arjmandi-Tash et al., 2019)
Size of Bridging Liquid Droplets	Increased bridging liquid droplet diameter will increase the size of the produced agglomerates (Orlewski et al., 2018)

2.4.1 Effect of Agitation Speed

As Table 2-3 shows, the size of the produced agglomerates decreases when there is an increase in agitation speed (Paradkar et al., 2002; Katta and Rasmuson, 2008; Pitt et al., 2018). The decrease in size with increased speed is due to the increased shear in the system as the agitation rate is increased. The increase in shearing may lead to attrition and breakage resulting in smaller sized agglomerates (Chaterjee et al., 2017). Increased shear causing an increase in particle breakage can also lead to a broader particle size distribution (H. Zhang et al., 2010b). Figure 2-4 shows a PSD for benzoic acid spherical agglomerates formed at different impeller speeds.
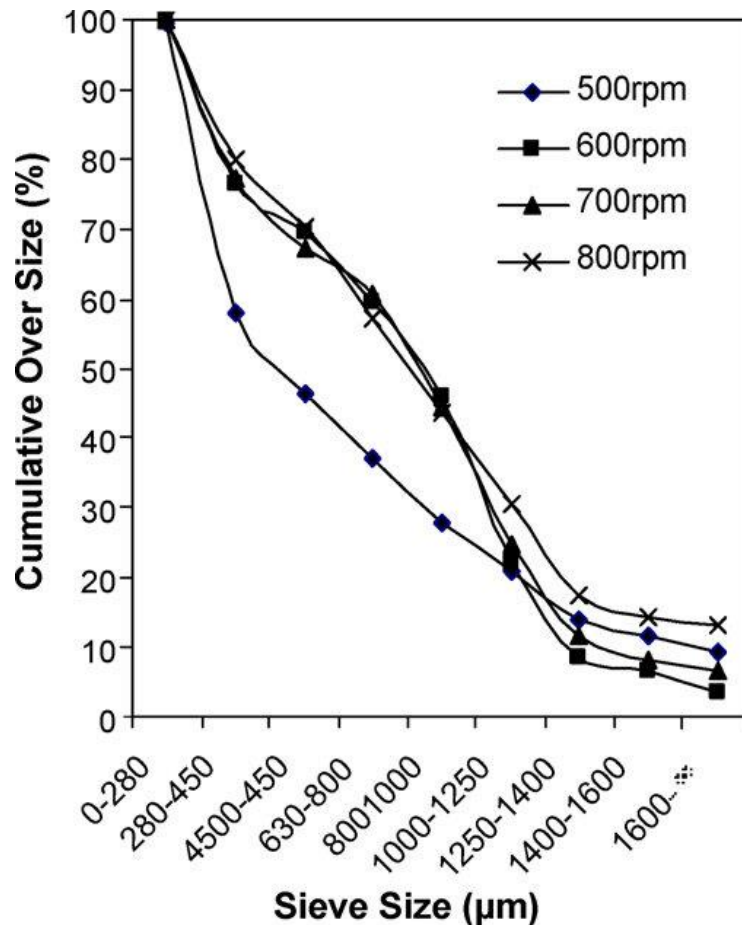
Figure 2-4 Impact of agitation speed on the particle size distribution of spherical agglomerates of benzoic acid, image from (Katta and Rasmuson, 2008)

2.4.2 Effect of Temperature Difference

Table 2-3 also shows that the agglomerate size decreases with an increase in the temperature difference between the good solvent and the bridging liquid (Kawashima et al., 1982). This can also be seen in Figure 2-5. Although the increase in temperature causes smaller agglomerates to form, the agglomerates take a shorter amount of time to become regularly shaped, dense particles with smooth surfaces (Maghsoodi and Yari, 2013). The change in size and density of the agglomerates with temperature may also be due to the influence on the initial crystallization of the primary particles (Kawashima et al., 1984; Pitt et al., 2018). The influence of temperature on solubility may account for temperature effecting spherical agglomerate properties (Chuahan et al., 2012). At lower temperatures, there is lower solubility of the powder in the system leading to an increase in the level of supersaturation; this promotes nucleation and smaller crystals (Thati and Rasmuson, 2012).
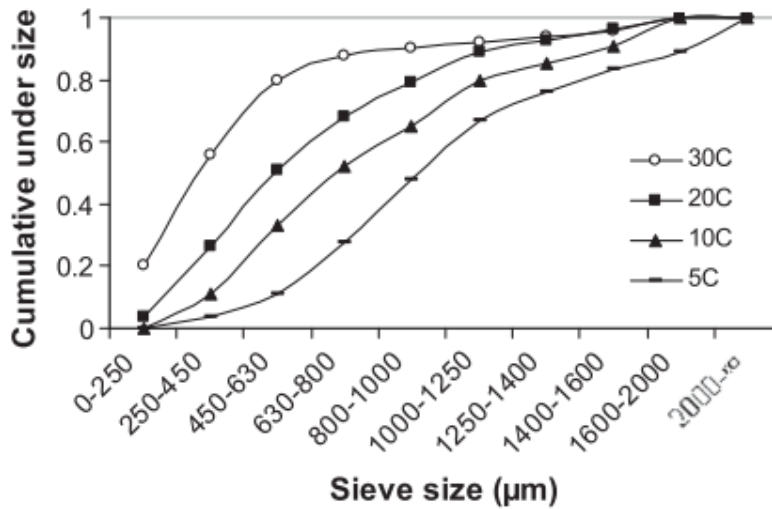
Figure 2-5 Impact of temperature on the particle size distribution, image from (Thati and Rasmuson, 2012)

2.4.3 Impact of Bridging Liquid to Solid Ratio (BSR)

The impact of BSR on the agglomeration process is more complex as there is a critical range for the BSR. This range is found empirically. If the BSR value falls within the critical range, then efficient agglomeration can occur. If the BSR is lower than the range, then there is no significant agglomeration, and if the value of BSR is higher than the range, the product has a paste-like consistency (Peña and Nagy, 2015; Pitt et al., 2018). The zero-growth regime for spherical agglomeration dominates the kinetics of agglomeration. The time in the zero-growth regime is sensitive and depends on process parameters, with the BSR being a key factor that influences the time in the zero-growth regime. As the BSR increases, the time in the zero-growth region decreases (Bemer, 1979). Figure 2-6 shows the impact of the BSR in the critical range on the PSD. It can be seen in Figure 2-6 that as the value of BSR increases the size of agglomerates increases and the distribution of agglomerate size is wider.
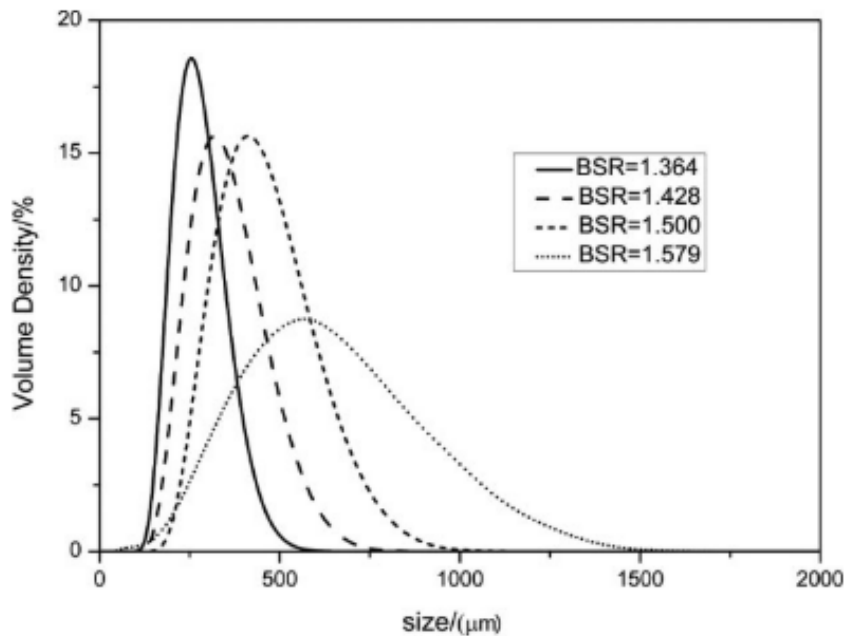
Figure 2-6 Impact of critical range BSR on the particle size distribution of spherical agglomerates, image from (Wu et al., 2015)

2.4.4   Effect of Feed Rate

The feed rate in spherical agglomeration is important as it influences the size and strength of the produced spherical agglomerates. At higher aqueous solution feed flow rates, the agglomerate size decreases (Kawashima et al., 1982; Thati and Rasmuson, 2011); this can be seen in Figure 2-7. This is due to the aqueous solution feed rate affecting the level of supersaturation in the spherical agglomeration process (Thati and Rasmuson, 2011).   Increased aqueous solution feed rate will increase the level of supersaturation resulting in more nuclei and smaller crystals (Thati and Rasmuson, 2012). The strong nuclei produced at high levels of supersaturation also explain why the fracture strength of agglomerates increases with increased aqueous solution feed rate (Thati and Rasmuson, 2011).
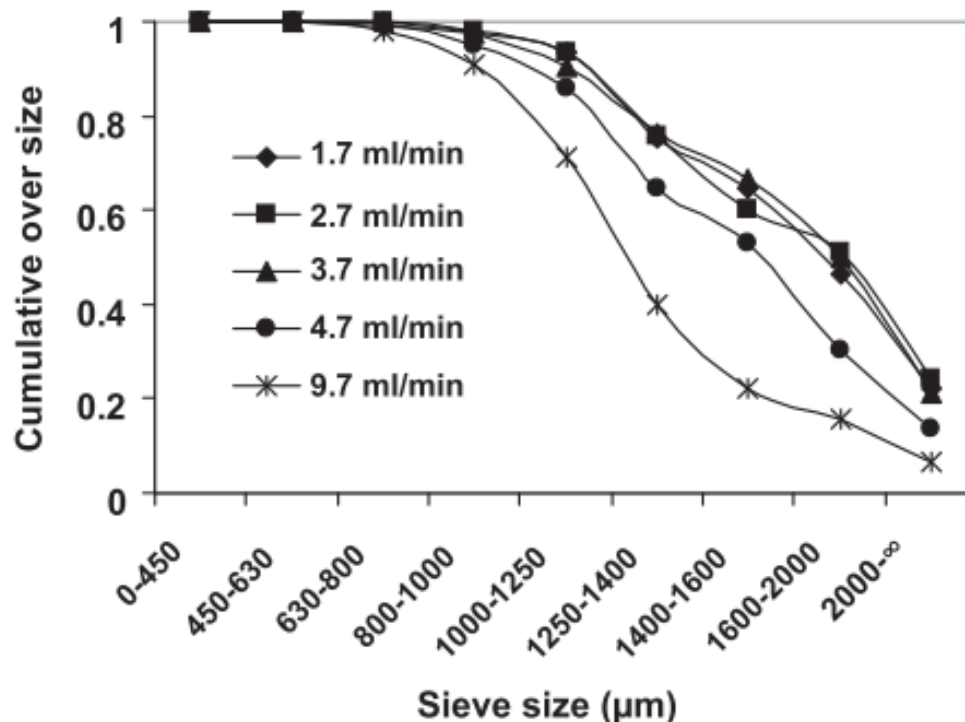
Figure 2-7 Impact of the feed rate on the particle size distribution, image from (Thati and Rasmuson, 2011)

When the feed rate of the bridging liquid is decreased the average agglomerate size decreases. This is to be expected as more bridging liquid in the system increases the chances of particle cohesion, increasing the size of the agglomerates that are formed (Kawashima et al., 1982). The injection point of the bridging liquid also impacts agglomerate size. If the bridging liquid is injected horizontally into the system, the agglomerates formed will be smaller than if the bridging liquid is injected vertically. This is due to the break-off point of the horizontally injected bridging liquid being at the capillary tip, compared to the external surface of the capillary when the bridging liquid injection is vertical. A smaller size bridging liquid droplet is formed when it breaks off from the capillary tip (Orlewski et al., 2018).

2.4.5   Effect of Solvent to Antisolvent Ratio

Another important parameter in the formation of spherical agglomerates is the solvent to antisolvent ratio, often called R_a (Tahara et al., 2015), or SASR (Peña and Nagy, 2015; Peña, Oliva, et al., 2017; Pitt et al., 2018; Peña et al., 2019). The ratio of solvent to antisolvent is critical as if the ratio is high then there is a lower level of supersaturation in the system. At low levels of supersaturation, the yield of spherical agglomerates decreases (Peña and Nagy, 2015). For the spherical agglomeration of albuterol

sulphate, it has been reported that the value of R_a should be lower than 0.01, which results in vast quantities of organic solvents being needed (Tahara et al., 2015).

2.4.6   Effect of Residence Time

Residence time has an impact on the particle size and properties of the produced agglomerates. Various studies have shown that as the residence time increases, the size of the agglomerates increases until an equilibrium point is reached (Kawashima et al., 1984; Tahara et al., 2015; Javadzedah et al., 2016; Chaterjee et al., 2017; Pitt et al., 2018). It is important to find an optimum residence time as the equilibrium status is due to long residence times, resulting in more breakage occurring, hence reducing the particle size. However, this is balanced by other particles agglomerating and increasing in size. If the residence time is too low, agglomeration will be incomplete due to inefficient effusion of good solvent and bridging liquid from the droplets (Javadzedah et al., 2016). Increasing the residence time also results in greater compressive strength and sphericity; some studies also observed an increase in density at higher residence times (Morishima et al., 1993; Pitt et al., 2018).

2.4.7   Effect of Solids Concentration

The concentration of the solids in the mixture influences the size of the agglomerates that are produced (Thati and Rasmuson, 2011; Peña, Burcham, et al., 2017). Increased solid concentration up to a limit also causes the agglomeration process to be faster with larger agglomerates produced. Once the limit is reached, increasing the concentration further has no impact on the final agglomerate size (Blandin et al., 2003; Pitt et al., 2018). If the surface of the solid particles is rough, then a higher concentration is needed compared to fine, smooth particles (Maghsoodi and Yari, 2013).

2.4.8   Effect of Primary Particle Size

The initial particle size is important in spherical agglomeration as it influences the nucleation mechanism that will occur. If the particle size is greater than the size of the bridging liquid droplets, then distribution nucleation will occur. The agglomerates formed through distribution nucleation are less dense and have a broader size distribution than those formed via the immersion mechanism. It is favourable to have small initial particles as this allows for greater control of the particle size distribution as they will undergo immersion nucleation (Arjmandi-Tash et al., 2019). A schematic of the different nucleation mechanisms is shown in Figure 2-1.

2.4.9   Effect of Bridging Liquid Droplet Diameter

Large droplets of bridging liquid results in large agglomerates being formed and a wider particle size distribution. This is due to the larger droplets being able to be penetrated by more of the initial solid particles. The droplets containing more solid will result in larger agglomerates. The broad size distribution could be due to the droplets breaking into smaller droplets which will create smaller agglomerates (Orlewski et al., 2018). If the droplets are much larger than the initial solid particle size, then immersion nucleation will take place which produces denser agglomerates and allows for greater control of the PSD (Arjmandi-Tash et al., 2019).

2.4.10 Effect of Mixing Conditions

There has been little consistency in the impeller geometries used in spherical agglomeration literature. Work by Chen et al., 2021 investigated the influence of three impeller configurations at different reactor scales. The impeller geometries used in this work were a pitched blade impeller, a double-layered pitched blade impeller, and a Maxblend impeller; these can be seen in Figure 2-8.
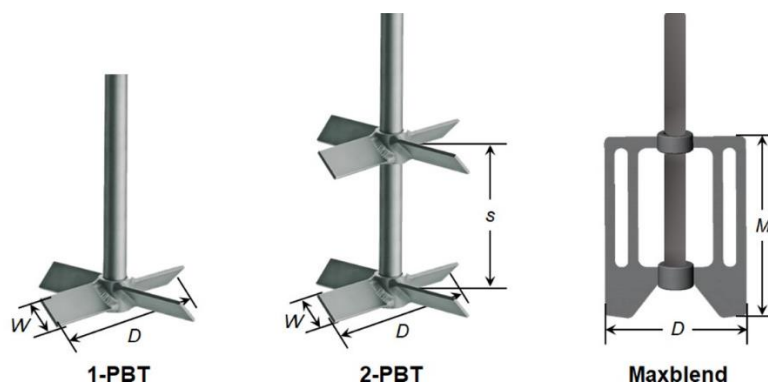
Figure 2-8 Impeller geometries used by (Chen et al., 2021)

The three impellers in Figure 2-8 were used in both 2 L and 10 L vessels to investigate scale-up of spherical agglomeration. Experiments were also performed at a 0.5 L scale, but these only used the single-layered pitched blade turbine. This work found that the Maxblend impeller needed lower agitation speeds than both configurations of pitched blade impellers. It was also found that scaling up spherical agglomeration was a relatively smooth process. However, larger scale systems tended to produce larger agglomerates and the PSD was also wider at larger scales. This can be seen in Figure 2-9.
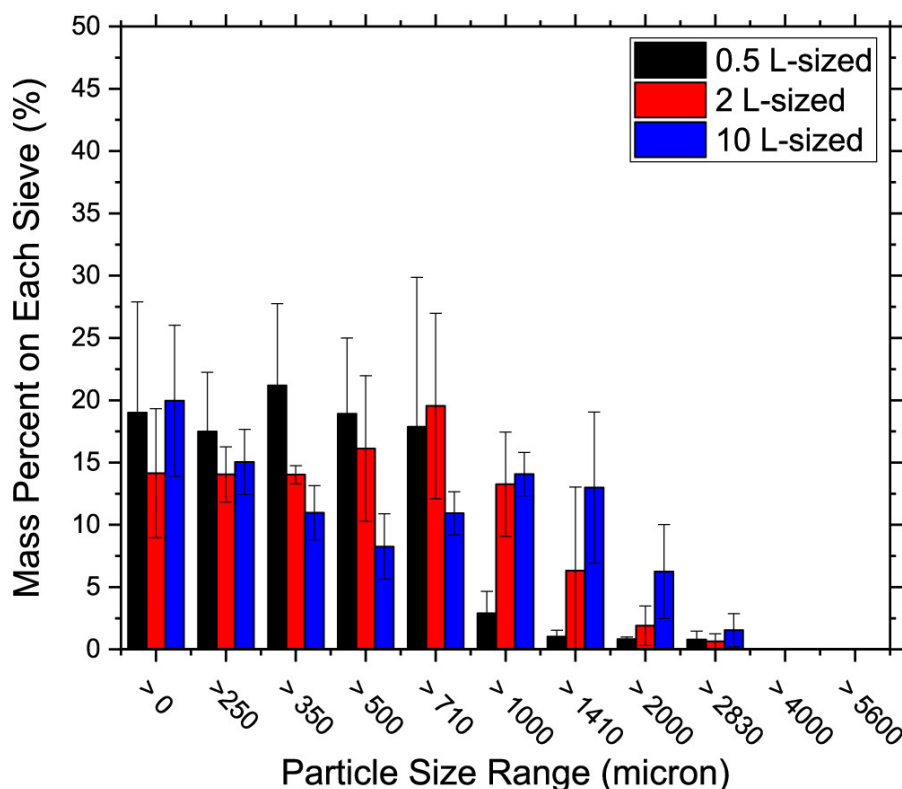
Figure 2-9 Particle size distribution of dimethyl fumarate agglomerates produced at varied reactor scales using a single-layered pitched blade impeller, image from (Chen et al., 2021)

2.5 Continuous Spherical Agglomeration

The pharmaceutical industry is showing increasing interest in continuous production as it has many benefits. In 2015 there was a publication by the FDA that contained guidelines to advance continuous manufacturing of pharmaceutical products. Many pharmaceutical companies, including Eli Lilly and Novartis, have developed commercial-scale continuous drug manufacture (Peng, 2017).

Continuous manufacturing can increase the safety of the process due to smaller reactor volumes being needed for the same production rate in comparison to batch. The smaller volumes are extremely important for reactions where there are harmful reactants. A fully continuous process offers greater quality control, and excipients can be added during the process to simplify the conversion of the API to a drug product (Johnson et al., 2019).

Continuous spherical agglomerate production using a series of mixed-suspension mixed-product removal (MSMPR) reactors has been investigated. This research had benzoic acid primary particles, ethanol solvent and water antisolvent mixed in the first reactor, with toluene bridging liquid added in the second reactor. The residence time, impeller speed and system volume were investigated for both tanks in the system. The BSR was also investigated, all parameters were found to have similar effects as they do in batch spherical agglomeration. The multi-stage stirred tank configuration allowed for increased control over the product end properties, and the resultant agglomerates had desirable characteristics that would allow them to undergo direct compression (Peña and Nagy, 2015).

2.6 Safety of Spherical Agglomeration for Pharmaceutical Manufacture

In the pharmaceutical industry, the safety and purity of tablets is a priority to ensure that medicines conform to guidelines and meet the needs of patients. Pharmaceutical products need to meet the guidelines of various organisations to be able to be sold globally. Regulatory authorities from Japan, Europe and the United States are involved in the International Conference on Harmonization (ICH) of technical requirements for registration of pharmaceuticals for human use. The ICH was formed to ensure that resources are used efficiently to ensure new medicines are available without compromising the safety and efficacy of drugs (Haleem et al., 2015).

In 2009, the ICH implemented the Q10 Pharmaceutical Quality Systems. This details a model pharmaceutical quality system (PQS) which was designed to ensure that product quality was met through a well performing process that has appropriate controls. Areas for improvement are also investigated for the PQS to further develop the understanding of the process (VanDuyse et al., 2021).

One approach taken by the pharmaceutical industry is Quality by Design (QbD). This approach was defined in ICH Q8 and Q9 guidelines (Pramod et al., 2016; Gyulai et al., 2018; VanDuyse et al., 2021). The principle of quality by design is that for most pharmaceutical products, the quality issues were due to poor design, therefore, quality must be incorporated into the process design. Quality is built in by systematically defining objectives of the product, increasing the levels of process understanding and process control based on process knowledge and risk management (Fukuda et al., 2018).

A study by Usha et al., 2008 investigated the stability, pharmacokinetics, pharmacodynamics and toxicity of spherical agglomerates of aceclofenac in a dichloromethane (DCM) and water solvent system with an acetone bridging liquid. Hydroxypropyl methylcellulose-50 cps (HPMC) was also present in the system as a hydrophilic polymer. Various process parameters including impeller speed and BSR were investigated. The dissolution behaviour of the spherical agglomerates was better than that of the aceclofenac crystals. Tablets were produced via direct compression of the optimal reaction conditions. The tablets of the spherical agglomerates were within acceptable limits of physiochemical properties and were found to be stable for 6 months (Usha et al., 2008).

Studies were also conducted on animal subjects to determine the concentration of the drug in the body over time. This study found that the spherically agglomerated aceclofenac had a higher blood plasma concentration over time compared to the marketed tablet and the unprocessed aceclofenac; this can be seen in Figure 2-10a. During the study on rats, there were no deaths of the test subjects and no differences in behaviour, appetite or physiological activities was observed. Haematological and

biochemical tests on the rats also did not show any changes, and this allowed for trials on human volunteers. As can be seen in Figure 2-10b, the tablet made of spherical agglomerates of aceclofenac (Tablet C) absorbs into the blood faster than the marketed tablet after oral administration. Analysis of Tablet C shows that it has a higher time of peak plasma concentration, and a higher peak plasma concentration suggesting that the spherical agglomerated material has an increased extent of absorption compared to the marketed tablet. As the spherical agglomerates in Tablet C have increased bioavailability, lower doses may be needed for tablets to achieve the same efficacy as the marketed tablet, and this would reduce the cost. Lower volumes of drug needed in the tablet could also lead to decreased likelihood of adverse reactions and toxicity (Usha et al., 2008). This work suggests that spherical agglomeration is a promising tool to increase bioavailability of API in the drug, therefore, reducing the mass needed in tablets which would then reduce the potential for adverse effects or toxicity. However, long-term studies into tablet stability and toxicity are needed, as well as pharmacokinetic studies before spherically agglomerated material in tablets can be produced industrially.
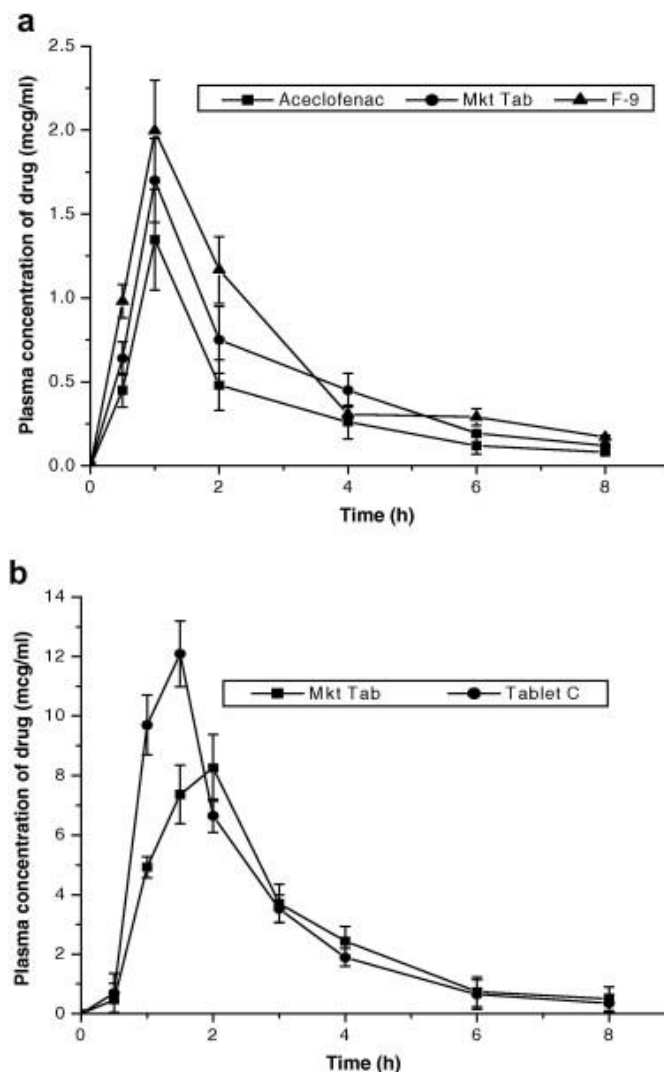
Figure 2-10 The concentration over time of drug in blood plasma for the pharmacokinetic study in (a) rats and (b) humans. F-9 is the spherical agglomerates of aceclofenac, Mkt Tab is the marketed tablet and Tablet C is the tablet produced from spherical agglomerates F-9, image from (Usha et al., 2008)

2.7 Sustainability of Spherical Agglomeration

The amount of waste generated by the pharmaceutical industry has been found to be higher than the waste from fine or bulk chemical production. Of all of the waste generated by pharmaceutical companies, GSK estimated that 70 % was solvent waste (Welton, 2015). Spherical agglomeration occurs in ternary solvent systems, and many solvents are harmful for the environment. Commonly used solvents are ethanol, toluene, dichloromethane (DCM) and chloroform. From Table 2-4, most of the commonly used solvents are classed as problematic or higher. This demonstrates that whilst spherical agglomeration is a promising technique for pharmaceutical manufacture, the solvent system and process design must be carefully considered to reduce the harmful effects that the solvents may have on the environment.

Table 2-4 Green solvent selection ranking guide for solvents used for spherical agglomeration, information from (Welton, 2015)

Classification	Solvents
Recommended	Water Ethanol Isopropyl acetate
Recommended or Problematic	Methanol Acetone Methyl acetate
Problematic	Heptane Toluene Chlorobenzene
Problematic or Hazardous	Cyclohexane Dichloromethane (DCM) Pyridine
Hazardous	Dimethyl ether Hexane Pentane
Highly Hazardous	Chloroform Dichloroethane Carbon tetrachloride

The Registration, Evaluation, Authorisation and Restriction of Chemicals (REACH) influences the import and use of chemicals in Europe. This organisation has added restrictions to toluene, DCM and chloroform due to their environmental impact and their potential to be hazardous to health (Byrne et al., 2016). Therefore, finding new solvents that are both more sustainable and less toxic than conventional spherical agglomeration solvents is extremely important.

Recent studies have investigated the possibility of using non-toxic and renewable bridging liquids for spherical agglomeration. In a study by Guo et al., 2022, oleic acid was successfully used as a bridging liquid for benzoic acid, L-leucine and aspirin. This shows that spherical agglomerates can be obtained with more sustainable solvents (Guo et al., 2022). Further research into improving the sustainability of spherical agglomeration is a research avenue that would increase the likelihood of spherical agglomeration being used industrially.

Another way to reduce the solvent use in the development stages of a spherical agglomeration process is through the development of accurate predictive models. These models would allow for a company

to input their API properties and various solvent systems to determine which systems are most likely to successfully form agglomerates. This would reduce the number of preliminary experiments required, lowering solvent consumption at the process development stage.

2.8 Gaps in Spherical Agglomeration Literature

The majority of studies relating to spherical agglomeration are carried out in small benchtop scale experiments and, therefore, it is unclear whether the optimal benchtop scale conditions will apply for spherical agglomerate production at an industrial scale as mixing and settling dynamics will differ at larger scales.

As spherical agglomeration processes require the powder to be mixed with solvent, there is often agitation involved which will influence the mixing patterns in the tank. The impact of flow patterns on the mechanisms of spherical agglomeration and the resultant products has not been thoroughly investigated. Different agitator types, agitation speeds, reactor geometries, and reactor scales will all result in different mixing patterns in the system.

2.9 High Shear Wet Granulation

The regimes that are thought to occur in the spherical agglomeration process are similar to those that occur in high shear wet granulation (HSWG). Understanding the impact that process parameters have on the regimes and product properties in HSWG can lead to a greater understanding of their impact on spherical agglomeration.

High shear wet granulation processes generally use a continuous stirred tank reactor (CSTR) with high agitation speeds being used to generate the necessary shear to increase the rate of mixing. Choppers are also present in these tanks to break up large granules to allow for the powder and binder to be redistributed throughout the reaction mixture (Briens and Logan, 2011).

In HSWG, a liquid binder is added to the powder that is to be granulated. Through agitation, the binder is distributed onto the powder surface causing granulation to occur through the mechanisms of nucleation, consolidation and growth (Campbell et al., 2011). During the consolidation and growth of the granules, they can also undergo attrition and breakage due to the shear imparted by the agitator (Chitu et al., 2011). The regimes occurring in HSWG are impacted by process parameters, and various studies have been conducted to find the influence of parameters such as agitation speed on the regimes of HSWG. In Figure 2-11, and Table 2-5 the impact of various parameters on specific regimes of granule formation can be seen. Many of these parameters can also be seen in Table 2-3 as influencing the formation of spherical agglomerates; this could be due to the mechanistic regimes in both processes being extremely similar.
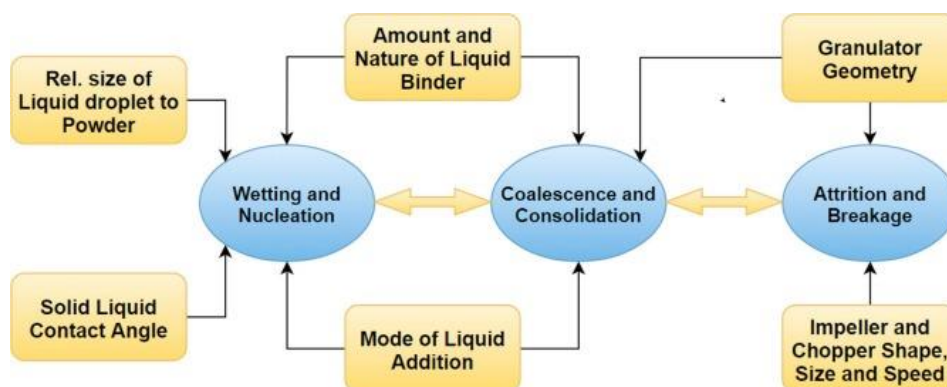
Figure 2-11 Regimes involved in HSWG and parameters that impact those regimes (Suresh et al., 2017)

Figure 2-11 shows that the nature of the binder has a large impact on both the wetting and nucleation and coalescence and consolidation regimes of HSWG. This is due to the availability of the binder being extremely important for these processes. In the wetting and nucleation regime, the binder makes contact with the powder and wets it allowing nuclei formation. The wetted nuclei then come into contact with other nuclei and loose powder and coalesce and consolidate (Suresh et al., 2017). If the binder is extremely viscous then it will not move around the granulation vessel as easily as a less viscous material resulting in lower availability of binder throughout the powder bed. Small amounts of binder will also decrease availability (Yu et al., 2017). This will result in less nuclei formation and lower rates of coalescence and consolidation causing fewer granules to form. Table 2-5 shows the impact of the equipment used for HSWG has on the mechanisms that occur in the granulation process.

Table 2-5 Impact of equipment parameters on granulation mechanisms, adapted from (Yu et al., 2017)

Mechanism	Impeller Speed	Impeller Type	Equipment Type
Nucleation and Wetting	✓		
Consolidation	✓		✓
Coalescence	✓	✓	
Attrition and Breakage	✓	✓	

In Table 2-5, the speed of agitation by the impeller is shown to impact on all regimes in granulation, whereas in Figure 2-11 the impeller speed is only shown to influence attrition and breakage. This is due to higher agitation speeds increasing the collision velocity between particles and other particles and the wall of the vessel. Above a certain velocity, this will lead to attrition and breakage. At velocities below this, there may be some breakage but also coalescence and consolidation (Yu et al., 2017). Therefore, Figure 2-11 only considers the impact on attrition and breakage as this is the mechanism that agitation speed has the largest impact on. Figure 2-12 shows increasing the tip speed of the impeller will lead to a reduction in the size of the produced granules at both reactor scales.
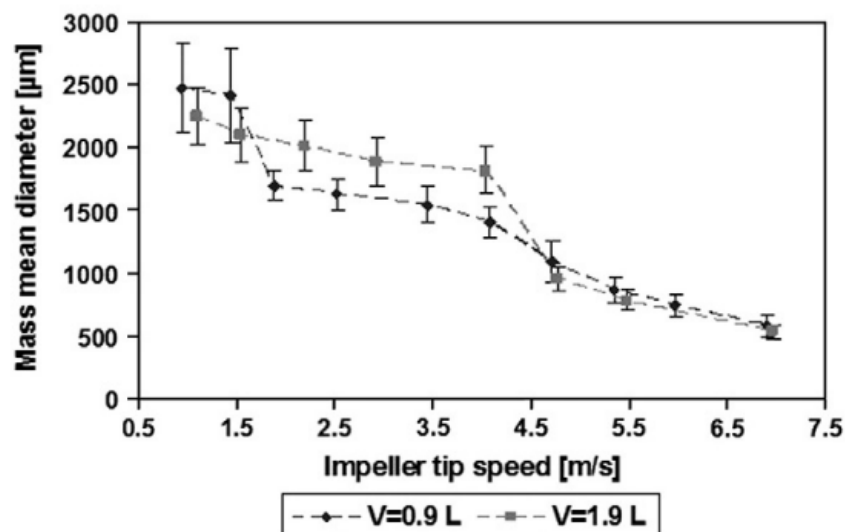
Figure 2-12 Influence of reactor scale and agitation speed on the size of granules in HSWG, image from (Chitu et al., 2011)

2.10 Stirred Tank Flow Characteristics

Stirred tank flow conditions are dependent on the geometry of the stirred tank and its various components. Impeller geometry, speed and size are all important parameters that influence flow in the tank. Other influential parameters are fluid properties and the dimensions of the tank and baffle system (Van Wazer et al., 1995). In an unbaffled stirred tank, the flow around the impeller is a circular flow pattern, shown in Figure 2-13; this induces vortex formation, reducing mixing efficiency.
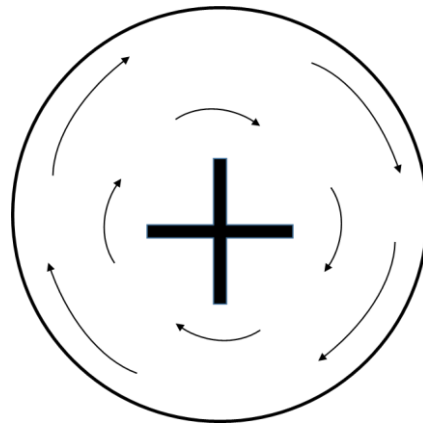
Figure 2-13 Aerial view of an unbaffled stirred tank with a circular flow pattern, adapted from (Van Wazer et al., 1995)

As well as circular flow, radial and axial flow are present in the stirred tank. In axial flow, mixing occurs up and down the length of the tank in a looping pattern. With radial flow, the fluid goes from the stirrer to the sides of the tank and then back towards the stirrer. Radial flow causes two mixing zones, one above and one below the impeller, however mixing occurs rapidly between the zones (Van Wazer et al., 1995; Couper et al., 2012). Figure 2-14 shows axial and radial flow profiles from a side and aerial view. As Table 2-5 shows, the impeller geometry influences mechanisms for HSWG, and will therefore influence spherical agglomeration mechanisms.
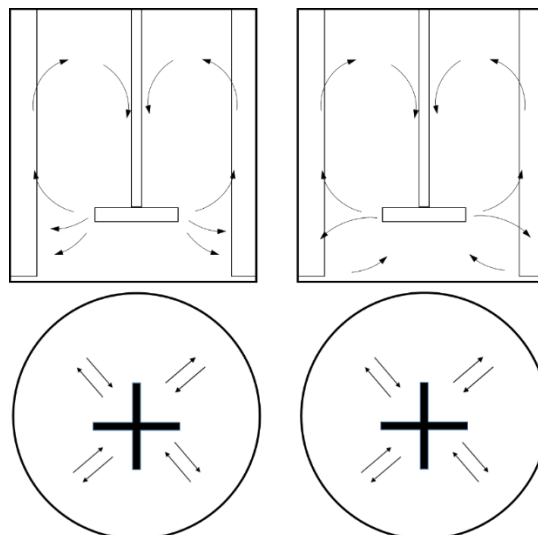
Figure 2-14 Varying flow patterns in stirred tanks left – axial flow, right – radial flow. Image adapted from (Couper et al., 2012)

To ensure that contact occurs between bridging liquid and particles, the particles need to be well suspended. Solid-liquid suspensions are agitated above the critical impeller speed (N_{js}) to ensure that no particles are stationary at the bottom of the tank for more than 2 s, Equation 2.2 is the calculation for N_{js} (Zwietering, 1958).

$$N_{js} = Sv^{0.1} \left[\frac{g(\rho_s - \rho_l)}{\rho_l}\right]^{0.45} X^{0.13} d_p^{0.2} d^{-0.85} \qquad (2.2)$$

Where:

N_{js} is the critical impeller speed for particle suspension (rps)

S is the Zwietering constant

v is the kinematic viscosity (m²/s)

g is the constant of acceleration due to gravity (m/s)

ρ_s is the solid density (kg/m³)

ρ_l is the liquid density (kg/m³)

X is the solid loading in the system

d_p is the diameter of particles (m)

d is the diameter of the impeller (m)

Equation 2.2, proposed by Zwietering, 1958, is an empirical correlation with a fitting parameter. In work by Devarajulu and Loganathan, 2016, Zwietering constants were determined for nine impeller geometries that promote varied levels of radial and axial flow. A selection of these impeller correlations can be seen in Table 2-6.

Table 2-6 A selection of impellers, and the Zwietering Constant equations derived by (Devarajulu and Loganathan, 2016)

Impeller	Zwietering Constant Equation
Radial Flow	$S = 8.54 \left(\frac{C}{T}\right)^{0.218} \left(\frac{H}{T}\right)^{-0.248}$
Radial Flow	$S = 13.98 \left(\frac{C}{T}\right)^{0.639} \left(\frac{H}{T}\right)^{-0.055}$
Axial Flow	$S = 10.42 \left(\frac{C}{T}\right)^{0.455} \left(\frac{H}{T}\right)^{-0.107}$
Axial	$S = 8.17 \left(\frac{C}{T}\right)^{0.329} \left(\frac{H}{T}\right)^{-0.120}$
C is impeller clearance (m), H is liquid height (m) and T is tank diameter (m)	

The correlations in Table 2-6 suggest that the critical impeller speed has a correlation to both the impeller clearance and the height of liquid in the tank (Devarajulu and Loganathan, 2016). Further studies found that the Zwietering constants can only be used for systems with the same geometry. The study also concludes that the influence of impeller clearance on critical impeller speed cannot be

separately accounted for in the Zwietering equation, and that experimental work is needed to derive accurate constants (Ayranci and Kresta, 2014).

There have been both experimental and computational fluid dynamics (CFD) investigations into influence of stirred tank geometry on the double loop flow pattern generated by radial flow impellers (Figure 2-14). These studies determined that at clearances below 30 % of the tank diameter, the radial flow pattern of a Rushton turbine is converted to a single-loop axial flow pattern (Montante et al., 1999; Zhu et al., 2019). Single-loop flow patterns are considered more effective at suspending solids than a double-loop pattern (Zhu et al., 2019). Increasing the impeller clearance to over 33 % of the tank diameter results in the double loop flow pattern, which creates segregation in the tank, resulting in undesirable mixing behaviour (Ochieng et al., 2008).
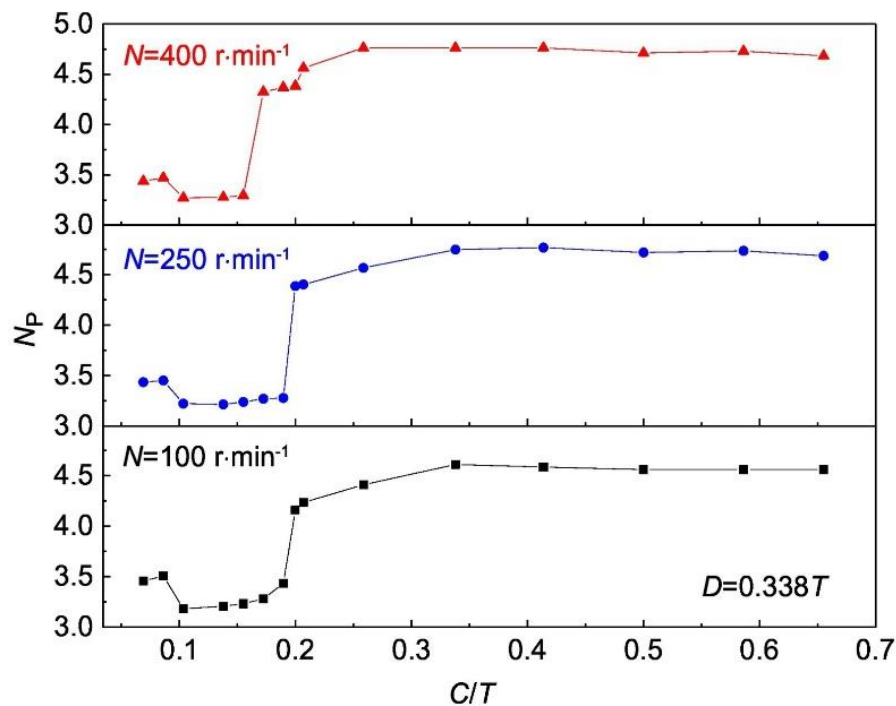
Figure 2-15 Influence of impeller clearance to tank diameter (C/T) on the impeller power number (Np) at multiple impeller speeds, image from (Zhu et al., 2019)

In Figure 2-15 it can be seen that not only does the impeller clearance influence the flow pattern of a radial impeller; it also influences the impeller power number. The decreased power number will reduce the power input needed to generate the impeller speed. Although clearance influences the impeller power number, it is not considered in the power number equation (Equation 2.3).

$$N_p = \frac{P}{\rho N^3 d^5}$$
(2.3)

Where:
N_p is the impeller power number
P is the required power input (W)
ρ is the fluid density (kg/m³)
N is the impeller rotation speed (rps)
d is the impeller diameter (m)

The transition from double-loop to single-loop also increases the macro mixing in the tank, reducing mixing time by approximately 16.4 % for the same impeller speed (Ochieng and Onyango, 2008). Both CFD and experimental studies found that the tracer was well dispersed with the axial flow pattern generated at low impeller clearances. Whilst this work highlights the importance of clearance on mixing and flow patterns in the tank, it has only been conducted with a Rushton turbine impeller. Investigations into the influence of clearance on mixing with different impeller geometries would be beneficial to understanding the importance of impeller configuration on mixing.

2.11 Modelling the Influence of Flow Characteristics on Spherical Agglomeration

CFD shows the flow patterns of the materials around the reactor and is a very useful tool to determine the degree and efficiency of mixing, as well as the shear profile in reactors. The basis of CFD analysis is Navier-Stokes equations. CFD is widely utilised in many industries as it can increase efficiency in mixing and fluid flow as it allows for the analysis of factors that influence flow such as particle size and pressure loss due to friction (Ofei and Ismail, 2016).

Population balance models (PBM) are widely used for granulation processes as they can determine the development of the product properties. PBM can range from simple one-dimensional models to more complex multi-dimensional models that solve simultaneous mechanisms (Yu et al., 2017).

As the mechanisms and regimes in spherical agglomeration are similar to those of HSWG, there will be similarities in the procedure for modelling HSWG and spherical agglomeration. The shear in both of these cases can be determined through a CFD model. This PhD thesis couples CFD simulations with PBM to determine the impact of flow characteristics on agglomerate production.

Analysis of CFD studies for slurries and suspensions are important, as although spherical agglomeration is mechanistically similar to HSWG, they differ greatly in the mixture composition. In HSWG, the mixture has a high volume of powder with lower liquid levels. Spherical agglomeration occurs in a ternary mixture resulting is a higher proportion of liquid to solid when compared to HSWG. This results in a spherical agglomeration mixture behaving more like a slurry or suspension.

2.11.1 CFD Modelling of HSWG

CFD studies of HSWG determine the flow patterns and mixing that occurs in the granulator. Table 2-7 shows a summary of CFD models used to investigate HSWG.

Table 2-7 Summary of CFD models of HSWG literature

Paper	Model System	Software	Process	Challenges	Advantages
CFD simulation of the high shear mixing process using kinetic theory of granular flow and frictional stress models – (Darelius et al., 2008)	CFD	ANSYS Fluent	• Eulerian-Eulerian approach o Particles are not treated individually but as a continuous medium • Kinetic theory of granular flow combined with frictional stress models. • Partial slip model used was derived for dilute particle systems and is a function of wall restitution for the particles	• Chopper flow could not be simulated as it impacts the flow pattern • High speed camera was used to find the velocity profiles close to the wall experimentally • Free slip model could not accurately predict the experimental bed height • Tangential wall velocity underpredicted	• Eulerian-Eulerian approach used allows for simulation of a large number of particles
Modelling of dense and complex granular flow in high shear mixer granulator – A CFD approach – (Ng et al., 2009)	CFD	ANSYS Fluent	• Eulerian approach • Segregated solver with implicit linearization – solves the model in 2 stages o 1st stage solves momentum equation for velocity profiles o 2nd stage Poisson type equation for pressure correction derived from continuity equation • Unsteady state with first-order temporal formulation	• Vertical swirl pattern cannot be accurately predicted with the continuum kinetic-frictional model • Over prediction of the tangential velocity at the wall	• Eulerian based continuum model can capture most features of the motion of solids

A compartmental CFD-PBM model of high shear wet granulation – (Yu et al., 2017)	CFD-PBM	ANSYS Fluent	• Constant volume Monte Carlo approach for the population balance model for internal and external coordinates • Two fluid CFD model based on the kinetic theory of granular flow • Sliding mesh approach used to allow for the rotation of the agitator	• Continuum based kinetic frictional model cannot successfully model the vertical swirl pattern as very complex • Large number of cells in the mesh needed to allow for accurate modelling of all parameters	• Less computationally expensive than DEM as it simulates bulk flow • Bed height can be well predicted
CFD simulation of transient particle mixing in a high shear mixer – (Nguyen et al., 2014)	CFD	ANSYS Fluent and MATLAB	• Eulerian-Eulerian multiphase framework used for particle flow • Kinetic theory of granular flow and the frictional stress model used in the transport equations • Solid velocity by the wall determined using a high-speed camera • Partial slip model was used for wall behaviour but needs further development to increase accuracy	• High-speed camera needed to determine the velocity of the particles near the wall and these differed to modelled wall velocities • Cohesivity could be incorporated into the frictional stress model and partial slip model can be further developed	• Rapid mixing behaviour can be captured by the model and this matches well with experimental results • Using a tracer allowed for the characterisation of the mixing mechanism
Analysis of mesoscale effects in high-shear granulation through a computational fluid dynamics-population balance coupled compartment model –	CFD-PBM	ANSYS Fluent and MATLAB	• CFD in fluent and data extracted to MATLAB for analysis • Coupled flow field and population balance solver • Uses kinetic theory of granular flow. Constant volume Monte Carlo (CVMC) method is used • Two-dimensional population balance model – solid and liquid	• Took 5 days for the system to reach steady state • Not accurate for flows of dense granular materials • Spatial compartmentalisation can influence the final granule size distribution	• Shows the stress and collision peak at the agitator blades for both aggregation and breakage

(Abrahamsson et al., 2018)				• Breakage and compaction mechanisms can be developed further	
Modelling dilute and dense granular flows in a high shear granulator – (Khalilitehrani et al., 2014)	CFD	ANSYS Fluent	• Standard kinetic theory of granular flow is used • Dense region modelled as a visco-plastic fluid • Cell size was equivalent to the size of 3-4 particles. Hexahedral mesh was used • Eulerian-Eulerian framework was used	• Viscosity is underestimated for intermediate particle concentrations – kinetic theory of granular flow needs modification to improve accuracy – underestimates viscosity	• Model matches the temperatures and volume fractions obtained experimentally • Velocity field is also captured quite well
Continuum modelling of multi-regime particle flows in high-shear mixing – (Khalilitehrani et al., 2015)	CFD	ANSYS Fluent	• Kinetic theory of granular flow is used for dilute region • Dense region treated with pseudo-plastic rheology • Eulerian-Eulerian framework • Sliding mesh used for the agitator rotation	• Overestimation of axial movement when using kinetic theory of granular flow + friction	• Good description of multi-regime granular flows especially in the intermediate range (neither dense nor dilute and the transition between these) • Matches experimental results well

As Table 2-7 shows, in CFD simulations of HSWG, an Eulerian-Eulerian approach is extremely common. The Eulerian-Eulerian approach is applicable to systems with a high volume of the dispersed phase. A Eulerian-Eulerian system is a two-fluid model that contains a continuous phase, the liquid, and a dispersed phase, the solid (Ofei and Ismail, 2016). In HSWG, there are large volume fractions of solids.

Another common feature of the CFD models in Table 2-7 is the use of the kinetic theory of granular flow (KTGF). The derivation of KTG is based on the classical kinetic theory of dense gases but this theory has been extended by considering interactions of non-ideal particles (Darelius et al., 2008). Statistical mechanics have been used to describe particle velocity, which is broken down to a local mean velocity and a random fluctuating velocity (Gantt and Gatzke, 2006).

The partial slip model is also consistently used by the CFD simulations shown in Table 2-7. This model was initially developed for dilute flow. Due to the partial slip model being based on dilute flow, it is based on coefficients of wall restitution which may reduce the relevance of this model for dense systems that are greatly impacted by frictional stress (Darelius et al., 2008). Partial slip is useful for system boundaries as using a no-slip condition can lead to overestimation of stresses in the system (Khalilitehrani et al., 2015). Using the partial slip model will allow for the range between no slip and free slip to be covered (Yu et al., 2017).

For stirred tank CFD simulations, a sliding mesh approach is often used for modelling the agitator; this can be seen in many of the models shown in Table 2-7. The sliding mesh approach allows for one part of the system geometry to rotate relative to the rest of the geometry. The fluxes of momentum across the geometry interface are matched for each time step (Darelius et al., 2008). Using the sliding mesh approach increases the accuracy of the model and reduces the need for experimental input although it does require more computational time (Jaworski et al., 1997).

2.11.2 CFD Modelling of Slurries and Suspensions

Although the mechanisms of spherical agglomerate formation are the same as high shear wet granulation, spherical agglomeration occurs in suspension. For this reason, the flow patterns in spherical agglomeration will be closer to that of slurries and suspension. A review of CFD modelling of slurries and suspensions has been carried out to identify appropriate CFD methodologies for suspension, and can be seen in Table 2-8.

The k-ε turbulence model is often used for the CFD modelling of slurries and suspensions. This model is one of the most common turbulence models and results in two extra transport equations being included to represent turbulence in the flow (Monk and Chadwick, 2017). The k parameter of the k-ε model is the turbulent kinetic energy; ε refers to the turbulent dissipation and this determines the scale of the turbulence (Mon Soe and Yu Khaing, 2017).

For CFD analysis of slurries and suspensions, the Euler-Granular multiphase model is commonly used. The major assumption of this model is that each phase present in the mixture coexists at all points in the vessel as interpenetrating continua. To solve the continuity and momentum equations for all phases present coefficients of interphase exchange and pressure are used (Gohel et al., 2012).

To simulate impeller rotation, a multiple reference frame (MRF) can be used. The MRF approach was proposed by Luo et al. 1994, in this approach a stationary portion of the reactor and a moving portion. In the case of a stirred tank reactor, the agitator and any flow that is within the confines of the agitator would be in the moving frame. The rest of the tank, including baffles and tank walls, are stationary in the CFD simulation (Patil et al., 2018). Using MRF generates an approximation of the results. However, it is considered to be a satisfactory approximation especially if the impact of the interactions between the agitator and baffles is weak (Gohel et al., 2012).

Table 2-8 Summary of slurry and suspension CFD modelling literature

Paper	Model Type	Software	Process	Advantages
CFD Modeling of Solid Suspension in a Stirred Tank: Effect of Drag Models and Turbulent Dispersion on Cloud Height – (Gohel et al., 2012)	CFD	ANSYS Fluent	• Euler-Granular theory – each phase coexists at all points in the vessel • One fluid phase and one solid phase • Kinetic Theory of Granular Flow • Hexahedral mesh – no mesh on the agitator • Consistent mesh density for most of tank with increased density at the walls	• Multiple reference frame approach used to model stirring action of agitator – successful as weak interaction between agitator and baffles • Drag models have limited impact on the results whilst still producing results that are close to experimental values
Experimental and CFD studies of solid-liquid slurry tank stirred with an improved Intermig impeller – (Zhao et al., 2014)	CFD	ANSYS Fluent	• Eulerian-Granular multiphase model • k-ε turbulence model • Agitator represented by unsteady sliding mesh	• Grid sizes have little impact on the results produced, therefore 260000 is acceptable and does not need increasing to 390000 or 520000
Computational Fluid Dynamics Simulation of the Solid Suspension in a Stirred Slurry Reactor – (Khopkar et al., 2006)	CFD	ANSYS Fluent	• Euler-Euler fluid model • Multiple reference frame used for agitation simulation • Used a commercial grid generator and tested gird sizes that generated between 10,000 and 800,000 cells • SUPERBEE limiter function was used to avoid nonphysical oscillations	• Useful for simulating large stirred tanks of slurry or suspension • Good agreementwith experimental data • 200,000 cells captured the flow pattern effectively
Solids Suspension Study in a Side-Entering Stirred Tank Through CFD Modeling – (Chen and Xiao, 2013)	CFD	ANSYS Fluent	• Eulerian-Granular multiphase model • k-ε turbulence model • Multiple reference frame approach used for rotation of the agitator • Tetrahedral elements that grow in size further away from the agitator	• Combining the Eulerian-Granular model with the k-ε turbulence model increases accuracy of model prediction • Flow patterns of liquid show that flow action undergoes compression due to solid particle presence so there can be poor mixing towards the top of the vessel

Analysis of Energy Dissipation in Stirred Suspension Polymerisation Reactors Using Computational Fluid Dynamics – (Nogueira et al., 2012)	CFD	CHAM PHOENICS 2008	- Cylindrical coordinate system - IPSA multiphase model k-ε turbulence model - Isothermal system and initially at rest - Used a non-slip boundary condition for the wall of the vessel	- Tested at multiple agitation speeds and the secondary forces that develop due to stirring were considered by habilitating the swirl option - Tested multiple reactor scales and had general rules for dimensions – diameter to height ratio of 5:18 and the agitator diameter is 0.9 times vessel diameter - Coalescence in bulk of liquid and breakage closest to agitator
A Study of the Mixing Performance of Different Impeller Designs in Stirred Vessels Using Computational Fluid Dynamics – (Torotwa and Ji, 2018)	CFD	ANSYS Fluent	- Multiple reference frame approach for rotation of agitator - Standard k-ε turbulence model was used - Reynolds-averaged Navier Stokes Equations is used as it is most realistic or the turbulent mixing - Pressure-based steady state and absolute velocity conditions used - Fluid flow and agitator were modelled as two separate regions that had interactions and a fine mesh was used for increased stability	- Generated velocity profiles matched the experimental results - Produced data allows for choosing optimal design of mixing equipment and scale up - Reynolds-averaged Navier Stokes was more realistic than Large Eddy Simulation or Direct Numerical Simulation - Impeller design impacts the performance and flow in a stirred vessel
CFD Predictions of Solids Distribution in Stirred Vessel – (Kubicki and Lo, 2012)	CFD	STAR-CCM+	- Eulerian multiphase model - Standard k-ε turbulence model was used - Multiple reference frame and Rigid body motion is used for the rotation of the agitator - Liquid and solid treated as interpenetrating continua - Mesh elements were polyhedral shaped	- Combining multiple reference frame and rigid body motion allows for better flow field prediction as it resolves the interactions between the agitator and the impeller - Finer mesh closer to the agitator reduced severity of gradients

2.11.3 Analysis of CFD Software

To be able to produce the CFD-PBM simulations for a stirred tank, the appropriate software must be chosen. Therefore, a software analysis needs to be completed to determine the simulation methodology.

2.11.3.1 *ANSYS Fluent*

ANSYS Fluent can be used for a wide variety of flow simulations due to it having extremely versatile code (Haghgoo, 2013). This results in Fluent being one of the most popular commercial CFD programs (Zou et al., 2018). Fluent contains powerful tools in a tightly integrated program allowing for results to be obtained quickly (Haghgoo, 2013). Although Fluent has high license costs, licenses were readily available through the University of Sheffield. The availability of licenses, increased support and an integrated platform made Fluent the CFD chosen package for this work.

2.11.3.2 *COMSOL*

COMSOL is a CFD package with a user-friendly graphical interface (Hysing, 2011). A major attraction of COMSOL compared to other CFD packages is the finite element method for numerically solving partial differential equations (Vladimir et al., 2012). COMSOL use is increasing due to it being widely accepted as a proper tool for heat transport simulation (Vlug, 2014). In comparison to other CFD software, COMSOL requires greater computing power due to it not using cell centred degrees of freedom (Hysing, 2011).

2.11.3.3 *STAR-CCM+*

STAR-CCM+ is a commercial CFD package that numerically simulates continuous mechanics problems (Hernandez-Perez et al., 2011). Many industries use STAR-CCM+ making it one of the most popular commercial CFD packages (Zou et al., 2018).

2.11.3.4 *OpenFoam*

OpenFoam is a free software used for CFD simulations. C++ coding is used to solve continuum mechanics problems easily and reliably (Jasak, 2009). There are two major versions of OpenFoam. One is developed by a corporation, and the other is community driven, and evolved independently to the main development branch (Beaudoin et al., 2014). A Linux operating system is required to run OpenFoam (Nilsson, 2006).

2.11.3.5 *Barracuda VR*

Barracuda VR can be used to simulate fluidised systems that involve chemical reactions of particulate solids, such as catalysts (Haghgoo, 2013). Making it applicable for modelling circulating fluidised beds to compare multiple drag models (Bandara et al., 2019). There is a simple, graphical user interface, including a logical workflow. The software also includes mesh generation and post-processing (Haghgoo, 2013).

2.11.3.6 *M-Star*

M-Star is a relatively new CFD software that uses a Lattice Boltzmann approach during CFD simulations. This reduces computational time for transient systems when compared to a conventional CFD package that calculates a Navier-Stokes based solution (Kuschel et al., 2023). CFD simulations of stirred tanks have been successfully performed in M-Star, with a particular emphasis on M-Star's ability to solve large eddy simulations (LES) in turbulent mixing (Giacomelli and Van den Akker, 2021; Kuschel et al., 2023; Hanspal et al., 2023).

2.11.3.7 *Comparison of Software*

To determine which CFD software is most suitable to use for this research a comparison of them is conducted. Table 2-9 shows the advantages and disadvantages of the different CFD software packages.

Table 2-9 Evaluation of various CFD software packages

Software	Advantages	Disadvantages
FLUENT	• Greater accuracy with reduced run-time for flow around a turbine blade compared to COMSOL (Vlug, 2014) • Integrated package that has both grid generation and post-processing (Haghgoo, 2013) • Allows the use of fine grids whilst using lower memory than COMSOL (Hysing, 2011) • Extremely versatile code that can be applied to many uses (Haghgoo, 2013) • Variable values can be found at all points in the system (Zou et al., 2018) • Includes complex pyrolysis model (Krusch et al., 2018)	• High license costs (Zou et al., 2018)
COMSOL	• User friendly with graphical user interface (Hysing, 2011) • Accurate calculation of heat transfer values (Vladimir et al., 2012) • Can be operated in conjunction with MATLAB (Vlug, 2014) • Can enter coupled systems of partial differential equations (Haghgoo, 2013)	• Relies heavily on direct solvers limiting it to certain applications (Hysing, 2011) • Processing time is increased for flow around turbine blade and results are less accurate compared to Fluent (Vlug, 2014)
STAR-CCM+	• One of the most popular CFD software (Zou et al., 2018) • Powerful mesh generator and has the ability to generate mesh for imported geometries (Podila and Rao, 2015) • Contains multiple overset interpolation methods and specifying the correct method can increase the accuracy of results (Chandar and Boppana, 2018)	• High license costs (Zou et al., 2018) • Values of variables can only be found at selected points (Zou et al., 2018) • Time consuming to create geometries in STAR packages, therefore a third-party software is often used (Podila and Rao, 2015)
OpenFoam	• Free to use software (Vlug, 2014) • Background meshes can have overset interfaces (Chandar and Boppana, 2018) • Allows for polynomial interpolation between meshes (Chandar and Boppana, 2018) • Continuously developed by both a company and users to produce different results (Beaudoin et al., 2014) • Communicates well with post-processing packages and mesh generators (Shademan et al., 2013)	• Requires Linux operating system (Vlug, 2014) • Not as user friendly as other CFD packages (Vlug, 2014)
Barracuda VR	• Accurate simulation of chemical reactions with particle/gas flows (Haghgoo, 2013)	• Does not include complex pyrolysis model (Hysing, 2011)

	• Good user interface with logical workflow, easy mesh generation and post-processing (Haghgoo, 2013)	• Over prediction of pressure drop in comparison with experimental results (Jayarathna et al., 2017)
M-Star	• Reduced computation time for a Lattice-Boltzmann solver compared to Navier-Stokes (Kuschel et al., 2023) • Proven track record for solving large eddy simulations in turbulent mixing (Giacomelli and Van den Akker, 2021)	• M-Star is a relatively new software and has less validation literature available with peer-reviewed papers published after October 2020 (M-Star Simulations, 2023), this is after this thesis had commenced

2.12 Population Balance Modelling

PBM is a useful tool for predicting product properties for many industrial processes. Equation 2.4 shows the one-dimensional population balance equation (Litster, 2016).

$$\frac{\partial Vn(x,t)}{\partial t} = \dot{Q}_{in}n_{,in}(x) - \dot{Q}_{ex}n_{,ex}(x) + \frac{\partial VGn(x,t)}{\partial x} + V\dot{b}(x) - V\dot{d}(x) \qquad (2.4)$$

Where:

V is the suspension volume (m³)

$n(x,t)$ is the number of particles of diameter x at time t

G is the growth of particles

$\dot{Q}_{in}$ and $\dot{Q}_{ex}$ are the volumetric flowrates in and out of the system volume (m³/s)

n_{in} and n_{ex} are the number of particles of size x in and out of the system volume (m⁻⁴)

$\dot{b}(x)$ is the frequency distribution of birth of particles of size x (m⁻⁴/s)

$\dot{d}(x)$ is the frequency distribution of death of particles of size x (m⁻⁴/s)

Equation 2.4 assumes that the system is a well-mixed control volume and focusses on particles of a specific size (x). The equation considers un-normalized size distributions in terms of volumetric flows (Litster, 2016).
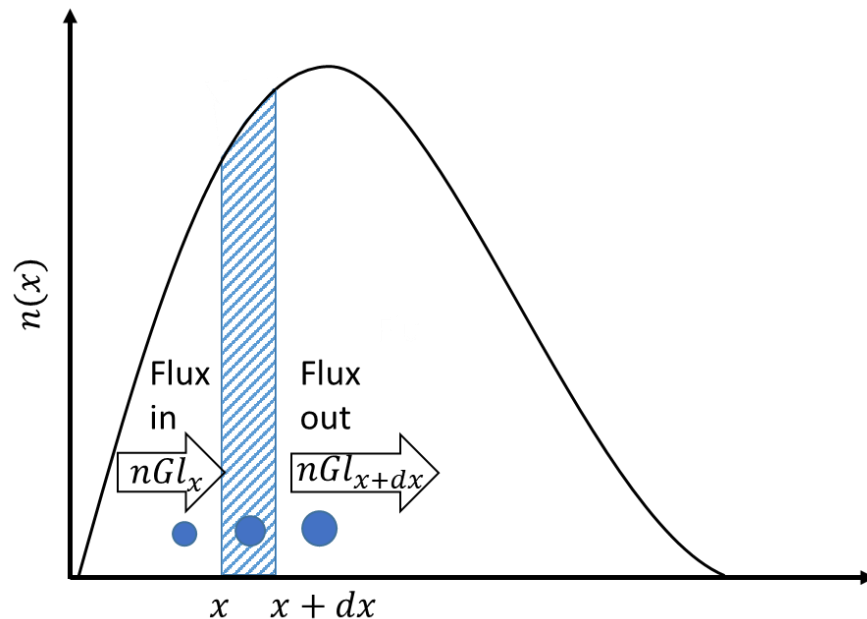
Figure 2-16 Differential growth changing the particle size distribution, image adapted from (Litster, 2016)

Figure 2-16 demonstrates the purpose of population balance modelling. The aim of a PBM is to determine the number of particles of size x to $x + dx$ in a specified control volume. Equation 2.4 considers the processes that effect the number of particles of the desired size range, termed $n(x)$. rticle size in a given volume.

Table 2-10 explains the terms in Equation 2.4, and how they are used to monitor the particle size in a given volume.

Equation Term	Explanation
$\dfrac{\partial V n(x,t)}{\partial t}$	The accumulation of particles of size x, in a control volume of size V, at a given time t
$\dot{Q}_{in} n_{,in}(x)$	The flow in of particles of size x into the control volume
$\dot{Q}_{ex} n_{,ex}(x)$	The flow out of the control volume of particles of size x
$\dfrac{\partial V G n(x,t)}{\partial x}$	The growth of particles of size x, in a control volume of size V, at a given time t
$V \dot{b}(x)$	Birth of particles of size x in the control volume, nucleation is an example of this
$V \dot{d}(x)$	Death of particles of size x in the control volume, breakage of particles is an example of this

Many industrial particulate processes, including crystallisation and high shear wet granulation have PBMs developed to predict product performance. Increased understanding of existing particulate PBMs will allow for improvements to population balance modelling of spherical agglomeration.

2.12.1 PBM for Granulation

Granulation is mechanistically similar to spherical agglomeration and therefore, there should be similarities in PBM construction for the two processes. As discussed in Section 2.9, there are three mechanisms involved in granulation, nucleation and wetting, coalescence and consolidation, and breakage and attrition. In the PBM framework, different kernels represent the different mechanisms. These kernels are discussed in the following sections.

2.12.1.1 *Nucleation and Wetting Kernel*

In the first stage of granulation, nuclei form through the wetting of the powder bed by a binder (Wildeboer et al., 2005). Nucleation is a rate process that influences granule properties and therefore needs including in a PBM for granulation (Bellinghausen et al., 2019). The mechanism of nuclei formation is complex, resulting in a nucleation kernel being challenging to develop (Wauters et al., 2003).

Models for nucleation consider the nucleation regime map proposed by Hapgood et al., 2003. The nucleation regime is determined by the drop penetration time and the dimensionless spray flux. Equation 2.5 is for drop penetration time and Equation 2.6 is for dimensionless spray flux (Hapgood et al., 2003). The regime map is shown in Figure 2-17.

$$\tau_p = 1.35 \frac{V_0^{2/3}}{\epsilon^2 R_{pore}} \frac{\mu}{\gamma_{LV} \, cos\theta_d} \tag{2.5}$$

Where:
τ_p is the drop penetration time (s)
V_0 is the volume of the liquid droplet (m³)
ϵ is the porosity of the powder bed
R_{pore} is the pore radius (m)
μ is the viscosity of the liquid (Pa.s)
γ_{LV} is the surface tension of the liquid (N/m)
θ_d is the liquid dynamic contact angle in a capillary (rad)

$$\varphi_a = \frac{3\dot{V}}{2\dot{A}d_d}$$
(2.6)

Where:
φ_a is the dimensionless spray flux
$\dot{V}$ is the volumetric spray rate (m³/s)
$\dot{A}$ is the area flux of powder (m²/s)
d_d is the diameter of the droplets (m)
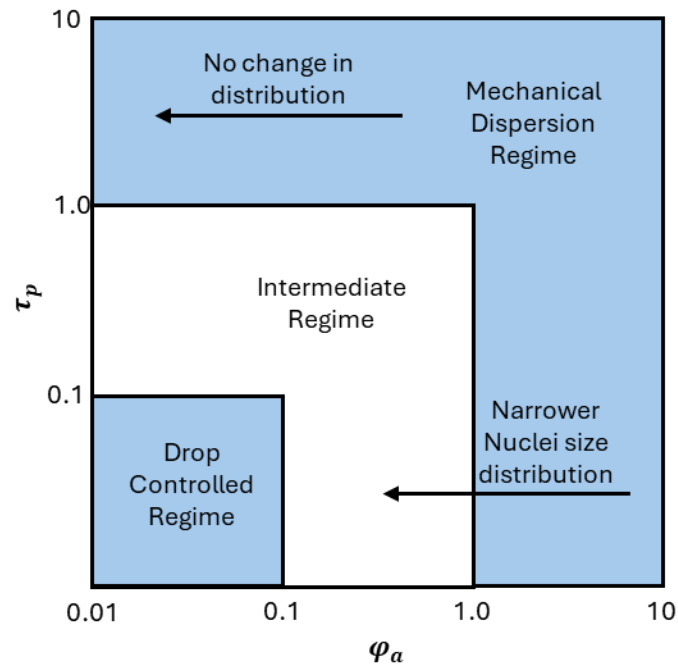
Figure 2-17 Nucleation regime map generated by (Hapgood et al., 2003), image reproduced from (Wildeboer et al., 2005)

Two commonly used nucleation models for a granulation PBM are the drop nucleation model by Barrasso and Ramachandran, 2015, and the model proposed by Hapgood et al., 2009 (Bellinghausen et al., 2019).

In the drop nucleation method, the droplets of binder have a lognormal size distribution. The liquid sprays onto a bed of fine powder, and the liquid fills the inter-particle voids. In this model, the droplet size, bed porosity and maximum pore saturation will influence the granule size. An assumption of this model is that the primary particles are much smaller than the binder droplets (Bellinghausen et al., 2019).

The nucleation model proposed by Hapgood et al., 2009, uses a Poisson distribution to estimate the nuclei size distribution. Using a probability function, such as a Poisson distribution, allows the model to predict the likelihood of events occurring in a specified region. In the Hapgood nucleation model, the Poisson distribution predicts the number of droplets that land in a certain area of the powder bed. Results for this model at low penetration time and low spray flux were consistent with experimental results. There was divergence between experiments and modelling results when the spray flux was greater than 0.5. This model would be most accurate for processes operating in the drop controlled nucleation regime (Hapgood et al., 2009).

Bellinghausen et al., 2019 recommended using the lognormal distribution method for nucleation PBMs if the spray flux is under five. With the lognormal distribution, there are model parameters that will need recalibrating for different operating conditions. This study found that the Poisson distribution model proposed by Hapgood et al., 2019, under predicts the size distribution of nuclei if the system is not operating within the drop-controlled regime (Bellinghausen et al., 2019). Hapgood et al., 2009, also highlighted the inaccuracy of the Poisson distribution method for nucleation regions other than the drop-controlled regime.

Overall, nucleation is a crucial process in granulation, but there is limited understanding of this process, as it is difficult to isolate nucleation. Although there are models such as lognormal distribution and the Hapgood model, there is still work needed to capture the kinetics of nucleation for granulation purposes.

2.12.1.2 *Coalescence and Consolidation Kernel*

More granulation mechanism research focusses on coalescence compared to the other granulation mechanisms, and therefore there are more coalescence kernels. Theoretical coalescence models in literature are useful for predicting whether the collision of two particles will result in them coalescing or rebounding (Iveson et al., 2001).

Iveson, 2001, proposed that there are two types of coalescence models. In class 1 models, the colliding particles will either stick together or rebound. For class 2 models, either the collided particles survive as one new particle, or they separate. Figure 2-18 shows a schematic diagram of the various coalescence models.
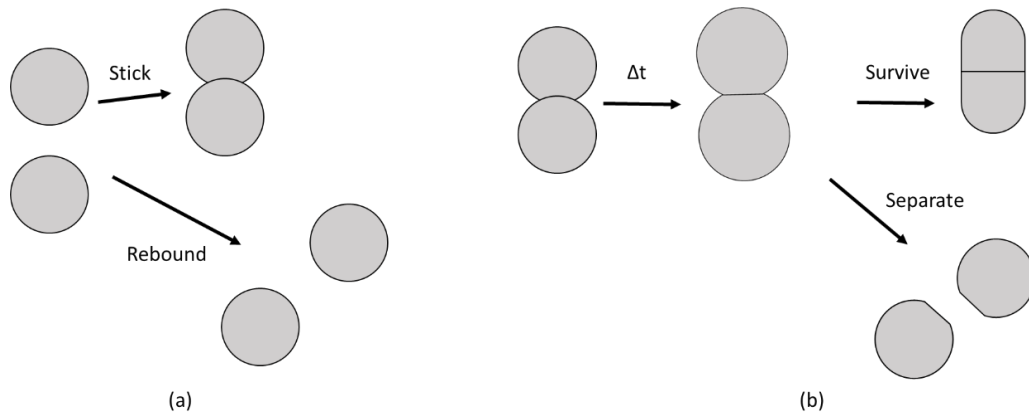
Figure 2-18 Schematic of the different coalescence model classifications, (a) class 1: stick or rebound, and (b) class 2: survive or separate, adapted from (Iveson, 2001)

A class 1 coalescence model operates with the assumption that granules move freely, and the elastic properties of the system are important. In this model, coalescence can only occur if the collision kinetic energy is dissipated. If the energy is not dissipated, the granules will rebound and not coalesce. Multiple coalescence models are class 1, but they differ in their selection of energy dissipation mechanisms. Some of these mechanisms are plastic deformation, elastic losses, and contact surface adhesion energy. A major assumption of class 1 models is that granules formed through coalescence will not undergo breakage due to subsequent impacts (Iveson, 2001). Figure 2-18(a) shows a class 1 coalescence model.

Class 2 coalescence models do not consider the elastic effects for initial collisions. This model assumes that either the granules are plastic, or they are surrounded by other granules and cannot move freely.

Due to the surrounding granules, collisions between granules will occur for a limited time and bonds develop between the granules in contact. The strength of the bond between granules needs to be sufficient to withstand other collisions and shear forces in the system. If the bond is strong enough, the bonded granules will coalesce (survive). If the bond is too weak then the granules will break apart (separate). Bond strength may be influenced by the contact time between particles, and the plastic deformation of granules (Iveson, 2001). A summary of coalescence models in literature and their classification can be seen in Table 2-11.

Table 2-11 Summary of existing coalescence models and which (Iveson, 2001) classification they fall under, information from model papers and (Iveson et al., 2001)

Model	Iveson 2001 Classification	Model Description
(Ouchiyama and Tanaka, 1975)	Class 2	This model is class 2 as it considers plastic deformation; the process is in a drum granulator, which consists of compression and separation zones.
(Ennis et al., 1991)	Class 1	The model considers head on collisions between particles that have a viscous fluid layer on them. The coefficient of restitution is used for calculating rebound velocity.
(Moseley and O'brien, 1993)	Class 1	In this model, the particle collisions occur at an angle. Elastic forces calculate the radial interaction force between particles.
(Simons et al., 1994)	Class 2	This model focusses on predicting the rupture energy of liquid bridges between particles, removing the need to use the Laplace-Young equation, which is complex and time consuming.
(Seville et al., 1998)	Class 2	The model considers visco-plastic sintering of particles and the contact time between particles.
(Thornton and Ning, 1998)	Class 1	This stick/bounce model considers elastic-plastic particle deformation. Collisions between particles occur head on. The coefficient of restitution is dependent on particle velocity parameters including the velocity of particle impact.

2.12.1.3 *Breakage and Attrition Kernel*

Although much of the development for PBM of granulation considers the coalescence kernel, there have been some developments in generating breakage kernels. Breakage is an important rate process in granulation as it influences the final product size distribution (Ramachandran et al., 2009). Table 2-12 summarises models developed for breakage during granulation.

Table 2-12 Description and limitation of breakage modelling for granulation

Model	Description	Limitations
(Biggs et al., 2003)	This model considers breakage to be negative aggregation. Aggregation is the only parameter involved in the model, which incorporates breakage by extending the aggregation equation to include a negative term (Biggs et al., 2003).	Breakage is a first-order rate process, but aggregation is second-order, meaning this model is inaccurate on a physical basis (Ramachandran et al., 2009).
(Salman et al., 2003)	Experimental observations of breakage due to impact in fertiliser granules developed an empirical breakage model. The probability of the impact causing damage to the granule is influenced by impact velocity, impact angle and particle size (Salman et al., 2003).	This model is limited to the experimental conditions and cannot be applied as a general breakage model (Ramachandran et al., 2009).
(Tan et al., 2004; Tan et al., 2005)	This model includes a binary breakage function. The binary function allows the granule to break into both small and large fragments. Other breakage models (fragmentation and attrition) were considered but the binary model improved the model accuracy when compared with experimental results (Tan et al., 2005).	This work used experimental data to fit model parameters, which may limit how appropriate this model is for other applications (Ramachandran et al., 2009).
(Dhanarajan and Bandyopadhyay, 2007)	This model considers breakage of granules to be directly proportional to the energy of impact. The breakage is also inversely proportional to the strength of the granule. There was good agreement between experimental and modelled results (Dhanarajan and Bandyopadhyay, 2007).	The assumption that binder content is the main factor in granule strength without considering binder properties limits the accuracy of the model. This model also neglected to consider velocity when calculating the kinetic energy of the granule (Ramachandran et al., 2009).

2.12.2 Modelling Spherical Agglomeration

Development of a PBM for spherical agglomeration will allow for prediction of agglomerate properties based on characteristics of the primary materials used in the process. Spherical agglomeration studies are often extremely system specific and require experimentation to determine the optimal conditions. A predictive PBM would reduce the number of experiments needed to design a spherical agglomeration process.

As spherical agglomeration is mechanistically similar to wet granulation, it can be assumed that a spherical agglomeration PBM has similar framework to a PBM for wet granulation. Modelling attempts of the various spherical agglomeration mechanisms are discussed in this section.

2.12.2.1 *Nucleation*

As Figure 2-1 shows, there are two pathways for nucleation in spherical agglomeration; the immersion mechanism and the distribution mechanism. For immersion nucleation to occur, the primary particles must be much smaller than the droplets of bridging liquid. The particles will then collide with the bridging liquid droplet and cover the droplet surface layer. The particles are then immersed into the bridging liquid droplet; this process continues until no more particles can fit inside the droplet (Pitt et al., 2018; Arjmandi-Tash et al., 2019; Ahmed et al., 2023). Figure 2-19 shows a schematic of the immersion mechanism. Distribution nucleation occurs when the primary particles are larger in size than the bridging liquid droplets. In this mechanism, the bridging liquid droplets stick to the outside of the particles, forming a liquid coating. This coating allows for aggregation between the particles, resulting in nuclei formation. In the immersion mechanism, the agglomerates grow to the size of the bridging liquid droplets. In theory using the immersion mechanism would allow for greater control over agglomerate properties; therefore, this is the favoured nucleation mechanism (Pitt et al., 2018; Arjmandi-Tash et al., 2019; Ahmed et al., 2023).
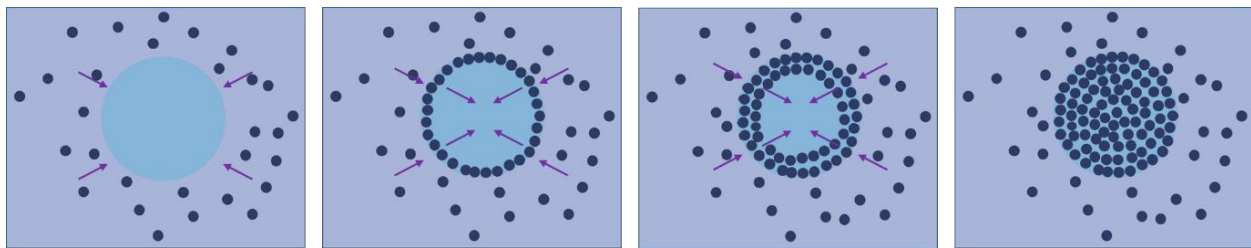
Figure 2-19 Schematic diagram of immersion in the spherical agglomeration process, adapted from (Arjmandi-Tash et al., 2019)

Arjmandi-Tash et al., 2019 proposed a mechanistic mathematical model for immersion nucleation in spherical agglomeration. For nucleation to occur, the primary particles need to collide with the bridging liquid droplets and the system needs to be undergoing agitation for this contact to occur. This model proposes that two scenarios that may occur when the particles collide with the bridging liquid (Arjmandi-Tash et al., 2019).

In the first scenario, the bridging liquid must preferentially wet the particles in comparison to the mother solution. The wettability of the particles in the bridging liquid allows the particles to penetrate into the droplets of the bridging liquid. Penetration into the droplets can occur at any collision velocity and surface tension, but these parameters may limit the immersion kinetics (Arjmandi-Tash et al., 2019).

For the second scenario, the bridging liquid does not wet the particles as well as the mother solution. In this system the particles will either stay at the droplet surface or rebound from it. Penetration of particles into the droplets can only occur if high impact velocities allow the particle to overcome the interfacial tension (Arjmandi-Tash et al., 2019).

The mathematical model proposed by Arjmandi-Tash et al., 2019 has been implemented into a PBM by Ahmed et al., 2023. gPROMS FormulatedProducts (Siemens, Process Systems Enterprise Ltd.) was used

for the PBM construction. This work used a HSWG framework with custom rate kernels to model spherical agglomeration (Ahmed et al., 2023). The nucleation kernel in this model is shown in Equation 2.7.

$$\dot{b}_{a,nuc}(x,t) = \frac{\dot{L}_{in,p} n_d(x,t)}{V_d} \tag{2.7}$$

Where:

$\dot{b}_{a,nuc}(x,t)$ is the birth of nuclei of size x at time t

$\dot{L}_{in,p}$ is the bridging liquid total volumetric flowrate (m³/s)

$n_d(x,t)$ is the bridging liquid number density (no/m⁴)

V_d is the volume of the formed nuclei, t assumed to be equal to the nuclei diameter (m³)

2.12.2.2 Growth

Initial attempts at modelling focused on the agglomeration in suspension method, with a view for applying the system to fine coal powder (Bemer, 1979). In the work by Bemer, 1979, experiments were performed using powdered glass in a binary solvent system. Observations from these experiments led to Bemer generating a PBM to predict agglomerate size. This model is called the coalescence-breakage model. The coalescence-breakage model includes collision induced coalescence, growth by layering, and breakage due to crushing. A coalescence frequency and efficiency model was used as the basis of Bemer's coalescence-breakage model and worked well for steady-state agglomerate size distribution predictions (Pitt et al., 2018).

Another approach to modelling growth in spherical agglomeration is through an agglomeration kernel, rather than coalescence. Madec et al., 2003; developed a multidimensional kernel for agglomeration in suspension. This kernel used a Monte Carlo solving approach. The agglomeration kernel included the bridging liquid composition, allowing for the model to determine if the BSR was within the optimal range for agglomeration. Equations 2.8-2.10 show the agglomeration kernel (Madec et al., 2003).

$$\beta = \beta_0 \left(L_i^3 + L_j^3\right)\left(\left(c_i + c_j\right)^\alpha \left(100 - \frac{c_i+c_j}{2}\right)^\delta\right)^\alpha \tag{2.8}$$

$$c_i = \frac{volume\ of\ liquid}{volume\ of\ agglomerate} \times 100 \tag{2.9}$$

$$\delta = \left(\frac{1-C_{opt}}{C_{opt}}\right)\alpha \tag{2.10}$$

Where:

β is the rate of agglomeration

β_0 is the agglomeration rate constant (m/s)

L_i and L_j are the agglomerating particle sizes (m)

c_i and c_j are the bridging liquid compositions in each particle (volume percentage)

δ is the solid particle weight coefficient

α is the liquid droplet weight coefficient

C_{opt} is the optimal value for bridging liquid composition

The derivation for C_{opt} means that agglomeration only occurs when particles have the correct amount of bridging liquid. If too much or too little bridging liquid is present a collision between particles is unable to occur (Madec et al., 2003; Pitt et al., 2018). The incorporation of the bridging liquid composition and the

liquid droplet weight coefficient ensure that particles must be sufficiently wetted for agglomeration to occur. This model did produce realistic agglomerate size distributions for spherical agglomerate processes, however it did not consider nucleation or growth (Madec et al., 2003).

Experimental data was incorporated into a modelling study by Blandin et al., 2005 that utilized the four-step agglomeration mechanism proposed by Bemer in 1979. The four mechanisms proposed are:

1. Primary particles become wetted by bridging liquid, causing nuclei formation
2. The nuclei collide with each other, resulting in compaction which reduces the mean diameter
3. Coalescence and consolidation lead to agglomerate growth. This stage is influenced by the system hydrodynamics, as well as process conditions, e.g. BSR and impeller speed
4. Agglomeration ends when the agglomerates cannot undergo more compaction

From the experimental study by Blandin, it was found that the agglomeration of salicylic acid microcrystals was strongly influenced by the BSR with the solids concentration having little influence on agglomeration. Blandin et al., 2003 also found that the agglomerate size was inversely proportional to the impeller speed. These observations influenced the formation of a model to predict the mean size of agglomerate products; this can be seen in Equation 2.11 (Blandin et al., 2005).

$$L_{NB} = \alpha C_s{}^{0.3} N_{PTD}{}^{-0.6} BSR^{2.1} \tag{2.11}$$

Where:
L_{NB} is the size of the agglomerate products
α is a proportionality constant influenced by material properties
C_s is the concentration of solids in the system (mol/m³)
N_{PTD} is the impeller speed (rps)
BSR is the bridging liquid to solid ratio

Equation 2.11 is an empirical correlation developed for one material system and therefore cannot be applied to general spherical agglomeration studies. Further work from Blandin et al., 2005 resulted in the generation of a spherical agglomeration model for the growth of agglomerates. The equations for this model are shown in Equations 2.12 to 2.18 (Blandin et al., 2005).

$$\frac{\partial \varphi(L,t)}{\partial t} = R_A(L,t) \tag{2.12}$$

$$r_{agg}(l,t) = K(i,j,t)N_i(t)N_j(t) \tag{2.13}$$

$$K(i,j,t) = f(i,j,t)eff(i,j,t) \tag{2.14}$$

$$f(i,j,t) = C_{coll}\alpha(i,j,t)\left(\frac{\pi}{4}\right)\left(S_i + S_j\right)^2 \left[\overline{u(S_i)^2} + \overline{u(S_j)^2}\right]^{0.5} \tag{2.15}$$

There are two equations for $eff(i,j,t)$ (Equations 2.16 and 2.17):

$$\text{If } f_{adh}(i,j,t) \geq f_{sep}(i,j,t) \quad then \quad eff(i,j,t) = \frac{f_{adh}(i,j,t)}{f_{sep}(i,j,t)} - 1 \tag{2.16}$$

$$\text{Otherwise } eff(i,j,t) = 0 \tag{2.17}$$

$$F_{adh}(i,j,y) \propto \left[\frac{def^{max}(i,j,t)}{L_p/2}\right]^2 (1 - P(t))F_{bridge}\left(\frac{S_i{}^2 + S_j{}^2}{S_i{}^3 + S_j{}^3}\right) \tag{2.18}$$

Where:

φ is the number density function (nb/ms³)

R_A is the rate distribution for agglomeration (m⁻⁴ s⁻¹)

L is the agglomerate particle size (m)

N_i and N_j are agglomerate particle concentration (nb/m³)

r_{agg} is the agglomeration rate (nb m⁻³ m⁻¹)

$K(i,j,t)$ is the agglomeration kernel

$f(i,j,t)$ is the meeting probability of agglomerates

$eff(i,j,t)$ is the efficiency of agglomeration

C_{coll} is a kinetic parameter that is determined through experimentation

$\alpha(i,j,t)$ is the target agglomeration efficiency

S_i and S_j are the agglomerate sizes (m)

u is the velocity of particle collision (m/s)

f_{adh} is the adhesive force between agglomerates (N)

f_{sep} is the disruptive force between agglomerates (N)

def^{max} is the radius of the contact surface (m)

$P(t)$ is the mean porosity of the agglomerates

F_{bridge} is the binding force at the point of contact between two agglomerates (N)

The model by Ahmed et al., 2023 considered agglomerate growth to occur by both layering and coalescence. The layering term was based on the immersion rate and collision rate limited regime developed by Arjmandi-Tash., et al 2019. The immersion rate limited model assumes a high rate of particle collisions with bridging liquid droplets. This results in a constant layer of particles on the droplet surface and agglomeration is limited by how quickly these particles immerse into the droplet. In the collision rate limited model, it is assumed that there are insufficient collisions for a constant layer at the surface of the droplets; the rate of collisions will limit agglomeration. Table 2-13 shows assumptions of both models.

Table 2-13 Assumptions for the immersion and collision rate limited models, adapted from (Arjmandi-Tash et al., 2019)

Model	Assumptions
Immersion rate limited	• There is a packed layer of primary particles on the surface of the droplets of bridging liquid • The immersion rate of the particles into the bridging liquid droplet limits agglomerate nucleation • Darcy's Law is used to calculate the imbibition of binder liquid in the particle layer, this calculates the immersion rate • The Kozeny-Carman equation is used to calculate the permeability of the particle layer
Collision rate limited	• Particle immersion into bridging liquid droplets is rapid • Nucleation of agglomerates is limited by the rate of collisions between the particles and droplets of bridging liquid • The bridging liquid droplets and primary particle sizes are greater than the turbulent microscale of Kolmogorov • The change of relative velocity between bridging liquid droplets and mother solution is negligible over the nucleation time.

Equation 2.19 is for immersion rate limited growth, and Equation 2.20 is for collision rate limited growth.

$$G(x,t) = C_{growth} \frac{2\Psi D_p \gamma \cos\theta}{15\mu_d x}(1-\varphi_{cp})\varphi_{cp} \qquad (2.19)$$

$$G(x,t) = C_{growth} 2\alpha \left[u(D_p)^2 + u(D_d)^2\right]^{\frac{1}{2}} \varphi_{Pb}(t) \qquad (2.20)$$

$$AgNu = \frac{15\mu_d \alpha \left[u(D_p)^2 + u(D_d)^2\right]^{1/2} \varphi_{Pb} D_d}{2\varphi\gamma\cos(\theta)\varphi_{cp}{}^2 D_p} \qquad (2.21)$$

Where:

$G(x,t)$ is the growth of an individual agglomerate, also shown as $\left(\frac{\partial x}{\partial t}\right)_x$

C_{growth} is a kinetic parameter found through experimentation

Ψ is the sphericity of the particles

D_p is the primary particle diameter (m)

γ is the bridging liquid and mother solution interfacial tension (J/m^2)

θ is the contact angle between the bridging liquid and the particles (°)

μ_d is the bridging liquid viscosity (N s/m^2)

x is the agglomerate diameter (m)

φ_{cp} is the critical-packing liquid volume fraction

α is the target efficiency

$u(D_p)$ is the relative velocity of the particles and the mother solution (m/s)

$u(D_d)$ is the relative velocity of the bridging liquid droplets and the mother solution (m/s)

φ_{Pb} is the volume fraction of crystals in the mother solution

$AgNu$ is the agglomerate nucleation number

D_d is the bridging liquid droplet diameter (m)

A parameter termed the agglomerate nucleation number, or AgNu, is used to predict whether the system is immersion or collision rate limited. If AgNu is greater than one then the system is immersion rate limited and Equation 2.19 will be used in the model. Equation 2.20 is used when AgNu is under one and the system is collision rate limited (Ahmed et al., 2023). The calculation for AgNu is shown in Equation 2.21.

Growth by coalescence is also considered in the model by Ahmed et al., 2023. The coalescence is based on the work by Blandin, shown in Equations 2.12 to 2.18 (Blandin et al., 2005) and is used to describe the formation of large agglomerates due to collisions and coalescence between agglomerates (Ahmed et al., 2023) .

Since the initial observations by Bemer there have been improvements to population balance modelling for spherical agglomeration. The incorporation of bridging liquid properties by Madec et al., 2003 was extremely useful in ensuring that agglomeration can only occur when the system is within the acceptable BSR range which increased the accuracy of spherical agglomeration modelling. In the model by Blandin et al., 2005, the bridging liquid is also an important parameter that is considered. This model also considers the mechanisms behind agglomeration, including incorporating collision velocities between particles. Ahmed et al., 2023 combined Blandin's coalescence model with a layering model based on work by Arjmandi-Tash et al., 2019. In the model by Ahmed, two mechanisms of layered growth are proposed based on factors that can limit particle immersion into bridging liquid droplets. This model considers the collisions between bridging liquid droplets and particles to be a growth limiting factor. One area that could

be further developed in these models is the influence of reactor geometry on hydrodynamics and mixing in the system as improved mixing will increase the contact between bridging liquid and particles (Bemer, 1979; Madec et al., 2003; Blandin et al., 2005; Pitt et al., 2018; Ahmed et al., 2023).

2.12.2.3 *Breakage*

The mechanism of breakage for spherical agglomeration needs further investigation. The most recent model by Ahmed et al., 2023, does not consider agglomerate breakage due to insufficient research into breakage mechanisms to derive a breakage kernel for spherical agglomeration (Ahmed et al., 2023).

Studies by Thati and Rasmuson, 2011, observed the potential of breakage occurring in spherical agglomerates of benzoic acid (Thati and Rasmuson, 2011; Pitt et al., 2018). It was thought that this system may include breakage as there was a gradual change in particle size distribution after addition of feed material to a previously agglomerated benzoic acid system (Thati and Rasmuson, 2011).

In Section 2.4.1 it was discussed that increased impeller speed will result in larger agglomerates up to a point, where further increases to speed will cause a decrease in agglomerate size. This could be due to impeller speeds above a critical value resulting in increased breakage, as the particle velocity will increase and be too great for successful coalescence with other particles, but sufficient to cause breakage when they contact the tank walls (Pitt et al., 2018).

2.12.3 Software for Population Balance Modelling

Population balance models can be calculated using different software. For this work, gPROMS Formulated Products was chosen for the spherical agglomeration PBM. This software was chosen due to the ability to generate a flowsheet that allows users to change model parameters without the need to adjust the code. This would be attractive in a pharmaceutical company as it would allow for research staff to quickly generate models of various spherical agglomeration processes without needing to access or understand the code. An existing PBM for spherical agglomeration was developed in gPROMS Formulated Products by Ahmed et al., 2023. This PBM was used as the foundation of the PBM in this work, with modifications made to incorporate flow characteristics. Continuing to develop the model in gPROMS Formulated Products was a more efficient way of developing the model than rewriting a functional and well performing model in a different software.

2.13 Summary

Spherical agglomeration can be used to increase the ease of handling problematic particles. It is often used for needle-like crystals. However, there is little research about how the process can be applied to other difficult to process particles such as particles that stick together or have both hydrophilic and hydrophobic components.

Many papers state that spherical agglomerates have improved micrometric properties and, therefore, bioavailability is increased. However, there have not been studies directly comparing tablets made from spherical agglomerates to tablets made from granules of the same compound to see whether these properties are improved. Tablets consist of API and excipients such as surfactants to stabilize the tablet and increase shelf life. The process of producing tablets from spherical agglomerates could be investigated to see whether they can be easily blended with excipients to produce tablets that meet industry and consumer standards.

Many studies have been carried out using STRs for spherical agglomeration, however there is a lack of consistency in the apparatus used. Various studies have used 4-blade propeller agitators, others have used

magnetic stirrers, and some use 6-blade turbine agitators. These will all induce different flow patterns in the system which will impact the mixing of the powder and bridging liquid. If there is insufficient mixing, then there will be a lower yield of spherical agglomerates. Investigating the quality of mixing with different agitator types will allow for the optimal conditions for the apparatus to be identified.

PBMs are a useful predictive tool for the pharmaceutical industry. Previous works in spherical agglomeration PBM have based the models on a HSWG framework, due to mechanistic similarity between spherical agglomeration and wet granulation. Models for nucleation and growth of spherical agglomerates have been developed. However, breakage needs further investigation before it can be incorporated into a model. The current understanding of spherical agglomeration highlights the importance of contact between the bridging liquid and the particles. However, there needs to be more research into the influence of mixing on agglomerate formation, and how this could be incorporated into a PBM.

To identify the impact of mixing characteristics on the formation of spherical agglomerates, this PhD thesis will develop CFD simulations of STRs with various geometries. These simulations will be compared with experimental data, which will influence the generation of a predictive PBM for spherical agglomeration, which incorporates mixing characteristics.

Chapter 3 Materials and Methods

This thesis used experimental and modelling approaches to investigate the importance of flow characteristics on spherical agglomeration and incorporate these findings into a PBM. Section 3.3 describes the methodology for the experiments used to investigate the influence of flow characteristics on spherical agglomeration, with the results of these experiments in Chapter 4. The experimental methodology for the analysis and validation of the spherical agglomeration PBM is given in Section 3.4; with the results of these experiments in Chapter 7. Section 3.5 discusses the agglomerate characterisation methods utilised for all of the experiments conducted as part of this research. The methodology for the CFD investigation into the influence of impeller characteristics on spherical agglomeration are in Section 3.6, with the results of the CFD study in Chapter 5. The construction of the spherical agglomeration PBM is detailed in Chapter 6.

3.1   Materials

Two different diameters of monosized poly(methylmethacrylate) (PMMA) beads are the material systems used for this research.

The PMMA beads allow for comparison to the CFD simulations, as they are spherical and monosized, which allowed for simplifications of the particle geometry in the CFD. The experiments investigating the influence of impeller geometry used 52 µm PMMA beads. Section 3.3 discusses the methodology of these experiments.

During the validation of the PBM, further experiments were performed with the 52 µm PMMA beads. Experiments were also performed with the 20 µm PMMA beads to determine the influence that primary particle size has on agglomerate formation. The methodology for the validation experiments with the PMMA beads is given in Section 3.4.

Table 3-1 shows a summary of the various material systems used for the experiments. The two particle types tested for this research used the same solvent system. For both particle sizes, water was used as the suspending solvent, with toluene added as the bridging liquid. This will minimise the influence of density and viscosity differences that other solvents would have on the mixing behaviours in the system.

Table 3-1 Summary of the material systems used in the experiments

Material	Suspending Solvent	Bridging Liquid
52 (±2) µm PMMA Beads (Microbeads USA Spheromers CA 50)	Water Stuart Distinction Water Still D4000	Toluene (Sigma-Aldrich Anhydrous 99.8 %)
20 (±2) µm PMMA Beads (Microbeads USA Spheromers CA 20)	Water Stuart Distinction Water Still D4000	Toluene (Sigma-Aldrich Anhydrous 99.8 %)

3.1.1   Material Wettability

A First Ten Angstroms 200 goniometer measured the contact angle of the bridging liquid on the PMMA beads to ensure that the bridging liquid would sufficiently wet the particles. For all experiments performed as part of this thesis, toluene was used as the bridging liquid. Toluene was used as previous work by an MEng student, Guo J. Lian, found that toluene was the optimal bridging liquid for the PMMA

beads (Lian, 2020). Contact angle measurements were performed in this work to determine whether the contact angle was different for the 20 μm and 52 μm PMMA beads, so that the correct value could be used for PBM validation.

A thin layer of the PMMA beads was attached to a glass slide using adhesive tape. The slide was placed on the stand, directly below a syringe containing the bridging liquid, in this case toluene. A drop of bridging liquid was added to the powder, a high-speed camera recorded the droplet falling and contacting the particles. Measurement of the contact angle was recorded from the frame where the droplet first touches the PMMA beads. The FTA32 software analysed the image of the contact point to determine the contact angle of the bridging liquid and the powder. On occasion, a reference line had to be manually drawn for the software to be able to determine the correct contact angle. Figure 3-1 shows the goniometer used for contact angle measurements.
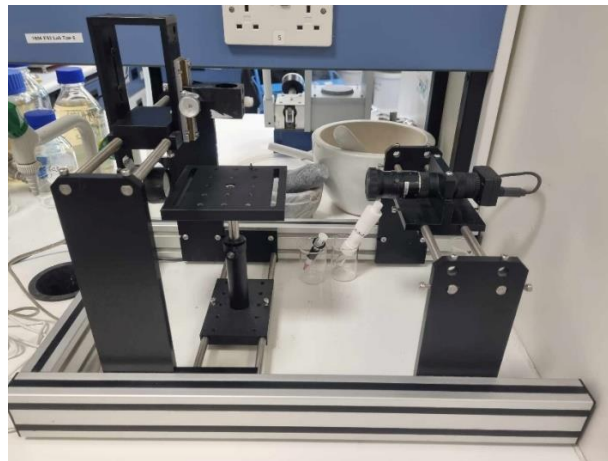
Figure 3-1 Image of the goniometer used to measure contact angle

Figure 3-2 shows one of the contact angle measurement images obtained for the 20 μm and 52 μm PMMA beads. In this figure it can be seen that the contact angle for the 52 μm beads is lower than the 20 μm beads. The measurements for each particle size were taken three times, and an average was calculated. The measured values and calculated average for contact angle are in Table 3-2.
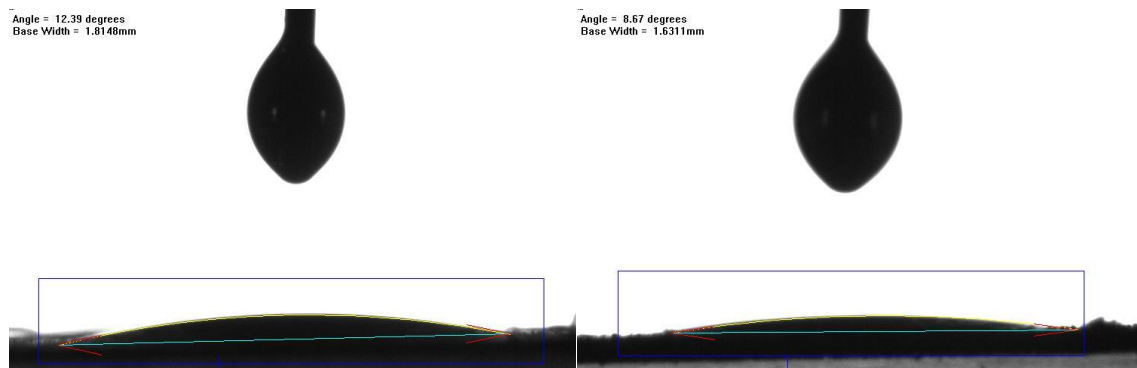
Figure 3-2 Contact angles measured for the different sized PMMA beads (l) 20 μm beads and (r) 52 μm beads

Table 3-2 Contact angle measurements for the 20 μm and 52 μm PMMA beads, with repeats

	20 μm PMMA Bead Contact Angle (°)	52 μm PMMA Bead Contact Angle (°)
Reading 1	12.39	8.67
Reading 2	13.46	8.35
Reading 3	14.55	8.96
Average	13.467	8.66
Standard Deviation	0.882	0.249

3.1.2   Determining System Composition

Section 2.4 discusses important parameters for successful spherical agglomeration, the solids concentration and bridging liquid to solid ratio (BSR) are two of these important parameters. The experimental system was 3 % wt/wt solution with a total mass of 600 g. Equation 3.1 shows the calculation for the mass of solid required. Equation 3.2 and 3.3 show the calculations for volume and mass of bridging liquid respectively.

$$m_p = m_t \frac{c_p}{100} \tag{3.1}$$

$$V_{BL} = BSR \frac{m_p}{\rho_p} \tag{3.2}$$

$$m_{BL} = V_{BL}\rho_{BL} \tag{3.3}$$

Where:
m_p is the mass of particles (kg)
m_t is the total system mass (kg)
c_p is the solids concentration (mol/m³)
V_{BL} is the volume of bridging liquid (m³)
BSR is the bridging liquid to solid ratio
ρ_p is the particle density (kg/m³)
m_{BL} is the mass of bridging liquid (kg)
ρ_{BL} is the bridging liquid density (kg/m³)

3.2   Equipment

All of the experiments used the set-up that is shown in Figure 3-4. The set-up consisted of a 1 L beaker, a baffle system and an impeller attached to a Caframo Light Torque Overhead Stirrer. The dimensions of the various equipment components are given in Figure 3-4 and Table 3-3.

Figure 3-3 Image of the tank and overhead stirrer used for the experiments
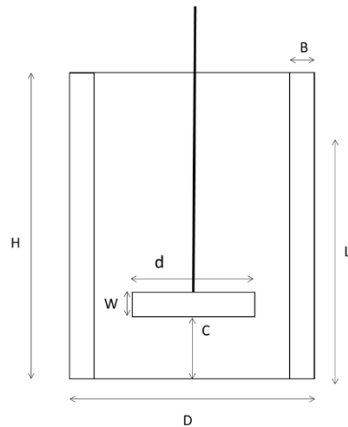
Figure 3-4 Schematic of the stirred tank set-up with the dimensions labelled according to Table 3-3

Table 3-3 Dimensions of the stirred tank system

Description	Symbol	Value (mm)
Vessel Diameter	D	90
Liquid Height	L	144
Vessel Height	H	180
Width of Impeller Blade	W	10
Impeller Diameter	D	50
Clearance	C	18-30
Baffle Width	B	9
Number of Baffles	n_B	4

The clearances in Table 3-3 were investigated as these are between 20 % and 33 % of the tank diameter. In previous studies, reducing a Rushton turbine impeller clearance to below 30 % of the tank diameter induced an axial flow pattern into the system (Montante et al., 1999; Zhu et al., 2019). The selected values for impeller clearance allow for an investigation into whether this phenomenon occurs for all radial impellers, whilst also investigating the influence of clearance on axial systems.

3.3 Influence of Impeller Geometry Experiments

3.3.1 Particle System

These experiments are agglomeration in suspension experiments, this type of spherical agglomeration occurs when crystals are suspended in a solvent, and the addition of bridging liquid induces agglomeration. This method allows for comparison to CFD simulations, as it is a binary mixture and having a ternary phase liquid system would increase the complexity of the CFD. Table 3-4 shows the composition of the experimental system used for the impeller geometry investigation, with an image of the 52 μm PMMA beads shown in Figure 3-5.

Table 3-4 Mass of components in the system

Material	Purpose In System	Mass (g)
52 (±2) μm PMMA Beads	Solid Particles	18
Water	Suspending Solvent	582
Toluene	Bridging Liquid	6.5025

—100 μm
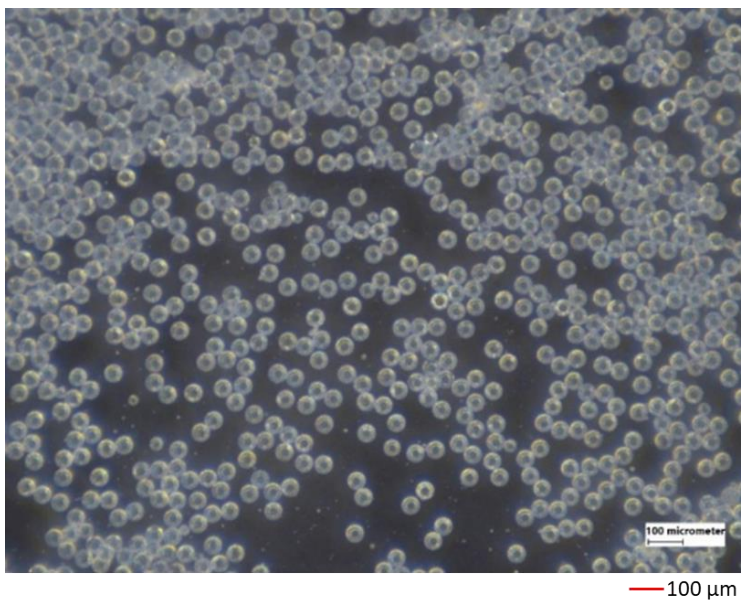
Figure 3-5 Image of the 52 (±2) μm PMMA beads used for the experiments, scale bar is 100 μm

Preliminary studies were conducted with a flat-blade impeller to determine the BSR of the system, values of 0.4, 0.5 and 0.6 were tested and it was determined that a BSR of 0.5 was the ideal value for this system.

3.3.2   Impeller Designs

These experiments used multiple impeller geometries to determine the influence that changing impeller geometry has on particle mixing. Figure 3-6 shows the chosen impellers. The four different impeller geometries promote various levels of radial and axial flow in the stirred tank, influencing the contact between bridging liquid and particles. Section 2.10 discusses the importance of impeller induced flow pattern on mixing in stirred tanks.

Table 3-5 Impeller geometries used for investigating influence of impeller geometry on spherical agglomeration, and which flow pattern the impeller promotes in the tank

Impeller Geometry	Diameter (mm)	Promoted Flow Pattern
Flat-Blade	50	Radial (Grenville et al., 2017)
Propeller	50	Axial (Couper et al., 2012)
Rushton Turbine	50	Radial (Grenville, 2016)
Pitched-Blade	50	Axial (Van Wazer et al., 1995)

Figure 3-6 Image of the four impellers used, from left-right, flat blade, propeller, Rushton turbine, pitched-blade

All four of the impeller geometries were tested at impeller speeds of 300 rpm, 450 rpm and 600 rpm. The clearance was also altered with experiments performed at clearances of 18 mm, 20 mm, 25 mm, 27 mm and 30 mm; giving a total of 60 experiments. Table 3-6 summarises the experiments performed for this work.

3.3.3   Experimental Approach and Methodology

To obtain a 3 % wt/wt solution of 52 μm PMMA beads in water, 18 g of PMMA beads was added to 582 g of distilled water. The system was agitated for 10 minutes to allow the system to equilibrate, and then the bridging liquid was added by pipette into the stirred tank. For a BSR of 0.5, there were 7.5 mL of toluene added. The system was agitated for a further 45 minutes to allow agglomerate formation. It was then passed through a Buchner funnel with a 90 mm diameter Millipore filter paper of 1.2 μm pore size, and left to dry at 21°C. Once dry, the agglomerates underwent analysis, and this analysis is discussed in Section 3.5. The impeller geometry, speed and clearance were varied for each experiment, the

experimental conditions can be seen in Table 3-6; this resulted in 60 experimental conditions performed, with two repeats for each impeller at 450 rpm and 25 mm clearance.

Table 3-6 Summary of experiments and CFD simulations performed. Each impeller speed and clearance value was tested for all four impeller geometries, (*indicates repeated experiments)

Impeller Geometry	Impeller Speed (rpm)	Impeller Clearance (mm)				
Flat-Blade	300	18	20	25	27	30
	450	18	20	25*	27	30
	600	18	20	25	27	30
Propeller	300	18	20	25	27	30
	450	18	20	25*	27	30
	600	18	20	25	27	30
Rushton	300	18	20	25	27	30
	450	18	20	25*	27	30
	600	18	20	25	27	30
Pitched-Blade	300	18	20	25	27	30
	450	18	20	25*	27	30
	600	18	20	25	27	30

3.4   PBM Validation Experiments

The purpose of these experiments was to evaluate a pre-existing PBM by Ahmed et al., 2023, and the PBM generated in Chapter 6. The experiments performed used the material systems specified in Table 3-1. The different sizes of PMMA beads allowed for investigation into the influence that particle diameter, and therefore, the bulk density, has on the agglomeration behaviour.

3.4.1   Impeller Geometries

The validation experiments used a 5 mm Rushton turbine, a 5 mm propeller and a 3 mm Rushton turbine impeller. The 5 mm Rushton turbine was determined to be the best impeller (see Chapter 5), with the 5 mm propeller being the worst. Using a 3 mm Rushton turbine will help determine whether impeller diameter is accurately included in the PBM. The three impeller geometries are shown in Figure 3-7.
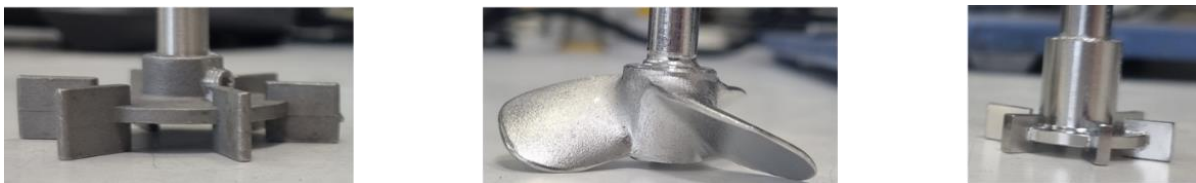
Figure 3-7 The impellers used for validation experiments, from left to right, 5 mm Rushton turbine, 5 mm propeller, 3 mm Rushton turbine

3.4.2   20 µm PMMA Bead Experiments

Figure 3-8 shows the 20 µm primary particles that were used for these experiments. These beads were used to investigate the accuracy of the PBM at predicting the influence of particle size in the system. For these experiments, PMMA beads were suspended in water and agitated for 10 minutes. After 10 minutes, the desired volume of bridging liquid was added into the system, which was then agitated for the specified agglomeration time. The product of one experiment was filtered and left to dry at 21 °C however, the

product dried as a sheet and was stuck to the filter paper. The experiment was repeated and the product was poured into metal trays and dried at 85 °C in an oven to determine if the drying process influenced the product. It was found that drying the agglomerates in an oven without filtering the product allowed the agglomerates to retain their shape. Therefore, all future validation experiments dried the product in an oven at 85 °C. A summary of experimental conditions for the PBM validation experiments with 20 μm PMMA beads is shown in Table 3-7.
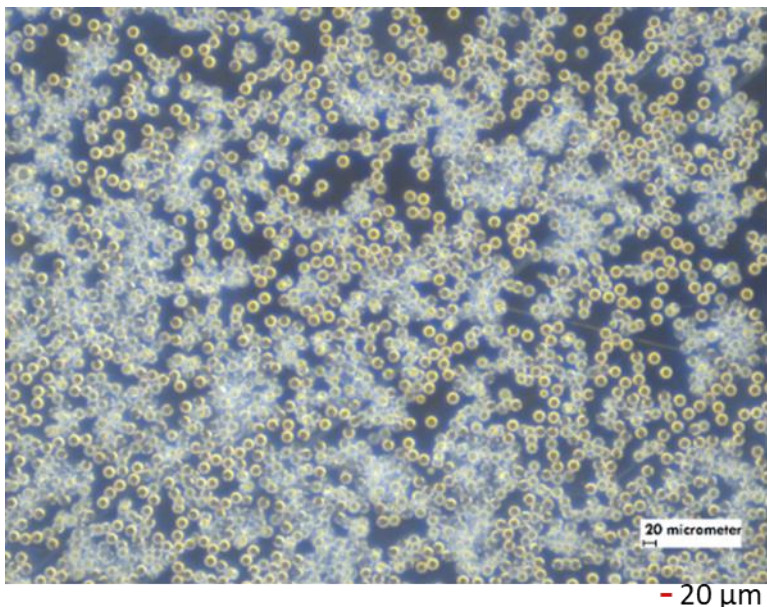
Figure 3-8 Image of 20 (±2) μm PMMA beads used for the experiments, scale bar is 20 μm

Table 3-7 Experimental conditions tested for the 20 μm beads as part of the PBM experimental validation

20 (±2) μm Validation Experiments	
Solid Particles	20 μm PMMA Plastic Beads
Solids Concentration	3 % wt/wt
Suspending Solvent	Water
Suspending Solvent and Powder Mass	600 g
Bridging Liquid	Toluene
BSR	0.38, 0.5, 0.64, 0.77
Impeller Speed	600
Agitation Time (min)	45, 90

3.4.3   52 μm PMMA Bead Experiments

The 52 μm PMMA beads used for these experiments can be seen in Figure 3-5. For these experiments, PMMA beads were suspended in water and agitated for 10 minutes. After 10 minutes, the desired volume

of toluene was added into the system as the bridging liquid, which was then agitated for the specified agglomeration time. Once the agglomeration time had been reached, the contents of the stirred tank were poured into metal trays and left to dry in an oven at 85 °C. Table 3-8 shows a summary of the experimental conditions that were investigated for the PBM validation with 52 μm PMMA beads.

Table 3-8 Experimental conditions tested for the 52 μm beads as part of the PBM experimental validation

52 (±2) μm Validation Experiments	
Solid Particles	52 μm PMMA Plastic Beads
Solids Concentration	3 % wt/wt and 4 % wt/wt
Suspending Solvent	Water
Suspending Solvent and Powder Mass	600 g
Bridging Liquid	Toluene
BSR	0.38, 0.5, 0.64, 0.77
Impeller Speed	600, 500
Agitation Time (min)	30, 45, 90

3.4.4 Summary of Experiments

A summary table of the experiments performed with the 52 μm PMMA beads can be seen in Table 3-9. Table 3-10 shows the experiments performed with the 20 μm PMMA beads.

Table 3-9 Summary of validation experiments performed with the 52 (±2) μm PMMA beads

Impeller Geometry	Solids Concentration	Impeller Speed (rpm)	Impeller Clearance (mm)	BSR	Agitation time (min)
50 mm Rushton Turbine	3 % wt/wt	600	25	0.5	45
50 mm Rushton Turbine	3 % wt/wt	600	25	0.5	90
30 mm Rushton Turbine	3 % wt/wt	600	25	0.5	45
50 mm Rushton Turbine	3 % wt/wt	600	25	0.64	45
50 mm Rushton Turbine	3 % wt/wt	600	25	0.38	45
50 mm Rushton Turbine	3 % wt/wt	600	25	0.77	45
50 mm Rushton Turbine	4 % wt/wt	500	25	0.5	30

Table 3-10 Summary of PBM validation experiments conducted with 20 (±2) μm PMMA beads as the primary particles

Impeller Geometry	Impeller Speed (rpm)	Impeller Clearance (mm)	BSR	Agitation time (min)
50 mm Rushton Turbine	600	25	0.5	45
50 mm Rushton Turbine	600	25	0.5	90
50 mm Propeller	600	25	0.5	45
50 mm Propeller	600	18	0.5	45
50 mm Propeller	600	25	0.5	90
50 mm Rushton Turbine	600	18	0.5	45
50 mm Rushton Turbine	600	25	0.64	45
50 mm Rushton Turbine	600	25	0.38	45
50 mm Rushton Turbine	600	25	0.77	45

The experiments summarised in Table 3-9 and Table 3-10 will allow for investigation into the accuracy of the PBM predicted PSD for spherical agglomeration systems with the following conditions:

- Primary particle size
- BSR
- Impeller geometry
- Impeller clearance
- Agitation time
- Impeller diameter
- Impeller speed
- Solids concentration

Impeller diameter, impeller speed and solids concentration were only varied for experiments with 52 μm PMMA beads as the primary material. The final experiment for the 52 μm particle size is based on experiments performed by Guo J Lian as part of an MEng research project[1]. Results from experiments by Guo J Lian were also used for model validation; these experiments were at a 300 mL scale, and more details are given in Chapter 7. The smaller impeller diameter of the 3 mm Rushton Turbine was only tested for the 52 μm PMMA beads because the impeller was not successful at agglomerating the larger particles, and therefore would not have been able to agglomerate the smaller primary particles as they are more difficult to entrain in the impeller flow pattern.

---

[1] Optimisation of the Spherical Agglomeration Process: Wetting and Nucleation, Guo Jung Lian 2020, cited as (Lian, 2020) throughout this thesis

3.5 Agglomerate Characterisation

For both sets of experiments, it was important to determine the PSD of the agglomerates. The size distribution data allows for comparisons between experimental and PBM predicted sizes. It is also useful as it gives insight into how well mixed the system is, as the agglomerates will be smaller and more delicate if there has been insufficient contact between the primary powder and the bridging liquid.

Image analysis was also performed on the agglomerates from both sets of experiments. These images will be useful to determine the sphericity of the agglomerates. It will also help identify if there is coalescence in the system.

3.5.1 Particle Size Analysis

The PSD was found using sieving. A Retsch AS 200 control sieving machine (Figure 3-9) was used with a series of Retsch sieves. To generate the particle size distribution, the mass of each empty sieve was recorded and the sieves were stacked into a large stack and a small stack, the arrangement of the stacks can be seen in Table 3-11. The powder was poured into the top sieve of the large stack and then placed onto the sieve shaker. It was shaken at an amplitude of 50 Hz for 15 minutes. The mass of sieve and powder on each sieve was recorded and the material on the sieves were collected. The material that was smaller than 710 µm was poured into the top sieve on the smaller stack. This was then placed on the sieve shaker and agitated at the same conditions as the larger material, with the mass of the sieves recorded after the agitation period had finished.

Figure 3-9 The Retsch sieve shaker with one of the sieve stacks used for PSD generation

Table 3-11 Sieve stacks used to generate the agglomerate PSD

Large Stack Sieve Size (µm)	Small Stack Sieve Size (µm)
2000	600
1700	500
1400	425
1180	355
1000	250
850	150
710	Collection Plate
Collection Plate (powder in this plate is put into 600 µm sieve in small stack)	

To generate the particle size distribution from the sieve data, the calculations shown in Equations 3.4 to 3.8 were performed.

$$m_i = m_{sp,i} - m_{s,i} \tag{3.4}$$

$$y_{m,i} = \frac{m_i}{\sum m_i} \tag{3.5}$$

$$f_{m,i} = \frac{y_{m,i}}{\Delta x_i} \tag{3.6}$$

$$y_i = \frac{y_{m,i}\bar{x}_i^{-3}}{\sum y_{m,i}\bar{x}_i^{-3}} \tag{3.7}$$

$$\bar{x}_{43} = \frac{\sum(y_{m,i}\bar{x}_i)}{\sum y_{m,i}} \tag{3.8}$$

Where:
m_i is the mass of powder in size interval i
$m_{sp,i}$ mass of the sieve and powder recorded for sieve size i
$m_{s,i}$ mass of sieve size i
$y_{m,i}$ is the mass fraction of particles size i
$f_{m,i}$ is the mass frequency of particles of size i
Δx_i is the difference between the interval of size i and $i+1$
$\bar{x}_i$ is the average of the interval i and $i+1$
$\bar{x}_{43}$ is the mean particle size of the distribution

3.5.2   Agglomerate Imaging

The agglomerates were imaged using a Pixelink D775CU-T camera with a TV lens 1/3" CS, the images were captured using UScope x64 software. The camera set-up is shown in Figure 3-10. To generate the images, a small sample of the powder was placed in a clear petri dish and the light was switched on to level 2. The images were taken with overhead lighting against a black background at zoom length settings of 0.58x and 2x. A scale bar was added using the UScope X64 software that has been calibrated to ensure accurate measurements.
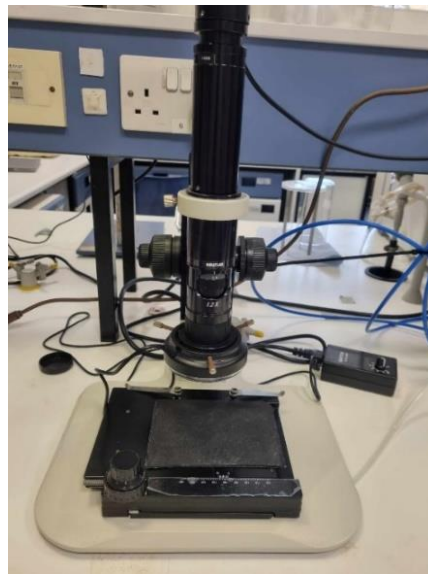
Figure 3-10 The Pixelink camera set-up used for obtaining agglomerate images

3.6   CFD Methodology

A comprehensive CFD software analysis, described in Section 2.11.3.7, determined that ANSYS Fluent was the preferred software for spherical agglomeration CFD studies. Using Fluent allows for CAD drawings of geometry, mesh generation and post-processing all in one integrated package (Haghgoo, 2013). Fluent is also widely used industrially, and is more user friendly than other available software, due to a larger number of tutorials and resources (Vlug, 2014). A summary of all CFD simulations performed for this research can be seen in Table 3-6.

3.6.1   Principles of CFD Simulations

The popularity of CFD simulations to predict the suspension of particles in a stirred tank has increased over the last 30 years as CFD predictions allow for design and optimisation of reactor geometry (Stuparu et al., 2021). It can also identify areas of inhomogeneity in a system, which may pose a safety risk in some processes (Egedy et al., 2012).

To generate a CFD simulation for a stirred tank there are steps that need to be followed to produce accurate simulations. The steps are:

- Generation of the geometry using CAD drawings
- Meshing the system
- Determine the governing equations, turbulence model and boundary conditions
- Data analysis

The geometry construction and meshing are crucial to the validity of the CFD simulation. To ensure that the CFD simulation is an accurate reflection of the equipment that is simulated, there must be consistency between the tank dimensions and properties.

Meshing of the system determines the accuracy of the simulation, but increased mesh density will lead to increased computation time (Parvizi et al., 2016). The two main approaches to CFD meshing are the structured and unstructured approach (Sadrehaghighi, 2018). A structured mesh consists of hexahedral elements that have implicit connectivity. The structured mesh approach is time consuming, especially for complex geometries, which may need to be manually broken into smaller components (Sosnowski et al., 2018). An unstructured mesh consists of tetrahedral elements andunstructured mesh generation is built in to many CFD software systems; therefore, the process can be automated (Sosnowski et al., 2018). The tetrahedral shape of this mesh also allows for adaptation around complex geometries, and it is preferable to use an unstructured mesh for moving meshes, such as simulating impeller rotation (Sadrehaghighi, 2018). A structured mesh will require fewer mesh elements than an unstructured mesh to produce the same simulation quality as hexahedral (structured) elements can be stretched further than tetrahedral (unstructured) elements, without decreasing the quality of the simulation results (Sosnowski et al., 2018).

Agglomeration in suspension occurs in a multiphase system in which particles are suspended in a solvent, and a bridging liquid is added to induce agglomeration. To accurately reflect this, the CFD simulations must consider multiphase flow. There are two main multiphase flow systems used in CFD simulations, they are Eulerian-Eulerian, or Lagrangian. In the Eulerian-Eulerian multiphase model, the solid particles are treated as a continuous phase (Gohel et al., 2012). The different phases are represented by their volume fraction at different points in the system. The mass and momentum balances are solved for each of the phases in the system using a Reynolds-averaged approach (Gu et al., 2020). The Lagrangian model considers solid material as individual particles, and approximates hydrodynamic forces using single-particle empirical models (Gohel et al., 2012). Multiple studies have determined that a Lagrangian approach requires greater computational time than an Eulerian-Eulerian approach (Zhang and Chen, 2007; Xu et al., 2020).

As spherical agglomeration occurs in a stirred tank, the system will be in turbulent flow. To model this correctly, the appropriate CFD turbulence model must be selected. One model that is commonly used for CFD simulations of stirred tanks is the k-ε turbulence model. This model assumes that the average velocity gradient is proportional to the Reynolds stress (Torotwa and Ji, 2018). In this model, the turbulent kinetic energy is the k term. The calculation (Equation 3.9) for the turbulent kinetic energy averages the fluctuating turbulent velocity in three directions (represented in Equation 3.9 by $\overline{u'}$, $\overline{v'}$ and $\overline{w'}$). The turbulent dissipation is represented by ε. Equation 3.10 shows the calculation for ε, in this equation the turbulent kinetic energy is related to the area using the diameter (D) to determine the turbulent dissipation ε (Gorman et al., 2021).

$$k = \frac{1}{2}\left(\overline{u'^2} + \overline{v'^2} + \overline{w'^2}\right) \tag{3.9}$$

$$\varepsilon = \frac{k^{3/2}}{0.3D} \tag{3.10}$$

The k-ε turbulence model is popular due to it producing results that are reasonably accurate in a lower computation time than other turbulence models (Torotwa and Ji, 2018). Two important parameters that need to be carefully considered when using the k-ε turbulence model is the mesh near the wall and the

wall treatment. These parameters influence the result of the turbulent boundary layer (Sadino-Riquelme et al., 2022). The k-ε turbulence model has produced some inaccurate results for recirculating flows, leading to variations of the k-ε model being developed (Lane, 2017).

Another turbulence model that can be used is the k-ω model. In this model k still refers to the turbulent kinetic energy, but ω is the turbulent frequency (Lee and Wahab, 2019). The k-ω model estimates the solution at the start of the run and has been shown to have difficulty converging to a solution. Often the k-ε model is run first and the solution of this is used as input for k-ω. For flows that demonstrate strong curvature, the k-ω model has improved accuracy compared to the k-ε model (Monk and Chadwick, 2017).

3.6.2   Geometry Construction

Construction of the various stirred tank geometries was performed in ANSYS Design Modeller 2019 R2, allowing for easy integration of the geometry into the CFD simulation through ANSYS Workbench. Figure 3-4 shows a schematic of the stirred tank, and the dimensions of the tank are shown in Table 3-3. Changing both impeller geometry and clearance resulted in construction of twenty stirred tank geometries. Table 3-12 shows the 20 stirred tank configurations constructed to determine the influence of impeller geometry on flow characteristics.

Table 3-12 Various impeller configurations in the stirred tank geometries produced for the spherical agglomeration CFD study

Impeller Geometry	Impeller Clearance (mm)
Flat-Blade	18
	20
	25
	27
	30
Propeller	18
	20
	25
	27
	30
Rushton Turbine	18
	20
	25
	27
	30
Pitched-Blade	18
	20
	25
	27
	30

Figure 3-11 shows CAD drawings for the stirred tanks with the various impeller geometries. It can be seen that there is a smaller cylindrical region inside the tank which is not present in an experimental system. This region was constructed to act as an "inner domain". This domain is rotated during CFD simulations to mimic the rotation of the impeller; the inner domain dimensions are in Table 3-13. These dimensions were chosen to allow for the rotation to occur in the bulk of the fluid. As the inner domain will rotate during simulations, it could not touch the bottom of the tank, or the baffles.
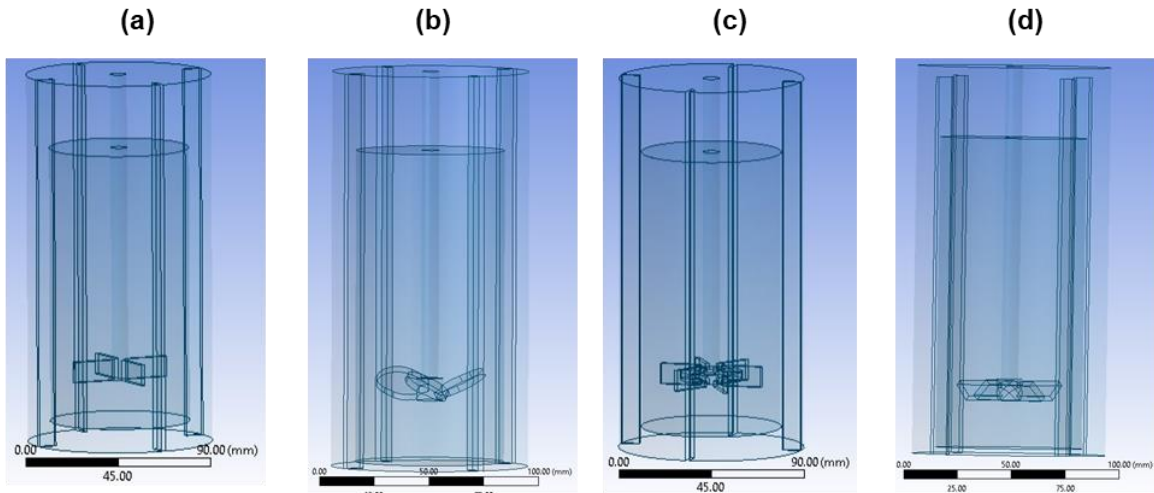
Figure 3-11 CAD drawings of the four impeller types simulated, with the laboratory equipment impellers shown below (a) flat-blade, (b) propeller, (c) Rushton turbine and (d) pitched-blade

Table 3-13 Dimensions of the inner domain for the CFD simulations

Description	Value (mm)
Inner Domain Height	142
Inner Domain Diameter	70
Inner Domain Clearance	2

3.6.3   Mesh Construction

Due to the complexity of the geometry, an unstructured, tetrahedral mesh shape was used for the CFD simulations. This meshing approach was selected as it is more suitable for geometries with a rotating

component (Sadrehaghighi, 2018). Figure 3-12 shows a cross section of the tank with a tetrahedral mesh. A mesh density analysis was performed to determine the optimal mesh size, the process of this is detailed in Section 3.6.5.
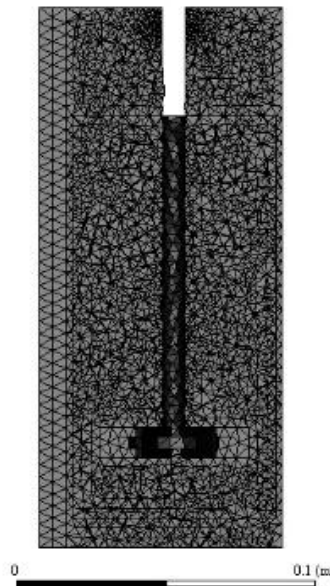
Figure 3-12 Image of the tank cross section with a 4 mm tetrahedral mesh that was used for CFD simulations

3.6.4   Simulation Construction

ANSYS Fluent 2019 R2 was used for the CFD simulations. The stirred tank was simulated as an Eulerian-Eulerian multiphase system, with water as the primary phase, and spherical solid particles as the secondary phase. The solid properties were chosen to reflect the size and density of spherical agglomerates produced when the 52 μm PMMA beads were the primary particles. The solid density was given as 1200 kg/m^3 as this is the density of PMMA. Monosized particles were used to reduce the computation time of the simulations. The particles size was specified as 500 μm due to this being the minimum size that is considered a spherical agglomerate when 52 μm PMMA beads are used as the primary particles.

Calculations of the impeller Reynolds number showed that the mixing behaviour in the system was turbulent as it ranged from 12,500 at 300 rpm to 25,000 at 600 rpm. Both the k-ε and k-ω turbulence model were tested for one CFD simulation. The k-epsilon model was used for all CFD simulations in this work as there was little variation in the results of the two models, and k-epsilon produced a solution in less time than k-omega.

In Table 3-14, the residual for the continuity equation is higher than the other residuals due to the mixing induced transient nature of the system. This results in fluctuations that influence the convergence of the continuity equation more than other residuals. Mass-averaged properties of the solid and liquid are classified as a mixture phase; the mixture is the input for the continuity equation (Equation 3.11), resulting in fluctuations for the continuity result (Stuparu et al., 2021). The agitation in the system also results in fluctuations in the continuity equation, as it will influence the velocity vector for each phase.

$$\frac{\partial(\alpha_q \rho_q)}{\partial t} + \nabla(\alpha_q \rho_q \vec{v}_q) = 0 \qquad (3.11)$$

Where:

α_q is the volume fraction for phase q

ρ_q is the density for phase q

$\vec{v}_q$ is the velocity vector for phase q

Table 3-14 Settings in Fluent used for all spherical agglomeration CFD simulations

CFD Setting	Value
Multiphase Model	Eulerian-Eulerian with two phases
Viscous Model	Standard k-epsilon turbulence model for a dispersed multiphase, preliminary simulations were performed with k-omega turbulence model for comparison but this did not influence results so k-epsilon was used for simulations of the 60 impeller configurations
Fluid Properties (modelled on water)	Density: 998 kg/m^3 Viscosity: 0.001003 kg/m.s
Solid Properties (assuming PMMA spherical particles)	Density: 1200 kg/m^3 Particle Size: 500 μm
Phase Interactions	Virtual Mass Modelling Coefficient: 0.5
Cell Zone Conditions	Inner Domain: Frame Motion, rotation axis direction 1, rotation speed is desired impeller speed Outer Domain: rotation axis direction 1
Cell Registers	Cylindrical region around impeller blades Radius: 0.025 m Height: 0.015 m
Method	Scheme: Phase Coupled SIMPLE Gradient: Green-Gauss Cell Based
Initialization	Solids inserted in cell register region
Residuals	Continuity:1e-03 u-solid, v-water, v-solid, w-water, w-solid, energy-p1, energy-p2, k-water, eps-water, vf-solid: 1e-05
Initial Conditions	Solid Volume Fraction: 0.1 Water Temperature: 300 K Solid Tempetature: 300K Water Turbulent Kinetic Energy: 1 m^2/s^2 Water Dissipation Rate: 1 m^2/s^3

As Table 3-14 shows, the fluid system was assumed to have the same viscosity as water, and was simulated as a Newtonian fluid. The values of water density and viscosity were used because the CFD simulations were performed as if the spherical agglomerates had already been formed, therefore, the amount of bridging liquid in the system was considered negligible. The viscosity in the system was assumed to be constant as water is a Newtonian fluid so it will have constant viscosity as agitation force is applied. The CFD simulations were validated by running an experiment with a mixture monosized red and clear glass beads suspended in water, the system was recorded, and the movement of the red beads was tracked in each frame. Appendix B - Impeller Geometry CFD Analysis shows a sequence of frames used in the CFD validation.

3.6.5   Mesh Density Analysis

The mesh for the created geometry occurred in ANSYS Mesher 2019 R2. The various areas of the tank geometry were labelled as "Named Sections" in ANSYS Mesher. These named sections determine the areas of contact between the different zones in the stirred tank. Contact sizing mesh was applied to the system due to there being contact between the moving area, classified as the inner domain, and the stagnant area, classified as the outer domain. The inner domain contains the agitator and the bulk of the moving fluid. The outer domain consists of the tank walls and baffles. A tetrahedral mesh was chosen for this system due to the flexibility of mesh construction, and the ability to simulate moving meshes to allow for impeller rotation (Sadrehaghighi, 2018).

Having a finer mesh will increase the accuracy of the results but will result in increased computational time. Simulations performed had the same set-up parameters at various mesh sizes until the results converged. This ensured that the mesh was sufficient to produce accurate results, whilst also ensuring that the computational time was not too long. The simulations to determine the ideal mesh density analysis simulated a flat blade impeller at a 25 mm clearance and an impeller speed of 450 rpm. Further CFD simulations used the best performing mesh from the mesh density analysis investigation. Table 3-15 shows the number of nodes and elements in the mesh for different mesh sizes, a graphical representation of the mesh density is shown in Figure 3-13. From Table 3-15, it can be seen that as the mesh size decreases, the number of nodes and elements increases rapidly. The increased mesh density, shown in Figure 3-13, reflects this increase.

Table 3-15 The number of nodes and elements for different mesh sizes tested as part of the mesh density analysis

Mesh Size (mm)	Number of Nodes	Number of Elements
6	10,487	46,898
5	17,329	81,483
4	30,868	151,303
3	66,917	341,675
2	207,652	1,110,692
1	1,495,923	8,436,968
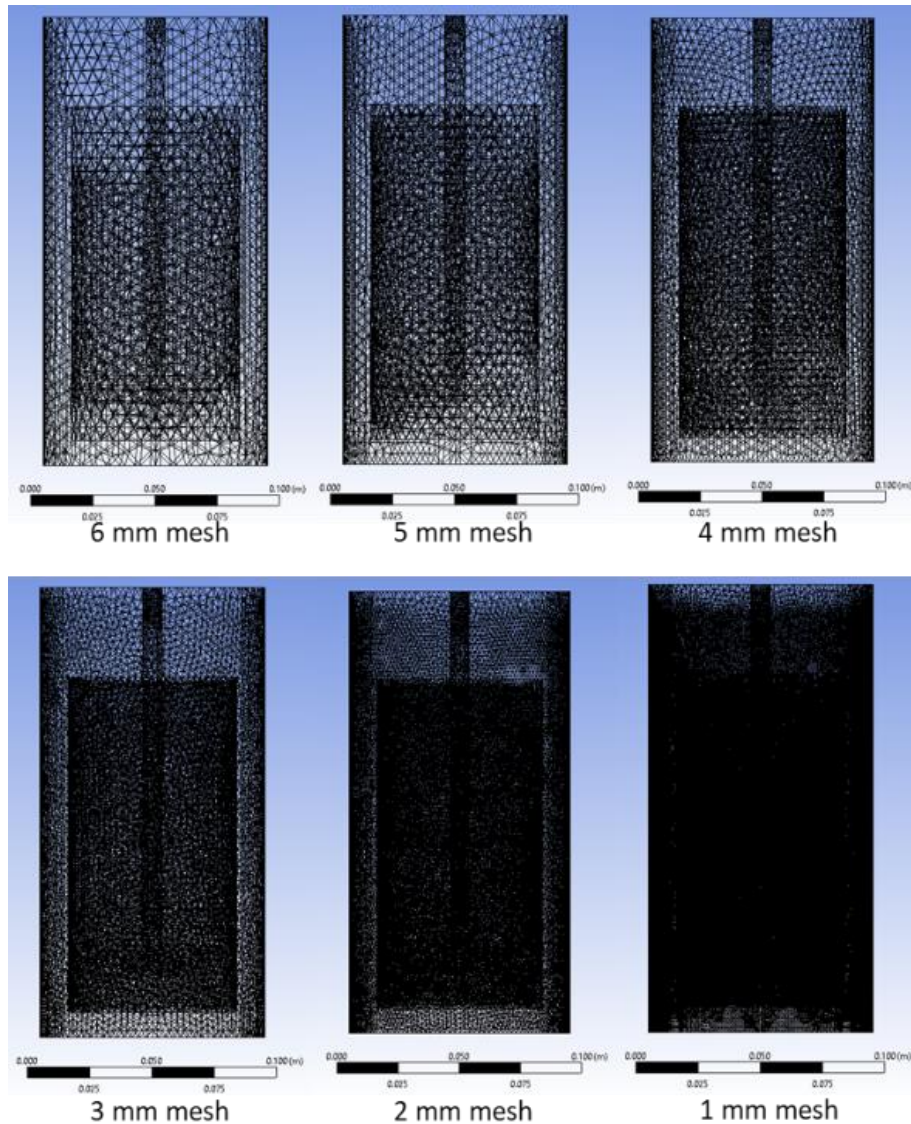
Figure 3-13 Schematics from ANSYS Mesh 2019 R2 for the various meshes tested as part of the mesh density analysis

3.6.6   Influence of Impeller Geometry Study CFD Simulations

The Mesh Density Analysis determined that a tetrahedral mesh with 4 mm mesh size was the best choice for the parametric CFD study. The geometries listed in Table 3-12 were simulated at 3 impeller speeds of 300 rpm, 450 rpm, and 600 rpm. A literature study investigated the impeller speeds used most often for spherical agglomeration studies of a similar volume. This study found that speeds between 200 and 700 rpm were most common; the number of studies that use different impeller speeds can be seen in Figure 3-14. The three impeller speeds for the different impeller configurations resulted in 60 CFD simulations performed as part of this thesis.
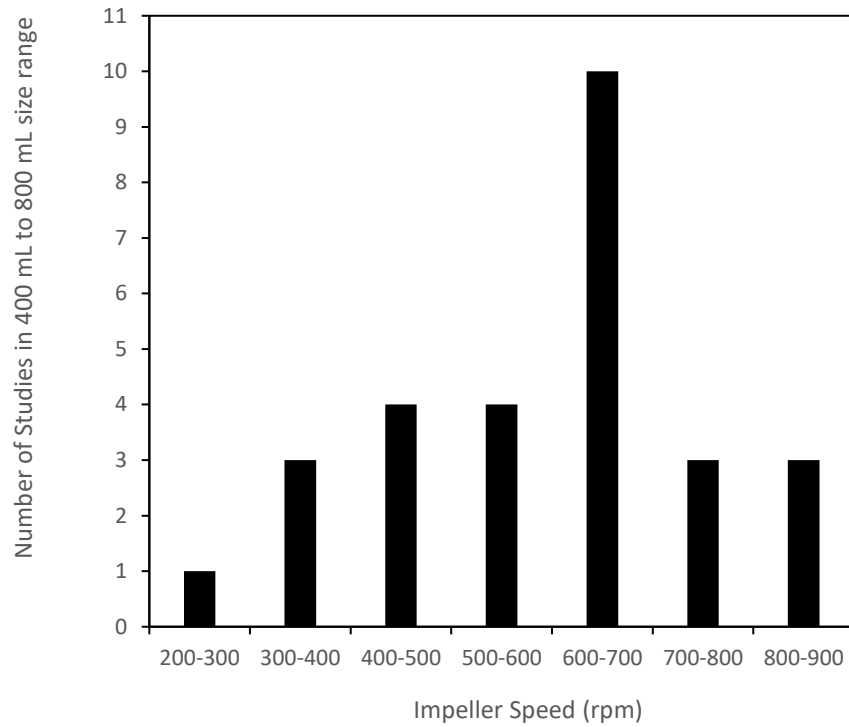
Figure 3-14 Impeller speed against number of experimental spherical agglomeration studies of similar liquid volume to the studied system

3.6.7   PBM Construction Simulations

Results from the 60 simulations of the parametric study produced fitting correlations for the velocity in the tank based on impeller characteristics. As these curves were fit with a 2nd order polynomial trendline, additional simulations were performed to increase the applicability of this trendline. Full details on the development of the fitting curves, and the additional simulations are in Chapter 6 of this thesis.

Chapter 4   Experimental Investigation into the Influence of Impeller Characteristics on Spherical Agglomeration

4.1   Introduction

From the literature review conducted in Chapter 2, it was found that due to the system specific nature of spherical agglomeration, the majority of research has focussed on determining the ideal solvent system to produce agglomerates. These studies have been useful in understanding parameters that influence agglomeration kinetics, however, there is little consistency in the equipment design. Spherical agglomeration occurs when an immiscible bridging liquid is added to a suspension of crystals. For successful agglomeration, there must be good contact between the bridging liquid and the crystals. A stirred tank system is commonly used for spherical agglomeration. In this equipment, the contact between the bridging liquid and crystals will be heavily influenced by the impeller characteristics. The aim of the work in this chapter is to investigate different impeller geometries, clearances and speeds to determine the influence that these parameters have on the formation of spherical agglomerates.

In this work, four different impeller geometries were investigated. The selected impellers were a flat blade impeller, a propeller impeller, a Rushton turbine impeller and a pitched blade impeller. These impellers were chosen as they promote different flow patterns in the tank. The Rushton turbine and flat blade impeller promote radial flow, whilst the pitched blade and propeller impeller promote axial flow (Van Wazer et al., 1995; Couper et al., 2012; Grenville et al., 2017). The different impeller geometries were all tested at clearances of 18 mm, 20 mm, 25 mm, 27 mm, and 30 mm with impeller speeds also being varied at 300 rpm, 450 rpm and 600 rpm. For each of the impeller conditions, toluene was added as the bridging liquid to a suspension of PMMA beads in water, and the system was agitated for 45 minutes. Section 3.3 details the full experimental methodology.

Figure 4-1 Image of the different impellers used in the experiments, from left to right – flat blade, propeller, Rushton turbine, pitched blade

From the experimental methodology (Section 3.3), 60 experimental conditions were investigated. Two repeats were performed for the experiments at 450 rpm and 25 mm clearance for each impeller. The data for these repeats, and standard deviations for the averages is given in Appendix A. As the repeated data was within an acceptable deviation, no repeats were performed for other conditions due to the large quantity of experiments this would have required. In this chapter, the results for each impeller are in individual sections, and a comparison of the results is given in Section 4.6. The PMMA beads used for these experiments are 52 µm. Therefore, any material in the particle size distribution (PSD) less than 500 µm is not considered a spherical agglomerate, even though it will have undergone growth.

To determine which impeller is most effective at generating spherical agglomerates, the following criteria will be considered; the agglomerates are sized between 500 µm and 1000 µm, there is a low value of the PSD span and the agglomerates are consistently spherical in shape.

4.2 Flat-Blade Impeller

The flat-blade impeller is a radial promoting impeller that has four blades with a 90 ° pitch. The PSD obtained for the spherical agglomeration experiments at different impeller clearances at an impeller speed of 300 rpm is shown in Figure 4-2. For an impeller speed of 300 rpm, there is a large portion of primary material for all impeller clearances, with 18 mm having the largest frequency of fine powder in the PSD. From Figure 4-2, it can be seen that for systems with an impeller speed of 300 rpm, clearances of 20 mm and 25 mm give the narrowest size distribution and produces the greatest mass of spherical agglomerates. In Figure 4-2, it can be seen that there is the lowest amount of primary material when the flat blade is used with an impeller clearance of 30 mm, however the PSD peaks for 30 mm are under 500 µm, suggesting limited agglomeration at this clearance. A clearance of 27 mm is the only one that produces a definitive peak that is greater than 500 µm.
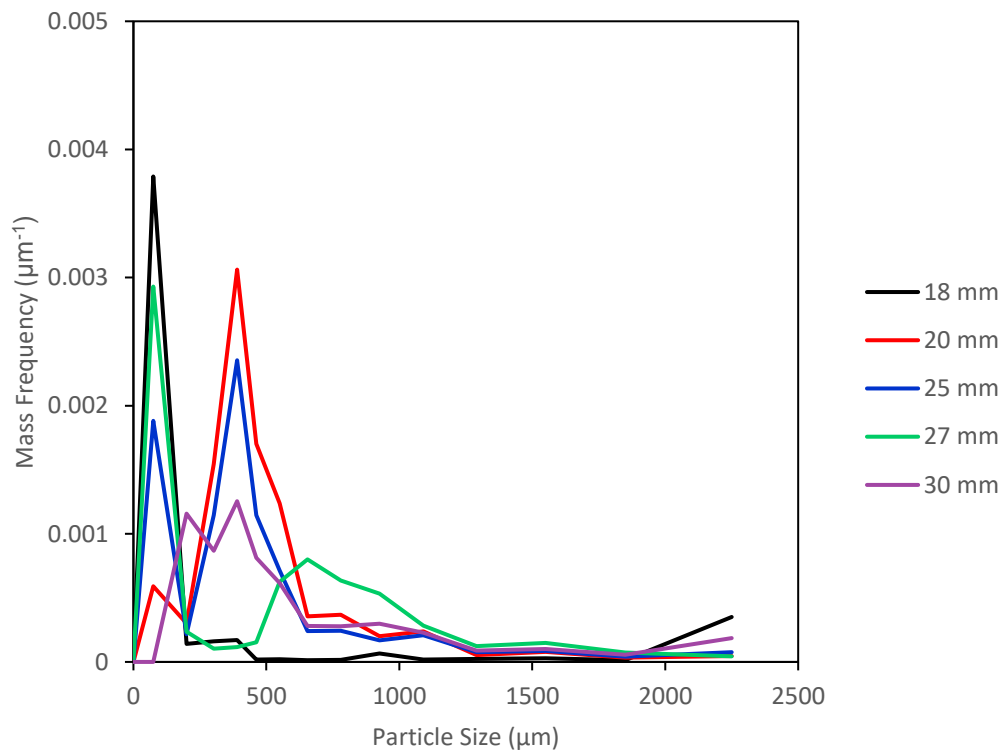
Figure 4-2 PSD for agglomerates produced by the flat blade impeller at a speed of 300 rpm for different clearances

The flat blade impeller rotating at 450 rpm forms more agglomerates between 500 µm and 1000 µm for all clearances compared to a speed of 300 rpm. Figure 4-3 shows the PSDs for agglomerates produced with the flat blade impeller at different clearances with a speed of 450 rpm. In this figure, the clearances of 18 mm and 30 mm have the lowest fraction of unagglomerated material, with the 30 mm clearance having the narrowest PSD.

At a speed of 450 rpm, the clearance of 25 mm produces the largest portion of fine material whilst also producing large agglomerates. In Figure 4-3, the clearance of 27 mm has the broadest PSD. This broad size distribution may be due to a clearance of 27 mm being a transition point in the flow pattern. Multiple studies have determined that a C/D ratio of 0.3 influences the shape and height of flow patterns for different impeller geometries. It has been found that lower clearances increased particle suspension with a flat blade impeller (Devarajulu and Loganathan, 2016).
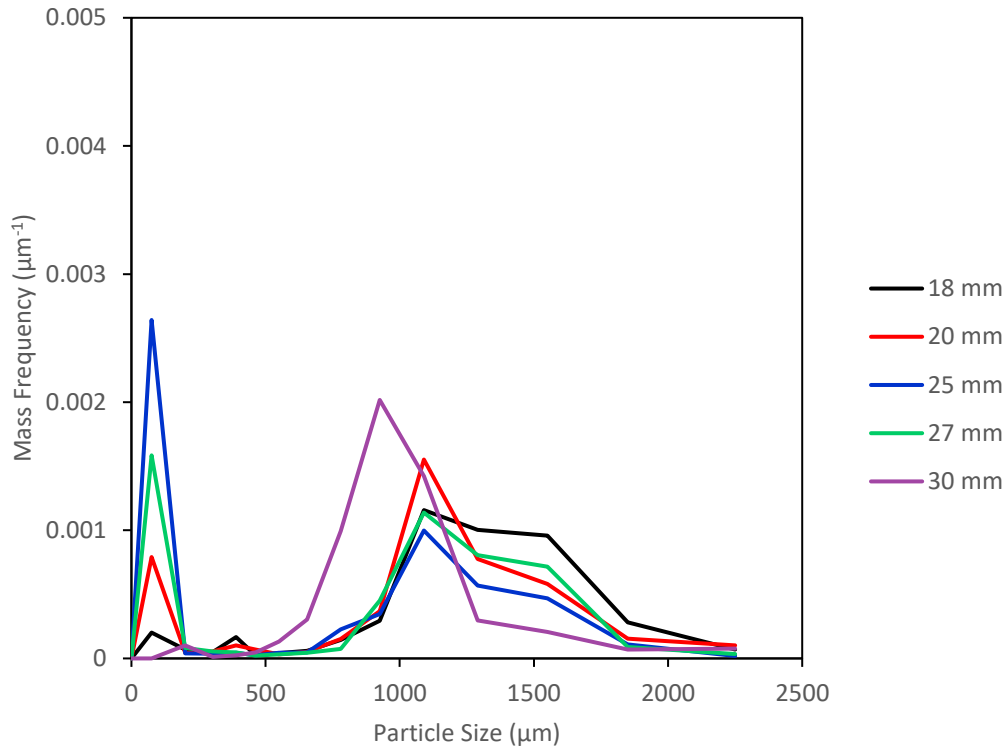
Figure 4-3 PSD for agglomerates produced by the flat blade impeller at a speed of 450 rpm for different clearances

At an impeller speed of 600 rpm, a clearance of 25 mm and 30 mm produce a fairly consistent PSD, with the 30 mm clearance producing larger granules, this can be seen in Figure 4-4. The agglomerates produced at 25 mm and 30 mm clearance have a peak at approximately 550 μm. Both clearances see a rapid decrease in the mass frequency from 550 μm to 700 μm. The PSD for 30 mm clearance has more agglomerates over this size than at the lower clearance, suggesting the increased clearance has less efficient mixing. The larger agglomerates at a clearance of 30 mm compared to 25 mm can be seen in Figure 4-5.

The clearance with the greatest portion of fines is with a clearance of 27 mm. This could be due to this clearance being a transition point between flow patterns. In a study by Devarajulu and Loganathan, 2016, it was observed that increasing the impeller clearance reduced particle suspension when a flat blade impeller was used. This is due to an increased suspension power being required by a flat blade impeller as the clearance increases (Chudacek, 1985).

Clearances of 18 mm and 20 mm have a similar PSD. For these clearances there is a relatively broad peek between approximately 600 μm and 1800 μm, with the maximum mass frequency at 110 μm. This peak

suggests a fairly uniform distribution of agglomerates, but they are much larger than at the clearances of 25 mm and 30 mm, this can also be seen in Figure 4-5.
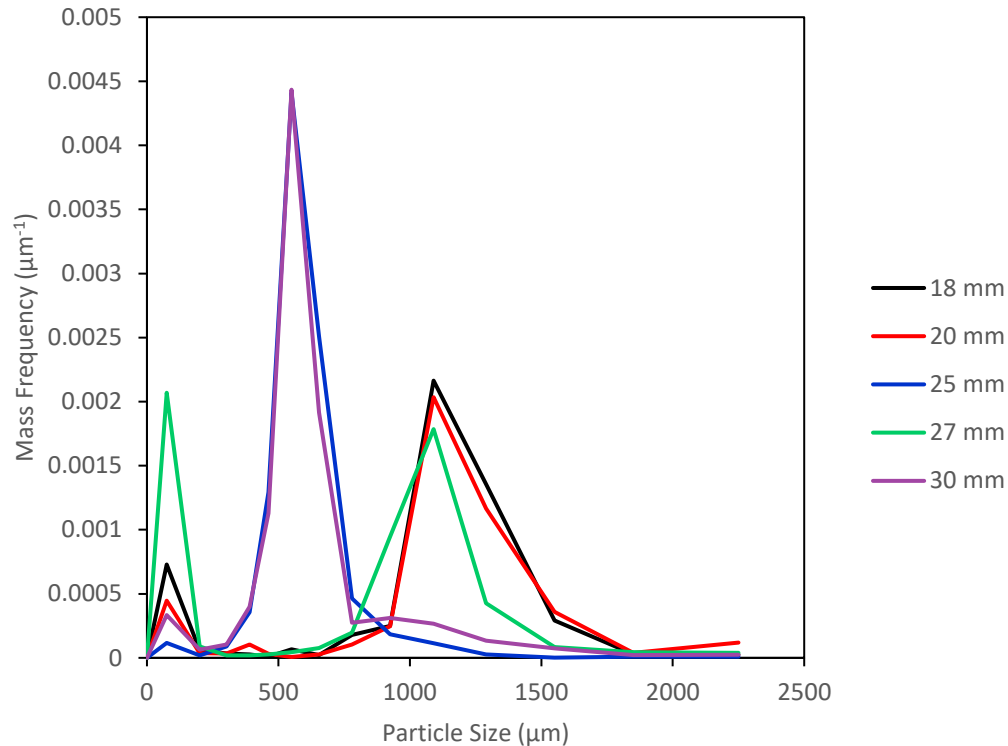
Figure 4-4 PSD for agglomerates produced by the flat blade impeller at a speed of 600 rpm for different clearances

Figure 4-5 shows images of spherical agglomerates produced by the flat blade impeller at varied impeller speeds and clearances. From this figure, it can be seen that an impeller speed of 300 rpm is not as effective at producing spherical agglomerates as increased impeller speeds. This is demonstrated by there being a few large agglomerates and a large mass of unagglomerated material. The agglomerates produced at 300 rpm are also of lower sphericity than agglomerated formed at increased impeller speeds.

The impeller condition that produces the best agglomerates appears to be an impeller speed of 600 rpm, with a clearance of 25 mm. These agglomerates are spherical in nature and the most consistently sized. The consistency in size is also shown in Figure 4-4, as the agglomerates produced at a clearance of 25 mm have the narrowest size distribution, and the lowest mass frequency of fine material. The increase in impeller clearance resulting in difficulties with particle suspension for a flat blade impeller has been observed in multiple studies (Chudacek, 1985; Devarajulu and Loganathan, 2016). In the study by Devarajulu and Loganathan, 2016, it was observed found that the ability of a flat blade impeller to suspend particles decreases at an impeller clearance to diameter ratio (C/D) above 0.3.

The highest impeller speed of 600 rpm will induce more shear on the system, increasing the consolidation and potential breakage of agglomerates, leading to a lower particle size (Chaterjee et al., 2017). Breakage phenomena in spherical agglomeration has not been investigated as well as the other mechanisms of formation, consolidation and growth.

	18 mm	20 mm	25 mm	27 mm	30 mm
300 rpm					
450 rpm					
600 rpm					

− 1000 µm

Figure 4-5 Images of agglomerates formed with the flat blade impeller at varied impeller speeds and clearances, the red scale bar is 1000 µm

Figure 4-6 shows the average particle size (d_{43}) for the agglomerates produced using a flat blade impeller at the various impeller speeds and clearances tested. The average size of agglomerates produced at a clearance of 18 mm and a speed of 300 rpm is just under 1000 µm although the mass frequency of particles is highest for sizes lower than 250 µm (Figure 4-2). This is due to this system also producing very large agglomerates due to inefficient mixing.

As Figure 4-6 shows, the largest average agglomerate size for all clearances other than 20 mm is for agglomerates produced at 450 rpm. From Figure 4-5, the agglomerates produced at 450 rpm appear to be more consistently spherical than agglomerates produced at 300 rpm, there is also less fine powder for 450 rpm agglomerates than those formed at 300 rpm. The increase in size between the agglomerates and 300 rpm and 450 rpm may be due to the increased impeller speed resulting in more contact between the primary particles and bridging liquid. In Figure 4-6, it can be seen that the agglomerates produced at 600 rpm are on average smaller than those at 450 rpm. This could be due to the increased impeller speed increasing the shear in the system, promoting consolidation and breakage of agglomerates, this phenomenon has also been observed in Chaterjee et al., 2017.
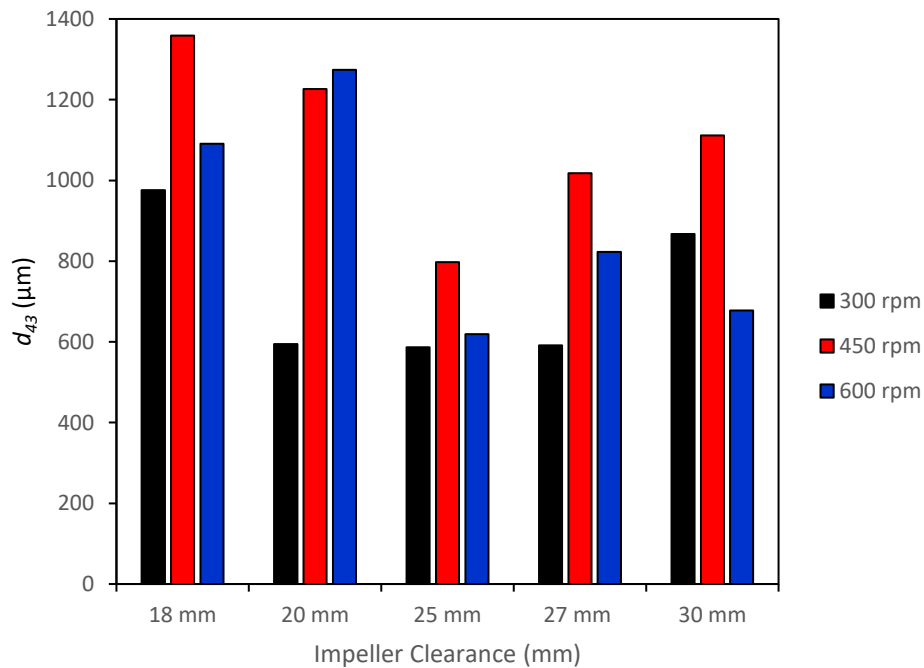
Figure 4-6 Average particle size for the flat blade impeller experiments at different impeller speeds and clearances, the standard deviation of the repeats for the experiment at 25 mm and 450 rpm was 0.441

4.3   Propeller

The propeller impeller has 3 blades at a 60 ° angle from the impeller shaft and it promotes axial flow in the tank. As discussed in Section 2.10, axial flow is a single loop flow pattern and is thought to give improved solid suspension compared to double loop (radial) flow impellers (Montante et al., 1999; Zhu et al., 2019). Figure 4-7 shows the PSD for spherical agglomerates produced using the propeller impeller at a speed of 300 rpm with different clearances. In Figure 4-7, it can be seen that all impeller clearances have

a large mass density of fine powder at impeller speeds of 300 rpm. For impeller clearances of 18 mm, 27 mm and 30 mm, the majority of the sieved material are unagglomerated fines (<500 µm). Clearances of 20 mm and 25 mm still have a large portion of unagglomerated material, but they also have very large masses of agglomerated material. The large portion of fines together with very large agglomerates is due to inefficient mixing in the system. Both Figure 4-7 and Figure 4-10 show that there is limited successful agglomeration for the propeller impeller at a speed of 300 rpm and, therefore, this configuration should not be considered for further spherical agglomeration studies. CFD simulations of this configuration were still performed to determine the velocity profiles in the tank (Chapter 5).
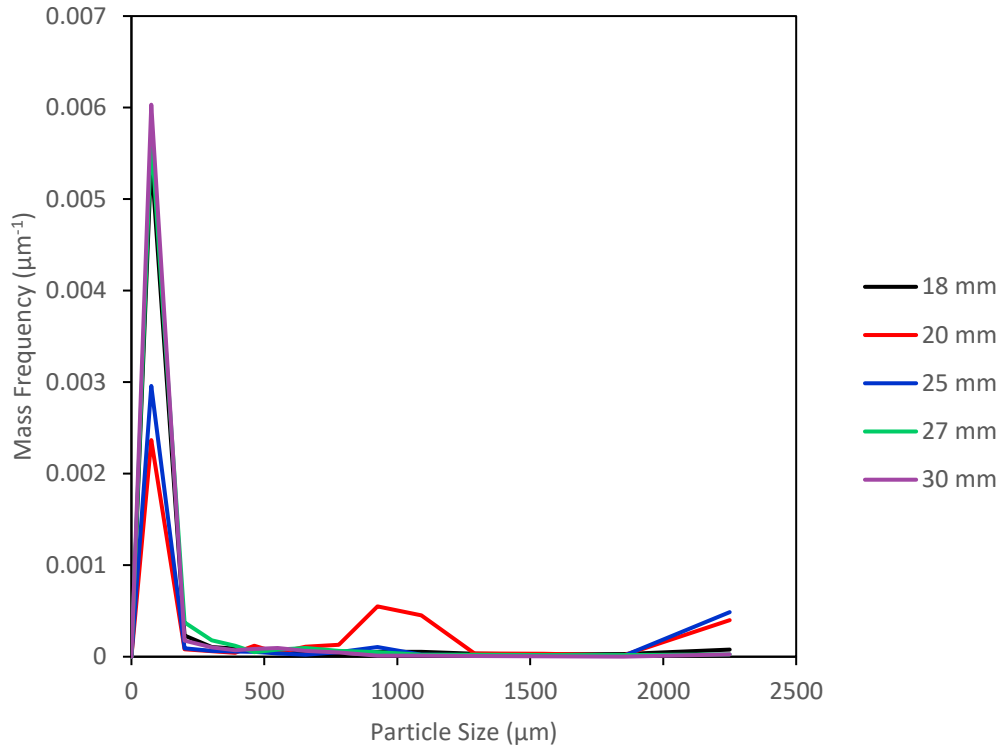
Figure 4-7 PSD for the propeller impeller with an impeller speed of 300 rpm at various clearances

In Figure 4-8, the PSD for the propeller impeller at a speed of 450 rpm can be seen for all five of the impeller clearances tested. When comparing Figure 4-8 with Figure 4-7, it is evident that a speed of 450 rpm greatly reduces the number of fines in the system, and also increases agglomerate formation. This is also corroborated by Figure 4-10. The lowest portion of fine material for the propeller impeller at 450 rpm is with an impeller clearance of 30 mm. The agglomerates produced at this clearance appear to be larger and more consistently spherical than agglomerates produced at lower clearances.

For clearances of 25 mm and below there is a trimodal size distribution. The first peak for these distributions are below 250 µm; this is unagglomerated primary material. There is then a peak at approximately 500 µm, with the third one at 1000 µm. These peaks are likely due to poor mixing between the primary particles and the bridging liquid leading to inefficient bridging liquid distribution.
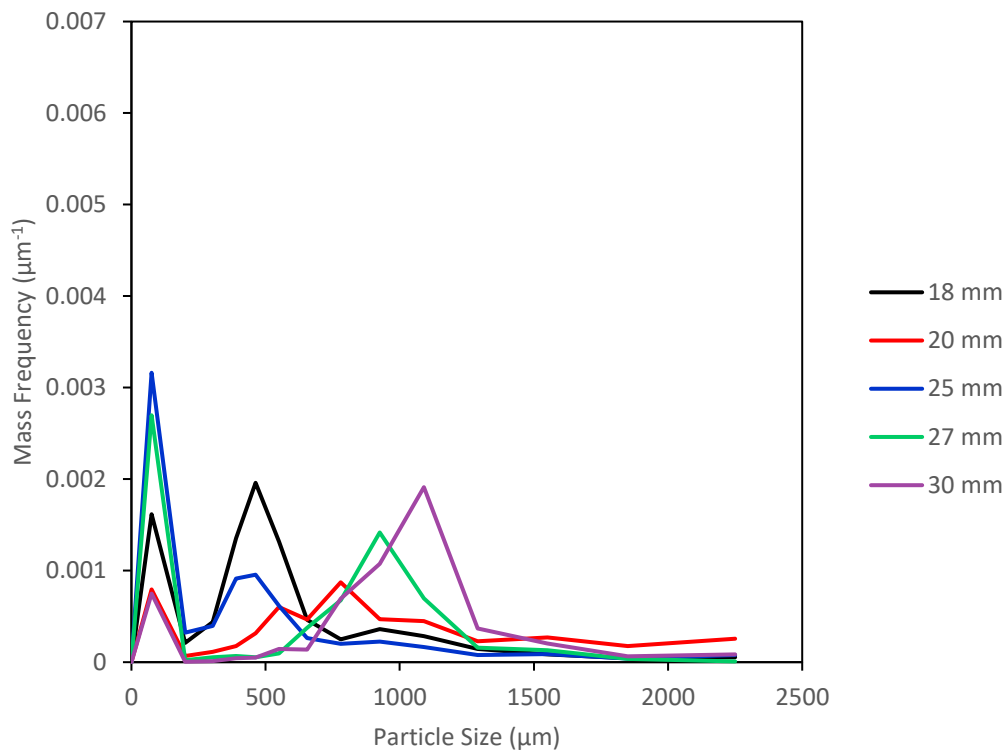
Figure 4-8 PSD for the propeller impeller with an impeller speed of 450 rpm at varied impeller clearances

Figure 4-9 shows the PSD for the propeller impeller at different clearances with a speed of 600 rpm. Impeller clearances of 27 mm and below have a bimodal distribution. For these clearances there is a high mass frequency of particles below 250 µm. This is unagglomerated material due to inefficient mixing.

Clearances of 18 mm and 20 mm have a peak at approximately 500 µm. This suggests that although there are lots of fines at these clearances, there is still successful agglomeration. This suggests that the impeller flow characteristics are not sufficient to provide efficient mixing and contact between the bridging liquid and the primary particles. The higher clearances, 25 mm and 27 mm, have their second peak over 1000 µm; this is due to coalescence between agglomerates leading to larger agglomerate structures.

The impeller clearance of 30 mm gives a trimodal distribution for the particle mass frequency. This clearance also has a relatively large portion of fine material, but also has two further peaks in the distribution, one at approximately 1100 µm and the final peak at approximately 1550 µm. These peaks suggest that there is inefficient mixing of the bridging liquid and the solid particles.

Although there is still a high portion of fines for all clearances, there are fewer fines at 600 rpm than at 300 rpm (Figure 4-7). This can also be seen by comparing agglomerate images in Figure 4-10. The reduction in fines at higher impeller speeds is due to the particles having a higher collision velocity. From Equation 2.15, it can be seen that increasing the particle collision velocity will increase the adhesive force between

agglomerates, resulting in more successful agglomerations in the system (Blandin et al., 2005; Ahmed et al., 2023).
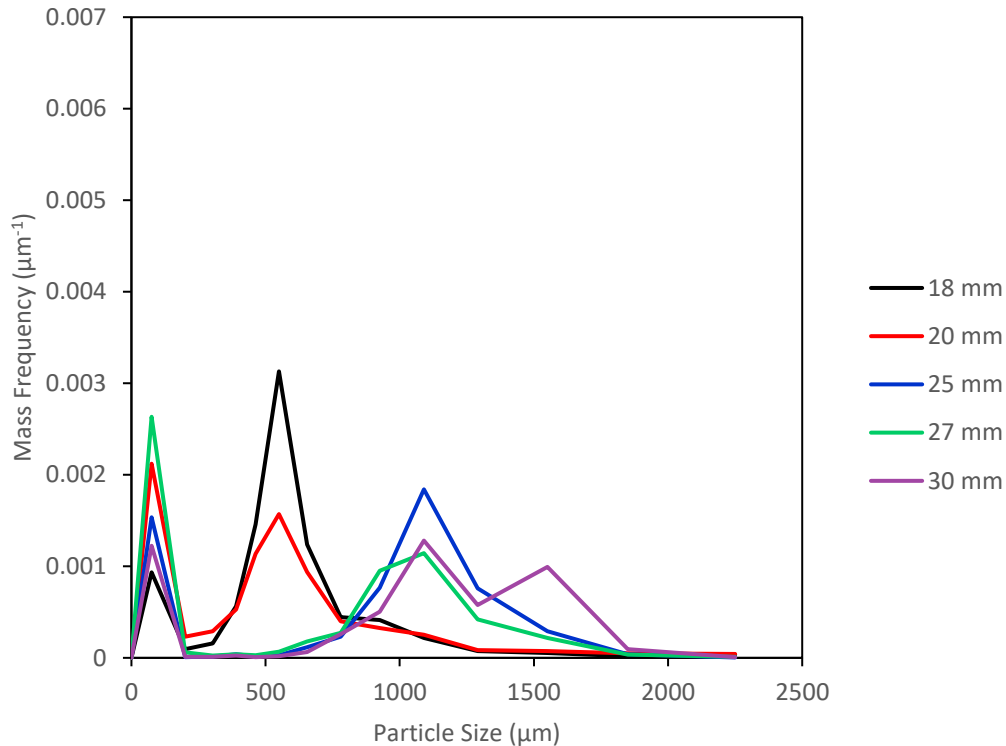
Figure 4-9 PSD for the propeller impeller at different clearances with an impeller speed of 600 rpm

Figure 4-10 shows images of the agglomerates produced with the propeller impeller at different impeller speeds and clearances. It can be seen that an impeller speed of 300 rpm is insufficient for successful agglomerate production. The many fine particles with a few, very large agglomerates in the images suggest that some particles are not suspended and therefore there is no contact with bridging liquid, whilst others are overwetted, resulting in oversized agglomerates. The lack of suspension may be due to some areas of the tank operating at velocities under the critical particle suspension velocity. Chapter 5 presents the results of a corresponding CFD investigation into the influence of impeller geometry on velocity profiles in the tank.

In Figure 4-10, the agglomerates for all impeller clearances and speeds are not as spherical as ones produced using a flat blade impeller (Figure 4-5). The lack of sphericity for these agglomerates may be due to the propeller impeller not imparting sufficient shear on the system to induce consolidation within the agglomerates (Dogon and Golombok, 2015).

	18 mm	20 mm	25 mm	27 mm	30 mm
300 rpm					
450 rpm					
600 rpm					

− 1000 µm

Figure 4-10 Images of the agglomerates formed using the propeller impeller at varies impeller speeds and clearances, the scale bar is 1000 µm

In Figure 4-11, the average size of the agglomerates at varied impeller speeds and clearances can be seen. There is not a clear correlation between the impeller clearance and speed with the average particle size. This is due to the bimodal and trimodal distributions present in all PSDs. As can be seen in most agglomerate images (Figure 4-10), all impeller configurations have a wide variety of particle shapes and sizes. This shows inefficient mixing in the system as not all particles were able to contact the bridging liquid.

The images in Figure 4-10 and the mean particle size shown in Figure 4-11 suggest that an impeller speed of 600 rpm and a clearance of 25 mm would be the optimal impeller configuration for spherical agglomerate production with a propeller impeller. The agglomerates produced under these conditions are the most consistently spherical in shape and have an average particle size over 500 μm, whilst being under 1000 μm. The PSD in Figure 4-9 however, shows that the majority of sieved material is either under 250 μm, with the large size peak being over 1000 μm. This bimodal distribution suggests that even though these agglomerates appear consistent in shape, the propeller impeller is not an ideal impeller geometry for spherical agglomeration.
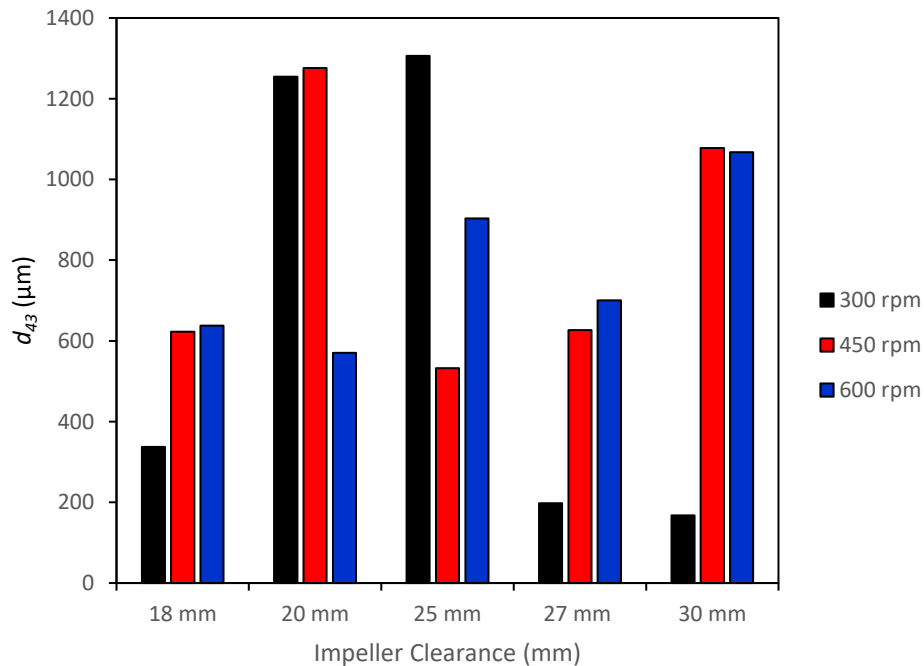
Figure 4-11 Average particle size for the propeller impeller at various impeller speeds and clearances, the standard deviation of the repeats for the experiment at 25 mm and 450 rpm was 0.592

4.4   Rushton Turbine

The Rushton turbine impeller is an impeller that promotes radial flow. It has a disc perpendicular to the impeller shaft, and six blades coming from the shaft and through the disc at a 90 ° blade pitch. The Rushton turbine used for this work can be seen in Figure 3-5.

Figure 4-12 shows the PSD of spherical agglomerates produced using a Rushton turbine impeller with an impeller speed of 300 rpm at different impeller clearances. At an impeller speed of 300 rpm, there are still fines present in the system for each impeller clearance, but they have all been successful at forming

agglomerates as every distribution has a peak above 500 μm. The 25 mm clearance has the largest proportion of fines in the system, suggesting that this clearance does not promote even mixing and particle suspension throughout the tank.

A clearance of 30 mm produces the largest agglomerates, with two of the peaks in the trimodal distribution being over 1000 μm and 1500 μm. There are still fines produced with this impeller clearance however, this is the lowest mass frequency of fines. The reduction in fines and production of larger agglomerates at a 30 mm clearance may be due to this being the only tested clearance that produces a double loop flow pattern (Montante et al., 1999; Zhu et al., 2019).
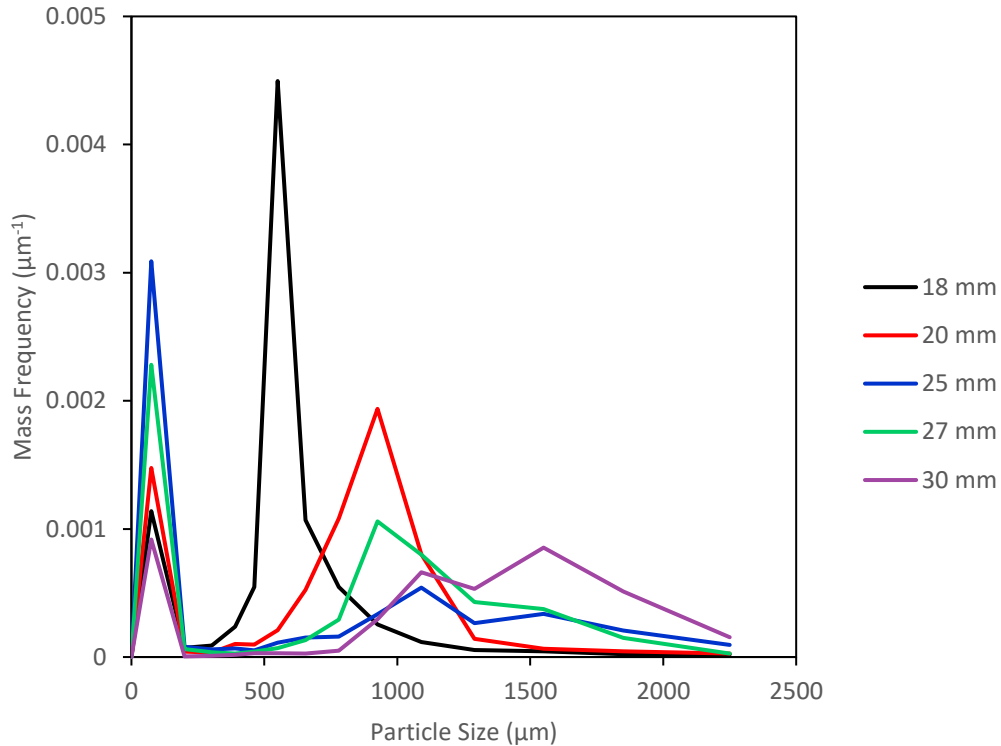
Figure 4-12 PSD for the agglomerates produced with the Rushton turbine at different clearances with an impeller speed of 300 rpm

The agglomerate PSDs in Figure 4-13 are for agglomerates formed with a Rushton turbine at an impeller speed of 450 rpm, at different impeller clearances. An impeller clearance of 20 mm produces the least amount of fines, and has a relatively narrow distribution that peaks at approximately 550 μm. The low portion of fines with a narrow distribution suggests that this impeller configuration provides increased contact between the bridging liquid and primary particles in comparison to other systems. Due to the low clearance of this impeller, the Rushton turbine will be generating a single loop flow pattern within the tank, which is considered to be beneficial for particle suspension (Montante et al., 1999; Zhu et al., 2019).

At 450 rpm, the largest portion of fines produced with the Rushton turbine are at an impeller clearance of 30 mm. This is at a C/D value of 0.33 which will result in a fully formed double loop pattern. This double loop may be reducing the suspension of particles in comparison to lower clearances, resulting in fewer particles having contact with the bridging liquid (Montante et al., 1999; Zhu et al., 2019).
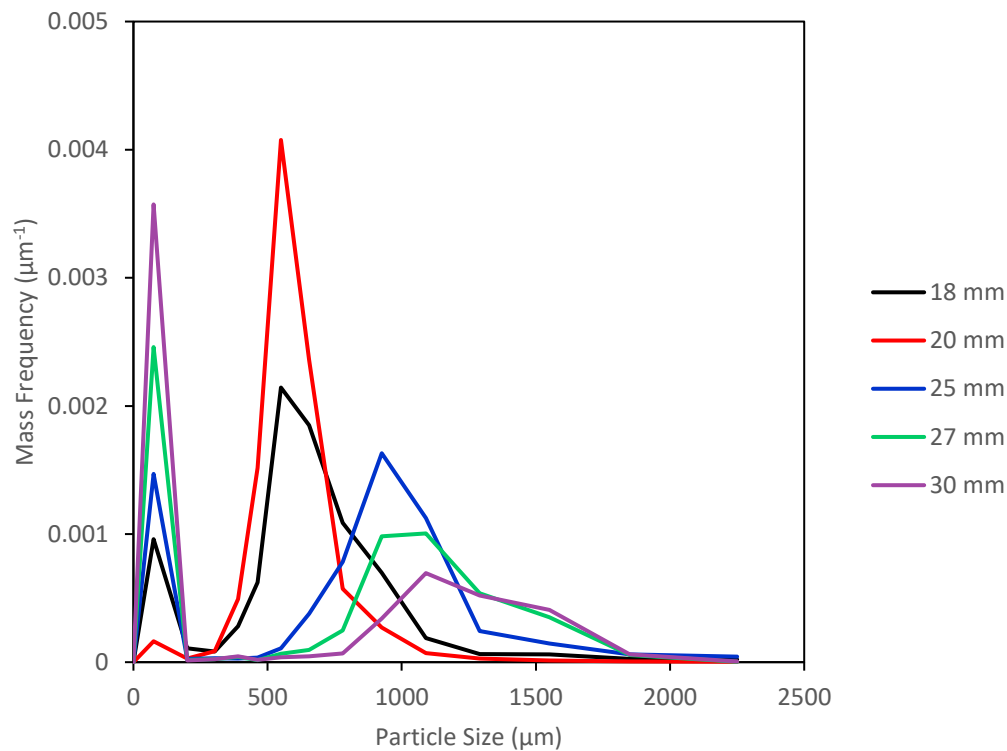
Figure 4-13 PSD for spherical agglomerates formed using a Rushton turbine at 450 rpm impeller speed, with various clearances

Figure 4-14 shows the PSD for spherical agglomerates produced using a Rushton turbine impeller at different clearances, with an impeller speed of 600 rpm. The PSD for an 18 mm clearance is similar to the PSD for an 18 mm clearance Rushton turbine at 300 rpm (Figure 4-12), however, the 600 rpm distribution has a third peak at approximately 1300 μm. This third peak suggests that whilst the clearance of 18 mm gives the fewest fines, and the bulk of the agglomerates are between 500 μm and 900 μm, there is a significant portion of oversized agglomerates. The presence of oversized agglomerates suggest that there is not even dispersion of bridging liquid throughout the tank, resulting in some particles being able to agglomerate more than others.

The impeller clearance of 27 mm at 600 rpm gives a PSD with 4 peaks. In this distribution, two of the peaks are below 500 μm, suggesting a large amount of fines in the system. The most prominent peak is at approximately 900 μm, with a shallower peak at 1500 μm. The values of these peaks demonstrate inefficient mixing in the system resulting in oversized agglomerates and a large portion of fines. The clearance of 27 mm is at a C/D value of 0.3, this clearance is the transition point between a radial flow impeller producing a single loop flow pattern or a double loop flow pattern. Operating at this transition point may have resulted in fluctuations and variations in flow pattern over the course of the experiment, leading to inefficient mixing (Montante et al., 1999; Zhu et al., 2019).
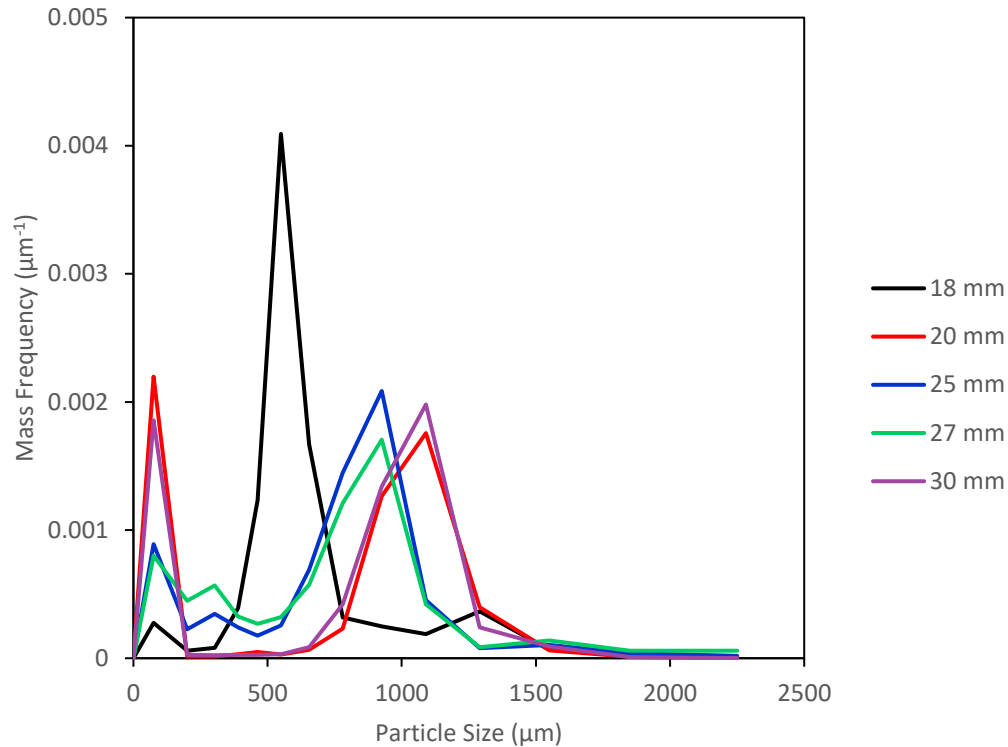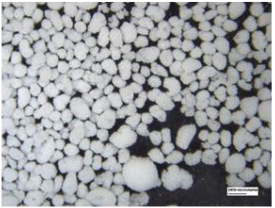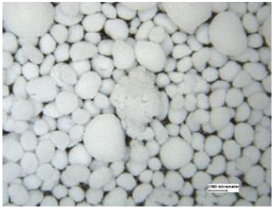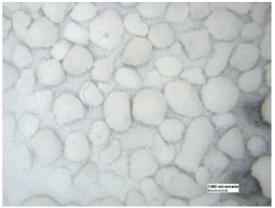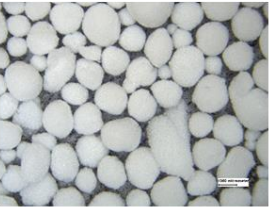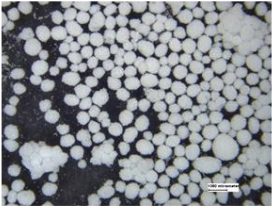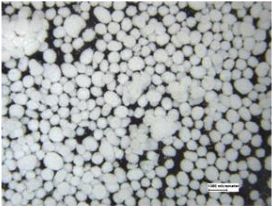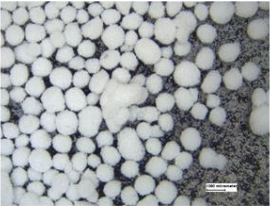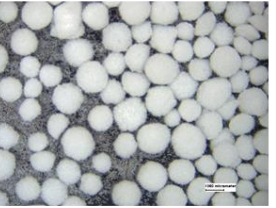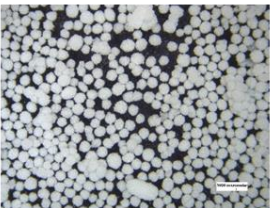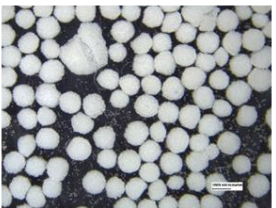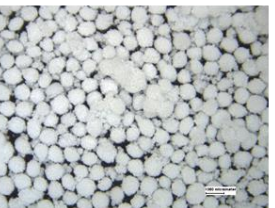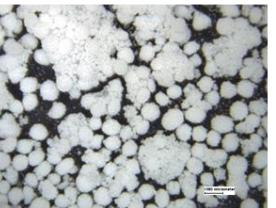
Figure 4-14 PSD of spherical agglomerates produced using a Rushton turbine at 600 rpm with various clearances

Figure 4-15 shows images of the spherical agglomerates produced using a Rushton turbine at different impeller speeds and clearances. The majority of the agglomerates in these images are spherical in appearance, with the non-spherical agglomerates being considerably larger than the bulk of the agglomerates. The larger agglomerates, with lower sphericity, will have been formed by coalescence of the spherical agglomerates (Pitt et al., 2018; Cheng et al., 2020).

The agglomerates formed at a speed of 600 rpm and a clearance of 27 mm have a broad range of sizes, this matches the PSD shown in Figure 4-14. This image contains very large coalesced masses, as well as primary material and smaller agglomerates, demonstrating the inefficient suspension of particles, and dispersion of bridging liquid at this condition. Agglomerates produced at the same speed, with a 30 mm clearance have a narrower distribution (Figure 4-14) and the agglomerates are more consistent in shape and size (Figure 4-15). This suggests that the clearance of 27 mm is undergoing a transition and fluctuations between double and single loop flow patterns, causing ineffective mixing (Montante et al., 1999; Zhu et al., 2019).

Although the PSDs for 18 mm at 300 rpm and 600 rpm were similar, the images of the agglomerates show that the 600 rpm agglomerates are more consistently spherical in shape. The improved sphericity at 600 rpm can be due to the increased impeller speed causing more consolidation in the system (Thati and Rasmuson, 2012; Saini et al., 2013). The consistency in the size and sphericity of agglomerates may be improved with a longer mixing time (Peña and Nagy, 2015).

	18 mm	20 mm	25 mm	27 mm	30 mm
300 rpm					
450 rpm					
600 rpm					

− 1000 µm

Figure 4-15 Images of spherical agglomerates formed with the Rushton turbine impeller at various impeller speeds and clearances, the scale bar is 1000 µm

The average particle size for the spherical agglomerates produced using a Rushton turbine at various impeller speeds and clearances can be seen in Figure 4-16. The mean for the majority of the impeller configurations in between 580 µm and 870 µm. The consistency across clearances and impeller speeds suggest that flow patterns and velocities produced by a Rushton turbine impeller are beneficial for promoting contact between the primary particles and the bridging liquid, inducing agglomeration.

Rushton turbine impellers have increased power consumption. It has also been found that increased Rushton turbine clearances will increase the power requirements (Devarajulu and Loganathan, 2016). In the spherical agglomeration PBM by Ahmed et al., 2023, the power consumption is used to estimate the energy dissipation in the system (Equations 6.2 to 6.4). The energy dissipation is used for calculating velocity of particle and fluid interactions, as well as the separation force (Blandin et al., 2005; Arjmandi-Tash et al., 2019; Ahmed et al., 2023). Therefore, increased clearance will increase the power consumption in the system, resulting in higher velocities in the system. Increased velocities will result in more successful collisions, and consolidation of the agglomerates.

The impeller speed of 300 rpm at a clearance of 30 mm gives agglomerates with a mean size of 1410 µm. In the PSD for this configuration (Figure 4-12) there were 3 peaks; one was the fines, and the other two were both over 1000 µm. The agglomerate images (Figure 4-15) show that agglomerates produced at 300 rpm with a 30 mm clearance are consistently large, and mostly spherical. The large agglomerates may be due to the increased clearance causing high power consumption, and therefore increased collision velocities (Devarajulu and Loganathan, 2016). The system however, is at a low impeller speed so there may not be sufficient shear to induce agglomerate breakage or consolidation, reducing the number of fines as proposed by Chaterjee et al., 2017.
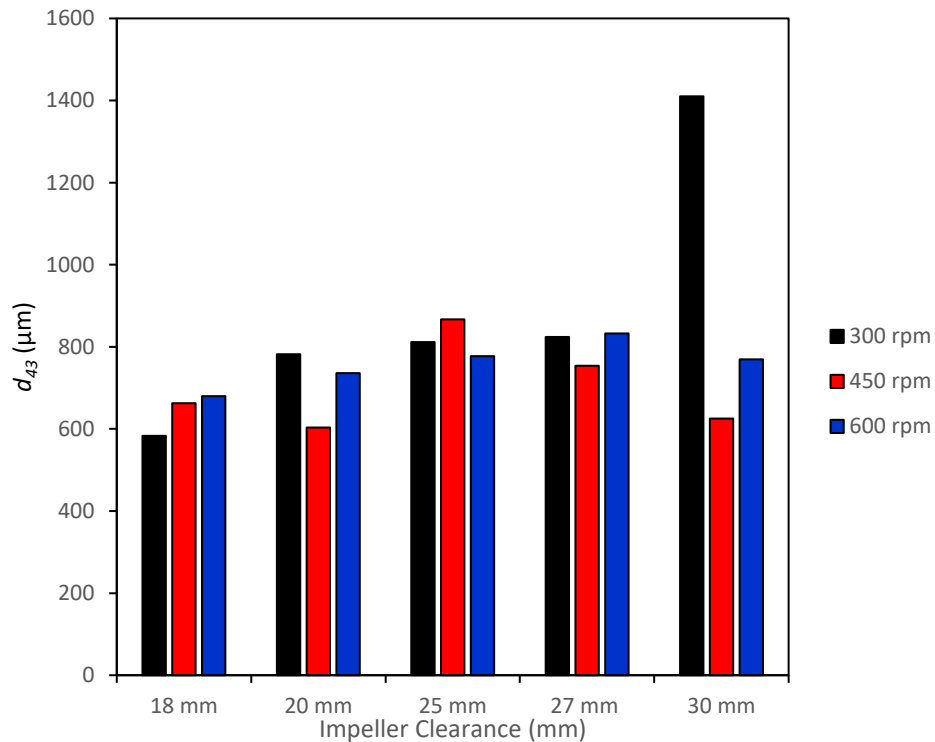
Figure 4-16 Average particle size of agglomerates formed using the Rushton turbine impeller at various impeller speeds and clearances, the standard deviation of the repeats for the experiment at 25 mm and 450 rpm was 0.19

4.5   Pitched-Blade Impeller

The pitched blade impeller for this work has four blades that exit the shaft at a 45 ° blade pitch; this impeller can be seen in Figure 3-5. Figure 4-17 shows the PSD of spherical agglomerates produced with a pitched blade impeller at 300 rpm with various impeller clearances. It can be seen that clearances of 18 mm, 20 mm and 30 mm had large mass frequencies of fines in the PSD. There was some agglomeration occurring at a clearance of 25 mm. However, this peak is below 500 µm and is considered unagglomerated material.

All clearances produced some agglomerated material (greater than 500 µm) at a speed of 300 rpm, but the mass of this is much lower than the mass of fines produced. A clearance of 27 mm was most effective at producing agglomerates as it has two peaks after 500 µm. The 27 mm PSD is a trimodal distribution which shows that even though this clearance was the best of the system, it still had mixing inefficiencies in the tank.
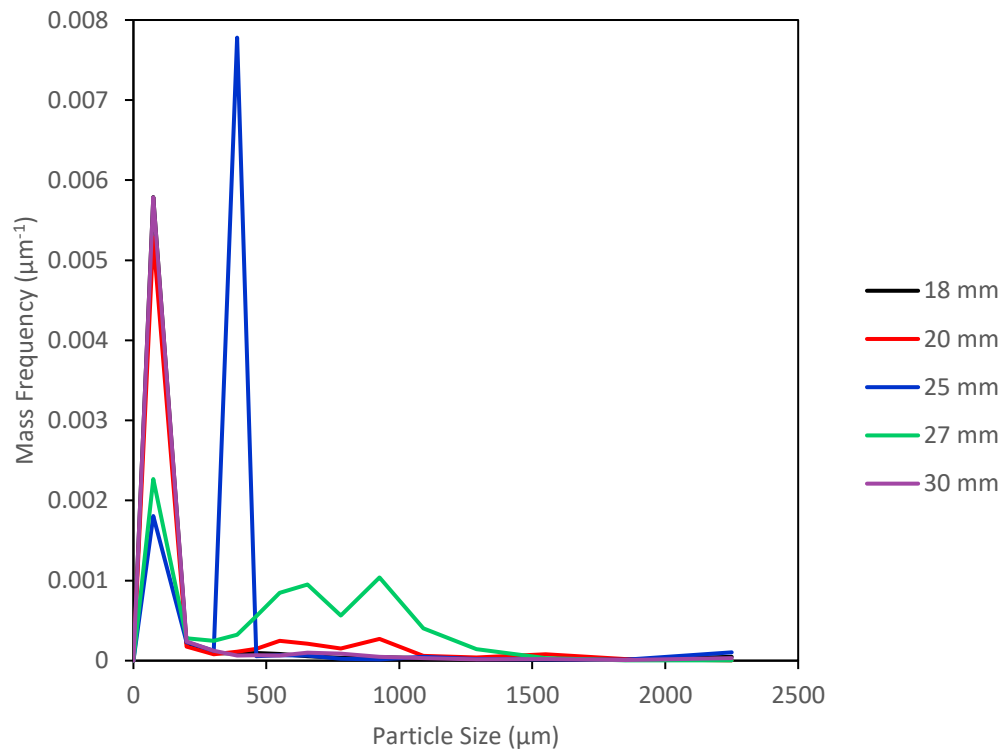
Figure 4-17 PSD for the spherical agglomerates formed with a pitched blade impeller at an impeller speed of 300 rpm at various impeller clearances

Figure 4-18 shows the PSD for pitched blade impeller agglomerates produced at a speed of 450 rpm with different impeller clearances. For each clearance tested, the PSD has a bimodal distribution. The first peak for all clearances is below 250 µm, meaning that there was still unagglomerated fines after 45 minutes of agglomeration time.

As can be seen in Figure 4-18, the second peak of the bimodal distributions was lowest for a clearance of 27 mm. This second peak was also the narrowest distribution for the 450 rpm impeller speed with a pitched blade impeller. This suggests that an impeller clearance of 27 mm for a 450 rpm impeller speed

promotes improved mixing between the bridging liquid and primary particles. A study by Kresta and Wood., 1993 found that at an impeller clearance that is 30 % of the tank diameter, the flow pattern reaches both the top and bottom of the tank, increasing suspension. As the tank diameter is 90 mm, a 27 mm clearance will be 30 % of the tank diameter, resulting in a full circulation loop of the tank. This full single loop will draw down less dense material and suspend any settled particles, resulting in even mixing between the bridging liquid and particles (Kresta and Wood, 1993).
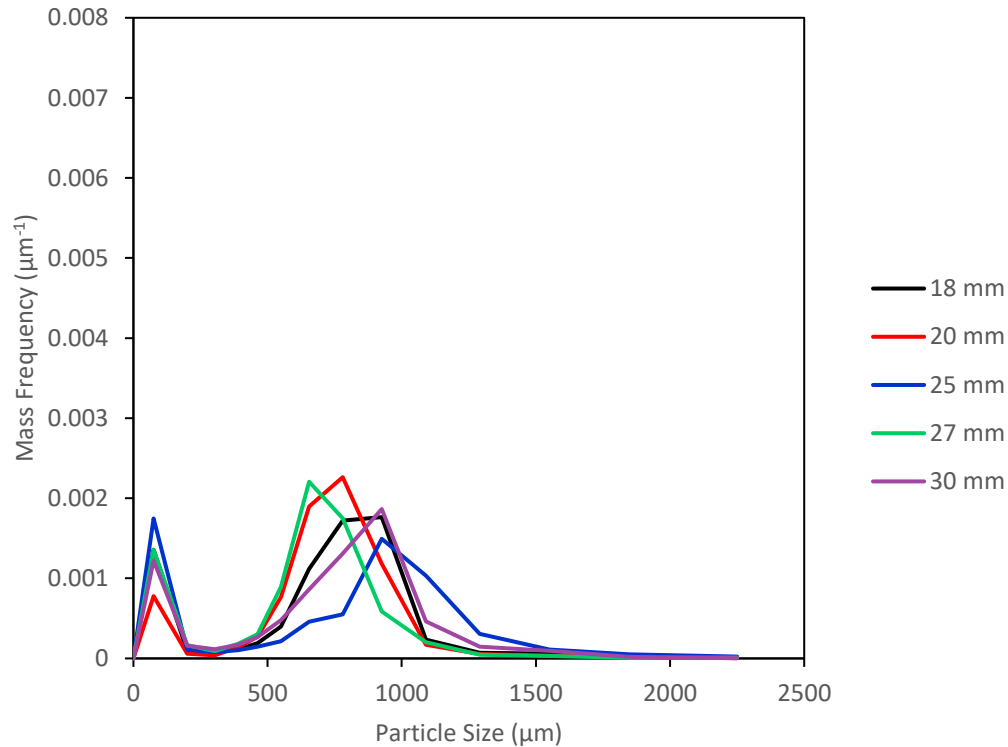
Figure 4-18 PSD for the pitched-blade impeller spherical agglomerates formed at impeller speed of 450 rpm and various impeller clearances

Figure 4-19 shows the PSD for agglomerates produced with a pitched blade impeller at a speed of 600 rpm with various clearances. All clearances produce a bimodal distribution, with the first peak representing unagglomerated material under 500 µm. The other peak for all clearances is over 900 µm. This suggests that the higher impeller speed increases particle suspension, encouraging contact between the bridging liquid and primary particles, inducing agglomeration.

The 27 mm impeller clearance has the fewest fines in the system, and a symmetrical second peak. This suggests that this impeller clearance increases the suspension of particles, resulting in better agglomeration. The improved suspension is due to the clearance to tank diameter ratio being 0.3. This value allows for the single loop pattern of the axial system to cover the full liquid height (Kresta and Wood, 1993).
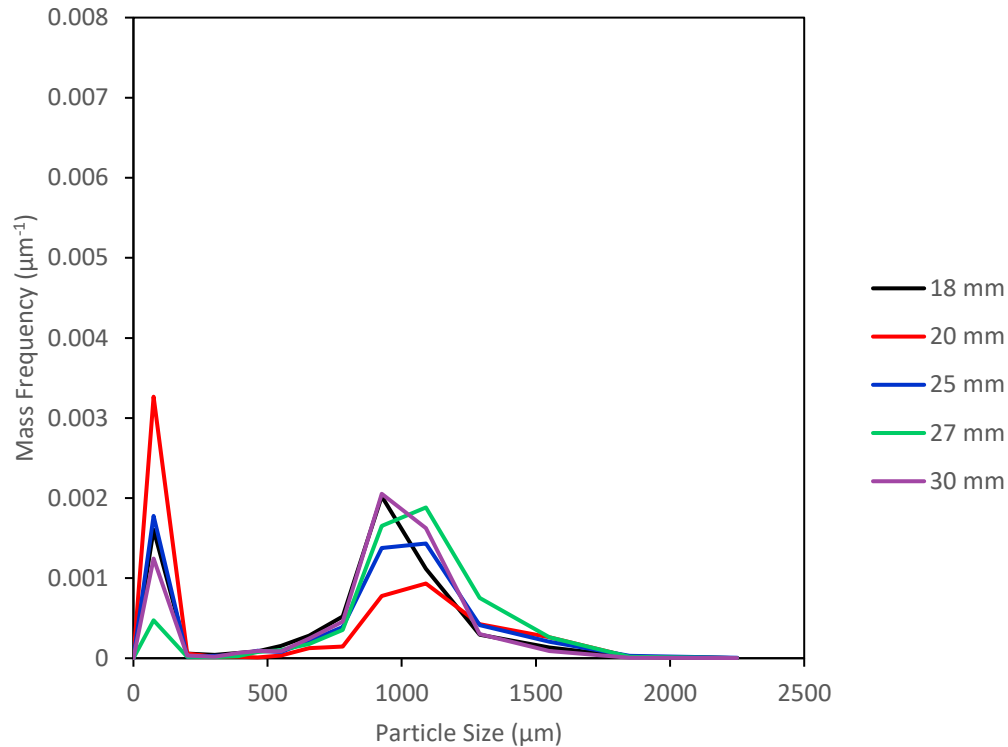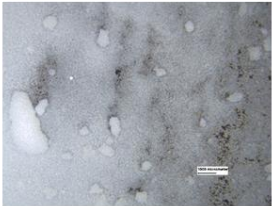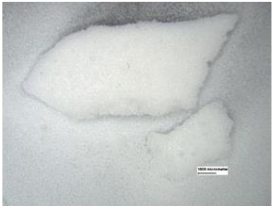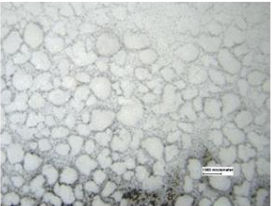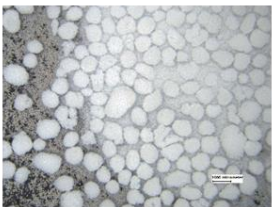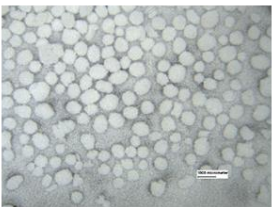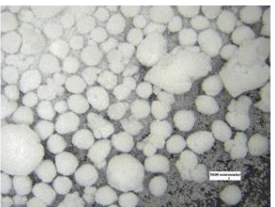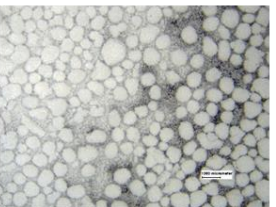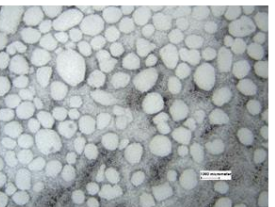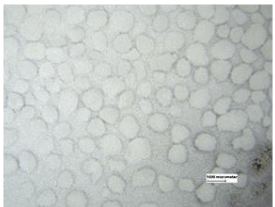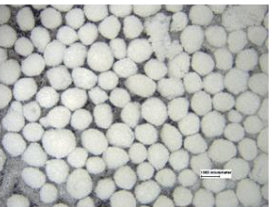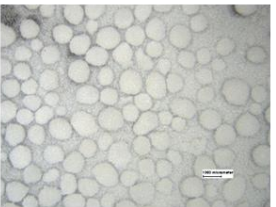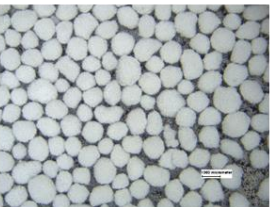
Figure 4-19 PSD of spherical agglomerates formed with a pitched blade impeller at different impeller clearances, with an impeller speed of 600 rpm

Figure 4-20 shows images of the agglomerates formed using a pitched blade turbine at various impeller speeds and clearances. From Figure 4-20, it can be seen that for all impeller speeds the 27 mm clearance produces agglomerates that are relatively consistent in shape and size. As previously mentioned, a clearance of 27 mm will give a clearance to tank diameter ratio of 0.3. This ratio allows for the flow in the tank to cover the full range of liquid depth, improving mixing between the particles and bridging liquid (Kresta and Wood, 1993).

An impeller speed of 300 rpm is not sufficient for successful spherical agglomeration using a pitched blade impeller, this can be seen in both Figure 4-17 and Figure 4-20. In Figure 4-20, the images at 300 rpm have large masses of fine material with a few, very large agglomerates. This shows that this speed is not able to induce agglomeration. One reason for this is that the system may be operating under the critical impeller speed for particle suspension (N_{JS}). CFD simulations were performed for the 60 impeller configurations to investigate the velocity profiles in the tank. The results of the CFD study are shown in Chapter 5.

	18 mm	20 mm	25 mm	27 mm	30 mm
300 rpm					
450 rpm					
600 rpm					

− 1000 µm

Figure 4-20 Images of the spherical agglomerates formed using a pitched blade impeller at various impeller clearances and speeds, the scale bar is 1000 µm

The average particle sizes for the agglomerates produced at different impeller speeds and clearances with the pitched blade impeller are shown in Figure 4-21. The average particle size of agglomerates at 300 rpm are consistently smaller than agglomerates produced at higher impeller speeds. The unsuccessful agglomeration at low impeller speeds is due to these speeds producing insufficient shear to induce agglomeration and consolidation (Dogon and Golombok, 2015).

Agglomerates produced at 450 rpm have an average particle size between 600 µm and 800 µm for all impeller clearances, with the clearance of 27mm producing the smallest average agglomerate size. From Figure 4-20, the agglomerates produced at a clearance of 27 mm and a speed of 450 rpm have increased sphericity in comparison with agglomerates produced at different clearances with a speed of 450 rpm.

At impeller speeds of 600 rpm, the agglomerates are generally larger than agglomerates formed at lower speeds. The exception to this, is the average size at a clearance of 20 mm. This may be due to the PSD at 600 rpm being wider yet shallower than the PSD for the same clearance at 450 rpm. In Figure 4-19, the agglomerates produced at a clearance of 20 mm and 600 rpm have a wide PSD (750 µm to 1750 µm) but at a very low mass frequency of 0.01. This is different to the agglomerates at 20 mm and 450 rpm as they have a narrower distribution (500 µm to 1250 µm) but the maximum frequency is much higher at approximately 0.025 at a size of 800 µm.
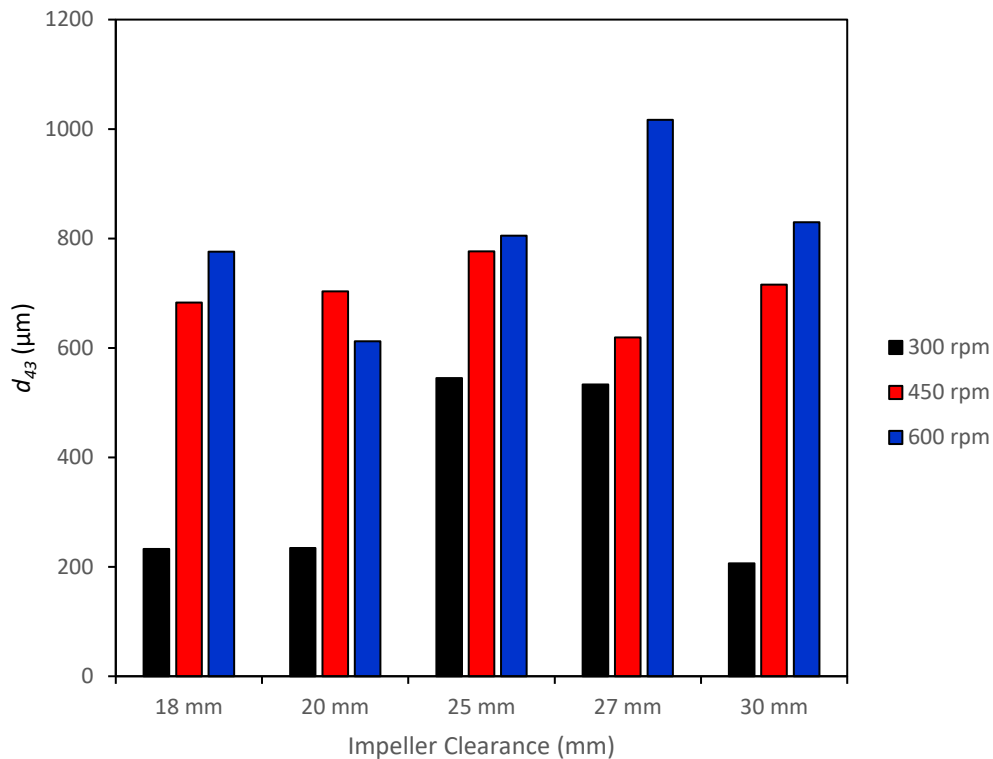
Figure 4-21 Average particle size for spherical agglomerates formed with a pitched blade impeller at different impeller speeds and clearances, the standard deviation of the repeats for the experiment at 25 mm and 450 rpm was 0.463

4.6   Discussion

The span of the particle size distribution quantifies the spread of the data, and it is calculated using Equation 4.1. Figure 4-22 shows the calculated PSD span for the different impeller geometries, speeds and clearances.

$$Span = \frac{d_{90} - d_{10}}{d}$$

(4.1)

Where:

d_{90} is the diameter that 90 % of the distribution is smaller than (µm)
d_{50} is the median of the particle size distribution; 50 % of the particles are smaller than this size (µm)
d_{10} is the diameter that 10 % of the particles are smaller than (µm)

(a)

(b)

(c)
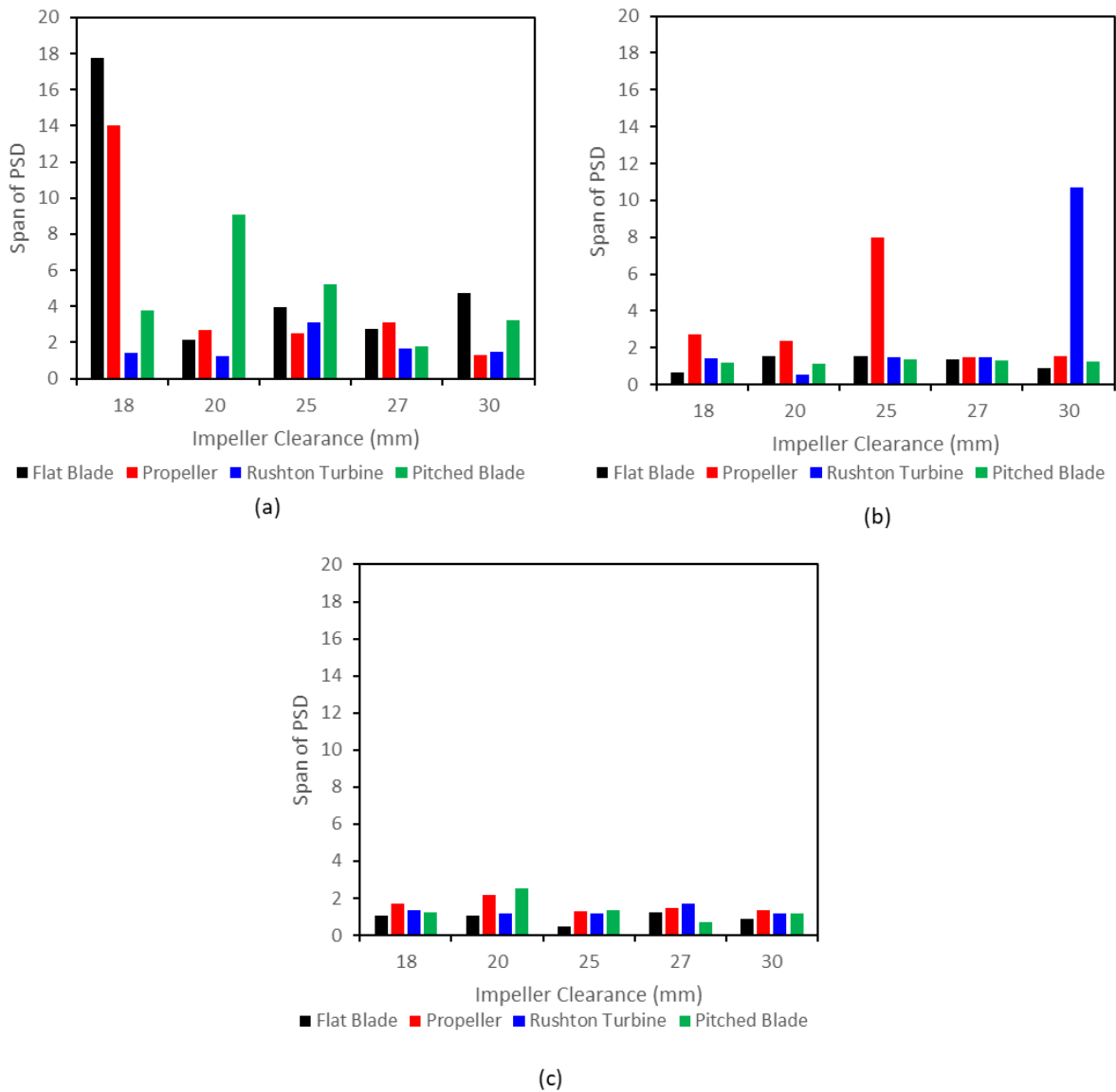
Figure 4-22 Span of the particle size distribution for the four impeller geometries at different clearances and impeller speeds, (a) 300 rpm, (b) 450 rpm and (c) 600 rpm

Figure 4-23 shows images of spherical agglomerates produced with different impeller geometries and clearances at a speed of 450 rpm. The agglomerate images for the different impeller conditions for speeds of 300 rpm and 600 rpm are shown in Figure A-5 and Figure A-6 in Appendix A, respectively. From these figures, it can be seen that impeller speed, geometry and clearance have a large influence on the size and shape of spherical agglomerates.

The impeller speed of 300 rpm was the poorest performing impeller speed for all impellers. This can be seen from the agglomerate images in Figure A-5. These agglomerates are less consistent in size and have reduced sphericity compared to agglomerates formed at higher speeds (Figure 4-23 and Figure A-6). Figure 4-22 shows the span of the particle size distribution for the impellers at different speeds and clearances. At an impeller speed of 300 rpm (Figure 4-22a) there is more variation in PSD for the different impeller geometries and clearances than at higher impeller speeds, suggesting that an impeller speed of 300 rpm is not able to successfully produce consistent spherical agglomerates. The increased impeller speeds producing more consistent agglomerates can be due to increased speeds improving suspension of particles (Jafari et al., 2012). At increased impeller speeds, the impeller tip speed is higher, resulting in higher shear forces in the system. Increased shear forces exponentially increase the agglomeration rate constant, resulting in faster agglomeration, leading to increased contact between the bridging liquid and particles (Chen et al., 2021). Increased impeller speeds also increase agglomerate consolidation, resulting in increased sphericity (Chaterjee et al., 2017).

From the results presented in Figure A-5, Figure 4-23 and Figure A-6, the Rushton turbine and flat blade impellers produced agglomerates with increased sphericity compared to the other impellers, especially at higher impeller speeds. The Rushton turbine and flat blade impellers increasing the sphericity of the agglomerates may be due to them promoting radial flow in the system compared to the propeller and pitched blade impellers which both promote axial flow (Van Wazer et al., 1995; Couper et al., 2012; Grenville et al., 2017). Radial flow impellers impart greater levels of shear on the system than an axial flow impeller. Increased shear forces will increase agglomeration as increased shear rates result in fluid layers that contain suspended particles moving at higher speeds (Dogon and Golombok, 2015). At impeller speeds of 450 rpm and above (Figure 4-22b and Figure 4-22c), the span of the flat blade impeller is consistently below 2 for all clearances, suggesting that these conditions promote consistent mixing and agglomeration in the tank. The Rushton turbine follows a similar trend, apart from at an impeller speed of 450 rpm with a clearance of 30 mm. This deviation from a narrow span can be seen in Figure 4-13 as the PSD shows a bimodal distribution of fine material under 200 µm and then a very broad peak between 750 µm and 1700 µm.

As demonstrated in Figure 4-20, the agglomerates produced by the pitched blade impeller were more consistent in size and sphericity with increasing impeller speed. This is further demonstrated by the span of the PSD in Figure 4-22, which also shows an increase in consistency as impeller speed is increased as the results at 450 rpm and 600 rpm are consistently below 2 with limited variation when compared to the results at 300 rpm. From the agglomerate images in Figure 4-20, it appears that an impeller speed of 600 rpm and clearances of 25 mm and above are able to produce agglomerates that are consistently sized and spherical, although these conditions still produce a large amount of fine powder. As Figure A-5, Figure 4-23 and Figure A-6 show, the pitched blade impeller produces agglomerates that are more consistent in shape and size than the propeller impeller, even though they both promote axial flow in the system. This may be due to the pitched blade impeller having a larger impeller power number than the propeller

impeller (Van Wazer et al., 1995; Couper et al., 2012). In the spherical agglomeration PBM by Ahmed et al., 2023, the power requirements are used to calculate the velocity of interactions between the liquid and fluid in the system. Impellers with increased power numbers will have higher power requirements, leading to increased velocity of the liquid and particle interactions (Blandin et al., 2005; Arjmandi-Tash et al., 2019; Ahmed et al., 2023). The increased velocities will result in more agglomerates being produced.

Of the tested impellers, the propeller was the least successful at producing agglomerates that are spherical in appearance within the desired size range of 500 μm to 1000 μm. The average particle sizes for this impeller, shown in Figure 4-11, are inconsistent across the various impeller speeds and clearances. The PSD for all configurations of the propeller impeller (Section 4.3), show that this impeller produces a large proportion of fine material. The spherical agglomerates produced using the propeller were not consistently spherical (Figure 4-10). This could be due to the low shear of the axial flow pattern not producing a sufficient velocity for effective particle suspension (Dogon and Golombok, 2015; Grenville et al., 2017).

In Figure 4-10, an impeller speed of 600 rpm and a clearance of 25 mm appears to form agglomerates that are the most consistent in sphericity and size for a propeller impeller. As Figure 4-11 shows, this impeller configuration produces a d_{43} that falls within the desired size range of 500 μm to 1000 μm, although it is towards the upper limit of this range. From the PSD, shown in Figure 4-8, there is a very broad peak that ranges from approximately 500 μm to 1750 μm, with the highest mass frequency at 1100 μm. This suggests that although the agglomerate images look consistent, there is still a broad range of particle sizes produced at this condition. The impeller speed and clearance that appears to produce the most consistent agglomerates for the propeller impeller produces less consistent agglomerates than the other impellers tested in this work. This suggests that the propeller impeller is unlikely to be successful at producing spherical agglomerates that are consistent in both size and sphericity.
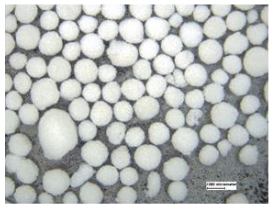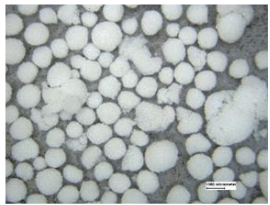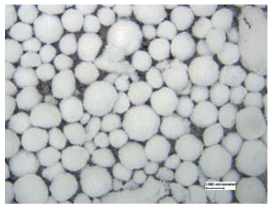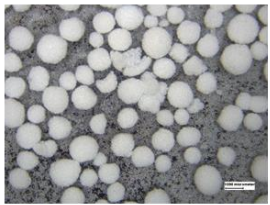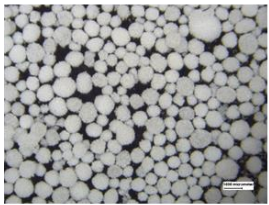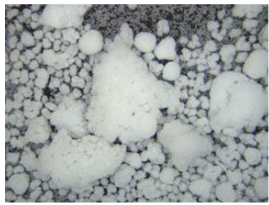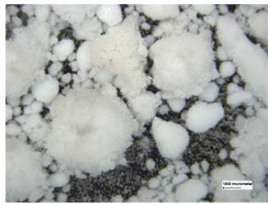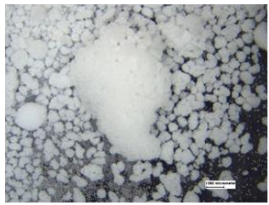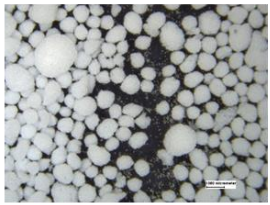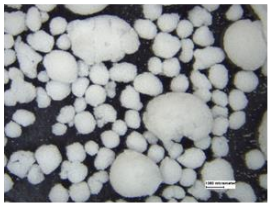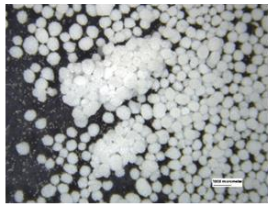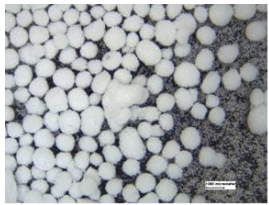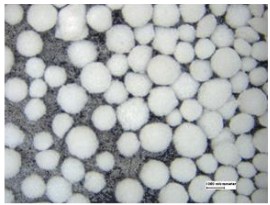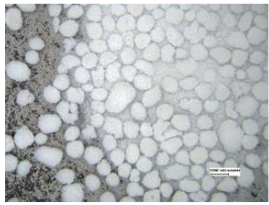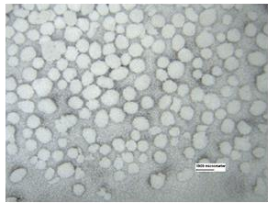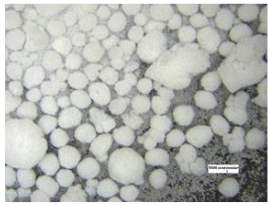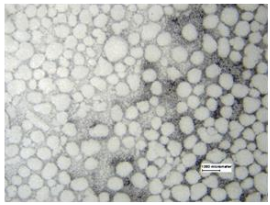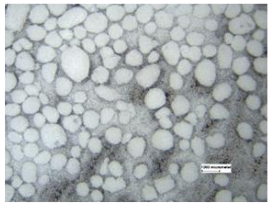
Based on the criteria outlined in Section 4.1, the Rushton turbine appears to be the most promising impeller for spherical agglomerate production at the impeller speeds and clearances tested in this work. This is due to the d_{43} of agglomerates produced by the Rushton turbine being consistently in the size range of 500 μm to 1000 μm. From the values of span that were calculated using Equation 4.1, only 2 of the 15 simulations produced PSDs with a span greater than 2, compared to 5 for the flat blade and pitched blade impellers, or 8 for the propeller impeller. As the Rushton turbine consistently produced PSDs with low values for span it is able to produce agglomerates more consistently. From the agglomerate images, the agglomerates produced by the Rushton turbine appear to be more spherical in shape than other impeller configurations, although this has not been quantified. The best to worst performing impeller based on the criteria established in this chapter are Rushton turbine, flat blade, pitched blade and propeller.

The results in this chapter suggest a correlation between impeller power number and improved spherical agglomerate characteristics. Of the four impellers tested, the power number in decreasing order would be Rushton turbine, flat blade impeller, pitched blade impeller and propeller impeller (Grenville et al., 2017). This is the same order as most consistent to least consistent spherical agglomerates formed, suggesting that increased power number increases the likelihood of producing spherical agglomerates that are consistent in size and sphericity. Increased power number will result in higher power requirements in the system, especially at increased clearances (Devarajulu and Loganathan, 2016). As the PBM for spherical agglomeration includes power consumption in the velocity calculations, increased

power number increases particle collision velocity, resulting in increased agglomeration (Blandin et al., 2005; Arjmandi-Tash et al., 2019; Ahmed et al., 2023).

Three impeller configuration parameters were investigated in this chapter; impeller geometry, impeller clearance and impeller speed. The impeller speed is the only parameter investigated in this work that can be specified as part of the PBM by Ahmed et al., 2023. As the results in this chapter show, impeller geometry and clearance have a significant influence on agglomerate properties. Therefore, they should be incorporated into the PBM. One way to do this would be to incorporate the impeller power number for the different impellers into the agglomeration and layering kernels. The power number would be used to calculate power consumption, which is a parameter that is used to calculate the collision velocity.

From the results, it can be seen that clearance does influence agglomerate production. However, the experimental results alone are insufficient to be able to include this in the PBM. To further investigate the influence of clearance in the stirred tank, CFD simulations of the various impeller configurations were performed to determine the velocity profiles in the tank. The results of these CFD simulations are presented in Chapter 5.

	18 mm	20 mm	25 mm	27 mm	30 mm
Flat Blade Impeller					
Propeller Impeller					
Rushton Turbine Impeller					
Pitched Blade Impeller					

— 1000 μm

Figure 4-23 Images of the agglomerates produced with different impeller geometries and clearances at an impeller speed of 450 rpm, the red line is a scale bar of 1000 μm

4.7   Conclusion

As can be seen from Figure 4-23, the impeller geometry and clearance have an enormous effect on spherical agglomerates. Due to the large influence of these impeller characteristics, it is essential that the impeller geometry and clearance are incorporated into a PBM for spherical agglomeration. The PBM by Ahmed et al., 2023 is the most recent and robust PBM for spherical agglomeration, but this model only considers impeller diameter and impeller speed. Therefore, adapting this PBM to incorporate the impeller geometry and clearance would improve the accuracy of the model. This would increase the likelihood of the PBM being used to aid the design of a spherical agglomeration process.

From the experimental results in this chapter, there is a clear correlation between increased impeller power number, and increased consistency of agglomerate size and sphericity. Of the four impellers tested, the Rushton turbine impeller has the highest power number. This impeller produced the largest portion of agglomerates within the desired size range of 500 μm to 1000 μm, and they appeared spherical in shape. This differs from the propeller impeller, which had the lowest power number and was the least consistent impeller with regards to agglomerate size and sphericity. In the PBM, the power requirements are used to calculate the velocity of particle and fluid interactions (Ahmed et al., 2023). Increased power number leads to increased power requirements and would result in increased velocities in the system. In the PBM by Ahmed et al., 2023 the power number is given as a fixed value and is not calculated as part of the model. Allowing the model to calculate the power number for different impeller geometries could lead to the PBM being applicable to different stirred tank geometries.

The impeller clearance has also been shown to influence the formation of spherical agglomerates. The influence varies with each impeller geometry and speed. From the experimental results alone, it is difficult to identify and parametrise the influence of impeller clearance. Therefore, CFD simulations that correspond to each impeller configuration tested in this chapter were performed. Including the velocity profiles from the CFD simulations with different impeller geometries and clearances in the PBM could improve the validity of the model. The results of the CFD simulations are shown in Chapter 5.

Chapter 5 CFD Investigation into the influence of flow characteristics on spherical agglomeration

5.1 Introduction

Chapter 4 discusses the results of an experimental study conducted to investigate how changing impeller characteristics influences spherical agglomeration. The experimental study did find an influence of the impeller geometry, speed and clearance. In this chapter, CFD simulations of the experimental equipment configurations were performed to understand the velocity profiles in the tank. Section 5.5 is a comparison of the CFD and experimental results to determine the importance of flow profiles on agglomerate production.

5.2 Mesh Density Analysis

The mesh density analysis was performed to determine the optimal mesh size for the CFD investigation into the influence of impeller geometry on spherical agglomeration. In Figure 5-1, the number of iterations for the simulation to converge is plotted against the number of nodes that are simulated. This figure shows that there is an exponential relationship between the number of nodes and the number of iterations required. A lower number of nodes, or a larger mesh size, would reduce the computation time needed for the simulations (Sadrehaghighi, 2018). A reduced computation time for a larger mesh was expected due to the number of nodes decreasing rapidly as the mesh size is increased. This can be seen in Figure 3-13.
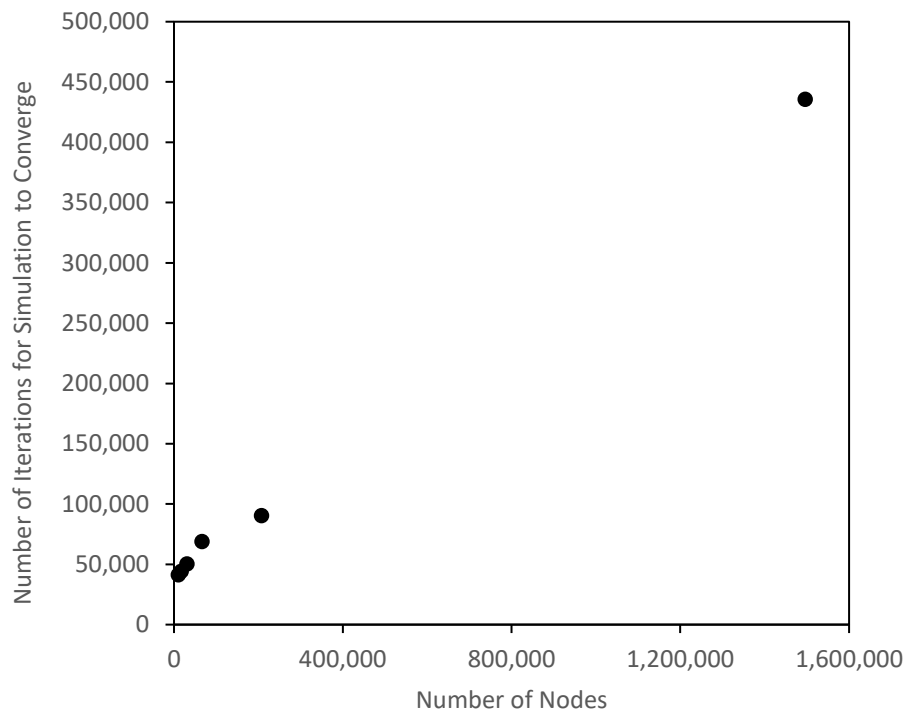
Figure 5-1 The number of iterations for the simulation to converge against the number of nodes for the different mesh sizes

Figure 5-2 shows the volume weighted average velocity magnitude for the solid particles and the fluid for different mesh values. There are fluctuations between 6 mm and 5 mm mesh, but when the mesh is 4 mm or smaller, the results are fairly constant. The maximum velocity magnitude values are also constant at a

mesh size of 4 mm and below; these results can be seen in Appendix B. Based on the results in Figure 5-1 and Figure 5-2, it was determined that the mesh size for the CFD simulations would be 4 mm. This value was chosen to give results that are not influenced by mesh size, whilst also reducing the overall computation time.
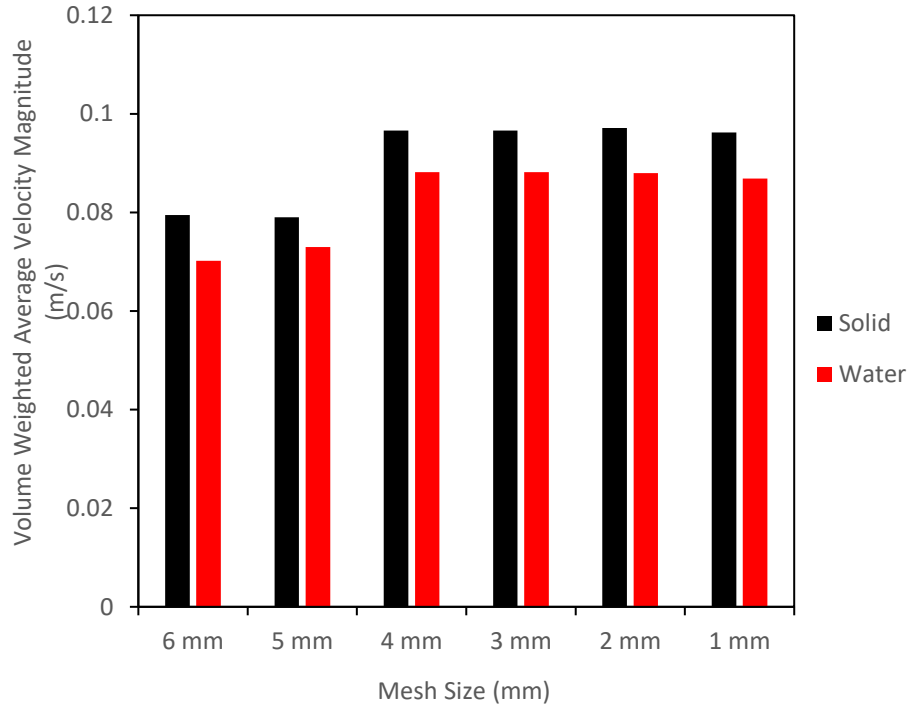
Figure 5-2 Volume weighted average velocity magnitude of the solid particles and liquid at different mesh sizes, results from CFD simulations

5.3 Influence of Impeller Geometry on Velocity Profile

As discussed in Section 4.1, the CFD study considered four impeller geometries which were each simulated at three impeller speeds and five impeller clearances. To determine the influence of the flow characteristics in the tank, the solid and liquid velocity magnitudes for the simulations were considered. The velocity in the tank will influence the rate of collisions of particles with both the bridging liquid and other particles, influencing agglomerate formation. Chapter 3 details the CFD simulation methodology used for investigating the influence of impeller characteristics on mixing in stirred tanks.

The volume weighted average velocity magnitude of both the solid and the liquid have been plotted against impeller clearance for the various impeller speeds and geometries to determine the influence that the impeller configuration has on the system velocities. Section 5.5 presents a comparison between the CFD and experimental results to determine the significance of impeller design on spherical agglomerate formation.

The just suspended impeller speed (N_{js}) was calculated using Equation 2.2 for each impeller geometry and clearance. The results of these calculations were converted into velocities using the just suspended impeller tip speed calculation, shown in Equation 5.1.

$$I_{js} = d\,\pi\,N_{js}$$

(5.1)

99

Where:

I_{js} is the just suspended impeller tip speed (m/s)

d is the impeller diameter (m)

N_{js} is the just suspended impeller speed (rps)

The results of Equation 5.1 are shown in Table 5-1. It can be seen that the just suspended impeller speed increases with clearance. The three impeller speeds tested were 300 rpm, 450 rpm and 600 rpm; these values are all greater than the calculated values of N_{js}. The volume weighted average (VWA) velocity magnitude of solid and water for each impeller configuration was found from the CFD simulations. In the following sections, the VWA velocity magnitude values were compared to the calculated I_{js} values. It is expected that systems operating under I_{js} would not lead to successful agglomeration.

Table 5-1 Calculated values of just suspended impeller speed and impeller tip speed for the impellers at different clearances

Impeller Geometry	Clearance (mm)	C/D	N_{js} (rps)	I_{js} (m/s)
Flat Blade	18	0.200	2.408	0.378
	20	0.222	2.576	0.405
	25	0.278	2.971	0.467
	27	0.300	3.120	0.490
	30	0.333	3.338	0.524
Propeller	18	0.200	2.318	0.364
	20	0.222	2.400	0.377
	25	0.278	2.582	0.406
	27	0.300	2.649	0.416
	30	0.333	2.742	0.431
Rushton	18	0.200	2.897	0.455
	20	0.222	2.964	0.466
	25	0.278	3.112	0.489
	27	0.300	3.164	0.497
	30	0.333	3.238	0.509
Pitched Blade	18	0.200	2.414	0.379
	20	0.222	2.532	0.398
	25	0.278	2.803	0.440
	27	0.300	2.903	0.456
	30	0.333	3.045	0.478

5.3.1   Flat-Blade Impeller

The flat-blade impeller has four blades, and a blade pitch of 90°; this impeller increases the radial flow in the system. Figure 5-3 shows the VWA velocity magnitude for the solid particles against impeller clearance to vessel diameter ratios (C/D) at different impeller speeds. There is a decrease in VWA velocity magnitude for all impeller speeds as the clearance ratio increases. For all values of C/D, the highest velocity magnitude is with an impeller speed of 600 rpm. It is expected that higher impeller speeds would result

in increased VWA velocity magnitude as the impeller will be rotating at higher tips speeds, resulting in increased velocities in the rest of the tank.

The VWA solid velocity magnitude at 300 rpm is lower than the calculated I_{js} value for all clearances. This suggests that particles at this impeller speed will not be well suspended in the tank, resulting in poor agglomeration.

For all impeller speeds tested, the VWA velocity magnitudes at low C/D values are higher than, or close to the I_{js} values for those clearances. This suggests that lower clearances are favourable for a flat-blade impeller. The drastic decrease in VWA solid velocity magnitude at C/D of 0.3 and above suggest a transition in flow pattern for this impeller. In work by Montante et al., 1999 and Zhu et al., 2019 it was observed that for a Rushton turbine impeller, there is a transition from a single loop to double loop flow pattern in the system at C/D greater than 0.3. A flat blade impeller also promotes radial flow in the tank, suggesting a flow pattern transition also occurs at these clearances for a flat blade impeller.
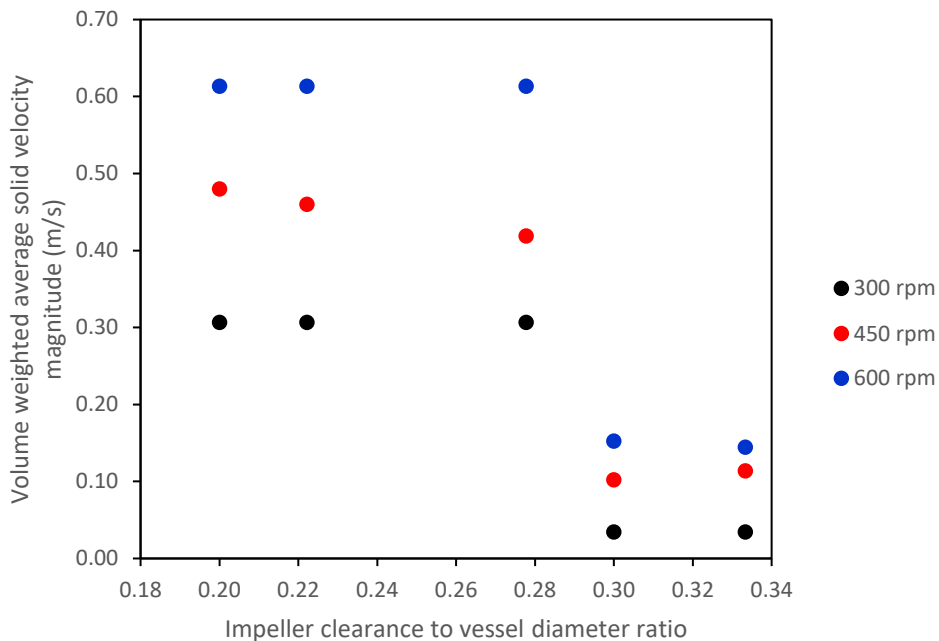
Figure 5-3 Volume weighted average solid velocity magnitude against clearance to vessel diameter ratio for a flat blade impeller at different impeller speeds

The VWA velocity magnitude for the water in the simulations can be seen in Figure 5-4. This profile for water looks similar to the profile for the solid particles. There are, however, differences between the solid and liquid velocity magnitude profiles. For the three impeller speeds tested, the VWA velocity magnitude profiles are consistent for C/D values of 0.28 and below. At an impeller speed of 600 rpm, the water has a larger velocity magnitude than the solid at a C/D of 0.3. When the C/D is further increased to 0.33, the solid velocity magnitude is larger than the water velocity magnitude. An impeller speed of 450 rpm produces similar values for both the solid and the water velocity magnitude for all clearances, with the biggest difference being between the values for a C/D of 0.33. For the impeller speed of 300 rpm, the VWA velocity magnitude for the water is almost double the solid VWA velocity magnitude.
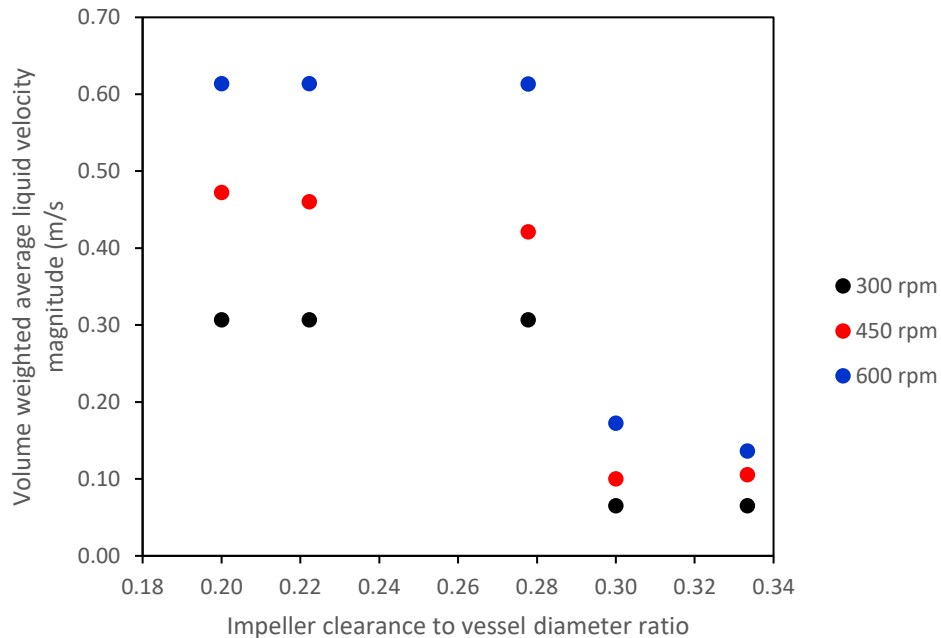
Figure 5-4 Volume weighted average water velocity magnitude against clearance to vessel diameter ratio for a flat blade impeller at different impeller speeds

The CFD contours, shown in Table 5-2 show a clear difference in the solid velocity magnitude profile at different C/D ratios. CFD contours for all impeller configurations can be found in Appendix B. The lower C/D ratios have a more uniform flow distribution with areas of high velocity. For a C/D of 0.33, there is a much smaller flow pattern, and this is closer to the impeller. It was also found that the VWA velocity magnitude for both the solid and the liquid decreases at C/D>0.3. In a study by Devarajulu & Loganathan., 2016, it was observed that a flat blade impeller with six blades was effective at suspending solids at C/D<0.25, suggesting that lower clearances would favour a flat blade impeller.

The results in Figure 5-3, Figure 5-4 and the CFD contours suggest that this transition occurs at 0.28<C/D<0.3 four a flat blade impeller with four blades. The study by Devarajulu & Loganathan., 2016 does not have published data for 0.25<C/D<0.3. Therefore, the transition for the six blade impeller that they tested may also occur between these values but it was not observed in their work. There may also be a difference between the results obtained by Devarajulu & Loganathan., 2016, and this work due to the difference in the number of impeller blades. Increasing the number of impeller blades will increase the impeller power number, leading to higher power consumption in the system. The spherical agglomeration PBM by Ahmed et al., 2023 suggests that increased power consumption will increase particle velocity, which may lead to improved suspension for all particles.

Table 5-2 CFD contours of solid velocity magnitude for the flat blade impeller at different impeller speeds and C/D ratios

C/D – 0.20 300 RPM	C/D – 0.20 450 RPM	C/D – 0.20 600 RPM
C/D – 0.28 300 RPM	C/D – 0.28 450 RPM	C/D – 0.28 600 RPM
C/D – 0.33 300 RPM	C/D – 0.33 450 RPM	C/D – 0.33 600 RPM
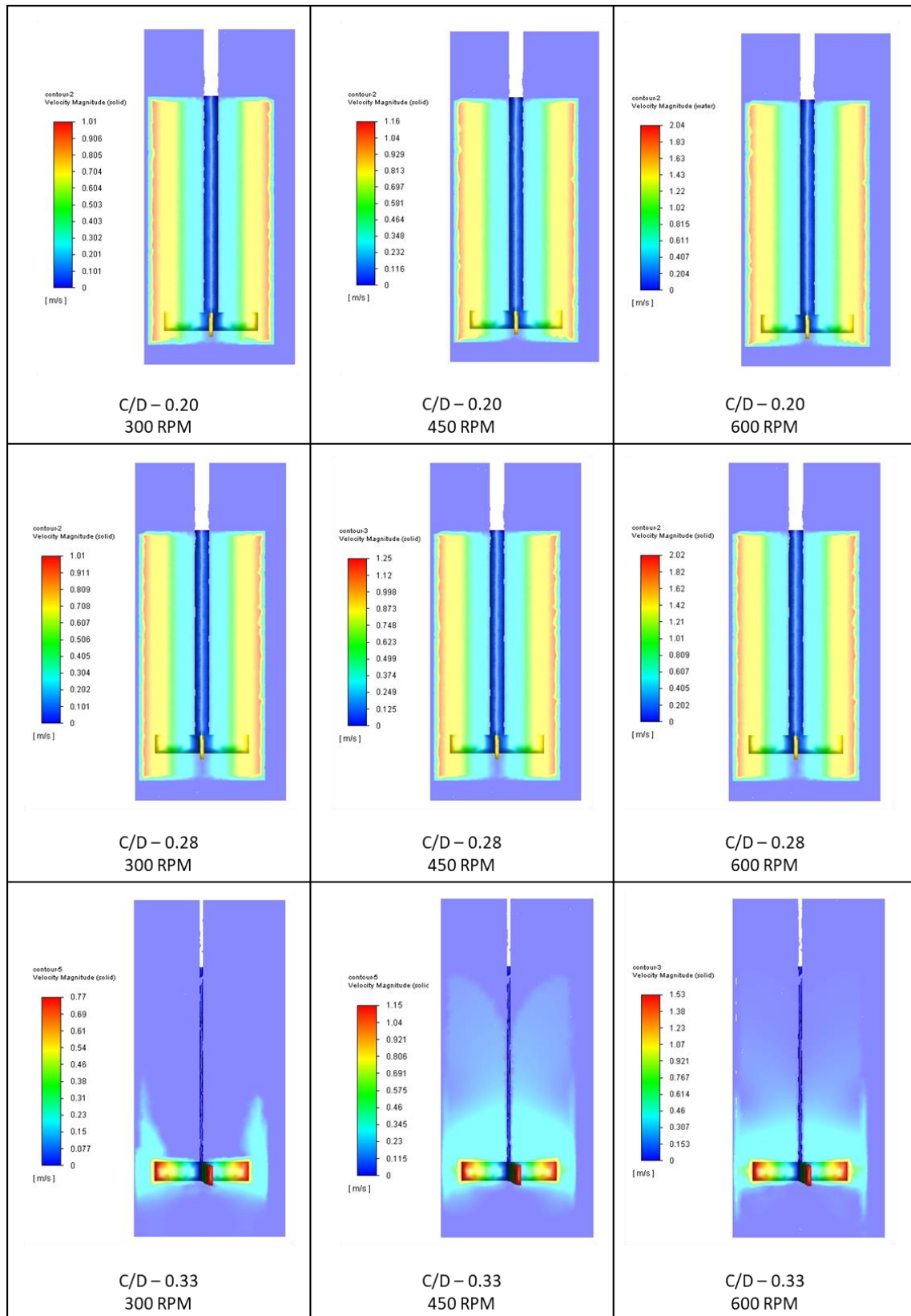
5.3.2　Propeller

The propeller impeller geometry has three curved blades at a 60 ° pitch. This impeller promotes axial flow in the stirred tank. The volume weighted averages for solid velocity magnitude at different impeller speeds and C/D are shown in Figure 5-5. For the propeller impeller, the solid particle VWA velocity magnitude increases with increased impeller speed for all values of C/D. This is expected as increased impeller speed will lead to a higher impeller tip speed, resulting in greater velocity in the system (Chen et al., 2021).

With impeller speeds of 450 rpm and 300 rpm, the VWA solid velocity magnitude decreases slightly as C/D increases. This decrease may be due to the increased value of N_{js}. For all impeller speeds and clearances, the VWA solid velocity magnitudes are lower than the calculated value of I_{js} shown in Table 5-1. The VWA solid velocity magnitude being much lower than these values suggest that more particles have settled to the bottom of the tank at higher clearances. At an impeller speed of 600 rpm, the VWA solid velocity magnitude increases with impeller C/D values. This suggests that the agglomerate formation in the system will improve with increased clearance at 600 rpm. The increase in particle suspension at C/D>0.28 may be due to a trend observed by Kresta and Wood, 1993. In this work, they determined that when C/D>0.3 for a pitched blade impeller then the single loop flow pattern reaches the top and bottom of the tank. As a pitched blade impeller also imparts axial flow in a stirred tank, it can be assumed that C/D will have a similar influence for flow generated by a propeller impeller.
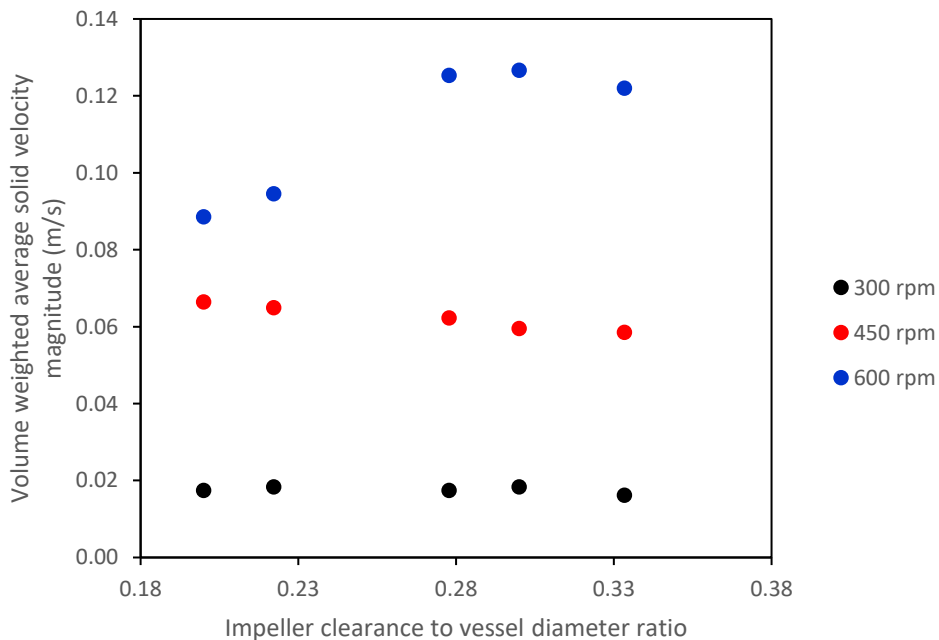
Figure 5-5 Volume weighted average solid velocity magnitude against clearance to vessel diameter ratio for a propeller impeller at different impeller speeds

The VWA liquid velocity magnitude is shown in Figure 5-6. The results for 600 rpm and 300 rpm follow a similar trend as the VWA solid velocity magnitude profiles in Figure 5-5. At an impeller speed of 450 rpm, the VWA liquid velocity magnitude is greater than the solid VWA velocity magnitude, and it increases with increasing C/D ratios. This may be due to the increased C/D causing the flow pattern to cover more of the

liquid height than it does at lower clearances. A study by Kresta and Wood, 1993 observed this trend for axial flow impellers.
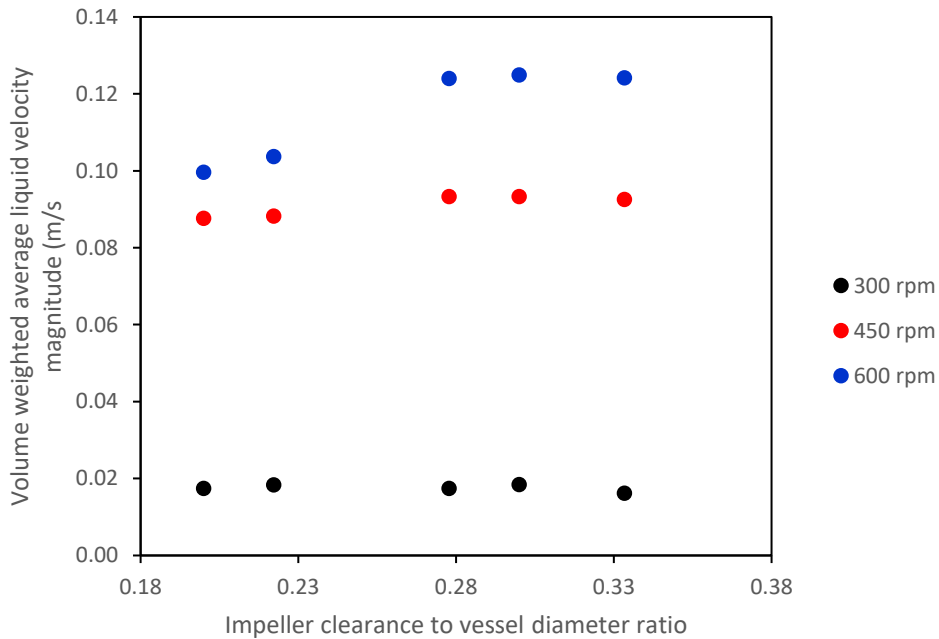
Figure 5-6 Volume weighted average water velocity magnitude against clearance to vessel diameter ratio for a propeller impeller at different impeller speeds

A selection of solid velocity magnitude CFD contours for the propeller impeller are shown in Table 5-3; with the remaining contours given in Appendix B - Impeller Geometry CFD Analysis. From Table 5-3, it can be seen that increasing the impeller speed increases the maximum solid velocity magnitude at all C/D values. The flow pattern from the impeller also reaches increased heights in the tank with an increase in impeller speed. This is due to increasing impeller speeds resulting in higher velocities in the tank, and more particles being entrained in the flow.

At an impeller speed of 300 rpm, the flow of the particles appears to have settled towards the bottom of the tank, under the impeller. This suggests that an impeller speed of 300 rpm is insufficient for particle suspension, and will therefore not be suitable for spherical agglomeration as it will not facilitate mixing between the particles and the bridging liquid.

The shape of the flow profile is fairly consistent across C/D ratios for an impeller speed of 450 rpm. This suggests that whilst this speed is sufficient for improved particle suspension when compared to a speed of 300 rpm, it is insufficient to suspend particles across the full height of fluid in the tank.

Increased C/D values lead with an impeller speed of 600 rpm lead to a flow pattern that covers the entirety of the liquid height in the tank. This correlates with the findings of a study by Kresta and Wood, 1993. This study, and the CFD results shown here suggest that increased C/D ratios and higher impeller speeds will lead to improved mixing between the bridging liquid and solid particles, increasing agglomerate production.

Table 5-3 Solid velocity magnitude CFD contours for the propeller impeller at varied impeller C/D and speeds

C/D − 0.20 300 RPM	C/D − 0.20 450 RPM	C/D − 0.20 600 RPM
C/D − 0.28 300 RPM	C/D − 0.28 450 RPM	C/D − 0.28 600 RPM
C/D − 0.33 300 RPM	C/D − 0.33 450 RPM	C/D − 0.33 600 RPM
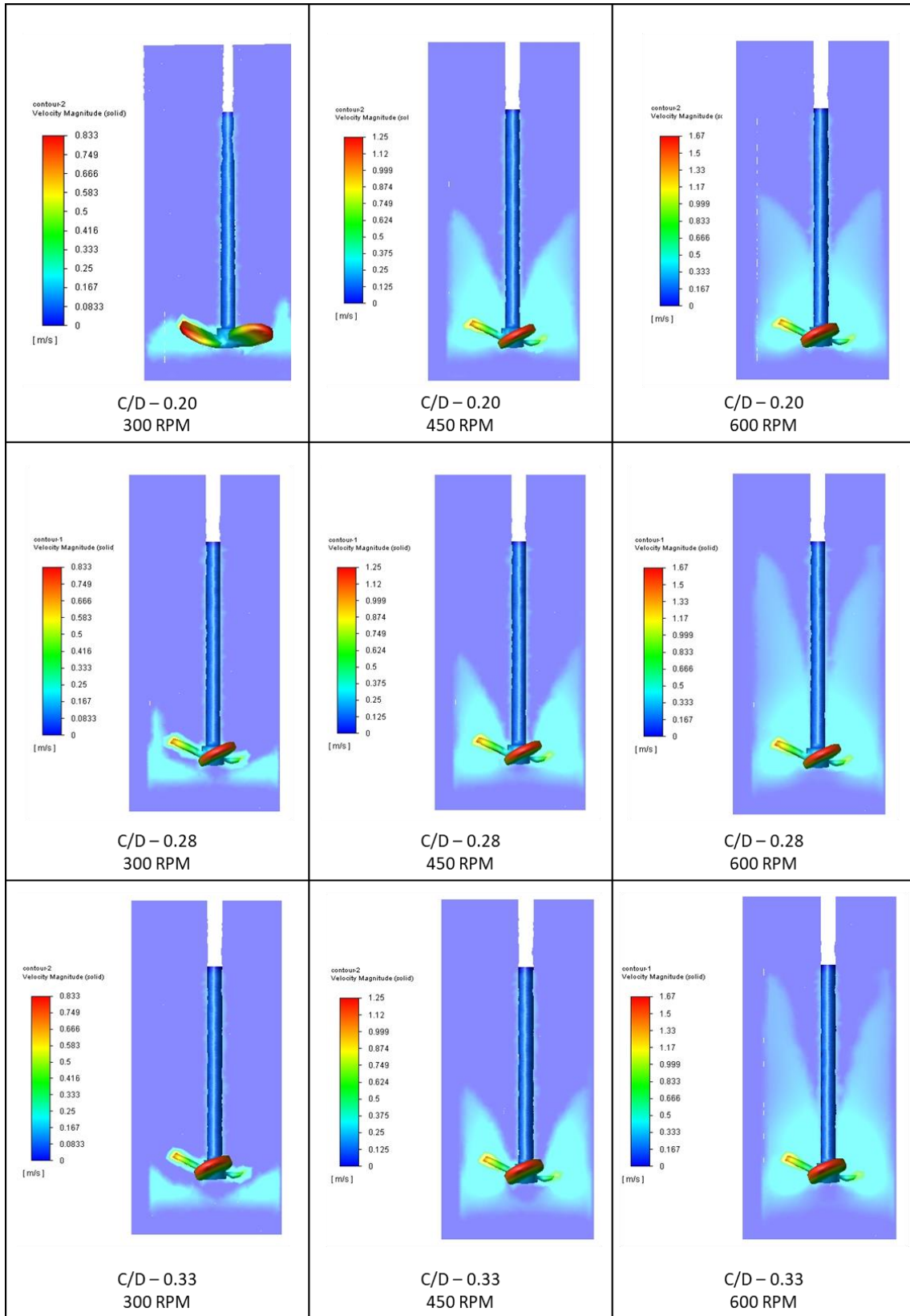
5.3.3 Rushton Turbine

The Rushton turbine impeller has 6 blades that leave a circular disk at a 90 ° pitch. This impeller promotes radial flow in the system. The VWA solid velocity magnitude profile for a Rushton turbine at different impeller speeds and clearances is shown in Figure 5-7. It can be seen that for all impeller speeds, the highest value of VWA solid velocity magnitude is at a C/D of 0.33. This value is much greater than values at lower C/D values. The increase of VWA solid velocity magnitudes correlates to studies by Montante et al., 1999 and Zhu et al., 2019. In this research and the studies by Montante et al., 1999 and Zhu et al., 2019, it was found that C/D for a Rushton turbine has a large influence on the flow pattern in the tank. At C/D values below 0.3, the system operates with a single loop flow pattern, similar to that induced by an axial flow impeller. Increasing the clearance to give C/D>0.3 will lead to the formation of the double loop flow pattern that is expected by a radial impeller (Figure 2-14).
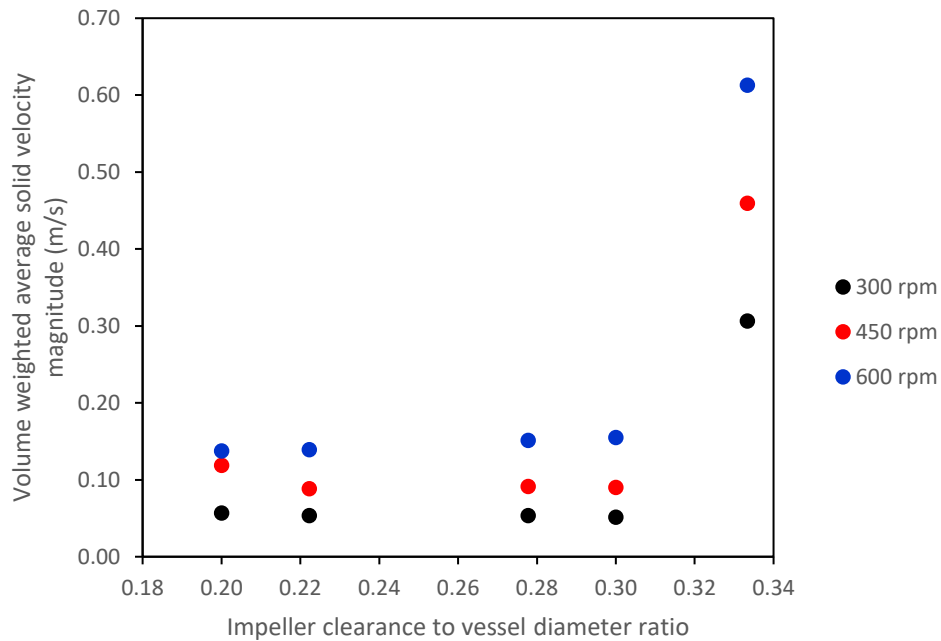
Figure 5-7 Volume weighted average solid velocity magnitude against clearance to vessel diameter ratio for a Rushton turbine impeller at different impeller speeds

The VWA liquid velocity magnitude for a Rushton turbine impeller is shown in Figure 5-8, and follows a similar trend to the VWA solid velocity magnitude, in that the velocity value is much larger at C/D of 0.33 compared to the lower C/D ratios. The VWA liquid velocity magnitudes at C/D<0.3 are lower than the VWA solid velocity magnitude for the same conditions. This may be due to the lower clearances inducing a single loop flow pattern, which is thought to be better at suspending solid particles (Montante et al., 1999; Zhu et al., 2019).

The VWA velocity profiles suggest that a C/D value of 0.33 and an impeller speed of 600 rpm for the Rushton turbine will be most effective at producing spherical agglomerates as this is above the calculated value of I_{js}, shown in Table 5-1.
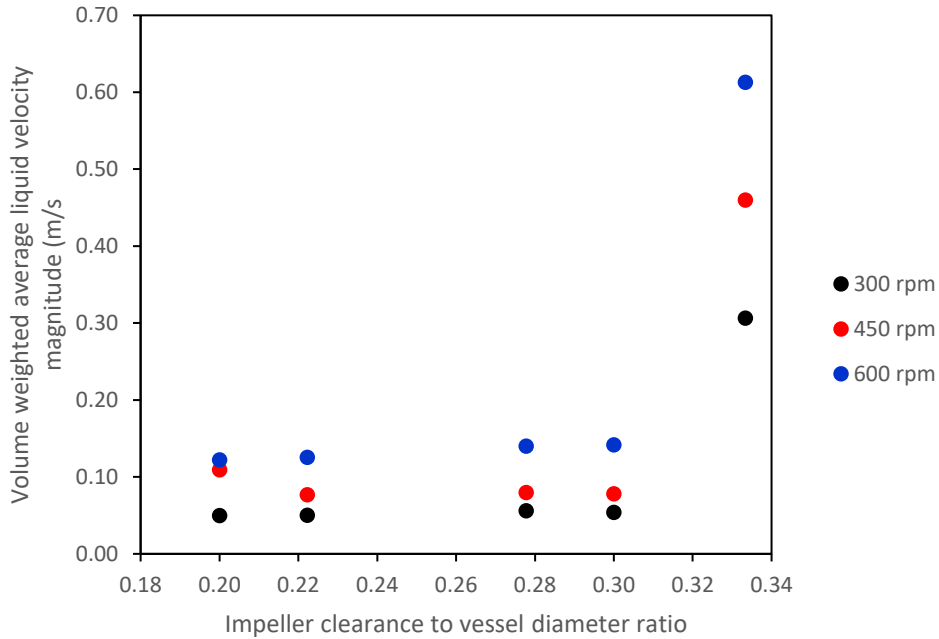
Figure 5-8 Volume weighted average water velocity magnitude against clearance to vessel diameter ratio for a Rushton turbine impeller at different impeller speeds

CFD contours of solid velocity magnitude for the Rushton turbine at selected impeller speeds and clearances can be seen in Table 5-4, with the results from the remaining simulations given in Appendix B. It can be seen that increasing the impeller speed increases the maximum velocity in the system.

The flow profile at C/D of 0.33 is very different to the profiles at lower C/D values for all impeller speeds. This is due to the trend also observed by Montante et al., 1999 and Zhu et al., 2019, in which a C/D>0.3 allows for a double loop flow pattern to form when a Rushton turbine is used. At lower clearances, the Rushton turbine will produce a single loop flow pattern, similar to that of an axial impeller. The results obtained at C/D of 0.33 have a higher maximum solid velocity magnitude than the lower clearances, suggesting that the double loop pattern induced at this clearance will result in higher velocities in the system. In a study by Devarajulu and Loganathan, 2016, it was found that increasing the clearance for a Rushton turbine impeller increases the impeller power number. In the model for spherical agglomeration developed by Ahmed et al., the power consumption is correlated to the energy dissipation in the system. The energy dissipation is used for calculating the velocities of the interactions between the particles and the bridging liquid, as well as the separation force between particles (Ahmed et al., 2023). This would suggest that the collision velocity in the system would increase at higher C/D values. This can be observed in Figure 5-7 although the increase at C/D>0.3 is less steep than at higher C/D ratios.

Table 5-4 CFD contours of solid velocity magnitude for the Rushton turbine impeller at different speeds and (C/D) ratios

C/D – 0.20 300 RPM	C/D – 0.20 450 RPM	C/D – 0.20 600 RPM
C/D – 0.28 300 RPM	C/D – 0.28 450 RPM	C/D – 0.28 600 RPM
C/D – 0.33 300 RPM	C/D – 0.33 450 RPM	C/D – 0.33 600 RPM
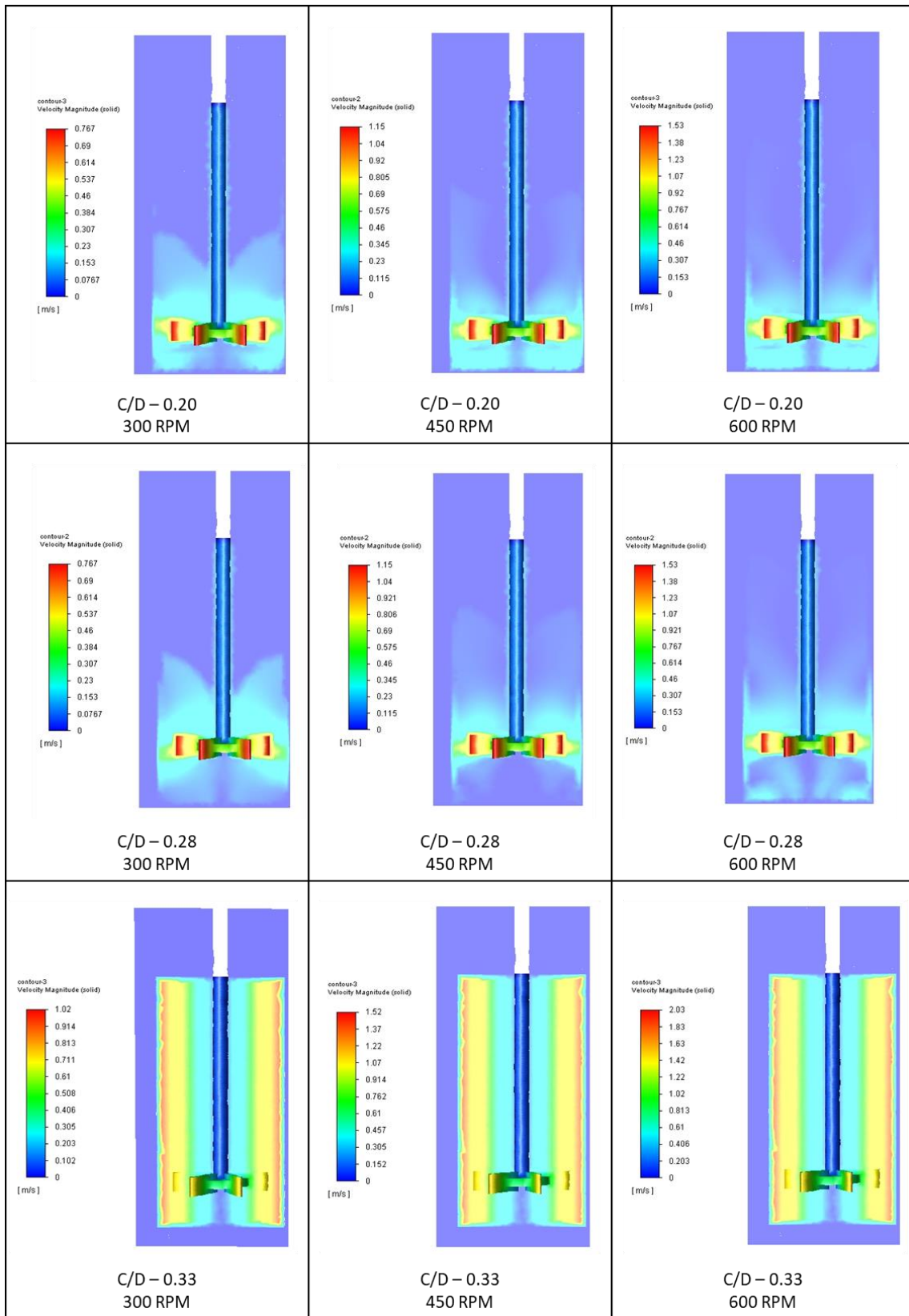
5.3.4 Pitched-Blade Impeller

The pitched blade impeller has four-blades coming out of the impeller shaft at a 45 ° pitch. This impeller promotes axial flow in the system. The VWA solid velocity magnitude for a pitched blade impeller at different impeller speeds and C/D ratios can be seen in Figure 5-9. The VWA solid velocity magnitude for all impeller speeds decreases with an increase in clearance up to C/D<0.3. After this the VWA solid velocity magnitude increases. Increased clearances for a pitched blade impeller have been shown to increase the impeller power number (Devarajulu and Loganathan, 2016). The spherical agglomeration PBM by Ahmed et al., 2023 uses power consumption in the calculation of the velocity of solid and liquid interaction, as well as separation forces. In the model, increasing power consumption would increase the velocities in the system. This suggests that spherical agglomerate production with a pitched blade impeller will be improved at increased C/D values as the velocities in the system will be greater.
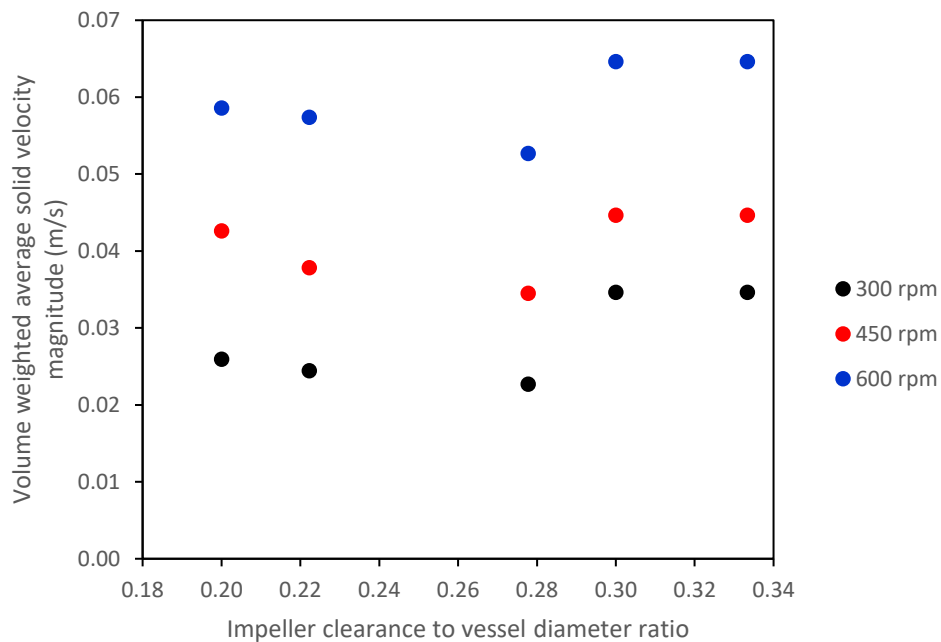
Figure 5-9 Volume weighted average solid velocity magnitude against clearance to vessel diameter ratio for a pitched blade impeller at different impeller speeds

The VWA liquid velocity magnitude at different impeller speeds and C/D ratios for the pitched blade impeller is shown in Figure 5-10. The VWA liquid velocity magnitude is higher than the VWA solid velocity magnitude for all conditions tested. This suggests that the pitched blade impeller is more effective at mixing liquids than it is at suspending solid particles.

The low values of VWA velocity magnitude for both solids and liquids with the pitched blade impeller suggest that this impeller will not be effective at producing spherical agglomerates. These results do suggest that the best agglomerates produced by a pitched blade impeller would be at C/D>0.3 and an impeller speed of 600 rpm as this gives the greatest value of VWA velocity magnitude for the solid and liquid.
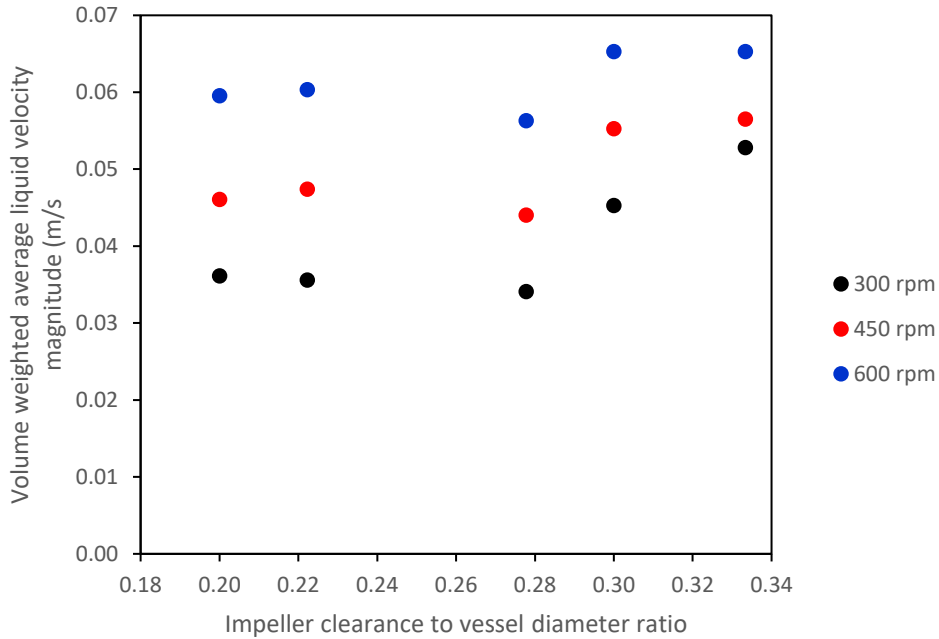
Figure 5-10 Volume weighted average water velocity magnitude against clearance to vessel diameter ratio for a pitched blade impeller at different impeller speeds

Table 5-5 shows a selection of CFD contours of the solid velocity magnitude at various C/D ratios and impeller speeds for the pitched blade impeller. The other contours can be found in Appendix B - Impeller Geometry CFD Analysis. The contours for 300 rpm show that particle suspension is directly around the impeller and towards the bottom of the tank. This demonstrates that this impeller speed is too low for particle suspension, and it suggests that 300 rpm is insufficient for successfully producing spherical agglomerates.

At an impeller speed of 450 rpm, the flow pattern appears to cover less area in the tank as C/D increases. This may be due to the increase in C/D leading to particles that have settled towards the bottom of the tank not becoming entrained in the flow pattern and therefore, not suspended. Increased C/D for a pitched blade impeller has been shown to extend the height of the flow pattern, with a C/D>0.3 covering the full liquid height (Kresta and Wood, 1993). The flow pattern for a C/D of 0.33 at an impeller speed of 450 rpm does not reach this height, suggesting that the velocity imparted on the particles is too low for them to stay suspended as they move further from the impeller.

The velocity profiles in Table 5-5 at an impeller speed of 600 rpm show that with increasing C/D ratios, the flow profiles cover a greater portion of the liquid height in the tank. This correlates with the findings of the study by Kresta and Wood, 1993. As the increasing C/D at 600 rpm leads to a greater height of flow pattern within the liquid height, it suggests that an impeller speed of 600 rpm is sufficient for particle suspension. The increased particle suspension at this speed and high C/D values mean that these conditions will be more successful at producing spherical agglomerates than lower C/D ratios and impeller speeds with a pitched blade impeller.

Table 5-5 Solid velocity magnitude CFD contours for the pitched blade impeller at various speeds and C/D ratios

C/D – 0.20 300 RPM	C/D – 0.20 450 RPM	C/D – 0.20 600 RPM
C/D – 0.28 300 RPM	C/D – 0.28 450 RPM	C/D – 0.28 600 RPM
C/D – 0.33 300 RPM	C/D – 0.33 450 RPM	C/D – 0.33 600 RPM
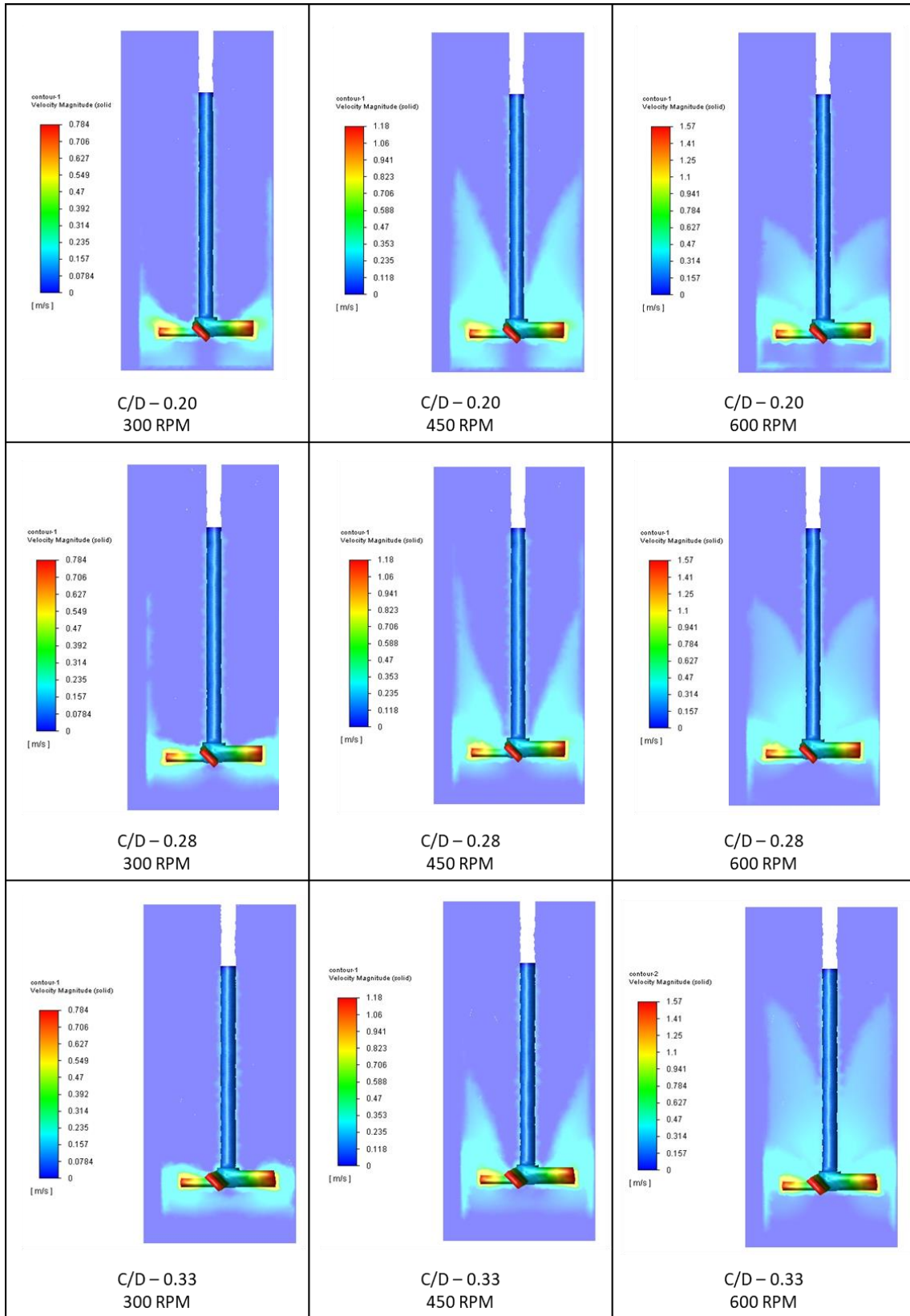
5.4　Influence of Impeller Geometry on Particle Suspension

Spherical agglomerates form due to contact between the bridging liquid and the primary particles in a stirred tank. Therefore, it is important to understand the suspension behaviour of the particles as this will determine the likelihood of contact between the particles and the bridging liquid. Tables 5-6 to 5-9 show CFD contours of solid volume fraction for the impeller configurations.

The CFD solid volume fraction contours for the flat blade impeller in Table 5-6 show that there is a clear change in solid suspension as the clearance is increased. This is a similar trend to the CFD contours and volume weighted average velocity magnitude profiles, shown in Table 5-2 and Figure 5-3 and Figure 5-4. In Table 5-6, the solid volume fraction is constant throughout the whole height of the tank at C/D≤0.28At increased C/D ratios, the solid particles are not as well suspended, and the highest volume fraction settles to the bottom of the tank. The velocity magnitude values in Figure 5-3 show that at C/D≤0.28 the velocity magnitude is much higher than at increased C/D values. This suggests that at higher clearances the velocity magnitude is insufficient for particle suspension. The trend of volume fraction contour is the same for all impeller speeds, suggesting that clearance has a larger influence on particle suspension than impeller speed for a flat blade impeller. At a C/D ratio of 0.33, however, increasing the impeller speed does increase the volume fraction of solids that are closer to the impeller, suggesting that when the impeller induces laminar flow, impeller speed is more important for particle suspension than impeller clearance.

Table 5-6 CFD contours of the solid volume fraction for the flat blade impeller at different impeller speeds and C/D
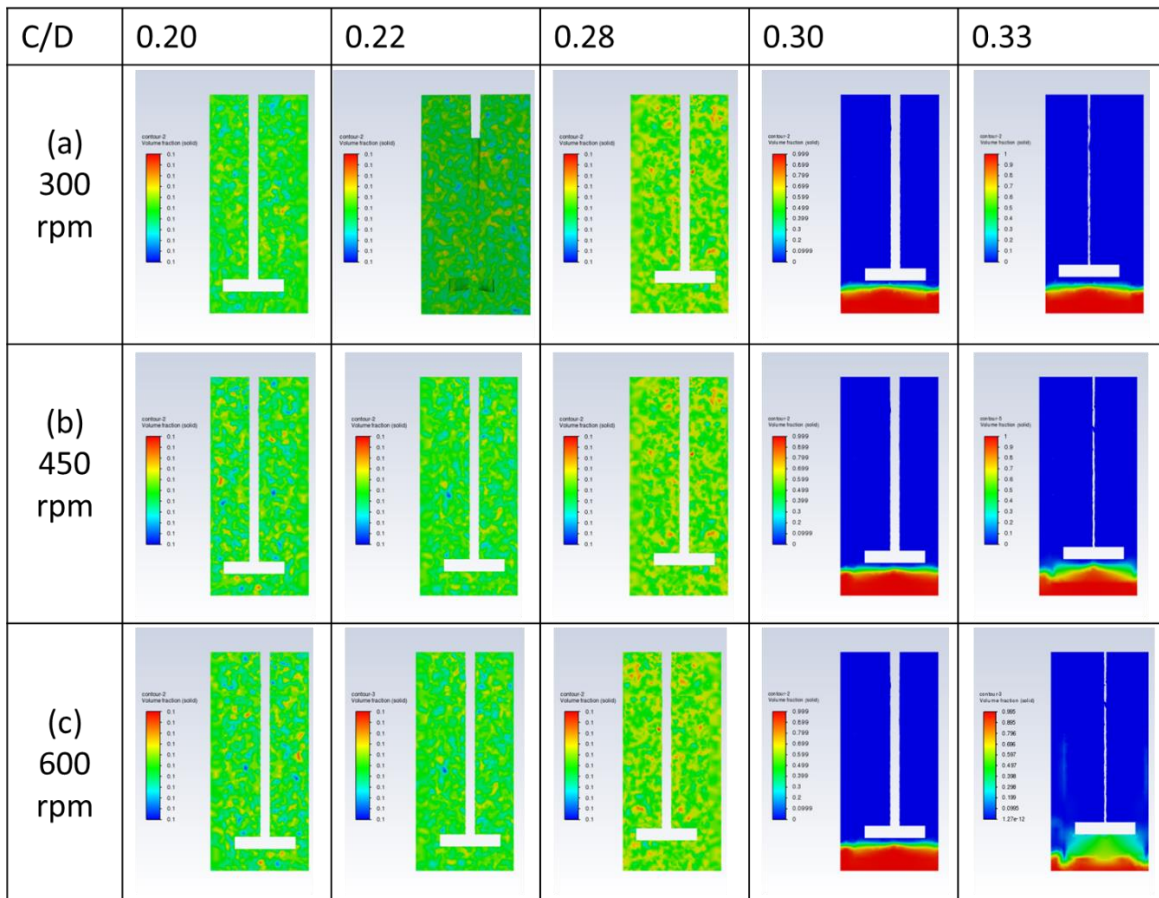
Table 5-7 shows the CFD contours of solid volume fraction for the propeller impeller at different impeller speeds and clearances. For all impeller speeds and clearances, a large portion of the solids are settled on the bottom of the tank, suggesting that the propeller impeller is inefficient at particle suspension. As the impeller speed is increased, the highest volume fraction of solids does form a peak in the centre of the tank underneath the impeller. The velocity magnitude values shown in Figure 5-5 and Figure 5-6 show that increasing the impeller speed leads to increased velocity in the system, therefore increasing the suspension of particles. In Table 5-7, the shape of the solid volume fraction is consistent across the increasing C/D ratios for each impeller speed. Therefore, the impeller speed has a greater influence on solid suspension than the clearance for a propeller impeller.

Table 5-7 CFD contours of the solid volume fraction for the propeller impeller at different impeller speeds and clearance to diameter ratios
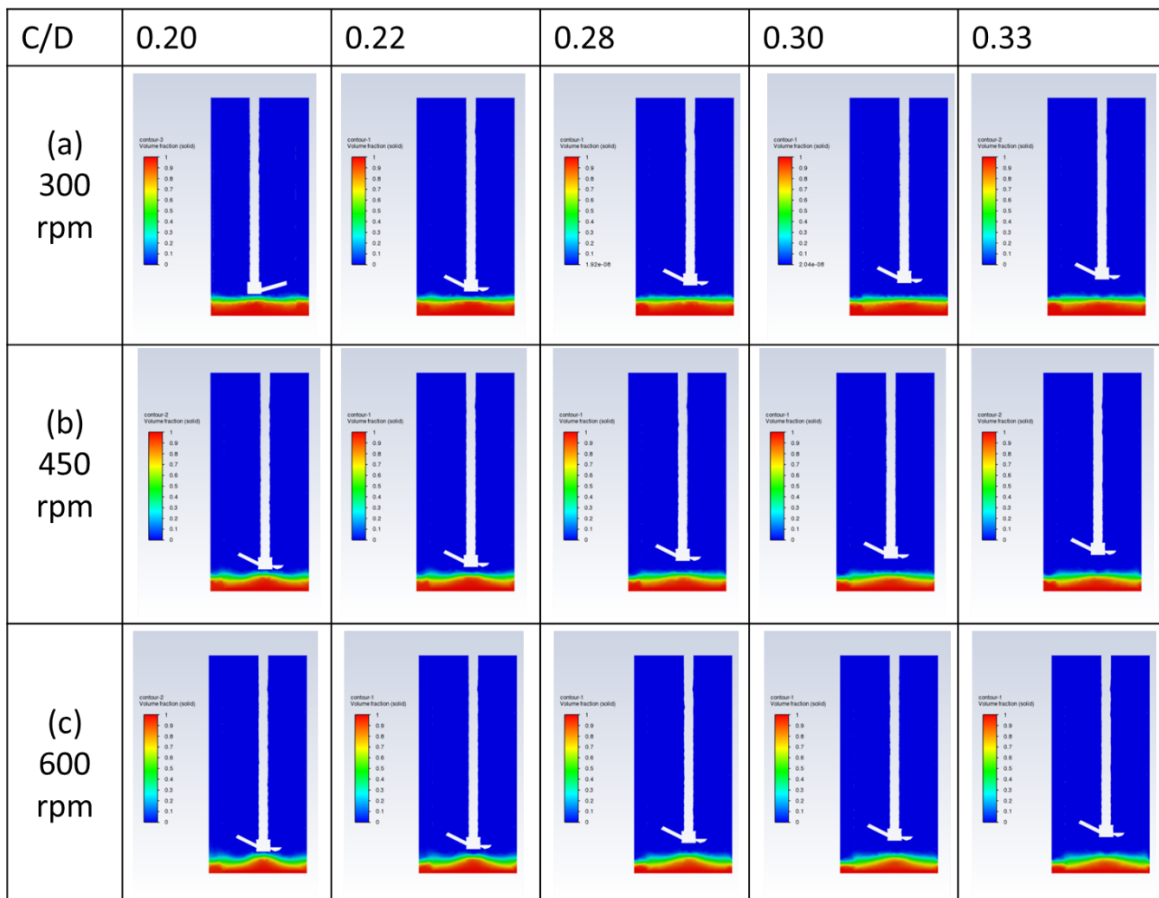
The solid volume fraction CFD contours for a Rushton turbine impeller at different impeller speeds and clearances can be seen in Table 5-8. In Table 5-8, there is a clear difference in the solid volume fraction contour at C/D of 0.33 compared to the other clearances for all impeller speeds. This is similar to the trend observed in Table 5-4, where the velocity profile changes at higher clearances as the Rushton turbine is able to form the double loop flow pattern associated with radial impellers (Montante et al., 1999; Zhu et al., 2019). In both the results for the flat blade impeller (Table 5-6) and the Rushton turbine impeller (Table 5-8), the double loop flow pattern allows for consistent particle suspension. This may be due to the velocity magnitude values obtained with the double loop pattern being much higher than the velocity magnitude values obtained when the radial impeller can only produce a single loop flow pattern.

In Table 5-8, at C/D≤0.3, there is a clear influence of impeller speed on the volume fraction of particles in the tank. As the impeller speed is increased, there is a greater volume fraction of particles above the impeller. This suggests that increased impeller speeds will improve the suspension of particles, leading to increased contact between the bridging liquid and the particles, resulting in more spherical agglomeration occurring.

Table 5-8 CFD contours of the solid volume fraction for the Rushton turbine impeller at different impeller speeds and clearance to diameter ratios

C/D	0.20	0.22	0.28	0.30	0.33
(a) 300 rpm					
(b) 450 rpm					
(c) 600 rpm					
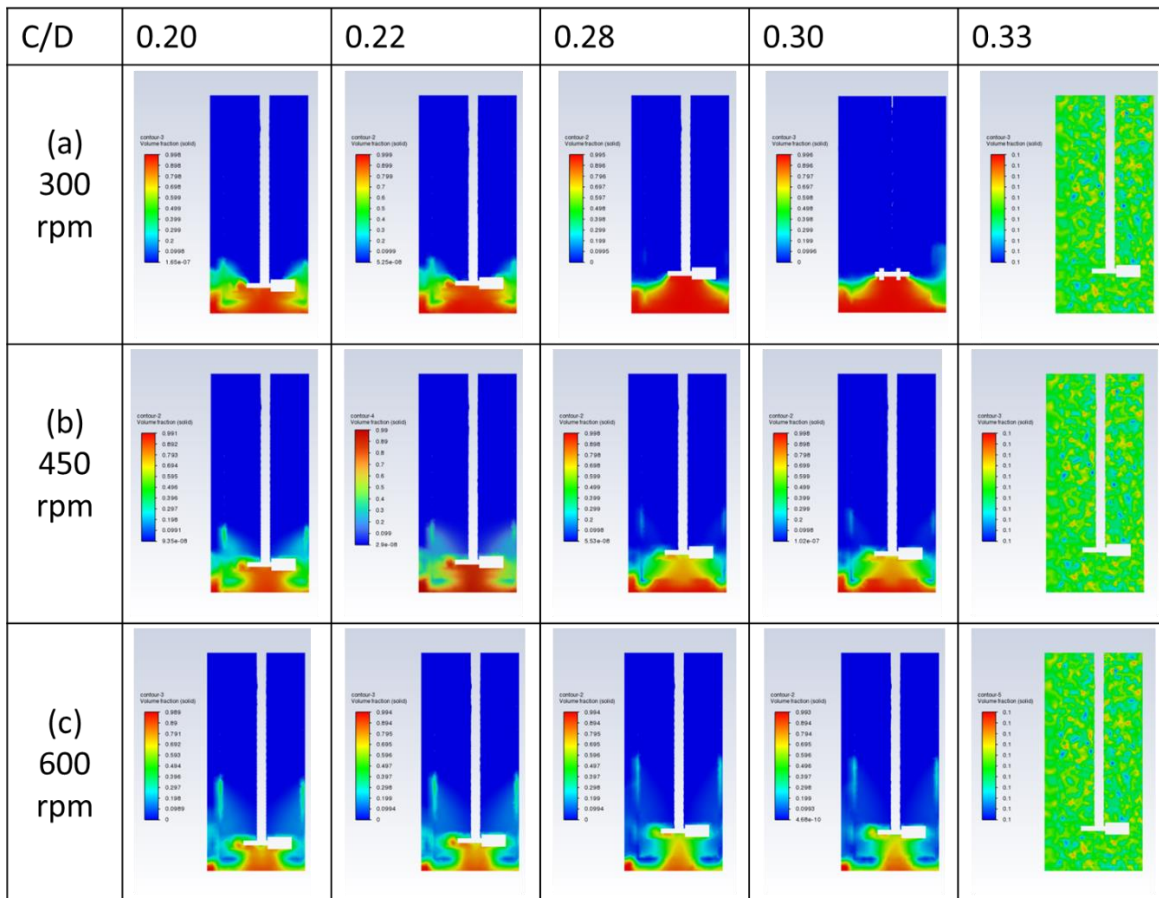
Table 5-9 shows the solid volume fraction CFD contours for the pitched blade impeller at various impeller speeds and clearances. Increasing the impeller speed increased the suspension of particles in the tank, as higher solid volume fractions are observed closer to the impeller at increased impeller speeds. The shapes of the solid volume fraction contours are fairly consistent across the C/D values for 300 rpm and 450 rpm. However, at the highest tested impeller speed of 600 rpm the clearance influences the shape, with C/D≤0.28 showing higher values of solid volume fraction near the edges of the tank than C/D≥0.3.

Table 5-9 CFD contours of the solid volume fraction for the pitched blade impeller at different impeller speeds and clearance to diameter ratios
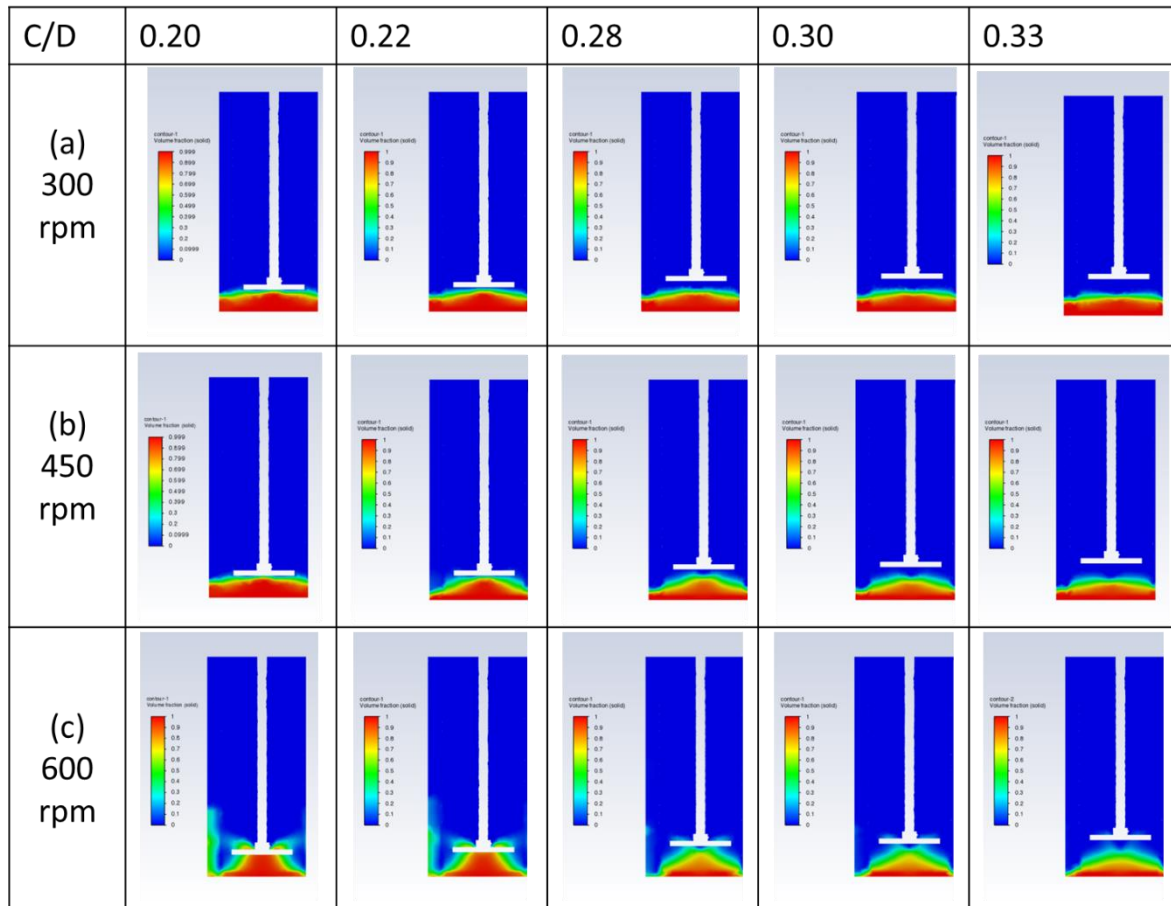
The volume fraction contours show that when an impeller is producing a single loop flow pattern, the impeller speed has a greater influence on particle suspension than the impeller clearance. However, the results suggest that the double loop flow pattern is better for suspending particles, due to these contours showing a uniform distribution of the particles in the tank (Table 5-6a,b,c at C/D≤0.28 and Table 5-8a,b,c at C/D=0.33). One limitation of these results is that the CFD simulations were performed with monosized particles of 500 μm diameter. This size was chosen to represent a spherical agglomeration product, but it does not consider the suspension behaviour of the much smaller primary material particles which would be very different.

5.5 Influence of Impeller Geometry on Spherical Agglomeration

In this section, the results of the CFD study into the influence of impeller geometry on flow patterns in the tank will be compared with the experimental results from Chapter 4. These experiments tested the same impeller speeds and C/D values for the four impeller geometries to determine which flow system is most effective at producing spherical agglomerates.

Figure 5-11 shows the VWA velocity magnitude profile for solid and liquid for the different impeller geometries and C/D ratios at a speed of 450 rpm. From the simulation results for all four impellers, the VWA velocity magnitude is lower for the impellers that promote axial flow in the tank. The propeller and pitched blade impellers promote axial flow patterns in the tank. In the experimental study, the propeller

116

impeller was the worst performing impeller as it produced very large agglomerates, whilst still having a large portion of primary material left in the product. The flow pattern of the four impeller geometries investigated in this work were studied by Matzke et al., 2022. This study found that even at high Reynolds numbers, the propeller impeller had the shortest circulation loop of the four impellers (Matzke et al., 2022). The short circulation loop would result in poor contact between the bridging liquid and particles, resulting in limited spherical agglomeration for the propeller impeller.

The CFD results for all impellers show that as the impeller speed is increased, the VWA velocity magnitude for both the solid and the liquid increases. These results are to be expected as the increased impeller speed will increase the impeller tip speed, which will result in faster velocities in the tank. It was determined in the experimental study that an impeller speed of 300 rpm was insufficient for the production of spherical agglomerates for all impellers.

Figure B- 2in Appendix B - Impeller Geometry CFD Analysis shows the volume weighted average solid and liquid velocity magnitude for the different impeller geometries and C/D ratios for an impeller speed of 300 rpm. The same profiles for speeds of 450 rpm and 600 rpm are in Figure 5-11 and Figure B-3respectively. As the speed is increased from 300 rpm to 450 rpm there is a much larger change in VWA velocity magnitude for both solid and liquid than when the speed is increased from 450 rpm to 600 rpm. The low values of VWA velocity magnitude at 300 rpm suggest that the mixing in the tank will be inefficient, leading to inconsistency in the agglomerates. This was observed in the experimental study.

The pitched blade impeller was not consistent at producing spherical agglomerates in the experimental study. From the CFD simulations, it appeared that high C/D values and increased impeller speeds were the most effective conditions for spherical agglomerate formation. The experimental results for the pitched blade impeller (Section 4.5) were most consistent for impeller speeds of 450 rpm and 600 rpm. Of the pitched blade experiments, the ideal configuration based on the PSD, the agglomerate images and the value of d_{43} was determined to be at C/D of 0.33 with an impeller speed of 600 rpm. In the CFD study, this condition produced the greatest VWA velocity for both the solid and the liquid, as well as the flow pattern that covered the most area of the fluid in the tank for this impeller.

The VWA velocity magnitude at higher impeller speeds was lower for the pitched blade impeller than the propeller impeller. In the experimental study, however, the pitched blade impeller produced more agglomerates that were more consistent in shape and size than the propeller impeller. From the CFD contours (Table 5-5), it became apparent that the flow pattern of the pitched blade impeller increased the suspension of particles that were settling towards the bottom of the tank. The flow profile also reaching high in the tank to draw the bridging liquid downwards, increasing contact between bridging liquid and particles at high speeds and C/D ratios. The flow images for the propeller impeller, shown in Table 5-3, also suggest that this impeller forms a deeper vortex in the system than the pitched blade impeller, which would also lead to inefficient mixing and uneven contact between bridging liquid particles (Schober and Fitzpatrick, 2005; Dickey, 2015). This would result in the propeller producing very large agglomerates whilst also having a large mass of primary material remaining.

The flat blade impeller had a transition of flow pattern when C/D>0.3. This was observed in the VWA velocity magnitude graphs, and also the CFD contours. From the experimental results this trend is harder to observe. The experimental images at 450 rpm and 600 rpm all show well-formed agglomerates that had consistent sphericity. This may be due to the VWA velocity magnitude for solid and liquid for a flat blade impeller being greater than the values for the pitched blade and propeller impellers at all impeller

speeds, this can be seen in Figure B- 2, Figure 5-11 and Figure B- 3. As the system is operating at a greater velocity than the axial flow impellers, it is able to produce agglomerates that are spherical in shape and fairly consistent in size.

In the experimental study, the Rushton turbine was the best performing impeller for spherical agglomerate production. The CFD contours shown in Table 5-4 show that for C/D<0.3, the flow pattern is similar to that of an axial impeller, which is thought to be more effective at particle suspension than the conventional double loop pattern produced by a radial impeller (Montante et al., 1999; Zhu et al., 2019). The contours for the Rushton turbine show that the solid velocity magnitude is higher both above and below the impeller, demonstrating that particles that were settling towards the bottom of the reactor will be caught in this flow at the bottom of the tank, resulting in them becoming entrained in the flow field and therefore undergoing agglomeration. For the Rushton turbine at a C/D of 0.33, the flow pattern is different. This flow pattern does not reach the bottom of the tank, but does cover a substantial portion below the impeller, and it reaches the full height of the liquid in the tank. The velocities for this C/D ratio are also higher than for lower C/D values at the same speed. This suggests that whilst the flow may not reach the bottom of the tank, particles are unable to settle, especially at 600 rpm which has a VWA solid and liquid velocity magnitude greater than the calculated value of suspension velocity (I_{js}), as shown in Table 5-1.

As Table 5-9 shows, for all impeller speeds and clearances, the CFD solid volume fraction contours for the pitched blade impeller are higher in the tank than the corresponding solid volume fraction contours for the propeller impeller (Table 5-7). This suggests that the pitched blade impeller will provide better particle suspension than the propeller impeller, leading to more spherical agglomeration occurring. In the experimental study conducted in Chapter 4, the pitched blade impeller did produce agglomerates that were more consistent in size and shape than the propeller impeller.
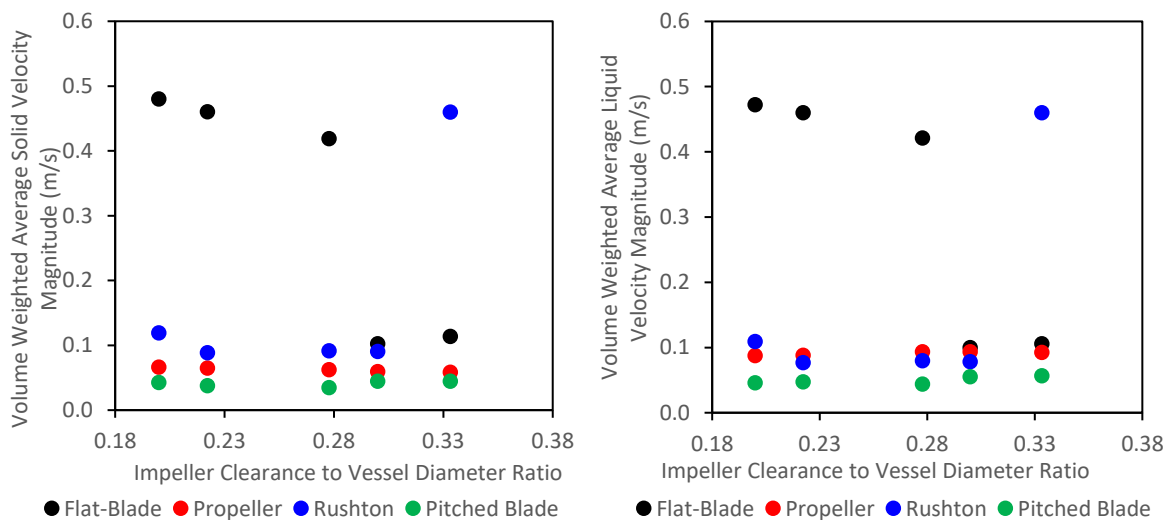
Figure 5-11 Volume weighted average velocity magnitude from the CFD simulations for different impeller geometries and clearances to diameter ratios at a speed of 450 rpm, (left – solid, right – liquid)

5.6 Conclusion

The CFD results correlate well with the experimental study. The CFD simulations show that the double loop flow pattern obtained by the flat blade impeller at C/D<0.28, and the Rushton turbine impeller at C/D>0.33 produced the highest velocities in the system. The increased velocities are due to the increased power requirements for generating a double loop flow pattern leading to increased energy dissipation in the system. The spherical agglomeration PBM by Ahmed et al., 2023 determined that energy dissipation was a major factor in the velocity of particle liquid interactions and separation forces. Increased velocity in the system increases the likelihood of agglomerate formation. This can be seen for all impellers, as increased impeller speeds resulted in greater VWA velocity magnitude in the CFD simulations, and improved agglomeration in the experimental study.

The pitched blade impeller had lower velocities in the system than the propeller, but it performed better in the experiments. This could be due to the large vortex that was formed by the propeller impeller leading to inefficient mixing in the system. The inefficient mixing would increase the likelihood of the system producing a few very large agglomerates whilst still retaining a high mass of primary material.

In the experimental study, it was observed that there was a correlation between impeller power number, and the likelihood of successful spherical agglomeration. From the CFD study, it is clear that the velocities in the tank are greater for radial flow promoting impellers than axial flow promoting impellers. Incorporating the power number and the influence that clearance has on the velocity profile will increase the accuracy of the PBM. Chapter 6 details the process of adapting the spherical agglomeration PBM by Ahmed et al., 2023, to incorporate the influence of the impeller geometry. The results of experimentally validating the PBM are presented in Chapter 7.

Chapter 6 Construction of a Population Balance Model for Spherical Agglomeration

The aim of this work is to develop a population balance model which is capable of predicting the effect of changing impeller type and speed on agglomerate properties. Starting with the spherical agglomeration PBM produced by Ahmed et al., 2023, flow characteristics identified from the experimental and CFD study in Chapters 4 and 5 respectively have been incorporated to achieve this aim.

Ahmed et al., 2023 developed a spherical agglomeration PBM in Siemens PSE gPROMS Formulated Products. This model uses a high shear wet granulator (HSWG) framework, with customised agglomeration and layering kernels. Using the HSWG framework is possible due to the mechanistic similarity between HSWG and spherical agglomeration.

In the PBM by Ahmed et al., 2023, the agglomeration kernel is derived from Blandin's coalescence model and the layering kernel is derived from work by Arjmandi-Tash. Breakage is not considered in the model due to limited research into breakage during spherical agglomeration (Ahmed et al., 2023; Arjmandi-Tash et al., 2019; Blandin et al., 2005). Section 2.12 of the literature review discusses in detail the development of PBMs for both high shear wet granulation and spherical agglomeration.

Alterations to the PBM by Ahmed et al., 2023 were conducted to incorporate flow characteristics into the PBM. The HSWG flowsheet that was used as the basis of the model is shown in Figure 6-1, with Table 6-1 explaining the function of each block on the flowsheet.
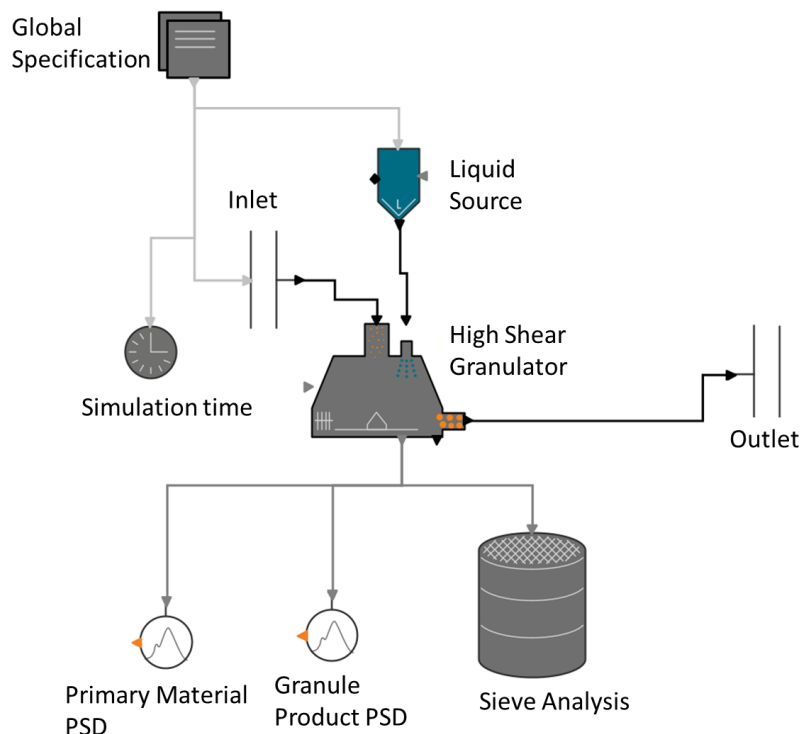
Figure 6-1 Flowsheet for the spherical agglomeration PBM in Siemens PSE gPROMS Formulated Products

Table 6-1 Description of model parameters in the Siemens PSE gPROMS Formulated Products flowsheet in Figure 6-1

Flowsheet Item	Description
Global Specification	Used to determine the material system, the boundaries of the particle size, and the number of grid points that the model uses to calculate PSD
Liquid Source	Specify the bridging liquid mass fraction, flow rate and temperature for the system
Inlet	Needed to fulfil the flowsheet design but does not influence results
Simulation Time	Specify the length of time the model simulates the agglomeration
High Shear Granulator	This block is specified by the user to determine which models are used for the calculation. The user can also specify the initial PSD, the bridging liquid droplet size, the impeller geometry and other important parameters for the spherical agglomeration PBM.
Outlet	Needed to fulfil the flowsheet design but does not influence results
Primary Material PSD	Monitors the size of the primary material in the system; this size is specified via the high shear granulator icon
Granule Product PSD	Monitors the size of the agglomerates in the system; the PSD is a result of the model
Sieve Analysis	This is used to analyse the Granule Product PSD to produce distribution curves and calculate the mean, d_{10}, d_{50} and d_{90} of the agglomerates. The number of sieves used can be specified

6.1 PBM Adaptation Methodology

As the experimental and CFD results show a large influence of both impeller geometry and clearance on the flow patterns in the tank, both of these parameters must be incorporated into the PBM by Ahmed et al., 2023.

The experimental study in Chapter 4 demonstrated a clear link between the impeller geometry and the consistency in size and shape of agglomerates. It was determined that as the impeller power number increased, so did the consistency of the agglomerate product. Therefore, incorporating impeller power number is an ideal way to include the impeller geometry in the PBM. Section 6.2 covers the correlations for power number and how they are incorporated into the PBM.

To include the impeller clearance, a fitting parameter was developed for the velocity equations based on the CFD results. For each impeller geometry and C/D ratio, a fitting equation was developed based on impeller speed. The process of developing the fitting parameters is shown in Section 6.3. Figure 6-2

summarises the approach taken to modify the PBM by Ahmed et al., 2023 to include the impeller geometry and clearance.
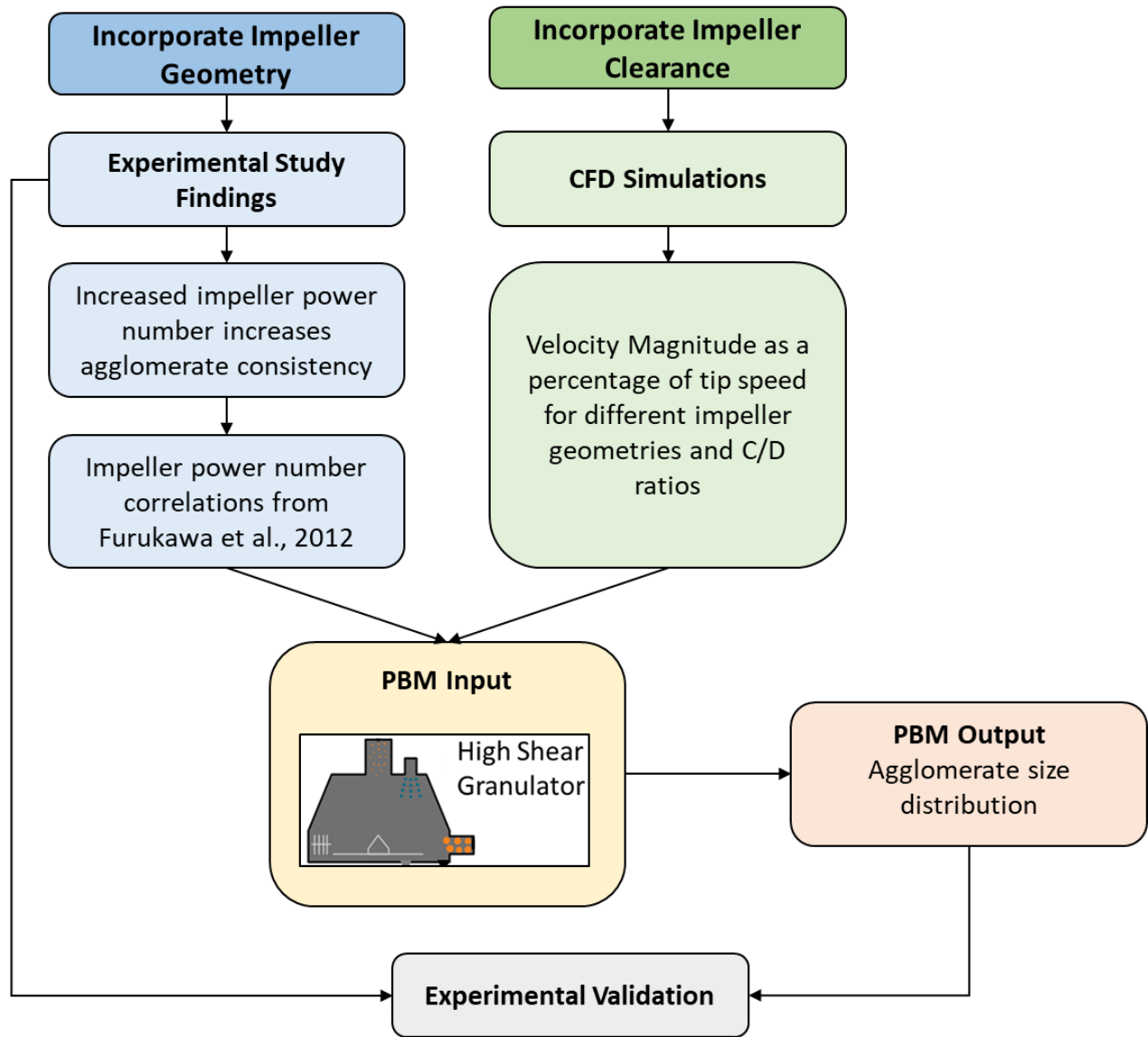
Figure 6-2 Diagram of the findings from this work that informed modifications to the PBM by Ahmed et al., 2023 to incorporate impeller geometry and clearance

6.2 Incorporating Impeller Geometry

From the experimental study in Chapter 4, it could be seen that agglomerates were more consistent in shape and size when an impeller with increased impeller power number was used. In the Ahmed et al., 2023 model, the power number is used for calculating the impeller power requirements for both the agglomeration and layering kernels. Further details of the PBM by Ahmed et al., 2023 are discussed in Section 2.12.2 of the literature review in this thesis.

Equation 6.1 is the power calculation used in the PBM.

$$P = \frac{N_P d^5 n^3}{v} \tag{6.1}$$

Where:

P is impeller power consumption (W)

N_P is the impeller power number

d is the impeller diameter (m)

n is the impeller rotational speed (rps)

v is the volume of the suspended fluid (m³)

The impeller power consumption is employed in both the agglomeration and layering kernel to calculate the velocity of the interactions between the particles and the fluid. The velocity calculations can be seen in Equations 6.2 and 6.3. Equation 6.4 shows the calculation for the separation force, which also involves the power that is imparted into the system. The separation force calculation is utilised in the agglomeration kernel, but it is not part of the layering kernel.

$$u(D_p) = \left[\frac{(\rho_{agg} - \rho_{L1})^3}{200 \rho_{L1} \mu_{L1} (2\rho_{agg} + \rho_{L1})} \right]^{1/2} S_i^{3/5} P^{2/5} \tag{6.2}$$

$$u(D_d) = \left[\frac{(\rho_{agg} - \rho_{L1})^3}{200 \rho_{L1} \mu_{L1} (2\rho_{agg} + \rho_{L1})} \right]^{1/2} S_j^{3/5} P^{2/5} \tag{6.3}$$

$$f_{sep}(i,j,t) \approx \rho_{L1} \left[P(S_i + S_j) \right]^{2/3} S_i^2 \tag{6.4}$$

Where:

u is velocity (m/s)

D_p is the particle size (m)

ρ_{agg} is the density of the agglomerates (kg/m³)

ρ_{L1} is the density of the suspending liquid (also called mother solution) (kg/m³)

μ_{L1} is the viscosity of the suspending liquid (also called mother solution) (Pa.s)

S_i is agglomerates of size i

S_j is agglomerates of size j

P is the impeller power requirement (W)

D_d is the size of bridging liquid droplets (m)

$f_{sep}(i,j,t)$ is the separation force of particles (N)

In the PBM by Ahmed et al., 2023 a fixed value for power number is used, with N_P being assumed to be 0.6. To determine if altering power number will influence the PSD produced by the PBM, the value of power number was modified in the equations. The PSD from the PBM with different power numbers can be seen in Figure 6-3. This shows that including power number values for the individual impellers will produce different results for the product particle size. Section 6.2 shows the process used to incorporate the impeller geometry into the spherical agglomeration PBM.
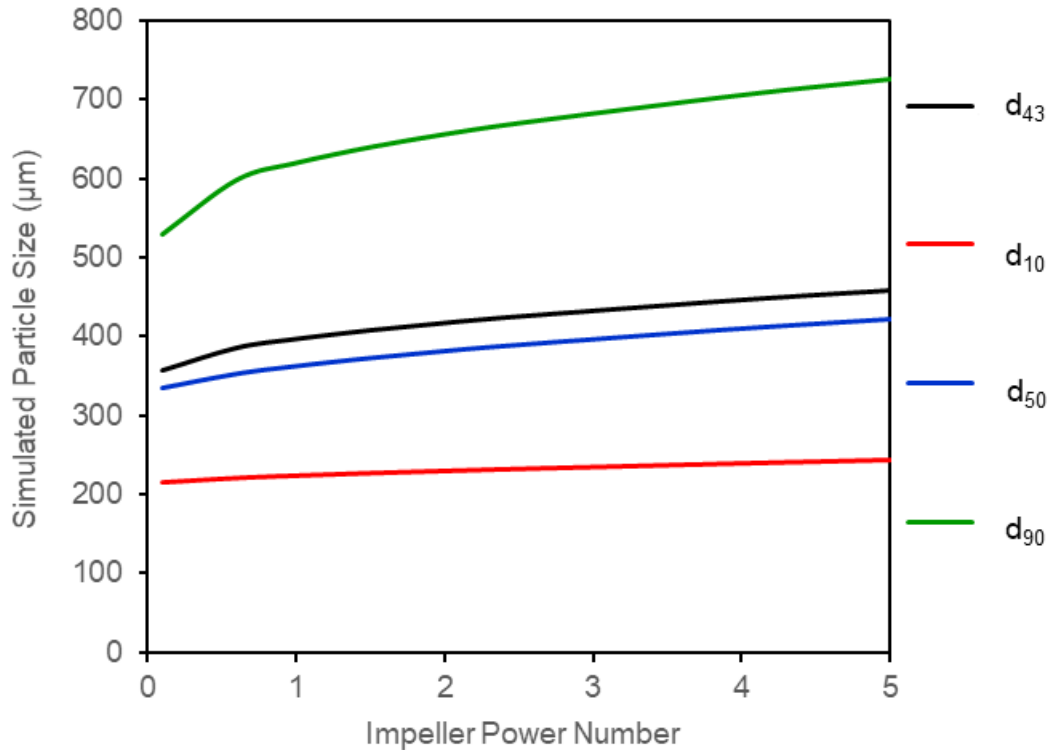
Figure 6-3 Particle size distributions when altering the power number in the PBM

As Figure 6-3 shows, changing the value of power number in Equation 6.1 produces a different particle size distribution for spherical agglomerates. This demonstrates that incorporating the power number for different impeller geometries will influence the PBM results. Increasing the power number appears to increase the average particle size (d_{43}).

6.2.1 Power Number Correlations Used for Modifying the PBM

Predictive correlations for impeller power number were determined by Furukawa et al., 2012. The correlations developed have been shown to have good agreement with measured values from experiments (Furukawa et al., 2012). To allow for consideration of flow patterns in the stirred tank, the Furukawa et al., 2012 correlations were incorporated into the power equation of the PBM. There are correlations from Furukawa et al., 2012 for the four impellers investigated in this research (Figure 3-6). All impellers have common equations involved in calculating the power number; these are presented in Equations 6.5 to 6.16 (Table 6-2). The equations for the Rushton turbine and flat blade impeller are all the same, and are presented in Section 6.2.2. The pitched blade impeller equations are given in Section 6.2.3, and the propeller impeller equations are shown in Section 6.2.4.

The calculations used are from Furukawa et al., 2012

b is impeller blade height (m)
D is the diameter of the stirred tank (m)
d is the diameter of the impeller (m)
f is the friction factor (-)
$f \sim$ is the approximate friction factor (-)

H is the height of liquid in the tank (m)

h_B is the length of the baffles (m)

N_P is the power number (-)

N_{P0} is the unbaffled power number (-)

N_{Pmax} is the fully baffled power number (-)

n is the impeller speed (rps)

n_B is the number of baffles in the tank (-)

n_p is the number of blades on the impeller (-)

P is the impeller power consumption (W)

Re_d is the Reynolds number of the impeller (-)

Re_G is the modified Reynolds number (-)

θ is the impeller blade pitch (°)

μ is the viscosity of the liquid (Pa.s)

ρ is the liquid density (kg/m^3)

$\beta, \eta, \gamma, X, C_L, C_{tr}, C_t, m, x$ are all calculation parameters with no units

Table 6-2 Equations from Furukawa et al., 2012 that are used for all impeller geometries to incorporate impeller geometry into the spherical agglomeration PBM by Ahmed et al., 2023

Equations Used for All Impeller Power Number Calculations

$$\beta = \frac{2\ln\left(D/d\right)}{\left[\left(D/d\right) - \left(d/D\right)\right]}$$

(Furukawa et al., 2012)   (6.5)

$$\eta = 0.711 \left[\frac{0.157 + \left[n_p \ln\left(D/d\right)\right]^{0.611}}{n_p^{0.52}\left[1 - \left(d/D\right)^2\right]}\right]$$

(Furukawa et al., 2012)   (6.6)

$$\gamma = \left[\frac{\eta \ln\left(D/d\right)}{\left(\beta D/d\right)^5}\right]^{1/3}$$

(Furukawa et al., 2012)   (6.7)

$$X = \gamma n_p^{0.7} \sin\left(\theta/H\right)^{1.6}$$

(Furukawa et al., 2012)   (6.8)

$$N_{P0} = f\left[\frac{1.2\pi^4\beta^2}{8d^3/(D^2H)}\right]$$

(Furukawa et al., 2012)   (6.9)

$$Re_d = \frac{nd^2\rho}{\mu}$$

(Furukawa et al., 2012)   (6.10)

$$Re_G = Re_d \left[\frac{\pi \eta \ln(D/d)}{4d/\beta D} \right]$$

<div align="right">(Furukawa et al., 2012)   (6.11)</div>

$$C_L = 0.215 \eta n_p (d/H) \left[1 - (d/D)^2 \right] + 1.83 (b \sin \theta / H) \left(n_p / 2 \sin \theta \right)^{1/3}$$

<div align="right">(Furukawa et al., 2012)   (6.12)</div>

$$C_{tr} = 23.8 \left(\frac{d}{D} \right)^{-3.24} b \sin \left(\frac{\theta}{D} \right)^{-1.18} X^{-0.74}$$

<div align="right">(Furukawa et al., 2012)   (6.13)</div>

$$f\sim = 0.0151 \left(\frac{d}{D} \right) C_t^{0.308}$$

<div align="right">(Furukawa et al., 2012)   (6.14)</div>

$$f = \frac{C_L}{Re_G} + C_t \left\{ \left[\left(C_{tr}/Re_G \right) + Re_G \right]^{-1} + \left(f\sim/C_t \right)^{1/m} \right\}^m$$

<div align="right">(Furukawa et al., 2012)   (6.15)</div>

$$N_p = \left[(1 + x^{-3})^{-1/3} \right] N_{Pmax}$$

<div align="right">(Furukawa et al., 2012)   (6.16)</div>

6.2.2 Rushton Turbine and Flat Blade Impeller Equations

Table 6-3 Equations from Furukawa et al., 2012 that are used for the Rushton turbine and flat blade impeller to incorporate impeller geometry into the spherical agglomeration PBM by Ahmed et al., 2023

Equations used for the Rushton Turbine and Flat Blade Impeller Power Number Calculations

$$C_t = \left[(1.96 X^{1.19})^{-7.8} + 0.25^{-7.8} \right]^{-1/7.8}$$

<div align="right">(Furukawa et al., 2012)   (6.17)</div>

$$m = \left[(0.71 X^{0.373})^{-7.8} + 0.333^{-7.8} \right]^{-1/7.8}$$

<div align="right">(Furukawa et al., 2012)   (6.18)</div>

$$x = \frac{4.5 \left(\frac{B_w}{D} \right) n_B^{0.8}}{N_{Pmax}^{0.2}} + \frac{N_{P0}}{N_{Pmax}}$$

<div align="right">(Furukawa et al., 2012)   (6.19)</div>

$$N_{Pmax} = \begin{cases} 10 \left(\frac{n_p^{0.7} b}{d} \right)^{1.3} & \frac{n_p^{0.7} b}{d} \leq 0.54 \\[2mm] 8.3 \left(\frac{n_p^{0.7} b}{d} \right) & 0.54 < \frac{n_p^{0.7} b}{d} \leq 1.6 \\[2mm] 10 \left(\frac{n_p^{0.7} b}{d} \right)^{0.6} & 1.6 < \frac{n_p^{0.7} b}{d} \end{cases}$$

<div align="right">(Furukawa et al., 2012)   (6.20)</div>

6.2.3 Pitched Blade Impeller Equations

Table 6-4 Equations from Furukawa et al., 2012 that are used for the pitched blade impeller to incorporate impeller geometry into the spherical agglomeration PBM by Ahmed et al., 2023

Equations used for the Pitched Blade Impeller Power Number Calculations

$$C_t = \left[\left(1.96X^{1.19}\right)^{-7.8} + 0.25^{-7.8}\right]^{-1/7.8}$$	(Furukawa et al., 2012)	(6.21)
$$m = \left[\left(0.71X^{0.373}\right)^{-7.8} + 0.333^{-7.8}\right]^{-1/7.8}$$	(Furukawa et al., 2012)	(6.22)
$$x = \frac{4.5\left(\frac{B_w}{D}\right)n_B{}^{0.8}}{\left(\frac{2\theta}{\pi}\right)^{0.72}N_{Pmax}{}^{0.2}} + \frac{N_{P0}}{N_{Pmax}}$$	(Furukawa et al., 2012)	(6.23)
$$N_{Pmax} = 8.3\left(\frac{2\theta}{\pi}\right)^{0.9}\left(n_p{}^{0.7}b\sin\left(\frac{\theta}{d}\right)^{1.6}\right)$$	(Furukawa et al., 2012)	(6.24)

6.2.4 Propeller Impeller Equations

Table 6-5 Equations from Furukawa et al., 2012 that are used for the propeller impeller to incorporate impeller geometry into the spherical agglomeration PBM by Ahmed et al., 2023

Equations used for the Propeller Impeller Power Number Calculations

$$C_t = \left[\left(3X^{1.5}\right)^{-7.8} + 0.25^{-7.8}\right]^{-1/7.8}$$	(Furukawa et al., 2012)	(6.25)
$$m = \left[\left(0.8X^{0.373}\right)^{-7.8} + 0.333^{-7.8}\right]^{-1/7.8}$$	(Furukawa et al., 2012)	(6.26)
$$x = \frac{4.5\left(\frac{B_w}{D}\right)n_B{}^{0.8}}{N_{Pmax}{}^{0.2}} + \frac{N_{P0}}{N_{Pmax}}$$	(Furukawa et al., 2012)	(6.27)
$$N_{Pmax} = 6.5\left(n_p{}^{0.7}b\sin\left(\frac{\theta}{d}\right)^{1.6}\right)^{1.7}$$	(Furukawa et al., 2012)	(6.28)

The work by Furukawa et al., 2012 also produced a power number correlation for a helical ribbon impeller. This has not been incorporated into the PBM as they are commonly used for agitating high viscosity fluids and not suspending solids (Ameur et al., 2013; Delaplace et al., 2000).

6.2.5 Incorporating Impeller Selection into the PBM

To ensure that the correct calculations were used for each impeller geometry, a dropdown box was created on the agglomeration parameter input page to allow for the correct impeller equations to be used; this can be seen in Figure 6-4. The impeller selection dropdown box is only available on the agglomeration parameter page, but the selected impeller will also be used for calculations in the layering kernel, as the impeller geometry does not change during an experiment. To construct the dropdown box, the Interface Language section of the High Shear Granulator block was edited. The code for this edit can be seen in Appendix C - PBM Construction and Validation.
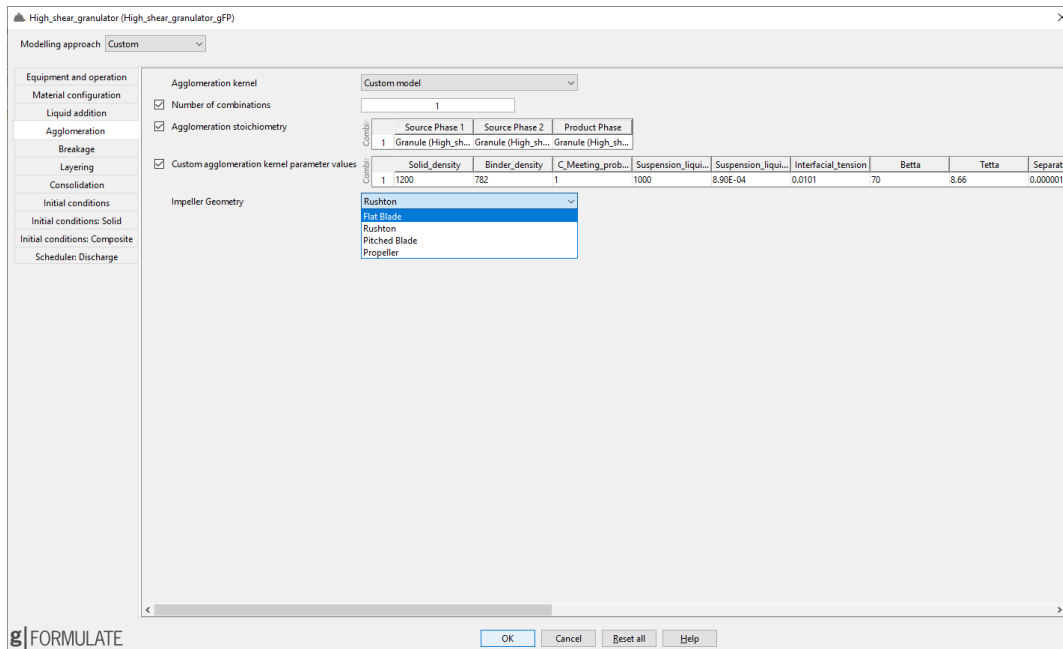
Figure 6-4 Impeller selection dropdown on spherical agglomeration PBM

To incorporate the impeller geometry into the custom agglomeration and layering kernels, each impeller geometry had to be added as a PARAMETER to both custom kernel pages. Each impeller was defined as an integer and given a default value of 0 as only one impeller would be used at a time.

The calculation parameters shown in Section 6.2.1, were classed as VARIABLES in the PBM kernels. The variables that needed to be specified were SET as parameter_names in the model to allow them to be specified through the flowsheet. Although values such as impeller clearance and speed will remain constant during an experiment, they will need to be specified on both the agglomeration and layering kernel. This is to allow the model to be used at multiple scales which would require a broad range of variables that could not be easily incorporated into a dropdown list.

Of the variables specified in Section 6.2.1, the following need to be specified for the model:

- b is impeller blade height (m)
- D is the diameter of the stirred tank (m)
- d is the diameter of the impeller (m)
- H is the height of liquid in the tank (m)
- h_B is the length of the baffles (m)
- n is the impeller speed (rpm)
- n_B is the number of baffles in the tank
- n_p is the number of blades on the impeller
- θ is the impeller blade pitch (°)
- μ is the viscosity of the liquid (Pa.s)
- ρ is the liquid density (kg/m^3)

These parameters are all things that would be known when constructing a simulation of the spherical agglomeration process.

A FOR loop was used for the equations that were specific to each impeller. The power number correlations by Furukawa et al., 2012 contain equations for an unbaffled and a fully baffled power number. To incorporate this, an IF statement was used that states if there is fewer than 1 baffle in the system, then the power number is equal to the unbaffled power number, otherwise it is calculated using Equation 6.16. This IF statement can be seen in Figure 6-5.

```
248 IF Number_of_baffles<1 THEN
249 Power_Number=Unbaffled_power_number;
250 else
251 Power_Number=ABS(Fully_Baffled_Power_Number*((1+(Small_x^(-3)))^(-1/3)));
252 END
```

Figure 6-5 IF statement to ensure that the number of baffles is incorporated into the PBM

The IF statement in Figure 6-5 was part of the communal equations, but the calculation of Fully_Baffled_Power_Number and Small_x are impeller specific, as well as CT and m. The value of the impeller blade pitch in radians (Thetar in the PBM) was also considered impeller specific because the model would produce errors for the pitched blade impeller at 45 °. These errors were not present when the impeller pitch was 46 °, therefore, an IF statement was used in the Pitched Blade Impeller equations to say that the value of Thetar was based on the Pitched_Blade_Pitch, which was assigned 46 ° on the model page. This IF statement can be seen in Figure 6-6

```
330 IF blade_Pitch>44.9 AND blade_pitch<45.1 THEN
331 Thetar=(Pitched_Blade_Pitch*pi)/180;
332 ELSE
333 Thetar=(Blade_Pitch*pi)/180;
334 END
```

Figure 6-6 IF statement used to set the blade pitch to 46 ° to prevent an error in running the PBM with a pitched blade impeller

A FOR loop was chosen for this purpose as the equations only needed to be performed when the specific impeller was selected. This would minimise computation time as the model would not calculate any results for the other three impeller geometries. For each impeller geometry, the values of CT, m, Small_x, Thetar and Fully_Baffled_Power_Number were calculated in the FOR loop. The full code for the Agglomeration Kernel and the Layering Kernel can be seen in Appendix C - PBM Construction and Validation.

6.3   Incorporating Impeller Clearance

Both the experimental and CFD simulation results in Chapter 4 and Chapter 5 respectively show that impeller clearance influences spherical agglomeration. The influence of clearance on the system varies for each impeller geometry (Figure 5-2-Figure 5-10). Therefore, the fitting parameters can be incorporated into the model for each geometry.

To allow for the clearance to be incorporated for the impellers at different speeds, the velocity magnitude as a percentage of impeller tip speed that was found using Equation 5.1. Table 6-6 shows the impeller tip speed, the VWA velocity magnitude for solid and water, as well as the VWA velocity magnitude as percentage of tip speed for a flat blade impeller. These values for the other impellers can be found in Appendix C - PBM Construction and Validation.

Table 6-6 The solid and water VWA velocity magnitudes, the impeller tip speed and VWA velocity magnitude as a percentage of tip speed for flat blade impeller

Impeller Geometry	Impeller Speed (rpm)	Impeller Clearance (mm)	Clearance to Vessel Diameter Ratio	Impeller Tip Speed (m/s)	Volume Weighted Average Solid Velocity Magnitude (m/s)	Solid VWA velocity magnitude as % of Tip Speed	Volume Weighted Average Water Velocity Magnitude (m/s)	Water VWA velocity magnitude as % of Tip Speed
Flat-Blade	300	18	0.200	0.785	0.307	39.066	0.307	39.066
Flat-Blade	300	20	0.222	0.785	0.307	39.064	0.307	39.064
Flat-Blade	300	25	0.278	0.785	0.307	39.058	0.307	39.058
Flat-Blade	300	27	0.300	0.785	0.035	4.410	0.065	8.312
Flat-Blade	300	30	0.333	0.785	0.035	4.410	0.065	8.312
Flat-Blade	450	18	0.200	1.178	0.480	40.744	0.472	40.093
Flat-Blade	450	20	0.222	1.178	0.460	39.064	0.460	39.064
Flat-Blade	450	25	0.278	1.178	0.419	35.555	0.421	35.744
Flat-Blade	450	27	0.300	1.178	0.102	8.674	0.100	8.493
Flat-Blade	450	30	0.333	1.178	0.114	9.669	0.106	8.966
Flat-Blade	600	18	0.200	1.571	0.614	39.066	0.614	39.066
Flat-Blade	600	20	0.222	1.571	0.614	39.064	0.614	39.064
Flat-Blade	600	25	0.278	1.571	0.614	39.058	0.614	39.058
Flat-Blade	600	27	0.300	1.571	0.152	9.704	0.172	10.971
Flat-Blade	600	30	0.333	1.571	0.145	9.203	0.136	8.668

This VWA velocity magnitude as percentage of tip speed (Table 6-6) was plotted against impeller speed for the different impeller clearance to tank diameter ratios and a 2nd order polynomial trendline was found for all systems. To ensure that the polynomial is an accurate prediction, extra simulations were performed to add in other points to the system. Details of these can be found in Table 6-7, with the results graphs in Figure 6-7 to Figure 6-10.

Table 6-7 Additional CFD simulations performed to validate the polynomial curves to develop the velocity fitting equations

Impeller Geometry	Impeller Clearance (mm)	C/D ratio	Impeller Speed (rpm)	Impeller Tip Speed (m/s)
Flat-Blade	18	0.2	400	1.047
	20	0.22	250	0.654
	25	0.28	500	1.309
	27	0.3	700	1.833
	30	0.33	550	1.440
Propeller	18	0.2	400	1.047
	20	0.22	250	0.654
	25	0.28	500	1.309
	27	0.3	700	1.833
	30	0.33	550	1.440
Rushton Turbine	18	0.2	400	1.047
	20	0.22	250	0.654
	25	0.28	500	1.309
	27	0.3	700	1.833
	30	0.33	550	1.440
Pitched-Blade	18	0.2	400	1.047
	20	0.22	250	0.654
	25	0.28	500	1.309
	27	0.3	700	1.833
	30	0.33	550	1.440

6.3.1 Velocity Fitting Curves for the Flat Blade Impeller

The fitting curves for the flat blade impeller can be found in Figure 6-7, and the equations for the trendlines are given in Table 6-8. In Figure 6-7, the VWA solid and liquid velocity magnitude as a percentage of tip speed is lower for C/D values of 0.3 and above. For the flat blade impeller, the increased clearance reduces particle velocity. This may be due to increased C/D values limiting particle suspension with a flat blade impeller (Devarajulu and Loganathan, 2016).

The profiles for the VWA solid velocity magnitude as a percentage of tip speed are similar to the VWA liquid velocity magnitude as a percentage of tip speed profiles. In Figure 6-7, it can be seen that the C/D<0.28 and C/D>0.3 are in two distinct regions of the graph. The lower C/D values are above 35 % of the impeller tip speed for all impeller speeds, and C/D>0.3 is below 10 % for all impeller speeds. This correlates with the CFD contours shown for the flat blade impeller in both Table 5-2 and Appendix B - Impeller Geometry CFD Analysis.
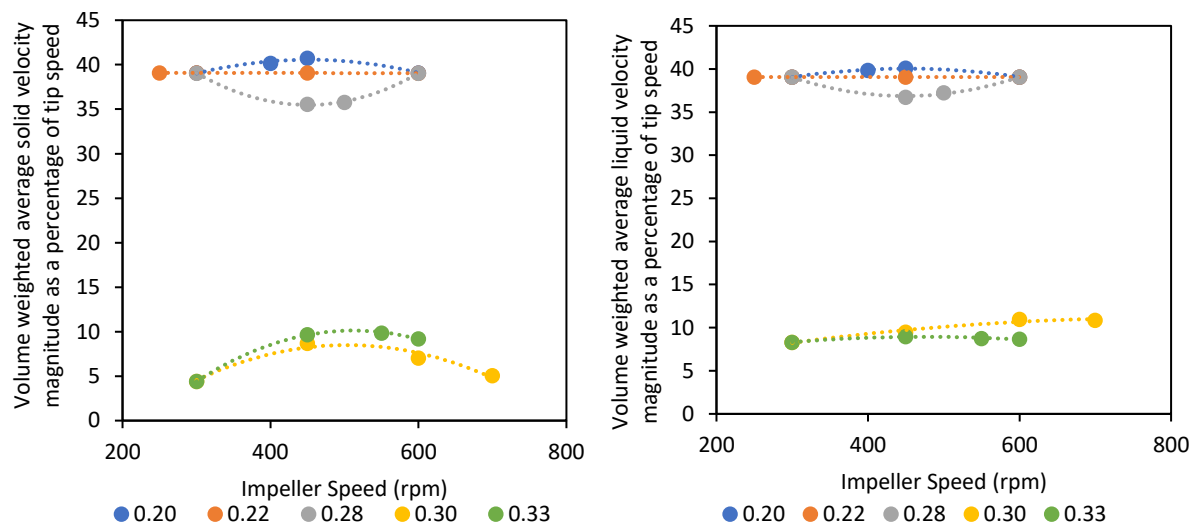
Figure 6-7 Flat blade impeller volume weighted average solid(left) and liquid (right) velocity magnitude as a percentage of tip speed against impeller speed for various impeller clearance to tank diameter ratios used to develop velocity fitting parameters.

6.3.2 Velocity Fitting Curves for the Propeller Impeller

Figure 6-8 shows the fitting curves for the propeller impeller and the equations for the curve trendlines are given in Table 6-8. The propeller impeller has a greater range in VWA solid velocity magnitude as a percentage of impeller tip speed, compared to VWA liquid velocity magnitude as a percentage of tip speed. For all impeller speeds and C/D values, the liquid velocity magnitude is between 6 % and 9 % of the impeller tip speed. For the propeller impeller, lower C/D ratios have lower values of velocity magnitude as a percentage of tip speed. This could be due to the low C/D having a shorter circulation loop of the flow pattern compared to increased clearances. This was also observed by Kresta and Wood, 1993.

At lower impeller speeds the solid particles have a low VWA velocity magnitude as percentage of impeller tip speed for all clearances. This is due to the low impeller speeds not providing sufficient velocities in the system to cause particles to become entrained in the flow. The propeller CFD contours, shown in Table 5-3and Appendix B - Impeller Geometry CFD Analysis show that for an impeller speed of 300 rpm the velocity magnitude profile in the tank is low and close to the impeller. This suggests that particles settle

towards the bottom of the tank, leading to limited contact between the bridging liquid and the particles, reducing spherical agglomerate formation.
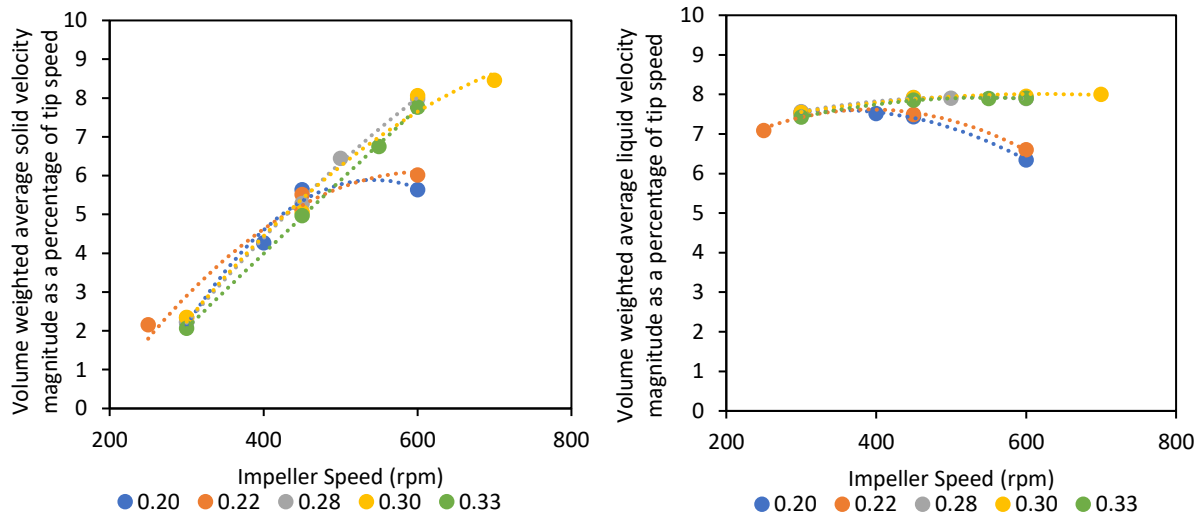
Figure 6-8 Propeller impeller volume weighted average solid (left) and liquid (right) velocity magnitude as a percentage of tip speed against impeller speed for various impeller clearance to tank diameter ratios used to develop velocity fitting parameters.

6.3.3 Velocity Fitting Curves for the Rushton Turbine Impeller

The fitting curves for the Rushton turbine impeller can be found in Figure 6-9 and the equations for the trendlines are given in Table 6-8. The graphs for the VWA solid and liquid velocity magnitude are very similar for the Rushton turbine impeller. These graphs show that a C/D of 0.33 gives the highest VWA velocity magnitude as a percentage of impeller tip speed. For all impeller speeds tested, the Rushton turbine at C/D of 0.33 gives between 35 % and 40 % of the impeller tip speed, with lower C/D values being between 5 % and 10 %. This can be due to a trend observed by Montante et al., 1999 and Zhu et al., 2019. In their work, it was observed that a Rushton turbine operating at C/D below 0.3 will form a single loop flow pattern. This pattern is produced by axial impellers. When C/D is greater than 0.3, the flow pattern is the double loop pattern that is associated with a radial impeller (Montante et al., 1999; Zhu et al., 2019).

The CFD contours for the Rushton turbine impeller, shown in Table 5-4 and Appendix B - Impeller Geometry CFD Analysis, show that there is a clear transition in the flow profile in the tank with a C/D ratio of 0.33. For ratios below this, the flow pattern follows a single loop pattern, with the maximum velocity in the tank being at the tip of the impeller blades. The contour for C/D of 0.33 has a different flow pattern. This pattern shows that the impeller tip speed is not the maximum speed observed for this impeller clearance. As the double loop flow pattern increases the power number and ,therefore, power consumption of the system, this will lead to an increase in the velocity of interactions between solid and liquid in the PBM (Ahmed et al., 2023). This will result in increased agglomeration.

133
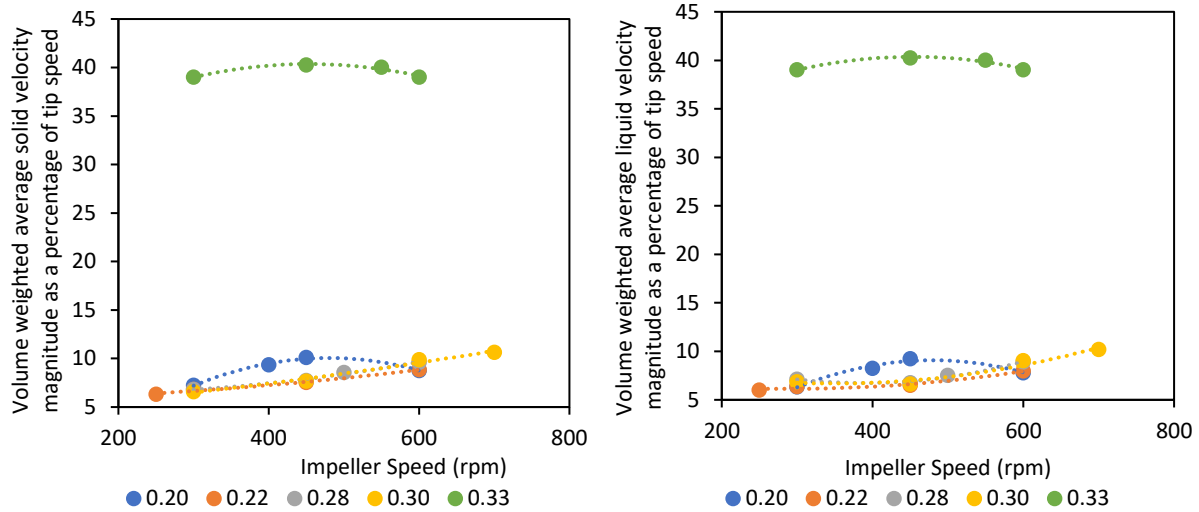
Figure 6-9 Rushton turbine impeller volume weighted average solid(left) and liquid (right) velocity magnitude as a percentage of tip speed against impeller speed for various impeller clearance to tank diameter ratios used to develop velocity fitting parameters.

6.3.4 Velocity Fitting Curves for the Pitched Blade Impeller

The fitting curves for the pitched blade impeller can be found in Figure 6-10 and the equations for the trendlines are given in Table 6-8. For a pitched blade impeller, the VWA solid velocity magnitude as a percentage of tip speed is below 5 %, with the VWA liquid velocity magnitude as a percentage of impeller tip speed being between 4 % and 9 %. The lowest values of VWA solid velocity magnitude as a percentage of impeller tip speed are with impeller speeds greater than 600 rpm and C/D values of 0.3 and 0.33. This could be due to a trend observed by Kresta and Wood, 1993, in which increasing the clearance for a pitched blade impeller increased the height of the flow pattern circulation loop. When C/D was 0.3 and above, this loop covers the full height of liquid in the tank. It may be that with the large circulation loop, the impeller speeds are insufficient to entrain particles in the full loop, leading to particle velocities much lower than the critical velocity, resulting in particle settling (Sharma and Shaikh, 2003).
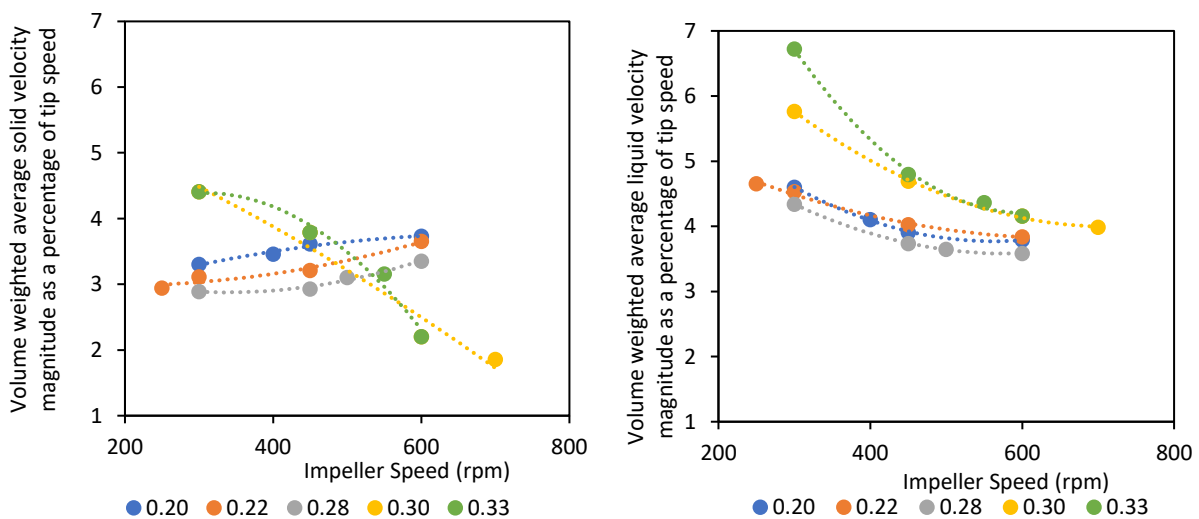
Figure 6-10 Pitched blade impeller volume weighted average solid(left) and liquid (right) velocity magnitude as a percentage of tip speed against impeller speed for various impeller clearance to tank diameter ratios used to develop velocity fitting parameters.

134

Table 6-8 Fitting equations from the graphs in Figure 6-7 to Figure 6-10

Impeller Geometry	C/D	Solid Fitting Equation	Solid R^2	Liquid Fitting Equation	Liquid R^2
Flat Blade	0.2	$y = -7E\text{-}05x^2 + 0.0603x + 26.93$	0.961	$y = -4E\text{-}05x^2 + 0.0389x + 31.263$	0.990
	0.22	$y = -1E\text{-}07x^2 + 8E\text{-}05x + 39.05$	0.986	$y = -2E\text{-}07x^2 + 0.0001x + 39.047$	0.968
	0.28	$y = 0.0002x^2 - 0.1431x + 67.71$	0.999	$y = -1E\text{-}04x^2 - 0.0882x + 56.666$	0.993
	0.3	$y = -1E\text{-}04x^2 + 0.096x - 15.66$	0.946	$y = -1E\text{-}05x^2 + 0.019x + 3.6335$	0.966
	0.33	$y = -0.0001x^2 + 0.1291x - 22.99$	0.999	$y = -2E\text{-}05x^2 + 0.019x + 4.3938$	0.963
Propeller	0.2	$y = -6E\text{-}05x^2 + 0.069x - 12.85$	0.974	$y = -2E\text{-}05x^2 + 0.0143x + 5.07$	0.997
	0.22	$y = -3E\text{-}05x^2 + 0.0401x - 6.18$	0.958	$y = -2E\text{-}05x^2 + 0.0186x + 3.98$	0.975
	0.28	$y = -1E\text{-}05x^2 + 0.0308x - 5.89$	0.999	$y = -7E\text{-}06x^2 + 0.0077x + 5.92$	0.986
	0.3	$y = -2E\text{-}05x^2 + 0.0361x - 6.78$	0.986	$y = -4E\text{-}06x^2 + 0.0055x + 6.30$	0.963
	0.33	$y = -2E\text{-}06x^2 + 0.0204x - 3.90$	0.999	$y = -8E\text{-}06x^2 + 0.0088x + 5.518$	0.995
Rushton Turbine	0.2	$y = -9E\text{-}05x^2 + 0.0849x - 10.30$	0.991	$y = -9E\text{-}05x^2 + 0.0832x - 10.87$	0.966
	0.22	$y = 7E\text{-}06x^2 + 0.0011x + 5.71$	0.991	$y = 2E\text{-}05x^2 - 0.0105x + 7.62$	0.959
	0.28	$y = 1E\text{-}05x^2 - 0.0039x + 6.622$	0.989	$y = 5E\text{-}05x^2 - 0.0379x + 14.08$	0.978
	0.3	$y = 5E\text{-}06x^2 + 0.0057x + 4.34$	0.983	$y = 3E\text{-}05x^2 - 0.0213x + 10.42$	0.956
	0.33	$y = -6E\text{-}05x^2 + 0.0521x + 28.53$	0.951	$y = -6E\text{-}05x^2 + 0.0521x + 28.53$	0.951
Pitched Blade	0.2	$y = -3E\text{-}06x^2 + 0.0041x + 2.32$	0.969	$y = 1E\text{-}05x^2 - 0.0136x + 7.60$	0.999
	0.22	$y = 4E\text{-}06x^2 - 0.0014x + 3.10$	0.959	$y = 5E\text{-}06x^2 - 0.0067x + 6.05$	0.992
	0.28	$y = 7E\text{-}06x^2 - 0.0048x + 3.68$	0.976	$y = 1E\text{-}05x^2 - 0.0113x + 6.84$	0.999
	0.3	$y = -3E\text{-}06x^2 - 0.0041x + 5.96$	0.964	$y = 1E\text{-}05x^2 - 0.0147x + 9.2353$	0.999
	0.33	$y = -2E\text{-}05x^2 + 0.0149x + 2.10$	0.977	$y = 3E\text{-}05x^2 - 0.0329x + 14.134$	0.997

6.3.5   Incorporating the Influence of Clearance in the PBM

In the model, FOR loops were used to allow specific equations to be calculated for the individual impellers, with a series of IF statements inside these FOR loops being used for the clearance based velocity fits. The clearance to vessel diameter ratio (C/D) is given as a range in the IF statements. A range was used to allow the model to be applied to values other than the specific C/D values that were tested as part of this work. The C/D ranges are shown in Table 6-9. The ranges were chosen based on how much the clearance influenced the sphericity and size of the agglomerates from the results in Chapter 5.

Table 6-9 Clearance to diameter ranges used for velocity fitting parameter IF statements in the PBM

Tested C/D	C/D Range
0.20	C/D<0.21
0.22	0.21<C/D<0.26
0.27	0.26<C/D<0.29
0.30	0.29<C/D<0.31
0.33	C/D>0.31

Figure 6-11 shows the code for a flat blade impeller. These equations are shown in Section 6.2.2, with the velocity fit parameters taken from Table 6-8. The common equations shown in Table 6-2 are outside of the FOR loop as they will be calculated for all impellers. The same format was used for the other impeller geometries with their respective equations from Section 6.2 and Table 6-8. The full code for the agglomeration and layering kernels can be found in Appendix C - PBM Construction and Validation.

```
255 FOR i := 1 TO Flat_Blade  DO
256 CT=(((1.96*(Capital_X)^1.19)^(-7.8))+(0.25^(-7.8)))^(-1/7.8);
257 m=(((0.71*(Capital_X)^0.373)^(-7.8))+(0.333^(-7.8)))^(-1/7.8);
258 Small_x=((4.5*((Baffle_Width/Vessel_Diameter)*(Number_of_Baffles^(0.8))))/(Fully_Baffled_Power_Number^(0.2)))+(Unbaffled_Power_Number/Fully_Baffled_Power_Number);
259 Thetar=(Blade_Pitch*pi)/180;
260 IF (Number_of_Blades^0.7)*(Impeller_Blade_Height/Impeller_Diameter)<=0.54 THEN
261 Fully_Baffled_Power_Number=10*((Number_of_Blades^0.7)*(Impeller_Blade_Height/Impeller_Diameter))^1.3;
262 ELSE IF (Number_of_Blades^0.7)*(Impeller_Blade_Height/Impeller_Diameter)>0.54 AND (Number_of_Blades^0.7)*(Impeller_Blade_Height/Impeller_Diameter)<=1.6 THEN
263 Fully_Baffled_Power_Number=8.3*((Number_of_Blades^0.7)*(Impeller_Blade_Height/Impeller_Diameter));
264 ELSE
265 Fully_Baffled_Power_Number=10*((Number_of_Blades^0.7)*(Impeller_Blade_Height/Impeller_Diameter))^0.6;
266 END
267 END
268 IF Clearance_Diameter_Ratio<0.21  THEN
269     Particle_Velocity_Fit=( (-7E-05*(Impeller_Speed^2))+(0.0603*Impeller_Speed)+26.93)/100;
270     Liquid_Velocity_Fit= ((-4E-05*(Impeller_Speed^2))+(0.0389*Impeller_Speed)+31.263)/100;
271     ELSE IF Clearance_Diameter_Ratio>0.21 AND Clearance_Diameter_Ratio<0.26 THEN
272     Particle_Velocity_Fit=((-1e-07*(Impeller_Speed^2))+(8e-05*Impeller_Speed)+39.05)/100;
273     Liquid_Velocity_Fit=((-2e-07*(Impeller_Speed^2))+(0.0001*Impeller_Speed)+39.047)/100;
274     ELSE IF Clearance_Diameter_Ratio>0.26 AND Clearance_Diameter_Ratio <0.29 THEN
275     Particle_Velocity_Fit=((0.0002*(Impeller_Speed^2))-(0.1431*Impeller_Speed)+67.706)/100;
276     Liquid_Velocity_Fit=((-1e-04*(Impeller_Speed^2))-(0.0882*Impeller_Speed)+56.666)/100;
277     ELSE IF Clearance_Diameter_Ratio>0.29 AND Clearance_Diameter_Ratio<0.32 THEN
278     Particle_Velocity_Fit=((-1e-04*(Impeller_Speed^2))+(0.096*Impeller_Speed)-15.659)/100;
279     Liquid_Velocity_Fit=((-1e-05*(Impeller_Speed^2))+(0.019*Impeller_Speed)+4.3938)/100;
280     ELSE
281     Particle_Velocity_Fit=((-0.0001*(Impeller_Speed^2))+(0.1291*Impeller_Speed)-22.986)/100;
282     Liquid_Velocity_Fit=   ((-2e-05*(Impeller_Speed^2))+(0.019*Impeller_Speed)+4.3938)/100;
283     END
284     END
285     END
286     END
287 END
```

Figure 6-11 Equations used to calculate the velocity fits, and the power number for the flat-blade impeller. The full code can be seen in Appendix C - PBM Construction and Validation

To ensure the system accurately predicts spherical agglomeration, the material properties and equipment geometries must be specified in the model. The parameters were specified in the agglomeration tab and layering tab in the High Shear Granulator block on the flowsheet. Table 6-10 shows the user specified parameters needed for both the agglomeration and layering kernels.

In Table 6-10, the impeller geometry is only shown as a user specified parameter for the agglomeration kernel. As the impeller geometry does not change throughout the process of the simulation, the model has been designed to use the geometry specified in the agglomeration kernel for the layering kernel as well. The impeller geometry is selected from a dropdown list on the agglomeration tab (Figure 6-4).

Table 6-10 Parameters specified by the user in the agglomeration and layering kernels of the PBM

Agglomeration	Layering	Both
• Meeting Probability • Half-filling Angle (Betta) • Separation Distance • Minimum Value of BSR Range (BSRmin) • Maximum Value of BSR Range (BSRmax) • Agglomeration Efficiency	• Critical Packing Liquid Volume Fraction (Fecp) • Sphericity • Growth Coefficient (C_Growth)	• Solid Density • Bridging Liquid Density • Bridging Liquid Viscosity • Suspension Liquid Density • Suspension Liquid Viscosity • Interfacial Tension • Contact Angle (Tetta) • Impeller Geometry • Impeller Diameter • Suspension Volume • Impeller Speed • Impeller Clearance • Vessel Diameter • Number of Impeller Blades • Blade Pitch (Thetar) • Impeller Blade Height • Baffle Width • Liquid Depth • Number of Baffles • Impeller Geometry

As shown in Table 6-1, the global specifications were used to specify the number of grid points, and particle size range. For this system, a maximum particle size of 3500 μm was chosen. The standard grid configuration follows a $\sqrt{2}$ system from the initial particle size, which is 1 μm for this model. To meet this convention, the system was specified to have 30 grid points. This number of grid points covers the desired particle size and factors in leeway in case larger primary material is specified.

6.4 Summary of PBM Modification

The PBM by Ahmed et al., 2023 was modified by allowing the user to select the impeller geometry for the model. Each impeller has different equations to calculate the impeller power number, the power number is calculated using correlations developed by Furukawa et al., 2012. To include the impeller clearance, velocity fitting parameters were developed from the CFD results. These alterations to the PBM change

the calculations in both the agglomeration and layering kernel. Figure 6-12 summarises the influence of the PBM modifications on the velocity and separation force calculations in the PBM.

Agglomeration Kernel

$$u(S_i) = V_{PF}\left[\frac{(\rho_{agg} - \rho_{L1})^3}{200\rho_{L1}\mu_{L1}(2\rho_{agg} + \rho_{L1})}\right]^{1/2} S_i^{3/5}P^{2/5}$$

$$u(S_j) = V_{LF}\left[\frac{(\rho_{agg} - \rho_{L1})^3}{200\rho_{L1}\mu_{L1}(2\rho_{agg} + \rho_{L1})}\right]^{1/2} S_j^{3/5}P^{2/5}$$

$$f_{sep}(i,j,t) \approx \rho_{L1}\left[P(S_i + S_j)\right]^{2/3}S_i^2$$

High Shear Granulator

Layering Kernel

$$u(S_i) = V_{PF}\left[\frac{(\rho_{agg} - \rho_{L1})^3}{200\rho_{L1}\mu_{L1}(2\rho_{agg} + \rho_{L1})}\right]^{1/2} S_i^{3/5}P^{2/5}$$

$$u(S_j) = V_{LF}\left[\frac{(\rho_{agg} - \rho_{L1})^3}{200\rho_{L1}\mu_{L1}(2\rho_{agg} + \rho_{L1})}\right]^{1/2} S_j^{3/5}P^{2/5}$$
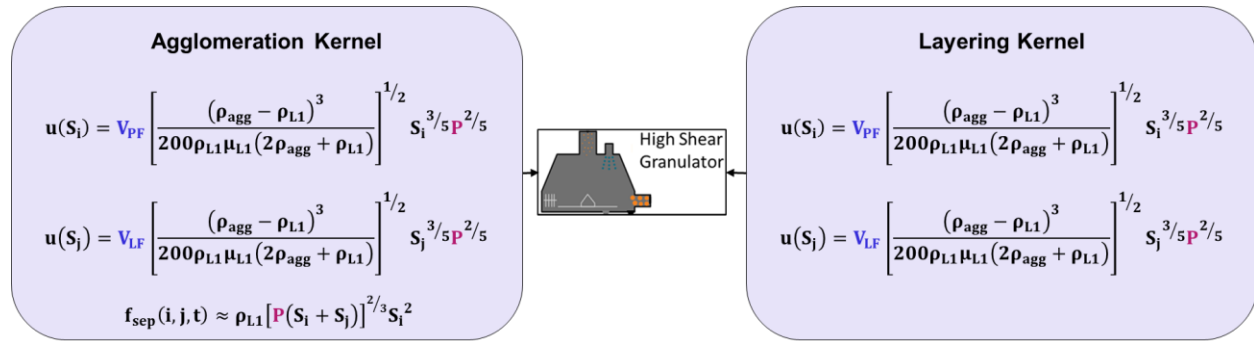
Figure 6-12 Diagram of modified equations and how they feed into the different custom kernels in the PBM for spherical agglomeration, blue terms show the inclusion of impeller clearance, red terms show the inclusion of impeller geometry

6.5   Preliminary PBM Evaluation

Preliminary simulations were performed to determine whether the power number calculations and clearance correlations influence the PSD from the PBM. Table 6-11 summarises these simulations.

Table 6-11 Methodology of preliminary simulations to investigate the incorporation of flow characteristics into the PBM. The specified speeds and clearances will be tested for the different impeller geometries

Impeller Geometry	Impeller Speed (rpm)	Impeller Clearance (mm)
Flat Blade Impeller, Propeller Impeller, Rushton Turbine Impeller, Pitched Blade Impeller	450	40
	600	15
	1000	25
	700	29
	1000	40
	200	40
	100	10
	800	45
	800	20
	100	30
	100	24

These simulations assumed a 40 μm PMMA primary particle with a toluene bridging liquid and a BSR of 0.5. The impeller speeds and clearances in Table 6-11 were also tested for the flat blade impeller without baffles to determine how well this is incorporated into the PBM.

6.6   Results of the Preliminary Simulations

The results of the preliminary simulations for the four impeller geometries are shown in Figure 6-13. This figure also shows the results of the different impeller speeds from the model developed by Ahmed et al., 2023. This model did not allow for the impeller geometry and clearance to be selected, so these results were obtained by changing the impeller speed to the values specified in Table 6-11. The preliminary

simulation results show that changing the impeller speed and clearance have an effect on the d_{43} of the PBM.

When a flat blade impeller is used, the d_{43} decreases as the clearance is increased for most simulations at the same impeller speed. The preliminary simulations tested three clearances at an impeller speed of 100 rpm. As the clearance was increased from 10 mm to 24 mm, the d_{43} increased from 585 µm to 683 µm; this then decreased to 487 µm with a clearance of 30 mm. The clearance of 10 mm may have been too low to generate a circulation loop that would reach the top of the tank, limiting the contact between the bridging liquid and particles. At increased impeller speeds of 800 rpm and 1000 rpm, the d_{43} decreased with increasing clearance. At 800 rpm the d_{43} decreased from 918 µm to 818 µm with an increase in clearance from 20 mm to 45 mm. When the impeller speed was 1000 rpm the d_{43} decreased from 976 µm to 730 µm with a clearance increase from 25 mm to 40 mm. The decrease in d_{43} at higher clearances could be due to the flat blade impeller demonstrating improved particle suspension at lower clearances (Devarajulu and Loganathan, 2016). Improved particle suspension will lead to greater contact between the bridging liquid and particles, leading to larger agglomerates forming, and fewer fines in the system.

There are fluctuations in the PBM d_{43} when a propeller impeller is used. However, these are less pronounced than with a flat blade impeller. There is not much difference between the values of d_{43} when the impeller speed is increased from 100 rpm to 200 rpm. For the three clearances tested at 100 rpm, the d_{43} was 483 µm. At an impeller speed of 200 rpm, the d_{43} is 484 µm. At higher impeller speeds, increasing the clearance will lead to a greater value of d_{43}. This can be seen for the results at both 800 rpm and 1000 rpm, with 1000 rpm providing a larger difference in d_{43} than at 800 rpm. For an impeller speed of 1000 rpm and a clearance of 25 mm the d_{43} was 492 µm, and this increased to 553 µm when the clearance was increased to 40 mm. This may be due to increased impeller clearance leading to the flow circulation loop covering a larger volume of the fluid in the tank, resulting in increased particle suspension at higher impeller speeds and clearance (Kresta and Wood, 1993). This increased particle suspension will lead to more contact between the bridging liquid and solid particles, resulting in more agglomerates forming.

The PBM results for the Rushton turbine impeller show that the d_{43} with this impeller is influenced by impeller speed and clearance. At impeller speeds of 800 rpm and under, increasing the impeller clearance leads to an increase in the value of d_{43}. At an impeller speed of 100 rpm, there is a 10 µm increase in d_{43} as the impeller clearance increases from 10 mm and 24 mm. With a further increase in clearance to 30 mm, the d_{43} increases by 100 µm to 598 µm. This rapid increase can be due to a trend observed by Montante et al., 1999 and Zhu et al., 2019. In that work, it was observed that increasing the impeller clearance to diameter (C/D) ratio to 0.3 leads to the flow pattern of a Rushton turbine impeller changing from a single loop, or axial, flow pattern to the double loop flow pattern that is expected from a radial impeller (Montante et al., 1999; Zhu et al., 2019). Although this double loop flow pattern is thought to be less efficient at particle suspension, it does lead to increased power consumption in the system. In the PBM, the power consumption is used to calculate the velocity of interactions of particles and fluid. Increasing these velocities will lead to increased agglomeration in the system.

A pitched blade impeller shows minor fluctuations in the d_{43} at different impeller speeds and clearances compared to the other impellers that were tested. This impeller has the most consistent values of d_{43} for most impeller speeds and clearances tested, with values for simulations of impeller speeds 600 rpm and below being between 482 µm and 484.4 µm. At higher impeller speeds it can be seen that increased impeller speeds lead to an increase in the value of d_{43}. At an impeller speed of 1000 rpm, the d_{43} is 494

μm with a clearance of 25 mm. When the clearance increased to 40 mm, the d_{43} also increased to 523 μm. This increase can be due to a trend observed by Kresta and Wood, 1993. This work observed that increasing the impeller clearance with an axial impeller, the flow pattern reached higher levels in the tank, with a C/D of 0.3 covering the full height of the tank (Kresta and Wood, 1993). The increased circulation of particles will lead to more contact between the bridging liquid and particles, resulting in larger agglomerates.

The d_{43} from the PBM by Ahmed et al., 2023 at different impeller speeds can also be seen in Figure 6-13. This PBM does not include impeller geometry or clearance so the results at different clearances are consistent for the same impeller speeds. The results from Ahmed et al., 2023 are higher than the results for the other impellers, except when a flat blade impeller is used at a speed of 1000 rpm and a clearance of 25 mm. This suggests that including the impeller geometry and clearance in the model will lead to increased accuracy of the model predictions.
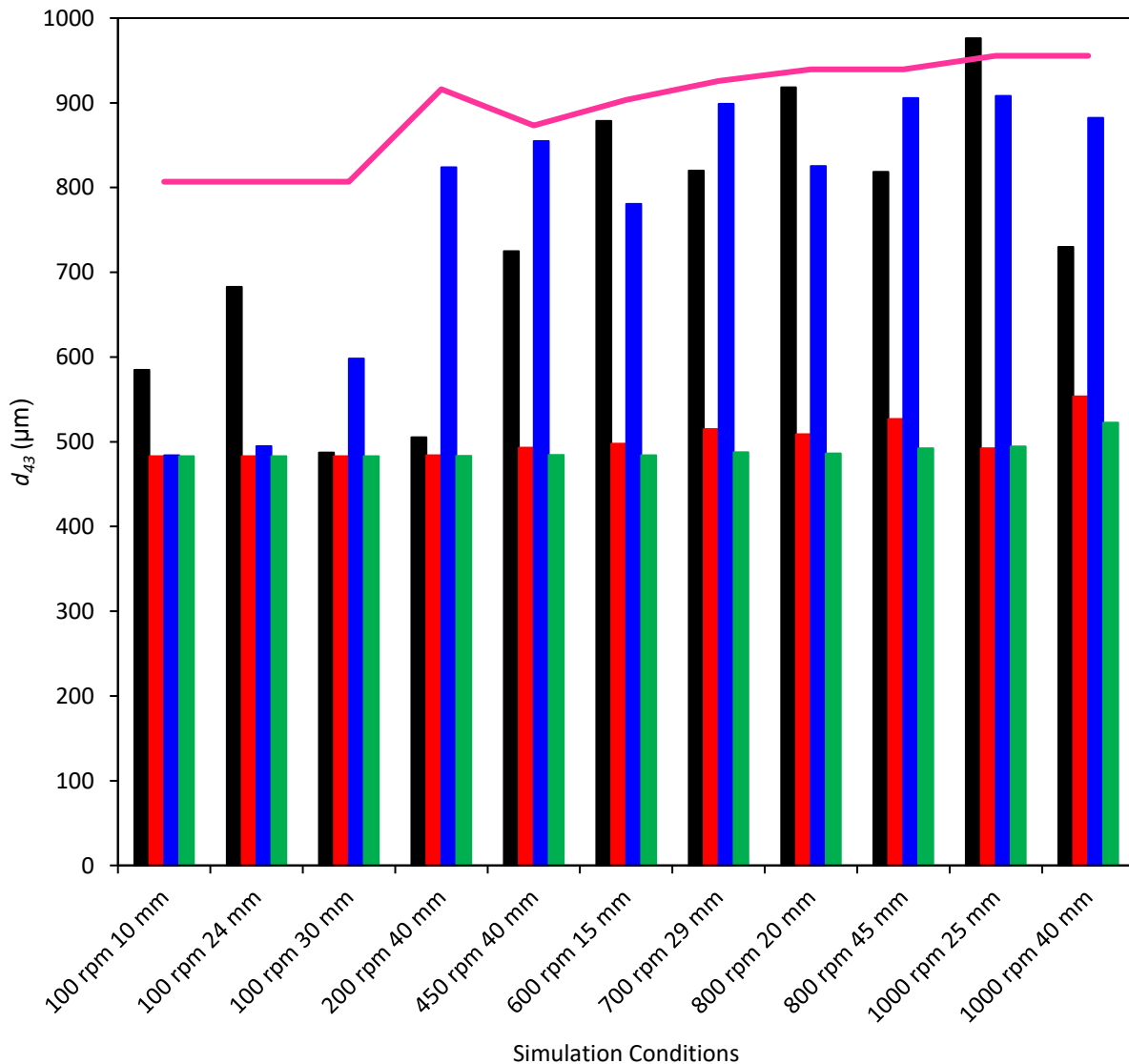
Figure 6-13 Results of the preliminary simulations with the different impellers, and from the model by Ahmed et al., 2023

From Figure 6-14 it can be seen that the influence of having baffles in a stirred tank system is reflected in the PBM. For the conditions simulated with the flat blade impeller at an impeller speed of 450 rpm and above, there is a clear difference between the results for a baffled and unbaffled stirred tank. The PBM results suggest that the d_{43} of the system will be higher if the stirred tank is baffled. It has been shown in many studies of stirred tanks, that baffling in the system reduces vortex formation and improves mixing efficiency. Having baffles in the tank will improve agglomeration as it will improve the contact between bridging liquid and particles. The PBM results with the power number incorporated accurately reflects the expected behaviour of a spherical agglomeration process with and without baffles.

The unbaffled results follow a similar trend that at high impeller speeds, increased impeller clearance will reduce the value of d_{43} from the PBM. This is expected with a flat blade impeller as it has been shown in work by Devarajulu and Loganathan, 2016 that increased impeller clearance is less effective at particle suspension for a flat blade impeller. Reduced particle suspension in the spherical agglomeration process will limit contact between the bridging liquid and particles, reducing the formation of agglomerates.
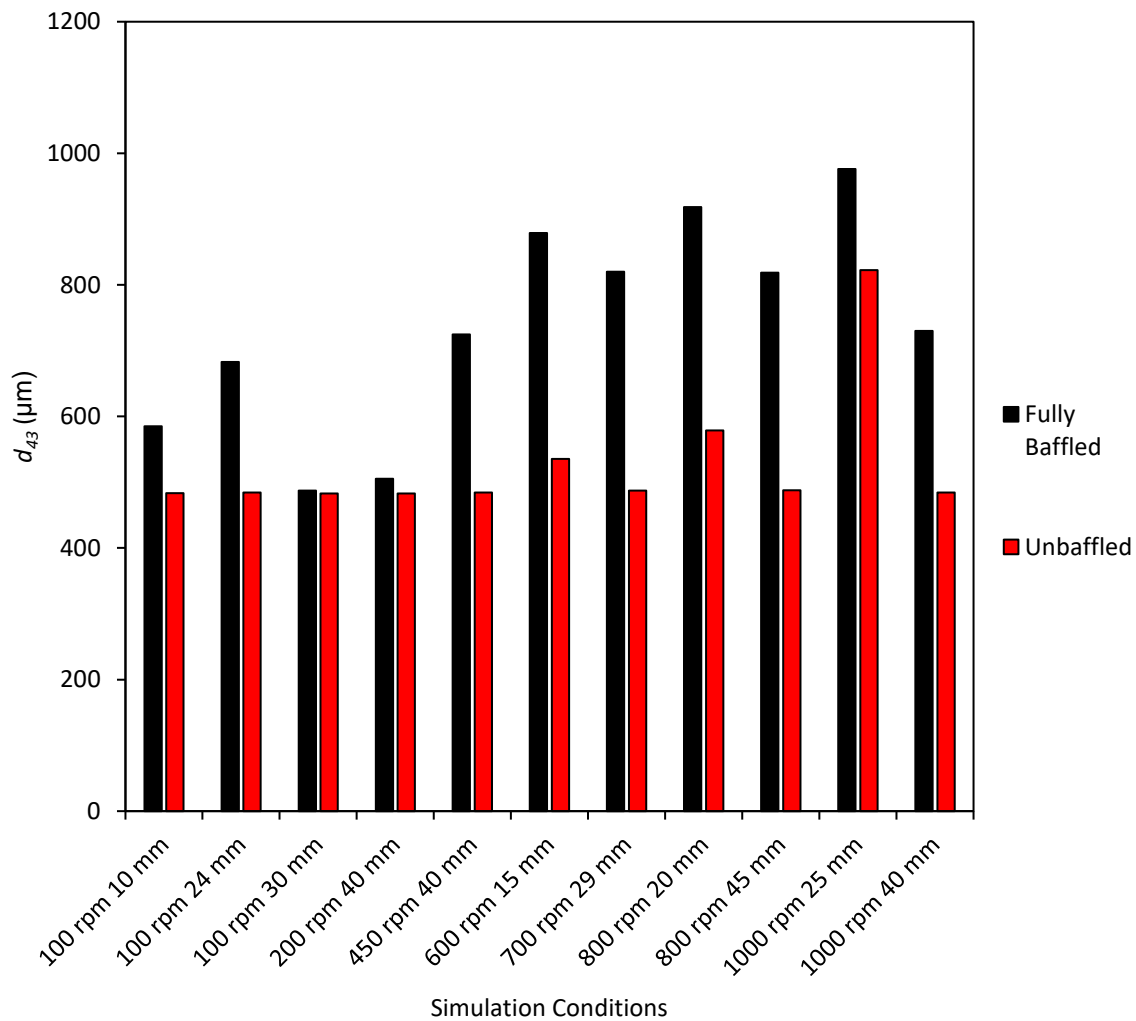
Figure 6-14 Fully baffled and unbaffled d_{43} from the PBM with a flat blade impeller

6.7 Conclusions

As the experimental study in Chapter 4 demonstrated, the impeller geometry and clearance have significant influence on the formation of spherical agglomerates. Therefore, they need to be considered in a population balance model for spherical agglomeration. In this work, the PBM by Ahmed et al., 2023 was modified to incorporate impeller geometry and clearance based on findings from the experimental study and the CFD simulations.

Impeller power number correlations by Furukawa et al., 2012 were used to incorporate the impeller geometry. The preliminary simulations show that the different impeller geometries produce different values of d_{43}, showing that the impeller geometry is considered in the model. The Rushton turbine and flat blade impellers produce larger d_{43} values than the pitched blade and propeller impellers. In the experimental study, it was found that the Rushton turbine and flat blade impeller produced more consistently sized agglomerates with increased sphericity than the pitched blade and propeller impeller. This suggests that including the power number correlations as a way to incorporate impeller geometry will increase the accuracy of the PBM against experimental data.

The impeller clearance was also incorporated into the PBM by using velocity fitting parameters that were developed from the CFD simulation results. From the preliminary simulations, the clearance does influence the d_{43} predicted by the PBM. As the velocity fitting parameters are different for each impeller geometry, the d_{43} shows different levels of variation for each impeller. The Rushton turbine and flat blade impeller show more of a change in d_{43} with clearance at all speeds, whereas the pitched blade impeller and propeller impeller show variation at impeller speeds of 800 rpm and above.

Another advantage of using the impeller power number correlations by Furukawa et al., 2012 is that they enable the number of baffles in the system to be altered. The preliminary simulation results in this chapter show that including baffles in the system increases the agglomerate d_{43}. Increased agglomerate size is expected as baffles reduce vortex formation in stirred tanks, improving mixing efficiency.

From the preliminary simulations in Section 6.6, it appears that results of the PBM with the impeller geometry and clearance accurately reflect the expected behaviour of different impeller configurations. This suggests that the impeller power number correlations by Furukawa et al., 2012 and the velocity fitting parameters from the CFD simulations are an effective way of incorporating impeller geometry and clearance into the PBM for spherical agglomeration.

To determine the accuracy of the model predictions, the model results need to be compared to an experimental study. Chapter 7 shows the results of experiments and simulations that were performed to validate the model. There were three stages of experimental validation considered for Chapter 7. To determine the effectiveness of incorporating power number and impeller clearance into the model, this model will be used to simulate the same 60 experimental conditions outlined in Section 3.3. The PBM was also used to model the experiments outlined in Section 3.4. These experiments tested the accuracy of the model against multiple investigation parameters including primary particle size, BSR and agglomeration time. PBM simulations were also performed that correspond to experiments completed by Lian, 2020 as part of a MEng research project. Full details of these experiments are given in Section 7.4. This work was at a 300 mL scale and investigated the influence of multiple parameters, including type of bridging liquid, BSR and agitation time, on the formation of PMMA spherical agglomerates (Lian, 2020). Table 6-12 shows the model validation simulations that were performed.

Table 6-12 Simulations performed to compare to the results of validation experiments

Impeller Geometry	Impeller Speed (rpm)	Impeller Clearance (mm)	Primary Particle Size (µm)	Primary Particle Mass (g)	Solution Volume (mL)	Bridging Liquid	BSR	Agitation Time (min)
50 mm Flat Blade	300	18	52	18	600	Toluene	0.5	45
50 mm Flat Blade	300	20	52	18	600	Toluene	0.5	45
50 mm Flat Blade	300	25	52	18	600	Toluene	0.5	45
50 mm Flat Blade	300	27	52	18	600	Toluene	0.5	45
50 mm Flat Blade	300	30	52	18	600	Toluene	0.5	45
50 mm Flat Blade	450	18	52	18	600	Toluene	0.5	45
50 mm Flat Blade	450	20	52	18	600	Toluene	0.5	45
50 mm Flat Blade	450	25	52	18	600	Toluene	0.5	45
50 mm Flat Blade	450	27	52	18	600	Toluene	0.5	45
50 mm Flat Blade	450	30	52	18	600	Toluene	0.5	45
50 mm Flat Blade	600	18	52	18	600	Toluene	0.5	45
50 mm Flat Blade	600	20	52	18	600	Toluene	0.5	45
50 mm Flat Blade	600	25	52	18	600	Toluene	0.5	45
50 mm Flat Blade	600	27	52	18	600	Toluene	0.5	45
50 mm Flat Blade	600	30	52	18	600	Toluene	0.5	45
50 mm Propeller	300	18	52	18	600	Toluene	0.5	45
50 mm Propeller	300	20	52	18	600	Toluene	0.5	45
50 mm Propeller	300	25	52	18	600	Toluene	0.5	45
50 mm Propeller	300	27	52	18	600	Toluene	0.5	45
50 mm Propeller	300	30	52	18	600	Toluene	0.5	45
50 mm Propeller	450	18	52	18	600	Toluene	0.5	45
50 mm Propeller	450	20	52	18	600	Toluene	0.5	45
50 mm Propeller	450	25	52	18	600	Toluene	0.5	45
50 mm Propeller	450	27	52	18	600	Toluene	0.5	45
50 mm Propeller	450	30	52	18	600	Toluene	0.5	45
50 mm Propeller	600	18	52	18	600	Toluene	0.5	45
50 mm Propeller	600	20	52	18	600	Toluene	0.5	45
50 mm Propeller	600	25	52	18	600	Toluene	0.5	45
50 mm Propeller	600	27	52	18	600	Toluene	0.5	45

50 mm Propeller	600	30	52	18	600	Toluene	0.5	45
50 mm Rushton Turbine	300	18	52	18	600	Toluene	0.5	45
50 mm Rushton Turbine	300	20	52	18	600	Toluene	0.5	45
50 mm Rushton Turbine	300	25	52	18	600	Toluene	0.5	45
50 mm Rushton Turbine	300	27	52	18	600	Toluene	0.5	45
50 mm Rushton Turbine	300	30	52	18	600	Toluene	0.5	45
50 mm Rushton Turbine	450	18	52	18	600	Toluene	0.5	45
50 mm Rushton Turbine	450	20	52	18	600	Toluene	0.5	45
50 mm Rushton Turbine	450	25	52	18	600	Toluene	0.5	45
50 mm Rushton Turbine	450	27	52	18	600	Toluene	0.5	45
50 mm Rushton Turbine	450	30	52	18	600	Toluene	0.5	45
50 mm Rushton Turbine	600	18	52	18	600	Toluene	0.5	45
50 mm Rushton Turbine	600	20	52	18	600	Toluene	0.5	45
50 mm Rushton Turbine	600	25	52	18	600	Toluene	0.5	45
50 mm Rushton Turbine	600	27	52	18	600	Toluene	0.5	45
50 mm Rushton Turbine	600	30	52	18	600	Toluene	0.5	45
50 mm Pitched Blade	300	18	52	18	600	Toluene	0.5	45
50 mm Pitched Blade	300	20	52	18	600	Toluene	0.5	45
50 mm Pitched Blade	300	25	52	18	600	Toluene	0.5	45
50 mm Pitched Blade	300	27	52	18	600	Toluene	0.5	45
50 mm Pitched Blade	300	30	52	18	600	Toluene	0.5	45
50 mm Pitched Blade	450	18	52	18	600	Toluene	0.5	45
50 mm Pitched Blade	450	20	52	18	600	Toluene	0.5	45
50 mm Pitched Blade	450	25	52	18	600	Toluene	0.5	45
50 mm Pitched Blade	450	27	52	18	600	Toluene	0.5	45
50 mm Pitched Blade	450	30	52	18	600	Toluene	0.5	45
50 mm Pitched Blade	600	18	52	18	600	Toluene	0.5	45
50 mm Pitched Blade	600	20	52	18	600	Toluene	0.5	45
50 mm Pitched Blade	600	25	52	18	600	Toluene	0.5	45
50 mm Pitched Blade	600	27	52	18	600	Toluene	0.5	45
50 mm Pitched Blade	600	30	52	18	600	Toluene	0.5	45
50 mm Rushton Turbine	600	25	52	18	600	Toluene	0.5	45
50 mm Rushton Turbine	600	25	20	18	600	Toluene	0.5	45

50 mm Rushton Turbine	600	25	20	18	600	Toluene	0.5	90
50 mm Propeller	600	25	20	18	600	Toluene	0.5	45
50 mm Propeller	600	18	20	18	600	Toluene	0.5	45
50 mm Propeller	600	25	20	18	600	Toluene	0.5	90
50 mm Rushton Turbine	600	18	20	18	600	Toluene	0.5	45
50 mm Rushton Turbine	600	25	52	18	600	Toluene	0.5	90
30 mm Rushton Turbine	600	25	52	18	600	Toluene	0.5	45
50 mm Rushton Turbine	600	25	52	18	600	Toluene	0.64	45
50 mm Rushton Turbine	600	25	20	18	600	Toluene	0.64	45
50 mm Rushton Turbine	600	25	52	18	600	Toluene	0.38	45
50 mm Rushton Turbine	600	25	20	18	600	Toluene	0.38	45
50 mm Rushton Turbine	600	25	20	18	600	Toluene	0.77	45
50 mm Rushton Turbine	600	25	52	18	600	Toluene	0.77	45
50 mm Rushton Turbine	1000	25	52	24	600	Toluene	0.5	30
30 mm Rushton Turbine	1000	0.15	52	12	300	Isopropyl Acetate	0.5	30
30 mm Rushton Turbine	1000	0.15	52	12	300	n-butyl Acetate	0.5	30
30 mm Rushton Turbine	1000	0.15	52	12	300	Toluene	0.5	30
30 mm Rushton Turbine	1000	0.15	52	12	300	Toluene	0.6	30
30 mm Rushton Turbine	1000	0.15	52	15	300	Toluene	0.5	30
30 mm Rushton Turbine	500	0.15	52	12	300	Toluene	0.5	30
30 mm Rushton Turbine	1000	0.15	52	12	300	Toluene	0.5	45
30 mm Rushton Turbine	1000	0.15	52	12	300	Kerosene	0.5	30

Chapter 7 Experimental Validation of Spherical Agglomeration PBM

7.1 Introduction

To ensure that the PBM accurately predicts spherical agglomeration, experiments were performed to determine the accuracy of the model. The PBM generated results for the same spherical agglomeration setup as the experiments and the results are compared. Comparing the results of the PBM generated in this work with results from the PBM by Ahmed et al., 2023, allows for the determination of the success at incorporating flow characteristics into a spherical agglomeration PBM.

There are three experimental systems used to validate the model. The PBM will simulate the conditions of the experiments to investigate the influence of impeller geometry on spherical agglomeration. Section 3.3 discusses the experimental methodology, with the results in Chapter 4. As the impeller geometry experiments informed the development of the PBM, two other experimental systems were tested. For further model validation, additional experiments were performed with both 52 μm and 20 μm PMMA beads that were suspended in distilled water with a toluene bridging liquid, as discussed in Section 3.4. These experiments tested the accuracy of the PBM predictions of PSD for different primary particle sizes, BSR, agitation time and impeller diameter. The third validation system used results obtained by Guo Jung Lian to validate the system. Using the results from Lian, 2020 will allow for analysis of how well the model predicts spherical agglomeration with various bridging liquids. This system volume was 300 mL (Lian, 2020). As the other validation experiments in this work were conducted at a 600 mL volume, this could give an insight into the accuracy of the model at different scales.

7.2 Influence of Impeller Geometry Results

To determine the effectiveness of including the power number and impeller clearance in the PBM, the model was used to simulate the 60 experimental conditions detailed in Section 3.3. The d_{43} was used as the comparison point between the experimental and PBM results. Sections 7.2.1 to 7.2.4 show the d_{43} results of the PBM with flow that was developed in this work, for various impeller geometries, clearances and speeds. These results are compared to the PBM produced by Ahmed et al., 2023 to determine whether including the impeller geometry has improved the prediction of the PBM. Section 7.2.5 summarises the experimental validation findings.

7.2.1 Flat Blade Impeller

The d_{43} values obtained by the PBM developed in this work to include flow, the experimental studies and the PBM by Ahmed et al., 2023 for the flat blade impeller at different clearances and speeds is shown in Figure 7-1. The PBM by Ahmed et al., 2023 gives constant d_{43} at each speed as the model does not consider the impeller clearance.

For the flat blade impeller at 300 rpm (Figure 7-1a), the d_{43} predicted by the model developed in this work was closer to experimental results than the PBM by Ahmed et al., 2023 for clearances of 20 mm, 25 mm and 27 mm. These agglomerates produced at these clearances at 300 rpm were more spherical in shape (Figure 4-5) and had fewer fines in the PSD than the other clearances (Figure 4-2).

For an impeller speed of 450 rpm (Figure 7-1b), the PBM with flow suggests that the clearance has limited influence on the d_{43} of the system as it ranges between 816 μm and 872 μm. The experimental results, however, show a clear influence of the clearance, with the d_{43} decreasing as the clearance increases to 25 mm, with an increase from 27 mm to 30 mm. This pattern is different than the velocity profiles obtained

from the CFD simulations that can be seen in Section 5.3.1. Due to the PBM with flow developed in this work following the CFD velocity profiles rather than the experimental PSD profile, the PBM by Ahmed et al., 2023 is a closer to the experimental values. The percentage difference between experimental data and the two PBMs evaluated in this section are shown in Appendix C - PBM Construction and Validation.

As Figure 7-1c shows, at an impeller speed of 600 rpm and clearances of 25 mm and above, the PBM that was developed in this work to include flow is better than the model by Ahmed et al., 2023 for predicting the d_{43}. From the agglomerate images in Figure 4-4, the 25 mm and 30 mm are consistently spherical, with the majority of them being between 500 µm and 800 µm in size. For these conditions, the PBM with flow is an over prediction for d_{43}. This may be due to the increased impeller speed, increasing the shear in the system which leads to more consolidation of the agglomerates. Increased consolidation would reduce the average particle size. The percentage difference between the d_{43} for the experimental results and the PBM with flow at a speed of 600 rpm and a clearance of 27 mm is under 0.4 %.
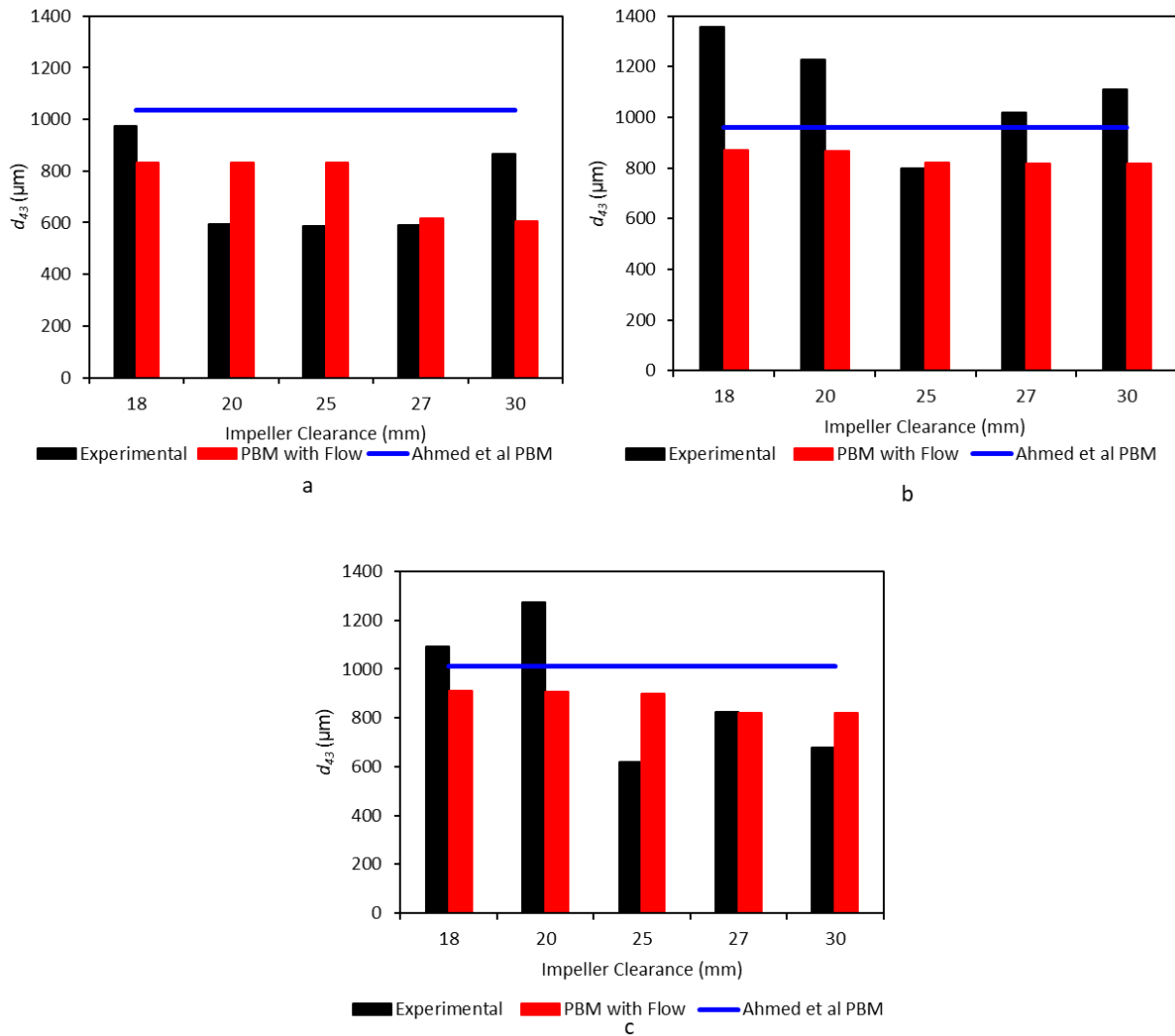
Figure 7-1 Average particle size (d_{43}) from the experimental study, PBM with flow and PBM by Ahmed et al., 2023 for agglomerates produced using the flat blade impeller at different clearances and impeller speeds. (a – 300 rpm, b – 450 rpm, c – 600 rpm)

147

7.2.2 Propeller Impeller

In Chapter 4, it was determined that the propeller impeller was the least successful impeller geometry for producing spherical agglomerates of consistent size and sphericity. This was due to the experimental products having a large portion of fine material, with some very large agglomerates. The d_{43} from the experimental study, the PBM with flow and the PBM by Ahmed et al., 2023 for a propeller impeller at different impeller speeds and clearances can be seen in Figure 7-2.

For the propeller at 300 rpm (Figure 7-2a), the PBM with flow is closer to experimental results than the PBM by Ahmed et al., 2023 for clearances of 18 mm, 27 mm and 30 mm. The agglomerate images, in Figure 4-10, show that these impeller clearances have a large portion of fine powder, but still produce some agglomerates within the desired size range. Clearances of 20 mm and 25 mm produce a few agglomerates that are very large which will skew the d_{43}. The increased d_{43} means that the PBM developed by Ahmed et al., 2023 being closer than the PBM developed in this work for these clearances. This can be seen in Figure 7-2a.

The d_{43} for the propeller impeller at 450 rpm from the experimental study, PBM with flow and the PBM by Ahmed et al., 2023 is shown in Figure 7-2b. The PBM with flow is a more accurate prediction for agglomerates produced at clearances of 18 mm, 25 mm and 27 mm. From the agglomerate images in Figure 4-10, the agglomerates formed at these conditions are a mix of particle sizes. This is also shown in the agglomerate PSD in Figure 4-8. The agglomerates formed at 20 mm and 30 mm with a speed of 450 rpm (Figure 7-2b) have a much larger d_{43}, meaning the results of these experiments are closer to the PBM by Ahmed et al., 2023. From Figure 4-8, the PSD for the 20 mm clearance has 4 distinct peaks, suggesting inefficient mixing and consolidation in the system. The PSD for the agglomerates formed at 30 mm shows two distinct peaks, one below 250 μm, and one at approximately 1250 μm. This broad range of peak sizes suggest inefficient mixing. From the agglomerate images in Figure 4-10, the clearance of 27 mm and 450 rpm gave the most consistent agglomerates, this condition is accurately predicted by the PBM with flow.

Figure 7-2c shows that with an impeller speed of 600 rpm the PBM with flow is a close prediction to the experimental data for clearances of 18 mm, 20 mm and 27 mm. From the agglomerate PSD in Figure 4-9, it can be seen that for the clearances of 18 mm and 20 mm, the PSD has a peak approximately 550 μm. This peak is within the desired range of agglomerates. The 27 mm PSD has a peak over 1000 μm, but also has the largest portion of fines in the system for agglomerates produced at 600 rpm with the propeller impeller. This broad range will result in an average particle size close to the predicted values. From Figure 7-2c, the PBM by Ahmed et al., 2023 is closer to the experimental results for clearances of 25 mm and 30 mm. In Figure 4-10, it can be seen that at a clearance of 30 mm, there are very large agglomerates formed skewing the results. The clearance of 25 mm produces agglomerates with consistent shape and sphericity, however, they are very large with the PSD showing a peak over 1000 μm (Figure 4-9).

As the impeller speed is increased, the range of the d_{43} predicted by the PBM with flow also increases. At 300 rpm the d_{43} ranges from 487.1 μm to 487.6 μm. A larger range is observed at 450 rpm, with the d_{43} ranging from 495.5 μm to 497.9 μm. A broader range from 503.2 μm to 514.5 μm is observed at an impeller speed of 600 rpm. This limited change is expected as the power number calculations do not consider the impeller clearance, and at 300 rpm, the propeller velocity fits (Figure 6-8) are consistent in value. Although the velocity fit profiles are close for all values, there is a larger difference between the

VWA velocity magnitude as percentage of tip speed for both solid and liquid as the impeller speed is increased.

For the propeller impeller, the developed model is closer to the experimental values of d_{43} than the PBM by Ahmed et al., 2023 for 9 of the 15 simulations. The impeller conditions that result in a d_{43} closer to the Ahmed et al., 2023 PBM are when there are agglomerates that are much larger than the desired size range due to inefficient mixing, hindering agglomeration. Appendix C - PBM Construction and Validation shows the percentage difference between the experimental d_{43}, and the d_{43} that is predicted by the PBM developed in this work and the PBM by Ahmed et al., 2023.
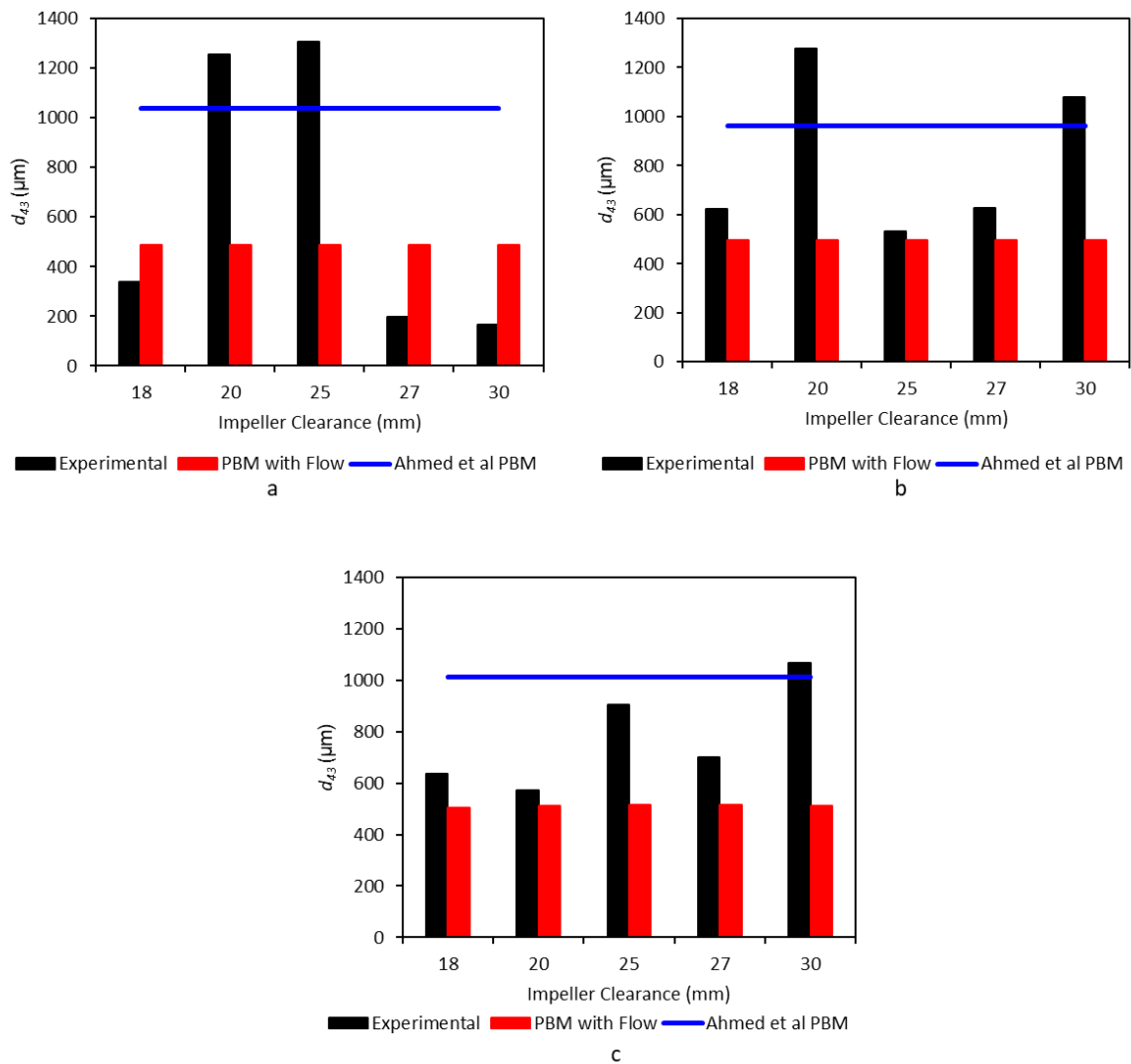
Figure 7-2 Average particle size (d_{43}) from the experimental study, PBM with flow and PBM by Ahmed et al., 2023 for agglomerates produced using the propeller impeller at different clearances and impeller speeds. (a – 300 rpm, b – 450 rpm, c – 600 rpm)

7.2.3 Rushton Turbine Impeller

Figure 7-3 shows the average particle size from the experimental study, the PBM with flow that was developed in this work, and the PBM by Ahmed et al., 2023 for spherical agglomerates produced with the Rushton turbine at various impeller speeds and clearances.

Figure 7-3a shows that with a Rushton turbine at 300 rpm, the PBM with flow reflects the experimental trend as the d_{43} increases with clearance, but the largest increase is between the clearances of 27 mm and 30 mm. With a clearance of 30 mm, the d_{43} from the PBM with flow is, however, a large underprediction for the experimental results. This may be due to the low impeller speed limiting shear in the system, reducing consolidation. The PBM with flow can be improved by incorporating the shear forces in the system that influence agglomeration. At the lower impeller speed of 300 rpm, the PBM by Ahmed et al., 2023 is a better prediction for clearances of 20 mm to 30 mm. However, the difference between the PBM with flow and the PBM by Ahmed et al., 2023 is very close for clearances of 20 mm, 25 mm and 27 mm. From Figure 4-11 it can be seen that the PSD for the Rushton turbine at 18 mm clearance and 300 rpm speed produces a large peak at approximately 550 µm, suggesting that this the best impeller clearance for the low speed. The agglomerate images in Figure 4-14 show that these agglomerates are less spherical than those at increased speeds.

With an impeller speed of 450 rpm (Figure 7-3b), all of the experimental d_{43} values are lower than the d_{43} proposed by Ahmed et al., 2023. From Figure 4-15, the agglomerates produced at this speed have improved sphericity compared to agglomerates at 300 rpm and are visibly larger than those produced by a Rushton turbine at 600 rpm. As Figure 7-3b shows, for all impeller clearances other than 25 mm, the d_{43} predicted by the PBM with flow is closer to the experimental d_{43} than the PBM by Ahmed et al., 2023. In the PSD shown in Figure 4-13, it can be seen that this condition produces a very large peak that is greater than 1000 µm. This shows that the agglomerates formed at this condition are very large. Clearances of 27 mm and 30 mm also have PSD peaks greater than 1000 µm, but they do have a greater portion of fines in the system, which would lower the d_{43}.

As Figure 7-3c shows, at an impeller speed of 600 rpm, the experimental and PBM with flow values are close, with this model providing an improved prediction from the PBM developed by Ahmed et al., 2023 for all impeller clearances. In Figure 4-15, it can be seen that agglomerates produced by a Rushton turbine at 600 rpm are relatively consistent in size and sphericity for all clearances. The least spherical agglomerates at this speed is for a clearance of 27 mm. Here, the agglomerates at this clearance appear less spherical and consistent in size. The percentage difference between experimental results and both PBMs investigated in this section can be seen in Appendix C - PBM Construction and Validation.
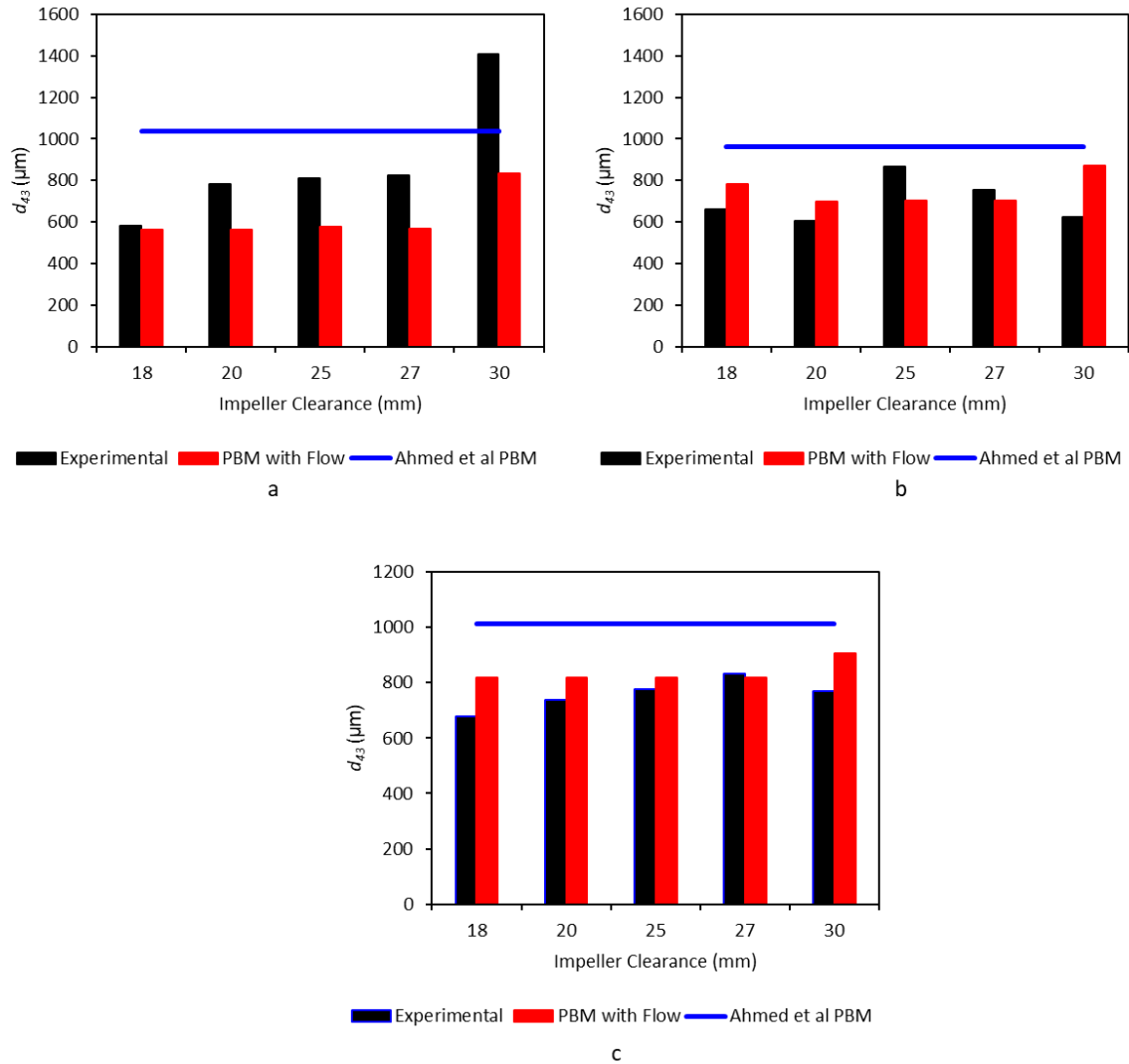
Figure 7-3 Average particle (d_{43}) size from the experimental study, PBM with flow and PBM by Ahmed et al., 2023 for agglomerates produced using the Rushton turbine impeller at different clearances and impeller speeds. (a – 300 rpm, b – 450 rpm, c – 600 rpm)

7.2.4   Pitched Blade Impeller

Figure 7-4 shows the d_{43} from the experimental study, the PBM with flow that includes flow and the PBM by Ahmed et al., 2023 for agglomerates produced with a pitched blade impeller at various impeller speeds and clearances.

The d_{43} from PBM with flow for the pitched blade impeller does not vary much with impeller speed and clearance, the lowest d_{43} is 483.3 µm at an impeller speed of 300 rpm (Figure 7-4a). The maximum d_{43} for this impeller geometry is 486.5 µm at an impeller speed of 600 rpm (Figure 7-4c). This limited increase is due to low variation in the calculated power number for a pitched blade impeller. The correlations by Furukawa et al., 2012 use the sin function on the blade pitch divided by reactor dimensions, and the results of some of these calculations are very close to 0. At an impeller clearance of 25 mm, the power number for a pitched blade impeller is 0.0215 for all impeller speeds. This is much lower than the expected power number of 1.5 that is commonly reported in literature (Grenville et al., 2017). The consistently low

151

value of power number for this impeller will result in low velocity of solid and liquid interactions, limiting the likelihood of successful agglomerations in the PBM. The power number being much lower than anticipated explains why the PBM with flow often results in underpredictions of d_{43} for the pitched blade impeller.

As Figure 7-4b and Figure 7-4c show, the PBM with flow underpredicts all experimental data at impeller speeds of 450 rpm and 600 rpm. The underpredictions are due to the limited variation in the d_{43} from the PBM with flow across all impeller speeds. Therefore, the PBM by Ahmed et al., 2023 is closer to the experimental results for 8 of the 15 simulations. Both the PBM with flow d_{43} and the PBM by Ahmed et al., 2023 d_{43} do not vary with clearance, therefore they are both inaccurate for the pitched blade impeller. Appendix C - PBM Construction and Validation shows the percentage difference between experimental results and both PBMs investigated in this section.
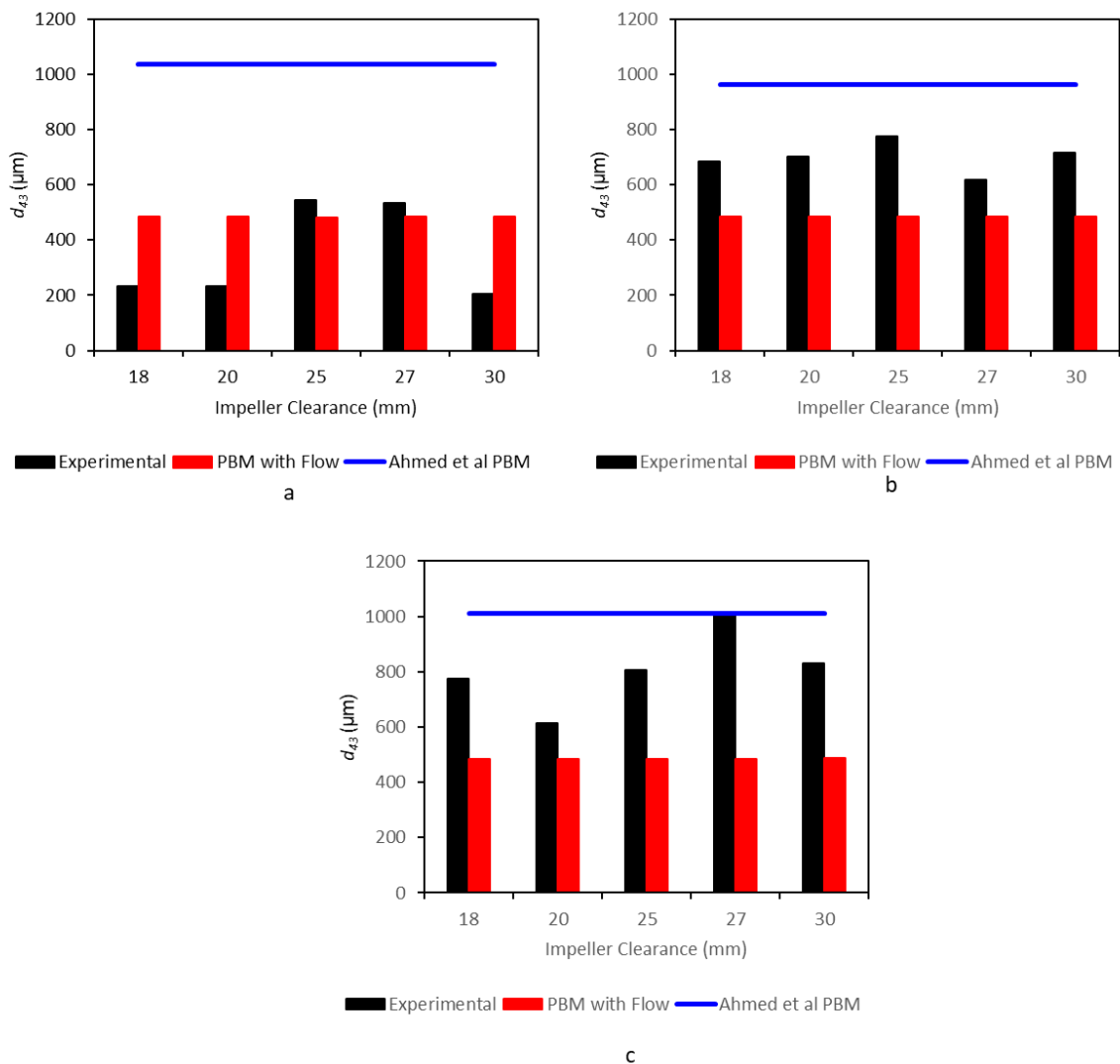
Figure 7-4 Average particle (d_{43}) size from the experimental study, PBM with flow and PBM by Ahmed et al., 2023 for agglomerates produced using the pitched blade impeller at different clearances and impeller speeds. (a – 300 rpm, b – 450 rpm, c – 600 rpm)

7.2.5   Evaluation of the PBM with flow at Predicting the Influence of Impeller Geometry

The comparison between the PBM with flow and experimental results show that there are definite discrepancies between the PBM predictions and experimental d_{43}. As there was little variation in the predictions of d_{43} for both the PBM with flow that was developed in this work, and the PBM by Ahmed et al., 2023 for the pitched blade impeller, both PBMs are considered ineffective for this impeller geometry. Therefore, the validation of the PBM will consider the results of the flat blade impeller, propeller impeller and Rushton turbine impeller. The PBM developed in this work was closer to the experimental data for 60 % of the 45 simulations than the PBM by Ahmed et al., 2023. This suggests that the PBM developed in this work has increased prediction accuracy when compared to the PBM by Ahmed et al., 2023, but further improvements need to be made.

One parameter that may limit the effectiveness of the PBM with flow at predicting spherical agglomeration is the growth coefficient. For all simulations, this was set at a value of 0.69 as this had been established in previous work as an acceptable value for the PMMA, toluene system. The value of growth coefficient may need changing with each impeller geometry and clearance to increase the effectiveness of the PBM with flow at predicting spherical agglomeration. Currently, the growth coefficient is found through experiments (Ahmed et al., 2023). It would be useful to develop correlations to predict the growth coefficient, reducing the number of experiments required to use the PBM.

Another reason for differences between the PBM and experiments is that the PBM assumes a consistent size of the bridging liquid droplets. The simulation procedure states that the bridging liquid is added as droplets that are 500 μm in diameter. This is difficult to ensure in an experimental setting as the droplets may break up in the stirred tank. In the PBM, the bridging liquid droplets are much larger than the primary particle size. Therefore, the PBM will assume that spherical agglomeration follows the immersion mechanism, with coalescence occurring when agglomerates are greater than the bridging liquid droplet size. It is assumed that experiments are also following the immersion mechanism due to the large droplets leaving the pipette and the small primary particle size, but it is difficult to confirm this.

It is also extremely important to increase the accuracy of predictions of d_{43} when using a pitched blade impeller. The calculated value of power number for this impeller using the correlations by Furukawa et al. were much lower than literature values. To ensure that this was not an issue with how the equations were implemented in gPROMS, calculations of these correlations were also performed in MATLAB and Microsoft Excel, and the same value of 0.0215 was obtained, these calculations can be seen in Appendix C. Therefore, improvements need to be made to the pitched blade power number correlations in order for them to be accurate in the PBM.

7.3   Further Validation Experiments

The experiments used for validation in Section 7.2 were also used for the development of the PBM. To determine the accuracy of the PBM at predicting agglomerate properties, further experiments were performed. These experiments used the Rushton turbine impeller and the propeller impeller as they were determined in Chapter 4 to be the most and least efficient impellers for spherical agglomeration respectively.

In the following sections, the experiments detailed in Section 3.4 were performed, these allowed for an understanding of how accurate the model is at predicting the influence of primary particle size, BSR,

agitation time and impeller diameter. These parameters were investigated as they had been determined to influence spherical agglomeration in Section 2.4.

7.3.1   Influence of Primary Particle Size

Figure 7-5 shows the average particle size for spherical agglomerates produced using 20 µm PMMA beads with both a Rushton turbine and propeller impeller. The PBM with flow is an overprediction for the experimental d_{43} when a Rushton turbine is used, but it underpredicts for the propeller impeller.

The PBM predicting larger agglomerates with a Rushton turbine than a propeller is due to the Rushton turbine having a much higher power number than the propeller impeller. For a clearance of 25 mm, the PBM calculated power number is 4.76 for a Rushton turbine and 0.094 for a propeller impeller. In the PBM, increased power number will lead to increased collision velocity and increased adhesive forces between particles, resulting in more agglomerate formation (Blandin et al., 2005; Ahmed et al., 2023).

As a result of inefficient mixing in the system, a large d_{43} was observed for the propeller impeller. The inefficient mixing in the system would result in the bridging liquid not circulating the full tank, limiting the number of particles that contact the bridging liquid, leading to very large agglomerates. Due to the low power number, there is limited shearing in the system which reduces consolidation of the agglomerates (Dogon and Golombok, 2015).

Due to the underprediction of the PBM with flow for the propeller impeller, the PBM by Ahmed et al., 2023 is much closer to the experimental result than the PBM developed as part of this work. The PBM by Ahmed et al., 2023 is, however, not as close as the PBM with flow for the Rushton turbine impeller.

During the experiments with 20 µm particles, it appeared as though there were fewer particles entrained in the flow, with more of them being pushed towards the tank wall. The CFD simulations that were used for model construction considered monosized particles of 500 µm; this is much larger than a 20 µm particle size. It would be useful to run CFD simulations with smaller particle sizes to determine whether these particles undergo different velocity profiles than the larger particles.

In Figure 7-6, the average particle size for spherical agglomerates produced using 52 μm primary particles with both a Rushton turbine and propeller impeller at a clearance of 25 mm and speed of 600 rpm can be seen. This figure also shows the d_{43} predicted by both the PBM developed in this work and the PBM by Ahmed et al., 2023.

As with the d_{43} for 20 μm particles, the PBM overpredicts for the Rushton turbine impeller, and underpredicts for the propeller impeller. The PBM with flow results for the 52 μm PMMA beads are much closer to the experimental results than they were when 20 μm PMMA beads were used.

The Rushton impeller gives larger agglomerates than the propeller impeller both experimentally and from the PBM with flow. This is due to the Rushton turbine having a greater power number than the propeller impeller. Increased power number will result in greater velocities of the interactions between the solid particles and the bridging liquid, resulting in more agglomeration.
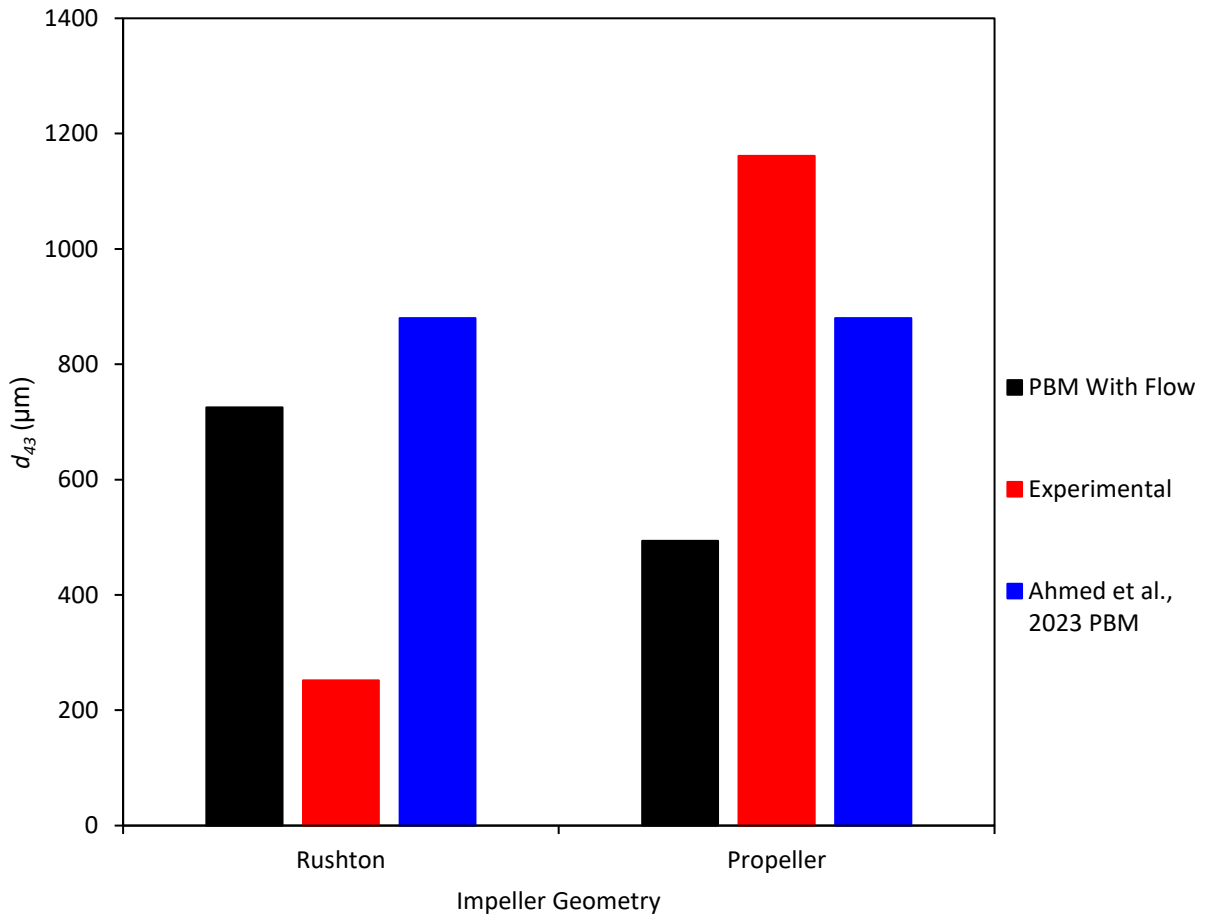
Figure 7-6 Average particle size (d_{43}) from PBM with flow, experimental investigation and the PBM by Ahmed et al., 2023 for agglomerates produced using 52 μm PMMA beads with different impellers

From both Figure 7-5 and Figure 7-6, it is clear that primary particle size does alter the results of both the PBM with flow and the PBM by Ahmed et al., 2023. For a primary particle size of 20 μm, neither of the

models are accurate at predicting the d_{43} of the experimental agglomerates for both the Rushton turbine and propeller impeller. The PBM with flow is more accurate at predicting the d_{43} with a primary particle size of 52 µm, with a 5 % overprediction for the Rushton turbine, and a 16 % underprediction for the propeller.

Another reason for discrepancies between the simulation and experimental data is that the simulations were performed with the same growth coefficient. From the results in Section 7.2, the impeller geometry appears to influence the growth coefficient. The growth coefficient of 0.69 was determined for the particle size of 52 µm. The smaller particle size of 20 µm may have a different growth coefficient due to the different contact angle between the PMMA beads and the toluene bridging liquid.

In the simulation construction, the different values of contact angle between toluene and PMMA were used for the different particle sizes; these values van be seen in Table 3-2. Changing the contact angle for the different particle sizes was done as the contact angle is an indicator of how well the bridging liquid wets the particles, with a lower contact angle suggesting better agglomeration. The contact angle for 52 µm beads was lower than that for 20 µm beads. Altering the contact angle may not be sufficient to increase the model accuracy due to PMMA swelling upon contact with toluene (Papanu et al., 2003; Doumenc et al., 2008; Vayer et al., 2017). The swelling behaviour may influence the agglomeration of the particles and, therefore, would need to be considered for further development of the model.

7.3.2   Influence of BSR

Figure 7-7 shows the average particle size from both experimental studies and simulations using the PBM with flow at different values of BSR. A range from 0.38 to 0.77 of BSR was investigated to determine whether the PBM could be used for predicting the optimal BSR, reducing the need for as many preliminary experiments when designing a spherical agglomeration process.

For particle sizes of 20 µm, the PBM with flow overpredicts the d_{43} at all values of BSR tested. These overpredictions have been apparent for all simulations with an initial particle size of 20 µm and are thought to be due to the growth coefficient in the PBM being for a particle size of 52 µm. The velocity fits from the CFD simulations were also developed with much larger particles so the PBM with flow may not be able to accurately predict the suspension behaviour of the small particles.

With a primary particle size of 52 µm, the PBM is an accurate prediction for d_{43} with a BSR of 0.5. This is the condition that was used to determine the growth coefficient in the model, so it is expected that it would be an accurate representation of the model conditions. At a lower BSR of 0.38, the PBM with flow is an overprediction of the experimental d_{43}. This may be that the growth coefficient is set too high for this BSR.

At BSRs of 0.64 and above, the experimental results show very large agglomerates, suggesting that these values of BSR are too high to produce spherical agglomerates within the desired size range. The model d_{43} does increase with increased BSR values, but it is much lower than the experimental values. From these results, it appears that the PBM does not accurately consider the influence of BSR. This is an extremely important parameter that needs to be carefully considered by the PBM.

The experimental results at a BSR of 0.77 for the 52 µm PMMA beads shows a decrease in d_{43} compared to the BSR of 0.64. This decrease is due to the increased level of paste formation with a BSR of 0.77 limiting

the product that could undergo sieve analysis. With the increased BSR, the beads formed a paste and stuck to both the impeller and the tank walls; this can be seen in Figure 7-8.
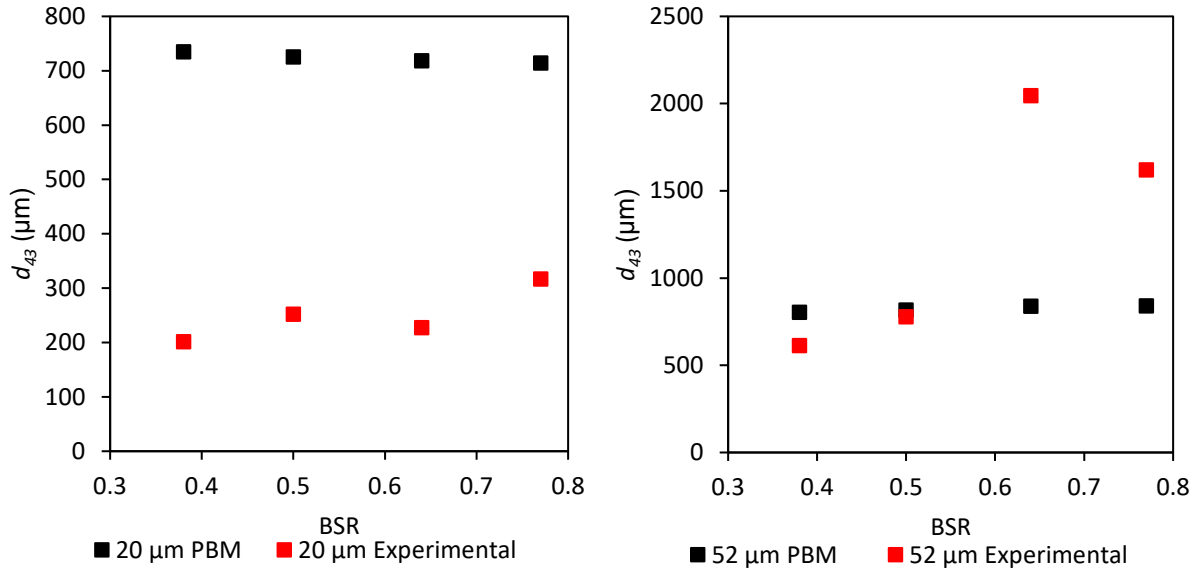
Figure 7-7 Average particle size (d_{43}) from the PBM with flow and experimental studies for different BSR values for agglomerates produced using primary particles of both 20 µm (left) and 52 µm (right)

Figure 7-8 Image of the paste in the reactor and on the impeller when a BSR of 0.77 was used with 52 µm PMMA beads

7.3.3 Influence of Agitation Time

Figure 7-9 shows the d_{43} value obtained at different agitation times for both a Rushton turbine and a propeller impeller. The d_{43} values are from both experimental results and the PBM with flow. The initial

particle size for these experiments was 20 μm and, therefore, they have limited success with spherical agglomerate formation.

For 20 μm particles, the increased agitation time with a propeller impeller reduces the d_{43} experimentally but increases it in the PBM with flow. The reduced experimental size is due to consolidation resulting in more consistently sized agglomerates, rather than a few very large agglomerates after 45 minutes. This can be seen in Figure 7-10.

As Figure 7-9 shows, the PBM predicts an increase in d_{43} for the Rushton turbine agglomerates as residence time increases. This also happens with the experimental d_{43}. However, the experimental d_{43} is much lower than the PBM d_{43}, potentially due to the incorrect growth coefficient being used for 20 μm particles. At 90 minutes, the values of the experimental and PBM d_{43} are close for the propeller impeller.
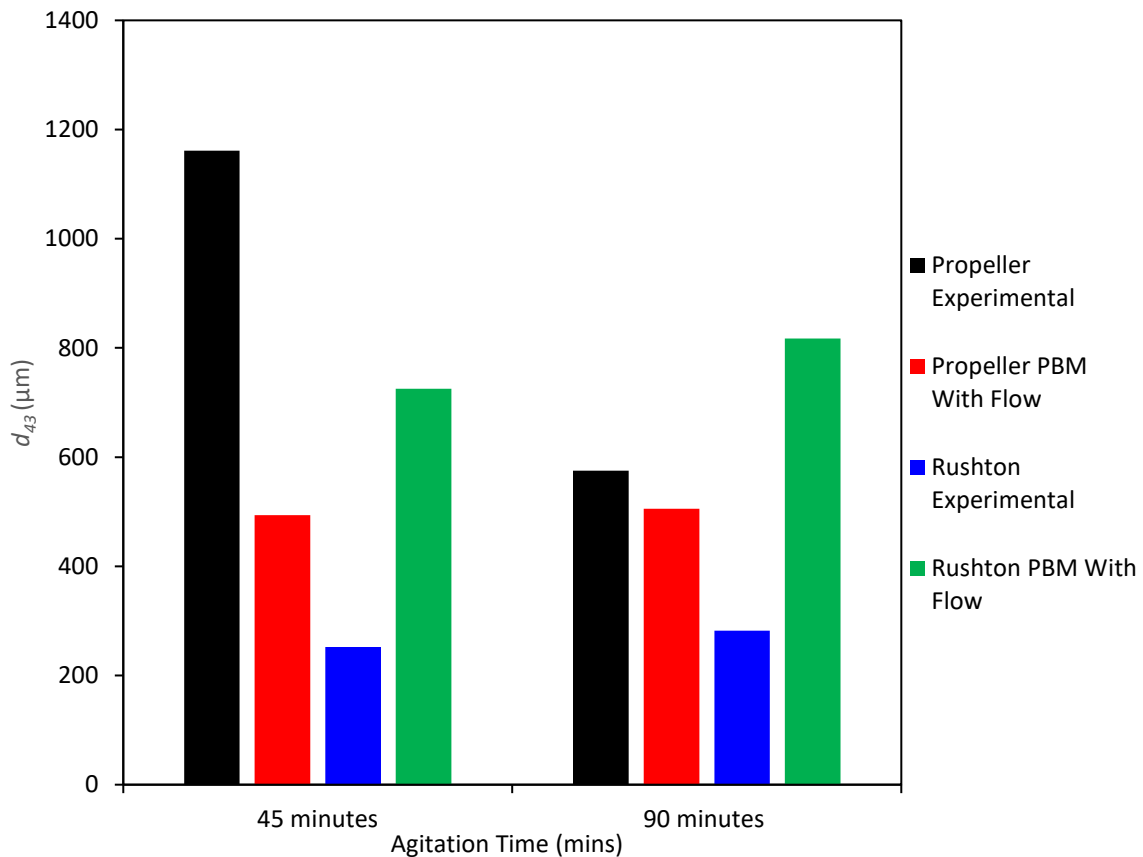
Figure 7-9 Average particle size (d_{43}) from the PBM with flow and experimental studies for spherical agglomerates produced with a Rushton turbine or propeller impeller at agitation times of 45 minutes or 90 minutes with primary material of 20 μm

In Figure 7-10, there is very little change between the agglomerate images for the Rushton turbine at 45 minutes and at 90 minutes. This is consistent with the d_{43} value for this impeller as there is little variation as the agitation time increases. The agglomerate images for the propeller impeller are very different. At 45 minutes, the image shows a very large agglomerate and some much smaller agglomerates. The image at 90 minutes show smaller agglomerates that are much more consistent in size. The propeller agglomerates at 90 minutes look similar to those formed by the Rushton turbine at 45 minutes, suggesting

that increased agitation time with a propeller induces enough shear on the system that it is comparable to the shear of a Rushton turbine with a much shorter agitation time.
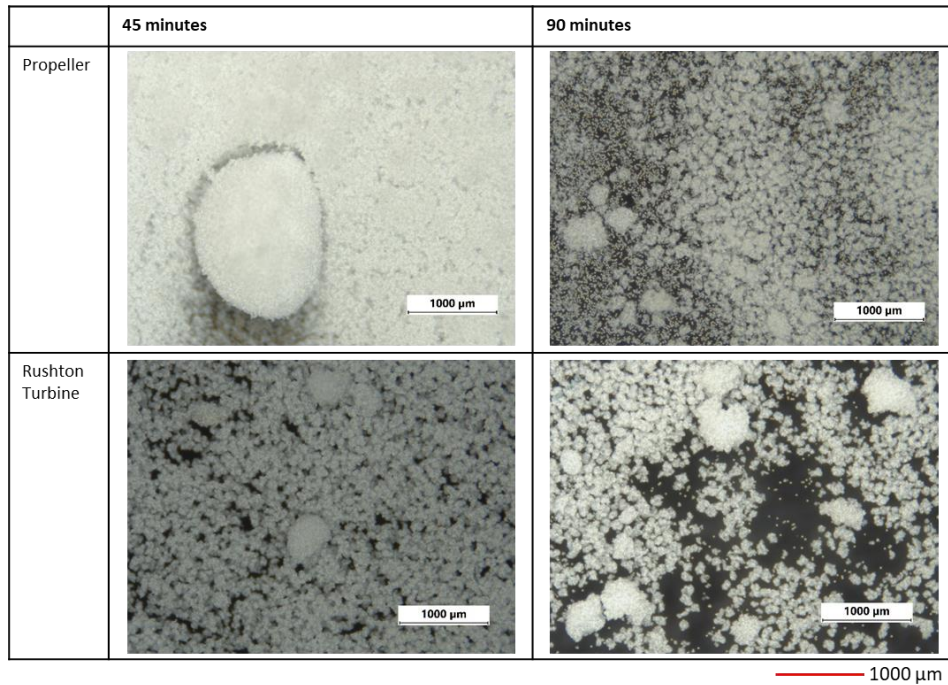
Figure 7-10 Images of agglomerates formed using 20 μm PMMA beads with a Rushton turbine or propeller impeller at 45 minute and 90 minute agitation time, scale bar is 1000 μm

Figure 7-11 shows the d_{43} for agglomerates produced at different agitations times using a Rushton turbine impeller and 52 μm PMMA beads. The PBM prediction is accurate for an agitation time of 45 minutes. However, it only predicts a slight increase in d_{43} at 90 minutes whereas the experimental d_{43} is almost double the d_{43} at 45 minutes. This suggests that the PBM assumes agglomeration finishes too early.
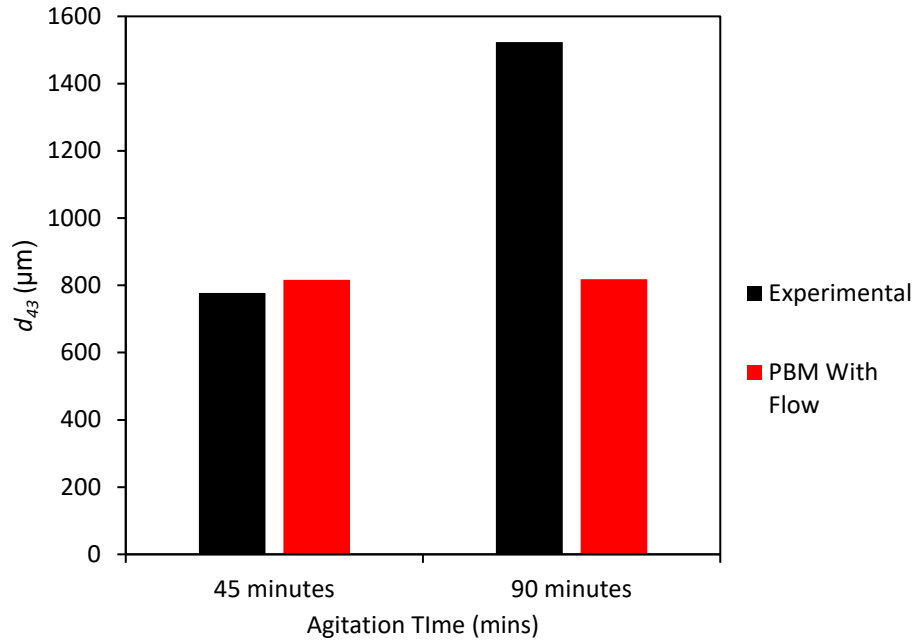
Figure 7-11 Average particle size (d_{43}) from experimental data and PBM with flow of agglomerates formed using a Rushton turbine impeller at different agitation times

The agglomerates formed at 45 minutes and 90 minutes can be seen in Figure 7-12. These images show that the agglomerates at 90 minutes are much larger and more consistently spherical than the ones formed at 45 minutes. The longer agitation time will increase consolidation in the system, resulting in dense agglomerates that are spherical in shape.
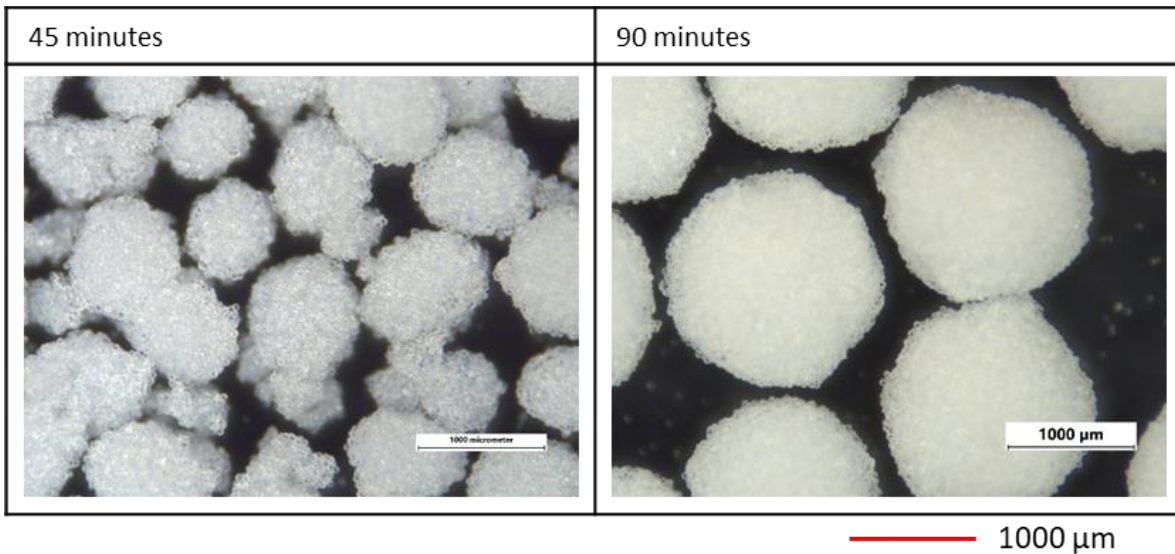
Figure 7-12 Images of agglomerates formed from 52 μm PMMA beads with a Rushton turbine at different agitation times, scale bar is 1000 μm

7.3.4   Influence of Impeller Diameter

Figure 7-13 shows the d_{43} of agglomerates produced using a 3 mm diameter Rushton turbine or a 5 mm diameter Rushton turbine. The results show the experimental d_{43} as well as the predicted d_{43} from the PBM developed in this work and the PBM by Ahmed et al., 2023.

Both PBMs predict that the impeller diameter does influence the d_{43} of the agglomerates, with an increased diameter leading to a larger d_{43}. The model developed in this work has a closer d_{43} to the experimental value than the PBM developed by Ahmed et al., 2023. However, both models are a significant overestimation in d_{43} for the 3 mm Rushton turbine. As was observed in Section 7.2, the impeller geometry has a clear influence on the agglomerate formation, but this is not always accurately reflected by the PBM in this work. The smaller impeller diameter could impart different velocity profiles in the system, reducing the mixing between particles and bridging liquid.
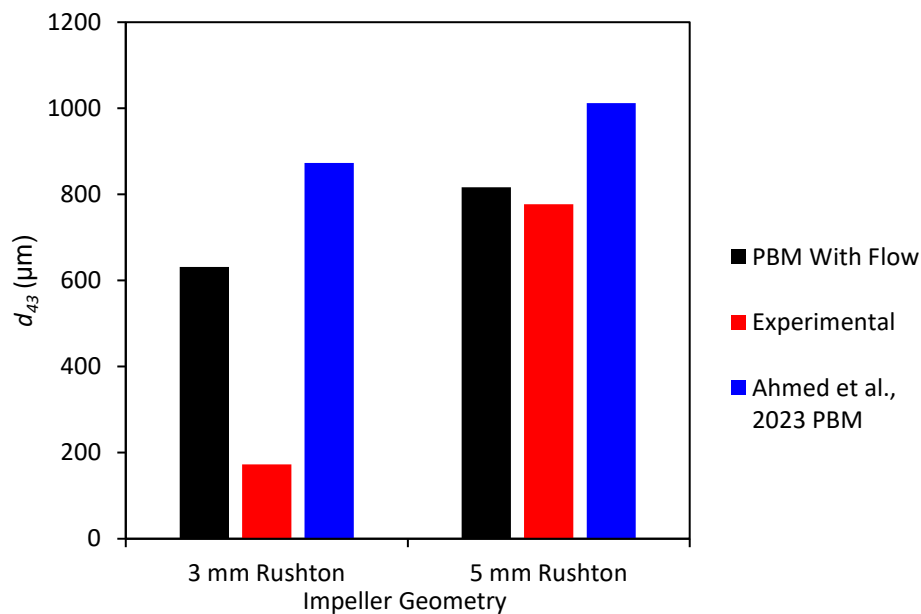
Figure 7-13 Average particle size (d_{43}) from the PBM with flow, experimental investigation and the PBM by Ahmed et al., 2023 of spherical agglomerates formed using Rushton turbine impellers of 3 mm or 5 mm diameter, initial particle size 52 μm

An image of the agglomerates formed using the 3 mm Rushton turbine can be seen in Figure 7-14. These agglomerates are not consistent in shape. Some of the larger agglomerates seen in this figure had only agglomerated in one direction, resulting in thin sheets of agglomerated material rather than spheres. The products of this experiment were not very strong and easily broke during sieving, resulting in a low d_{43} value. The flat shape of some agglomerates, and how easily they break, suggest that a 3 mm Rushton turbine does not induce consolidation in the system, likely due to low shear forces. CFD simulations of this impeller could be performed to investigate the flow pattern and shear forces with an impeller diameter to take diameter ratio of 0.3. If these were found to be different then the PBM should be adapted to include this, increasing the accuracy of the PBM as a predictive tool.
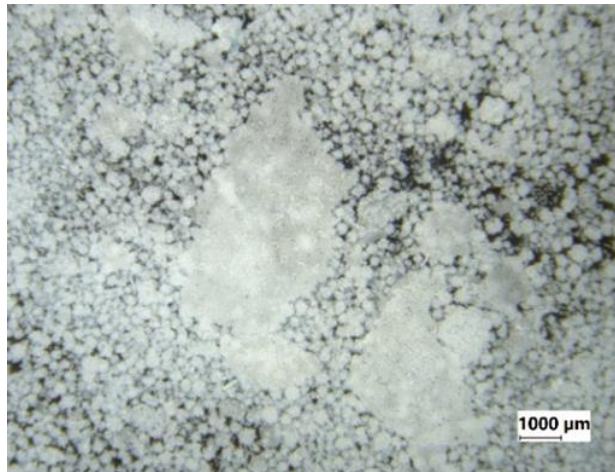
— 1000 µm

Figure 7-14 Agglomerates formed with 3 mm Rushton turbine impeller, scale bar is 1000 µm

7.4 Previous Spherical Agglomeration Research Experiments

Results obtained by Guo Jung Lian as part of a MEng Research Project at the University of Sheffield were also used to validate the model. These experiments used 52 µm PMMA beads, suspended in water, with various bridging liquids. Table 7-1 shows a summary of experiments from Lian, 2020 that were simulated as part of this work.

Table 7-1 Summary of experiments performed by Guo Jung Lian for his MEng work that are used to validate the model, information from (Lian, 2020)

Bridging Liquid	BSR	Water Mass (g)	Powder Mass (g)	Impeller Speed (rpm)	Agitation Time (min)
Isopropyl Acetate	0.5	288	12	1000	30
n-butyl Acetate	0.5	288	12	1000	30
Toluene	0.5	288	12	1000	30
Toluene	0.6	288	12	1000	30
Toluene	0.5	285	15	1000	30
Toluene	0.5	288	12	500	30
Toluene	0.5	288	12	1000	45
Kerosene	0.5	288	12	1000	30

7.4.1 Influence of Bridging Liquid Type

The bridging liquid is extremely important in spherical agglomeration as it induces the agglomeration of the particles. For the simulations of the various bridging liquids, the viscosity, interfacial tension, contact angle and volume of bridging liquid was altered. The bridging liquid volume was different for the different bridging liquids even though the BSR is the same, as this depends on the bridging liquid density (Equation

3.3). Additional bridging liquid was also added to account for the solubility of Isopropyl acetate and n-butyl acetate in water.

Table 7-2 Bridging liquid properties used in the simulations of work from Lian, 2020

Bridging Liquid	Density (kg/m^3)	Solubility in Water (g/L)	Viscosity (Pa.s)	Interfacial Tension (N/m)	Contact Angle (°)	Mass Added (g)
Isopropyl Acetate	870	31	0.0005	0.0145	14.3	13.28
n-Butyl Acetate	880	6.8	0.00069	0.022	22.9	6.31
Toluene	872	0.526	0.00055	0.0354	8.7	4.36
Kerosene	795	0	0.00164	0.0487	35.5	3.9

Figure 7-15 shows the experimental results and both the PBM with flow and the PBM by Ahmed et al., 2023 predictions of d_{43} for spherical agglomerates of PMMA produced with different bridging liquids. Images of the experimental agglomerates are shown in Figure 7-16. Based on the contact angles shown in

Table 7-2, toluene should be most effective at agglomerate production, with kerosene being the worst performing bridging liquid. The experimental data in Figure 7-15 and Figure 7-16 show a clear correlation that increased bridging liquid contact angle reduces the size, sphericity and consistency of agglomerates.

From Figure 7-15, the PBM developed as part of this work predicts a d_{43} lower than the PBM by Ahmed et al., 2023 for all bridging liquids. This lower prediction may be due to the PBM assuming a faster agglomeration than occurs experimentally. In Section 7.3.3, it was found that increasing the agitation time increased the consistency of the agglomerates as they were more spherical after 90 minutes of agitation compared to 45 minutes (Figure 7-10 and Figure 7-12). Another reason that the PBM with flow may be underpredicting the d_{43} for toluene and isopropyl acetate is that the smaller impeller diameter has lower power consumption than the 50 mm impeller diameter used for the experiments conducted in this work. The PBM uses the power consumption to calculate the velocity of solid and liquid interactions, therefore, lower power consumption will result in lower velocities in the system, reducing the predicted d_{43}. As the PBM developed in this work uses the impeller diameter to calculate more parameters in the power consumption equation, the PBM produces lower results than the PBM by Ahmed et al., 2023.

The PBM prediction of d_{43} is closest for n-butyl acetate as a bridging liquid. In the work by Lian, 2020 this was not considered to be the optimal bridging liquid due to the large proportion of unagglomerated material in the PSD, however, agglomerates did form. In Figure 7-16, it can be seen that the agglomerates formed with n-butyl acetate are very inconsistent in size and not spherical.
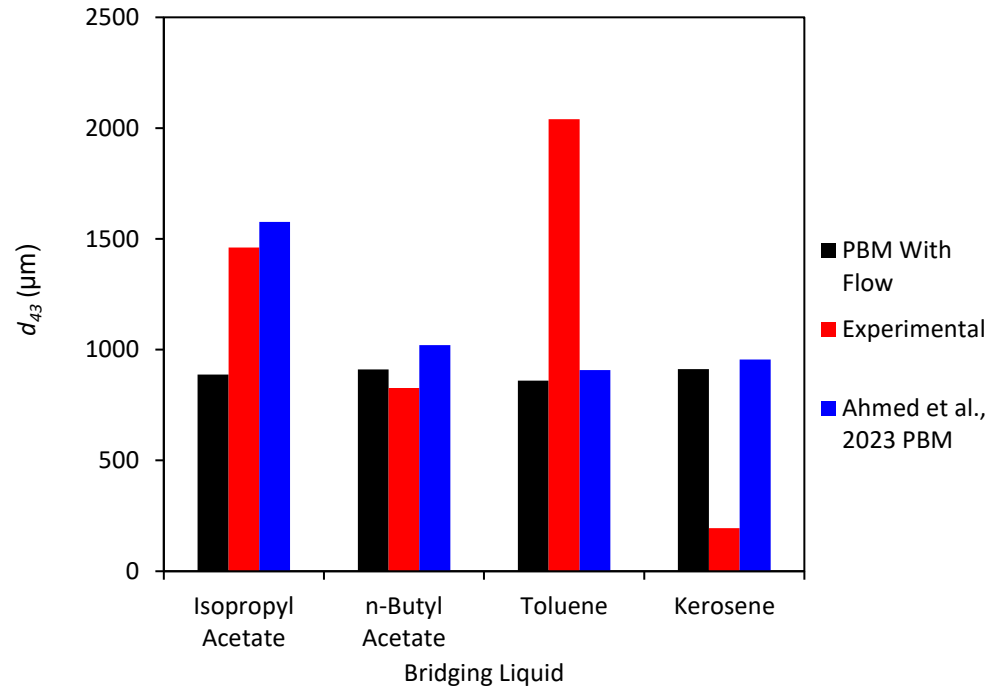
Figure 7-15 Influence of bridging liquid on the PBM and experimental d_{43} of PMMA agglomerates, data from (Lian, 2020)
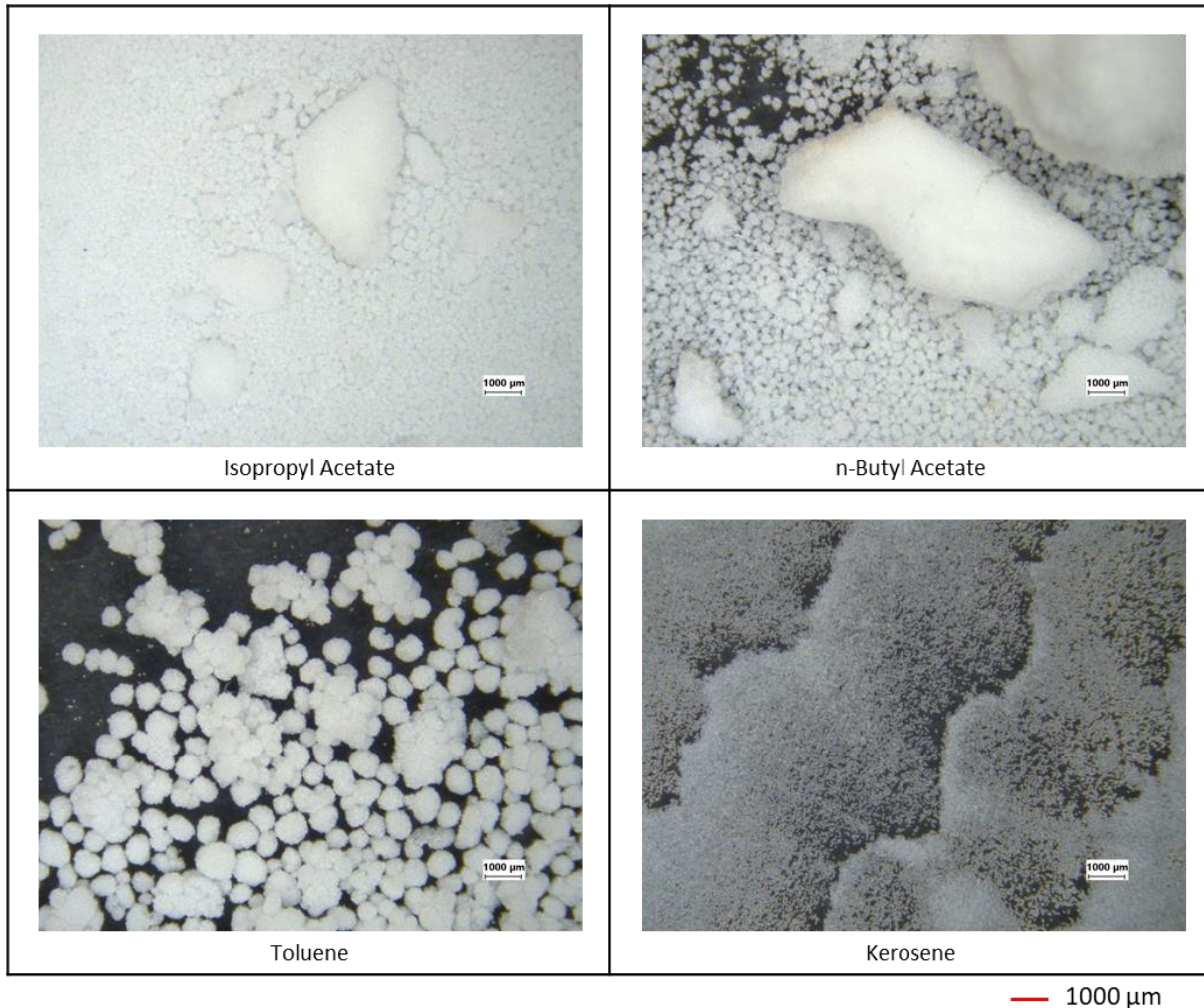
Figure 7-16 Images of the PMMA agglomerates formed with different bridging liquids, agglomerates made as part of (Lian, 2020), scale bar is 1000 μm

When simulating the experimental conditions in the PBM with flow and the PBM by Ahmed et al., 2023 the growth coefficient was 0.69 for all bridging liquids. This was done for consistency between the different PBMs, however, this value would be different for the different bridging liquids. The growth coefficient is found experimentally, and as the data in this section is from experiments that were performed for Lian, 2020 it was not possible to determine an accurate growth coefficient for the different bridging liquids.

7.4.2 Influence of Various Process Parameters

In the work by Lian, 2020, toluene was considered as the best bridging liquid for spherical agglomeration. This bridging liquid was then used for investigations into the influence of BSR, solids concentration, impeller speed and agitation time. Details of the simulations performed are shown in Table 7-3. Figure 7-17 shows the d_{43} from the experimental study, the PBM developed in this work and the PBM by Ahmed et al., 2023 for the different process parameters. Images of the agglomerates formed at different conditions are shown in Figure 7-18.

Table 7-3 Details of the simulations performed to investigate the influence of various process parameters on PMMA agglomerates with toluene as bridging liquid, experiments performed by (Lian, 2020)

Condition	Solids Mass (g)	Bridging Liquid Mass (g)	Impeller Speed (rpm)	Agitation Time (min)
Base Case	12	4.4	1000	30
Increased BSR	12	5.2	1000	30
Increased Solids Concentration	15	5.5	1000	30
Reduced Impeller Speed	12	4.4	500	30
Increased Agitation Time	12	4.4	1000	45

With toluene as the bridging liquid, increasing the BSR reduced the d_{43} of the experimental results, however, both the PBM developed in this work and the PBM by Ahmed et al., 2023 predicted an increase in d_{43}. In the agglomerate images, shown in Figure 7-18, the agglomerates appear more consistently spherical and larger at a higher BSR. Although the agglomerates appear larger, the d_{43} is lower with an increased BSR of 0.6. It may be that the increased BSR resulted in a more consistent distribution of bridging liquid in the tank, resulting in fewer agglomerates forming, but the agglomerates that did form were consistently large in size. Figure 7-16 also shows the base case agglomerates formed at the lower BSR of 0.5. In the lower BSR system, uneven BSR distribution caused some areas that formed very large agglomerates, and others that formed smaller agglomerates. The variation in agglomerate size will have skewed the d_{43} to be larger than the agglomerates formed at an increased BSR.

The d_{43} for the PBM predictions and experimental results with an increased solids concentration can also be seen in Figure 7-17. This figure shows that with increased solids concentration, the d_{43} decreases compared to the base case. The agglomerates shown in Figure 7-18 show that the agglomerates are similar in sphericity to the base case agglomerates, however, there are more agglomerates of lower size in the image. The agglomerates with increased solids concentration appear to have undergone less consolidation than the base case agglomerates, as it is possible to see the backlighting through some of the agglomerates with an increased solids concentration. In the PBM developed in this work and the PBM by Ahmed et al., 2023 predicted that the d_{43} would increase with an increased solids concentration. In Table 7-3, it can be seen that with the increased solids concentration, a greater mass of bridging liquid was added to the system. The PBM may assume that all bridging liquid added is used to form agglomerates, but this does not happen in a spherical agglomeration experiment.

The PBM was also tested against the base case with a reduced impeller speed of 500 rpm. In Figure 7-17, it can be seen that for the experimental results, reducing the impeller speed increases the d_{43}. This is different to the results of both the PBM developed in this work and the PBM by Ahmed et al., 2023. The increased d_{43} with a lower impeller speed for the experimental agglomerates could be due to lower impeller speed reducing shear in the system, leading to less breakage. At lower shear there will be less consolidation in the system, causing the agglomerates to be larger. Figure 7-18 shows that not only are the agglomerates produced at a lower impeller speed larger than the base case, they are also less spherical. The lower sphericity of agglomerates produced at reduced impeller speed is due to the lack of consolidation in the system.

Both the PBM developed in this work and the PBM by Ahmed et al., 2023 do not show a difference in d_{43} when the agitation time increased from 30 minutes to 45 minutes; this can be seen in Figure 7-17. The experimental results, however, do show that increasing the agitation time reduces the value of d_{43} by approximately 600 μm. From Lian, 2020, increasing the agitation time did increase the size of agglomerates, even though the d_{43} was lower. In the agglomerate images in Figure 7-18, the agglomerates at an increased agitation time appear larger and more consistent in size than the agglomerates from the base case. This suggests that increased agitation time leads to agglomerates that are consistently large, whilst the base case has a much broader distribution, with some very large agglomerates skewing the d_{43}. The fact that both PBMs do not show a difference in d_{43} with agitation time suggests that the model assumes the agglomeration process is much faster than it occurs experimentally.

For all of the different process parameters investigated, both the PBM developed in this work and the PBM by Ahmed et al., 2023 underpredicted the d_{43} compared to the experimental data. The d_{43} from the PBM developed in this work was lower than the PBM by Ahmed et al., 2023 for all conditions. This suggests that the growth coefficient used for the simulations did not allow for the PBM to represent the system. Due to the PMMA-toluene system used in this work also being used in the Lian, 2020 work a growth coefficient of 0.69 was used. This is determined experimentally and, therefore, should be adapted for different process parameters. There was, however, limited data to determine the growth coefficient for the specific experiments simulated. The generation of a mathematical correlation for the growth coefficient is important in ensuring the spherical agglomeration PBM is applicable to more systems.
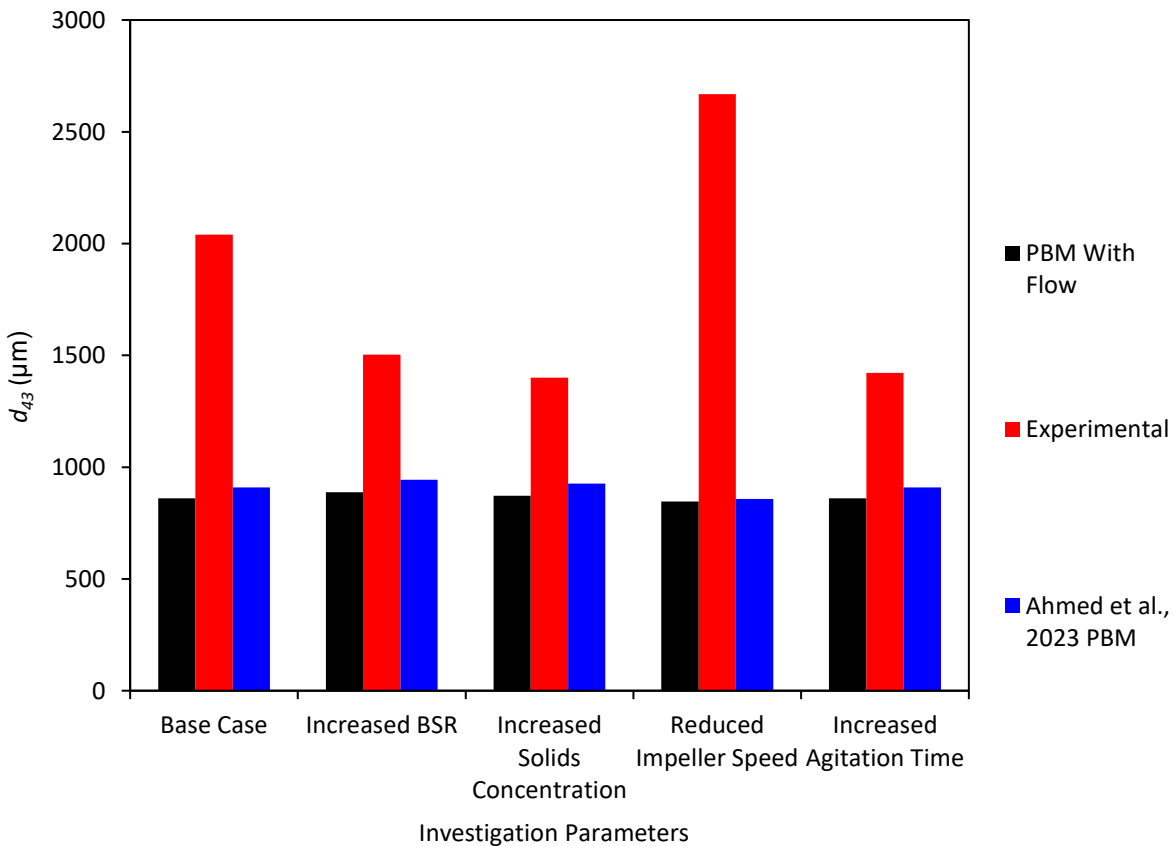
Figure 7-17 Influence of different process parameters on the PBM and experimental d_{43} of PMMA agglomerates with a toluene bridging liquid, data from (Lian, 2020)

167
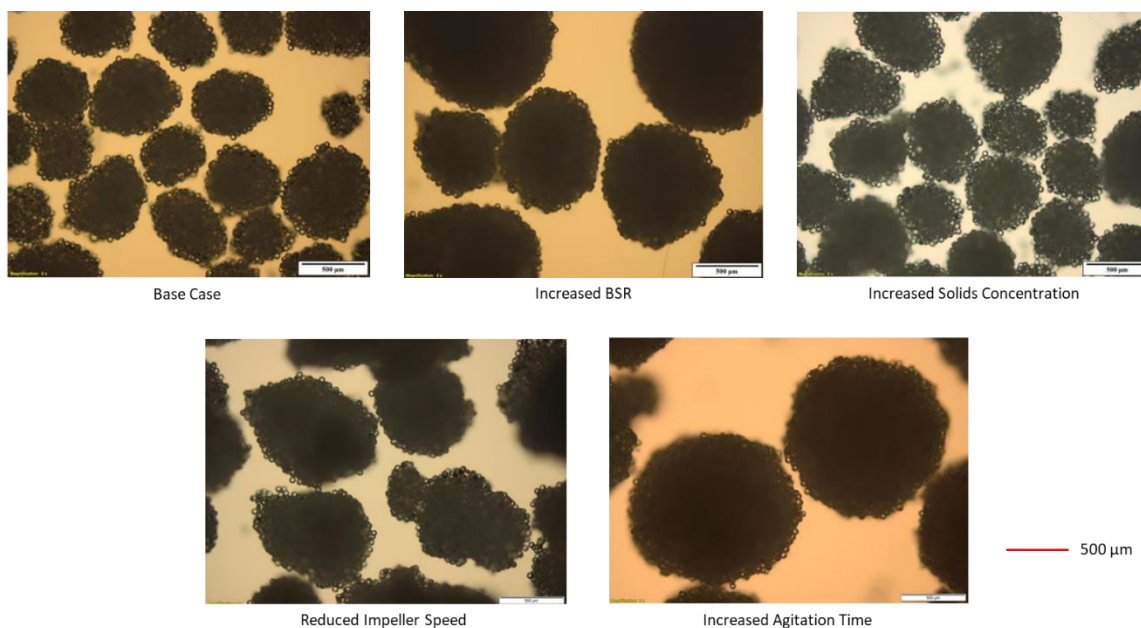
Figure 7-18 Images of the PMMA agglomerates with a toluene bridging liquid at different process parameters, scale bar is 500 µm, images from (Lian, 2020)

7.5 Conclusion

The PBM developed in this work has incorporated the influence of the impeller geometry and clearance to produce different particle size distributions for spherical agglomeration. The previous iteration of the PBM that was developed by Ahmed et al., 2023 only considered impeller diameter and speed.

Impeller power number was used to incorporate the impeller geometry into the PBM. This has worked better for the radial flow impellers tested than the axial impellers. For the radial impellers, the power number is close to expected values from literature, but it is much lower than expected for axial impellers. A pitched blade impeller is expected to have a power number of approximately 1.5, but the PBM is calculating this to be 0.0215. To improve the PBM prediction with axial flow impellers, the correlations for power number should be adapted to more accurately reflect the power imparted on the system.

All simulations in this work have used a growth coefficient of 0.69 as this was determined and appropriate value for the 52 µm PMMA beads, toluene and water system with a flat blade impeller and a BSR of 0.5. The results throughout this chapter suggest that the growth coefficient will change with impeller geometry, initial particle size, impeller diameter and BSR. Therefore, the development of a way to calculate the growth coefficient with minimal experimentation would improve the model accuracy.

The PBM validation experiments considered two primary particle sizes, 20 µm and 52 µm. Predictions of d_{43} were closer to the experimental results for an initial particle size of 52 µm than for 20 µm particles. The difference in accuracy with different particle sizes may be due to the growth coefficient being influenced by primary particle size. Another reason for this discrepancy may be that the smaller particles are less likely to become entrained in the flow pattern, limiting contact with the bridging liquid. If the 20 µm particles are not caught in the flow patter, then the velocity fitting parameters developed from the CFD simulations will not be applicable to low particle sizes. This could be tested by running CFD simulations

168

with a range of primary particle sizes to determine if the velocity fitting parameters need to be altered for different primary particle sizes.

In the model, it is assumed that the bridging liquid droplet size is consistently 500 µm, however, this is very difficult to control in an experimental setting. Due to the lack of control over bridging liquid droplet size the PBM results may not apply to the experiment even though it has the corresponding geometry, BSR and agitation time. A method to control the droplet size, or measure it in the tank would be useful to increase the accuracy of the model.

In this work the PBM by Ahmed et al., 2023 was modified to include the impeller geometry and clearance due to these parameters greatly influencing the sphericity and PSD of spherical agglomerates. These modifications resulted in the PBM developed in this work producing d_{43} values that are closer to experimental results than the PBM by Ahmed et al., 2023 for 56.4 % of the experimental results. The PBM with flow has a major advantage when compared to previous iterations of the spherical agglomeration PBM as it produces different results for different impeller geometries and clearances.

Chapter 8 Investigation into particle motion and settling in cascading MSMPRs

8.1 Introduction

The research contained in this chapter was conducted as part of a four-month industrial placement at a Pfizer research site and focussed on an active pharmaceutical ingredient (API) crystallisation process. While this chapter does not explicitly examine spherical agglomeration, the subject matter, computational flow characteristics of pharmaceutical crystallisers, is highly relevant to the thesis. Information gained through the spherical agglomeration CFD simulations, shown in Chapter 5, influenced the parametric study presented in this chapter, and the results of this chapter inform the overall thesis conclusion. The work in this chapter would be useful in designing industrial spherical agglomeration processes as the product of crystallisations will be used as feed material for spherical agglomeration. Being able to control the size of the crystals for spherical agglomeration will allow for control of whether the process follows the immersion or distribution mechanism.

MSMPR crystallisers are often utilised in the development stage of API manufacture to produce drug crystals that undergo further processing to produce tablets. A lab scale (300 mL) arrangement of three MSMPRs in series is shown in Figure 8-1; these tanks formed the basis of the CFD simulations.
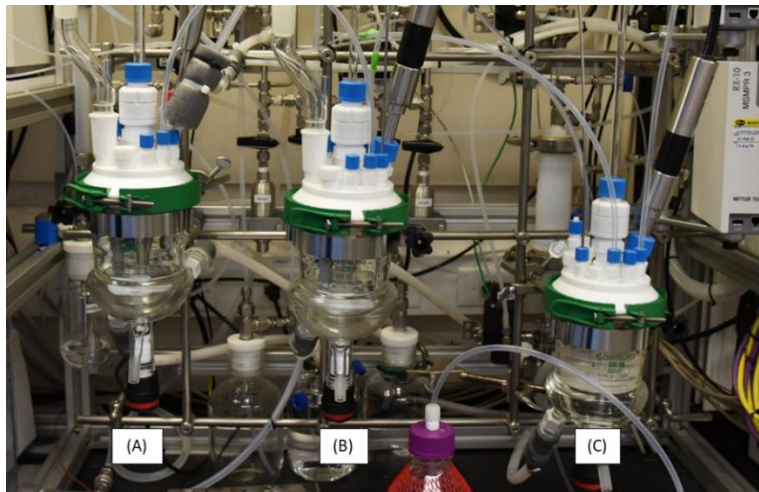
Figure 8-1 Image of the lab-scale MSMPRs in series

Complex withdrawals and transfers between the tanks in Figure 8-1 typically occur at regular intervals during the crystallisation process. The transfer process begins with a rapid withdrawal from tank C resulting in 40 mL of liquid withdrawn from the tank in 2 seconds. Tank B then undergoes a withdrawal at the same flowrate (20 mL/s) with the withdrawn transferring into tank C over a period of 4 seconds, giving a flowrate of 10 mL/s.   There is then a withdrawal from tank A at 20 mL/s for 2 seconds; the withdrawn liquid is injected into tank B at a rate of 10 mL/s. Tank A will then undergo an injection of feed material to ensure there is sufficient material for continuous crystal production.

Withdrawals occur at every 1/10th of the total crystallisation time; Figure 8-2 shows the volume in tank C as the withdrawal occurs, assuming a 30 minute crystallisation time. Tank C contains the crystallisation product. The CFD study focussed on the withdrawal from Tank C to ensure that the crystals withdrawn from this tank were representative of the final crystal product. This research will improve product

recovery from the system without needing to perform multiple experiments, saving both time and resources, which is incredibly important in API development.
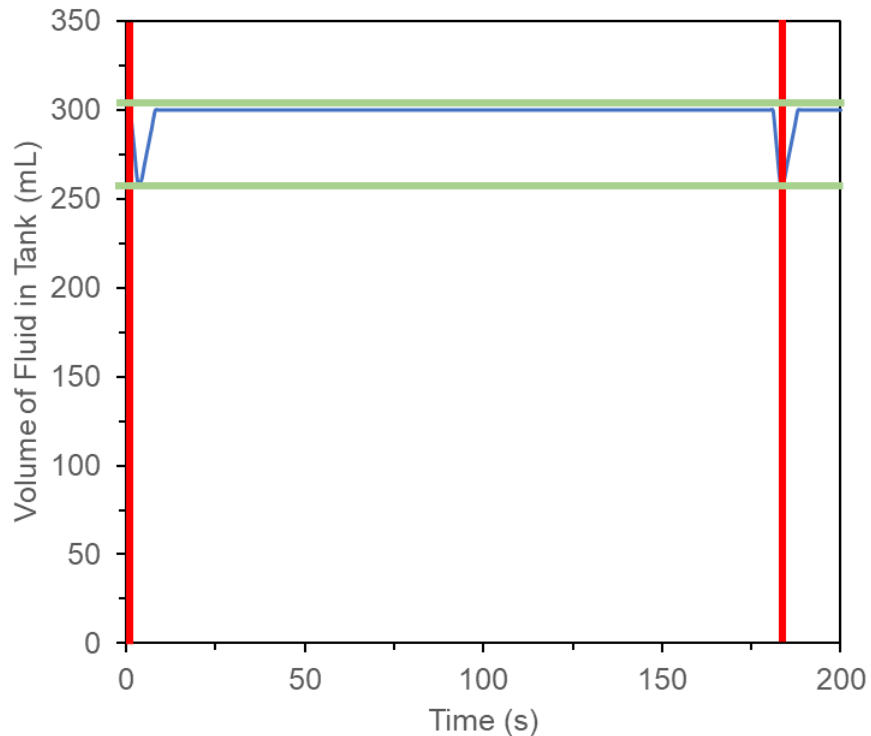
Figure 8-2 Graphical representation of the fluid volume in tank C, assuming a 30 minute residence time, the green lines show the change in volume as 10 % of the initial volume, the red lines represent the time between withdrawals, equivalent to 10 % of the overall residence time

8.1.1 Aim

The aim for the research in this chapter is to use CFD simulations to identify aspects of reactor configurations that will maximise the withdrawal of representative crystals from the sampling dip tube.

8.1.2 Objectives

The objectives to achieve the aim were as follows:

- Construct a representative geometry of the lab-scale equipment
- Investigate settling characteristics in the tank and identify issues with particle suspension
- Design and conduct a parametric study to identify improvements to stirred tank configurations that will maximise the number of withdrawn particles and ensure the withdrawn particles are a representative sample of the particle size distribution (PSD) in the tank

8.2 Methodology

M-Star CFD (M-Star Simulations, LLC) was utilised for the CFD study, as the Lattice-Boltzmann solver has demonstrated successful results for mixing turbulent systems in stirred tanks. Both M-Star (M-Star Simulations, LLC) and ANSYS Fluent were available to use during the placement. M-Star CFD (M-Star Simulations, LLC) was chosen due to it having reduced computation times when compared to other CFD software. this was attractive due to the time constraints of the placement. More information about M-

Star CFD (M-Star Simulations, LLC) is given in Section 2.11.3.7. Table 8-13 summarises all simulations performed as part of this research.

8.2.1   Simulation Construction

Simulation construction occurred in multiple stages to ensure the results obtained accurate. The stages are as follows:

- Geometry construction – tank geometry construction used a combination of M-Star CFD (M-Star Simulations, LLC) built in computer aided design (CAD) and other CAD software.
- Establishing a particle and solvent system – a material system was selected that allowed for simulations results to be comparable to a crystallisation experiment.
- Constructing inlet and withdrawal system – the simulation needed to contain particle and solvent withdrawal through the dip tube at regular intervals, with some particles being recycled.
- Lattice density analysis –lattice density evaluation performed to ensure there are sufficient lattice points for an accurate result, without unnecessarily increasing the computation time.
- Initial simulations –performed to ensure that the withdrawal system is working accurately and identify areas for simulation improvement.
- Scaling the withdrawals and inlets – the inlets and withdrawals were scaled to fit as many as possible into a shorter simulation time, reducing computational requirements
- Adding probes to the system – increased similarity with laboratory equipment. Probes act as baffles in the system and will therefore change the flow pattern from the initial simulations.
- Design of Experiments Simulations –the final simulations performed to determine the optimal equipment configuration. The simulations optimised both the number of particles withdrawn and how representative the withdrawn particle size distribution was compared to the inlet particles.

8.2.2   Stirred Tank Geometry

Stirred tank geometry construction occurred in the M-Star CFD (M-Star Simulations, LLC) CAD system, with the exception of the impeller. ANSYS Design Modeller (Figure 8-3) was used to create the geometry for the custom impeller used in this equipment. Figure 8-3 shows the customised impeller and the CAD version. Table 8-1 shows the values of parameters used in CFD simulations of the crystallisation vessel.

Table 8-1 Values of stirred tank simulation parameters

Geometry Component	Value
Vessel Diameter	85 mm
Vessel Height	130 mm
Fluid Height	65 mm
Impeller Diameter	61.6-77 mm
Shaft Diameter	10 mm
Impeller Speed	250-350 rpm
Impeller Clearance	5-15 mm
Dip Tube Diameter	6.4 mm
Inlet Diameter	6.4 mm
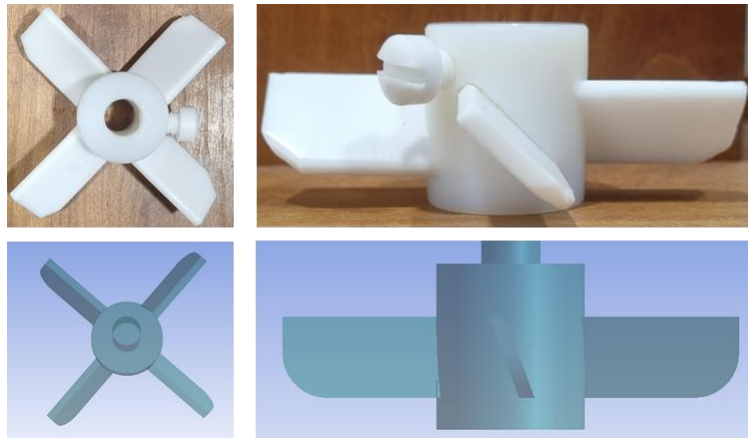
Figure 8-3 Impeller used in the stirred tanks and the CAD versions created in ANSYS Design Modeller

Table 8-1 shows the equipment geometry used for preliminary simulations to configure the particle inlet and withdrawal system. Following the preliminary simulations, probes were added into the system. These probes are in the laboratory equipment (Figure 8-1) to record inline measurements and act as baffles. Section 8.2.8 discusses the added probes.

8.2.3 Particle and Solvent System

To reflect an industrial crystallisation process the solvent and particle system needed careful selection. Ethanol is a commonly used crystallisation solvent and was the selected suspending solvent for the CFD simulations. Table 8-2 shows the fluid properties used in the simulation.

Table 8-2 Properties of the fluid in the system, they were based on ethanol, a commonly used solvent in crystallisation

Fluid Property	Value
Density (kg/m^3)	789
Viscosity (m^2/s)	1.52x10^{-6}
Surface Tension (N/m)	0.022
Volume (mL)	300

Table 8-3 shows the simulated particle properties. The density chosen is similar to typical crystallisation primary particles. To simplify the simulations, the particles are both spherical, and inertial. Spherical particles simplify the particle size distribution. Inertial particles mean that no growth or particle-particle interactions occur in the simulations. Including growth and particle-particle interactions requires CFD-DEM simulations, greatly increasing the computation time. To eliminate the need to model growth, the PSD of the inserted particles was 50-200 μm, similar to that of a crystallisation product. Figure 8-4 shows a uniform size distribution; this distribution allows for easy analysis of how representative the withdrawals from the system were, as the withdrawals should also contain a uniform number of particles in each size fraction.

Table 8-3 Properties of the simulated particles

Particle Property	Value
Density (kg/m³)	1300
Particle Shape	Spherical
Particle Type	Inertial
Size Distribution	50-200 μm Uniform Distribution
Drag Force Model	Free Particle
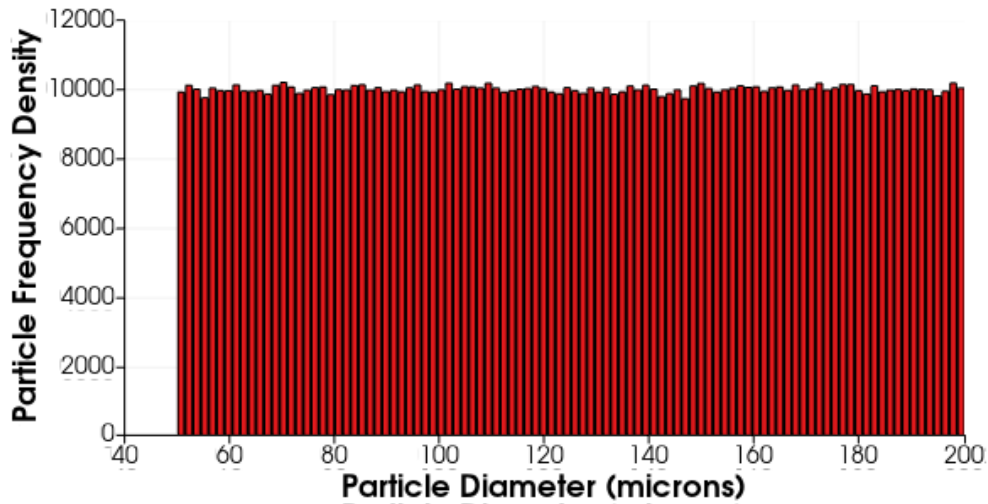
Figure 8-4 Particle size distribution of the particles that are injected into the stirred tank

8.2.4 Constructing the Withdrawal System

Initial construction of the withdrawal system allowed for a withdrawal every 3 minutes as experimentally the withdrawals occur every $1/10^{th}$ of the 30-minute residence time. To match the experimental conditions specified in Section 8.1, the inlet and outlets velocities calculated result in a 20 mL/s outlet and a 10 mL/s inlet through the dip tube diameters specified in Table 8-1. The outlet and inlet velocity calculation is in Equation 8-1; the results are in Table 8-4.

$$v = \frac{Q}{A}$$

(8-1)

Where:
v = velocity (m/s)
Q = flowrate (m³/s)
A = surface area of the dip tube (m²)

Table 8-4 Values of inlet and outlet velocity, calculated using Equation 8-1

	Flowrate (m³/s)	Surface Area (m²)	Velocity (m/s)
Inlet	0.000020	0.000032	0.62
Outlet	0.000010	0.000032	0.31
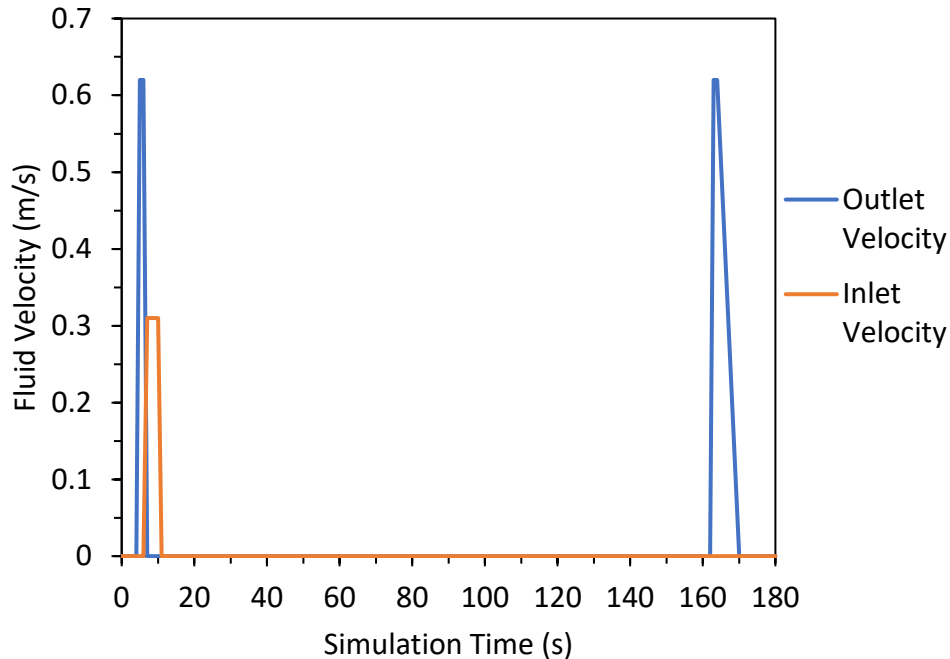
Figure 8-5 Graphical representation of the inlet and outlet velocities for a 180s simulation

Figure 8-5 shows the inlet and outlet velocities when the withdrawals occur at 1/10th of the residence time. In Section 8.2.7, alterations of the timing between withdrawals allows for generation of more outlet data in a shorter computation time without flow field and influencing the results.

8.2.5   Lattice Density Analysis

A lattice density analysis ensures that insufficient lattice points do not alter the accuracy of simulation results. In M-Star CFD (M-Star Simulations, LLC), the mathematical extent of the model is represented by the lattice. Increasing the lattice density in the same geometric area will result in more calculation points during the simulation.

Performing simulations using lattice densities of 90, 100, 110, 125 and 150 allowed for investigation into their influence on the results. The default value in M-Star CFD (M-Star Simulations, LLC) was a lattice density of 100. Increasing lattice density ensured that the data had sufficient accuracy with a lower computation time. A simulation with a lattice density of 90 determined if having 100 lattice points would greatly increase computation time.

The various lattice densities, shown in Figure 8-6, tested in a 30 s simulation with one particle withdrawal that began at 1 s and ended at 3 s. The withdrawn particles were of a uniform size distribution between 100 μm and 1000 μm. This differed from the particle size shown in Figure 8-4 as the PSD changed after the lattice density analysis simulations.
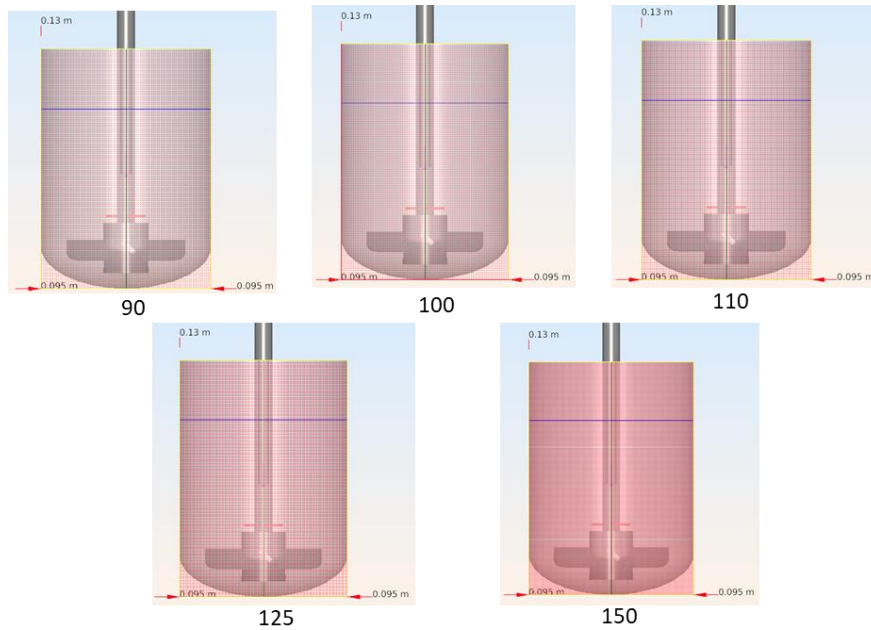
Figure 8-6 Geometries of the stirred tank with various lattice densities

8.2.6   Initial Simulations

Initial simulations determine mixing and settling behaviour of different particle sizes in the tank using the standard laboratory equipment conditions. The simulated equipment configuration is in Table 8-5.

To investigate particle settling across the height of the tank, zones were constructed in M-Star CFD (M-Star Simulations, LLC) using the cylindrical output surface tool. The zones do not interfere with the simulation process but would allow for results across varying zones in the reactor, shown in Figure 8-7, being readily available in results files.

Some simulations used the PSD shown in Figure 8-4; others simulated monosized particles to investigate whether there was a maximum diameter of well-suspended particles in the system. For monosized investigations, one injection of 100,000 particles occurred at 5 s simulation time and there was no withdrawal in this system. The total simulation time was 60 s.

Table 8-5 Properties of the stirred tank used for the initial simulations

Geometry Component	Value
Vessel Diameter	85 mm
Vessel Height	130 mm
Fluid Height	65 mm
Impeller Diameter	77 mm
Shaft Diameter	10 mm
Impeller Speed	250 rpm
Impeller Clearance	5 mm
Dip Tube Diameter	6.4 mm
Inlet Diameter	6.4 mm

176
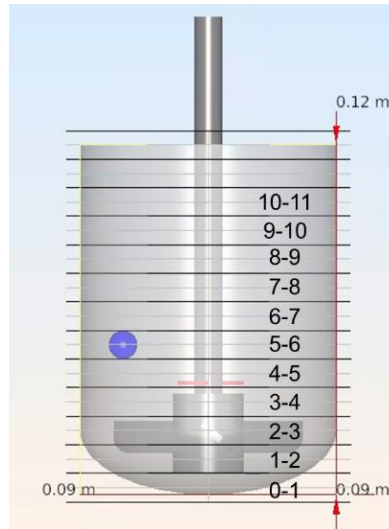
Figure 8-7 Geometry of the stirred tank with vertical zones added to investigate suspension of different sized particles

8.2.7   Scaling the withdrawals and inlets

To enable six withdrawals to occur in a 180 s simulation time, the withdrawals and inlets were scaled, allowing the generation of more results in a shorter computation time. To ensure that the increased withdrawal rate would not influence the particle suspension; the fluid velocity curve was plotted against simulation time (Figure 8-8). From Figure 8-8, the mean fluid velocity plateaued after 3 s, suggesting stable velocity. The particles injection occurred after 5 seconds simulation time into a stable fluid system. To ensure that the particles were fully suspended, the first withdrawal was set to occur at 15 seconds simulation time. Table 8-6 showing the specific velocities and particle numbers for the injections, as well as the outlet velocity for the scaled withdrawals and inlets.
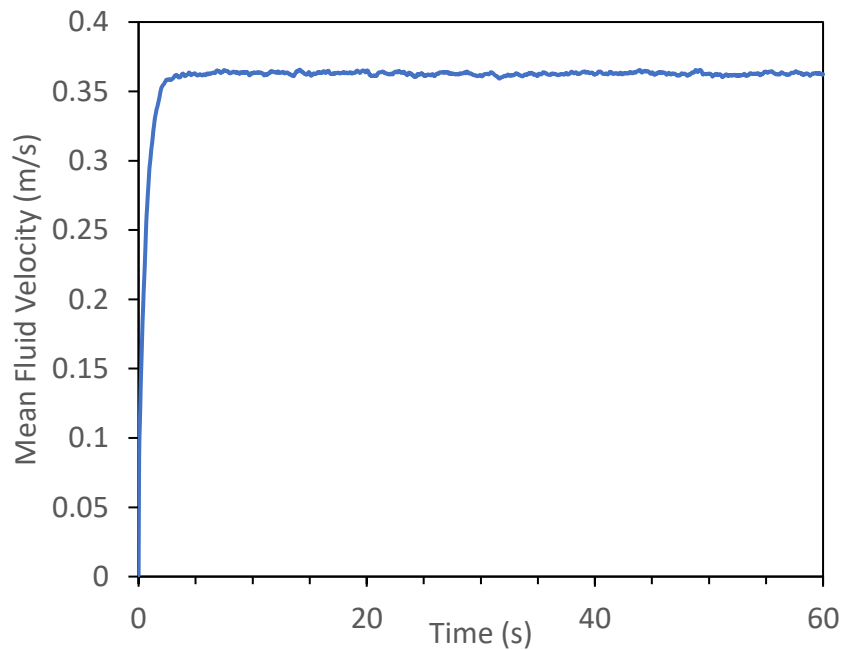
Figure 8-8 Fluid velocity as a function of simulation time (s)

For the multiple withdrawal system, simulations performed utilised the uniform size distribution specified in Figure 8-4.

Table 8-6 Velocities and particle injection values for the scaled outlet simulations

Simulation Time (s)	Particle Injection	Fluid Outlet Velocity (m/s)	Fluid Injection Velocity (m/s)
5	1,000,000	0	0
15	0	0.62	0
30	100,000	0	0.31
45	0	0.62	0
60	100,000	0	0.31
75	0	0.62	0
90	100,000	0	0.31
105	0	0.62	0
120	100,000	0	0.31
135	0	0.62	0
150	100,000	0	0.31
165	0	0.62	0

8.2.8   Adding probes to the system

Addition of probes to the simulation geometry increased the accuracy of the simulations to the lab-scale stirred tank system. These probes also acted as baffles. Table 8-7 shows the dimensions of the probes in the MSMPRs used in the lab (Figure 8-1); these probes were included in the CFD geometry. Figure 8-9 shows the CAD drawing of the tank after probe addition.

Table 8-7 Name and dimensions of the probes added to the tank to refine the geometry

Probe Name	Diameter (mm)	Clearance (mm)	Insertion Angle (°)
Probe 1	12	50	20
Probe 2	12.7	50	90
Thermocouple	3.175	40	90
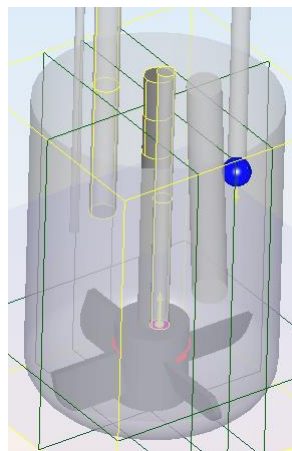
Figure 8-9 CAD drawing of the stirred tank after adding the probes

The geometry used for all of the DoE simulations is in Figure 8-9. The DoE specification is in Section 8.2.9, with the results for these simulations in Section 8.4.3.

8.2.9 Design of Experiment Simulations

The CFD study followed a central composite design of experiments (DoE) that was generated using Stat-Ease Inc. Design Expert®. The three parameters investigated in the DoE influence mixing and settling of particles in the tank. The DoE investigates the influence of impeller diameter, speed, and clearance, due to the influence that the flow pattern had on spherical agglomeration. Chapter 5 discusses the influence of flow characteristics on spherical agglomeration, with both CFD simulations and experiments performed to determine the importance of flow. Table 8-8 shows the template for the central composite DoE constructed using Design-Expert.

Table 8-8 Central Composite DoE produced by Design-Expert

Std	Run	A:A	B:B	C:C
		Diameter (mm)	Speed (rpm)	Clearance (mm)
1	6	-0.59	-0.59	-0.59
2	15	0.59	-0.59	-0.59
3	11	-0.59	0.59	-0.59
4	10	0.59	0.59	-0.59
5	1	-0.59	-0.59	0.59
6	9	0.59	-0.59	0.59
7	3	-0.59	0.59	0.59
8	12	0.59	0.59	0.59
9	5	-1	0	0
10	14	1	0	0
11	19	0	-1	0
12	16	0	1	0
13	4	0	0	-1
14	13	0	0	1
15	2	0	0	0
16	17	0	0	0
17	7	0	0	0
18	8	0	0	0
19	18	0	0	0

Due to the tank diameter, the maximum impeller diameter, given a value of 1 in the DoE, was 77 mm. The minimum diameter is be 80% of the maximum diameter, denoted by -1 in the central composite DoE, with value being 61.6 mm. The midpoint is the DoE 0 value and was 90% of the maximum diameter and the other diameters were calculated. The impeller diameters used for the DoE are in Table 8-9, with Figure 8-10 showing the CAD drawing of the tank with the smallest and largest impeller diameter.

Table 8-9 Values of impeller diameter that will be used for the DoE

DoE Code	Diameter (mm)
-1	61.6
-0.59	64.7
0	69.3
0.59	73.9
1	77

61.6 mm   77 mm
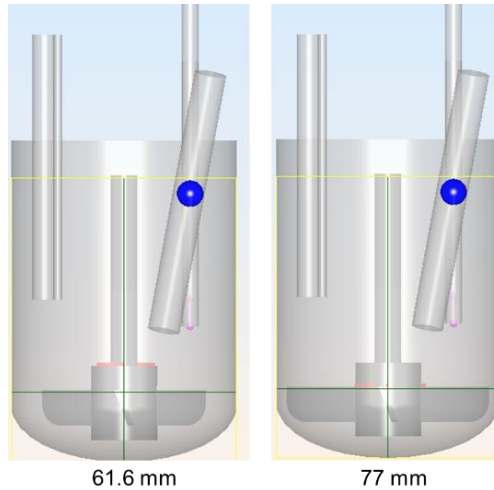
Figure 8-10 CAD drawing of tank used in DoE simulations with minimum size (61.6mm) and maximum size (77mm) impeller diameter

The impeller speed varied between 250 rpm and 350 rpm. Table 8-10 shows the range of impeller speed values tested within the DoE.

Table 8-10 Values of impeller speed that will be used for the DoE

DoE Code	Speed (rpm)
-1	250
-0.59	270
0	300
0.59	330
1	350

Simulations performed utilised various impeller clearances within the reactor due to this influencing the flow pattern, and therefore, the particle suspension in spherical agglomeration studies. Information on the influence of impeller clearance on spherical agglomeration is in Chapter 5. Due to the size of the largest impeller diameter, as seen in Table 8-9, the minimum clearance allowed for the system is 5 mm with 15 mm being the maximum clearance. Table 8-11 shows the different values of clearance tested for the DoE.

Table 8-11 Values of impeller clearance that will be simulated for the CFD DoE

DoE Code	Clearance (mm)
-1	5
-0.59	7
0	10
0.59	13
1	15

Table 8-12 shows the DoE from Table 8-8 with the values from Tables 8-9, 8-10 and 8-11 inserted to give a simulation plan. This resulted in a maximum of 19 simulations.

Table 8-12 Central Composite DoE with the parameter values included, the blue shaded rows are the central values of the simulation

		A:A	B:B	C:C
Std	Run	Diameter (mm)	Speed (rpm)	Clearance (mm)
1	6	64.7	270	7
2	15	73.9	270	7
3	11	64.7	330	7
4	10	73.9	330	7
5	1	64.7	270	13
6	9	73.9	270	13
7	3	64.7	330	13
8	12	73.9	330	13
9	5	61.6	300	10
10	14	77.0	300	10
11	19	69.3	250	10
12	16	69.3	350	10
13	4	69.3	300	5
14	13	69.3	300	15
15	2	69.3	300	10
16	17	69.3	300	10
17	7	69.3	300	10
18	8	69.3	300	10
19	18	69.3	300	10

Figure 8-11 shows a screenshot from M-Star CFD (M-Star Simulations, LLC) post processing that shows particles falling from the reactor, this error occurred for simulations with a lattice density of 100. To stop this, the lattice density was increased to 150 for the DoE parametric study simulations.
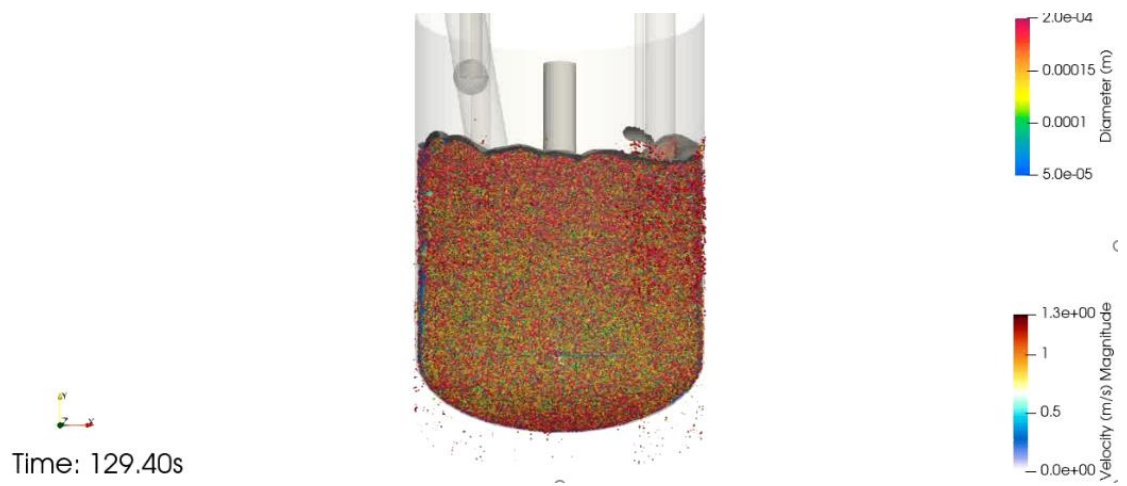
Figure 8-11 Particles falling from reactor when a complex simulation had a lattice density of 100

Table 8-13 Summary of all CFD simulations performed to investigate settling in MSMPRs

No.	Purpose	Simulation Time (s)	Lattice Density	Primary PSD	Impeller Speed (RPM)	Impeller Clearance (mm)	Impeller Diameter (mm)	Probes	Inlet	Outlet
1	Lattice Density Analysis	30	100	100,000 uniform 100-1000 µm, in from start	300	10	77	Dip Tube	No	20 mL/s for 2 s starting at 1 s
2	Lattice Density Analysis	30	90	100,000 uniform 100-1000 µm, in from start	300	10	77	Dip Tube	No	20 mL/s for 2 s starting at 1 s
3	Lattice Density Analysis	30	110	100,000 uniform 100-1000 µm, in from start	300	10	77	Dip Tube	No	20 mL/s for 2 s starting at 1 s
4	Lattice Density Analysis	30	125	100,000 uniform 100-1000 µm, in from start	300	10	77	Dip Tube	No	20 mL/s for 2 s starting at 1 s
5	Lattice Density Analysis	30	150	100,000 uniform 100-1000 µm, in from start	300	10	77	Dip Tube	No	20 mL/s for 2 s starting at 1 s
6	Initial Simulation	60	100	Uniform, 50-200 µm, injected in	300	10	77	Dip Tube	100,000 particles at 5s	No

7	Initial Simulation	60	100	Monosized, 50 μm, injected in	300	10	77	Dip Tube	100,000 particles at 5s	No
8	Initial Simulation	60	100	Monosized, 75 μm, injected in	300	10	77	Dip Tube	100,000 particles at 5s	No
9	Initial Simulation	60	100	Monosized, 100 μm, injected in	300	10	77	Dip Tube	100,000 particles at 5s	No
10	Initial Simulation	60	100	Monosized, 125 μm, injected in	300	10	77	Dip Tube	100,000 particles at 5s	No
11	Initial Simulation	60	100	Monosized, 130 μm, injected in	300	10	77	Dip Tube	100,000 particles at 5s	No
12	Initial Simulation	60	100	Monosized, 135 μm, injected in	300	10	77	Dip Tube	100,000 particles at 5s	No
13	Initial Simulation	60	100	Monosized, 150 μm, injected in	300	10	77	Dip Tube	100,000 particles at 5s	No
14	Initial Simulation	60	100	Monosized, 175 μm, injected in	300	10	77	Dip Tube	100,000 particles at 5s	No
15	Initial Simulation	60	100	Monosized, 200 μm, injected in	300	10	77	Dip Tube	100,000 particles at 5s	No
16	Initial Simulation	60	100	Monosized, 250 μm, injected in	300	10	77	Dip Tube	100,000 particles at 5s	No
17	Initial Simulation	60	100	Monosized, 300 μm, injected in	300	10	77	Dip Tube	100,000 particles at 5s	No

18	Scaled Withdrawal System	190	100	Uniform, 50-200 μm, injected in	300	10	77	Dip Tube	1,000,000 particles at 5s, then injection of 100,000 particles and 10 mL/s fluid over 2 s after 30 s simulation time, repeat this every 30 s	20 mL/s for 2 s every 30 s after 15 s simulation time
19	Adding in probes	30	100	Uniform, 50-200 μm, injected in	300	10	77	All probes	100,000 particles at 5s	No
20	Adding in probes	190	100	Uniform, 50-200 μm, injected in	300	10	77	All probes	1,000,000 particles at 5s, then injection of 100,000 particles and 10 mL/s fluid over 2 s after 30 s simulation time, repeat this every 30 s	20 mL/s for 2 s every 30 s after 15 s simulation time
21	Altering the impeller hub	40	100	Uniform, 50-200 μm, injected in	300	15	74 (with hub)	All probes	1,000,000 particles at 5s, then injection of 100,000 particles and 10 mL/s fluid at 30 s	20 mL/s for 2 s after a 15 s simulation time
22	Altering the impeller hub	40	100	Uniform, 50-200 μm, injected in	300	15	74 (no hub)	All probes	1,000,000 particles at 5s, then injection of 100,000 particles	20 mL/s for 2 s after a 15 s simulation time

									and 10 mL/s fluid at 30 s	
23	Altering the impeller hub	40	100	Uniform, 50-200 µm, injected in	300	15	88 (with hub)	All probes	1,000,000 particles at 5s, then injection of 100,000 particles and 10 mL/s fluid at 30 s	20 mL/s for 2 s after a 15 s simulation time
24	Altering the impeller hub	40	100	Uniform, 50-200 µm, injected in	300	15	88 (no hub)	All probes	1,000,000 particles at 5s, then injection of 100,000 particles and 10 mL/s fluid at 30 s	20 mL/s for 2 s after a 15 s simulation time
25	Altering the impeller hub	40	100	Uniform, 50-200 µm, injected in	300	15	54 (no hub)	All probes	1,000,000 particles at 5s, then injection of 100,000 particles and 10 mL/s fluid at 30 s	20 mL/s for 2 s after a 15 s simulation time
26	Altering the impeller hub	40	100	Uniform, 50-200 µm, injected in	300	15	4 (with hub)	All probes	1,000,000 particles at 5s, then injection of 100,000 particles and 10 mL/s fluid at 30 s	20 mL/s for 2 s after a 15 s simulation time
27	Reducing Fallen Particle Number	190	110	Uniform, 50-200 µm, injected in	300	10	77	All probes	1,000,000 particles at 5s, then injection of 100,000 particles and 10 mL/s fluid over 2 s after 30 s simulation time,	20 mL/s for 2 s every 30 s after 15 s simulation time

									repeat this every 30 s	
28	Reducing Fallen Particle Number	190	125	Uniform, 50-200 µm, injected in	300	10	77	All probes	1,000,000 particles at 5s, then injection of 100,000 particles and 10 mL/s fluid over 2 s after 30 s simulation time, repeat this every 30 s	20 mL/s for 2 s every 30 s after 15 s simulation time
29	Reducing Fallen Particle Number	190	150	Uniform, 50-200 µm, injected in	300	10	77	All probes	1,000,000 particles at 5s, then injection of 100,000 particles and 10 mL/s fluid over 2 s after 30 s simulation time, repeat this every 30 s	20 mL/s for 2 s every 30 s after 15 s simulation time
30	Design of Experiments	190	150	Uniform, 50-200 µm, injected in	300	10	69.3	All probes	1,000,000 particles at 5s, then injection of 100,000 particles and 10 mL/s fluid over 2 s after 30 s simulation time, repeat this every 30 s	20 mL/s for 2 s every 30 s after 15 s simulation time

31	Design of Experiments	190	150	Uniform, 50-200 μm, injected in	300	10	69.3	All probes	1,000,000 particles at 5s, then injection of 100,000 particles and 10 mL/s fluid over 2 s after 30 s simulation time, repeat this every 30 s	20 mL/s for 2 s every 30 s after 15 s simulation time
32	Design of Experiments	190	150	Uniform, 50-200 μm, injected in	270	7	64.7	All probes	1,000,000 particles at 5s, then injection of 100,000 particles and 10 mL/s fluid over 2 s after 30 s simulation time, repeat this every 30 s	20 mL/s for 2 s every 30 s after 15 s simulation time
33	Design of Experiments	190	150	Uniform, 50-200 μm, injected in	270	7	73.9	All probes	1,000,000 particles at 5s, then injection of 100,000 particles and 10 mL/s fluid over 2 s after 30 s simulation time, repeat this every 30 s	20 mL/s for 2 s every 30 s after 15 s simulation time
34	Design of Experiments	190	150	Uniform, 50-200 μm, injected in	330	7	64.7	All probes	1,000,000 particles at 5s, then injection of 100,000 particles	20 mL/s for 2 s every 30 s after 15 s simulation time

									and 10 mL/s fluid over 2 s after 30 s simulation time, repeat this every 30 s	
35	Design of Experiments	190	150	Uniform, 50-200 µm, injected in	330	7	73.9	All probes	1,000,000 particles at 5s, then injection of 100,000 particles and 10 mL/s fluid over 2 s after 30 s simulation time, repeat this every 30 s	20 mL/s for 2 s every 30 s after 15 s simulation time
36	Design of Experiments	190	150	Uniform, 50-200 µm, injected in	270	64.7	13	All probes	1,000,000 particles at 5s, then injection of 100,000 particles and 10 mL/s fluid over 2 s after 30 s simulation time, repeat this every 30 s	20 mL/s for 2 s every 30 s after 15 s simulation time
37	Design of Experiments	190	150	Uniform, 50-200 µm, injected in	270	13	73.9	All probes	1,000,000 particles at 5s, then injection of 100,000 particles and 10 mL/s fluid over 2 s after 30 s simulation time,	20 mL/s for 2 s every 30 s after 15 s simulation time

									repeat this every 30 s	
38	Design of Experiments	190	150	Uniform, 50-200 µm, injected in	330	13	64.7	All probes	1,000,000 particles at 5s, then injection of 100,000 particles and 10 mL/s fluid over 2 s after 30 s simulation time, repeat this every 30 s	20 mL/s for 2 s every 30 s after 15 s simulation time
39	Design of Experiments	190	150	Uniform, 50-200 µm, injected in	330	13	73.9	All probes	1,000,000 particles at 5s, then injection of 100,000 particles and 10 mL/s fluid over 2 s after 30 s simulation time, repeat this every 30 s	20 mL/s for 2 s every 30 s after 15 s simulation time
40	Design of Experiments	190	150	Uniform, 50-200 µm, injected in	300	10	61.6	All probes	1,000,000 particles at 5s, then injection of 100,000 particles and 10 mL/s fluid over 2 s after 30 s simulation time, repeat this every 30 s	20 mL/s for 2 s every 30 s after 15 s simulation time

41	Design of Experiments	190	150	Uniform, 50-200 µm, injected in	300	10	77	All probes	1,000,000 particles at 5s, then injection of 100,000 particles and 10 mL/s fluid over 2 s after 30 s simulation time, repeat this every 30 s	20 mL/s for 2 s every 30 s after 15 s simulation time
42	Design of Experiments	190	150	Uniform, 50-200 µm, injected in	250	10	69.3	All probes	1,000,000 particles at 5s, then injection of 100,000 particles and 10 mL/s fluid over 2 s after 30 s simulation time, repeat this every 30 s	20 mL/s for 2 s every 30 s after 15 s simulation time
43	Design of Experiments	190	150	Uniform, 50-200 µm, injected in	350	10	69.3	All probes	1,000,000 particles at 5s, then injection of 100,000 particles and 10 mL/s fluid over 2 s after 30 s simulation time, repeat this every 30 s	20 mL/s for 2 s every 30 s after 15 s simulation time
44	Design of Experiments	190	150	Uniform, 50-200 µm, injected in	300	5	69.3	All probes	1,000,000 particles at 5s, then injection of 100,000 particles	20 mL/s for 2 s every 30 s after 15 s simulation time

									and 10 mL/s fluid over 2 s after 30 s simulation time, repeat this every 30 s	
45	Design of Experiments	190	150	Uniform, 50-200 μm, injected in	300	15	69.3	All probes	1,000,000 particles at 5s, then injection of 100,000 particles and 10 mL/s fluid over 2 s after 30 s simulation time, repeat this every 30 s	20 mL/s for 2 s every 30 s after 15 s simulation time

8.3   Results and Discussion

There are four sections of simulation results presented and analysed in this section of Chapter 8; they are:

- Lattice density analysis
- Initial simulations
- Multiple withdrawal simulations
- Design of experiment simulations

The first three sections cover the results that were important in the development of the simulation process to be able to construct the design of experiments. The purpose of the DoE results is to optimise the equipment configuration in order to maximise particle withdrawal and increase how representative the withdrawal is of particles in the system.

8.3.1   Lattice Density Analysis

As discussed in Section 8.2.5, the lattice density analysis is important to ensure that the number of calculation points does not limit the accuracy of the results in the system. Lattice density analysis is also useful as after a certain number of lattice points the results are consistent and increasing the lattice density will not provide further clarity but will increase computation time.

Figure 8-12 shows that increasing the number of lattice points in the system will result in an exponential increase in the computation time for a 30 s simulation. An increase in lattice density from 125 to 150 causes the simulation time to double.
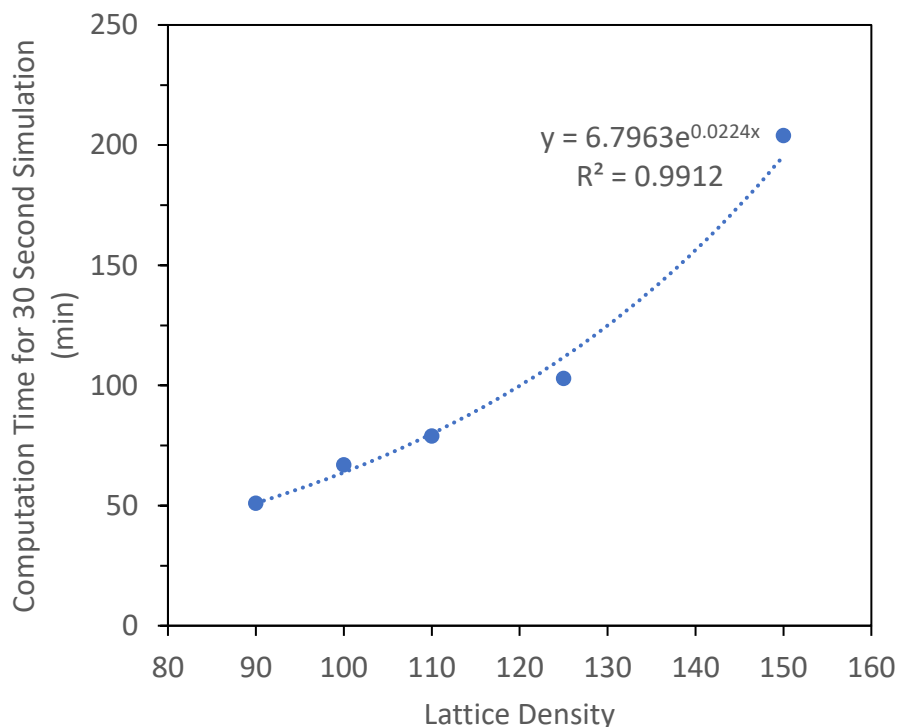
Figure 8-12 Influence of lattice density on computation time for a 30 s simulation

The fluid velocity for the system at varying lattice densities is in Figure 8-13. From this, it is possible to see that there are minimal fluctuations in the values of minimum fluid mean velocity. The results for maximum fluid mean velocity do show more variation than the minimum.
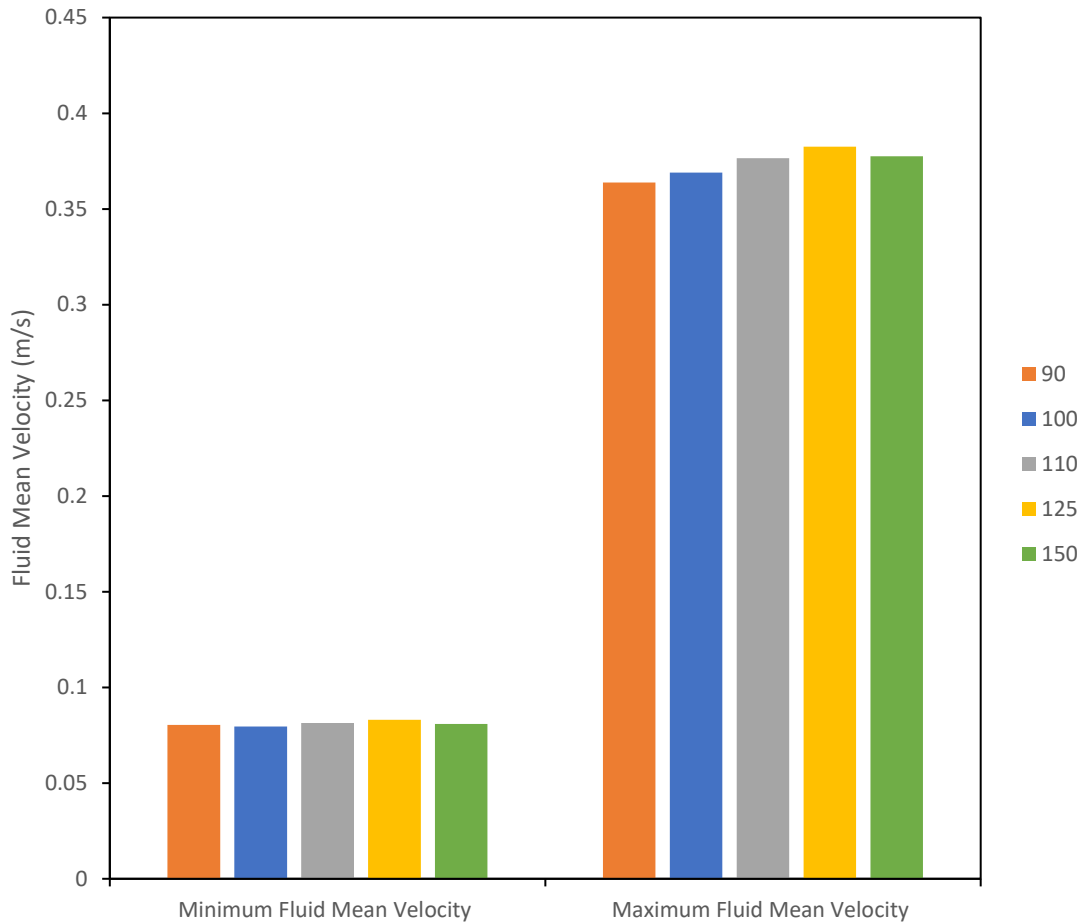
Figure 8-13 Minimum and maximum fluid mean velocity in the tank at varied lattice densities

From Figure 8-13, the percentage difference for both minimum and maximum mean fluid velocity is less than 5 % for all values of lattice density tested. The results were also consistent for the particle properties, the particle results can be seen in Appendix D. Future simulations utilise a lattice density of 100 due to the minimal difference in values and the shorter computation time. An error occurred for complex simulations with a lattice density of 100, with particles falling out of the reactor (Figure 8-11). To eliminate this error, the DoE simulations had an increased lattice density of 150.

8.3.2 Initial Simulations
The initial simulations conducted determined whether the geometry allowed for suspension of particles in the system. As discussed in Section 8.2.6, simulations performed used two main variations to the particle size. One set of simulations were conducted with the uniform particle size distribution shown in Figure 8-4 and others were simulated with only monosized particles, ranging from 50 μm to 300 μm.

Figure 8-14 shows the number of particles in the various regions of the tank (refer to Figure 8-7 for tank regions). In Figure 8-14, more particles settle towards the bottom of the tank over time. Between 30 s and 60 s of simulation time, over 10,000 particles sink to the bottom region of the tank (0-1 cm). The particle insertion into the system occurs at 5 s and the particles are entrained into the flow by 10 s simulation time. After 10 s simulation time, all of the other regions in the tank face a steady decrease in particle count with the 10-11 cm region having the fewest particles present.
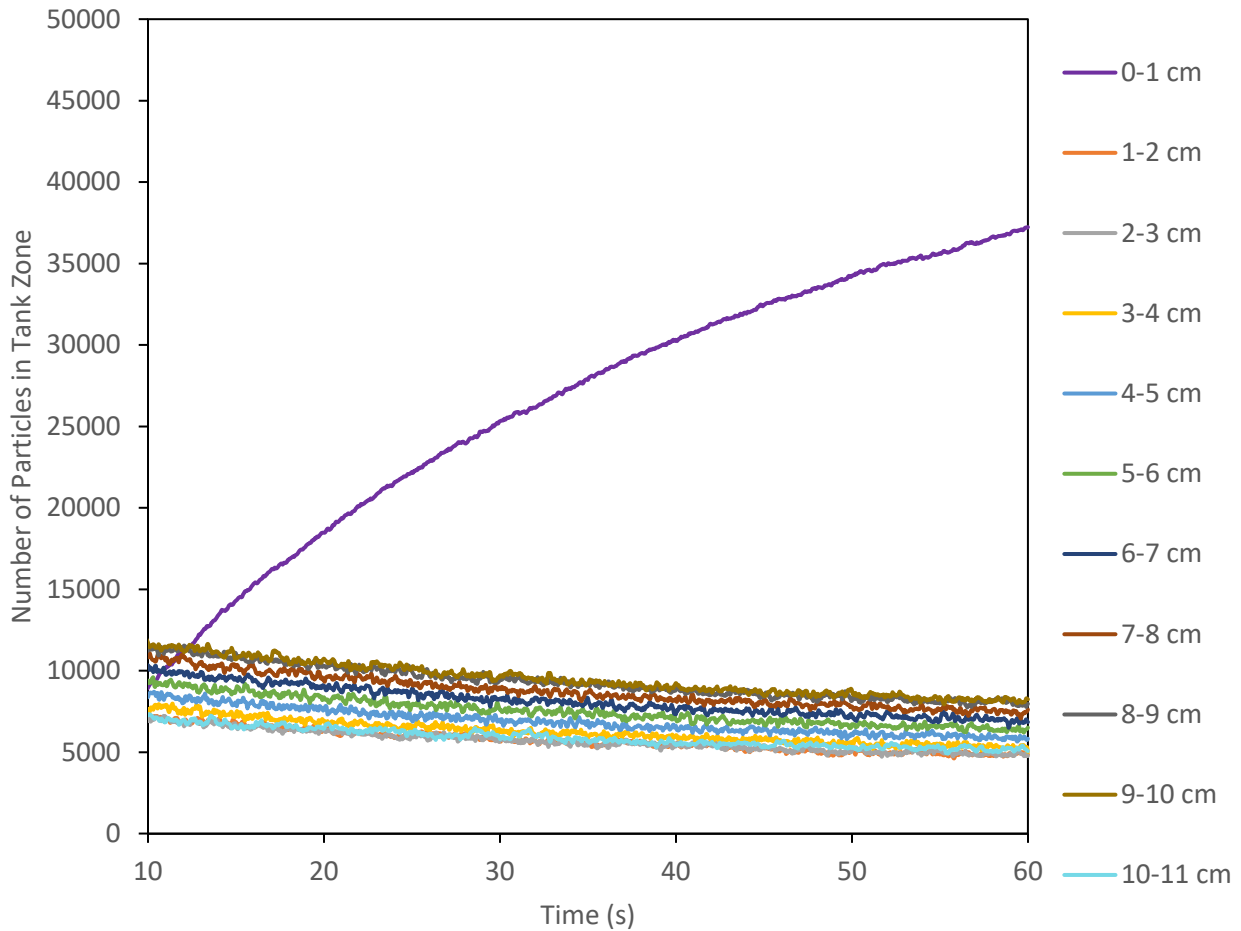
Figure 8-14 Number of particles in vertical regions of the stirred tank

Figure 8-15 shows a plot of the mean particle diameter in various vertical tank regions (Figure 8-7) against simulation time. This allows for an investigation into the relationship between particle settling and the size of the particles. As the particle diameter in the bottom of the tank, region 0-1 cm, is the highest, it does suggest that particles with larger diameters settle more readily. Impeller configuration will influence particle settling behaviours. For the uniform particle size distribution, the mean particle diameter for a well-suspended system for the various regions would be 125 μm as this would be the mean particle size of the inserted particles.
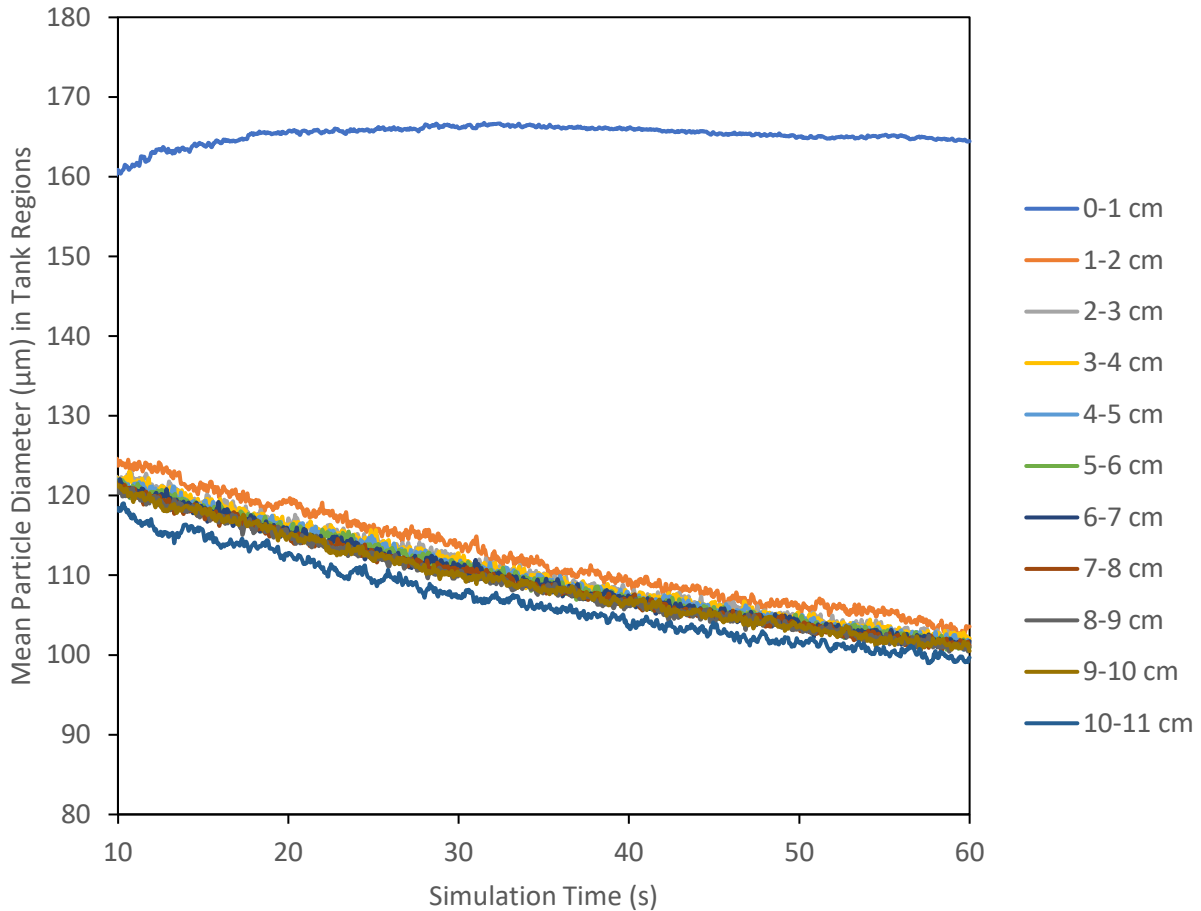
Figure 8-15 Mean particle diameter in various regions in the tank over the course of the simulation time

8.3.2.2 *Monosized Particle Suspension*

The results in Figure 8-15 suggest larger particle diameters are more likely to settle to the bottom of the tank. Construction of monosized simulations allowed for investigation into the influence of particle diameter on settling in the stirred tank. Figure 8-16 shows the number of particles in each vertical reactor height (Figure 8-7) for each simulation with monosized particles.

In the stirred tank system, there is a change in suspension behaviour for particles that are greater than 130 μm. In Figure 8-16, particle sizes of 135 μm and above the greatest number of particles is in the 0-1 cm region at the bottom of the tank. For particle sizes of 200 μm, 250 μm and 300 μm, all of the particles were in the bottom 2 cm of the tank. From Figure 8-17, there was some variation between the smaller particle sizes. In the simulations that have particle diameters under 100 μm, very few particles have settled to the bottom region of the tank in 60s, with approximately 3 times as many particles settling to the bottom region for particle sizes between 100 μm and 130 μm.
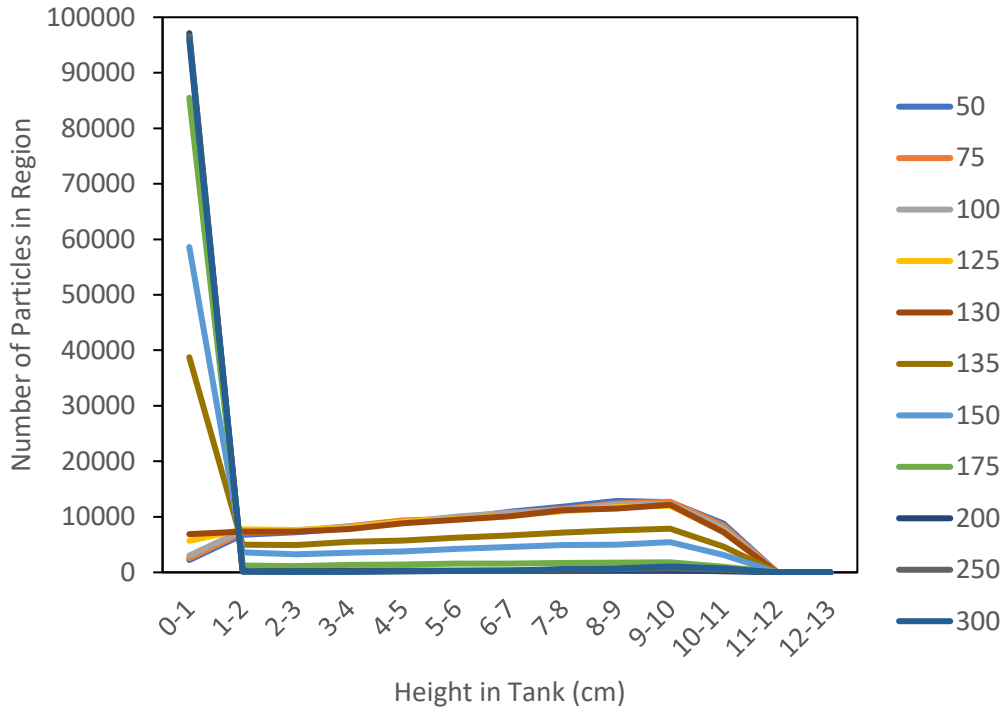
Figure 8-16 Suspension of monosized particles in various reactor zones after 60 s simulation time
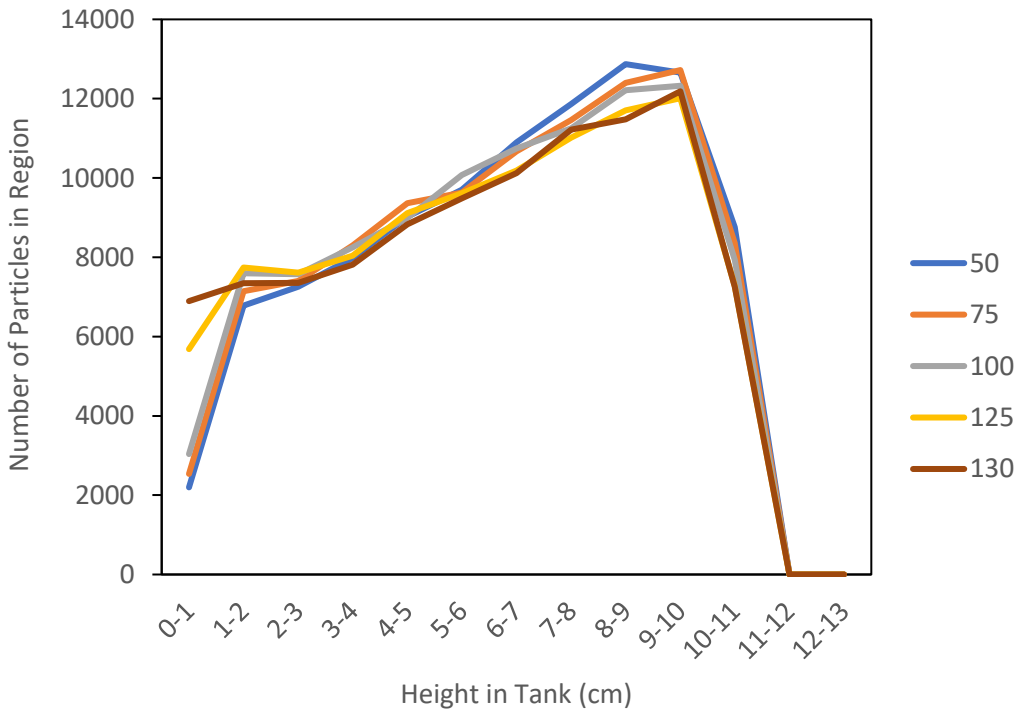
Figure 8-17 Suspension of monosized particles that are under 130 μm

197
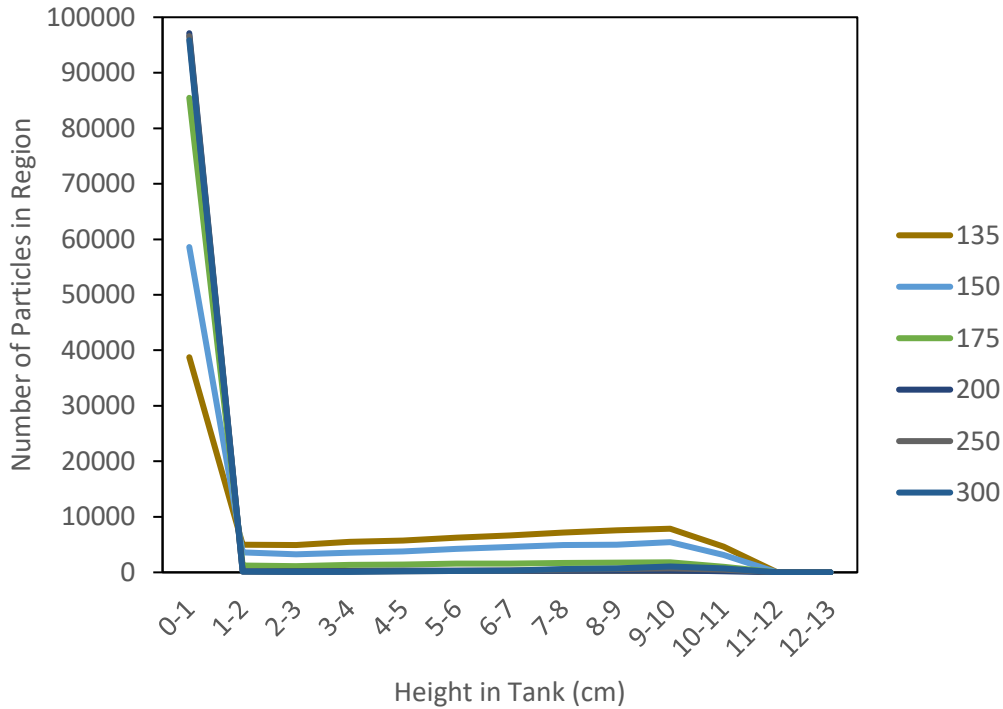
Figure 8-18 Suspension of particles 135 μm and above in the 60 s monosized particle simulations

In Figure 8-18, there is a difference in suspension characteristics at sizes of 175 μm and above. For the particles of 135 μm and 150 μm, the largest number of particles are in the bottom region of the tank, but there are over 5,000 particles in each of the other regions suggesting that although the system is not well suspended, there are some particles entrained in the flow pattern induced by the impeller. When the particles are 175 μm or greater there is very little suspension of the particles, with over 85 % of them having sank to the bottom of the stirred tank. Due to the lack of suspension of particles that are 175 μm or larger, it is expected that these sizes will have limited presence in the withdrawn particle data.

8.3.3   Multiple Withdrawal System

To increase the number of withdrawal results for each simulation, simulations performed contained multiple scaled withdrawals, resulting in a withdrawal every 30 seconds. For these simulations, the particle size distribution shown in Figure 8-4 was suspended. Figure 8-19 shows the suspension of particles in the tank over the 180 s simulation time, whilst the multiple withdrawals and inlets were occurring. The number of particles in the tank increases over the course of the simulation time. This suggests that the number of particles withdrawn from the system is much lower than the expected value of 10 % based on the description in Section 8.1.

The largest number of particles in the tank are in the bottom region (0-1 cm of the tank) and this increases over time suggesting particle settling. This increase in number of particles settling over time may be due to more particles entering the system. There is also the possibility that the velocity of the inlet may act as a jet that pushes the particles further down the tank.
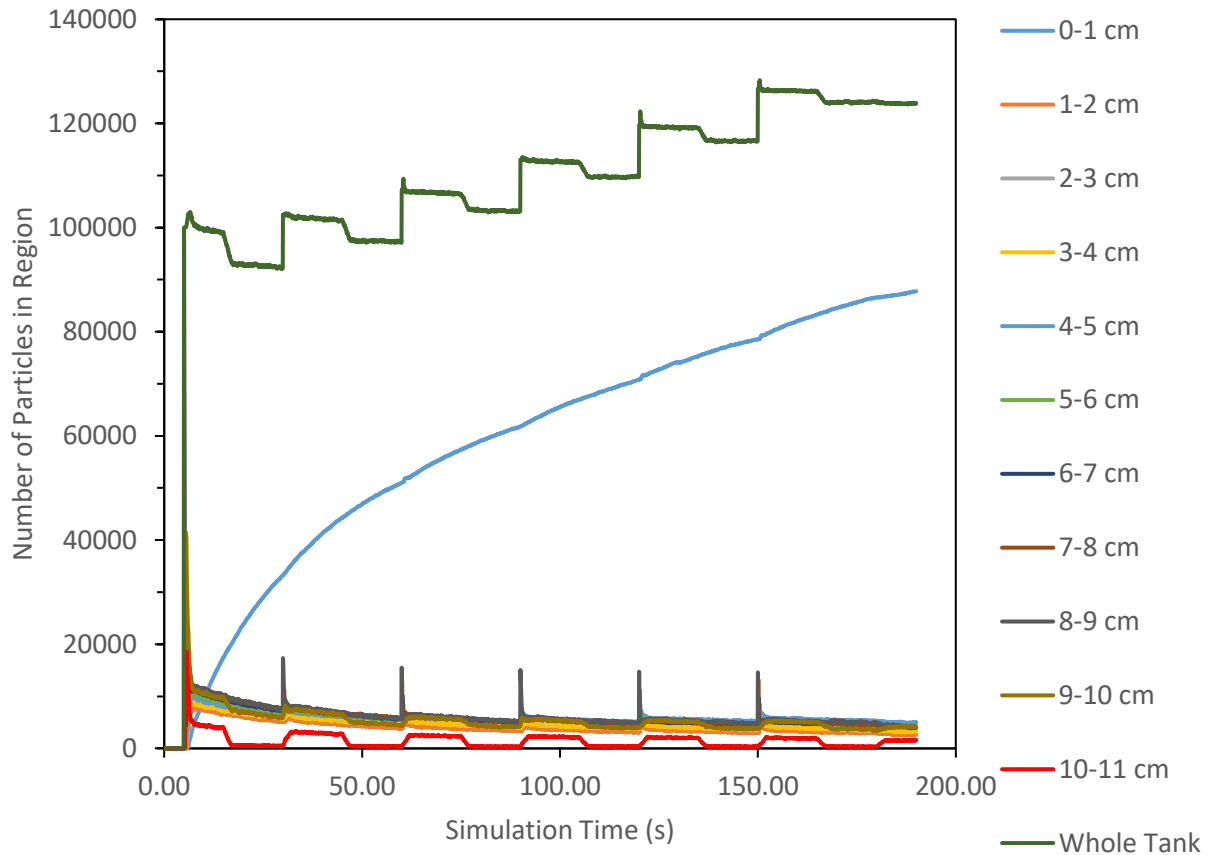
Figure 8-19 Number of particles in various regions of the tank over the simulation time when there are multiple withdrawals and inlets

Figure 8-20 has similar results to Figure 8-15, which showed the mean particle diameter in different tank regions for a 60 s simulation time, without withdrawals. In both Figure 8-20 and Figure 8-15, the bottom of the tank has the largest mean particle diameter. This is due to the larger particles settling more readily to the bottom of the tank compared to smaller particles, as was seen in the monosized particle suspension, shown in Section 8.3.2.2.

The larger particles settling to the bottom of the tank also explains why the mean particle diameter for the higher zones in the tank is much lower than expected. The mean diameters for the higher regions in Figure 8-20 are lower than the higher regions in Figure 8-15. This may be due to the simulation time for the results in Figure 8-20 being 180 s compared to the 60 s simulation time for Figure 8-15, meaning that the particles have a longer time to settle towards the bottom of the tank. Another reason for the difference in mean particle diameter could be that the results in Figure 8-20 are from simulations with multiple withdrawals and inlets, but there were no withdrawals or inlets occurring during the simulation for Figure 8-15. The velocity involved in injecting new particles and fluid into the system may act as a jet and push the larger particles towards the bottom of the tank, promoting settling and the discrepancy in mean diameter throughout the tank.
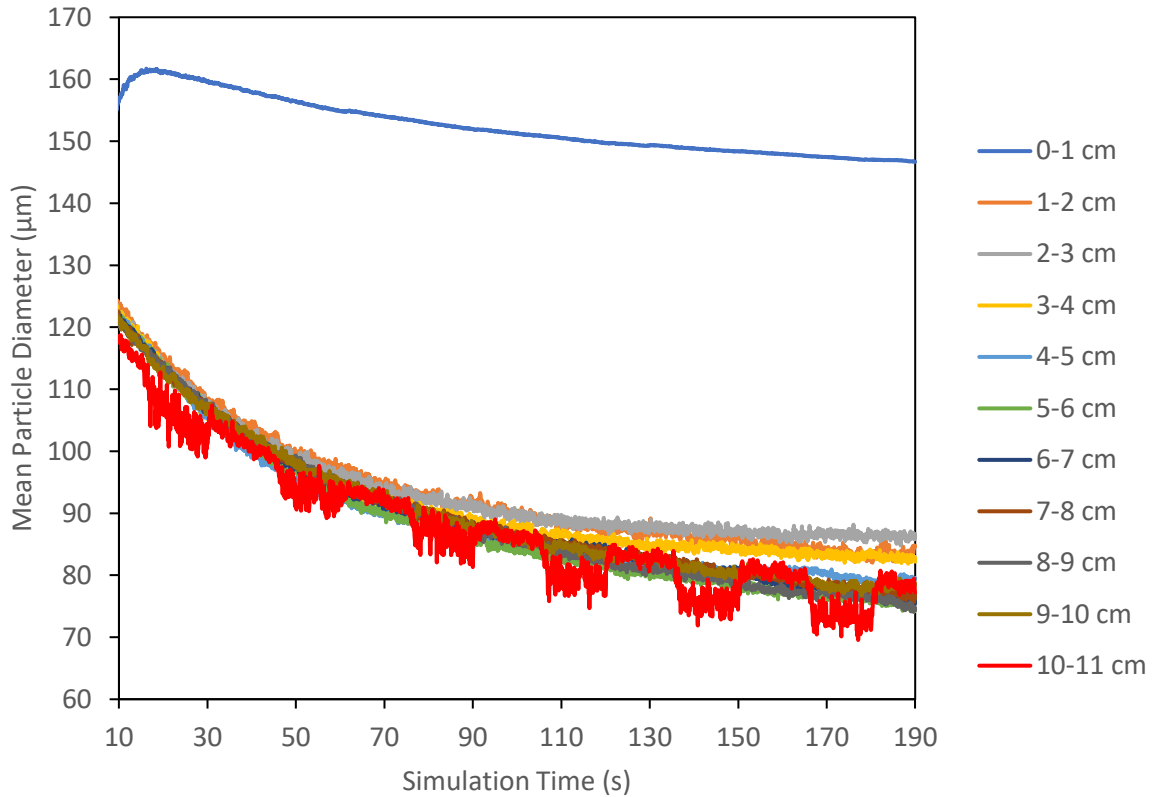
Figure 8-20 Mean particle diameter in various tank regions over time when there are multiple withdrawals and inlets

As the larger particles are more likely to settle at the bottom of the tank it seems likely that there will be fewer large particles present in the withdrawals from the system. Figure 8-21 shows the particle size distribution by number of particles withdrawn from the tank.

In Figure 8-21 it can be seen that for particles under 100 µm are well represented in the withdrawal. For particles over this size there are still some exiting the system, however this is a lot fewer than expected. The largest particle sizes in the system have the fewest number of particles exiting the tank through the dip tube outlet. This is expected as the majority of these particles have settled towards the bottom of the tank. From the monosized, simulations shown in Figure 8-18, over 80 % of the particles had settled to the bottom of the tank when the particle size was greater than 175 µm.
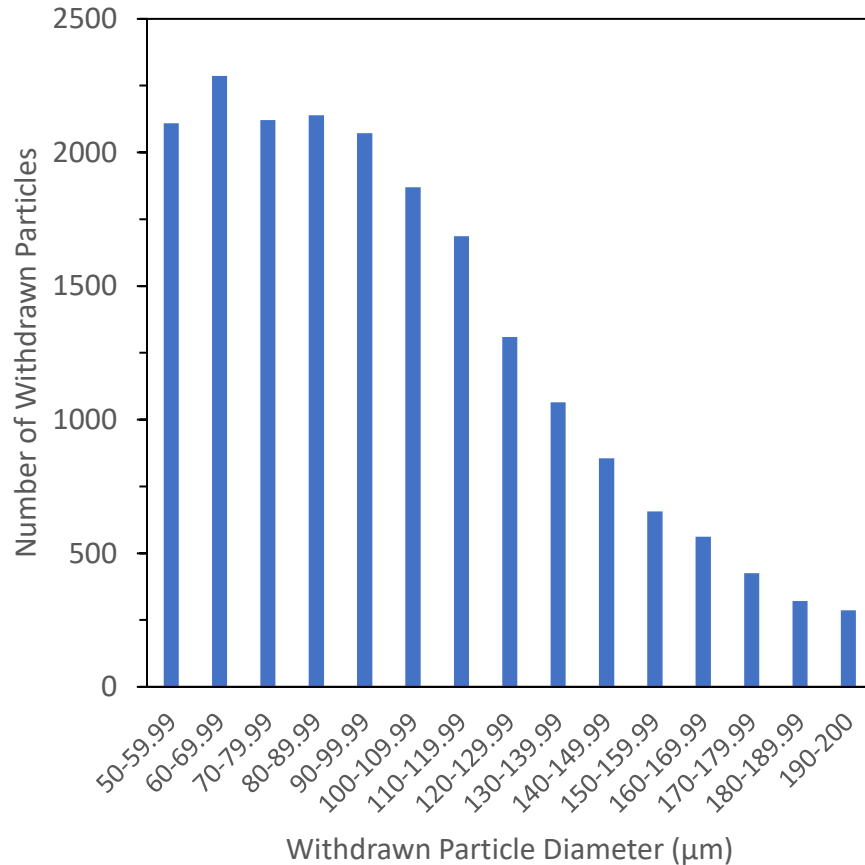
Figure 8-21 Diameter of withdrawn particles when there are multiple withdrawals and inlets

The monosized simulations showed that there was a clear divide in the settling behaviour of different particle sizes. Particles under 130 μm were relatively well suspended and the smallest portion of particles for these sizes had settled to the bottom of the tank. For particles that are between 130 μm and 175 μm a large portion of the particles do settle towards the bottom of the tank but the majority of the particles are still entrained in the impeller flow and are suspended. Particles larger than 175 μm are not well suspended and readily settled towards the bottom of the tank. The reduced suspension of large particles limits the number that reach the outlet and are withdrawn from the system.

8.3.4   Design of Experiments Simulations

The DoE aims to maximise the number of withdrawn particles and increase how representative of the initial PSD the withdrawn particle distribution is. Section 8.3.4.2 discusses increasing the number of particles withdrawn and Section 8.3.4.3 discusses how to increase the representative nature of the withdrawal. Design Expert ® used simulation results to produce predictions stirred tank designs that would improve particle withdrawal.

8.3.4.1   *Running central points to reduce the number of simulations*

This work used a central composite DoE as consistency in two simulations of the central point runs (simulations 15 to 19 in Table 8-12) allows for the elimination of other central point runs. To investigate

whether the central point simulations are consistent, reducing the number of necessary simulations, a plot of withdrawn particle sizes for two runs of the central point simulations, shown in Figure 8-22.

From Figure 8-22 the number of withdrawn particles is very similar for most sizes, with minor fluctuations. For every size interval, the number of particles removed from the simulation were within a percentage difference of 1%. This difference is considered negligible, therefore; reducing the number of simulations needed to 16.
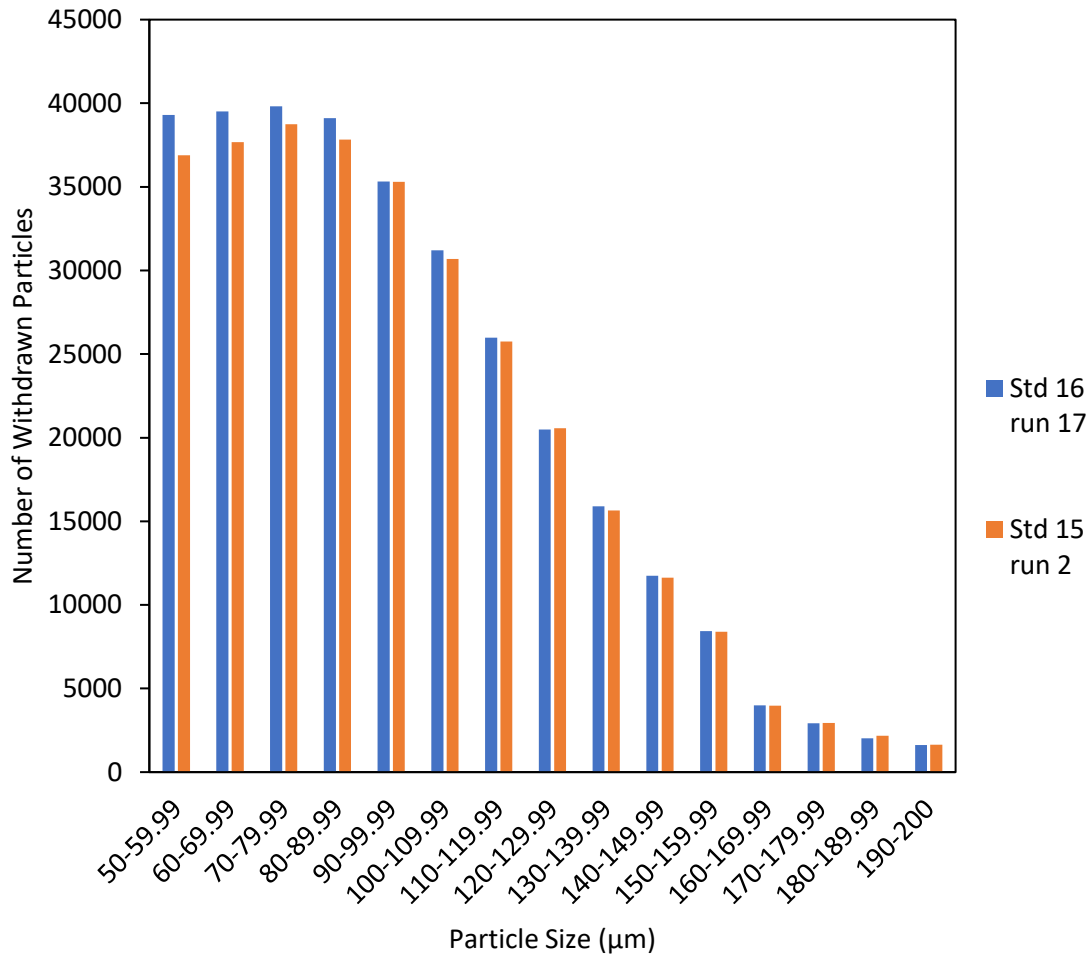
Figure 8-22 Number and diameter of particles withdrawn from the central point simulations

8.3.4.2 *Maximising Number of Particles Withdrawn*

Increasing the number of particles withdrawn from the system through a parametric CFD study was one aim of this research. The equipment parameters matched the values specified in the DoE shown in Table 8-12. There were 16 simulations needed due to two runs of the central point being consistent in Section 8.3.4.1. The number of particles withdrawn for the DoE simulations are in Figure 8-23.

From Figure 8-23 the DoE simulations resulted in a wide variety of particle removal numbers. Simulation 8 had the lowest number of particles withdrawn with 168,841 particles removed. Simulation 3 resulted in the greatest number of withdrawn particles, with 515,418 particles removed from the system. The total number of particles removed, as well as the equipment configuration specified in the DoE are in Table 8-14.

Approximately 350,000 more particles were withdrawn in simulation 3 than simulation 8. These two simulations had the same impeller speed of 330 rpm, which is on the higher end of the simulated impeller speed range (250 – 350). There were two differences in the simulated conditions, simulation 3 had a smaller impeller diameter and clearance, with a diameter of 64.70 mm and a clearance of 7 mm compared to simulation 8 having an impeller diameter of 73.88 mm and a clearance of 13 mm. The smaller impeller diameter with a lower clearance will be able to sit closer to the bottom of the tank and agitate the particles that were beginning to settle to the bottom of the tank. Once particles become entrained in the impeller flow pattern, they will be well suspended and therefore more able to be withdrawn from the tank.

Simulation 8, which had the lowest number of withdrawn particles, had a large impeller diameter, a high speed and a high clearance. When comparing this with simulation 7 it becomes apparent that a smaller impeller diameter is favoured for this system. This can be inferred due to simulation 7 having the same impeller speed and clearance as simulation 8, but it has a lower impeller diameter of 64.7 mm. This change results in an increased particle removal rate of 472,667.

Reducing the impeller diameter also had a positive impact at lower impeller speeds. In simulation 5 and simulation 6 there is consistency in the impeller clearance, with a value of 13 mm for both systems; they are also both agitated at a speed of 270 rpm. In simulation 6, which has an impeller diameter of 73.88 mm, there are 287,920 particles removed from the system. Simulation 5 has a smaller impeller diameter of 64.7 mm but the number of removed particles increased to 328,115. Reducing the diameter will result in an increase in withdrawn particles due to the smaller impeller diameter having a greater amount of distance from the wall. The distance between the blades and the wall will promote upflow of the particles, resulting in a greater number of them being suspended and therefore able to enter the withdrawal dip tube.

Simulation 7 resulted in the second highest number of particles removed from the system during the withdrawals. The simulation with the largest number of withdrawn particles was simulation 3. This simulation resulted in 515,418 particles removed through the six simulated withdrawals. Simulation 3 has a lower clearance than simulation 7. Both simulations have the smaller impeller diameter of 64.7 mm, and a high impeller speed of 330 rpm. For smaller impeller diameters the increasing clearance reduces the number of particles withdrawn as many particles will sink lower into the tank and the smaller diameter has less power than the larger impeller to be able to cause particles that are much lower than the impeller to become entrained in the flow pattern (Gao et al., 2021). The increased suspension rate results in a greater number of particles withdrawn from the system.
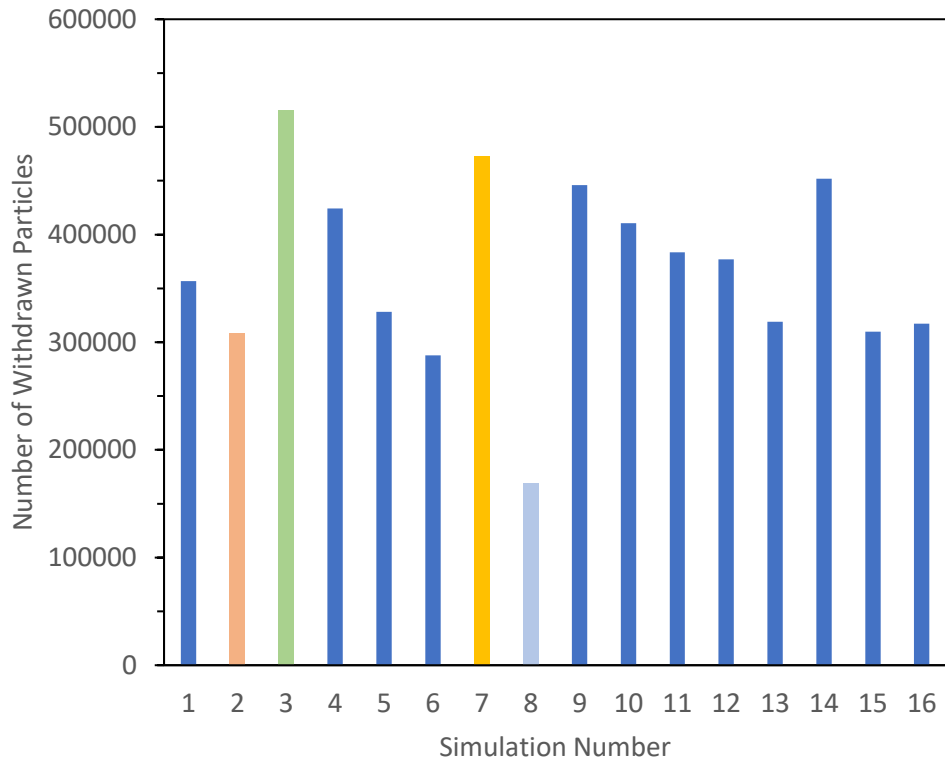
Figure 8-23 Number of particles removed in the 16 simulations performed for the DoE

Table 8-14 Number of particles removed for the DoE with the reactor conditions specified

Simulation Number	Number of Particles Removed	Impeller Diameter (mm)	Impeller Speed (rpm)	Impeller Clearance (mm)
1	356,879	64.7	270	7
2	308,441	73.9	270	7
3	515,418	64.7	330	7
4	424,085	73.9	330	7
5	328,115	64.7	270	13
6	287,920	73.9	270	13
7	472,667	64.7	330	13
8	168,841	73.9	330	13
9	445,787	61.6	300	10
10	410,686	77.0	300	10
11	383,471	69.3	250	10
12	376,964	69.3	350	10
13	319,018	69.3	300	5
14	451,777	69.3	300	15
15	309,839	69.3	300	10
16	317,326	69.3	300	10

Figure 8-24 shows a cubic plot obtained by inputting the data into the Design Expert software. This figure shows a predicted number of particles removed during the withdrawals at varying reactor conditions. The lowest predicted number of withdrawn particles is 141,550. The conditions that would obtain this result are the lowest values for impeller diameter, impeller speed, and impeller clearance. For the range of points that were tested, this simulation would occur with an impeller diameter of 61.6 mm, an impeller speed of 250 rpm and an impeller clearance of 5 mm.

For a smaller impeller diameter with low clearance, the impeller speed is the most important factor in determining how well suspended the particles are, based on the results shown in Figure 8-24. The simulation with the highest number of particles removed, 605,269, has the same impeller diameter and clearance as the simulation with the lowest number of particles removed; but, the impeller speed is 350 rpm which is the maximum of the range that was tested.
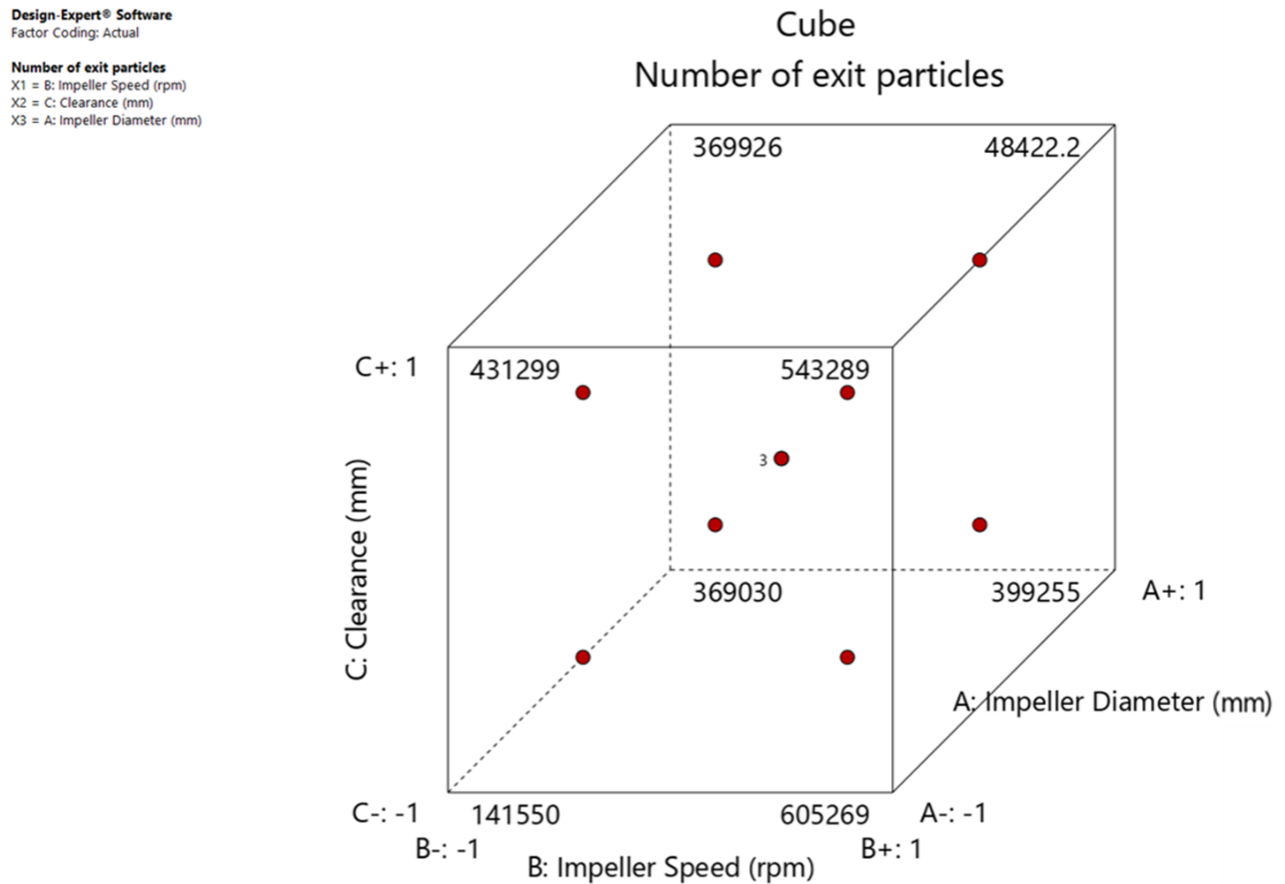
Figure 8-24 Cubic DoE result to from Design Expert for maximising the number of withdrawn particles

For larger impeller diameters, it is preferable to have both a high impeller speed and a high clearance, although for this condition the impeller speed is the driving force for increased particle withdrawal. Table 8-15 shows the number of withdrawn particles for the different simulation conditions used for the DoE.

Table 8-15 Predicted number of particles removed at the corner points of the DoE cubic results shown in Figure 8-24

Impeller Diameter (mm)	Impeller Speed (rpm)	Impeller Clearance (mm)	Number of Exit Particles
77	350	5	399,255
77	350	15	484,222
61.6	350	5	605,269
61.6	350	15	543,289
77	250	5	369,030
77	250	15	369,926
61.6	250	5	141,550
61.6	250	15	431,299

From the DoE predictions in Table 8-15, a small diameter with a high speed and low clearance results in the greatest number of particles removed from the system. CFD simulations of this condition would investigate the accuracy of the prediction. If the prediction and simulation match, then this would be a good candidate for experimental validation. The confirmation simulations and experimental validation were outside of the scope of the research conducted during the industrial placement.

8.3.4.3 *Increasing Representation of Primary Particle Size in Withdrawn PSD*

The simulations also aimed to ensure that the withdrawal of the particles was representative of the particles that are present in the tank. This was done because the simulations were based on tank C in Figure 8-1; this tank contains the product of the crystallisation and it is important to ensure that all sizes of the product will be removed from the system. The particles inserted into the system were of a uniform size distribution and were in the size range of 50 μm to 200 μm. A uniform distribution was chosen, as this would result in the withdrawn particles also having a uniform distribution. Figure 8-25 shows what a cumulative size distribution of the withdrawn particles would look like if the withdrawal was fully representative of the injected particle distribution.
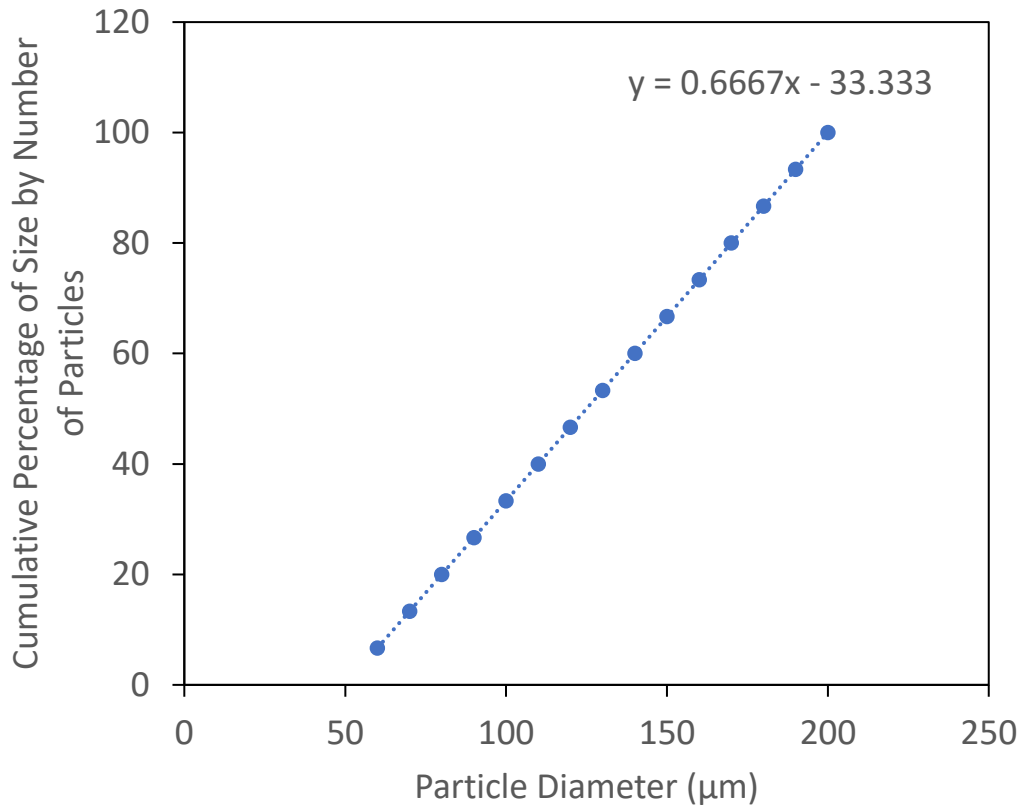
Figure 8-25 Cumulative number of withdrawn particles for a fully representative particle withdrawal, used for comparison with DoE results

To analyse the DoE simulations, a plot of the withdrawn particles cumulative PSD with a linear trendline was plotted in Microsoft Excel. The gradient of the line was used as optimisation input in Design Expert with the objective to produce a simulation condition that would give results as close to the line gradient for the fully presentative withdrawal in Figure 8-25. A selection of cumulative percentage of size by number of particle simulation results, shown in Figure 8-26. The chosen values are the same simulations as the highlighted values in Figure 8-23 which showed the number of particles removed for the simulations performed as part of the DoE. The cumulative PSD for all 16 of the simulations are in in Appendix D. Figure 8-26 shows that there are simulations that have results that are similar to the idealised representative withdrawal results.

In Figure 8-26 the result for simulation 2 has a non-linear shape whereas simulations 3, 7, and 8 have increased linearity. The difference in linearity of the plotted points is demonstrated by the R^2 value calculated for the trendline. Table 8-16 shows the simulation parameters, the number of withdrawn particles, the linear trendline equation, and the R^2 values for all of the DoE simulations.
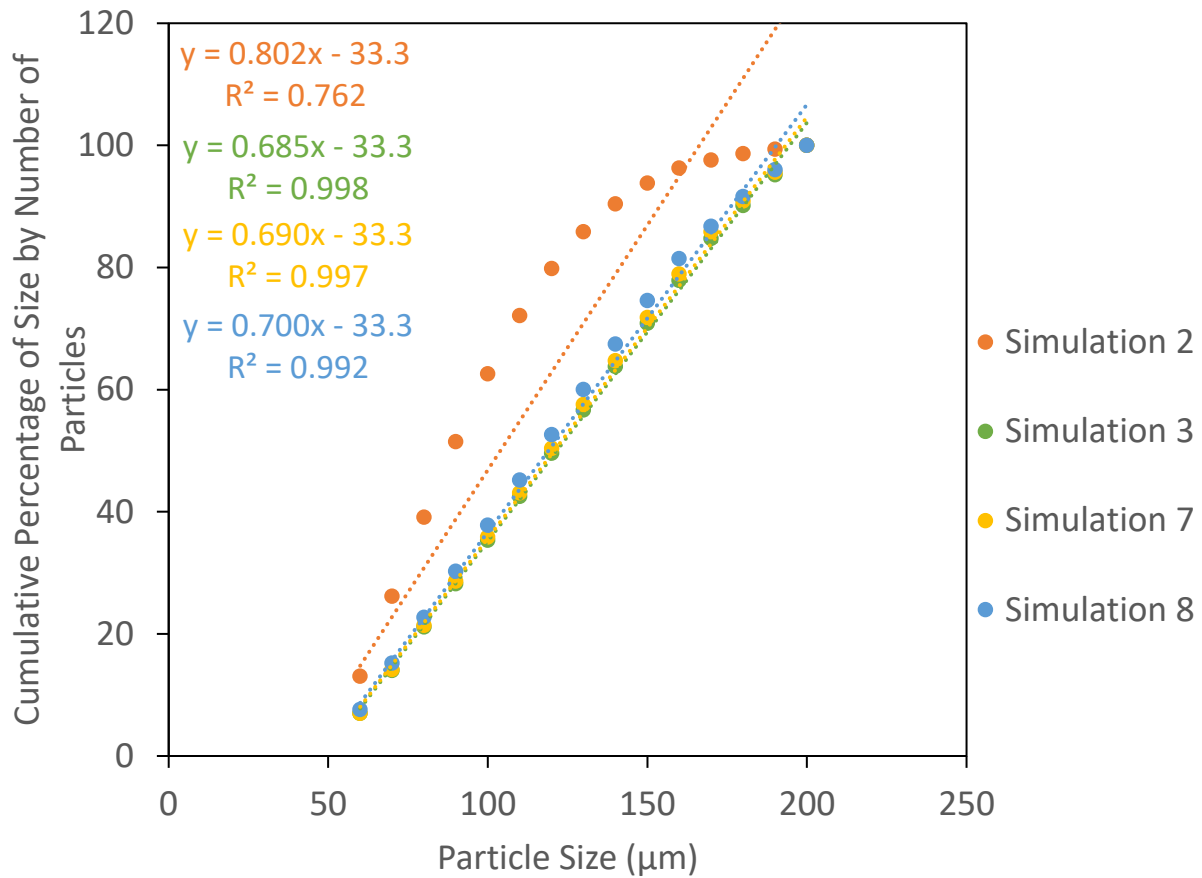
Figure 8-26 Cumulative percentage PSD for selected DoE results; these results were selected to compare with the highlighted results in Section 8.3.4.2, which discussed maximising the number of withdrawn particles

The withdrawn particles from simulation 8 follow a linear trend and has a fairly representative withdrawal. The equation of the line is close to the one for representative withdrawal shown in Figure 8-25 and it has an R^2 value that is very close to 1. However, the number of particles withdrawn is the lowest of all of the simulations, suggesting that this is not an optimal configuration for the system.

From Table 8-16 there appears to be less of a clear pattern of how the reactor conditions influence the representative nature of the particle withdrawal in comparison to how the impeller properties increase the number of particles withdrawn from a system.

Simulation 10 has the equation closest to the equation for the representative graph. For this system, there is an impeller diameter of 77 mm, an impeller speed of 300 rpm and an impeller clearance of 10 mm. These conditions also resulted in 410,686 particles withdrawn from the system. From the DoE, this system has the largest diameter but the midpoint values for impeller speed and clearance.

Table 8-16 Results of the cumulative PSD linear trendline for the DoE simulations

Simulation Number	Predicted Number of Particles Removed	Impeller Diameter (mm)	Impeller Speed (rpm)	Impeller Clearance (mm)	Trendline Equation	R^2 Value
1	356,879	64.7	270	7	y=0.797x-33.3	0.793
2	308,441	73.9	270	7	y=0.802x-33.3	0.762
3	515,418	64.7	330	7	y-0.685x-33.3	0.998
4	424,085	73.9	330	7	y=0.701x-33. 3	0.990
5	328,115	64.7	270	13	y=0.8x-33. 3	0.778
6	287,920	73.9	270	13	y=0.795x-33. 3	0.813
7	472,667	64.7	330	13	y=0.690x=33. 3	0.997
8	168,841	73.9	330	13	y=0.7x-33.3	0.992
9	445,787	61.6	300	10	y=0.758x-33.3	0.934
10	410,686	77.0	300	10	y=0.683-33.3	0.997
11	383,471	69.3	250	10	y=0.779x-33.3	0.866
12	376,964	69.3	350	10	y=0.684x-33.3	0.998
13	319,018	69.3	300	5	y=0.796x-33.3	0.791
14	451,777	69.3	300	15	y=0.711x-33.3	0.986
15	309,839	69.3	300	10	y=0.797x-33.3	0.802
16	317,326	69.3	300	10	y=0.799x-33.3	0.791

The DoE simulation condition that increased the number of particles removed from the system was simulation 3. In simulation 3, the diameter is 64.7 mm, the impeller speed is 330 rpm and the clearance is 7 mm. These conditions resulted in 515,418 particles removed. Simulation 3 also had a fairly representative withdrawal; this can be seen in Figure 8-26, and Table 8-16. For simulation 3, the gradient is 0.6853 with an R^2 value of 0.9979. This shows that the simulation cumulative distribution is close to the optimal cumulative distribution.

Predictions from Design Expert ® suggest that a small impeller diameter, rotating at a high impeller speed will increase both the number of particles removed, as well as the representation of the initial PSD within the withdrawal. A lower clearance favours particle removal, whereas a higher clearance favours PSD representation. This will be useful for designing crystallisation processes with particles that readily settle to the bottom of the tank. From this research the settled particles are better suspended, and therefore, more represented in the withdrawn PSD, with a small diameter, high speed, and higher value of impeller clearance. Experiments with those parameters will increase the consistency between the withdrawn PSD and the particles in the tank.

Figure 8-27 is a cubic DoE result that produced by Design Expert. From this figure, it is apparent that the higher impeller speed results in gradients that are close to the optimal representative withdrawal. From the 16 simulations that were conducted, 11 of them were with impeller speeds of 300 rpm and above, and eight of these simulations had a gradient between 0.68 and 0.76 with an R^2 value greater than 0.93. This suggests that the higher impeller speeds do increase the suspension of particles of all sizes in the

distribution, resulting in an increase in how representative the withdrawn PSD is. Impeller diameter and clearance seem to have less of an influence for the representative nature of the particle withdrawal.
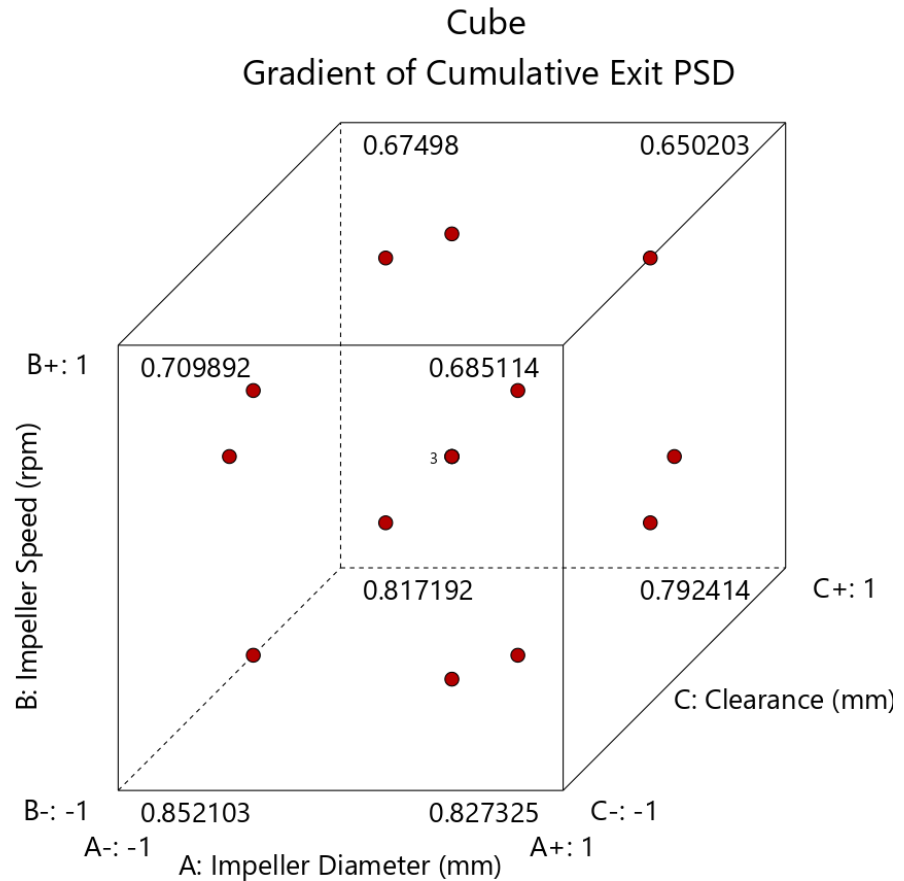
Figure 8-27 Cubic DoE result for optimising the representative nature of the withdrawn particles

From Figure 8-27, two conditions may result in the optimal representation in the withdrawn PSD. The first simulation would give a gradient of 0.67498. The reactor configuration would have an impeller diameter of 61.6 mm, an impeller speed of 350 rpm, and an impeller clearance of 15 mm. From Table 8-15 this condition also predicts a large number of particles withdrawn. The other option of simulation would result in a gradient of 0.650203. In this simulation, there would be an impeller speed of 350 rpm, an impeller diameter of 77 mm and an impeller clearance of 15 mm. The predicted withdrawal value from Design Expert, shown in Table 8-15, is 484,222. As these values are predictions from the DoE software, it would be beneficial to run simulations with these conditions to determine how accurate the predictions are. Experimental validation would also increase confidence in the CFD predictions; however, this fell out of the scope of the industrial placement research.

8.4 Conclusion

During this work, CFD simulations performed with the aim of improving product removal from a series of stirred tanks used for crystallisation. Performed simulations investigated the influence of impeller diameter, impeller speed and impeller clearance. The selected investigation parameters alter the flow

characteristics, mixing, and particle suspension in spherical agglomeration research, shown in Chapter 4, Chapter 5, Chapter 6 and Chapter 7.

The results from the monosized investigations were expected as they showed that the larger particles settle more readily, resulting in fewer of them in the withdrawn particles. Altering impeller geometry will influence flow patterns in the tank, increasing the number of larger particles suspended. A smaller impeller at a high speed and low clearance will increase the suspension of the particles that have sank towards the bottom of the tank over the course of the simulation. This is due to the low clearance for a smaller diameter impeller increasing the velocity underneath the impeller (Gao et al., 2021). The increased velocity will result in more particles becoming entrained in the flow, improving their suspension. As they are better suspended, they will be more likely to contact the outlet, leading to a larger number of particles withdrawn from the system.

Based on both the results of the performed simulations, and the predicted values produced by Design Expert ®, the equipment design that increased the number of particles removed from the system will have a small impeller diameter, a high impeller speed, and a low impeller clearance. With each withdrawal in the lab equipment, there are 10 % of the total number of particles removed with each withdrawal. For the CFD simulations, this would mean that there are 600,000 particles removed. The DoE simulation results all had lower numbers of removed particles than expected. The central composite design predicted a simulation that resulted in over 600,000 particles removed. This simulation had a small impeller diameter at a high speed and low clearance.

The other optimisation area was ensuring that the PSD at the outlet was representative of the PSD of the particles in the tank. The uniform distribution used for the CFD simulations helped identifying any particle sizes not represented at the outlet, as the withdrawn PSD should contain equal proportions of every particle size. Design Expert also suggests that a high impeller speed has the greatest influence on how representative the withdrawn PSD is, with the predicted gradients closest to 0.66 all being at the higher impeller speed. Interestingly, the small impeller diameter and high impeller speed were both in the optimal design to both maximise the number of particles withdrawn, and the representative nature of the withdrawn PSD. The difference in the predictions were for the impeller clearance. A lower impeller clearance favoured a greater number of particles withdrawn from the system, whilst the higher clearance improved the representation in the withdrawn PSD.

To increase the confidence in the DoE predictions, CFD simulations of the conditions that increased the number of withdrawn particles, and the uniformity of the withdrawal PSD should be performed. Experimental validation of these conditions would also increase the confidence in the CFD simulations. The experiments would use a small diameter impeller at high speed, with the clearance being either 5 mm or 15 mm.

Chapter 9 Conclusion and Future Work

9.1 Conclusion

The experimental study conducted as part of this work, shows that the impeller geometry is an important parameter in the formation of spherical agglomerates. It was determined from the work within this thesis that of the four impellers tested, there was a clear correlation between impeller power number and agglomeration. Against a criteria of consistent agglomerate size and shape, the impeller performance from best to worst was the Rushton turbine impeller, the flat blade impeller, the pitched blade impeller and then the propeller impeller. Decreased impeller power number resulted in a decrease of agglomerates within the desired size range, and reduced agglomerate sphericity. The relationship between impeller power number and performance was incorporated into the PBM using correlations by Furukawa et al., 2012.

As evidenced by the CFD simulations in both Chapter 5 and Chapter 8, as well as the experimental study in Chapter 4; clearance is an important parameter for suspension of solids. For the Rushton turbine, a lower clearance hinders the formation of the double loop flow pattern, resulting in a promotion of axial behaviour, this was evident in the experimental and CFD results for the Rushton turbine impeller as the agglomerate characteristics changed at C/D values of 0.3 and higher (Montante et al., 1999; Zhu et al., 2019). The clearance also influenced results for axial impellers. In Chapter 8 a custom pitched blade impeller was used for CFD studies into the suspension of crystalline material, in this work it was found that low clearances for small diameter impellers improved particle suspension at high speeds as this combination results in higher velocity underneath the impeller, preventing particles from settling to the bottom of the tank (Gao et al., 2021).

CFD simulations for the various impeller geometries used in the spherical agglomeration study showed expected flow patterns based on previously published literature. It was observed that at C/D ratio of 0.3 and above, a Rushton turbine impeller was able to form the double loop flow pattern that is expected of a radial impeller. For a flat blade impeller, increasing the clearance reduced the particle suspension in the tank. This has also been observed by Devarajulu and Loganathan, 2016. Utilising the velocity magnitude from the CFD simulations as a percentage of impeller tip speed allowed the influence of clearance to be incorporated into the PBM.

Generating predictive models for pharmaceutical applications is important as it will reduce the number of preliminary experiments needed to design a process. Reducing the number of exploratory experiments is beneficial to pharmaceutical companies as it means less material is used. This is advantageous as there is often a small amount of API manufactured initially. Another advantage that comes from the reduction of preliminary experiments is that less solvent is used when developing a spherical agglomeration process. Lowering the solvent requirements will increase the sustainability of the pharmaceutical development stage.

The PBM developed in this work does show alterations in particle size predictions with different impeller geometries, speeds, and clearances. This shows that incorporating power number and using the velocity fitting equations derived from the CFD simulations works to include flow characteristics in the PBM. From the experimental validation of the PBM, it is apparent that PBM predictions are less accurate with a pitched blade impeller due to the calculated power number being much lower than published values. The PBM developed in this work produced d_{43} values closer to the experimental studies than the PBM by

Ahmed et al., 2023 for 60 % of the simulations based on the experiments to investigate the influence of different impeller geometry, clearance, and speed on spherical agglomerate characteristics. This shows that incorporating flow characteristics has improved the PBM, however, there are still improvements to be made.

One factor in the PBM that needs to be carefully considered is the growth coefficient. The growth coefficient is a kinetic parameter that is found experimentally, and is system dependent (Arjmandi-Tash et al., 2019; Ahmed et al., 2023). For all PBM simulations, a value of 0.69 was used for the growth coefficient as it was the same material system. From the results, it appears that the growth coefficient needs to consider impeller properties and primary particle size. Incorporating these into a calculation for growth coefficient would increase the accuracy of the model and limit preliminary experiments.

9.2   Future Work

The following recommendations for future work would increase the validity and applicability of the spherical agglomeration PBM for various systems:

- Perform experiments with various particle shapes and solvent systems to compare to the PBM as spherical agglomeration would be most often used to improve micromeritic properties of needle-like crystals.

- Develop modified correlations based on the power number correlations in Furukawa et al., 2012 to improve the accuracy of power number for pitched blade and propeller impellers, as these are calculated to be much lower than expected values from literature.

- Run CFD simulations with varied particle sizes to determine if the velocity fit correlations are accurate for both primary material and very large agglomerates. The new fits can then be incorporated into the PBM.

- Design an experimental method to control and measure droplet size within the stirred tank. The PBM uses the bridging liquid droplet size to determine the nucleation mechanism, therefore, droplet control in an experimental system will increase the validity of the PBM predictions.

- Develop a mathematical model to predict the growth coefficient for different systems and process parameters to increase the applicability of the PBM.

- Perform further characterisation of the agglomerates produced with varied impeller geometries, speeds and clearances to determine the influence of mixing profiles on micromeritic properties such as hardness and porosity.

As spherical agglomeration is a relatively new topic for pharmaceutical applications compared with other processes such as high shear wet granulation (HSWG), there are other research avenues which would also be useful. As spherical agglomeration is mechanistically similar to HSWG, it can be assumed that the breakage mechanism occurs during the formation of spherical agglomerates. Breakage is an important mechanism to understand, however, it has not been thoroughly investigated for this process.

References

Abrahamsson, P.J., Kvist, P., Reynolds, G., Yu, X., Niklasson Björn, I., Hounslow, M.J. and Rasmuson, A. 2018. Analysis of mesoscale effects in high-shear granulation through a computational fluid dynamics–population balance coupled compartment model. *Particuology*. **36**, pp.1–12.

Ahmed, B., Arjmandi-Tash, O., Litster, J.D. and Smith, R.M. 2023. Mechanistic modelling of spherical agglomeration processes. *Powder Technology*. **417**.

Arjmandi-Tash, O., Tew, J.D., Pitt, K., Smith, R. and Litster, J.D. 2019. A new mathematical model for nucleation of spherical agglomerates by the immersion mechanism. *Chemical Engineering Science: X*. **4**, p.100048.

Avdeef, A., Fuguet, E., Llinàs, A., Ràfols, C., Bosch, E., Völgyi, G., Verbic, T., Boldyreva, E. and Takács-Novák, K. 2016. Equilibrium solubility measurement of ionizable drugs - consensus recommendations for improving data quality. *ADMET and DMPK*. **4**(2), pp.117–178.

Ayranci, I. and Kresta, S.M. 2014. Critical analysis of Zwietering correlation for solids suspension in stirred tanks. *Chemical Engineering Research and Design*. **92**(3), pp.413–422.

Bachmann, J., Woche, S.K., Goebel, M.O., Kirkham, M.B. and Horton, R. 2003. Extended methodology for determining wetting properties of porous media. *Water Resources Research*. **39**(12), pp.1–14.

Bandara, J.C., Thapa, R., Nielsen, H.K., Moldestad, B.M.E., Eikeland, M.S., Bandara, J.C., Thapa, R., Nielsen, H.K. and Britt, M.E. 2019. Circulating fluidized bed reactors – part 01 : analyzing the effect of particle modelling parameters in computational particle fluid dynamic (CPFD) simulation with experimental validation. *Particulate Science and Technology*., pp.1–14.

Beaudoin, M., Nilsson, H., Page, M., Magnan, R. and Jasak, H. 2014. Evaluation of an improved mixing plane interface for OpenFOAM. *IOP Conference Series: Earth and Environmental Science*.

Bellinghausen, S., Gavi, E., Jerke, L., Ghosh, P.K., Salman, A.D. and Litster, J.D. 2019. Nuclei size distribution modelling in wet granulation. *Chemical Engineering Science: X*. **4**, p.100038.

Bemer, G.G. 1979. Agglomeration in Suspension: a Study of Mechanisms and Kinetics. *Technische Hogeschool Delft, Afdeling der Werktuigbouwkunde (Report) WTHD*. (120).

Bezuglyi, B.A., Tarasov, O.A. and Fedorets, A.A. 2001. Modified Tilting-Plate Method for Measuring Contact Angles. *Colloid Journal*. **63**(6), pp.668–674.

Bharti, N., Bhandari, N., Sharma, P., Singh, K. and Kumar, A. 2013. Spherical Crystallization: A Novel Drug Delivery Approach. *Asian journal of biomedical & pharmaceutical sciences*. **3**(18), pp.10–16.

Biggs, C.A., Sanders, C., Scott, A.C., Willemse, A.W., Hoffman, A.C., Instone, T., Salman, A.D. and Hounslow, M.J. 2003. Coupling granule properties and granulation rates in high-shear granulation. *Powder Technology*. **130**, pp.162–168.

Blandin, A.F., Mangin, D., Rivoire, A., Klein, J.P. and Bossoutrot, J.M. 2003. Agglomeration in suspension of salicylic acid fine particles: Influence of some process parameters on kinetics and agglomerate final size. *Powder Technology*. **130**(1–3), pp.316–323.

Blandin, A.F., Mangin, D., Subero-Couroyer, C., Rivoire, A., Klein, J.P. and Bossoutrot, J.M. 2005. Modelling of agglomeration in suspension: Application to salicylic acid microparticles. *Powder Technology*. **156**(1), pp.19–33.

Briens, L. and Logan, R. 2011. The effect of the chopper on granules from wet high-shear granulation using a PMA-1 granulator. *AAPS PharmSciTech*. **12**(4), pp.1358–1365.

Byrne, F.P., Jin, S., Paggiola, G., Petchey, T.H.M., Clark, J.H., Farmer, T.J., Hunt, A.J., Robert McElroy, C. and Sherwood, J. 2016. Tools and techniques for solvent selection: green solvent selection guides. *Sustainable Chemical Processes*. **4**(1).

Campbell, G.A., Clancy, D.J., Zhang, J.X., Gupta, M.K. and Oh, C.K. 2011. Closing the gap in series scale up of high shear wet granulation process using impeller power and blade design. *Powder Technology*. **205**(1–3), pp.184–192.

Chadwick, K., Davey, R.J., Mughal, R. and Marziano, I. 2009. Crystallisation from water-in-oil emulsions as a route to spherical particulates: Glycine and the hydrochloride salts of glutamic acid and ephedrine. *Organic Process Research and Development*. **13**(6), pp.1284–1290.

Chandar, D.D.J. and Boppana, V.B.L. 2018. A Comparitive Study of Different Overset Grid Solvers Between OpenFOAM, STAR-CCM+ and ANSYS-Fluent. *AIAA Aerospace Sciences Meeting, 2018*. (210059).

Chaterjee, A., Gupta, M.M. and Srivastava, B. 2017. Spherical crystallization: A technique use to reform solubility and flow property of active pharmaceutical ingredients. *International Journal of Pharmaceutical Investigation*. **7**(1), pp.4–9.

Chen, C.W., Lee, H.L., Yeh, K.L. and Lee, T. 2021. Effects of Scale-Up and Impeller Types on Spherical Agglomeration of Dimethyl Fumarate. *Industrial and Engineering Chemistry Research*. **60**(30), pp.11555–11567.

Chen, J. and Xiao, W. 2013. Solids suspension study in a side-entering stirred tank through CFD modeling. *International Journal of Chemical Reactor Engineering*. **11**(1), pp.331–346.

Cheng, X., Li, F., Luo, L., Ding, Z., Zeng, L., Mao, Y., Huang, X. and Hao, H. 2020. On the selection of wetting liquid for spherical agglomeration of cefotaxime sodium. *Powder Technology*. **363**, pp.593–601.

Chitu, T.M., Oulahna, D. and Hemati, M. 2011. Wet granulation in laboratory-scale high shear mixers: Effect of chopper presence, design and impeller speed. *Powder Technology*. **206**(1–2), pp.34–43.

Chuahan, N., Satapara, V., Sorathiya, K., Parmar, K., Raval, M. and Patel, P. 2012. Spherical Crystallization : an Aspect To Increase the Pysicochemical Properties of Drugs. *International Journal of Pharmaceutical Innovations*. **2**(4), pp.37–47.

Chudacek, M.W. 1985. Solids suspension behaviour in profiled bottom and flat bottom mixing tanks. *Chemical Engineering Science*. **40**(3), pp.385–392.

Couper, J.R., Penney, W.R., Fair, J.R. and Walas, S.M. 2012. Mixing and Agitation *In*: *Chemical Process Equipment*. Elsevier, pp.277–327.

Darelius, A., Rasmuson, A., van Wachem, B., Niklasson Björn, I. and Folestad, S. 2008. CFD simulation of the high shear mixing process using kinetic theory of granular flow and frictional stress models. *Chemical Engineering Science*. **63**(8), pp.2188–2197.

Devarajulu, C. and Loganathan, M. 2016. Effect of Impeller Clearance and Liquid Level on Critical Impeller Speed in an Agitated Vessel using Different Axial and Radial Impellers. *Journal of Applied Fluid Mechanics*. **9**(6), pp.1735–3645.

Dhanarajan, A.P. and Bandyopadhyay, R. 2007. An Energy-Based Population-Balance Approach to Model Granule Growth and Breakage in High-Shear Wet Granulation Processes. *AAPS PharmSciTech*. **8**(3).

Dickey, D.S. 2015. *Fluids and Solids Handling* [Online]. Available from: www.aiche.org/cep.

Dogon, D. and Golombok, M. 2015. Particle agglomeration in sheared fluids. *Journal of Petroleum Exploration and Production Technology*. **5**(1), pp.91–98.

Doumenc, F., Bodiguel, H. and Guerrier, B. 2008. Physical aging of glassy PMMA/toluene films: Influence of drying/swelling history. *European Physical Journal E*. **27**(1), pp.3–11.

Egedy, A., Varga, T. and Chován, T. 2012. CFD Modelling and Video Analysis Based Model Validation for a Stirred Reactor. *Computer Aided Chemical Engineering*. **30**(June), pp.1123–1127.

Ennis, B.J., Tardos, G. and Pfeffer, R. 1991. A microlevel-based characterization of granulation phenomena. *Powder Technology*. **65**, pp.251–272.

Fukuda, I.M., Pinto, C.F.F., Moreira, C.D.S., Saviano, A.M. and Lourenço, F.R. 2018. Design of experiments (DoE) applied to pharmaceutical and analytical quality by design (QbD). *Brazilian Journal of Pharmaceutical Sciences*. **54**(Special Issue), pp.1–16.

Furukawa, H., Kato, Y., Inoue, Y., Kato, T., Tada, Y. and Hashimoto, S. 2012. Correlation of power consumption for several kinds of mixing impellers. *International Journal of Chemical Engineering*.

Galet, L., Patry, S. and Dodds, J. 2010. Determination of the wettability of powders by the Washburn capillary rise method with bed preparation by a centrifugal packing technique. *Journal of Colloid and Interface Science*. **346**(2), pp.470–475.

Gantt, J.A. and Gatzke, E.P. 2006. Kinetic theory of granular flow limitations for modeling high-shear mixing. *Industrial and Engineering Chemistry Research*. **45**(20), pp.6721–6727.

Gao, S., Meng, L., Wei, D., Zhao, Q., Wang, X. and Hou, D. 2021. Influence of the impeller diameter and off-bottom clearance on the flow velocity distribution characteristics near the bottom inside a flotation machine. *Minerals*. **11**(1), pp.1–19.

Giacomelli, J.J. and Van den Akker, H.E.A. 2021. A spectral approach of suspending solid particles in a turbulent stirred vessel. *AIChE Journal*. **67**(2).

Glomme, A., März, J. and Dressman, J.B. 2005. Comparison of a miniaturized shake-flask solubility method with automated potentiometric acid/base titrations and calculated solubilities. *Journal of Pharmaceutical Sciences*. **94**(1), pp.1–16.

Gohel, S., Joshi, S., Azhar, M., Horner, M. and Padron, G. 2012. CFD modeling of solid suspension in a stirred tank: Effect of drag models and turbulent dispersion on cloud height. *International Journal of Chemical Engineering*. **2012**.

Gorman, J., Bhattacharyya, S., Cheng, L. and Abraham, J.P. 2021. *Turbulence Models Commonly Used in CFD* [Online]. Available from: www.intechopen.com.

Gregory, M. 2014. Measuring water solubility of platinum group metal containing substances. *Johnson Matthey Technology Review*. **58**(4), pp.212–216.

Grenville, R.K. 2016. Characterizing impeller performance with examples of process results. *Process Development Symposium 2016: Development Challenges in Sustainable Processing*. (April), pp.104–121.

Grenville, R.K., Giacomelli, J.J., Padron, G. and Brown, D.A.R. 2017. Mixing: Impeller performance in stirred tanks. *Chemical Engineering (United States)*. **124**(8), pp.42–51.

Gu, D., Ye, M. and Liu, Z. 2020. Computational fluid dynamics simulation of solid-liquid suspension characteristics in a stirred tank with punched circle package impellers. *International Journal of Chemical Reactor Engineering*. **18**(9).

Guo, S., Feng, S., Yu, C., Liu, Y., Li, K., Chen, M., Han, D. and Gong, J. 2022. Design of spherical agglomerates via crystallization with a non-toxic bridging liquid: From mechanism to application. *Powder Technology*. **408**.

Gyulai, O., Kovács, A., Sovány, T., Csóka, I. and Aigner, Z. 2018. Optimization of the critical parameters of the spherical agglomeration crystallization method by the application of the Quality by Design approach. *Materials*. **11**(4).

Haghgoo, M.R. 2013. *A comparison of CFD Software packages to find the suitable one for numerical modeling of gasification process*.

Haleem, R.M., Salem, M.Y., Fatahallah, F.A. and Abdelfattah, L.E. 2015. Quality in the pharmaceutical industry - A literature review. *Saudi Pharmaceutical Journal*. **23**(5), pp.463–469.

Hanspal, N., DeVincentis, B. and Thomas, J.A. 2023. Modeling multiphase fluid flow, mass transfer, and chemical reactions in bioreactors using large-eddy simulation. *Engineering in Life Sciences*. **23**(2).

Hapgood, K.P., Litster, J.D. and Smith, R. 2003. Nucleation regime map for liquid bound granules. *AIChE Journal*. **49**(2), pp.350–361.

Hapgood, K.P., Tan, M.X.L. and Chow, D.W.Y. 2009. A method to predict nuclei size distributions for use in models of wet granulation. *Advanced Powder Technology*. **20**(4), pp.293–297.

Hernandez-Perez, V., Abdulkadir, M. and Azzopardi, B.J. 2011. Grid generation issues in the CFD modelling of two-phase flow in a pipe. *Journal of Computational Multiphase Flows*. **3**(1), pp.13–26.

Holaň, J., Štěpánek, F., Billot, P. and Ridvan, L. 2014. The construction, prediction and measurement of co-crystal ternary phase diagrams as a tool for solvent selection. *European Journal of Pharmaceutical Sciences*. **63**, pp.124–131.

Hoorfar, M. and Neumann, A.W. 2004. Axisymmetric Drop Shape Analysis (ADSA) for the determination of surface tension and contact angle. *Journal of Adhesion*. **80**(8), pp.727–743.

Huhtamäki, T., Tian, X., Korhonen, J.T. and Ras, R.H.A. 2018. Surface-wetting characterization using contact-angle measurements. *Nature Protocols*. **13**(7), pp.1521–1538.

Hysing, S.-R. 2011. Evaluation of CFD codes on a two-phase flow benchmark reference test case.

Iveson, S.M. 2001. Granule coalescence modelling: including the effects of bond strengthening and distributed impact separation forces. *Chemical Engineering Science*. (56), pp.2215–2220.

Iveson, S.M., Litster, J.D., Hapgood, K. and Ennis, B.J. 2001. Nucleation, growth and breakage phenomena in agitated wet granulation processes: a review. *Powder Technology*. **117**, pp.3–39.

Jafari, R., Tanguy, P.A. and Chaouki, J. 2012. Characterization of minimum impeller speed for suspension of solids in liquid at high solid concentration, using gamma-ray densitometry. *International Journal of Chemical Engineering*.

Jasak, H. 2009. OpenFOAM : Open source CFD in research and industry. *International Journal of Naval Architecture and Ocean Engineering*. **1**, pp.89–94.

Javadzedah, Y., Vazifehsal, Z., Dizaj, S.M. and Mokhtarpour, M. 2016. Spherical Crystallization of Drugs *In*: *Advanced Topics in Crystallization* [Online]., p.21. Available from: https://www.intechopen.com/books/advanced-biometric-technologies/liveness-detection-in-biometrics.

Jaworski, Z., Wyszynski, M.L., Moore, I.P.T. and Nienow, A.W. 1997. Sliding mesh computational fluid dynamics-a predictive tool in stirred tank design. *Proceedings of the Institution of Mechanical Engineers, Part E: Journal of Process Mechanical Engineering*. **211**(3), pp.149–156.

Jayarathna, C.K., Moldestad, B.E. and Tokheim, L. 2017. Validation of results from Barracuda ® CFD modelling to predict minimum fluidization velocity and pressure drop of Geldart A particles method. , pp.76–82.

Jiang, H., Müller-Plathe, F. and Panagiotopoulos, A.Z. 2017. Contact angles from Young's equation in molecular dynamics simulations. *Journal of Chemical Physics*. **147**(8).

Jitkar, S., Thipparaboina, R., Chavan, R.B. and Shastri, N.R. 2016. Spherical Agglomeration of Platy Crystals: Curious Case of Etodolac. *Crystal Growth and Design*. **16**, pp.4034–4042.

Johnson, M.D., May, S.A., Kopach, M.E., Groh, J.M., Braden, T., Shankarraman, V. and Merritt, J.M. 2019. Design and Selection of Continuous Reactors for Pharmaceutical Manufacturing. *Chemical Engineering in the Pharmaceutical Industry*., pp.367–385.

Katta, J. and Rasmuson, Å.C. 2008. Spherical crystallization of benzoic acid. *International Journal of Pharmaceutics*. **348**(1–2), pp.61–69.

Kawashima, Y., Kurachi, Y. and Takenaka, H. 1982. Preparation of spherical wax matrices of sulfamethoxazole by wet spherical agglomeration technique using a CMSMPR agglomerator. *Powder Technology*. **32**(2), pp.155–161.

Kawashima, Y., Naito, M., Lin, S.Y. and Takenaka, H. 1983. *Experimental Study of the Kinetics of the Spherical Crystallization of Ayllline Sodium Theophylline Monohydrate*.

Kawashima, Y., Okumura, M. and Takenaka, H. 1984. The effects of temperature on the spherical crystallization of salicylic acid. *Powder Technology*. **39**(1), pp.41–47.

Keshwani, B., Jaimini, M. and Sharma, D. 2015. SPHERICAL CRYSTALLISATION: A REVOLUTION IN THE FIELD OF PARTICLE ENGINEERING. *International Journal of Current Pharmaceutical Research*. **7**(4).

Khalilitehrani, M., Abrahamsson, P.J. and Rasmuson, A. 2014. Modeling dilute and dense granular flows in a high shear granulator. *Powder Technology*. **263**, pp.45–49.

Khalilitehrani, M., Gómez-Fino, E.M., Abrahamsson, P.J. and Rasmuson, A. 2015. Continuum modeling of multi-regime particle flows in high-shear mixing. *Powder Technology*. **280**, pp.67–71.

Khopkar, A.R., Kasat, G.R., Pandit, A.B. and Ranade, V. V. 2006. Computational fluid dynamics simulation of the solid suspension in a stirred slurry reactor. *Industrial and Engineering Chemistry Research*. **45**(12), pp.4416–4428.

Kresta, S.M. and Wood, P.E. 1993. The Mean Flow Field Produced by a 45' Pitched Blade Turbine: Changes in the Circul&on Pattern Due to Off Bottom Clearance. *The Canadian Journal of Chemical Engineering*. **71**, pp.42–53.

Krishna, E.H., Gupta, V.R.M. and Jyothi, S. 2012. Spherical crystallisation - A modern technique for direct compression of pharmaceutical substances. *Asian Journal of Pharmaceutical and Clinical Research*. **5**(SUPPL.4), pp.114–117.

Krusch, S., Scherer, V., Solimene, R. and Senneca, O. 2018. Assessment of coal pyrolysis kinetics for Barracuda or Ansys Fluent. *Energy Procedia*. **158**, pp.1999–2004.

Kubicki, D. and Lo, S. 2012. Cfd predictions of solids distribution in stirred vessel. . (December), pp.1–5.

Kulkarni, P.K., Dixit, M. and Jain, A. 2011. Spherical agglomeration of naproxan by solvent change method. *Stamford Journal of Pharmaceutical Sciences*. **4**(1), pp.1–8.

Kuschel, M., Wutz, J., Salli, M., Monteil, D. and Wucherpfennig, T. 2023. CFD supported scale up of perfusion bioreactors in biopharma. *Frontiers in Chemical Engineering*. **5**.

Kwok, D.Y., Gietzelt, T., Grundke, K., Jacobasch, H.J. and Neumann, A.W. 1997. Contact angle measurements and contact angle interpretation. 1. Contact angle measurements by axisymmetric drop shape analysis and a goniometer sessile drop technique. *Langmuir*. **13**(10), pp.2880–2894.

Lane, G.L. 2017. Improving the accuracy of CFD predictions of turbulence in a tank stirred by a hydrofoil impeller. *Chemical Engineering Science*. **169**, pp.188–211.

Lee, H.C. and Wahab, A.K.A. 2019. Performance of different turbulence models in predicting flow kinematics around an open offshore intake. *SN Applied Sciences*. **1**(10).

Lian, G.J. 2020. *Optimisation of the Spherical Agglomeration Process: Wetting and Nucleation*. MEng Thesis, Sheffield: The University of Sheffield.

Liao, D., Li, M., Wang, J., Zhang, M., Qiu, M. and An, C. 2023. A review on the preparation and characterization methods of spherical explosive crystals. *Journal of Materials Research and Technology*. **27**, pp.3098–3118.

Litster, J. 2016. Design and processing of particulate products. *Design and Processing of Particulate Products*.

Madec, L., Falk, L. and Plasari, E. 2003. Modelling of the agglomeration in suspension process with multidimensional kernels. *Powder Technology*. **130**(1–3), pp.147–153.

Maghsoodi, M., Derakhshandeh, K. and Yari, Z. 2012. On the mechanism of agglomeration in suspension. *Advanced Pharmaceutical Bulletin*. **2**(1), pp.25–30.

Maghsoodi, M. and Yari, Z. 2013. Effect of Temperature on Corrosion Control. *Iran Journal Basic Medical Science*. **17**, pp.344–350.

Matzke, M., Behrens, C., Jongebloed, N., Steins, D., Ulbricht, M. and Schultz, H.J. 2022. Investigation and Visualization of Flow Fields in Stirred Tank Reactors Using a Fluorescence Tracer Method. *Chemie-Ingenieur-Technik*. **94**(8), pp.1131–1140.

Mon Soe, T. and Yu Khaing, S. 2017. Comparison of Turbulence Models for Computational Fluid Dynamics Simulation of Wind Flow on Cluster of Buildings in Mandalay. *International Journal of Scientific and Research Publications*. **7**(8), pp.337–350.

Monk, D. and Chadwick, E.A. 2017. Comparison of Turbulence Models Effectiveness for a Delta Wing at Low Reynolds Numbers. *7th European Conference for Aeronautics and Space Sciences (EUCASS).*, p.1303.

Montante, G., Lee, K.C., Brucato, A. and Yianneskis, M. 1999. An experimental study of double-to-single-loop transition in stirred vessels. *Canadian Journal of Chemical Engineering*. **77**(4), pp.649–659.

Morishima, K., Kawashima, Yoichi, Kawashima, Yoshiaki, Takeuchi, H., Niwa, T. and Hino, T. 1993. *Micromeritic characteristics and agglomeration mechanisms spherical crystallization of bucillamine by the spherical agglomeration and the emulsion solvent diffusion methods 57 in the*.

Moseley, I.L. and O'brien, T.J. 1993. A MODEL FOR AGGLOMERATION IN A FLUIDIZED BED. *Chemical Engineering Science*. **48**(17), pp.3043–3050.

M-Star Simulations, LLC. 2023. M-Star Peer-Reviewed Validation.

Ng, B.H., Ding, Y.L. and Ghadiri, M. 2009. Modelling of dense and complex granular flow in high shear mixer granulator-A CFD approach. *Chemical Engineering Science*. **64**(16), pp.3622–3632.

Nguyen, D., Rasmuson, A., Niklasson Björn, I. and Thalberg, K. 2014. CFD simulation of transient particle mixing in a high shear mixer. *Powder Technology*. **258**, pp.324–330.

Nilsson, H. 2006. Evaluation of OpenFOAM for CFD of turbulent flow in water turbines.

Nogueira, E.S., Pinto, J.C. and Vianna, A.S. 2012. Analysis of energy dissipation in stirred suspension polymerisation reactors using computational fluid dynamics. *Canadian Journal of Chemical Engineering*. **90**(4), pp.983–995.

Ochieng, A. and Onyango, M.S. 2008. Homogenization energy in a stirred tank. *Chemical Engineering and Processing: Process Intensification*. **47**(9–10), pp.1853–1860.

Ochieng, A., Onyango, M.S., Kumar, A., Kiriamiti, K. and Musonge, P. 2008. Mixing in a tank stirred by a Rushton turbine at a low clearance. *Chemical Engineering and Processing: Process Intensification*. **47**(5), pp.842–851.

Ofei, T.N. and Ismail, A.Y. 2016. Eulerian-Eulerian Simulation of Particle-Liquid Slurry Flow in Horizontal Pipe. *Journal of Petroleum Engineering*. **2016**, pp.1–10.

Orlewski, P.M., Ahn, B. and Mazzotti, M. 2018. Tuning the particle sizes in spherical agglomeration. *Crystal Growth and Design*. **18**(10), pp.6257–6265.

Ouchiyama, N. and Tanaka, T. 1975. The Probability of Coalescence in Granulation Kinetics. *Industrial and Engineering Chemistry Process Design and Development*. **14**(3), pp.286–289.

Papanu, J.S., Hess, D.W., Soane (Soong), D.S. and Bell, A.T. 2003. Swelling of Poly(methyl Methacrylate) Thin Films in Low Molecular Weight Alcohols. *Journal of Applied Polymer Science* .

Paradkar, A.R., Pawar, A.P., Chordiya, J.K., Patil, V.B. and Ketkar, A.R. 2002. Spherical crystallization of celecoxib. *Drug Development and Industrial Pharmacy*. **28**(10), pp.1213–1220.

Parvizi, S., Keshavarz Alamdari, E., Hassan Hashemabadi, S. and Aosati, S. 2016. CFD Simulation and Experimental Study of Impeller Speed and Clearance Effects in the Mixer of Copper Solvent Extraction Unit. *Indian Journal of Science and Technology*. **9**(S1).

Patil, H., Patel, A.K., Pant, H.J. and Venu Vinod, A. 2018. CFD simulation model for mixing tank using multiple reference frame (MRF) impeller rotation. *ISH Journal of Hydraulic Engineering*. **00**(00), pp.1–10.

Peña, R., Burcham, C.L., Jarmer, D.J., Ramkrishna, D. and Nagy, Z.K. 2017. Modeling and optimization of spherical agglomeration in suspension through a coupled population balance model. *Chemical Engineering Science*. **167**.

Peña, R., Jarmer, D.J., Burcham, C.L. and Nagy, Z.K. 2019. Further Understanding of Agglomeration Mechanisms in Spherical Crystallization Systems: Benzoic Acid Case Study. *Crystal Growth and Design*. **19**(3), pp.1668–1679.

Peña, R. and Nagy, Z.K. 2015. Process Intensification through Continuous Spherical Crystallization Using a Two-Stage Mixed Suspension Mixed Product Removal (MSMPR) System. *Crystal Growth and Design*. **15**(9), pp.4225–4236.

Peña, R., Oliva, J.A., Burcham, C.L., Jarmer, D.J. and Nagy, Z.K. 2017. Process Intensification through Continuous Spherical Crystallization Using an Oscillatory Flow Baffled Crystallizer. *Crystal Growth and Design*. **17**(9), pp.4776–4784.

Peng, K. 2017. *An Equipment Selection Methodology for Continuous Manufacturing of Small-Molecule Drugs*.

Pierce, E., Carmona, F.J. and Amirfazli, A. 2008. Understanding of sliding and contact angle results in tilted plate experiments. *Colloids and Surfaces A: Physicochemical and Engineering Aspects*. **323**(1–3), pp.73–82.

Pitt, K., Peña, R., Tew, J.D., Pal, K., Smith, R., Nagy, Z.K. and Litster, J.D. 2018. Particle design via spherical agglomeration: A critical review of controlling parameters, rate processes and modelling. *Powder Technology*. **326**, pp.327–343.

Podila, K. and Rao, Y.F. 2015. A Comparative Study of the Commercial Cfd Codes : ANSYS Fluent and STAR-CCM+ To Simulate Nuclear Fuel Bundles *In*:, pp.0–24.

Pramod, K., Tahir, Ma., Charoo, N., Ansari, S. and Ali, J. 2016. Pharmaceutical product development: A quality by design approach. *International Journal of Pharmaceutical Investigation*. **6**(3), p.129.

Puechagut, H.G., Bianchotti, J. and Chiale, C.A. 1998. Preparation of norfloxacin spherical agglomerates using the ammonia diffusion system. *Journal of Pharmaceutical Sciences*. **87**(4), pp.519–523.

Ramachandran, R., Immanuel, C.D., Stepanek, F., Litster, J.D. and Doyle, F.J. 2009. A mechanistic model for breakage in population balances of granulation: Theoretical kernel development and experimental validation. *Chemical Engineering Research and Design*. **87**(4), pp.598–614.

Río, O. and Neumann, A. 1997. Axisymmetric Drop Shape Analysis: Computational Methods for the Measurement of Interfacial …. *Journal Of Colloid And Interface Science*. **147**(196), pp.136–147.

Sadino-Riquelme, M.C., Rivas, J., Jeison, D., Donoso-Bravo, A. and Hayes, R.E. 2022. Computational modelling of mixing tanks for bioprocesses: Developing a comprehensive workflow. *Canadian Journal of Chemical Engineering*. **100**(11), pp.3210–3226.

Sadrehaghighi, I. 2018. Mesh Generation in CFD. *CFD Open Series*. **1**(July), p.151.

Saini, P., Kumar, A. and Visht, S. 2013. Spherical Agglomeration : A Novel Technique Of Particulate Modification & Developing Niche Drug Delivery System. *Ijbr*. **6**(2), pp.86–101.

Salman, A.D., Fu, J., Gorham, D.A. and Hounslow, M.J. 2003. Impact breakage of fertiliser granules. *Powder Technology*. **130**, pp.359–366.

Schober, C. and Fitzpatrick, J.J. 2005. Effect of vortex formation on powder sinkability for reconstituting milk powders in water to high solids content in a stirred-tank. *Journal of Food Engineering*. **71**(1), pp.1–8.

Seville, J.P.K., Silomon-Pflug, H. and Knight, P.C. 1998. Modelling of sintering in high temperature gas fluidisation. *Powder Technology*. **97**, pp.160–169.

Shademan, M., Barron, R.M. and Balachandar, R. 2013. Evaluation of OpenFOAM in Academic Research and Industrial Applications. . (September 2015).

Sharma, R.N. and Shaikh, A.A. 2003. Solids suspension in stirred tanks with pitched blade turbines. *Chemical Engineering Science*. **58**(10), pp.2123–2140.

Simons, S.J.R., Seville, J.P.K. and Adams, M.J. 1994. AN ANALYSIS OF THE RUPTURE ENERGY OF PENDULAR LIQUID BRIDGES. *Chemical Englneerlng Science*. **49**(14), pp.2331–2339.

Sosnowski, M., Krzywanski, J., Grabowska, K. and Gnatowska, R. 2018. Polyhedral meshing in numerical analysis of conjugate heat transfer. *EPJ Web of Conferences*. **180**, pp.4–9.

Stuparu, A., Susan-Resiga, R. and Bosioc, A. 2021. CFD simulation of solid suspension for a liquid–solid industrial stirred reactor. *Applied Sciences (Switzerland)*. **11**(12).

Suresh, P., Sreedhar, I., Vaidhiswaran, R. and Venugopal, A. 2017. A comprehensive review on process and engineering aspects of pharmaceutical wet granulation. *Chemical Engineering Journal*. **328**, pp.785–815.

Tahara, K., O'Mahony, M. and Myerson, A.S. 2015. Continuous spherical crystallization of albuterol sulfate with solvent recycle system. *Crystal Growth and Design*. **15**(10), pp.5155–5156.

Tan, H.S., Salman, A.D. and Hounslow, M.J. 2004. Kinetics of fluidised bed melt granulation: IV. Selecting the breakage model. *Powder Technology*. **143–144**, pp.65–83.

Tan, H.S., Salman, A.D. and Hounslow, M.J. 2005. Kinetics of fluidised bed melt granulation V: Simultaneous modelling of aggregation and breakage *In*: *Chemical Engineering Science*., pp.3847–3866.

Tavana, H., Lam, C.N.C., Grundke, K., Friedel, P., Kwok, D.Y., Hair, M.L. and Neumann, A.W. 2004. Contact angle measurements with liquids consisting of bulky molecules. *Journal of Colloid and Interface Science*. **279**, pp.493–502.

Teipel, U., Heintz, T. and Krause, H.H. 2000. Crystallization of Spherical Ammonium Dinitramide (ADN) Particles. *Propellants, Explosives, Pyrotechnics*. **25**(2), pp.81–85.

Thati, J. and Rasmuson, Å.C. 2011. On the mechanisms of formation of spherical agglomerates. *European Journal of Pharmaceutical Sciences*. **42**(4), pp.365–379.

Thati, J. and Rasmuson, Å.C. 2012. Particle engineering of benzoic acid by spherical agglomeration. *European Journal of Pharmaceutical Sciences*. **45**(5), pp.657–667.

Thornton, C. and Ning, Z. 1998. A theoretical model for the stick/bounce behaviour of edhesive, elastic-plastic spheres. *Powder Technology*. **99**, pp.154–162.

Torotwa, I. and Ji, C. 2018. A study of the mixing performance of different impeller designs in stirred vessels using computational fluid dynamics. *Designs*. **2**(1), pp.1–16.

Usha, A.N., Mutalik, S., Reddy, M.S., Ranjith, A.K., Kushtagi, P. and Udupa, N. 2008. Preparation and, in vitro, preclinical and clinical studies of aceclofenac spherical agglomerates. *European Journal of Pharmaceutics and Biopharmaceutics*. **70**(2), pp.674–683.

VanDuyse, S.A., Fulford, M.J. and Bartlett, M.G. 2021. ICH Q10 Pharmaceutical Quality System Guidance: Understanding Its Impact on Pharmaceutical Quality. *AAPS Journal*. **23**(6).

Vayer, M., Vital, A. and Sinturel, C. 2017. New insights into polymer-solvent affinity in thin films. *European Polymer Journal*., p.93.

Veseli, A., Žakelj, S. and Kristl, A. 2019. A review of methods for solubility determination in biopharmaceutical drug characterization. *Drug Development and Industrial Pharmacy*. **45**(11), pp.1717–1724.

Vladimir, G., Michal, O., Radim, P. and Martin, Z. 2012. Benchmark of COMSOL multiphysics via in-depth floor slab test - Transient cases. *Energy Procedia*. **14**, pp.744–749.

Vlug, M.W. 2014. *2D Numerical model of droplet breakup in emulsions development of a numerial model to predict the number and size after breakup of droplets in simple shear flow*.

Wauters, P.A.L., Scarlett, B., Liu, L.X., Litster, J.D. and Meesters, G.M.H. 2003. A population balance model for high shear granulation. *Chemical Engineering Communications*. **190**(10), pp.1309–1334.

Van Wazer, J.R., Lyons, J.W., Kim, K.Y. and Colwell, R.E. 1995. *7 Fluid Flow and Mixing*.

Welton, T. 2015. Solvents and sustainable chemistry. *Proceedings of the Royal Society A: Mathematical, Physical and Engineering Sciences*. **471**(2183).

Wildeboer, W.J., Litster, J.D. and Cameron, I.T. 2005. Modelling nucleation in wet granulation *In*: *Chemical Engineering Science*., pp.3751–3761.

Wu, S., Li, K., Zhang, T. and Gong, J. 2015. Size Control of Atorvastatin Calcium Particles Based on Spherical Agglomeration. *Chemical Engineering and Technology*. **38**(6), pp.1081–1087.

Xu, Z., Han, Z. and Qu, H. 2020. Comparison between Lagrangian and Eulerian approaches for prediction of particle deposition in turbulent flows. *Powder Technology*. **360**, pp.141–150.

Yu, X., Hounslow, M.J., Reynolds, G.K., Rasmuson, A., Bjorn, I.N. and Abrahamsoson, P.J. 2017. A Compartmental CFD-PBM Model of High Shear Wet Granulation. *AIChE Journal*. **63**(2), pp.438–458.

Yuan, Y. and Lee, T.R. 2013. Surface science techniques *In*: *Springer Series in Surface Sciences*.

Zhang, H., Chen, Y., Wang, J. and Gong, J. 2010. Investigation on the spherical crystallization process of cefotaxime sodium. *Industrial and Engineering Chemistry Research*. **49**(3), pp.1402–1411.

Zhang, Z. and Chen, Q. 2007. Comparison of the Eulerian and Lagrangian methods for predicting particle transport in enclosed spaces. *Atmospheric Environment*. **41**(25).

Zhao, H.L., Zhang, Z.M., Zhang, T.A., Liu, Y., Gu, S.Q. and Zhang, C. 2014. Experimental and CFD studies of solid-liquid slurry tank stirred with an improved Intermig impeller. *Transactions of Nonferrous Metals Society of China*. **24**(10), pp.2650–2659.

Zhu, Q., Xiao, H., Chen, A., Geng, S. and Huang, Q. 2019. CFD study on double- to single-loop flow pattern transition and its influence on macro mixing efficiency in fully baffled tank stirred by a Rushton turbine. *Chinese Journal of Chemical Engineering*. **27**(5), pp.993–1000.

Zou, Y., Zhao, X. and Chen, Q. 2018. Comparison of STAR-CCM+ and ANSYS Fluent for simulating indoor airflows. *Building Simulation*. **11**(1), pp.165–174.

Zwietering, T.N. 1958. Suspending of solid particles in liquid by agitators. *Chemical Engineering Science*. **9**.

Appendix A - Impeller Geometry Experiments

Flat Blade Impeller PSD

Table A- 1 Mass frequency for each repeat with a flat blade impeller at a clearance of 25 mm and a speed of 450 rpm, the average and standard deviation for the repeats is also shown

Sieve Size (μm)	Repeat 1 Mass Frequency	Repeat 2 Mass Frequency	Repeat 3 Mass Frequency	Average Mass Frequency	Standard Deviation
150	0.0027011	0.0025985	0.0026230	0.0026413	0.0000438
250	0.0000379	0.0000381	0.0000382	0.0000381	0.0000001
355	0.0000361	0.0000385	0.0000343	0.0000363	0.0000017
425	0.0000424	0.0000476	0.0000463	0.0000454	0.0000022
500	0.0000245	0.0000266	0.0000251	0.0000254	0.0000009
600	0.0000433	0.0000458	0.0000443	0.0000444	0.0000010
710	0.0000479	0.0000446	0.0000462	0.0000462	0.0000013
850	0.0002199	0.0002438	0.0002168	0.0002268	0.0000121
1000	0.0003479	0.0003255	0.0003680	0.0003471	0.0000173
1180	0.0009767	0.0009895	0.0010285	0.0009982	0.0000220
1400	0.0005689	0.0005613	0.0005753	0.0005685	0.0000057
1700	0.0004788	0.0004605	0.0004639	0.0004677	0.0000079
2000	0.0001087	0.0001115	0.0001100	0.0001101	0.0000012
2500	0.0000194	0.0000199	0.0000198	0.0000197	0.0000002

Figure A- 1 Calculated and average value of d_{43} for experiments performed with a flat blade impeller at a clearance of 25 mm and a speed of 450 rpm, error bar represents standard deviation of measurements

Propeller Impeller PSD

Table A- 2 Mass frequency for each repeat with a propeller impeller at a clearance of 25 mm and a speed of 450 rpm, the average and standard deviation for the repeats is also shown

Sieve Size (µm)	Repeat 1 Mass Frequency	Repeat 2 Mass Frequency	Repeat 3 Mass Frequency	Average Mass Frequency	Standard Deviation
150	0.0024785	0.0027575	0.0026878	0.0026413	0.0001186
250	0.0000369	0.0000395	0.0000380	0.0000381	0.0000011
355	0.0000353	0.0000375	0.0000361	0.0000363	0.0000009
425	0.0000443	0.0000486	0.0000432	0.0000454	0.0000023
500	0.0000281	0.0000246	0.0000235	0.0000254	0.0000020
600	0.0000402	0.0000446	0.0000483	0.0000444	0.0000033
710	0.0000475	0.0000423	0.0000489	0.0000462	0.0000028
850	0.0002464	0.0002104	0.0002237	0.0002268	0.0000149
1000	0.0003247	0.0003727	0.0003438	0.0003471	0.0000197
1180	0.0009969	0.0010176	0.0009802	0.0009982	0.0000153
1400	0.0005591	0.0005740	0.0005725	0.0005685	0.0000067
1700	0.0004486	0.0004846	0.0004699	0.0004677	0.0000148
2000	0.0001145	0.0001007	0.0001151	0.0001101	0.0000067
2500	0.0000191	0.0000200	0.0000199	0.0000197	0.0000004

Figure A- 2 Calculated and average value of d_{43} for experiments performed with a propeller impeller at a clearance of 25 mm and a speed of 450 rpm, error bar represents standard deviation of measurements

Rushton Turbine Impeller PSD

Table A- 3 Mass frequency for each repeat with a Rushton turbine impeller at a clearance of 25 mm and a speed of 450 rpm, the average and standard deviation for the repeats is also shown

Sieve Size (μm)	Repeat 1 Mass Frequency	Repeat 2 Mass Frequency	Repeat 3 Mass Frequency	Average Mass Frequency	Standard Deviation
150	0.0024785	0.0027575	0.0026878	0.0026413	0.0001186
250	0.0000369	0.0000395	0.0000380	0.0000381	0.0000011
355	0.0000353	0.0000375	0.0000361	0.0000363	0.0000009
425	0.0000443	0.0000486	0.0000432	0.0000454	0.0000023
500	0.0000281	0.0000246	0.0000235	0.0000254	0.0000020
600	0.0000402	0.0000446	0.0000483	0.0000444	0.0000033
710	0.0000475	0.0000423	0.0000489	0.0000462	0.0000028
850	0.0002464	0.0002104	0.0002237	0.0002268	0.0000149
1000	0.0003247	0.0003727	0.0003438	0.0003471	0.0000197
1180	0.0009969	0.0010176	0.0009802	0.0009982	0.0000153
1400	0.0005591	0.0005740	0.0005725	0.0005685	0.0000067
1700	0.0004486	0.0004846	0.0004699	0.0004677	0.0000148
2000	0.0001145	0.0001007	0.0001151	0.0001101	0.0000067
2500	0.0000191	0.0000200	0.0000199	0.0000197	0.0000004

Figure A- 3 Calculated and average value of d_{43} for experiments performed with a Rushton turbine impeller at a clearance of 25 mm and a speed of 450 rpm, error bar represents standard deviation of measurements

Pitched Blade Impeller PSD

Table A- 4 Mass frequency for each repeat with a pitched blade impeller at a clearance of 25 mm and a speed of 450 rpm, the average and standard deviation for the repeats is also shown

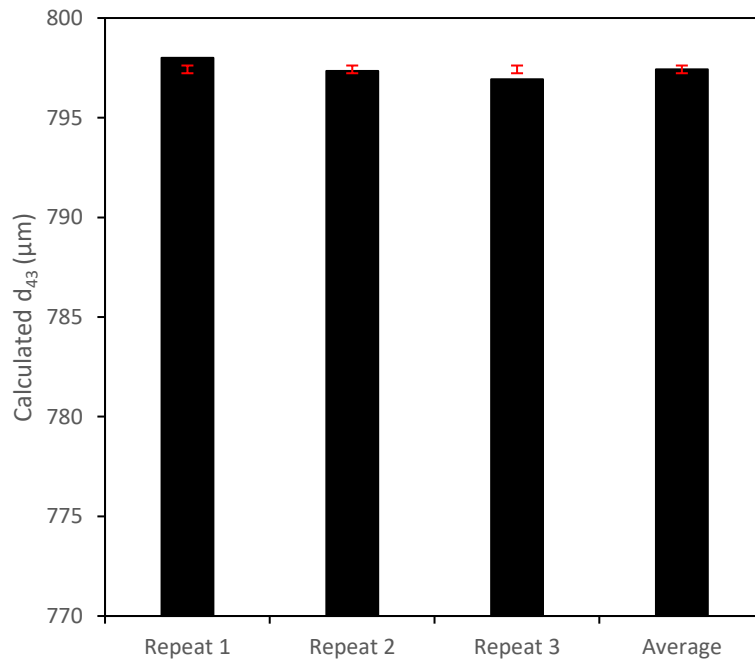| Sieve Size (μm)	Repeat 1 Mass Frequency	Repeat 2 Mass Frequency	Repeat 3 Mass Frequency	Average Mass Frequency	Standard Deviation
150	0.0017250	0.0017691	0.0017493	0.00174778	0.00001802
250	0.0001085	0.0001126	0.0001099	0.00011032	0.00000168
355	0.0000792	0.0000813	0.0000805	0.00008034	0.00000087
425	0.0000992	0.0001054	0.0001013	0.00010197	0.00000258
500	0.0001431	0.0001517	0.0001465	0.00014709	0.00000353
600	0.0002218	0.0002099	0.0002108	0.00021415	0.00000542
710	0.0004622	0.0004598	0.0004585	0.00046015	0.00000152
850	0.0005655	0.0005486	0.0005407	0.00055159	0.00001035
1000	0.0015266	0.0014874	0.0014637	0.00149254	0.00002594
1180	0.0010187	0.0010765	0.0010089	0.00103468	0.00002983
1400	0.0002982	0.0003124	0.0003098	0.00030677	0.00000615
1700	0.0001191	0.0001027	0.0001157	0.00011248	0.00000705
2000	0.0000521	0.0000468	0.0000505	0.00004975	0.00000222
2500	0.0000251	0.0000234	0.0000255	0.00002466	0.00000089
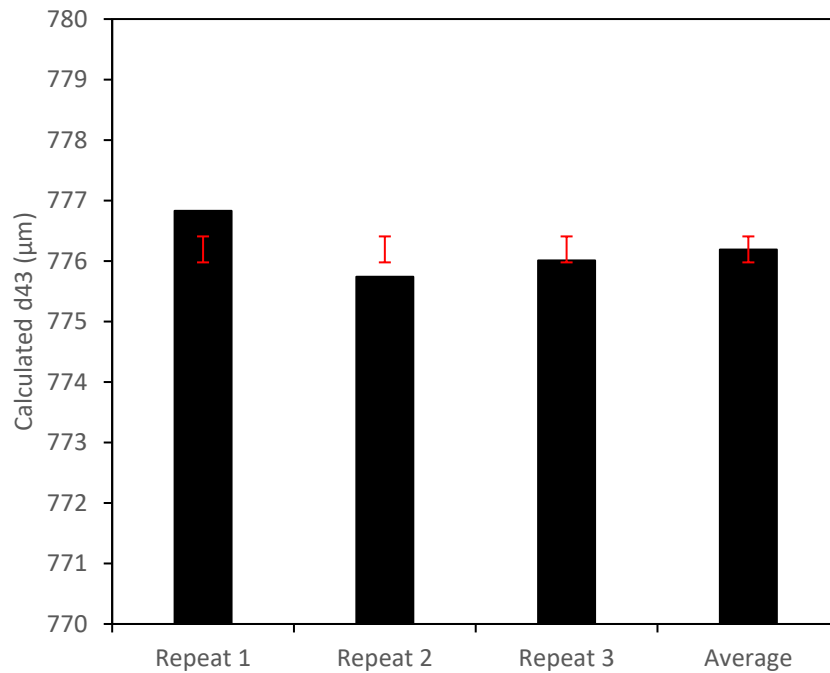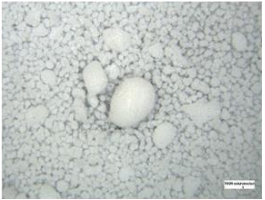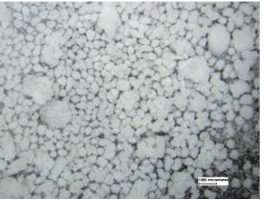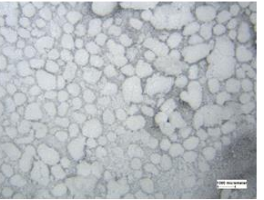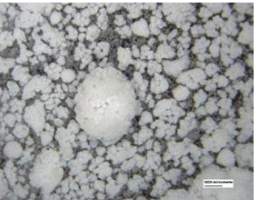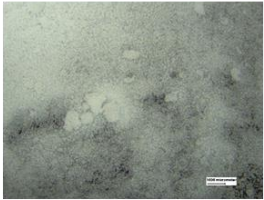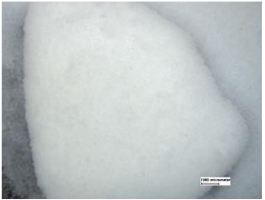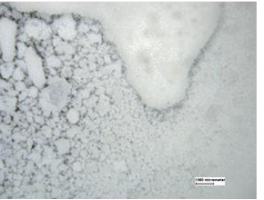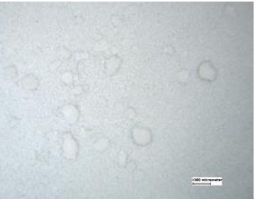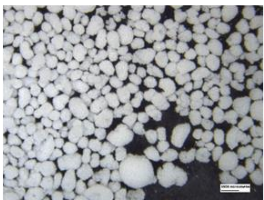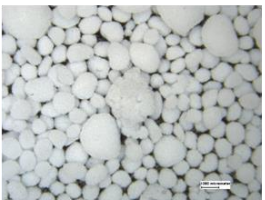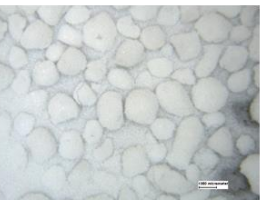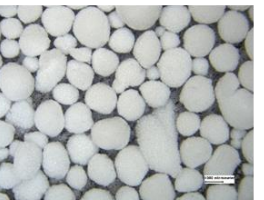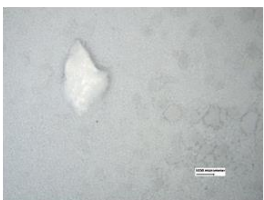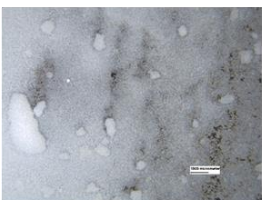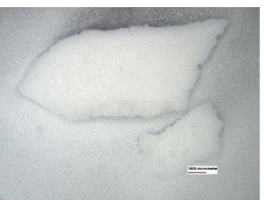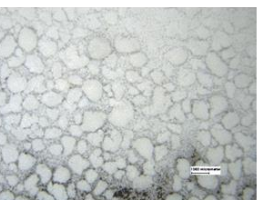
Figure A- 4 Calculated and average value of d_{43} for experiments performed with a pitched blade impeller at a clearance of 25 mm and a speed of 450 rpm, error bar represents standard deviation of measurements
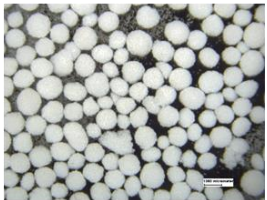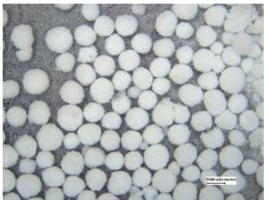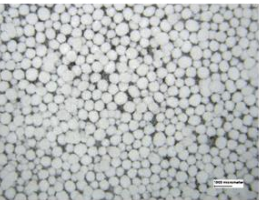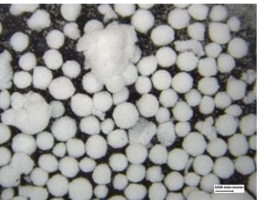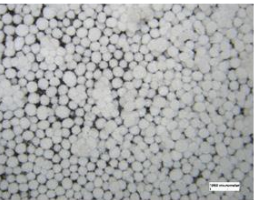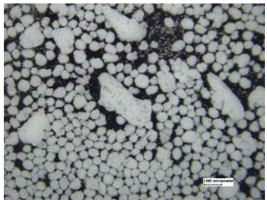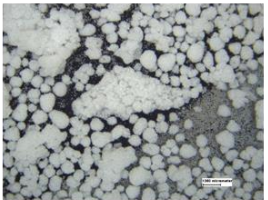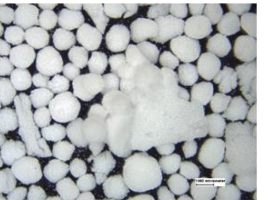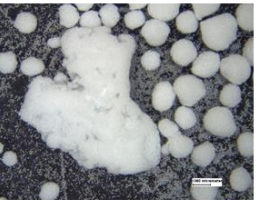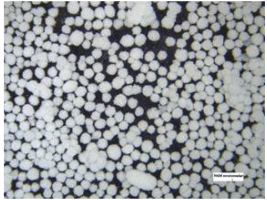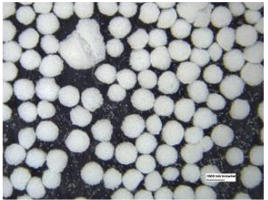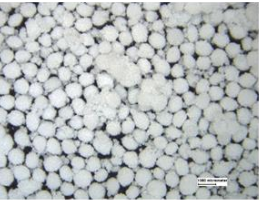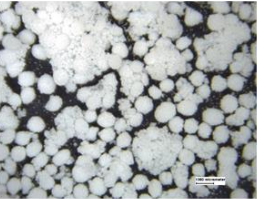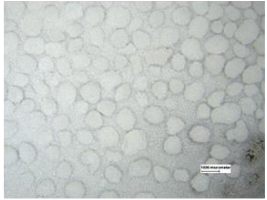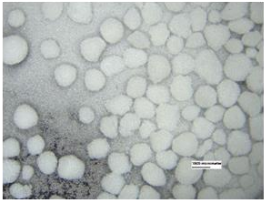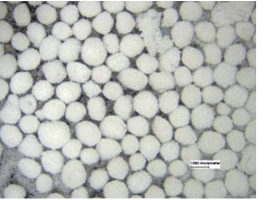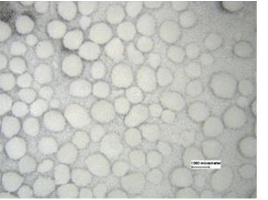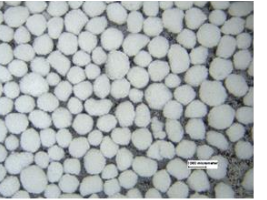
Agglomerate Images at 300 rpm

	18 mm	20 mm	25 mm	27 mm	30 mm
Flat Blade Impeller					
Propeller Impeller					
Rushton Turbine Impeller					
Pitched Blade Impeller					

━ 1000 μm

Figure A- 5 Images of the agglomerates produced with different impeller geometries and clearances at an impeller speed of 300 rpm, scale bar is 1000 μm

Agglomerate Images at 600 rpm

	18 mm	20 mm	25 mm	27 mm	30 mm
Flat Blade Impeller					
Propeller Impeller					
Rushton Turbine Impeller					
Pitched Blade Impeller					

▬ 1000 μm

Figure A- 6 Images of the agglomerates produced with different impeller geometries and clearances at an impeller speed of 600 rpm, scale bar is 1000 μm

Appendix B - Impeller Geometry CFD Analysis

CFD Contours

Flat Blade

Table B- 1 CFD contours of solid velocity magnitude for a flat blade impeller at different impeller C/D ratios and speeds

C/D − 0.22
300 RPM

C/D − 0.20
450 RPM

C/D − 0.22
600 RPM

C/D − 0.30
300 RPM

C/D − 0.30
450 RPM

C/D − 0.30
600 RPM
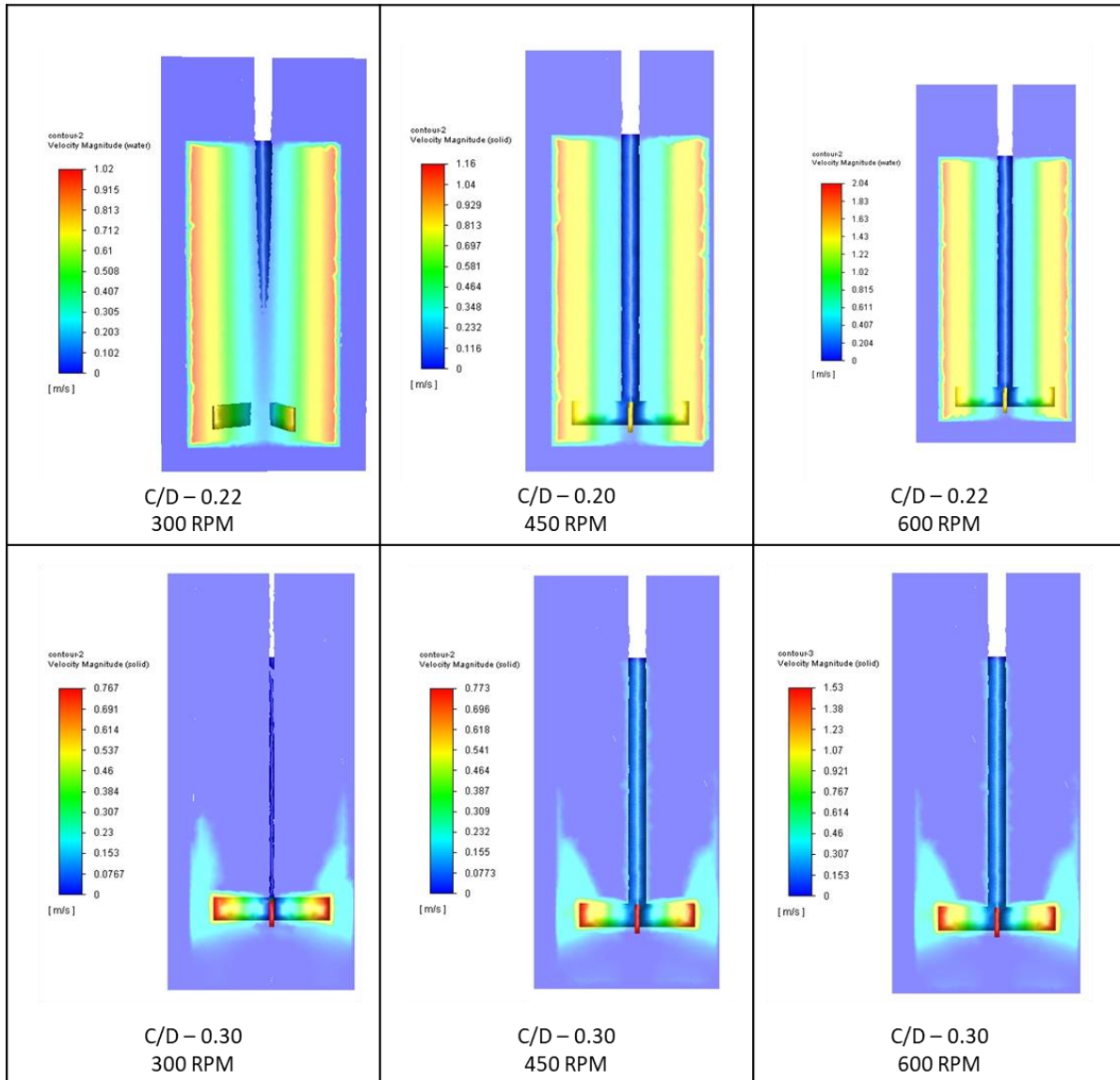
Propeller

Table B- 2 CFD contours of solid velocity magnitude for a propeller impeller at different impeller C/D ratios and speeds

| $C/D - 0.22$ 300 RPM | $C/D - 0.20$ 450 RPM | $C/D - 0.22$ 600 RPM |
| $C/D - 0.30$ 300 RPM | $C/D - 0.30$ 450 RPM | $C/D - 0.30$ 600 RPM |
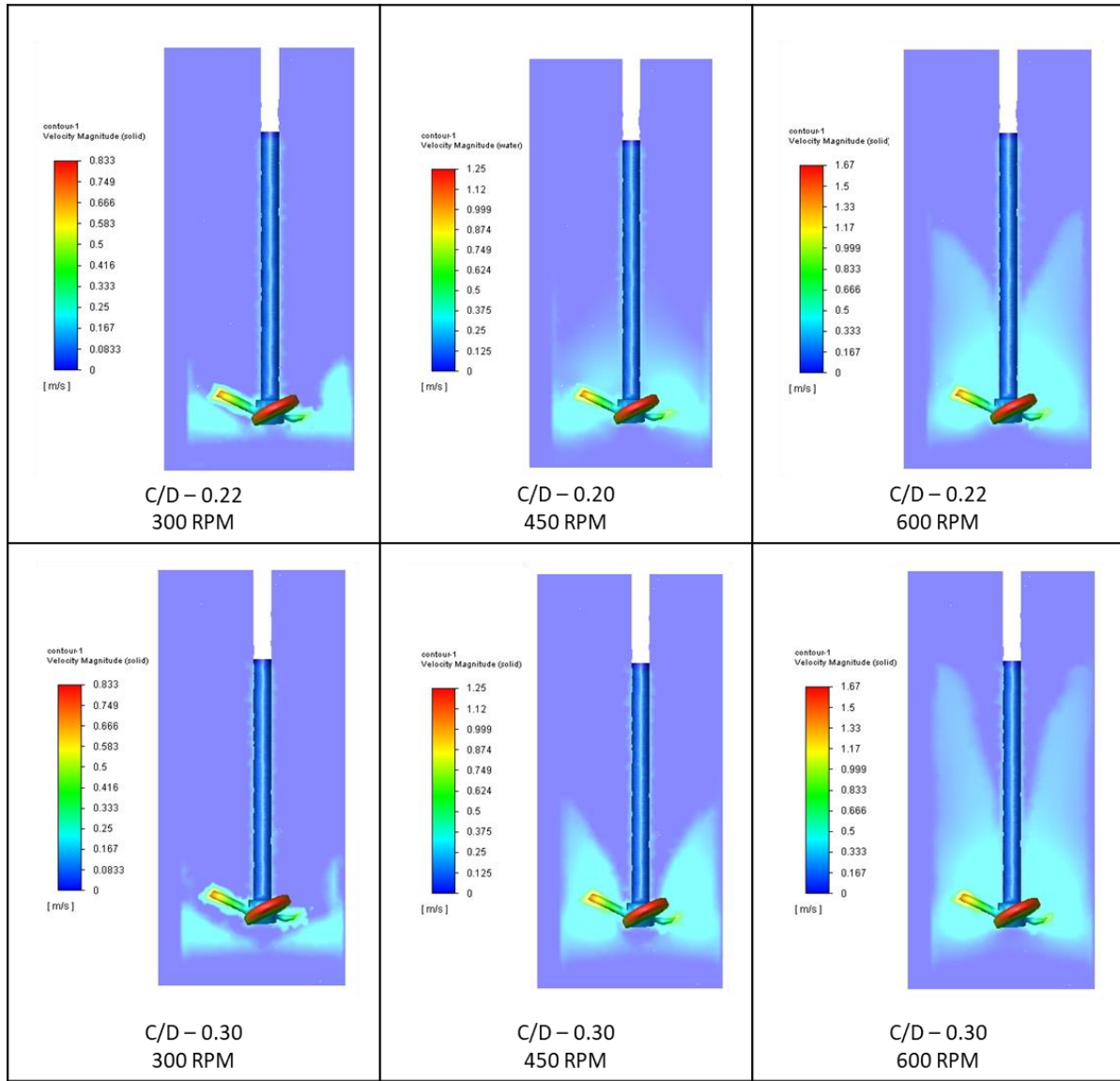
Rushton Turbine

Table B- 3 CFD contours of solid velocity magnitude for a Rushton turbine impeller at different impeller C/D ratios and speeds

C/D − 0.22 300 RPM	C/D − 0.20 450 RPM	C/D − 0.22 600 RPM
C/D − 0.30 300 RPM	C/D − 0.30 450 RPM	C/D − 0.30 600 RPM
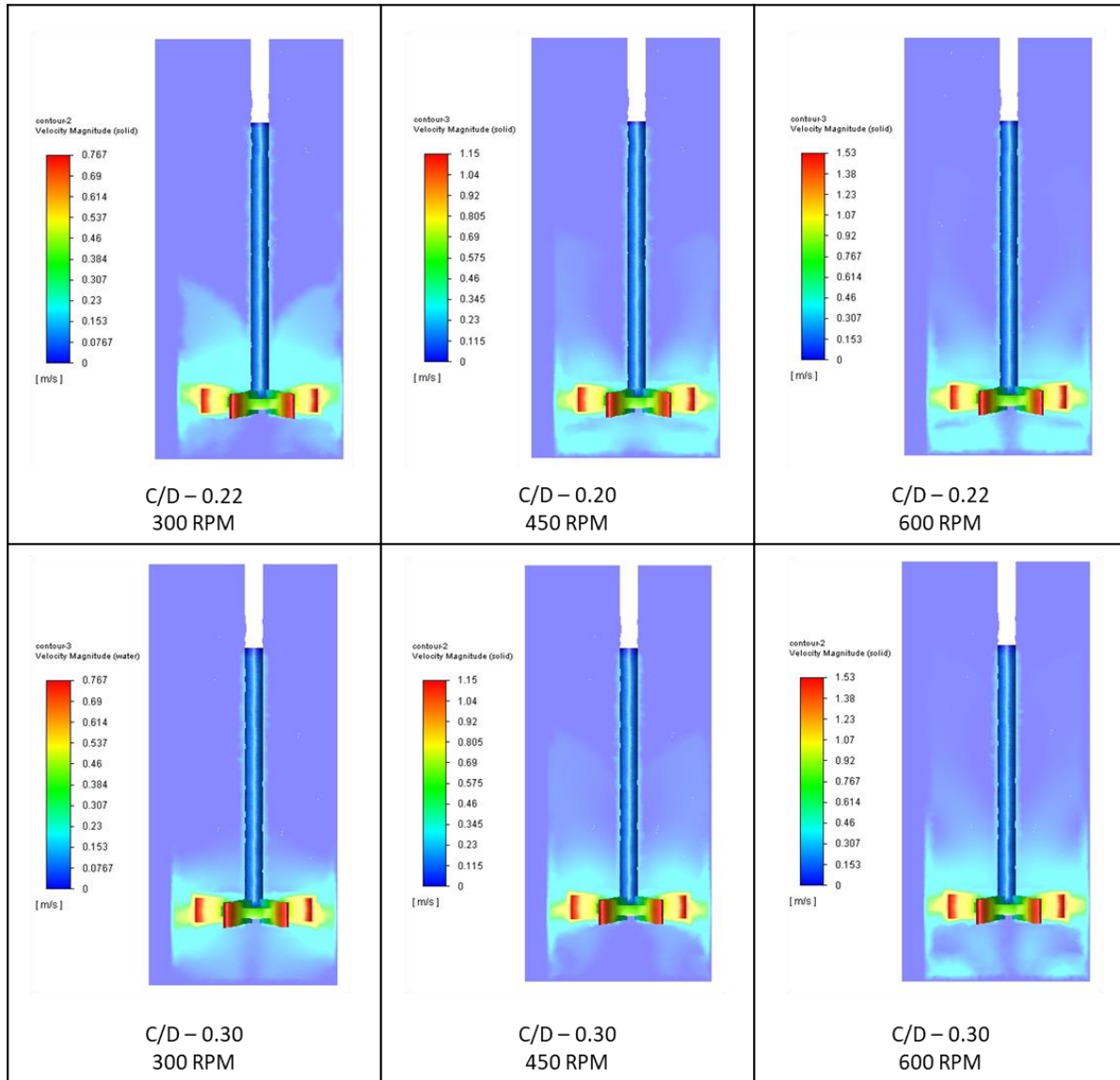
Pitched Blade

Table B- 4 CFD contours of solid velocity magnitude for a pitched blade impeller at different impeller clearance to diameter ratios (C/D) and speeds

| C/D – 0.22 300 RPM | C/D – 0.22 450 RPM | C/D – 0.22 600 RPM |
| C/D – 0.30 300 RPM | C/D – 0.30 450 RPM | C/D – 0.30 600 RPM |
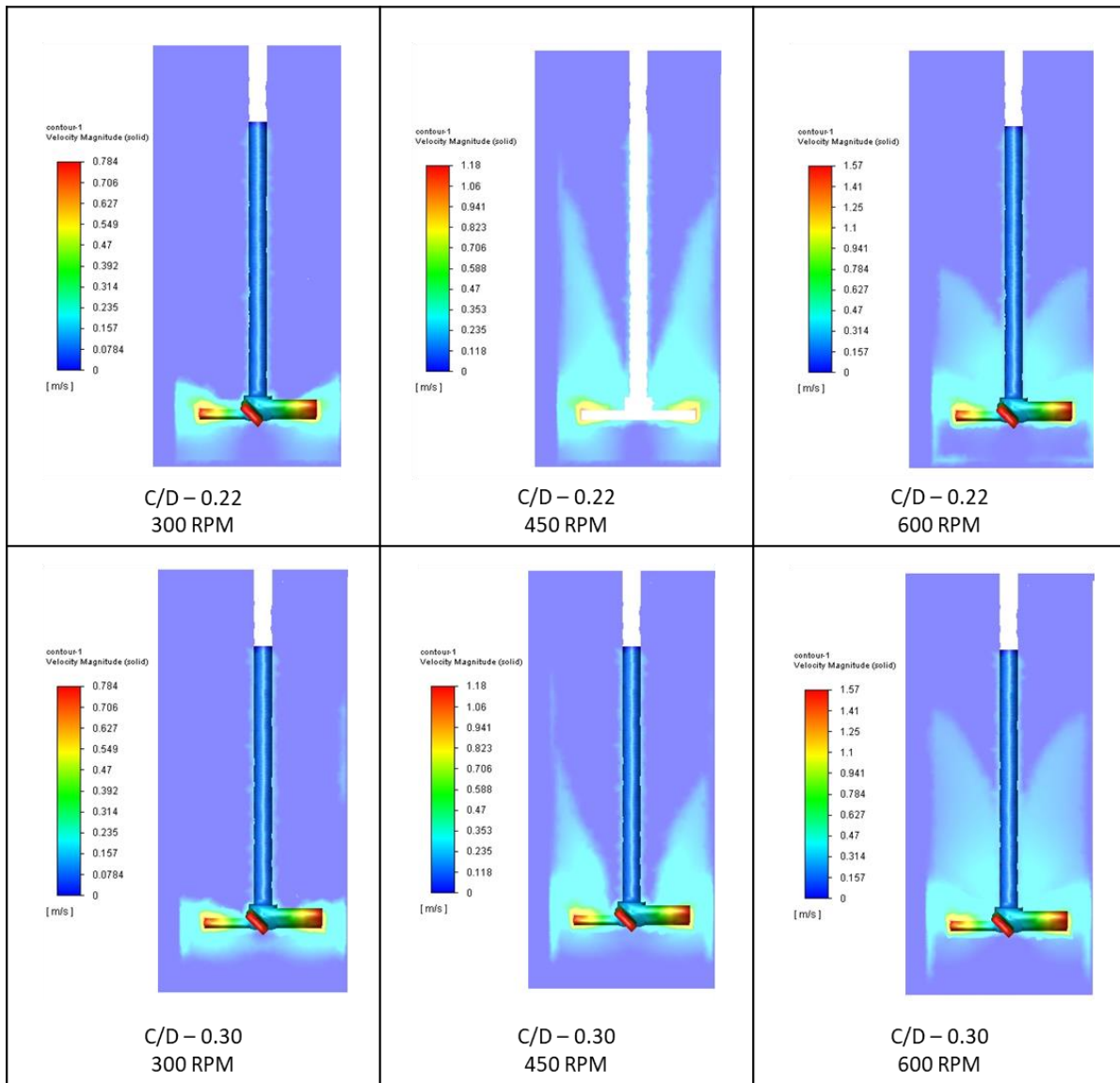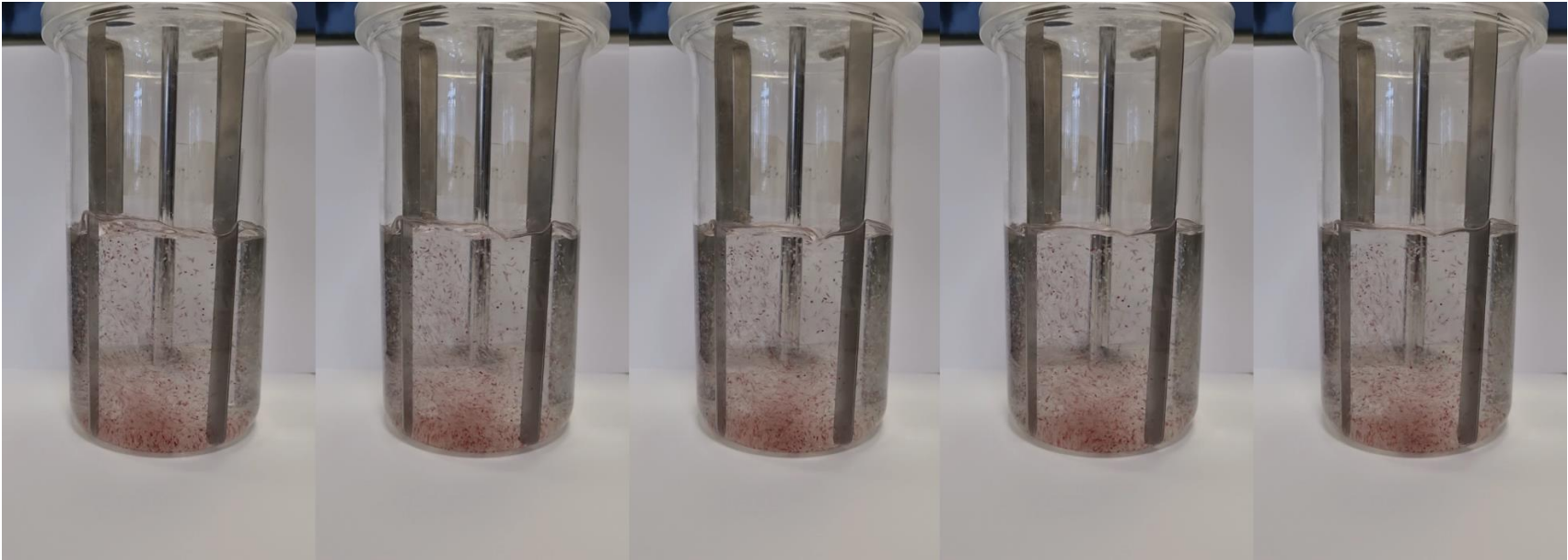
CFD Validation

Figure B- 1 A sequence of frames from the video used for CFD validation

VWA Velocity Magnitude Profile Graphs

300 rpm
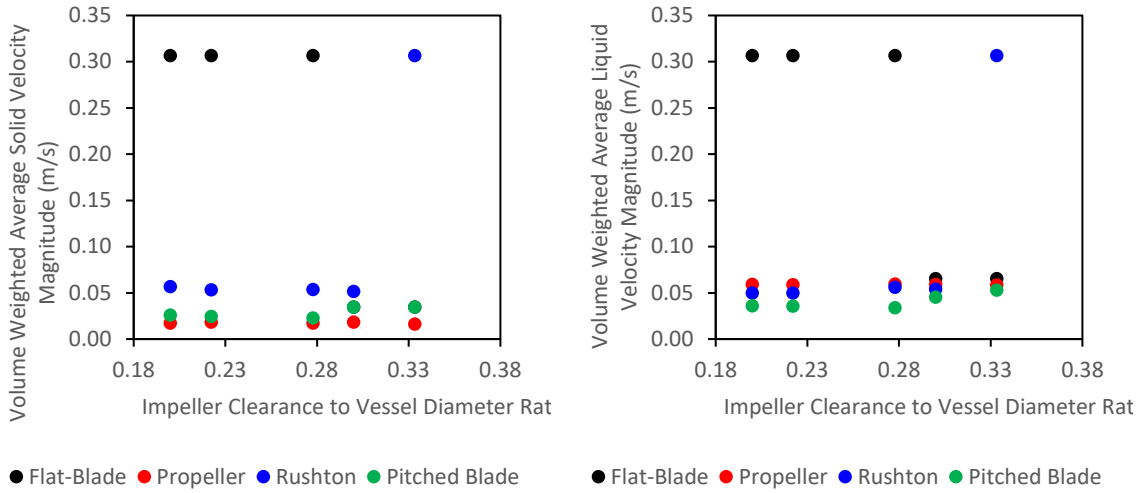
Figure B- 2 Volume weighted average velocity magnitude from the CFD simulations for different impeller geometries and clearance to diameter ratios at a speed of 300 rpm, (left – solid, right – liquid)

600 rpm
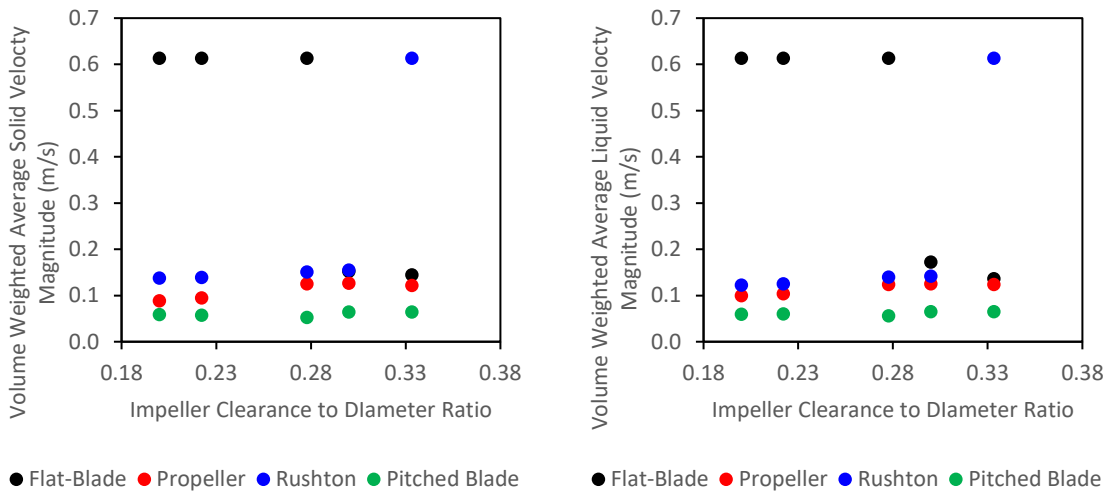
Figure B- 3 Volume weighted average velocity magnitude from the CFD simulations for different impeller geometries and clearance to diameter ratios at a speed of 600 rpm, (left – solid, right – liquid)

Appendix C - PBM Construction and Validation

Adding Impeller Geometry Drop Down Box

The following code was added to the high shear granulator block to produce the dropdown box option in the custom agglomeration specification page:

```xml
  <PMA>
<ID>High_shear_granulator_block.Agglomeration.agglomeration_kernels.Agglomeration_Custom.Custo
m_agglomeration_rate.Flat_Blade</ID>
<Name>High_shear_granulator_block.Agglomeration.agglomeration_kernels.Agglomeration_Custom.Cu
stom_agglomeration_rate.Flat_Blade</Name>
<Description>High_shear_granulator_block.Agglomeration.agglomeration_kernels.Agglomeration_Cust
om.Custom_agglomeration_rate.Flat_Blade</Description>

    <DefaultValue>0</DefaultValue>

  </PMA>



  <PMA>
<ID>High_shear_granulator_block.Agglomeration.agglomeration_kernels.Agglomeration_Custom.Custo
m_agglomeration_rate.Pitched_Blade</ID>
<Name>High_shear_granulator_block.Agglomeration.agglomeration_kernels.Agglomeration_Custom.Cu
stom_agglomeration_rate.Pitched_Blade</Name>
<Description>High_shear_granulator_block.Agglomeration.agglomeration_kernels.Agglomeration_Cust
om.Custom_agglomeration_rate.Pitched_Blade</Description>

    <DefaultValue>0</DefaultValue>

  </PMA>



  <PMA>
<ID>High_shear_granulator_block.Agglomeration.agglomeration_kernels.Agglomeration_Custom.Custo
m_agglomeration_rate.Propeller</ID>
<Name>High_shear_granulator_block.Agglomeration.agglomeration_kernels.Agglomeration_Custom.Cu
stom_agglomeration_rate.Propeller</Name>
<Description>High_shear_granulator_block.Agglomeration.agglomeration_kernels.Agglomeration_Cust
om.Custom_agglomeration_rate.Propeller</Description>

    <DefaultValue>0</DefaultValue>

  </PMA>



  <PMA>
<ID>High_shear_granulator_block.Agglomeration.agglomeration_kernels.Agglomeration_Custom.Custo
```

m_agglomeration_rate.Rushton</ID>
<Name>High_shear_granulator_block.Agglomeration.agglomeration_kernels.Agglomeration_Custom.Cu
stom_agglomeration_rate.Rushton</Name>
<Description>High_shear_granulator_block.Agglomeration.agglomeration_kernels.Agglomeration_Cust
om.Custom_agglomeration_rate.Rushton</Description>

    <DefaultValue>0</DefaultValue>

  </PMA>

    <PMA>
<ID>High_shear_granulator_block.Layering.Layering_models.Layering_custom_rate.Custom_layering_ki
netics.Flat_Blade</ID>
<Name>High_shear_granulator_block.Layering.Layering_models.Layering_custom_rate.Custom_layerin
g_kinetics.Flat_Blade</Name>
<Description>High_shear_granulator_block.Layering.Layering_models.Layering_custom_rate.Custom_la
yering_kinetics.Flat_Blade</Description>

    <DefaultValue>0</DefaultValue>

  </PMA>

    <PMA>
<ID>High_shear_granulator_block.Layering.Layering_models.Layering_custom_rate.Custom_layering_ki
netics.Pitched_Blade</ID>
<Name>High_shear_granulator_block.Layering.Layering_models.Layering_custom_rate.Custom_layerin
g_kinetics.Pitched_Blade</Name>
<Description>High_shear_granulator_block.Layering.Layering_models.Layering_custom_rate.Custom_la
yering_kinetics.Pitched_Blade</Description>

    <DefaultValue>0</DefaultValue>

  </PMA>

    <PMA>
<ID>High_shear_granulator_block.Layering.Layering_models.Layering_custom_rate.Custom_layering_ki
netics.Propeller</ID>
<Name>High_shear_granulator_block.Layering.Layering_models.Layering_custom_rate.Custom_layerin
g_kinetics.Propeller</Name>
<Description>High_shear_granulator_block.Layering.Layering_models.Layering_custom_rate.Custom_la
yering_kinetics.Propeller</Description>

    <DefaultValue>0</DefaultValue>

  </PMA>

```
    <PMA>
<ID>High_shear_granulator_block.Layering.Layering_models.Layering_custom_rate.Custom_layering_ki
netics.Rushton</ID>
<Name>High_shear_granulator_block.Layering.Layering_models.Layering_custom_rate.Custom_layerin
g_kinetics.Rushton</Name>
<Description>High_shear_granulator_block.Layering.Layering_models.Layering_custom_rate.Custom_la
yering_kinetics.Rushton</Description>

    <DefaultValue>0</DefaultValue>

  </PMA>

-----------------------------------------------

  <ModeSet id="Impeller Geometry">

    <Option id="Flat Blade"/>

    <Option id="Rushton"/>

    <Option id="Pitched Blade"/>

    <Option id="Propeller"/>

  </ModeSet>
<Section requiresMode="Agglomeration Custom user model">

        <PMA          id="High_shear_granulator_block.Agglomeration_dialog.number_of_possibilities"
required="OptionalOn" section="set"/>

        <PMA              id="High_shear_granulator_block.Agglomeration_dialog.agg_stoichiometry"
orderedSetType="Selection-Single"              required="OptionalOn"              section="set"
sourceOrderedSet="High_shear_granulator_block.Agglomeration_dialog.agglomeration_phases_availab
le"/>

        <PMA              id="High_shear_granulator_block.Agglomeration_dialog.kernel_parameters"
required="OptionalOn" section="assign"/>

        <ModeSelector modeSet="Impeller geometry"/>

        <Section requiresMode="Flat Blade">

          <PMA
id="High_shear_granulator_block.Agglomeration.agglomeration_kernels.Agglomeration_Custom.Custo
m_agglomeration_rate.Flat_Blade" required="Hidden" section="set" value="1"/>

          <PMA
id="High_shear_granulator_block.Layering.Layering_models.Layering_custom_rate.Custom_layering_ki
netics.Flat_Blade" required="Hidden" section="set" value="1"/>
```

```xml
        </Section>

        <Section requiresMode="Rushton">

            <PMA
id="High_shear_granulator_block.Agglomeration.agglomeration_kernels.Agglomeration_Custom.Custo
m_agglomeration_rate.Rushton" required="Hidden" section="set" value="1"/>

            <PMA
id="High_shear_granulator_block.Layering.Layering_models.Layering_custom_rate.Custom_layering_ki
netics.Rushton" required="Hidden" section="set" value="1"/>

        </Section>

        <Section requiresMode="Pitched Blade">

            <PMA
id="High_shear_granulator_block.Agglomeration.agglomeration_kernels.Agglomeration_Custom.Custo
m_agglomeration_rate.Pitched_Blade" required="Hidden" section="set" value="1"/>

            <PMA
id="High_shear_granulator_block.Layering.Layering_models.Layering_custom_rate.Custom_layering_ki
netics.Pitched_Blade" required="Hidden" section="set" value="1"/>

        </Section>

        <Section requiresMode="Propeller">

            <PMA
id="High_shear_granulator_block.Agglomeration.agglomeration_kernels.Agglomeration_Custom.Custo
m_agglomeration_rate.Propeller" required="Hidden" section="set" value="1"/>

            <PMA
id="High_shear_granulator_block.Layering.Layering_models.Layering_custom_rate.Custom_layering_ki
netics.Propeller" required="Hidden" section="set" value="1"/>

        </Section>
```

VWA Velocity Magnitude Results

Propeller Impeller

Table C- 1 Volume weighted average solid and liquid velocity magnitude as a percentage of impeller tip speed for a propeller impeller at different impeller speeds and clearances

Impeller Geometry	Impeller Speed (rpm)	Impeller Clearance (mm)	Clearance to Vessel Diameter Ratio	Impeller Tip Speed (m/s)	Solid Average Velocity (m/s)	Average as % of Tip Speed	Water Average Velocity (m/s)	Average as % Tip Speed
Propeller	300	18	0.200	0.785	0.017	2.220	0.059	7.552
Propeller	300	20	0.222	0.785	0.018	2.343	0.059	7.510
Propeller	300	25	0.278	0.785	0.017	2.220	0.059	7.567
Propeller	300	27	0.300	0.785	0.018	2.345	0.059	7.539
Propeller	300	30	0.333	0.785	0.016	2.064	0.058	7.428
Propeller	450	18	0.200	1.178	0.066	5.638	0.088	7.439
Propeller	450	20	0.222	1.178	0.065	5.515	0.088	7.493
Propeller	450	25	0.278	1.178	0.062	5.287	0.093	7.919
Propeller	450	27	0.300	1.178	0.060	5.057	0.093	7.921
Propeller	450	30	0.333	1.178	0.059	4.974	0.093	7.856
Propeller	600	18	0.200	1.571	0.089	5.642	0.100	6.344
Propeller	600	20	0.222	1.571	0.095	6.020	0.104	6.602
Propeller	600	25	0.278	1.571	0.125	7.979	0.124	7.897
Propeller	600	27	0.300	1.571	0.127	8.066	0.125	7.956
Propeller	600	30	0.333	1.571	0.122	7.766	0.124	7.906

Rushton Turbine Impeller

Table C- 2 Volume weighted average solid and liquid velocity magnitude as a percentage of impeller tip speed for a Rushton turbine impeller at different impeller speeds and clearances

Impeller Geometry	Impeller Speed (rpm)	Impeller Clearance (mm)	Clearance to Vessel Diameter Ratio	Impeller Tip Speed (m/s)	Solid Average Velocity (m/s)	Average as % of Tip Speed	Water Average Velocity (m/s)	Average as % Tip Speed
Rushton Turbine	300	18	0.200	0.785	0.057	7.229	0.050	6.350
Rushton Turbine	300	20	0.222	0.785	0.053	6.803	0.050	6.363
Rushton Turbine	300	25	0.278	0.785	0.053	6.810	0.056	7.124
Rushton Turbine	300	27	0.300	0.785	0.052	6.584	0.054	6.876
Rushton Turbine	300	30	0.333	0.785	0.307	39.025	0.307	39.025
Rushton Turbine	450	18	0.200	1.178	0.119	10.108	0.109	9.254
Rushton Turbine	450	20	0.222	1.178	0.089	7.528	0.077	6.506
Rushton Turbine	450	25	0.278	1.178	0.091	7.749	0.080	6.765
Rushton Turbine	450	27	0.300	1.178	0.090	7.676	0.078	6.625
Rushton Turbine	450	30	0.333	1.178	0.460	39.025	0.460	39.025
Rushton Turbine	600	18	0.200	1.571	0.138	8.758	0.122	7.781
Rushton Turbine	600	20	0.222	1.571	0.139	8.865	0.125	7.981
Rushton Turbine	600	25	0.278	1.571	0.151	9.627	0.140	8.905
Rushton Turbine	600	27	0.300	1.571	0.155	9.886	0.142	9.029
Rushton Turbine	600	30	0.333	1.571	0.613	39.025	0.613	39.025

Pitched Blade Impeller

Table C- 3 Volume weighted average solid and liquid velocity magnitude as a percentage of impeller tip speed for a pitched blade impeller at different impeller speeds and clearances

Impeller Geometry	Impeller Speed (rpm)	Impeller Clearance (mm)	Clearance to Vessel Diameter Ratio	Impeller Tip Speed (m/s)	Solid Average Velocity (m/s)	Average as % of Tip Speed	Water Average Velocity (m/s)	Average as % Tip Speed
Pitched Blade	300	18	0.200	0.785	0.026	3.302	0.036	4.599
Pitched Blade	300	20	0.222	0.785	0.024	3.114	0.036	4.533
Pitched Blade	300	25	0.278	0.785	0.023	2.891	0.034	4.338
Pitched Blade	300	27	0.300	0.785	0.035	4.410	0.045	5.765
Pitched Blade	300	30	0.333	0.785	0.035	4.410	0.053	6.724
Pitched Blade	450	18	0.200	1.178	0.043	3.616	0.046	3.909
Pitched Blade	450	20	0.222	1.178	0.038	3.211	0.047	4.024
Pitched Blade	450	25	0.278	1.178	0.035	2.929	0.044	3.737
Pitched Blade	450	27	0.300	1.178	0.045	3.789	0.055	4.692
Pitched Blade	450	30	0.333	1.178	0.045	3.789	0.057	4.798
Pitched Blade	600	18	0.200	1.571	0.059	3.729	0.060	3.789
Pitched Blade	600	20	0.222	1.571	0.057	3.653	0.060	3.840
Pitched Blade	600	25	0.278	1.571	0.053	3.353	0.056	3.584
Pitched Blade	600	27	0.300	1.571	0.065	4.115	0.065	4.156
Pitched Blade	600	30	0.333	1.571	0.065	4.115	0.065	4.156

Code for the Custom Agglomeration Kernel

```
PARAMETER
   Number_of_grid_points_1    AS INTEGER
   Number_of_grid_points_2    AS INTEGER
   Length_1              AS ARRAY(Number_of_grid_points_1) OF particle_length_gFP # in microns
   Length_2              AS ARRAY(Number_of_grid_points_2) OF particle_length_gFP # in microns
   Kernel_parameter_names     AS ORDERED_SET DEFAULT []
   conv_um_to_m           AS REAL DEFAULT 1e-6
   Flat_Blade         AS INTEGER DEFAULT 0
   Rushton           AS INTEGER DEFAULT 0
   Pitched_Blade      AS INTEGER DEFAULT 0
   Propeller          AS INTEGER DEFAULT 0


   # =======================================================================
   # USER AREA - BEGIN
   # -----------------------------------------------------------------------------------------------------------------------
   g_acceleration          AS REAL DEFAULT 9.8
   pi               AS REAL DEFAULT 3.14159265359
   # -----------------------------------------------------------------------------------------------------------------------
   # USER AREA - END
   # =======================================================================
PORT
   System_information       AS Sensor_information_gFP DIRECTION_BIDIRECTIONAL
VARIABLE
   Agglomeration_rate_kernel      AS ARRAY(Number_of_grid_points_1, Number_of_grid_points_2) OF
rate_constant_gFP
   Kernel_parameters           AS ARRAY(Kernel_parameter_names) OF custom_variable_gFP
   # =======================================================================
   # USER AREA - BEGIN
   # -----------------------------------------------------------------------------------------------------------------------
   # User inputs
      # Meeting probability variables:
Meeting_probability       AS ARRAY (Number_of_grid_points_1,Number_of_grid_points_2) OF no_type
Separation_force          AS ARRAY (Number_of_grid_points_1,Number_of_grid_points_2) OF no_type
Collision_energy          AS ARRAY (Number_of_grid_points_1,Number_of_grid_points_2) OF no_type
Deformation_energy        AS ARRAY (Number_of_grid_points_1,Number_of_grid_points_2) OF no_type
Deformation           AS ARRAY (Number_of_grid_points_1,Number_of_grid_points_2) OF no_type
Adhesive_force        AS ARRAY (Number_of_grid_points_1,Number_of_grid_points_2) OF no_type
Agglomeration_efficiency       AS  ARRAY  (Number_of_grid_points_1,Number_of_grid_points_2)  OF
no_type
Difference            AS ARRAY (Number_of_grid_points_1,Number_of_grid_points_2) OF no_type
C_Meeting_probability      AS no_type
C_Agglomeration_efficiency   AS no_type
Collision_velocity        AS ARRAY(Number_of_grid_points_1,Number_of_grid_points_2) OF no_type
```

Particle_fluid_velocity_1   AS ARRAY(Number_of_grid_points_1) OF no_type
Particle_fluid_velocity_2   AS ARRAY(Number_of_grid_points_2) OF no_type
Suspension_liquid_density   AS no_type #Suspension liquid density
Suspension_liquid_viscosity AS no_type #Suspension liquid viscosity
Power   AS no_type #average stirring power dissipated per unit of suspension mass
Target_efficiency   AS ARRAY(Number_of_grid_points_1,Number_of_grid_points_2) OF no_type
Agglomerate_density   AS no_type
Particle_tvelocity_parameter AS no_type
Solid_density   AS no_type
Binder_density   AS no_type
Agglomerate_porosity   AS no_type #average porosity as function of time
Agglomerate_bliquidfracion AS no_type
Agglomerate_sliquidfracion AS no_type
BSR   AS no_type
BSR_granule   AS no_type
Agglomeration efficiency variables:
S_saturation   AS no_type
Sigma_cap   AS no_type
Sigma_fun   AS no_type
Force_bridge   AS no_type
Size_primary   AS particle_length_gFP # in microns
Interfacial_tension   AS no_type
Betta   AS no_type
Tetta   AS no_type
Separation_distance   AS no_type
R_1   AS no_type
R_2   AS no_type
BSRmin   AS no_type
BSRmax   AS no_type
Impeller_diameter   AS no_type #in m
Suspension_volume   AS no_type #in ml
Impeller_speed   AS no_type #in rpm
z   AS no_type
y   AS no_type
x   AS no_type
t_residence   AS no_type
Test   AS no_type
Power_Number   AS no_type
Impeller_Clearance   AS no_type
Vessel_Diameter   AS no_type
Clearance_Diameter_Ratio   AS no_type
Particle_Velocity_Fit   AS no_type
Liquid_Velocity_Fit   AS no_type
Number_of_Blades   AS no_type

Blade_Pitch   AS no_type
Impeller_Blade_Height   AS no_type
Baffle_Width   AS no_type
Liquid_Depth   AS no_type
Number_of_Baffles   AS no_type
#Power Number Parameters to Calculate
Unbaffled_Power_Number   AS no_type
Fully_Baffled_Power_Number   AS no_type
Reynolds_Number   AS no_type
Modified_Reynolds_Number   AS no_type
Friction_Factor   AS no_type
CL   AS no_type
CT   AS no_type
m   AS no_type
CTR   AS no_type
Approx_Friction_Factor   AS no_type
Capital_X   AS no_type
Betar   AS no_type
Gammar   AS no_type
Etar   AS no_type
Small_x   AS no_type
Thetar   AS no_type
Pitched_Blade_Pitch   AS no_type

USER AREA - END
#==
SET
==
USER AREA - BEGIN

Name your kernel parameters as an ordered set. This will allow you to
assign their values directly in the dialog boxes of unit operations that consider agglomeration
Kernel_parameter_names := ["Solid_density",
"Binder_density",
"C_Meeting_probability",
"Suspension_liquid_density",
"Suspension_liquid_viscosity",
"Interfacial_tension",
"Betta",
"Tetta",
"Separation_distance",
"BSRmin",
"BSRmax",
"C_Agglomeration_efficiency",

```
"Impeller_diameter",
"Suspension_volume",
"Impeller_speed" ,
"Impeller_Clearance",
"Vessel_Diameter",
"Number_of_Blades",
"Blade_Pitch",
"Impeller_Blade_Height",
"Baffle_Width",
"Liquid_Depth",
"Number_of_Baffles"] ;
# -----------------------------------------------------------------------------------------------------------------------#
USER                               AREA                          -                            END
#=================================================================================
EQUATION
# ======================================================================
# USER AREA – BEGIN
# --------------------------------------------------------------------------------------------------
# If desired, equate your kernel parameters to local variables to make them easier to work with.
C_Meeting_probability = Kernel_parameters("C_Meeting_probability") ;
Suspension_liquid_density = Kernel_parameters("Suspension_liquid_density") ;
Suspension_liquid_viscosity = Kernel_parameters("Suspension_liquid_viscosity") ;
Solid_density=Kernel_parameters("Solid_density") ;
Binder_density=Kernel_parameters("Binder_density") ;
Interfacial_tension=Kernel_parameters("Interfacial_tension") ;
Betta=Kernel_parameters("Betta");
Tetta=Kernel_parameters("Tetta");
Separation_distance=Kernel_parameters("Separation_distance");
BSRmin=Kernel_parameters("BSRmin");
BSRmax=Kernel_parameters("BSRmax");
C_Agglomeration_efficiency=Kernel_parameters("C_Agglomeration_efficiency");
Impeller_diameter=Kernel_parameters("Impeller_diameter");
Suspension_volume=Kernel_parameters("Suspension_volume");
Impeller_speed=Kernel_parameters("Impeller_speed");
Impeller_Clearance=Kernel_parameters("Impeller_Clearance");
Vessel_Diameter=Kernel_parameters("Vessel_Diameter");
Number_of_Blades  = Kernel_parameters ("Number_of_Blades");
Blade_Pitch = Kernel_parameters ("Blade_Pitch");
Impeller_Blade_Height  = Kernel_parameters ("Impeller_Blade_Height");
Baffle_Width  = Kernel_parameters ("Baffle_Width");
Liquid_Depth = Kernel_parameters ("Liquid_Depth");
Number_of_Baffles  = Kernel_parameters ("Number_of_Baffles");
```

Agglomerate_density = (1-Agglomerate_porosity) *Solid_density + Agglomerate_bliquidfracion * Binder_density;

x=Agglomerate_sliquidfracion*Suspension_liquid_density*Suspension_liquid_density;

z=Agglomerate_bliquidfracion*Binder_density;#test

y=(1-Agglomerate_porosity)*Solid_density;#test

BSR_granule=Agglomerate_bliquidfracion/(1-Agglomerate_porosity);

Power=Power_Number*Impeller_diameter^5*(Impeller_speed/60)^3/(Suspension_volume*1e-6);

Clearance_Diameter_Ratio=Impeller_Clearance/Vessel_Diameter;

FOR i := 1 TO 1-Flat_Blade-Rushton-Pitched_Blade-Propeller DO
 Particle_Velocity_Fit=1;
 Liquid_Velocity_Fit= 1;
END

Betar=(2*log(Vessel_Diameter/Impeller_Diameter))/((Vessel_Diameter/Impeller_Diameter)-(Impeller_Diameter/Vessel_Diameter));

etar=   0.711   *   (0.157+((Number_of_Blades *(LOG(max(1.1,Vessel_Diameter/Impeller_Diameter)))^0.611)))/ max(1e-10,(Number_of_Blades^0.52)*(1-((Impeller_Diameter/Vessel_Diameter)^2)));

gammar=((etar*log(Vessel_Diameter/Impeller_Diameter))/(((betar*(Vessel_Diameter)/Impeller_Diameter))^5))^1/3;

Capital_X=(MAX(1e5,gammar*(Number_of_Blades^0.7)*Impeller_Blade_Height*((abs(sin(thetar/Liquid_Depth)))^1.6)));

Unbaffled_Power_Number=MAX(1e-10,Friction_Factor*((1.2*(pi^4)*(Betar^2))/((8*(Impeller_Diameter^3))/((Vessel_Diameter^3)*Liquid_Depth))));

Reynolds_Number=((Impeller_Speed/60)*Suspension_liquid_density*(Impeller_Diameter^2))/Suspension_liquid_viscosity;

Modified_Reynolds_Number=(MAX(1,((pi*Etar*log(Vessel_Diameter/Impeller_Diameter))/((4*Impeller_Diameter)/(Betar*Vessel_Diameter)))*Reynolds_Number));

CL=ABS((0.215*Etar*Number_of_Blades)*(Impeller_Diameter/Liquid_Depth)*(1-(Impeller_Diameter/Vessel_Diameter)^2)+1.83*(Impeller_Blade_Height*(sin(Thetar/Liquid_Depth)))*1.83*(Impeller_Blade_Height*(sin(Thetar/Liquid_Depth))));

CTR=23.8*((Impeller_Diameter/Vessel_Diameter)^(-3.24))*((Impeller_Blade_Height*abs(sin(Thetar/Vessel_Diameter)))^(-1.18))*(MAX(1e-10,Capital_X)^(-0.74));

Approx_Friction_Factor=0.0151*(Impeller_Diameter/Vessel_Diameter)*(CT^(0.308));

Friction_Factor=CL/Modified_Reynolds_Number+CT*(((((CTR/Modified_Reynolds_Number)+Modified_Reynolds_Number)^(-1))+((Approx_Friction_Factor/CT)^(1/m)))^m);

IF Number_of_baffles<1 THEN
Power_Number=Unbaffled_power_number;
else
Power_Number=ABS(Fully_Baffled_Power_Number*((1+(Small_x^(-3)))^(-1/3)));
END

#Flat Blade
FOR i := 1 TO Flat_Blade DO
CT=(((1.96*(Capital_X)^1.19)^(-7.8))+(0.25^(-7.8)))^(-1/7.8);
m=(((0.71*(Capital_X)^0.373)^(-7.8))+(0.333^(-7.8)))^(-1/7.8);
Small_x=((4.5*((Baffle_Width/Vessel_Diameter)*(Number_of_Baffles^(0.8))))/(Fully_Baffled_Power_Number^(0.2)))+(Unbaffled_Power_Number/Fully_Baffled_Power_Number);
Thetar=(Blade_Pitch*pi)/180;
IF (Number_of_Blades^0.7)*(Impeller_Blade_Height/Impeller_Diameter)<=0.54 THEN
Fully_Baffled_Power_Number=10*((Number_of_Blades^0.7)*(Impeller_Blade_Height/Impeller_Diameter))^1.3;
ELSE   IF   (Number_of_Blades^0.7)*(Impeller_Blade_Height/Impeller_Diameter)>0.54   AND (Number_of_Blades^0.7)*(Impeller_Blade_Height/Impeller_Diameter)<=1.6 THEN
Fully_Baffled_Power_Number=8.3*((Number_of_Blades^0.7)*(Impeller_Blade_Height/Impeller_Diameter));
ELSE
Fully_Baffled_Power_Number=10*((Number_of_Blades^0.7)*(Impeller_Blade_Height/Impeller_Diameter))^0.6;
END
END
IF Clearance_Diameter_Ratio<0.21 THEN
   Particle_Velocity_Fit=((-7E-05*(Impeller_Speed^2))+(0.0603*Impeller_Speed)+26.93)/100;
   Liquid_Velocity_Fit= ((-4E-05*(Impeller_Speed^2))+(0.0389*Impeller_Speed)+31.263)/100;
   ELSE IF Clearance_Diameter_Ratio>0.21 AND Clearance_Diameter_Ratio<0.26 THEN
   Particle_Velocity_Fit=((-1e-07*(Impeller_Speed^2))+(8e-05*Impeller_Speed)+39.05)/100;
   Liquid_Velocity_Fit=((-2e-07*(Impeller_Speed^2))+(0.0001*Impeller_Speed)+39.047)/100;

```
ELSE IF Clearance_Diameter_Ratio>0.26 AND Clearance_Diameter_Ratio <0.29 THEN
Particle_Velocity_Fit=((0.0002*(Impeller_Speed^2))-(0.1431*Impeller_Speed)+67.706)/100;
Liquid_Velocity_Fit=((-1e-04*(Impeller_Speed^2))-(0.0882*Impeller_Speed)+56.666)/100;
ELSE IF Clearance_Diameter_Ratio>0.29 AND Clearance_Diameter_Ratio<0.32 THEN
Particle_Velocity_Fit=((-1e-04*(Impeller_Speed^2))+(0.096*Impeller_Speed)-15.659)/100;
Liquid_Velocity_Fit=((-1e-05*(Impeller_Speed^2))+(0.019*Impeller_Speed)+4.3938)/100;
ELSE
Particle_Velocity_Fit=((-0.0001*(Impeller_Speed^2))+(0.1291*Impeller_Speed)-22.986)/100;
Liquid_Velocity_Fit=   ((-2e-05*(Impeller_Speed^2))+(0.019*Impeller_Speed)+4.3938)/100;
END
END
END
END
END

FOR i := 1 TO Rushton DO
CT=(((1.96*(Capital_X)^1.19)^(-7.8))+(0.25^(-7.8)))^(-1/7.8);
m=(((0.71*(Capital_X)^0.373)^(-7.8))+(0.333^(-7.8)))^(-1/7.8);
Small_x=((4.5*((Baffle_Width/Vessel_Diameter)*(Number_of_Baffles^(0.8))))/(Fully_Baffled_Power_Nu
mber^(0.2)))+(Unbaffled_Power_Number/Fully_Baffled_Power_Number);
Thetar=(Blade_Pitch*pi)/180;
IF (Number_of_Blades^0.7)*(Impeller_Blade_Height/Impeller_Diameter)<=0.54 THEN
Fully_Baffled_Power_Number=10*((Number_of_Blades^0.7)*(Impeller_Blade_Height/Impeller_Diamet
er))^1.3;
ELSE    IF     (Number_of_Blades^0.7)*(Impeller_Blade_Height/Impeller_Diameter)>0.54      AND
(Number_of_Blades^0.7)*(Impeller_Blade_Height/Impeller_Diameter)<=1.6 THEN
Fully_Baffled_Power_Number=8.3*((Number_of_Blades^0.7)*(Impeller_Blade_Height/Impeller_Diamet
er));
ELSE
Fully_Baffled_Power_Number=10*((Number_of_Blades^0.7)*(Impeller_Blade_Height/Impeller_Diamet
er))^0.6;
END
END
  IF  Clearance_Diameter_Ratio<0.21 THEN
  Particle_Velocity_Fit=((-9E-05*(Impeller_Speed^2))+(0.0894*Impeller_Speed)-10.306)/100;
  Liquid_Velocity_Fit= ((-9e-05*(Impeller_Speed^2))+(0.0832*Impeller_Speed)-10.865)/100;
  ELSE IF Clearance_Diameter_Ratio>0.21 AND Clearance_Diameter_Ratio<0.26 THEN
  Particle_Velocity_Fit=((7e-06*(Impeller_Speed^2))+(0.0011*Impeller_Speed)+5.7077)/100;
  Liquid_Velocity_Fit=((2E-05*(Impeller_Speed^2))-(0.0105*Impeller_Speed)+7.6219)/100;
  ELSE IF Clearance_Diameter_Ratio>0.26 AND Clearance_Diameter_Ratio <0.29 THEN
  Particle_Velocity_Fit=((1E-05*(Impeller_Speed^2))-(0.0039*Impeller_Speed)+6.6215)/100;
  Liquid_Velocity_Fit=((5e-05*(Impeller_Speed^2))-(0.0379*Impeller_Speed)+14.076)/100;
  ELSE IF Clearance_Diameter_Ratio>0.29 AND Clearance_Diameter_Ratio<0.32 THEN
  Particle_Velocity_Fit=((5e-06*(Impeller_Speed^2))+(0.0057*Impeller_Speed)+4.3427)/100;
```

```
    Liquid_Velocity_Fit=((3e-05*(Impeller_Speed^2))-(0.0213*Impeller_Speed)+10.424)/100;
    ELSE
    Particle_Velocity_Fit=((-6e-05*(Impeller_Speed^2))+(0.0521*Impeller_Speed)+28.531)/100;
    Liquid_Velocity_Fit=  ((-6e-05*(Impeller_Speed^2))+(0.0521*Impeller_Speed)+28.531)/100;
    END
    END
    END
    END
END

FOR i := 1 TO Pitched_Blade DO
IF blade_Pitch>44.9 AND blade_pitch<45.1 THEN
Thetar=(Pitched_Blade_Pitch*pi)/180;
ELSE
Thetar=(Blade_Pitch*pi)/180;
END
Ct=(((1.96*(Capital_X^1.19))^(-7.8))+(0.25^(-7.8)))^(-1/7.8);
m=(((0.71*(Capital_X^0.373))^(-7.8))+(0.333^(-7.8)))^(-1/7.8);
Fully_Baffled_Power_Number=MAX(1e-
10,8.3*(ABS(((2*thetar)/pi))^0.9)*((Number_of_Blades^0.7*Impeller_Blade_Height*(ABS((sin(thetar/Im
peller_Diameter))))^1.6)));
Small_x=(4.5*((Baffle_Width/Vessel_Diameter)*(Number_of_Baffles^0.8)))/((ABS((2*thetar/pi))^0.72)*(
Fully_Baffled_Power_Number^0.2))+(Unbaffled_Power_Number/Fully_Baffled_Power_Number);
  IF  Clearance_Diameter_Ratio<0.21 THEN
  Particle_Velocity_Fit=( (-3E-06*(Impeller_Speed^2))+(0.0041*Impeller_Speed)+2.3232)/100;
  Liquid_Velocity_Fit= ((1e-05*(Impeller_Speed^2))-(0.0136*Impeller_Speed)+7.5951)/100;
  ELSE IF Clearance_Diameter_Ratio>0.21 AND Clearance_Diameter_Ratio<0.26 THEN
  Particle_Velocity_Fit=((4E-06*(Impeller_Speed^2))-(0.0014*Impeller_Speed)+3.1023)/100;
  Liquid_Velocity_Fit=((5e-06*(Impeller_Speed^2))-(0.0067*Impeller_Speed)+6.0505)/100;
  ELSE IF Clearance_Diameter_Ratio>0.26 AND Clearance_Diameter_Ratio <0.29 THEN
  Particle_Velocity_Fit=((7E-06*(Impeller_Speed^2))-(0.0048*Impeller_Speed)+3.6786)/100;
  Liquid_Velocity_Fit=((1e-05*(Impeller_Speed^2))-(0.0113*Impeller_Speed)+6.8389)/100;
  ELSE IF Clearance_Diameter_Ratio>0.29 AND Clearance_Diameter_Ratio<0.32 THEN
  Particle_Velocity_Fit=((-3e-06*(Impeller_Speed^2))-(0.0041*Impeller_Speed)+5.9627)/100;
  Liquid_Velocity_Fit=((1e-05*(Impeller_Speed^2))-(0.0147*Impeller_Speed)+9.2353)/100;
  ELSE
  Particle_Velocity_Fit=((-2e-05*(Impeller_Speed^2))+(0.0149*Impeller_Speed)+2.0962)/100;
  Liquid_Velocity_Fit=  ((3e-05*(Impeller_Speed^2))-(0.0329*Impeller_Speed)+14.134)/100;
  END
  END
  END
  END
END
```

```
FOR i := 1 TO Propeller DO
Ct=(((3*(Capital_X^1.5))^(-7.8))+(0.25^(-7.8)))^(-1/7.8);
m=(((0.8*(Capital_X^0.373))^(-7.8))+(0.333^(-7.8)))^(-1/7.8);
Fully_Baffled_Power_Number=MAX(1e-
10,6.5*((Number_of_Blades^0.7)*(Impeller_Blade_Height*((ABS(SIN(thetar/impeller_Diameter)))^1.6)^
1.7)));
Small_x=(4.5*((Baffle_Width/Vessel_Diameter)*(Number_of_Baffles^0.8)))/((ABS((2*thetar/pi))^0.72)*(
Fully_Baffled_Power_Number^0.2))+(Unbaffled_Power_Number/Fully_Baffled_Power_Number);
Thetar=(Blade_Pitch*pi)/180;
IF  Clearance_Diameter_Ratio<0.21 THEN
   Particle_Velocity_Fit=( (-6E-05*(Impeller_Speed^2))+(0.069*Impeller_Speed)-12.835)/100;
   Liquid_Velocity_Fit= ((-2e-05*(Impeller_Speed^2))+(0.0143*Impeller_Speed)+5.0721)/100;
   ELSE IF Clearance_Diameter_Ratio>0.21 AND Clearance_Diameter_Ratio<0.26 THEN
   Particle_Velocity_Fit=((-3E-05*(Impeller_Speed^2))+(0.0401*Impeller_Speed)-6.1806)/100;
   Liquid_Velocity_Fit=((-2E-05*(Impeller_Speed^2))+(0.0186*Impeller_Speed)+3.9794)/100;
   ELSE IF Clearance_Diameter_Ratio>0.26 AND Clearance_Diameter_Ratio <0.29 THEN
   Particle_Velocity_Fit=((-1e-05*(Impeller_Speed^2))+(0.0308*Impeller_Speed)-5.8947)/100;
   Liquid_Velocity_Fit=((-7e-06*(Impeller_Speed^2))+(0.0077*Impeller_Speed)+5.9241)/100;
   ELSE IF Clearance_Diameter_Ratio>0.29 AND Clearance_Diameter_Ratio<0.32 THEN
   Particle_Velocity_Fit=((-2e-05*(Impeller_Speed^2))+(0.0361*Impeller_Speed)-6.7771)/100;
   Liquid_Velocity_Fit=((-4e-06*(Impeller_Speed^2))+(0.0055*Impeller_Speed)+6.2981)/100;
   ELSE
   Particle_Velocity_Fit=((-2e-06*(Impeller_Speed^2))+(0.0204*Impeller_Speed)-3.8957)/100;
   Liquid_Velocity_Fit=   ((-8e-06 *(Impeller_Speed^2))+(0.0088*Impeller_Speed)+5.5177)/100;
   END
   END
   END
   END
END

IF t_residence<181  then
Test=0;
else
Test=Max(1,ABS(Agglomerate_density-Suspension_liquid_density));
END

Particle_tvelocity_parameter=Liquid_Velocity_Fit*(32/225*(Test)^2*g_acceleration^2/Suspension_liqui
d_density/Suspension_liquid_viscosity)^(1/3);

   FOR              i:=1            TO            Number_of_grid_points_1            DO
Particle_fluid_velocity_1(i)=Particle_Velocity_Fit*SQRT(Max(0,((Test))^3/200/Suspension_liquid_density
/Suspension_liquid_viscosity/(2*Agglomerate_density+Suspension_liquid_density)))*(Length_1(i)*conv
_um_to_m)^(3/5)*Power^(2/5);
```

```
    END


    FOR                 j:=1              TO              Number_of_grid_points_2              DO
Particle_fluid_velocity_2(j)=Particle_Velocity_Fit*SQRT(Max(0,((Test))^3/200/Suspension_liquid_density
/Suspension_liquid_viscosity/(2*Agglomerate_density+Suspension_liquid_density)))*(Length_2(j)*conv
_um_to_m)^(3/5)*Power^(2/5);
    END


    FOR i:=1 TO Number_of_grid_points_1 DO
    FOR j:=1 TO Number_of_grid_points_2 DO
    Collision_velocity(i,j)=SQRT(Particle_fluid_velocity_1(i)^2+Particle_fluid_velocity_2(j)^2);
    Target_efficiency(i,j)=Particle_tvelocity_parameter*(Length_2(j)*
conv_um_to_m)/(2*g_acceleration*(Length_1(i)* conv_um_to_m))*Collision_velocity(i,j);
    Meeting_probability(i,j)=Max(0,C_Meeting_probability*Target_efficiency(i,j)*pi/4*((Length_1(i)*
conv_um_to_m)+(Length_2(j)* conv_um_to_m))^2*Collision_velocity(i,j));
    END
    END


    #Separation Force:
    FOR i:=1 TO Number_of_grid_points_1 DO
    FOR j:=1 TO Number_of_grid_points_2 DO
    If i<=j then

Separation_force(i,j)=Suspension_liquid_density*(Power*(Length_1(i)*conv_um_to_m+Length_2(j)*con
v_um_to_m))^(2/3)*(Length_1(i)*conv_um_to_m)^2;
    else
    Separation_force(i,j)=Separation_force(j,i);
    END
    END
    END


    #BSR_granule*(1-Agglomerate_porosity)/(Agglomerate_porosity):
    S_saturation=1;

    R_1=(Size_primary*conv_um_to_m*(1-
cos((Betta*pi/180)))+Separation_distance*conv_um_to_m)/(2*cos((Betta+Tetta)*pi/180));
    R_2=Size_primary*conv_um_to_m*sin((Betta*pi/180))/2+R_1*(sin(((Betta+Tetta)*pi/180))-1);
    Sigma_cap=8*(1-
Agglomerate_porosity)*Interfacial_tension/(Agglomerate_porosity)/(Size_primary*conv_um_to_m);

Force_bridge=pi*Size_primary*conv_um_to_m*Interfacial_tension*sin((Betta*pi/180))*(sin((Betta*pi/1
80)+(Tetta*pi/180))+Size_primary*conv_um_to_m/4*sin((Betta*pi/180))*(1/R_1-1/R_2));
```

```
    Sigma_fun=Max(0,Sigma_cap);

 #Collision energy:

  FOR i:=1 TO Number_of_grid_points_1 DO
  FOR j:=1 TO Number_of_grid_points_2 DO

  Collision_energy(i,j)=
pi/6*Agglomerate_density*((Length_1(i)*conv_um_to_m)^3*(Length_2(j)*conv_um_to_m)^3/((Length
_1(i)*conv_um_to_m)^3+(Length_2(j)*conv_um_to_m)^3))*(Particle_fluid_velocity_1(i)^2+Particle_flui
d_velocity_2(j)^2);

  Deformation_energy(i,j)=Max(0,(BSR-BSRmin)/Max(0.01,(BSRmax-BSRmin))*Collision_energy(i,j));

  END
  END


  FOR i:=1 TO Number_of_grid_points_1 DO
  FOR j:=1 TO Number_of_grid_points_2 DO


  If i<=j then
  Deformation(i,j)=Max(0.000001,Sqrt((Length_2(j)*conv_um_to_m/2)^2-(Max(0,
Length_2(j)*conv_um_to_m/2-
Sqrt(Max(0.0000000000000000001,(Deformation_energy(i,j)/((Sigma_fun)*pi*(Length_2(j)*conv_um_t
o_m/2+Length_1(i)*conv_um_to_m/2)))))))^2));
    ELSE
   Deformation(i,j)=Deformation(j,i);
     END
  END
  END


  FOR i:=1 TO Number_of_grid_points_1 DO
  FOR j:=1 TO Number_of_grid_points_2 DO
  Adhesive_force(i,j)=(Deformation(i,j)/(Size_primary*conv_um_to_m/2))^2*(1-
Agglomerate_porosity)*Force_bridge*((Length_1(i)*conv_um_to_m)^2+(Length_2(j)*conv_um_to_m)^
2)/((Length_1(i)*conv_um_to_m)^3+(Length_2(j)*conv_um_to_m)^3);

  END
  END

  FOR i:=1 TO Number_of_grid_points_1 DO
```

```
   FOR j:=1 TO Number_of_grid_points_2 DO

  Difference(i,j)= Adhesive_force(i,j)- Separation_force(i,j);

Agglomeration_efficiency(i,j)=C_Agglomeration_efficiency*((Difference(i,j)+ABS(Difference(i,j)))/2)/MAX
(1e-10,Separation_force(i,j));

  END
  END

  FOR i:=1 TO Number_of_grid_points_1 DO
  FOR j:=1 TO Number_of_grid_points_2 DO

  Agglomeration_rate_kernel(i,j)=Meeting_probability(i,j)* Agglomeration_efficiency(i,j);
    END
  END

ASSIGN
Pitched_Blade_Pitch:=46;
```

Code for the Custom Layering Kernel

```
PARAMETER

    Number_of_grid_points        AS INTEGER  # no_FVB

    Length                       AS ARRAY(Number_of_grid_points) OF particle_length_gFP # [microns] L_FVB

    Kinetic_parameter_names      AS ORDERED_SET DEFAULT []

   Flat_Blade        AS INTEGER DEFAULT 0

    Rushton          AS INTEGER DEFAULT 0

    Pitched_Blade      AS INTEGER DEFAULT 0

    Propeller         AS INTEGER DEFAULT 0

 # =====================================================================

 # USER AREA - BEGIN

 # ----------------------------------------------------------------------------------------------------------------------

  g               AS REAL DEFAULT 9.8

  pi              AS REAL DEFAULT 3.14159265359

 # ----------------------------------------------------------------------------------------------------------------------

 # USER AREA - END

 # =====================================================================

UNIT

    univ                       AS                             universal_parameters_gFP

VARIABLE

    Layering_growth_rate              AS  ARRAY(Number_of_grid_points)  OF  linear_growth_rate_gFP  #
[microns/second]

    Kinetic_parameters        AS ARRAY(Kinetic_parameter_names) OF custom_variable_gFP

 # =====================================================================

 # USER AREA - BEGIN

 # ----------------------------------------------------------------------------------------------------------------------

     # Declare local variables for intermediate calculations.

zee              AS no_type

UDp               AS no_type
```

```
UDd                          AS no_type #ARRAY(Number_of_grid_points) OF no_type

alpha                        AS no_type #ARRAY(Number_of_grid_points) OF no_type

mp                           AS no_type

fepb                         AS no_type

Size_primary                 As particle_length_gFP # in microns

Binder_viscosity             AS no_type #REAL DEFAULT 3.76E-04

Suspension_liquid_viscosity  AS no_type #REAL DEFAULT 8.90E-04

interfacial_tension          AS no_type #REAL DEFAULT 0.0502

teta                         AS no_type #REAL DEFAULT 60

fecp1                        AS no_type #REAL DEFAULT 0.36

Solid_density                AS no_type #REAL DEFAULT 1100

Binder_density               AS no_type #REAL DEFAULT 684

Suspension_liquid_density    AS no_type #REAL DEFAULT 1000

Power                        AS no_type #REAL DEFAULT 0.01

Suspension_volume            AS no_type #REAL DEFAULT 0.0005

TBSR                         AS no_type #REAL DEFAULT 0.55

sphericity                   AS no_type #REAL DEFAULT 0.43

t_residence                  AS no_type

Impeller_diameter            AS no_type #in m

Impeller_speed               AS no_type #in rpm

Agglomerate_size             AS particle_length_gFP # in microns

C_Growth                     AS no_type

t_coll                       AS no_type

t_imm                        AS no_type

AgNu                         AS no_type

TBSR_f                       AS no_type

Agglomerate_bliquidfracion   AS ARRAY(Number_of_grid_points) OF no_type

Power_Number                 AS no_type

Impeller_Clearance           AS no_type
```

Particle_Velocity_Fit   AS no_type

Liquid_Velocity_Fit   AS no_type

Clearance_Diameter_Ratio   AS no_type

Vessel_Diameter   AS no_type

Number_of_blades   AS no_type

Blade_pitch   AS no_type

Impeller_Blade_Height   AS no_type

Liquid_Depth   AS no_type

Number_of_baffles   AS no_type

Thetar   AS no_type

Betar AS no_type

Etar AS no_type

Gammar AS no_type

Capital_x   AS no_type

Reynolds_number AS no_type

Modified_reynolds_number AS no_type

CL AS no_type

CT AS no_type

m AS no_type

CTR AS no_type

Approx_Friction_factor AS no_type

Friction_factor AS no_type

Fully_baffled_power_Number AS no_type

Unbaffled_power_number AS no_type

small_x AS no_type

Baffle_width AS no_type

Pitched_Blade_Pitch AS no_type

 # ---

 # USER AREA - END

SELECTOR

   granule_presence AS ARRAY(Number_of_grid_points) OF (yes,no) DEFAULT no

PORT

   System_information   AS Sensor_information_gFP DIRECTION_BIDIRECTIONAL

SET

 # ==

 # USER AREA - BEGIN

 # ---

     # Name your kinetic parameters as an ordered set. This will allow you to

     # assign their values directly in the dialog boxes of unit operations

     # that consider consolidation.

     Kinetic_parameter_names := ["Binder_viscosity",

"Suspension_liquid_viscosity",

"interfacial_tension",

"teta",

"fecp",

"Solid_density",

"Binder_density",

"Suspension_liquid_density",

"Suspension_volume",

"sphericity",

"Impeller_diameter",

"Impeller_speed",

"C_Growth",

"Impeller_Clearance",

"Vessel_Diameter",

 "Number_of_blades",

"Blade_pitch",

"Impeller_blade_height",

"Liquid_Depth",

"Number_of_baffles",

"Baffle_width"] ;

```
 # ---------------------------------------------------------------------------------------------------------------------

 # USER AREA - END

 # ====================================================================
```

EQUATION

```
 # ====================================================================

 # USER AREA - BEGIN

 # ---------------------------------------------------------------------------------------------------------------------

     # If desired, equate your kinetic parameters to local variables to make them easier to work with.

     # Express the consolidation rate, or rate of decrease in porosity, in units of 1/s.

     # Note that this value should be positive for decreasing porosity.

     Binder_viscosity = Kinetic_parameters("Binder_viscosity") ;

     Suspension_liquid_viscosity=Kinetic_parameters("Suspension_liquid_viscosity") ;

     interfacial_tension=Kinetic_parameters("interfacial_tension") ;

     teta=Kinetic_parameters("teta") ;

     fecp1=MAX(1-10,Kinetic_parameters("fecp"));

     Solid_density=Kinetic_parameters("Solid_density");

     Binder_density=Kinetic_parameters("Binder_density");

     Suspension_liquid_density=Kinetic_parameters("Suspension_liquid_density");

     Suspension_volume=Kinetic_parameters("Suspension_volume");#in ml

     sphericity=Kinetic_parameters("sphericity");

     Impeller_diameter=MAX(1e-10,Kinetic_parameters("Impeller_diameter"));#in m

     Impeller_speed=Kinetic_parameters("Impeller_speed");#in rpm

     C_Growth=Kinetic_parameters("C_Growth");

     Impeller_Clearance=Kinetic_parameters("Impeller_Clearance");
```

```
Vessel_Diameter=MAX(1e-10,Kinetic_parameters("Vessel_Diameter"));

Number_of_blades= Kinetic_parameters("Number_of_Blades");

Blade_pitch        =Kinetic_parameters("Blade_pitch");

Impeller_Blade_Height    =Kinetic_parameters("Impeller_Blade_Height");

Liquid_Depth        =MAX(1e-10,Kinetic_parameters("Liquid_Depth"));

  Number_of_baffles =Kinetic_parameters("Number_of_Baffles");

  Baffle_width= Kinetic_parameters("Baffle_width");


FOR i := 1 TO 1-Flat_Blade-Rushton-Pitched_Blade-Propeller  DO

 Particle_Velocity_Fit=1;

   Liquid_Velocity_Fit= 1;

END
```

Clearance_Diameter_Ratio=Impeller_Clearance/Vessel_Diameter;

Betar=(2*log(Vessel_Diameter/Impeller_Diameter))/((Vessel_Diameter/Impeller_Diameter)-(Impeller_Diameter/Vessel_Diameter));

etar= 0.711*(0.157+((Number_of_Blades*(LOG(max(1.1,Vessel_Diameter/Impeller_Diameter)))^0.611)))/max(1e-10,(Number_of_Blades^0.52)*(1-((Impeller_Diameter/Vessel_Diameter)^2)));

gammar=((etar*log(Vessel_Diameter/Impeller_Diameter))/(((betar*(Vessel_Diameter)/Impeller_Diameter))^5))^1/3;

Capital_X=(MAX(1e-5,gammar*(Number_of_Blades^0.7)*Impeller_Blade_Height*((abs(sin(thetar/Liquid_Depth)))^1.6)));

Unbaffled_Power_Number=Friction_Factor*((1.2*(pi^4)*(Betar^2))/((8*(Impeller_Diameter^3))/((Vessel_Diameter^3)*Liquid_Depth)));

Reynolds_Number=((Impeller_Speed/60)*Suspension_liquid_density*(Impeller_Diameter^2))/Suspension_liquid_viscosity;

Modified_Reynolds_Number=(MAX(1,((pi*Etar*log(Vessel_Diameter/Impeller_Diameter))/((4*Impeller_Diameter)/(Betar*Vessel_Diameter)))*Reynolds_Number));

CL=ABS((0.215*Etar*Number_of_Blades)*(Impeller_Diameter/Liquid_Depth)*(1-(Impeller_Diameter/Vessel_Diameter)^2)+1.83*(Impeller_Blade_Height*(sin(Thetar/Liquid_Depth)))*1.83*(Impeller_Blade_Height*(sin(Thetar/Liquid_Depth))));

CTR=23.8*((Impeller_Diameter/Vessel_Diameter)^(-3.24))*((MAX(1e-10,Impeller_Blade_Height*abs(SIN(Thetar/Vessel_Diameter))))^(-1.18))*(MAX(1e-10,Capital_X)^(-0.74));

Approx_Friction_Factor=0.0151*(Impeller_Diameter/Vessel_Diameter)*(CT^(0.308));

Friction_Factor=CL/Modified_Reynolds_Number+CT*(((((CTR/Modified_Reynolds_Number)+Modified_Reynolds_Number)^(-1))+((Approx_Friction_Factor/CT)^(1/m)))^m);

IF Number_of_baffles<1 THEN

Power_Number=Unbaffled_power_number;

else

Power_Number=ABS(Fully_Baffled_Power_Number*((1+(Small_x^(-3)))^(-1/3)));

END

#Flat Blade

FOR i := 1 TO Flat_Blade DO

CT=(((1.96*(Capital_X)^1.19)^(-7.8))+(0.25^(-7.8)))^(-1/7.8);

m=(((0.71*(Capital_X)^0.373)^(-7.8))+(0.333^(-7.8)))^(-1/7.8);

Small_x=((4.5*((Baffle_Width/Vessel_Diameter)*(Number_of_Baffles^(0.8))))/(Fully_Baffled_Power_Number^(0.2)))+(Unbaffled_Power_Number/Fully_Baffled_Power_Number);

Thetar=(Blade_Pitch*pi)/180;

IF (Number_of_Blades^0.7)*(Impeller_Blade_Height/Impeller_Diameter)<=0.54 THEN

Fully_Baffled_Power_Number=10*((Number_of_Blades^0.7)*(Impeller_Blade_Height/Impeller_Diameter))^1.3;

ELSE   IF   (Number_of_Blades^0.7)*(Impeller_Blade_Height/Impeller_Diameter)>0.54   AND (Number_of_Blades^0.7)*(Impeller_Blade_Height/Impeller_Diameter)<=1.6 THEN

Fully_Baffled_Power_Number=8.3*((Number_of_Blades^0.7)*(Impeller_Blade_Height/Impeller_Diameter));

ELSE

Fully_Baffled_Power_Number=10*((Number_of_Blades^0.7)*(Impeller_Blade_Height/Impeller_Diameter))^0.6;

END

END

IF Clearance_Diameter_Ratio<0.21 THEN

   Particle_Velocity_Fit=((-7E-05*(Impeller_Speed^2))+(0.0603*Impeller_Speed)+26.93)/100;

   Liquid_Velocity_Fit= ((-4E-05*(Impeller_Speed^2))+(0.0389*Impeller_Speed)+31.263)/100;

   ELSE IF Clearance_Diameter_Ratio>0.21 AND Clearance_Diameter_Ratio<0.26 THEN

   Particle_Velocity_Fit=((-1e-07*(Impeller_Speed^2))+(8e-05*Impeller_Speed)+39.05)/100;

   Liquid_Velocity_Fit=((-2e-07*(Impeller_Speed^2))+(0.0001*Impeller_Speed)+39.047)/100;

   ELSE IF Clearance_Diameter_Ratio>0.26 AND Clearance_Diameter_Ratio <0.29 THEN

   Particle_Velocity_Fit=((0.0002*(Impeller_Speed^2))-(0.1431*Impeller_Speed)+67.706)/100;

   Liquid_Velocity_Fit=((-1e-04*(Impeller_Speed^2))-(0.0882*Impeller_Speed)+56.666)/100;

   ELSE IF Clearance_Diameter_Ratio>0.29 AND Clearance_Diameter_Ratio<0.32 THEN

   Particle_Velocity_Fit=((-1e-04*(Impeller_Speed^2))+(0.096*Impeller_Speed)-15.659)/100;

   Liquid_Velocity_Fit=((-1e-05*(Impeller_Speed^2))+(0.019*Impeller_Speed)+4.3938)/100;

   ELSE

   Particle_Velocity_Fit=((-0.0001*(Impeller_Speed^2))+(0.1291*Impeller_Speed)-22.986)/100;

   Liquid_Velocity_Fit=   ((-2e-05*(Impeller_Speed^2))+(0.019*Impeller_Speed)+4.3938)/100;

   END

   END

   END

   END

END

FOR i := 1 TO Rushton DO

Thetar=(Blade_Pitch*pi)/180;

CT=(((1.96*(Capital_X^1.19))^(-7.8))+(0.25^(-7.8)))^(-1/7.8);

m=(((0.71*(Capital_X^0.373))^(-7.8))+(0.333^(-7.8)))^(-1/7.8);

Small_x=((4.5*((Baffle_Width/Vessel_Diameter)*(Number_of_Baffles^(0.8))))/(Fully_Baffled_Power_Number^(0.2)))+(Unbaffled_Power_Number/Fully_Baffled_Power_Number);

IF (Number_of_Blades^0.7)*(Impeller_Blade_Height/Impeller_Diameter)<=0.54 THEN

Fully_Baffled_Power_Number=10*((Number_of_Blades^0.7)*(Impeller_Blade_Height/Impeller_Diameter))^1.3;

ELSE IF (Number_of_Blades^0.7)*(Impeller_Blade_Height/Impeller_Diameter)>0.54 AND (Number_of_Blades^0.7)*(Impeller_Blade_Height/Impeller_Diameter)<=1.6 THEN

Fully_Baffled_Power_Number=8.3*((Number_of_Blades^0.7)*(Impeller_Blade_Height/Impeller_Diameter));

ELSE

Fully_Baffled_Power_Number=10*((Number_of_Blades^0.7)*(Impeller_Blade_Height/Impeller_Diameter))^0.6;

END

END

IF Clearance_Diameter_Ratio<0.21 THEN

Particle_Velocity_Fit=((-9E-05*(Impeller_Speed^2))+(0.0894*Impeller_Speed)-10.306)/100;

Liquid_Velocity_Fit= ((-9e-05*(Impeller_Speed^2))+(0.0832*Impeller_Speed)-10.865)/100;

ELSE IF Clearance_Diameter_Ratio>0.21 AND Clearance_Diameter_Ratio<0.26 THEN

Particle_Velocity_Fit=((7e-06*(Impeller_Speed^2))+(0.0011*Impeller_Speed)+5.7077)/100;

Liquid_Velocity_Fit=((2E-05*(Impeller_Speed^2))-(0.0105*Impeller_Speed)+7.6219)/100;

ELSE IF Clearance_Diameter_Ratio>0.26 AND Clearance_Diameter_Ratio <0.29 THEN

Particle_Velocity_Fit=((1E-05*(Impeller_Speed^2))-(0.0039*Impeller_Speed)+6.6215)/100;

Liquid_Velocity_Fit=((5e-05*(Impeller_Speed^2))-(0.0379*Impeller_Speed)+14.076)/100;

ELSE IF Clearance_Diameter_Ratio>0.29 AND Clearance_Diameter_Ratio<0.32 THEN

Particle_Velocity_Fit=((5e-06*(Impeller_Speed^2))+(0.0057*Impeller_Speed)+4.3427)/100;

Liquid_Velocity_Fit=((3e-05*(Impeller_Speed^2))-(0.0213*Impeller_Speed)+10.424)/100;

ELSE

Particle_Velocity_Fit=((-6e-05*(Impeller_Speed^2))+(0.0521*Impeller_Speed)+28.531)/100;

Liquid_Velocity_Fit= ((-6e-05*(Impeller_Speed^2))+(0.0521*Impeller_Speed)+28.531)/100;

END

END

END

END

END

FOR i := 1 TO Pitched_Blade DO

Ct=(((1.96*(Capital_X^1.19))^(-7.8))+(0.25^(-7.8)))^(-1/7.8);

m=(((0.71*(Capital_X^0.373))^(-7.8))+(0.333^(-7.8)))^(-1/7.8);

Fully_Baffled_Power_Number=MAX(1e-10,8.3*(ABS(((2*thetar)/pi))^0.9)*((Number_of_Blades^0.7*Impeller_Blade_Height*abs((sin(thetar/Impeller_Diameter)))^1.6)));

Small_x=(4.5*((Baffle_Width/Vessel_Diameter)*(Number_of_Baffles^0.8)))/((ABS((2*thetar/pi))^0.72)*(Fully_Baffled_Power_Number^0.2))+(Unbaffled_Power_Number/Fully_Baffled_Power_Number);

IF blade_Pitch>44.9 AND blade_pitch<45.1 THEN

Thetar=(Pitched_Blade_Pitch*pi)/180;

ELSE

Thetar=(Blade_Pitch*pi)/180;

END

  IF Clearance_Diameter_Ratio<0.21 THEN

  Particle_Velocity_Fit=((-3E-06*(Impeller_Speed^2))+(0.0041*Impeller_Speed)+2.3232)/100;

  Liquid_Velocity_Fit= ((1e-05*(Impeller_Speed^2))-(0.0136*Impeller_Speed)+7.5951)/100;

  ELSE IF Clearance_Diameter_Ratio>0.21 AND Clearance_Diameter_Ratio<0.26 THEN

  Particle_Velocity_Fit=((4E-06*(Impeller_Speed^2))-(0.0014*Impeller_Speed)+3.1023)/100;

  Liquid_Velocity_Fit=((5e-06*(Impeller_Speed^2))-(0.0067*Impeller_Speed)+6.0505)/100;

  ELSE IF Clearance_Diameter_Ratio>0.26 AND Clearance_Diameter_Ratio <0.29 THEN

  Particle_Velocity_Fit=((7E-06*(Impeller_Speed^2))-(0.0048*Impeller_Speed)+3.6786)/100;

  Liquid_Velocity_Fit=((1e-05*(Impeller_Speed^2))-(0.0113*Impeller_Speed)+6.8389)/100;

  ELSE IF Clearance_Diameter_Ratio>0.29 AND Clearance_Diameter_Ratio<0.32 THEN

  Particle_Velocity_Fit=((-3e-06*(Impeller_Speed^2))-(0.0041*Impeller_Speed)+5.9627)/100;

  Liquid_Velocity_Fit=((1e-05*(Impeller_Speed^2))-(0.0147*Impeller_Speed)+9.2353)/100;

  ELSE

  Particle_Velocity_Fit=((-2e-05*(Impeller_Speed^2))+(0.0149*Impeller_Speed)+2.0962)/100;

```
      Liquid_Velocity_Fit=   ((3e-05*(Impeller_Speed^2))-(0.0329*Impeller_Speed)+14.134)/100;

      END

      END

      END

      END

END


FOR i := 1 TO Propeller DO


Ct=(((3*(Capital_X^1.5))^(-7.8))+(0.25^(-7.8)))^(-1/7.8);

m=(((0.8*(Capital_X^0.373))^(-7.8))+(0.333^(-7.8)))^(-1/7.8);

Fully_Baffled_Power_Number=MAX(1e-
10,6.5*((Number_of_Blades^0.7)*(Impeller_Blade_Height*((ABS(SIN(thetar/impeller_Diameter)))^1.6)^
1.7)));

Small_x=(4.5*((Baffle_Width/Vessel_Diameter)*(Number_of_Baffles^0.8)))/((ABS((2*thetar/pi))^0.72)*(
Fully_Baffled_Power_Number^0.2))+(Unbaffled_Power_Number/Fully_Baffled_Power_Number);

Thetar=(Blade_Pitch*pi)/180;

IF  Clearance_Diameter_Ratio<0.21 THEN

   Particle_Velocity_Fit=( -6E-05*(Impeller_Speed^2))+(0.069*Impeller_Speed)-12.835)/100;

   Liquid_Velocity_Fit= ((-2e-05*(Impeller_Speed^2))+(0.0143*Impeller_Speed)+5.0721)/100;

   ELSE IF Clearance_Diameter_Ratio>0.21 AND Clearance_Diameter_Ratio<0.26 THEN

   Particle_Velocity_Fit=((-3E-05*(Impeller_Speed^2))+(0.0401*Impeller_Speed)-6.1806)/100;

   Liquid_Velocity_Fit=((-2E-05*(Impeller_Speed^2))+(0.0186*Impeller_Speed)+3.9794)/100;

   ELSE IF Clearance_Diameter_Ratio>0.26 AND Clearance_Diameter_Ratio <0.29 THEN

   Particle_Velocity_Fit=((-1e-05*(Impeller_Speed^2))+(0.0308*Impeller_Speed)-5.8947)/100;

   Liquid_Velocity_Fit=((-7e-06*(Impeller_Speed^2))+(0.0077*Impeller_Speed)+5.9241)/100;

   ELSE IF Clearance_Diameter_Ratio>0.29 AND Clearance_Diameter_Ratio<0.32 THEN

   Particle_Velocity_Fit=((-2e-05*(Impeller_Speed^2))+(0.0361*Impeller_Speed)-6.7771)/100;

   Liquid_Velocity_Fit=((-4e-06*(Impeller_Speed^2))+(0.0055*Impeller_Speed)+6.2981)/100;
```

ELSE

Particle_Velocity_Fit=((-2e-06*(Impeller_Speed^2))+(0.0204*Impeller_Speed)-3.8957)/100;

Liquid_Velocity_Fit= ((-8e-06 *(Impeller_Speed^2))+(0.0088*Impeller_Speed)+5.5177)/100;

END

END

END

END

END

Power=Power_Number*Impeller_diameter^5*(Impeller_speed/60)^3/(Suspension_volume*1e-6);

zee=(32/225*abs(Solid_density-Suspension_liquid_density)^2*g^2/(Suspension_liquid_density*Suspension_liquid_viscosity))^(1/3);

UDp=Particle_Velocity_Fit*(abs(Solid_density-Suspension_liquid_density)^3/(200*Suspension_liquid_density*Suspension_liquid_viscosity*(2*Solid_density+Suspension_liquid_density)))^0.5*(Size_primary/1000000) ^(3/5)*Power^(2/5);

UDd=Liquid_Velocity_Fit*(abs(Binder_density-Suspension_liquid_density)^3/(200*Suspension_liquid_density*Suspension_liquid_viscosity*(2*Binder_density+Suspension_liquid_density)))^0.5*(Agglomerate_size/1000000)^(3/5)*Power^(2/5);

alpha=zee*(Size_primary/1000000)/(2*g*(Agglomerate_size/1000000))*(UDp^2+UDd^2)^0.5;

t_coll=(Agglomerate_size/1000000)*log(1/(1-TBSR_f*(1-fecp1)/fecp1))/2/alpha/(UDp^2+UDd^2)^0.5/fepb/TBSR_f;#;

t_imm=15*Binder_viscosity*(Agglomerate_size/1000000)^2*(1-fecp1)/4/sphericity/(Size_primary/1000000)/interfacial_tension/Cos((teta*pi/180))/fecp1^3;

AgNu=t_imm/t_coll;

IF t_residence<181 then

Layering_growth_rate=0;

else

IF AgNu>1 then

Layering_growth_rate=C_Growth*1000000*(sphericity*(Size_primary/1000000)*interfacial_tension*Cos((teta*pi/180))*(1-fecp1)*fecp1/15/Binder_viscosity/(t_residence-180))^0.5*MAX(0,TANH(1e3*(Agglomerate_bliquidfracion-fecp1)));

else

Layering_growth_rate=C_Growth*1000000*alpha*2*(UDp^2+UDd^2)^0.5*fepb*MAX(0,TANH(1e3*(Agglomerate_bliquidfracion-fecp1)));

END

END

--

USER AREA - END

==

==

ASSIGN

TBSR_f:= 0.4389031;

Pitched_Blade_Pitch:=46;

MATLAB Code for Pitched Blade Impeller Power Number
Calculations

```
>> Number_of_Blades=4;

Blade_Pitch=46;

Impeller_Blade_Height=0.01;

Baffle_Width=0.01;

Impeller_Clearance=0.025;

Vessel_Diameter=0.09;

Impeller_Diameter=0.05;

Liquid_Depth=0.09;

Baffle_Length=0.18;

Impeller_Speed=600;

Number_of_Baffles=4;

Suspension_Liquid_Viscosity=0.001;

Suspension_Liquid_Density=1000;

Thetar=(Blade_Pitch*pi)/180

a=Vessel_Diameter/Impeller_Diameter

b=Impeller_Diameter/Vessel_Diameter

c=Thetar/Liquid_Depth

d=Impeller_Diameter/Liquid_Depth

e=sin(Thetar)

f=Thetar/Vessel_Diameter

g=Thetar/Impeller_Diameter

h=Thetar/pi

i=sin(g)

Betar=(2*log(Vessel_Diameter/Impeller_Diameter))/((Vessel_Diameter/Impeller_Diameter)-
(Impeller_Diameter/Vessel_Diameter))

Etar=0.711*(0.157+((Number_of_Blades*(log(a)))^0.611))/((Number_of_Blades^0.52)*((1-(b^2))))

Gammar=((Etar*log(a))/(((Betar*Vessel_Diameter)/Impeller_Diameter)^5))^(1/3)

Capital_X=Gammar*(Number_of_Blades^0.7)*Impeller_Blade_Height*(sin(c))^1.6
```

Reynolds_Number=((Impeller_Speed/60)*Suspension_Liquid_Density*(Impeller_Diameter^2))/Suspension_Liquid_Viscosity

Modified_Reynolds_Number=((pi*Etar*log(Vessel_Diameter/Impeller_Diameter))/((4*Impeller_Diameter)/(Betar*Vessel_Diameter)))*Reynolds_Number

CL=0.215*Etar*Number_of_Blades*d*(1-(b^2))+(Impeller_Blade_Height*sin(c)*1.83)*((Number_of_Blades/(2*e))^(1/3))

CT=((1.96*(Capital_X^(1.19))^(-7.8))+(0.25^(-7.8)))^(-1/7.8)

m=(((0.71*(Capital_X^0.373))^(-7.8))+(0.333^(-7.8)))^(-1/7.8)

CTR=23.8*((b)^(-3.24))*((Impeller_Blade_Height*abs(sin(f)))^(-1.18))*(Capital_X^(-0.74))

Approx_Friction_Factor=0.0151*(Impeller_Diameter/Vessel_Diameter)*(CT^(0.308))

Friction_Factor=CL/Modified_Reynolds_Number+CT*(((((CTR/Modified_Reynolds_Number)+Modified_Reynolds_Number)^(-1))+((Approx_Friction_Factor/CT)^(1/m)))^m)

Fully_Baffled_Power_Number=((2*h)^(0.9))*(Number_of_Blades^(0.7))*Impeller_Blade_Height*8.3*abs(i^(1.6))

Unbaffled_Power_Number=Friction_Factor*((1.2*(pi^4)*(Betar^2))/((8*(Impeller_Diameter^3))/((Vessel_Diameter^3)*Liquid_Depth)));

Small_x=((4.5*(Baffle_Width/Vessel_Diameter)*(Number_of_Baffles^0.8)/(((2*Thetar)/pi)^0.9)*(Fully_Baffled_Power_Number^0.2)))+(Unbaffled_Power_Number/Fully_Baffled_Power_Number);

Power_Number=abs(Fully_Baffled_Power_Number*((1+(Small_x^(-3)))^(-1/3)));

Results
Thetar =   0.8029

a =   1.8000

b =   0.5556

c =   8.9206

d =   0.5556

e =   0.7193

f =   8.9206

g =   16.0570

h =   0.2556

i =   -0.3420

Betar =   0.9447

Etar =   0.9218

Gammar =   0.3365

Capital_X =   0.0028

Reynolds_Number =   2.5000e+04

Modified_Reynolds_Number =   1.8089e+04

CL =   0.3169

CT =   8.3109e-04

m =   0.0790

CTR =   6.7406e+06

Approx_Friction_Factor =   9.4396e-04

Friction_Factor =   9.6148e-04

Fully_Baffled_Power_Number =   0.0215

Excel Calculation of Pitched Blade Impeller Power Number

Table C- 4 Calculation of pitched blade power number in Microsoft Excel

Symbol	Description	Value
b	Blade Height (m)	0.01
Bw	Baffle Width (m)	0.01
C	Clearance (m)	0.03
D	Vessel Diameter (m)	0.09
d	Impeller Diameter (m)	0.05
f	Friction Factor	
H	Liquid Depth (m)	0.09
hB	Baffle Length (m)	0.18
Np	Power Number	0.02151532
Np0	Unbaffled Power Number	0.073113672
Npmax	Fully Baffled Power Number	0.021511296
n	Impeller Speed (rps)	10
nB	Number of Baffles	4
np	Number of Impeller Blades	4
P	Power Consumption (W)	
Red	Impeller Reynolds Number	25000
ReG	Modified Reynolds Number	18088.88666
T	Shaft Torque (N.m)	
theta	Angle of Impeller Blade (degrees)	46
thetar	Angle of Impeller Blade (radians)	0.802851456
mu	Liquid Viscosity (Pa.s)	0.001
rho	Liquid Density (kg/m3)	1000
Eta	0.711((0.157+(npln(D/d))^0.611)/(np^0.52(1-d/D)^2))	0.921755
gamma	(eta*ln(D/d)/(beta*D/g)^5)^1/3	0.336537824
beta	2ln(D/d)/((D/d)-(d/D))	0.94465714
X	gamma*np^0.7*b*(sin^1.6)*theta/H	0.002773022
Ct	((1.96*X^1.19)^-7.8+(0.25)^-7.8)^-1/7.8	0.000831085
f~	0.0151(d/D)Ct^0.308	0.000943964
m	(0.71*X^0.373)^-7.8+(0.333)^-7.8)^(1/7.8)	0.08
Ctr	(23.8(d/D))^(-3.24)*(b*sin(theta/D)^(-1.18)*X^-0.74	6740581.946
CL	0.215*eta*np*(d/H)(1-(d/D)^2)+1.83(b*sin(theta/H)(np/2sin(theta)^(1/3)	0.31690169
f	CL/Reg+Ct*(((Ctr/Reg)+Reg)^-1+(f~/Ct)^(1/m))^m	0.000961484
x	(4.5*(Bw/D)*nB^0.8)/((2*theta/pi)^0.72*Npmax^0.2)+Np0/Npmax	12.12244025

Model Validation

Flat Blade Impeller

Table C- 5 The experimental, PBM with flow and Ahmed et al., 2023 average particle size (d_{43}) for agglomerates produced using a flat blade impeller at varied impeller speeds and clearances

Impeller Clearance (mm)	Impeller Speed (rpm)	Experimental d_{43} (µm)	Flow PBM d_{43} (µm)	Ahmed et al., PBM d_{43} (µm)	Flow PBM %diff	Ahmed %diff
18		975.92	833.68	1036.35	15.72	6.01
20		594.70	833.43	1036.35	33.43	54.16
25	300	586.90	831.01	1036.35	34.43	55.38
27		591.28	617.17	1036.35	4.28	54.69
30		867.07	603.93	1036.35	35.78	17.79
18		1358.52	872.31	961.60	43.59	34.22
20		1226.40	868.41	961.60	34.18	24.20
25	450	797.42	822.42	961.60	3.09	18.67
27		1017.94	816.21	961.60	22.00	5.69
30		1111.25	816.50	961.60	30.58	14.44
18		1090.56	910.14	1011.76	18.04	7.50
20		1273.92	907.46	1011.76	33.60	22.94
25	600	618.79	899.05	1011.76	36.93	48.20
27		822.66	819.64	1011.76	0.37	20.62
30		677.81	820.68	1011.76	19.07	39.53

Propeller Impeller

Table C- 6 The experimental, PBM with flow and Ahmed et al., 2023 average particle size (d_{43}) for agglomerates produced using a propeller impeller at varied impeller speeds and clearances

Impeller Clearance (mm)	Impeller Speed (rpm)	Experimental d_{43} (µm)	Flow PBM d_{43} (µm)	Ahmed et al., PBM d_{43} (µm)	Flow PBM %diff	Ahmed %diff
18	300	337.53	487.28	1036.35	36.31	101.73
20		1254.51	487.56	1036.35	88.05	19.05
25		1306.47	487.32	1036.35	91.33	23.06
27		198.11	487.29	1036.35	84.38	135.81
30		167.55	487.11	1036.35	97.63	144.33
18	450	622.90	495.47	961.60	22.79	42.75
20		1275.63	497.92	961.60	87.70	28.07
25		532.03	496.96	961.60	6.82	57.52
27		626.43	496.68	961.60	23.11	42.21
30		1078.07	496.14	961.60	73.93	11.42
18	600	637.51	503.21	1011.76	23.55	45.38
20		570.68	511.56	1011.76	10.92	55.75
25		903.13	514.52	1011.76	54.82	11.35
27		700.55	513.70	1011.76	30.78	36.35
30		1067.50	512.19	1011.76	70.31	5.36

Rushton Turbine Impeller

Table C- 7 The experimental, PBM with flow and Ahmed et al., 2023 average particle size (d_{43}) for agglomerates produced using a Rushton turbine impeller at varied impeller speeds and clearances

Impeller Clearance (mm)	Impeller Speed (rpm)	Experimental d_{43} (µm)	Flow PBM d_{43} (µm)	Ahmed et al., PBM d_{43} (µm)	Flow PBM %diff	Ahmed %diff
18	300	583.34	564.64	1036.35	3.26	55.94
20		782.02	561.65	1036.35	32.80	27.97
25		811.42	578.91	1036.35	33.45	24.35
27		823.70	569.93	1036.35	36.42	22.86
30		1410.00	833.36	1036.35	51.41	30.55
18	450	662.51	784.80	961.60	16.90	36.83
20		603.58	699.70	961.60	14.75	45.75
25		867.05	701.43	961.60	21.12	10.34
27		754.22	700.90	961.60	7.33	24.17
30		625.15	870.53	961.60	32.81	42.41
18	600	679.73	819.78	1011.76	18.68	39.26
20		735.94	817.20	1011.76	10.46	31.56
25		776.96	816.62	1011.76	4.98	26.25
27		832.57	817.26	1011.76	1.86	19.43
30		769.44	904.68	1011.76	16.16	27.21

Pitched Blade Impeller

Table C- 8 The experimental, PBM with flow and Ahmed et al., 2023 average particle size (d_{43}) for agglomerates produced using a pitched blade impeller at varied impeller speeds and clearances

Impeller Clearance (mm)	Impeller Speed (rpm)	Experimental d_{43} (µm)	Flow PBM d_{43} (µm)	Ahmed et al., PBM d_{43} (µm)	Flow PBM %diff	Ahmed %diff
18	300	232.76	483.34	1036.35	69.98	126.64
20		234.61	483.34	1036.35	69.29	126.16
25		544.87	483.31	1036.35	11.97	62.16
27		533.38	483.69	1036.35	9.77	64.08
30		206.54	484.08	1036.35	80.37	133.53
18	450	683.13	483.75	961.60	34.17	33.86
20		703.28	483.99	961.60	36.94	31.03
25		776.19	483.82	961.60	46.41	21.34
27		619.42	484.32	961.60	24.48	43.29
30		715.57	484.92	961.60	38.43	29.34
18	600	775.91	484.31	1011.76	46.28	26.39
20		612.24	484.99	1011.76	23.19	49.20
25		805.31	484.76	1011.76	49.69	22.72
27		1016.54	484.98	1011.76	70.80	0.47
30		829.71	486.53	1011.76	52.15	19.77

Appendix D - CFD Simulations for Settling in MSMPRs

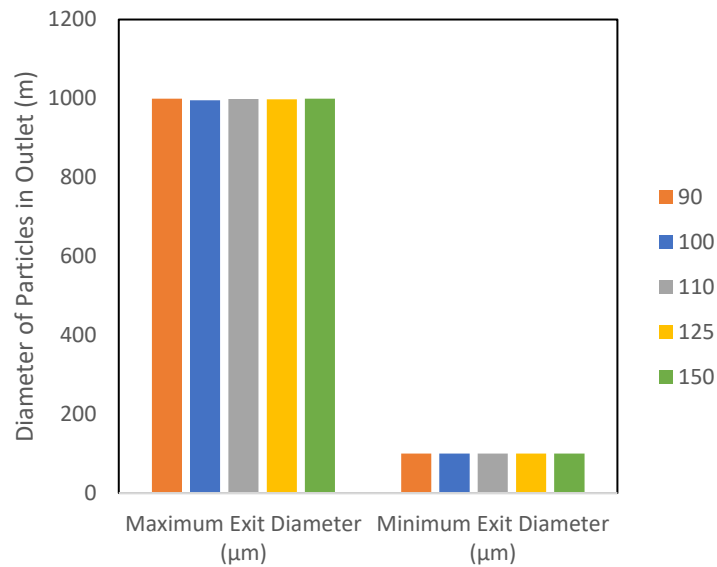## Lattice Density Analysis

Figure D- 1 Minimum and Maximum particle diameter withdrawn from the system at varying lattice density

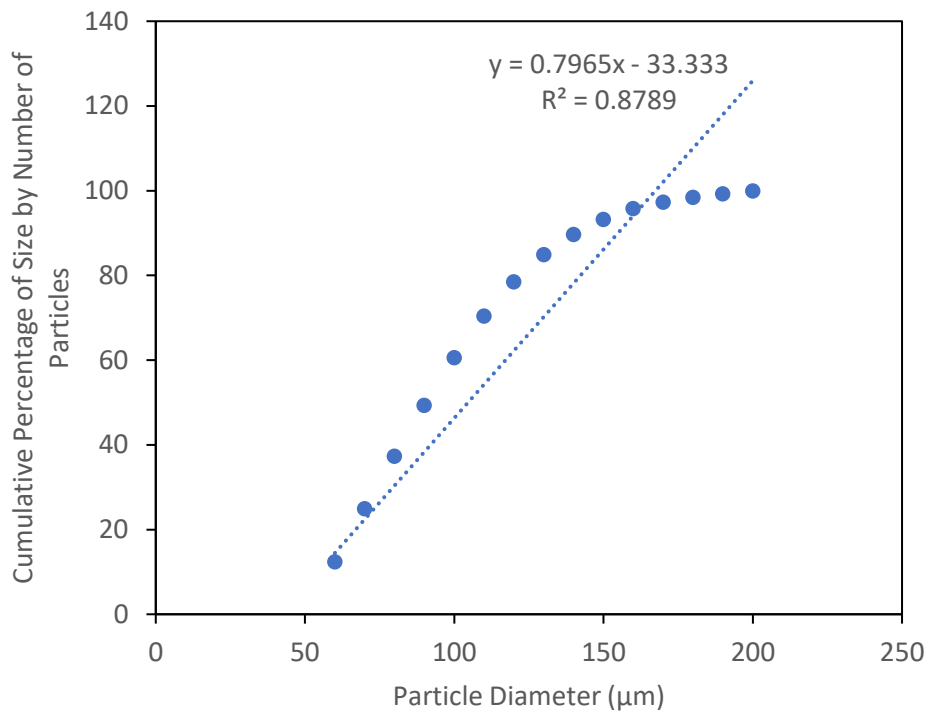## Parametric Study Representative PSD in Particle Withdrawal

Figure D- 2 Cumulative Percentage of Size by Number of Particles for DoE simulation 1, which has an impeller diameter of 64.7 mm, an impeller speed of 270 rpm, and an impeller clearance of 7 mm
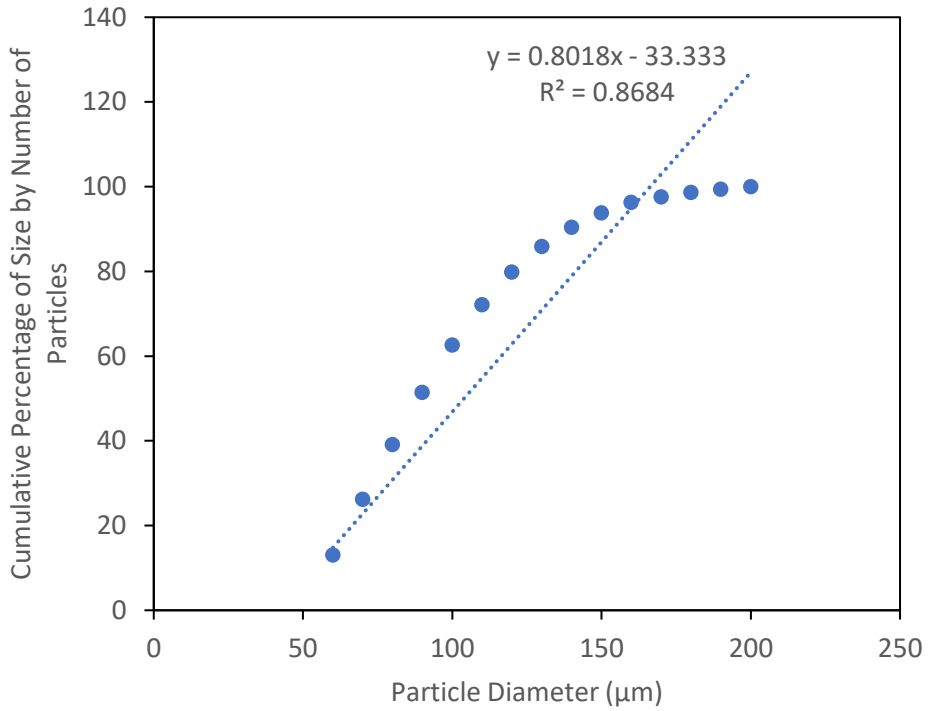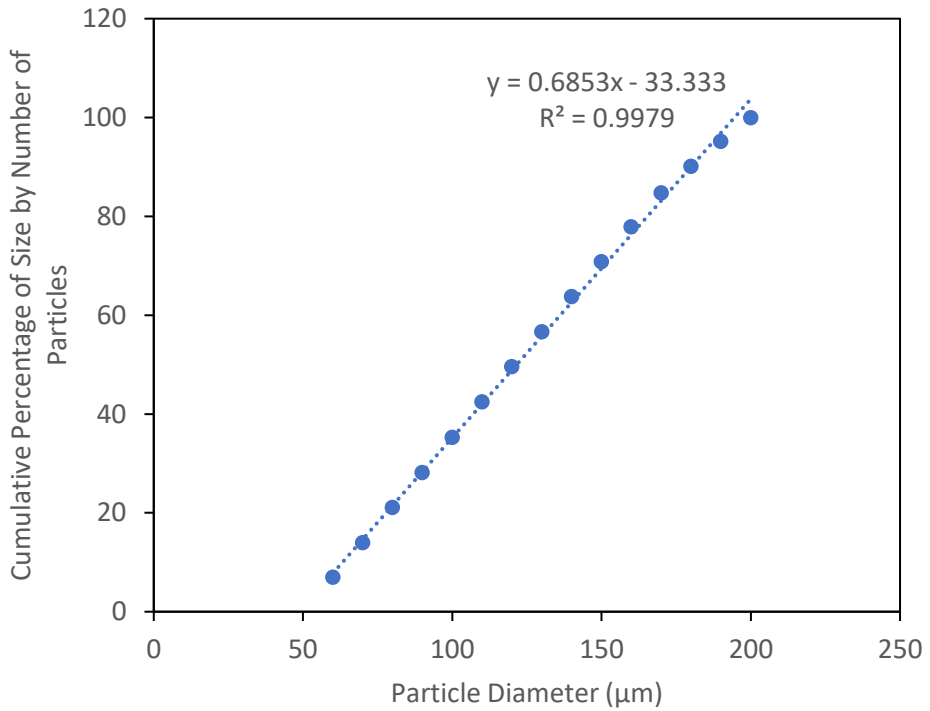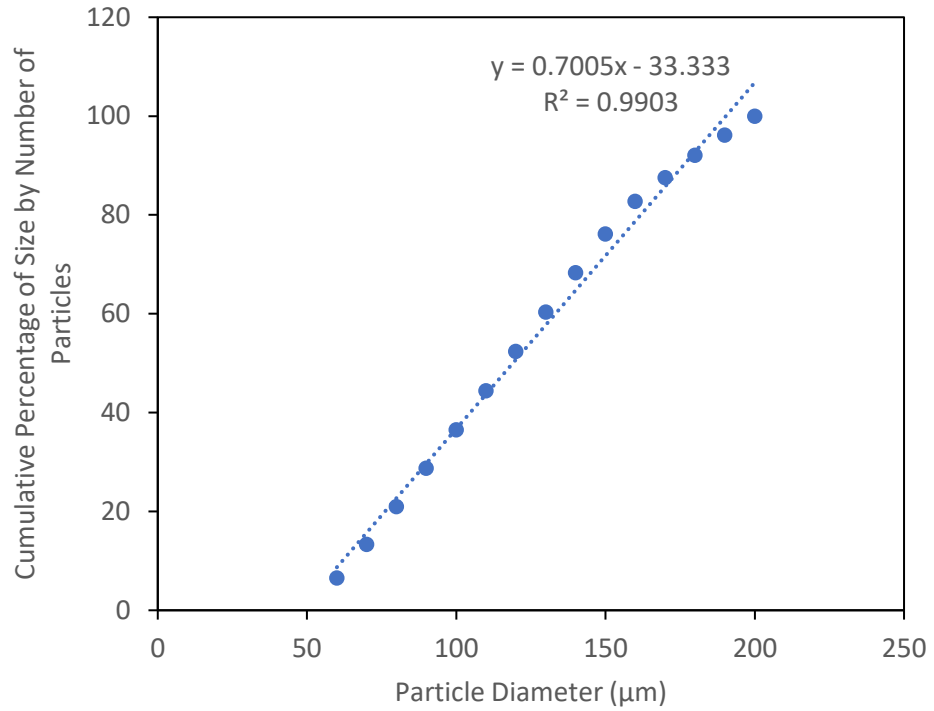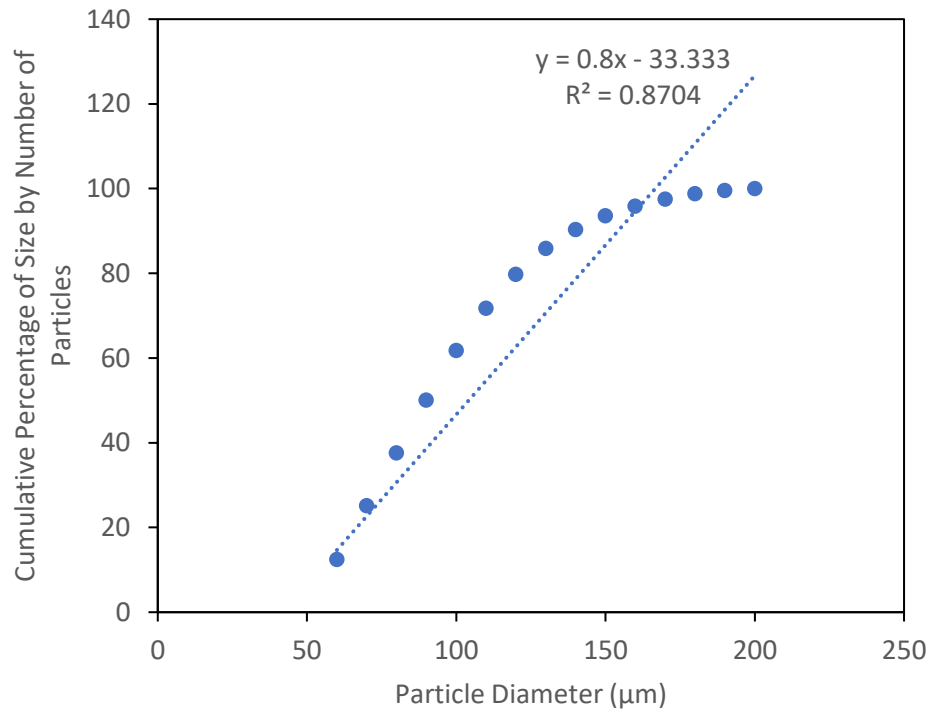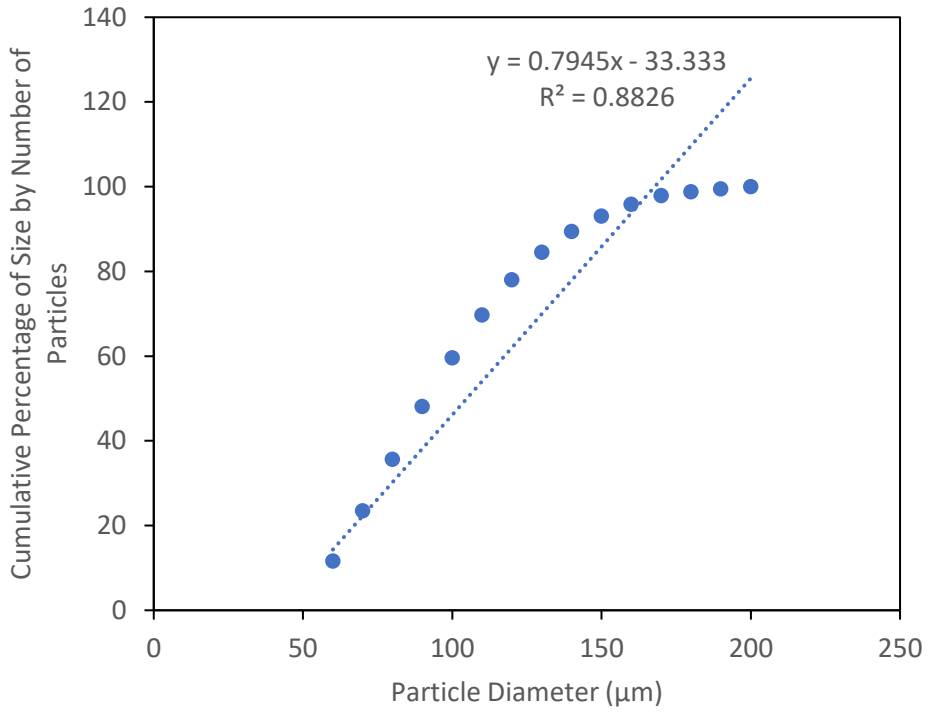
Figure D- 3 Cumulative Percentage of Size by Number of Particles for DoE simulation 2, which has an impeller diameter of 73.9 mm, an impeller speed of 270 rpm, and an impeller clearance of 7 mm
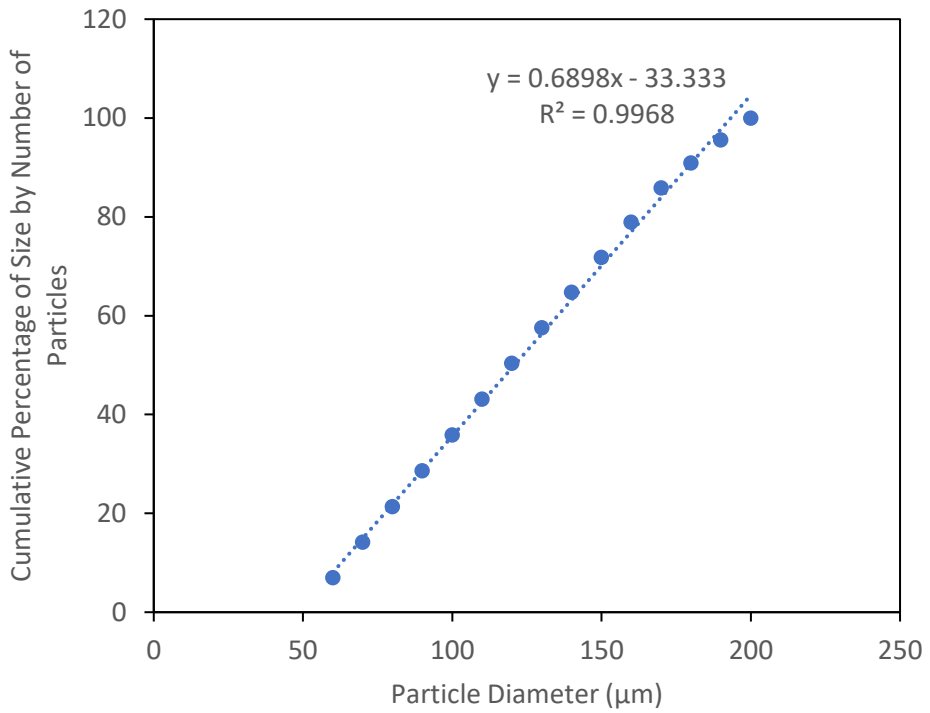

Figure D- 4 Cumulative Percentage of Size by Number of Particles for DoE simulation 3, which has an impeller diameter of 64.7 mm, an impeller speed of 330 rpm, and an impeller clearance of 7 mm

Figure D- 5 Cumulative Percentage of Size by Number of Particles for DoE simulation 4, which has an impeller diameter of 73.9 mm, an impeller speed of 330 rpm, and an impeller clearance of 7 mm

Figure D- 6 Cumulative Percentage of Size by Number of Particles for DoE simulation 5, which has an impeller diameter of 64.7 mm, an impeller speed of 270 rpm, and an impeller clearance of 13 mm
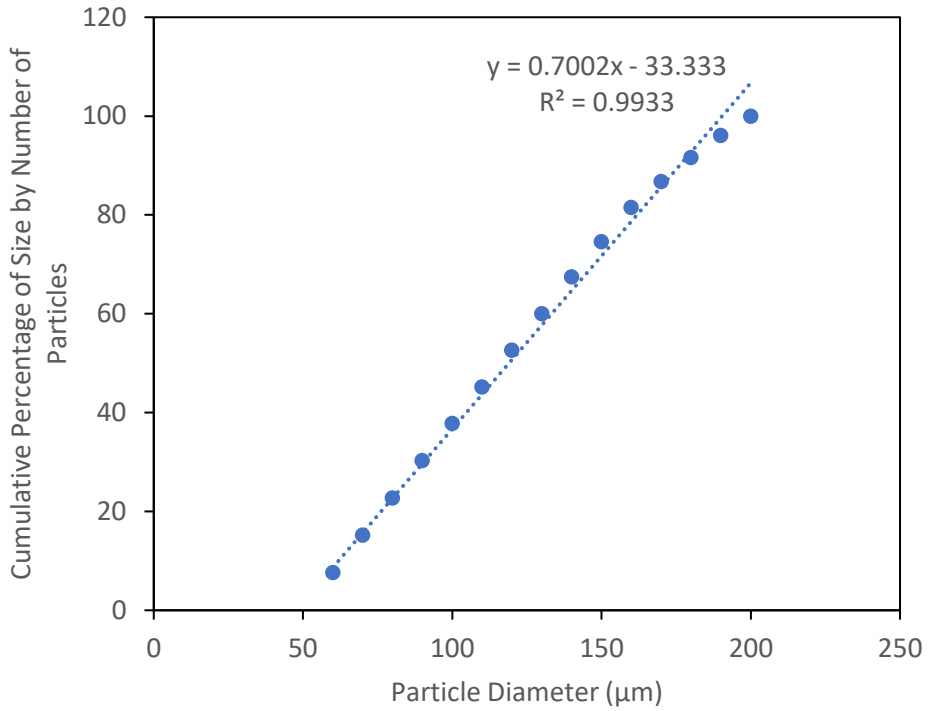
Figure D- 7 Cumulative Percentage of Size by Number of Particles for DoE simulation 6, which has an impeller diameter of 73.9 mm, an impeller speed of 270 rpm, and an impeller clearance of 13 mm
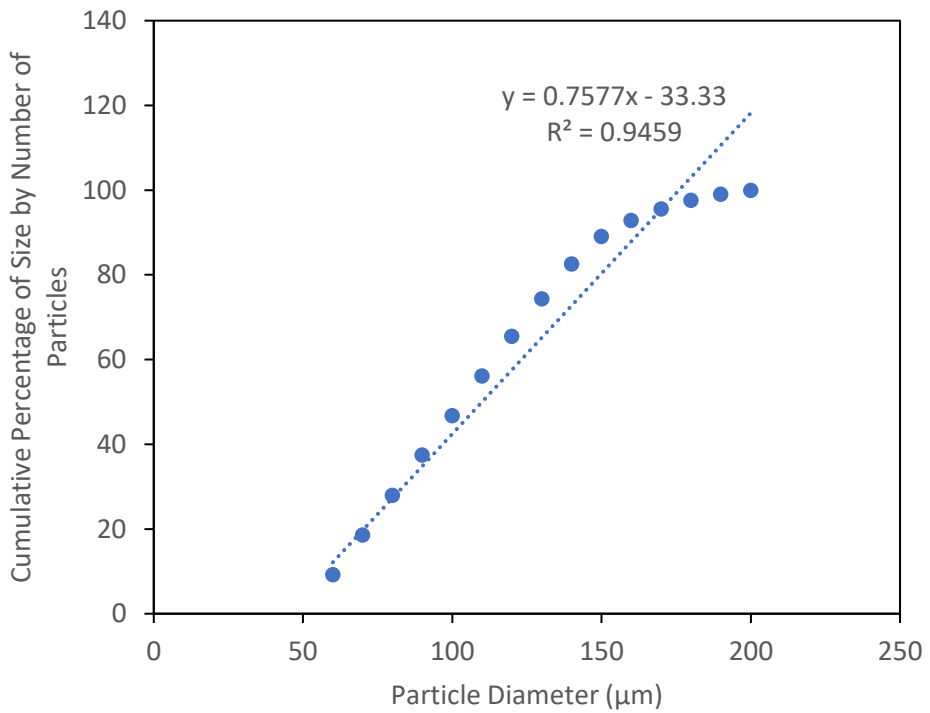

Figure D- 8 Cumulative Percentage of Size by Number of Particles for DoE simulation 7, which has an impeller diameter of 64.7 mm, an impeller speed of 330 rpm, and an impeller clearance of 13 mm

Figure D- 9 Cumulative Percentage of Size by Number of Particles for DoE simulation 8, which has an impeller diameter of 73.8 mm, an impeller speed of 330 rpm, and an impeller clearance of 13 mm

Figure D- 10 Cumulative Percentage of Size by Number of Particles for DoE simulation 9, which has an impeller diameter of 61.6 mm, an impeller speed of 300 rpm, and an impeller clearance of 10 mm
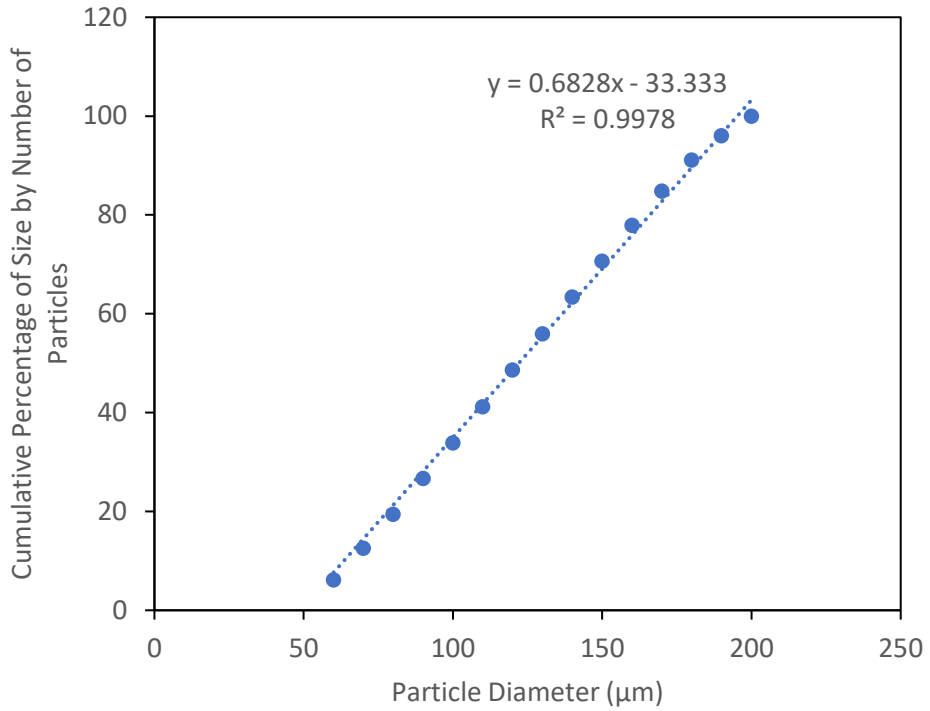
Figure D- 11 Cumulative Percentage of Size by Number of Particles for DoE simulation 10, which has an impeller diameter of 77 mm, an impeller speed of 300 rpm, and an impeller clearance of 10 mm
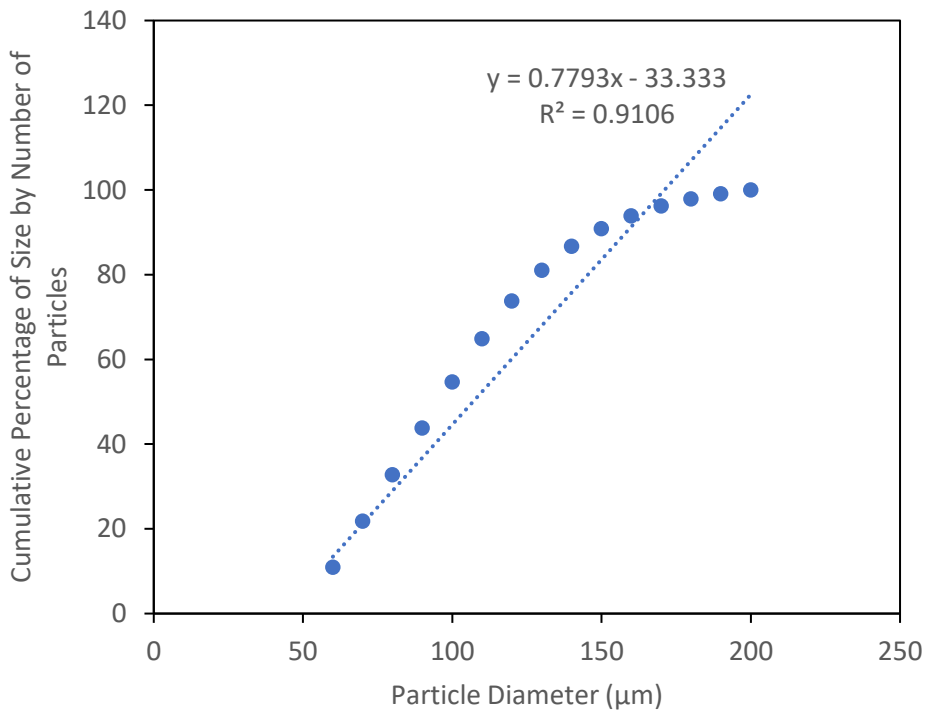

Figure D- 12 Cumulative Percentage of Size by Number of Particles for DoE simulation 11, which has an impeller diameter of 69.3 mm, an impeller speed of 250 rpm, and an impeller clearance of 10 mm
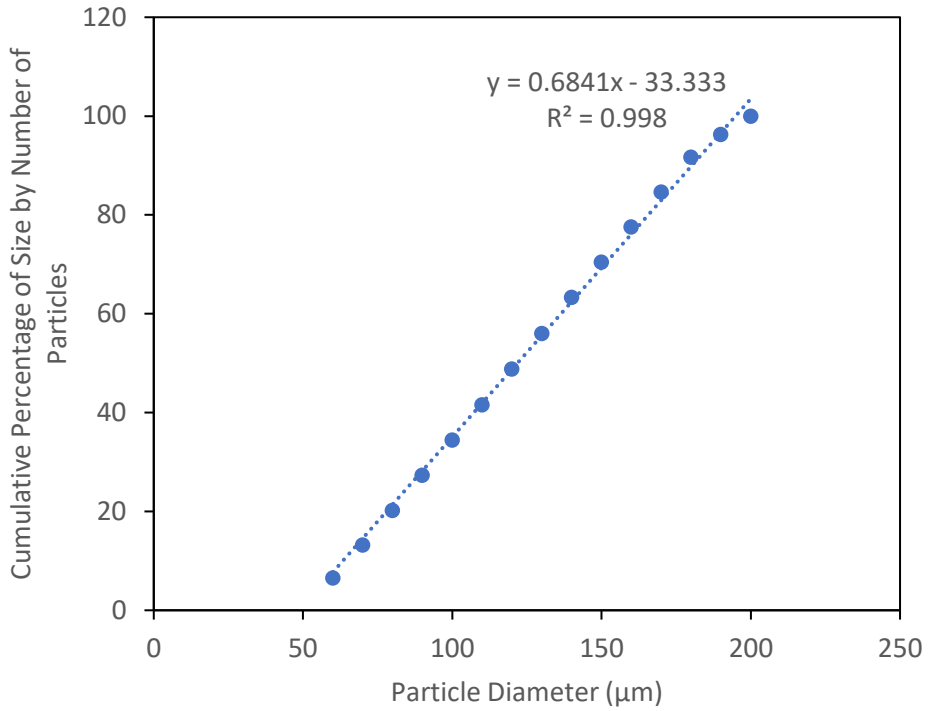
Figure D- 13 Cumulative Percentage of Size by Number of Particles for DoE simulation 12, which has an impeller diameter of 69.3 mm, an impeller speed of 350 rpm, and an impeller clearance of 10 mm

Figure D- 14 Cumulative Percentage of Size by Number of Particles for DoE simulation 13, which has an impeller diameter of 69.3 mm, an impeller speed of 300 rpm, and an impeller clearance of 5 mm
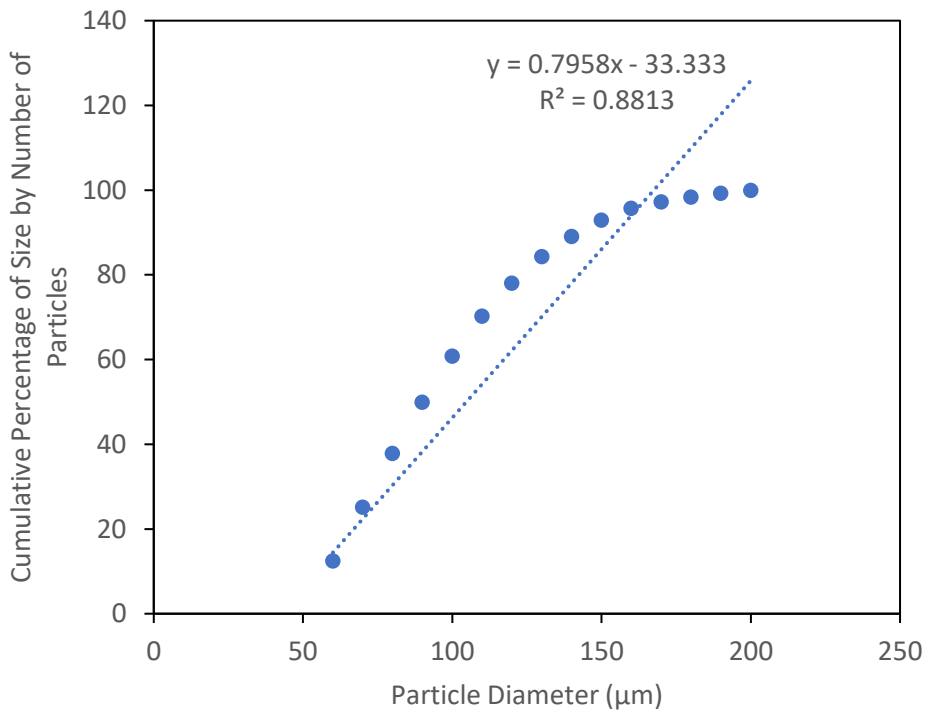
Figure D- 15 Cumulative Percentage of Size by Number of Particles for DoE simulation 14, which has an impeller diameter of 69.3 mm, an impeller speed of 300 rpm, and an impeller clearance of 15 mm
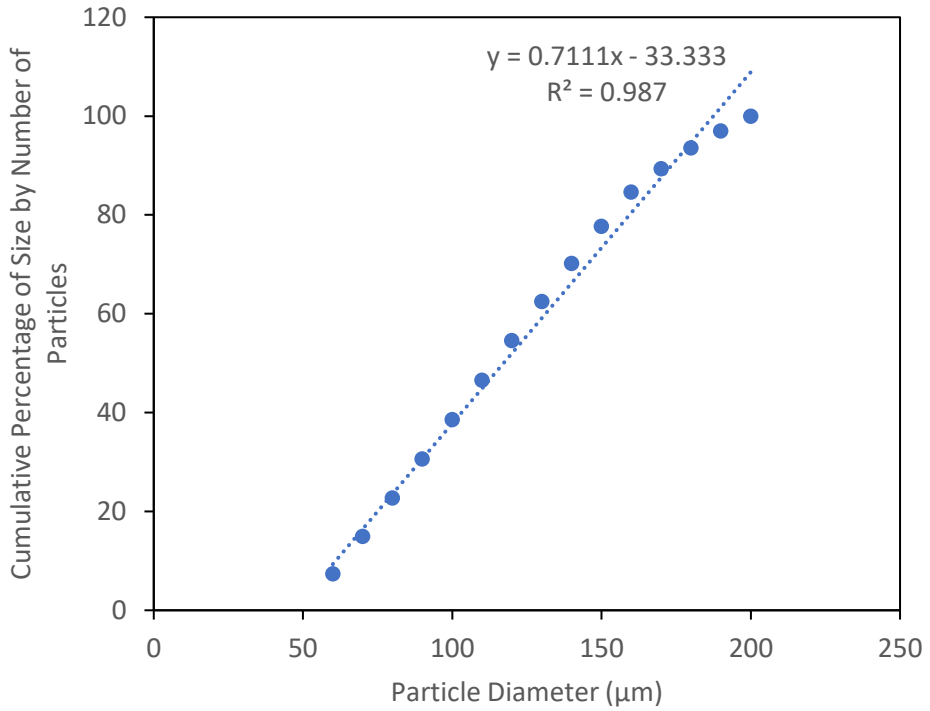

Figure D- 16 Cumulative Percentage of Size by Number of Particles for DoE simulation 15, which has an impeller diameter of 69.3 mm, an impeller speed of 300 rpm, and an impeller clearance of 10 mm

Figure D- 17 Cumulative Percentage of Size by Number of Particles for DoE simulation 16, which has an impeller diameter of 69.3 mm, an impeller speed of 300 rpm, and an impeller clearance of 10 mm
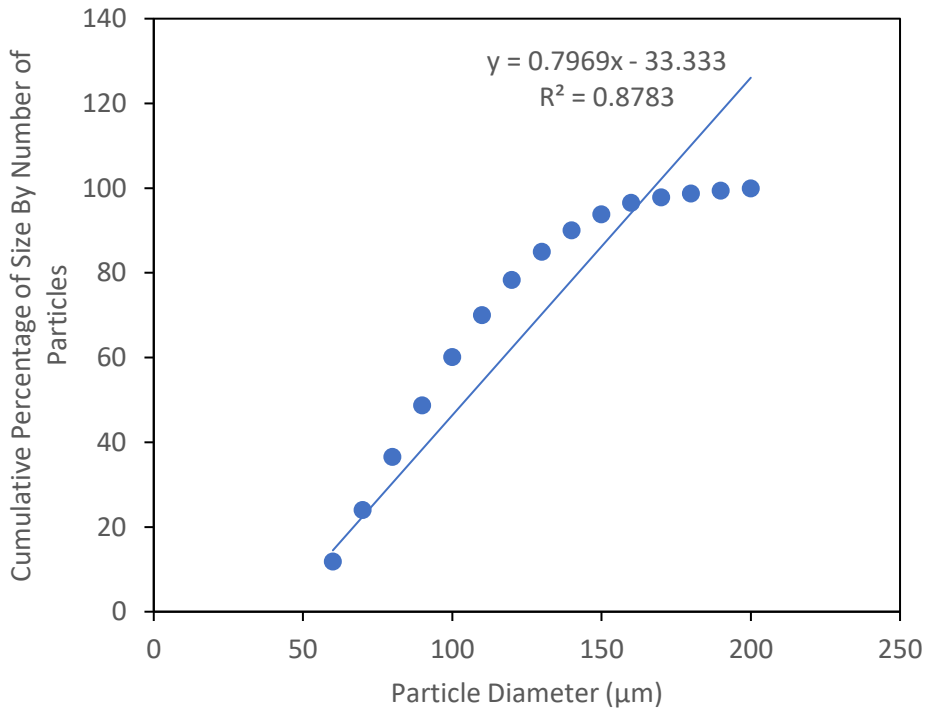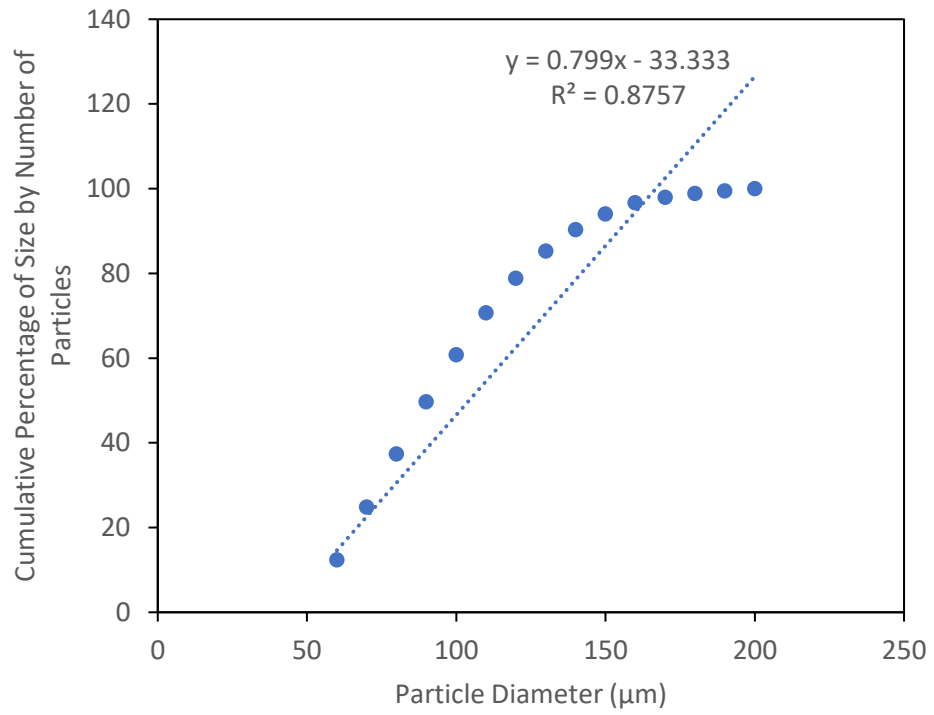
Appendix E - Publication of Work

Journal Articles in Preparation

A CFD and Experimental Investigation of the Influence of Flow Characteristics on Spherical Agglomeration

This article will discuss the results of an experimental analysis of the influence of impeller geometry, speed, and clearance on spherical agglomeration. The paper will also present the results of the corresponding CFD simulations to determine the flow pattern in the system. This work was presented in Chapters 4 and 5 of this thesis. Table E- 1 shows the writing stages and expected completion dates.

Table E- 1 Expected draft dates for journal article discussing CFD and experimental results for spherical agglomeration

Stage of Writing	Completed/Expected Completion Date
First Draft	Completed
Feedback from PDRA	Completed
Second draft based on PDRA feedback	Expected - 10/07/2024
Feedback from supervisors	Expected – 24/07/24
Final Draft	Expected – 14/08/24

Investigation Into Particle Motion and Settling in Cascading MSMPRs

The results from the industrial placement, presented in Chapter 8, will be discussed in this journal article. This paper will discuss the influence of impeller diameter, speed and clearance on the withdrawn particles from a crystallisation process. A central composite DoE was conducted to optimise the number of particles withdrawn from a system, as well as making sure all particle sizes are represented in the PSD of the withdrawn particles. Table E- 2 presents the stages of writing the journal article and the expected completion dates of the drafts.

Table E- 2 Expected draft dates for journal article discussing particle settling CFD simulations conducted as part of an industrial placement

Stage of Writing	Completed/Expected Completion Date
First Draft	Expected - 21/07/24
Feedback from PDRA	Expected -07/08/24
Second draft based on PDRA feedback	Expected - 14/08/24
Feedback from supervisors	Expected - 30/08/24
Final Draft – Send for legal approval	Expected - 15/09/24

Incorporating Flow Characteristics into a Population Balance Model for Spherical Agglomeration

This article will discuss the incorporation of flow into the PBM for spherical agglomeration, as well as the experimental validation of the PBM. The work in this journal article has been presented in Chapter 6 and 7 of this thesis. Table E- 3 shows the expected completion date of the various stages of writing the journal article

Table E- 3 Expected draft dates for a journal article discussing the modification and experimental validation of a PBM for spherical agglomeration that includes flow characteristics

Stage of Writing	Completed/Expected Completion Date
First Draft	Expected - 05/08/24
Feedback from PDRA	Expected - 26/08/24
Second draft based on PDRA feedback	Expected - 09/09/24
Feedback from supervisors	Expected - 13/10/24
Final Draft	Expected - 27/10/24

Conference Proceedings

AIChE Annual Meeting 2022 – Oral Presentation Abstract

Influence of Impeller Geometry on the Formation of Spherical Agglomerates

Spherical agglomeration is a promising particle size enlargement technique for pharmaceutical manufacturing, with ongoing research for industrial applications. In spherical agglomeration the primary crystals are suspended in a solvent system and a bridging liquid is added to create agglomerates. Most research is conducted at bench-top scale, with small, stirred tanks commonly used for spherical agglomerate production. While the effect of scale and impeller geometry is known to have strong effects on flow patterns and fluid and particle velocity profiles for suspensions in stirred tanks, little investigation has been conducted on these parameters for spherical agglomeration.

To investigate the effect of impeller configuration on spherical agglomeration, computational fluid dynamics (CFD) simulations were performed using ANSYS Fluent 19.1. Impeller geometries, clearances and speeds were varied. Flat-blade, pitched-blade, Rushton turbine and a propeller impeller were tested. These impellers were selected to vary the relative contributions of axial and radial flow on the velocity profile of the stirred tank. The geometry constructed for the CFD simulations was a replication of a 1 L stirred tank, used for complementary spherical agglomeration experiments. Standard geometric relationships for stirred tank design were used to determine the impeller clearances; tested clearances are between 1/5 to 1/3 of the tank diameter. Each impeller geometry and clearance were simulated for impeller speeds of 300 rpm, 450 rpm, and 600 rpm.

For the experiments, a suspension of monosized 52 µm PMMA plastic beads in water was used as model suspended particles, and toluene was added as a bridging liquid.

Increasing the impeller speed resulted in more spherical and denser agglomerates as increased collision velocity increases the rate of agglomeration and consolidation. Collision velocity also increased when radial flow was promoted in the tank; such as when a Rushton turbine or flat-blade impeller was used.

Lower clearances resulted in a broad particle size distribution; containing unagglomerated primary material and large, dense agglomerates which sank to the bottom of the tank, closer to the impeller flow field. Here they contacted more bridging liquid, increasing growth. This is more apparent at lower impeller speeds as there is insufficient shear to break the larger agglomerates and the velocities further away from the impeller are not high enough to allow for the smaller particles to become entrained in the flow field. This demonstrates that the clearance has a significant impact on mixing efficiency.

The CFD results have been useful to understand the flow behaviours in the stirred tank under the various operating conditions; and how these have influenced the formation of spherical agglomerates. Even though impellers induce the same type of flow in the tank the agglomerates do not undergo the same velocity or shear stress profiles, resulting in differences in the agglomerate formation. The results of the CFD simulations will be used to inform the derivation of an agglomeration kernel that will be implemented into a population balance model (PBM) for spherical agglomeration. This is done with the intention to predict ideal impeller design to produce spherical agglomerates with desired characteristics.
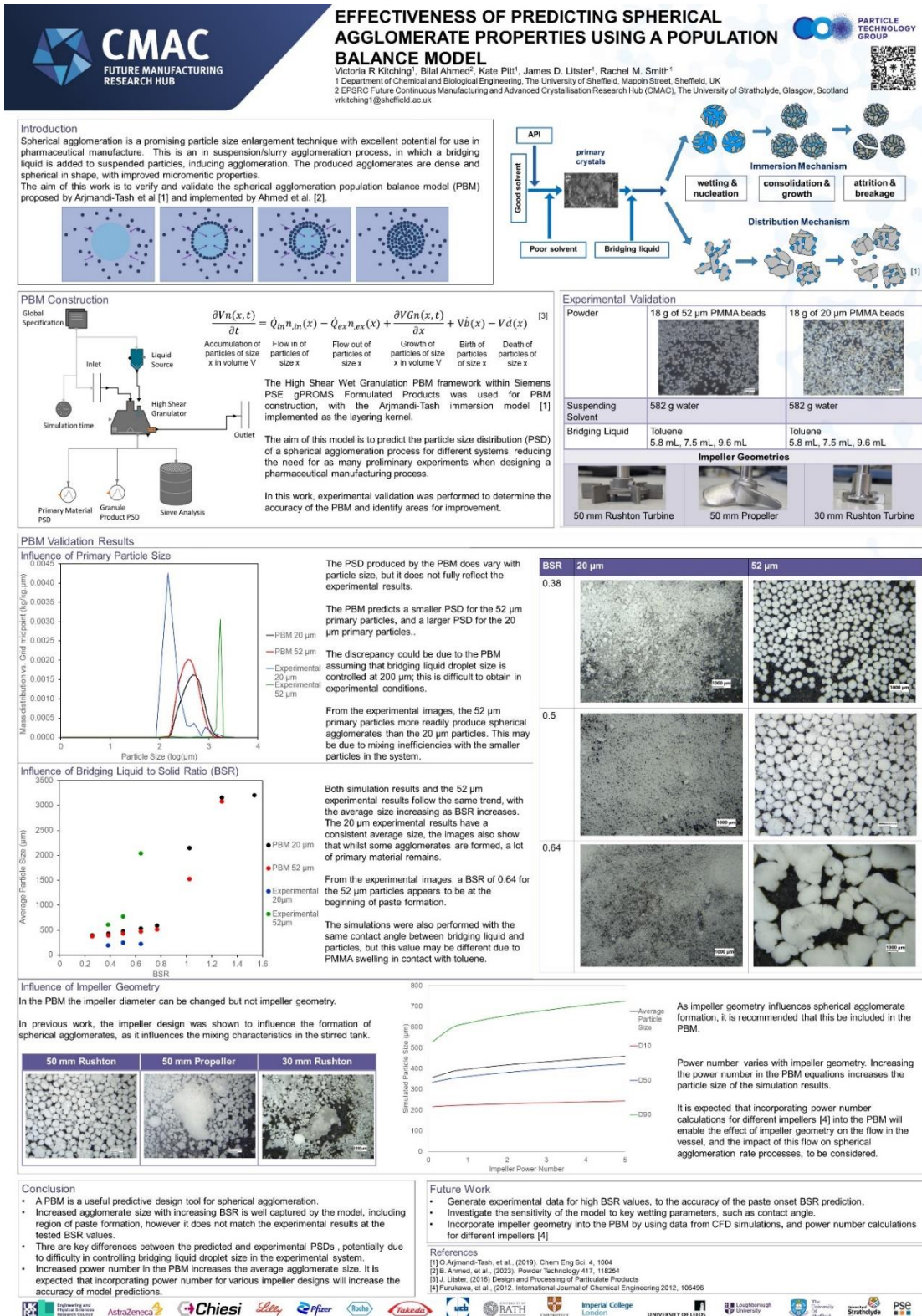
Figure E- 1 Poster presented at the 10th International Granulation Workshop in Sheffield, UK in 2023